

# Fluid and metal dynamics in rare-metal magmatic-hydrothermal systems: the case of the peraluminous Beauvoir granite (Massif Central, France)

Océane Rocher

▶ **To cite this version:**

Océane Rocher. Fluid and metal dynamics in rare-metal magmatic-hydrothermal systems: the case of the peraluminous Beauvoir granite (Massif Central, France). Earth Sciences. Université de Lorraine, 2025. English. ⟨NNT : 2025LORR0048⟩. ⟨tel-05328533⟩

**HAL Id: tel-05328533**

**https://hal.univ-lorraine.fr/tel-05328533v1**

Submitted on 23 Oct 2025

**HAL** is a multi-disciplinary open access archive for the deposit and dissemination of scientific research documents, whether they are published or not. The documents may come from teaching and research institutions in France or abroad, or from public or private research centers.

L'archive ouverte pluridisciplinaire **HAL**, est destinée au dépôt et à la diffusion de documents scientifiques de niveau recherche, publiés ou non, émanant des établissements d'enseignement et de recherche français ou étrangers, des laboratoires publics ou privés.



HAL Authorization

UNIVERSITÉ DE LORRAINE | BIBLIOTHÈQUES UNIVERSITAIRES

AVERTISSEMENT

Ce document est le fruit d'un long travail approuvé par le jury de soutenance et mis à disposition de l'ensemble de la communauté universitaire élargie.

Il est soumis à la propriété intellectuelle de l'auteur. Ceci implique une obligation de citation et de référencement lors de l'utilisation de ce document.

D'autre part, toute contrefaçon, plagiat, reproduction illicite encourt une poursuite pénale.

Contact bibliothèque : ddoc-theses-contact@univ-lorraine.fr
*(Cette adresse ne permet pas de contacter les auteurs)*

LIENS

Code de la Propriété Intellectuelle. articles L 122. 4
Code de la Propriété Intellectuelle. articles L 335.2- L 335.10
http://www.cfcopies.com/V2/leg/leg_droi.php
http://www.culture.gouv.fr/culture/infos-pratiques/droits/protection.htm

Thèse

Présentée et soutenue publiquement pour l'obtention du titre de

DOCTEUR DE l'UNIVERSITE DE LORRAINE

Mention : Géosciences

par Océane ROCHER

sous la direction de Julien MERCADIER et Antonin RICHARD

# Dynamiques des fluides et des métaux dans les systèmes magmatiques-hydrothermaux à métaux rares : cas du granite peralumineux de Beauvoir (Massif central)

Soutenue publiquement le 2 avril 2025

***Président du jury :*** *Anne-Sylvie André-Mayer*

**Directeurs de thèse :**

| | |
|---|---|
| M. Julien MERCADIER | Directeur de recherche, CNRS, GeoRessources, Nancy (France) |
| M. Antonin RICHARD | Maître de conférences, Université de Lorraine, GeoRessources, Nancy (France) |

**Rapporteurs :**

| | |
|---|---|
| Mme. Valérie BOSSE | Maître de conférences, Université Clermont Auvergne, Laboratoire Magmas et Volcans, Clermont-Ferrand (France) |
| M. Philippe MUCHEZ | Professeur, Department of Earth and Environmental Sciences, KU Leuven (Belgique) |

**Examinateurs :**

| | |
|---|---|
| M. Cyril CHELLE-MICHOU | Assistant professeur, Institute of Geochemistry and Petrology, Department of Earth Sciences, ETH Zurich, Zürich (Suisse) |
| Mme. Anne-Sylvie ANDRE-MAYER | Professeur, Université de Lorraine, GeoRessources, Nancy (France) |

**Invités :**

| | |
|---|---|
| M. Michel CUNEY | Directeur de recherche émérite, CNRS, GeoRessources, Nancy (France) |
| M. Patrick FULLENWARTH | Ingénieur géologue, Imerys Ceramics France - Kaolins de Beauvoir, Echassières (France) |
| M. Matthieu HARLAUX | Géologue de recherche, Bureau de Recherches Géologiques et Minières, Orléans (France) |

***Remerciements***

La fin de cette thèse est pour moi l'occasion d'exprimer ma reconnaissance à toutes les personnes qui m'ont accompagnée, soutenue et inspirée tout au long de cette aventure.

Je tiens tout d'abord à remercier sincèrement mes encadrants de thèse, Julien Mercadier et Antonin Richard, pour m'avoir fait confiance, m'avoir donné la chance de travailler sur ce projet passionnant et m'avoir guidée tout en me laissant l'espace de grandir. Je vous suis infiniment reconnaissante pour votre bienveillance, vos précieux conseils et toutes les opportunités que vous m'avez offertes. Merci à toi, Antonin, pour ta disponibilité exceptionnelle. Une pensée particulière pour toi, Julien, et tes *pep talks* qui m'ont grandement aidée à prendre confiance en moi. Je souhaite aussi remercier Christophe Ballouard, mon encadrant de l'ombre mais néanmoins toujours présent tout au long de ces années. Merci pour nos discussions inspirantes, ton aide précieuse sur le terrain, ton humour et tes talents de dessinateur de dinosaures et libellules géantes.

Je voudrais également remercier l'ensemble des membres de mon jury de thèse d'avoir accepté d'évaluer ce travail. Une reconnaissance particulière à Cyril Chelle-Michou, qui m'a chaleureusement accueillie à l'ETHZ et m'a permis de finaliser une grande partie de mes acquisitions auprès de son équipe. Je tiens aussi à remercier toutes les personnes que j'ai eu la chance de rencontrer pendant ces deux mois, en particulier Lorenzo, pour son aide précieuse dans les analyses, ainsi que Marcel, Julien, Dawid, Chetan, Sava, Adrianna, Anna, Diane, Thomas, Lison et Thibault.

Un grand merci à toutes celles et ceux qui ont enrichi mon cheminement scientifique, avec qui j'ai pu échanger et apprendre. Je pense notamment aux membres du projet Li-Beauvoir, en particulier Naïla, Bastien, Nicolas, Chloé, Steven et Patrick. Je remercie également Imerys et l'équipe exceptionnelle qui nous a accompagnés dans ce projet. Merci à Grégoire Jean, Patrick, Benjamin, Alyson, mais aussi Manon et Alex pour votre gentillesse, votre expertise et votre envie de partager. Merci à Oscar et Loïs pour votre confiance, votre bienveillance et le temps que vous m'avez accordé. Je remercie également Yanis, Jules, Pauline, Gaëlle, Rémi et Valentin, dont l'aide a été précieuse dans ma recherche. Un grand merci à Charles Gumiaux pour son implication dans la compréhension des données structurales. La liste de toutes les personnes qui ont contribué à mon évolution scientifique est longue. Je souhaite finalement sincèrement remercier Alexandre Tarantola, Michel Cuney, Lydéric France, Michel Cathelineau, Matthieu Harlaux, Eric Gloaguen et Jérémy Melleton pour nos discussions enrichissantes et vos précieux conseils.

J'ai eu la chance d'évoluer dans un laboratoire incroyable, et je tiens à remercier particulièrement Anne-Sylvie, le personnel administratif, Cédric Demeurie et Delphine Martin, et toute l'équipe technique. Merci à Alexandre Flammang pour sa réactivité et sa bonne humeur.

Merci à Lise Salsi, Andreï Lecomte, Olivier Rouer, Patrick Carr et Chantal Peiffert pour leur précieuse aide au cours de mes analyses. Merci aussi à Marie-Camille Caumon pour m'avoir guidée dans l'utilisation du Raman. Au CRPG, je souhaiterais remercier Nordine Bouden et Johan Villeneuve pour leur expertise et leur patience.

Je suis également profondément reconnaissante envers toutes les personnes qui ont contribué à faire de ces quelques années une expérience aussi riche humainement que scientifiquement. Merci à Naïla, grande vadrouilleuse qui est toujours là où on ne l'attend pas et qui a aussi toujours été là pour moi au cours de ces années. Merci pour ton écoute, ton soutien, ta générosité, et pour être cette personne lumineuse et folle, à la fois glamour et un peu déjantée. On a débuté cette aventure ensemble, je n'aurais pu rêver meilleure co-bureau... et surtout, je repars avec une amie pour la vie ! Merci Baptiste, maître incontesté des discours brefs et notre 'papa' à tous, pour nos discussions et séances de méditation. A présent, le bruit des vagues me fera penser à toi. Merci Caroline, notre spécialiste en plans loufoques, pour ton esprit créatif et ta bonne humeur. Je suis persuadée que notre carrière dans la chorale de Stitch n'est qu'à ses débuts ! Merci à Marjolène, Jean-Charles, Said, Lucas, Alix, Quentin, Hugo et Maxime pour tous les bons moments passés ensemble. Ces belles années, rythmées par des petits déjeuners, des apéros tarot et des rires, resteront gravées dans ma mémoire. Last but not least, thank you, Johan, with whom a beautiful friendship was born from an unexpected meeting. Thank you for our Zoom sessions, your eclectic musical shares, for broadening my cinematic horizons, and for encouraging me throughout this last year. Thank you for being an incredible friend, with whom I hope to share many more adventures.

Ma vie a été rythmée par de belles rencontres, des personnes bienveillantes et précieuses m'ayant beaucoup apporté. Merci à mon petit poulpe Jeanne, d'être l'amie adorable que tu es. Merci Anthony, rayon de soleil qui illumine mes journées, et pour ton influence sur ma culture photographique. Merci Juliette pour toutes ces sessions de travail, de me faire découvrir plein de jeux et surtout de partager ma passion des films de Noël. Je tiens également à remercier Sophie, Anne-Lise, Audrey, Marie, Pauline, Emilie, Claire, Victor et Jannik pour tous les bons moments que nous avons partagés. Je souhaiterais aussi remercier du fond du cœur les amis qui sont devenus de la famille. Merci Joséphine et Emma d'être des amies aussi extraordinaires sans qui la vie ne serait pas la même, merci pour tous les bons moments passés et à venir, pour votre écoute, votre douceur, votre bienveillance et votre soutien à toute épreuve.

Je voudrais enfin remercier du fond du cœur mes parents pour leur soutien indéfectible depuis toujours, sans lequel je ne serais jamais arrivée jusqu'ici. Merci à Florian et Zoé d'avoir fait les 400 coups avec moi, de me supporter (même si vous n'avez pas le choix) et d'être là pour moi. Enfin, un merci tout particulier à ma mamie Jojo, qui s'est toujours intéressée à mes discours de caillou et m'a toujours encouragée avec amour et fierté.

***Résumé***

Les systèmes magmatiques-hydrothermaux à métaux rares se développent généralement en relation avec l'intrusion de magmas felsiques fortement différenciés dans la croûte continentale supérieure. Ces magmas sont extrêmement enrichis en métaux lithophiles et halogènes tels que Li, F, Ta, Nb, Sn, W et Be, et leur évolution résulte d'une succession complexe de processus magmatiques et hydrothermaux, dont l'impact et l'importance relative demeurent encore débattus. La présente thèse se propose d'apporter des éléments de réponse à ces questions en étudiant l'histoire magmatique et hydrothermale du granite de Beauvoir, un granite peralumineux à métaux rares riche en phosphore (PHP-RMG), mondialement connu pour sa composition atypique et sa teneur en lithium et mis en place à la fin de l'orogenèse varisque dans le Massif central (France). Cette étude repose sur l'analyse *in-situ* élémentaire (majeurs et traces) et des isotopes d'oxygène de l'apatite et du quartz, ainsi que sur la caractérisation des inclusions fluides par microthermométrie, spectrométrie Raman et LA-ICP-MS.

La pétrographie et la géochronologie U-Pb de l'apatite révèlent quatre grandes phases magmatiques et hydrothermales, s'étendant de la cristallisation du magma, induisant une phase hydrothermale précoce, à deux phases hydrothermales tardives, non magmatiques, induites par l'activité tectonique régionale. La phase hydrothermale précoce, initiée par la dévolatilisation du liquide silicaté, apparaît comme une étape clé dans l'évolution du système de Beauvoir, où les processus magmatiques et hydrothermaux s'entremêlent. Cette transition magmatique-hydrothermale a été enregistrée à la fois dans la distribution des terres rares de l'apatite magmatique, la signature isotopique du quartz de l'unité B1, et le piégeage d'inclusions fluides et magmatiques primaires au sein du quartz. Cette influence marquée de la transition magmatique-hydrothermale sur la cristallisation de l'unité B1 s'est traduite par une augmentation de l'état d'oxydation du système, le rendant plus propice à la formation d'une première génération de cassitérite ($SnO_2$), la libération de fluides magmatiques riches en métaux, la résorption partielle des phénocristaux de quartz, suivie de la cristallisation tardive de quartz à texture snowball au sein d'un liquide silicaté résiduel, enrichi en volatiles.

Bien que la circulation de ces fluides magmatiques exsolvés ait significativement mobilisé les métaux vers les roches encaissantes, leur volume semble insuffisant pour expliquer les halos d'altération observés, notamment dans les micaschistes. Cela suggère une dynamique supra-solidus en système ouvert, marquée par l'infiltration significative de fluides magmatiques profonds. L'existence d'un tel système ouvert en conditions sub-solidus est mise en évidence par la signature isotopique en oxygène, de la chimie de l'apatite hydrothermale précoce et la composition des inclusions fluides identifiées dans le quartz magmatique. Ces données suggèrent une évolution progressive des fluides magmatiques exsolvés, marquée par des dynamiques d'ébullition, de refroidissement et surtout par leur interaction et mélange avec des fluides

météoriques oxydants, l'ensemble de ces processus ayant favorisé la précipitation d'une seconde génération de cassitérite, bien que cette dernière soit mineure.

Cette étude enrichit non seulement la compréhension du système de Beauvoir, mais apporte également des éléments clés au modèle génétique des systèmes magmatiques-hydrothermaux à métaux rares. Elle démontre de l'importance des dynamiques en système ouvert, tant lors des processus supra- que sub-solidus, et suggère des mécanismes de circulations fluides et de transport de métaux similaires à ceux des systèmes porphyres-épithermaux, bien que les volumes de magmas et de fluides impliqués soient considérablement plus faibles.

***Abstract***

Rare-metal magmatic-hydrothermal systems typically develop in association with the intrusion of highly differentiated felsic magmas into the upper continental crust. These magmas present exceptional enrichment in lithophile metals and halogens (e.g., Li, F, Ta, Nb, Sn, W, and Be) and evolve through a complex interplay of magmatic and hydrothermal processes, the relative importance and impact of which are still debated. This thesis aims to address these questions by investigating the magmatic and hydrothermal history of the Beauvoir granite, a world-class, highly-phosphorus, peraluminous rare-metal granite (PHP-RMG) emplaced during the late stages of the Variscan orogeny in the French Massif Central. The study combines *in-situ* analysis of major and trace elements, oxygen isotopes in apatite and quartz, as well as fluid inclusion characterisation through microthermometry, Raman spectroscopy, and LA-ICP-MS.

Petrographic and U-Pb geochronological analysis of apatite reveals four major magmatic and hydrothermal phases, spanning from the crystallisation of the magma to an early hydrothermal phase, followed by two late-stage, non-magmatic hydrothermal events driven by regional tectonic activity. The early hydrothermal phase, initiated by magma devolatilisation, constitutes a critical point in the Beauvoir system's evolution, where magmatic and hydrothermal processes are intertwined. This magmatic-hydrothermal transition is recorded in the rare earth element distribution of magmatic apatite, the isotopic signature of quartz from the B1 unit, and the entrapment of primary melt and magmatic fluid inclusions within quartz. The pronounced influence of this transition on crystallisation in unit B1 is reflected in an increase in the system's oxidation state, promoting the formation of the first cassiterite ($SnO_2$) generation, the release of metal-rich magmatic fluids, and partial resorption of quartz phenocrysts, followed by late-stage snowball-textured quartz crystallising from a residual, volatile-enriched melt.

While the circulation of exsolved magmatic fluids significantly mobilised metals into the surrounding rocks, the volume of fluids seems insufficient to explain the observed alteration halos, especially within the host mica schists. This suggests an open-system dynamic at the supra-solidus stage, with deep magmatic fluids significantly infiltrating the system. The existence of such open-system behaviour under sub-solidus conditions is confirmed by the oxygen isotopic signature and chemistry of the early hydrothermal apatite, and the composition of fluid inclusions hosted within magmatic quartz. These findings suggest a progressive evolution of exsolved magmatic fluids, characterised by boiling, cooling dynamics, and notably their interaction and mixing with oxidising meteoric fluids. Collectively, these processes favoured the precipitation of a second, albeit minor, cassiterite generation.

This study not only enhances the understanding of the Beauvoir system but also provides key insights into the genetic models of rare-metal magmatic-hydrothermal systems. It demonstrates the significance of open-system dynamics during both supra- to sub-solidus

processes and suggests that fluid circulation and metal transport mechanisms in these systems are analogous to those in porphyry-epithermal systems, albeit with much smaller magma and fluid volumes.

# *Table of content*

**Préambule (French)……...……..…..1**

**Part I. General introduction……..……..…6**

**1. Magmatic-hydrothermal systems and ore formation in the continental crust…….....…..7**

1.1. Fluid circulation processes leading to metal enrichment, transport and deposition.....8

1.2. Examples of mineralised magmatic-hydrothermal systems.....12

1.2.1. Porphyry-epithermal systems.....12

1.2.2. Sn-W granite-related systems.....16

1.3. Greisen and albitic alterations: key metasomatic processes in granitic systems.....19

**2. Peraluminous rare-metal granites……..…….……22**

2.1. Definition and classification of rare-metal granites.....22

2.2. Genesis models for highly evolved peraluminous rare-metal deposits.....25

2.3. PRMGs geometry, emplacement and textural features.....27

**3. The Beauvoir PRMG in the European Variscan belt……...28**

3.1. The Variscan orogeny.....28

3.2. Regional geology of the French Massif Central.....30

3.2.1. Structuration.....31

3.2.2. Tectono-metamorphic evolution.....32

3.2.3. Magmatic history.....32

3.2.3.i. Cambrian to Ordovician pre-orogenic magmatism.....32

3.2.3.ii. Late Devonian to Carboniferous magmatism.....33

3.2.3.iii. Late Carboniferous peraluminous rare-metal magmatism.....35

3.2.4. Focus on the Sioule metamorphic series.....36

3.3. The Echassières granitic complex.....37

**4. The expression of the Beauvoir magmatic-hydrothermal system……39**

4.1. Early hydrothermal stage.....40

4.1.1. Comprehensive overview.....40

4.1.2. Detailed dynamics and evolution of fluid circulation.....43

4.1.2.i. Early magmatic fluid circulation.....44

4.1.2.ii. High-temperature incursion of external fluids.....46

4.1.2.iii. Low-temperature fluid evolution.....47

4.1.3. Fluid circulation involved in extensive greisenisation of the Beauvoir PRMG....50
4.2. Late hydrothermal stages....52
**5. Key questions and research strategy....54**

**Part II. Unravelling the magmatic and hydrothermal evolution of rare-metal granites through apatite geochemistry and geochronology: the Variscan Beauvoir granite (French Massif Central) (published paper)....58**
**1. Introduction....59**
**2. Geological setting....64**
2.1. Regional geology....64
2.2. The Echassières granitic complex....66
2.3. The Beauvoir magmatic-hydrothermal system....68
2.4. Apatite occurences in the Beauvoir PRMG....70
**3. Material and methods....70**
3.1. Sampling strategy....70
3.2. Imaging and analytical methods....71
**4. Results....74**
4.1. Apatite petrography....74
4.1.1. Magmatic apatite....74
4.1.2. Early hydrothermal apatite....76
4.1.3. Late hydrothermal apatite....80
4.2. Halogens....80
4.3. Major and minor elements....80
4.4. Trace elements....82
4.5. Oxygen isotopes....84
4.6. U-Pb geochronology....87
**5. Discussion....90**
5.1. Timing of magmatic and hydrothermal episodes for the Beauvoir PRMG....90
5.2. Apatite as a proxy for magmatic evolution in PRMG systems....94
5.3. Apatite as a proxy to trace nature and dynamics of hydrothermal systems in PRMGs....97
5.4. Apatite as a window into mineralising processes within PRMGs....104
**6. Summary and conclusions....106**

**Part III. Insights of quartz into mechanisms influencing the magmatic-hydrothermal transition……..110**
**1. Introduction……..111**
**2. Petrographic insights into melt and fluid evolution……..……114**
2.1. Material and methods.....114
2.1.1. Studied material.....114
2.1.2. Quartz petrography and element mapping.....114
2.1.3. Fluid inclusion petrography.....115
2.2. Results.....115
2.2.1. Quartz petrography.....115
2.2.2. Fluid inclusion petrography.....121
2.3. Preliminary discussion and conclusions: snowball-textured quartz as a marker of extensive devolatilisation in the Beauvoir PRMG.....127
**3. Fluid inclusions as archives of fluid dynamics and metal mobility……..……129**
3.1. Material and methods.....129
3.1.1. Microthermometry.....129
3.1.2. Raman spectrometry.....130
3.1.3. Laser ablation – inductively coupled plasma – mass spectrometry.....131
3.1.3.i. Acquisition procedure.....131
3.1.3.ii. Data reduction.....131
3.1.3.iii. Data cleaning and exclusion criteria.....134
3.2. Results.....135
3.2.1. Microthermometry.....135
3.2.2. Trace gas content relative to the vapour phase.....138
3.2.3. Salinity calculations.....140
3.2.3.i. Absence of halite.....140
3.2.3.ii. Presence of halite.....143
3.2.4. Assessment of compositional variations between processing methods.....145
3.2.5. Chemical composition of fluid inclusions in the Beauvoir PRMG.....147
3.2.5.i. Chemical composition of the distinct FI types.....147
3.2.5.ii. Comparison of absolute concentrations across FI types.....154
3.2.5.iii. Comparison of element-to-Cl ratios across FI types.....155

3.3. Preliminary discussion and conclusions.....160

3.3.1. Magmatic nature of high-temperature fluids in the Beauvoir PRMG.....160

3.3.2. Insights into magmatic-hydrothermal processes derived from fluid inclusions.....162

3.3.2.i. Element partitioning during high-temperature phase separation.....162

3.3.2.ii. Dilution of magmatic fluids by low-salinity fluids?.....165

3.3.2.iii. Possible evidence of accidental trapping of Li-micas?.....168

3.3.2.iv. Processes triggering ore-bearing minerals precipitation?.....169

**4. Trace elements and oxygen isotopes in quartz as tracers of the magmatic-hydrothermal evolution.....171**

4.1. Material and methods.....171

4.1.1. Laser ablation – inductively coupled plasma – mass spectrometry.....171

4.1.2. Secondary ion mass spectrometry (SIMS).....172

4.2. Results.....173

4.2.1. Quartz trace elements.....173

4.2.2. Quartz and cassiterite oxygen isotopes.....175

4.3. Preliminary discussion and conclusions.....178

4.3.1. Al and Li incorporation in magmatic quartz of the Beauvoir PRMG: influence of melt composition, partitioning behaviour, and co-crystallising phases.....178

4.3.2. Temperature estimation of quartz crystallisation.....179

4.3.2.i. TitaniQ geothermobarometry.....179

4.3.2.ii. Oxygen thermometry.....181

4.3.3. Initial O isotopic signature of the melt and implications for its source.....184

4.3.4. Processes resulting in $\delta^{18}O$ variation in magmatic quartz.....185

4.3.4.i. Sub-solidus alteration and re-equilibration.....185

4.3.4.ii. Temperature-dependent isotopic fractionation.....188

4.3.4.iii. Magmatic system involving multiple $\delta^{18}O$ reservoirs.....188

4.3.4.iv. Oxygen isotopic fractionation in relation with devolatilisation processes.....189

**5. High-temperature magmatic fluid circulation in the Beauvoir PRMG.....189**

5.1. Material and methods.....190

5.1.1. Studied material.....190

5.1.2. Scanning electron microscope (SEM) and cathodoluminescence (CL) imaging.....190

5.1.3. Micro-XRF chemical mapping.....190

5.1.4. Secondary ion mass spectrometry (SIMS).....191

5.2. Results.....191

5.2.1. Petrography.....191

5.2.1.i. Drill core sample.....191

5.2.1.ii. Quarry sample.....192

5.2.1.iii. Fluid inclusion observations in the quarry sample.....195

5.2.2. Oxygen isotopes.....197

5.2.3. Quartz-cassiterite oxygen isotope thermometry.....198

5.2.4. Estimation of the O isotopic composition of the parent fluid.....198

5.3. Preliminary discussion and conclusions.....201

5.3.1. Magmatic fluid involvement in quartz-cassiterite greisen formation.....201

5.3.2. Influence of boiling processes on the O isotopic composition of the vapour phase.....202

**6. Conclusion.....202**

**Part IV. General discussion.....203**

**1. Impact of melt devolatilisation on crystallisation dynamics.....204**

**2. Meteoric fluid incursion and its role in the evolution of the Beauvoir system.....211**

**3. Dynamics and significance of hydrothermal mobility of metals in the Beauvoir magmatic-hydrothermal evolution.....213**

3.1. Characterisation of magmatic fluid metal enrichment and high-temperature metal mobility.....213

3.2. Unveiling the complex role of vapour and brine phases in metal transport and enrichment.....215

3.3. Open-system dynamics in supra-solidus magmatic-hydrothermal evolution.....216

**Conclusions and perspectives…….225**

**References……228**

**Appendices……...263**

# *List of figures*

Figure I.1. Schematic representation of the recurrent association between ore deposit types and specific tectonic settings (from Heinrich and Candela, 2014).....8

Figure I.2. Major types of hydrothermal fluids circulating within the Earth's crust (modified from Robb, 2020).....9

Figure I.3. Simplified conceptual diagram of the major elements and processes involved in the development mineralised magmatic-hydrothermal systems.....11

Figure I.4. Cross section of a typical continental subduction zone and arc magmatic system, highlighting the key steps that lead to (or hinder) porphyry ore formation (modified from Richards, 2022).....12

Figure I.5. Schematic model of a telescoped porphyry Cu system showing spatial relationships between a central multiphase porphyry stock and its host rocks, as well as the generalised alteration-mineralisation zoning pattern (modified from Sillitoe, 2010).....14

Figure I.6 Continental collision (A) transitioning to a post-collision setting (B), which is conducive to the development of Sn-W greisen systems (modified from Gourcerol et al., 2019).....16

Figure I.7. Conceptual time evolution of fluid circulation and greisen formation associated with granite crystallisation and cooling at Panasqueira (modified from Launay et al., 2021).....17

Figure I.8. Representation of morphological types of greisen systems (modified from Pirajno, 2009).....20

Figure I.9. Mineralogical-chemical diagram for the classification of major types of magmas: Alumina saturation index (A) versus differentiation index (B) (modified from Cuney, 2014 & Cuney and Marignac, 2015).....24

Figure I.10. Localisation of major domains involved in the Variscan orogeny in Western Europe (modified from Ballèvre et al., 2009).....29

Figure I.11. Schematic representation of the western European Variscan belt representing the main terranes and showing Variscan granitoids, as well as LCT pegmatites, rare-metal granites and rhyolites (modified from Ballouard et al. (2024)).....33

Figure I.12. Simplified geological context of the Echassières granitic complex in the northern part of the French Massif Central (FMC) (modified from Cuney et al. (1992) and Harlaux et al. (2017)).....36

Figure I.13. (a) Interpretative cross-section of the Echassières granitic complex based on geological data and gravimetric modeling (modified from Cuney and Autran, 1987); (b) Interpretative cross-section of the Beauvoir PRMG representing the vertical magmatic internal zoning composed by the three successive units B1, B2, and B3 (modified from Cuney et al. (1992) and Monnier et al. (2018)); (c) to (e) Macroscopic photographs of typical samples from the B1, B2, and B3 units, respectively.....38

Figure I.14. Chronology of the different magmatic and hydrothermal events (i to iv) that occurred in the Beauvoir PRMG between 315 Ma and the Eocene in parallel with the main regional hydrothermal events.....40

Figure I.15. Conceptual model illustrating fluid circulation during the early hydrothermal stage in the Beauvoir granite and highlighting the physico-chemical evolution of the involved fluids (adapted from Aïssa et al., 1987).....42

Figure I.16. Selected macrophotographs of early hydrothermal alterations within the Beauvoir PRMG.....43

Figure I.17. Diagram showing salinity versus homogenisation temperature $T_H$ for different generations of fluid inclusions in the Beauvoir granite (a) and the La Bosse stockwork (b) (from Harlaux et al., 2017).....45

Figure I.18. Major and trace element concentrations in L1-, V2-, and L2-type fluid inclusions from the Beauvoir granite and La Bosse stockwork, determined by LA-ICP-MS analysis (from Harlaux et al., 2017).....46

Figure I.19. Conceptual model deciphering the evolution of OH-rich greisen alteration in the Beauvoir magmatic-hydrothermal system (from Monnier et al., 2020).....51

Figure I.20. Selected macrophotographs of late hydrothermal alterations within the Beauvoir PRMG.....52

Figure II.1. (a) Schematic representation of the western European Variscan belt representing the main terranes and showing Variscan granitoids, as well as LCT pegmatites, rare-metal granites and rhyolites (modified from Ballouard et al. (2024)). (b) Simplified geological context of the Echassières granitic complex in the northern part of the French Massif Central (FMC) (modified from Cuney et al. (1992) and Harlaux et al. (2017)). (c) Interpretative cross-section of the Beauvoir PRMG representing the vertical magmatic internal zoning composed by the three successive units B1, B2, and B3 (modified from Cuney et al. (1992) and Monnier et al. (2018)).....65

Figure II.2. Paragenetic synthesis of magmatic and hydrothermal mineralogical associations of the Beauvoir system.....67

Figure II.3. Selected macrophotographs of investigated samples grouped by hosted apatite type.....75

Figure II.4. Petrographic characteristics of magmatic apatite (type I) within the three magmatic units of the Beauvoir PRMG (i.e., B1, B2 and B3).....76

Figure II.5. Petrographic characteristics of early hydrothermal apatite (type II) within the Beauvoir PRMG and host mica schists.....78

Figure II.6. Petrographic characteristics of late hydrothermal apatite (type III) within the Beauvoir PRMG.....79

Figure II.7. Sr, S and Mn ternary plot with indication on the As content (circle size) in apatite generations from the Beauvoir PRMG.....81

Figure II.8. Trace elements distribution normalised to the upper continental crust (CC) (Rudnick and Gao, 2003) for the distinct apatite generations from the Beauvoir PRMG.....83

Figure II.9. REE compositions of the different apatite generations from the Beauvoir PRMG.....84

Figure II.10. O isotopic composition of the distinct apatite generations from the Beauvoir PRMG system.....86

Figure II.11. Tera-Wasserburg diagrams for the different apatite generations from the Beauvoir PRMG.....89

Figure II.12. Chronology of the different magmatic and hydrothermal events that occurred in the Beauvoir PRMG between 315 Ma and the Eocene in parallel with the main regional geodynamic and hydrothermal events.....92

Figure II.13. Discriminant Sr/Y vs ∑LREE plot after O'Sullivan et al. (2020) to decipher the nature of the parent rock from apatite chemistry.....95

Figure II.14. Mn, Sr & S ternary diagram showing the geochemical evolution of hydrothermal apatite from the Beauvoir PRMG with colour scale representing $\delta^{18}O$ values.....99

Figure II.15. Br/I molar ratios of the distinct apatite generations within the Beauvoir PRMG with colour scale representing $\delta^{18}O$ values.....101

Figure II.16. Chemistry of CL textural micro-domains in early hydrothermal apatite IIa.....105

Figure II.17. Simplified cross-sections illustrating a schematic evolution of the Beauvoir magmatic-hydrothermal system, as revealed by apatite chemistry and U-Pb geochronology, along with corresponding regional geodynamic events.....108

Figure III.1. Macrophotographs of characterised Beauvoir granite samples, showing minimal to no visible alteration: (a) B1 unit, (b) B2 unit, and (c) B3 unit.....114

Figure III.2. Petrographic characteristics of magmatic quartz within the B1 unit.....117

Figure III.3. Petrographic characteristics of magmatic quartz within the B2 unit.....118

Figure III.4. Petrographic characteristics of magmatic quartz within the B3 unit.....119

Figure III.5. CL images and associated WDX element maps of aluminium in magmatic quartz crystals from the B1 unit of the Beauvoir PRMG.....120

Figure III.6. Petrography of melt and fluid inclusion assemblages (FIAs) in magmatic quartz from the B1 unit (-379.0 m) of the Beauvoir PRMG.....123

Figure III.7. Petrography of fluid inclusion assemblages (FIAs) in magmatic quartz from the B2 unit (-546.5 m) of the Beauvoir PRMG.....124

Figure III.8. Petrography of fluid inclusion assemblages (FIAs) in magmatic quartz from the B3 unit (-824.0 m) of the Beauvoir PRMG.....125

Figure III.9. Raman spectrometry identification of elongated, needle-shaped solids present in V2-type fluid inclusions hosted in magmatic quartz from the B1 unit of the Beauvoir PRMG.....126

Figure III.10. Conceptual model of the formation of snowball quartz in the B1 unit of the Beauvoir PRMG.....128

Figure III.11. Synthetic description of approaches used to process fluid inclusion LA-ICP-MS spectra and estimate salinity in the binary $H_2O$-NaCl system and ternary $H_2O$-NaCl-KCl system.....132

Figure III.12. Example of Li and Na spectra obtained by LA-ICP-MS for a L5-L6-type fluid inclusion hosted in magmatic quartz from the B1 unit of the Beauvoir PRMG.....134

Figure III.13. Transition phase temperatures ($T_e$, $T_m$ice, $T_d$Hh, $T_d$Hl and $T_H$) of fluid inclusions in magmatic quartz from the Beauvoir PRMG, determined through microthermometry.....137

Figure III.14. Halite dissolution temperature ($T_d$Hl) versus homogenisation temperature ($T_H$) for L2- and L7-type fluid inclusions in the Beauvoir PRMG.....138

Figure III.15. $CO_2$-$CH_4$-$N_2$ ternary diagram illustrating the trace gas content of fluid inclusions in the Beauvoir PRMG, with $H_2$ content represented by feature size, as determined by Raman spectrometry.....138

Figure III.16. Comparison of salinities obtained in the binary $H_2O$-NaCl system and the ternary $H_2O$-NaCl-KCl system for L2-type (a-b), V2-type (c-d), L3-L4-type (e-f), L5-L6-type (g-h), and L7-type (i-j) fluid inclusions.....141

Figure III.17. Comparison of $NaCl_{eq}$ and $KCl_{eq}$ contents estimated graphically using Na/K ratios and microthermometric measurements ($T_m$ice or $T_d$Hl) in the ternary phase diagram.....142

Figure III.18. Comparison of Li, Cl, K and Sn concentrations deriving from the binary $H_2O$-NaCl system and ternary $H_2O$-NaCl-KCl system for fluid inclusions in the Beauvoir PRMG.....147

Figure III.19. Major, minor and trace element contents of L2-, V2- , L3-L4-, L5-L6-, and L7-type fluid inclusions hosted in magmatic quartz from the Beauvoir granite.....151

Figure III.20. Boxplots illustrating the major, minor, and trace element contents normalised to Na concentrations for L2-, V2-, L3-L4-, L5-L6-, and L7-type fluid inclusions hosted in magmatic quartz from the Beauvoir granite.....152

Figure III.21. (a) Na/K vs. total salinity (NaCl + KCl), (b) Na/Li vs. total salinity, and (c) Nb/Ta vs. total salinity for fluid inclusions hosted in magmatic quartz from the Beauvoir PRMG.....153

Figure III.22. Evolution of concentrations in function of total salinity (NaCl + KCl) for the distinct fluid inclusion types in the Beauvoir PRMG.....157

Figure III.23. Evolution of element-to-Cl ratios in function of total salinity (NaCl + KCl) for the distinct fluid inclusion types in the Beauvoir PRMG.....159

Figure III.24. Salinity versus homogenisation temperature ($T_H$) for the distinct fluid inclusion types recognised in the Beauvoir PRMG.....161

Figure III.25. Partition coefficients between the L2 brine and V2 vapour formed through phase separation of the initial L1 magmatic fluids in the Beauvoir PRMG.....163

Figure III.26. Concentrations of representative elements vs. total salinity (NaCl + KCl) for the distinct FI types hosted in magmatic quartz from the Beauvoir PRMG, showing three main trends (i.e., possible precipitation, accidental trapping of Li-mica and dilution of magmatic fluids by meteoric water).....167

Figure III.27. Biplots of K vs. Li (a) and Rb vs. Li (b) for the distinct FI types hosted in magmatic quartz from the Beauvoir PRMG.....168

Figure III.28. Al vs. Li diagram showing a rough positive correlation between the two elements.....173

Figure III.29. SEM-CL images of magmatic quartz associated with Al and Li concentrations and $\delta^{18}O$ ratios along profiles A-B for the B1 (a-c), B2 (d-f) and B3 (g-i) units.....174

Figure III.30. Oxygen isotopic compositions of magmatic quartz (a-c) and cassiterite (d-e).....176

Figure III.31. Cathodoluminescence images of quartz grains from the B1 unit (a-b) and associated $\delta^{18}O$ profiles across grains (c-d).....177

Figure III.32. Cathodoluminescence image of magmatic quartz from the B2 unit (a) and associated $\delta^{18}O$ ratios of quartz at its contact with cassiterite (b).....178

Figure III.33. Temperatures (a) and pressures (b) of quartz crystallisation estimated using the TitaniQ thermobarometer (Thomas et al., 2010).....181

Figure III.34. Summary of crystallisation temperatures obtained through oxygen thermometry on magmatic minerals (Fouillac et al., 1987; Fouillac and Rossi, 1991; this study) and crystallisation experiments (Pichavant, 2022).....183

Figure III.35. Oxygen isotopic composition of quartz from the three magmatic units of the Beauvoir PRMG (excluding recrystallised zones within grains) (Fouillac et al., 1987; Fouillac and Rossi, 1991; this study) in comparison with values reported for other PRMGs (Žák et al., 2005; Michaud and Pichavant, 2020), LCT pegmatites (Taylor and Friedrichsen, 1983; Kontak and Kyser, 2009; Ashworth et al., 2020; Pfister et al., 2024), Variscan peraluminous leucogranites (Turpin et al., 1990b; Tartèse and Boulvais, 2010) and the Richemont rhyolitic dyke (Raimbault and Burnol, 1998). The $\delta^{18}O$ ratios of the Beauvoir melts were estimated using the crystal-melt temperature-dependent fractionation factor proposed by Zhao and Zheng (2003) for rhyolitic melt and a crystallisation temperature of ca. 670 to 550 °C (Pichavant, 2022).....184

Figure III.36. (a) $\delta^{18}O$ values of mica versus quartz, (b) albite versus quartz, and (c) topaz versus quartz for the Beauvoir PRMG (Fouillac et al., 1987; Fouillac and Rossi, 1991). O isotopic compositions of minerals from other PRMGs (Žák et al., 2005; Michaud and Pichavant, 2020), LCT pegmatites (Taylor and Friedrichsen, 1983; Kontak and Kyser, 2009; Ashworth et al., 2020; Pfister et al., 2024), Variscan peraluminous leucogranites (Turpin et al., 1990b; Tartèse and Boulvais, 2010) and the Richemont rhyolitic dyke (Raimbault and Burnol, 1998) are reported for comparison.....186

Figure III.37. $\delta^{18}O_{Qz}$ values for the two samples analysed from the B2 unit, positioned respectively above and below the B3 sample along the GPF1 drillhole.....187

Figure III.38. Petrographic characteristics of the greisen band from the drill core sample collected at 801 m depth along the historic GPF1 drillhole (B3 unit).....193

Figure III.39. Petrographic characteristics of quartz-cassiterite greisen collected from the Beauvoir quarry.....194

Figure III.40. Petrography of fluid inclusions (FIs) of likely primary origin hosted in greisen-related quartz and cassiterite from the quarry sample.....196

Figure III.41. O isotopic compositions of quartz (a-b) and cassiterite (c) from the high-temperature greisen within the Beauvoir PRMG.....197

Figure III.42. (a) Diagram showing pairs of $\delta^{18}O$ ratios for quartz and cassiterite used to estimate the temperature of O isotopic equilibrium, with equilibrium lines for temperatures ranging from 350 to 650 °C calculated using the equation proposed by Li et al. (2022). (b) Distribution of estimated temperatures for O isotope equilibrium between quartz and cassiterite. (c) $\delta^{18}O$ ratios estimated for the fluid from quartz data using temperature-dependent fractionation factors from Zheng (1993) and Vho et al. (2019). (d) $\delta^{18}O$ ratios estimated for the fluid from cassiterite data using temperature-dependent fractionation factors from Zheng (1991) and Li et al. (2022). (e) Comparison of fluid $\delta^{18}O$ ratios estimated from quartz cassiterite data using temperature-dependent fractionation factors of Vho et al. (2019) and Li et al. (2022), respectively.....200

Figure IV.1. Synthetic illustration of the magmatic-hydrothermal evolution of the Beauvoir PRMG.....209

Figure IV.2. Average concentrations for magmatic fluid inclusions (L1, L2, V2, and L7) hosted in magmatic quartz from the B1 unit of the Beauvoir PRMG versus average whole-rock concentrations of the B1 unit compiled from Burnol and Viallefond (1984); Pichavant et al. (1987a); Rossi et al. (1987); and Raimbault et al. (1995).....214

Figure IV.3. Mass balance approach proposed to estimate the volume of fluid required for the Beauvoir magmatic-hydrothermal system to generate the observed chemical overprint in the host mica schists, as expressed in the equation (IV.2).....218

Figure IV.4. Histogram representation of the estimated fluid volumes required for (a-c) the formation of the 1 km-wide alteration halo in the host mica schists and (d) the development of 10% greisenised zones within the Beauvoir intrusion.....220

Figure IV.5. Proposed open-system model for the genesis and magmatic-hydrothermal evolution of the Beauvoir PRMG.....223

Figure II.A1. Estimation of the interlaboratory reproducibility from the dispersion of apatite reference material lower intercept ages obtained during this study.....269

Figure II.A2. Detailed Tera-Wasserburg diagrams for apatite I and IIb from the Beauvoir PRMG.....270

Figure II.A3. Binary diagrams illustrating trends between Sr and S content and O isotopic composition of apatite.....271

Figure III.A1. Cathodoluminescence (CL) images revealing zonation in magmatic quartz from the B1 unit of the Beauvoir PRMG.....274

Figure III.A2. Cathodoluminescence (CL) images showing zonation in magmatic quartz from the B2 unit of the Beauvoir PRMG.....275

Figure III.A3. Cathodoluminescence (CL) images showing zonation in magmatic quartz from the B3 unit of the Beauvoir PRMG.....276

# *List of tables*

Table I.1. Summary of the main replacement reactions occurring during greisenisation and albitisation (Pirajno, 1992; Launay et al., 2019; Ballouard et al., 2020).....21

Table I.2. Synthesis of petrographic observations, microthermometric and Raman spectrometry results for the different fluid inclusion types identified in the Beauvoir granite, based on the studies of [1] Aïssa et al. (1987); [2] Aïssa (1987); [3] Harlaux et al. (2017); and [4] Monnier et al. (2020).....49

Table I.3. Chemical composition ranges for magmatic fluid inclusions hosted in magmatic quartz and topaz from the Beauvoir PRMG, as determined by LA-ICP-MS (from Harlaux et al., 2017).....50

Table II.1. Summary of samples and apatite characteristics.....73

Table III.1. Main minerals observed at the contact with magmatic quartz and as inclusions within magmatic quartz in the three units of the Beauvoir PRMG.....116

Table III.2. Synthesis of microthermometric and Raman spectrometry results for the different fluid inclusion types analysed in magmatic quartz from the Beauvoir PRMG.....139

Table III.3. Summary of salinity estimates in the $H_2O$-NaCl binary system and the $H_2O$-NaCl-KCl ternary system.....144

Table III.4. Percentage differences of elemental concentrations estimated in the $H_2O$-NaCl and $H_2O$-NaCl-KCl systems for fluid inclusions.....146

Table III.5. Summary of elements detected in fluid inclusions hosted in magmatic quartz from the Beauvoir PRMG by LA-ICP-MS, indicating the percentage of analyses in which each element was identified for each FI type, along with the corresponding median limit of detection (LOD) for each element.....149

Table IV.1. Summary of key arguments derived from the analysis of apatite, quartz, cassiterite, and fluid inclusions hosted in magmatic quartz, which collectively help reconstruct the supra- to sub-solidus history of the Beauvoir PRMG.....207

# PRÉAMBULE

La circulation de fluides hydrothermaux au sein de la croûte terrestre joue un rôle fondamental dans les processus de minéralisation, menant dans certains cas à des concentrations exceptionnelles en métaux, tant en termes de teneur que de volume. Ces fluides, riches en volatiles et métaux dissous, circulent souvent en lien avec une activité magmatique, donnant lieu au développement de systèmes magmatiques-hydrothermaux minéralisés. Une multitude de contextes géodynamiques permet le développement de tels systèmes, aussi bien en domaine continental qu'océanique. Les gisements de type porphyres et les gisements péribatholithiques à Sn-W constituent des exemples classiques de systèmes magmatiques-hydrothermaux, issus de l'intrusion de magmas intermédiaires à felsiques au sein de la croûte continentale supérieure (Robb, 2020). Ces systèmes illustrent parfaitement la complexité des interactions entre magmas, fluides et roches encaissantes, la circulation de fluides au sein et autour des corps intrusifs jouant un rôle crucial sur l'enrichissement en métaux et la distribution spatiale de la minéralisation (e.g., Dilles, 1987; Audétat et al., 2000b; Burnard and Polya, 2004; Sillitoe, 2010; Lecumberri-Sanchez et al., 2017; Legros et al., 2019).

Les granites peralumineux riches en métaux rares et les pegmatites de type lithium-césium-tantale (LCT) représentent des exemples emblématiques de systèmes magmatiques-hydrothermaux évolués, généralement mis en place lors des dernières phases du magmatisme granitique tardi-orogénique (Kovalenko et al., 1970; Linnen, 1998; Linnen and Cuney, 2005). Ces systèmes sont caractérisés par un enrichissement extrême en métaux lithophiles et halogènes (e.g., Li, F, Ta, Nb, Sn, et W), leurs teneurs excédant de plusieurs ordres de grandeur celles de la croûte continentale supérieure (Tischendorf, 1977; Romer and Pichavant, 2020). Les métaux se concentrent principalement dans des minéralisations disséminées au sein de l'intrusion, incluant des aluminosilicates de lithium et des oxydes de Nb-Ta-Sn (Linnen and Cuney, 2005; Černý and Ercit, 2005). La genèse de ces systèmes est largement attribuée à des processus magmatiques tels que la fusion partielle et la cristallisation fractionnée (e.g., Pichavant, 2022; Ballouard et al., 2023). Ainsi, l'étroite relation entre l'hydrothermalisme et le dépôt des métaux caractérisant les gisements de type porphyres et péribatholithiques à Sn-W est peu évidente au sein des granites et pegmatites à métaux rares, bien qu'ils se développent dans des contextes géologiques similaires.

Du métasomatisme a toutefois été documenté depuis longtemps au sein des granites et pegmatites à métaux rares, entraînant des modifications minéralogiques et géochimiques significatives (e.g., Černý, 1986; Schwartz, 1992). Ces processus, désignés par les termes d'albilitisation et de greisenisation, résultent de la circulation d'une phase volatile magmatique (MVP) – ou fluides magmatiques – exsolvée des magmas au cours de leur refroidissement et cristallisation (e.g., Štemprok, 1987; Halter et al., 1998; Monnier et al., 2020; Pfister et al., 2023). Bien que le rôle des fluides magmatiques, voire de liquides silicatés riches en volatiles (e.g., Badanina et al., 2004; Müller et al., 2018b; Kaeter et al., 2018; Ballouard et al., 2020a),

dans le transport et la concentration des métaux tels que Li, Nb, et Ta soit largement reconnu, l'ampleur des interactions entre magma, fluide et roche reste débattue. Par ailleurs, la contribution des fluides externes, en particulier d'origine météorique, est suggérée dans certains cas, leur timing et leur impact demeurant cependant souvent incertains (e.g., Witt, 1988; Cuney et al., 1992; Bettencourt et al., 2005). Ainsi, malgré les avancées significatives dans notre compréhension des systèmes granitiques peralumineux à métaux rares, de nombreuses interrogations subsistent quant à la nature exacte des processus magmatiques et hydrothermaux mis en jeu, ainsi que leur influence respective dans la formation et l'évolution de ces gisements.

Dans le contexte économique actuel, marqué par une transition énergétique rapide et un essor des technologies vertes, les gisements granitiques peralumineux à métaux rares suscitent un intérêt grandissant en raison de leur enrichissement en lithium (Li), tantale (Ta), niobium (Nb) ou encore étain (Sn). Ces métaux, classés parmi les matières premières critiques par la Commission européenne, occupent une place centrale dans divers secteurs industriels de pointe (European Commission, 2023). Le tantale et le niobium sont essentiels à la fabrication des superalliages et des composants électroniques avancés, tandis que le lithium joue un rôle clé dans des industries aussi variées que la pharmaceutique – pour le traitement des troubles bipolaires – et l'aéronautique, via les alliages légers d'aluminium-lithium (Dessemond et al., 2019; U.S. Geological Survey, 2024). Cependant, c'est dans le domaine des batteries lithium-ion que l'utilisation du lithium a explosé depuis 2015, cette application représentant aujourd'hui près de 90 % de la demande mondiale (Gloaguen et al., 2018; U.S. Geological Survey, 2024). L'augmentation continue de la demande mondiale pour ces métaux stratégiques, combinée à la dépendance aux saumures des lacs salés – méthode historiquement dominante pour l'extraction du lithium depuis les années 1990 – et la concentration géographique de la production dans quelques pays (Australie, Chili et Chine) soulèvent d'importants enjeux économiques et géopolitiques. Dans ce contexte, les granites peralumineux à métaux rares et pegmatites LCT apparaissent comme des alternatives prometteuses pour diversifier les sources d'approvisionnement et réduire la dépendance vis-à-vis des marchés extérieurs, tout en répondant aux attentes sociétales pour une exploitation durable.

Localisé dans la partie nord du Massif central (France), le granite de Beauvoir constitue un exemple exceptionnel et largement étudié de granite peralumineux à métaux rares, notamment grâce au programme de *Géologie Profonde de la France* (GPF) qui a permis l'implantation du sondage profond GPF1 sur le site d'Échassières en 1985 (Cuney and Autran, 1987). Ce granite se distingue son enrichissement remarquable en éléments fondants et lithophiles (Li, P, F, Rb, Cs, Be, Nb, Ta, Sn, W, U), en particulier dans sa zone apicale (Raimbault et al., 1995). Les teneurs en Li, Sn et Ta atteignent respectivement 0.1 à 1 pds.%, 0.02 à 0.4 pds.%, et 40 à 500 ppm, des valeurs nettement supérieures à celles de la croûte continentale supérieure (Li ~ 24 ppm; Sn ~

2.1 ppm; et Ta ~ 0.9 ppm; Rudnick and Gao, 2003). Depuis le milieu du XIX$^{e}$ siècle, sa partie superficielle kaolinisée est exploitée à ciel ouvert pour la production de kaolin. Actuellement géré par Imerys Ceramics France, ce site produit environ 30 000 tonnes de kaolin par an, ainsi que 60 tonnes de concentrés de cassitérite (Sn), minéraux du groupe de la columbite (Nb-Ta) et du pyrochlore (Nb-Ta-U) en tant que co-produits.

Face aux enjeux liés à la souveraineté énergétique et à l'approvisionnement en matières premières critiques, Imerys a lancé le projet EMILI (Exploitation de Micas Lithinifères), visant à développer une mine de lithium sur le site de Beauvoir. Ce projet, initié par une phase d'exploration cumulant plus de 33 000 m de sondages confirmant l'attractivité du gisement, serait constitué d'une mine souterraine, d'une usine de concentration et d'une usine de conversion qui permettraient de produire 34 000 tonnes d'hydroxyde de lithium d'ici 2030. Cette capacité de production pourrait équiper environ 700 000 véhicules électriques par an en batteries lithium-ion. Outre ses objectifs industriels, le projet EMILI offre une opportunité scientifique unique pour approfondir la compréhension des systèmes minéralisés liés aux granites peralumineux à métaux rares. Une collaboration entre Imerys et l'Université de Lorraine, via le LabEx Ressources21, a été établie pour la période 2021–2024. Ce partenariat structurant regroupe huit projets de recherche axés sur le granite de Beauvoir, parmi lesquels figure cette thèse dédiée à l'étude de son système magmatique-hydrothermal. Ce projet bénéficie d'un co-financement d'Imerys, ainsi que d'un accès privilégié aux données issues des campagnes de sondages et aux carottes de forage réalisées dans le cadre du projet EMILI.

Cette thèse se propose de réexaminer les relations complexes entre processus magmatiques et hydrothermaux au sein du granite peralumineux à métaux rares de Beauvoir, en vue d'éclaircir certaines controverses relatives aux dynamiques des fluides au cours des stades supra- à sub-solidus et à leur rôle dans la genèse et l'enrichissement en métaux stratégiques. Le manuscrit s'organise en quatre parties principales, entièrement rédigées en anglais, avec des introductions en anglais et français en début de chaque partie.

La **Partie I** explore l'état des connaissances sur les systèmes magmatiques-hydrothermaux, en s'intéressant aux processus de circulation des fluides, de transfert, transport et dépôt des métaux. Une approche progressive mène à examiner les systèmes associés aux magmas intermédiaires à felsiques mis en place dans la croûte continentale supérieure, tels que les porphyres, les gisements péribatholithiques à Sn-W, et les granites peralumineux à métaux rares (PRMG). Ces derniers sont abordés de manière détaillée dans la section 2, où sont présentés leur définition, classification, modèles de genèse et géométrie de mise en place. La troisième section retrace brièvement l'évolution de l'orogenèse varisque, en mettant particulièrement l'accent sur le Massif central, où l'évolution tardive de cette orogenèse est marquée par un épisode significatif de magmatisme à métaux rares, ayant notamment conduit à la formation du granite de Beauvoir. La section 4

s'intéresse aux connaissances actuelles sur l'évolution magmatique-hydrothermale de ce granite, en particulier aux dynamiques des fluides, leur origine, leur chronologie, ainsi qu'à leur impact sur la distribution des métaux. Au fil de cette Partie I, les zones d'ombre de l'évolution magmatique-hydrothermale des granites peralumineux à métaux rares, et en particulier du granite de Beauvoir, sont mises en lumière. Ces questionnements, ainsi que la stratégie scientifique adoptée pour y répondre, sont développés en conclusion de cette première partie.

La **Partie II** est consacrée à la caractérisation détaillée des différentes générations d'apatite, magmatiques et hydrothermales, rencontrées au sein du granite de Beauvoir. Cette étude a fait l'objet d'une publication dans le journal *Chemical Geology*, et repose sur une approche *in-situ* multidisciplinaire combinant la chimie élémentaire (éléments majeurs, traces et halogènes), les isotopes de l'oxygène et la géochronologie U-Pb. Elle permet d'établir un cadre global en apportant des contraintes sur quatre stades majeurs dans l'évolution magmatique et hydrothermale du granite de Beauvoir, depuis sa mise en place il y a environ 310–315 Ma (Duthou and Pin, 1987; Cheilletz et al., 1992; Melleton et al., 2015) jusqu'à l'altération supergène de type kaolinisation survenue à l'Éocène-Oligocène (Merceron et al., 1987; Charoy et al., 2003; Monnier et al., 2019). Outre la reconstitution des dynamiques de circulation des fluides lors de la transition magmatique-hydrothermale, cette étude permet également de mieux caractériser les épisodes hydrothermaux tardifs, non magmatiques, liés à des événements tectoniques régionaux. L'apatite se révèle ainsi être un minéral clé pour comprendre les processus magmatiques et hydrothermaux à l'origine des granites à métaux rares, et leur rôle dans la précipitation des métaux, en particulier de l'étain (Sn).

La **Partie III** est centrée sur la transition magmatique-hydrothermale du granite de Beauvoir, étape clé pendant laquelle les processus magmatiques et hydrothermaux interagissent de façon complexe et façonnent la distribution des métaux à l'échelle du système (e.g., Cuney et al., 1992; Harlaux et al., 2017, 2025). Cette étude s'attache essentiellement à caractériser le quartz magmatique du granite de Beauvoir, véritable archive géochimique enregistrant les signatures de ces processus magmatiques-hydrothermaux et ayant piégé de nombreuses populations d'inclusions fluides (Aïssa et al., 1987). Une approche multidisciplinaire, alliant pétrographie détaillée, analyse des éléments traces, isotopes de l'oxygène et étude des inclusions fluides piégées a été appliquée. Les résultats obtenus offrent un éclairage fondamental sur la dynamique de la transition magmatique-hydrothermale au sein du granite de Beauvoir et son influence sur la mobilisation des métaux.

La **Partie IV** synthétise l'ensemble des résultats afin de proposer un modèle de mise en place et d'évolution des dynamiques de circulations fluides, ainsi que de la mobilité hydrothermale des métaux au sein du granite de Beauvoir. Ce modèle permet de dégager des pistes pour enrichir les modèles actuels de genèse des granites peralumineux à métaux rares.

# PART I

# General introduction

## 1. Magmatic-hydrothermal systems and ore formation in the continental crust

The Earth's crust acts as a major reservoir for hydrothermal fluids originating from various sources, including seawater, formation brines, meteoric, metamorphic or magmatic fluids (Robb, 2020). The circulation of these hydrothermal fluids is proven to be a key element in mineralisation processes, sometimes leading to remarkable metal concentrations, both in terms of metal grade and volume. In certain geodynamic contexts, hydrothermal systems develop in association with magmatic activity, and are therefore designated as "magmatic-hydrothermal systems" (e.g., Hedenquist and Lowenstern, 1994; Heinrich and Candela, 2014). Understanding the formation of magmatic-hydrothermal ore deposits is crucial for addressing global metal demands, as they represent not only our most significant source of Cu, Mo, Sn, W, In, and Re, but also an important source of Au, Ag, Pb, Zn, and other minor and rare metals (Heinrich and Candela, 2014; Audétat and Edmonds, 2020).

Magmatic-hydrothermal systems result from the emplacement of melts within the Earth's crust, their subsequent cooling and crystallisation, the exsolution of magmatic fluids, melt-fluid-crystal interactions, and potential mixing dynamics between magmatic and external fluids (e.g., meteoric or metamorphic fluids) (Pirajno, 2009). They occur in a variety of tectonic settings, both in continental and oceanic domains, and are almost invariably associated with the intrusion of granitic magmas. Porphyry-epithermal deposits and Sn-W granite-related systems represents well-known magmatic-hydrothermal systems associated with the emplacement of felsic to intermediate magmas within the upper continental crust (Fig. I.1). In both systems, fluid circulation within and surrounding the intrusive bodies has been demonstrated as a crucial factor for metal enrichment, significantly influencing the spatial distribution of mineralisation (e.g., Dilles, 1987; Audétat et al., 2000b; Burnard and Polya, 2004; Sillitoe, 2010; Lecumberri-Sanchez et al., 2017; Legros et al., 2019).

Although highly peraluminous rare-metal granites (PRMGs; Linnen and Cuney, 2005) as well as lithium-cesium-tantalum (LCT) pegmatites (Černý and Ercit, 2005) constitute another example of magmatic-hydrothermal systems emplaced in similar geological settings, this relationship between hydrothermal processes and metal deposition appears to be less pronounced. The disseminated mineralisation they host, such as Li aluminosilicates along with Nb-Ta-Sn oxide minerals, is generally thought to have been primarily deposited at supra-solidus conditions. Although magmatic processes, such as partial melting and fractional crystallisation, appear to play a major role in metal enrichment and deposition within rare metal deposits (e.g., Linnen and Cuney, 2005; Pichavant, 2022; Ballouard et al., 2023), these systems are commonly affected by magmatic-hydrothermal processes, which in some cases lead to significant mineralogical and geochemical modifications (e.g., Schwartz, 1992; London et al., 1996; Badanina et al., 2004; Linnen et al., 2019; Ballouard et al., 2020a; McNeil et al., 2020; Launay et al., 2021) (section 2.2

of Part I). In most cases, the impact of magmatic-hydrothermal to hydrothermal processes on rare-metal mineralisation is considered negligible, as has been proposed for the Beauvoir peraluminous granite (France; Raimbault et al., 1995). However, some of these magmatic mineralisation have undergone intense sub-solidus reworking, such as the Cínovec granite cupola where Li, Sn, and W-rich greisens formed (Johan and Johan, 2001; Webster et al., 2004). Magmatic-hydrothermal systems associated with rare-metal granite deposits have been relatively understudied over the years, and the role of magmatic-hydrothermal to hydrothermal processes in rare metal enrichment and their (re)distribution remains thus poorly quantified.

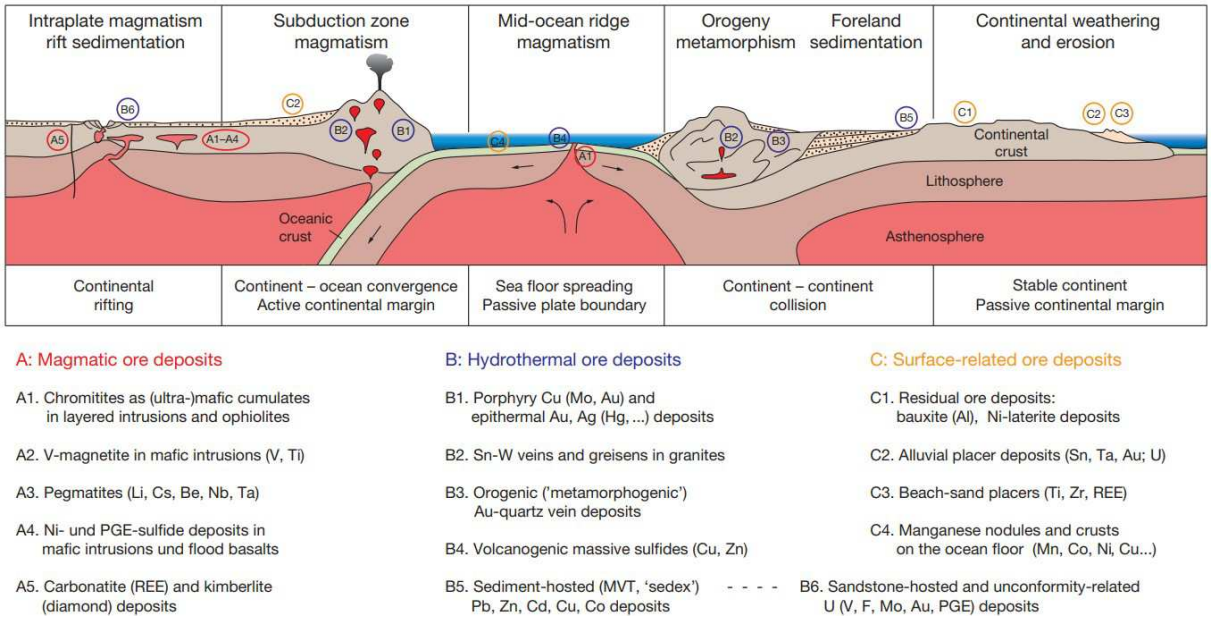



*Figure I.1. Schematic representation of the recurrent association between ore deposit types and specific tectonic settings (from Heinrich and Candela, 2014). This figure is not exhaustive and depends on the classifications considered.*

In this section, the fundamental characteristics of magmatic-hydrothermal systems are first defined and summarised, followed by an overview of typical granitoid-related hydrothermal deposits, including porphyry-epithermal and Sn-W perigranitic ore systems. These deposits will serve as a comparative framework for understanding magmatic-hydrothermal systems that develop in and around peraluminous rare-metal granites, such as the Beauvoir intrusion. As previously mentioned, even though the relationship between hydrothermalism and mineralisation remains unclear in PRMGs, they typically exhibit evidence of greisen and albitic alterations, which are explored in detail in the final section.

### 1.1. Fluid circulation processes leading to metal enrichment, transport and deposition

The development of magmatic-hydrothermal systems is characterised by a continuous transition from an initially purely magmatic system dominated by crystal-melt interactions to a system dominated by crystal-melt-fluid phase interactions, ultimately resulting in a purely hydrothermal system associated with fluid-rock interactions (Audétat and Edmonds, 2020). This

transition is accompanied by the progressive cooling of the intrusion and the circulating fluids, whose nature can evolve as the system progresses.

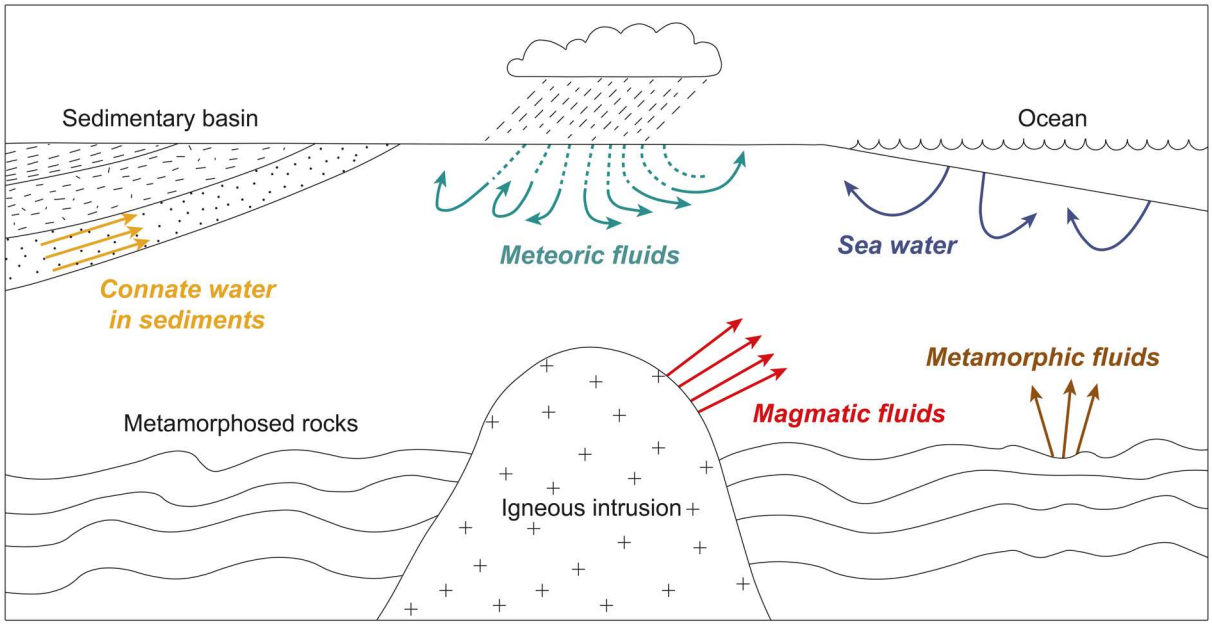



*Figure I.2. Major types of hydrothermal fluids circulating within the Earth's crust (modified from Robb, 2020).*

The term "hydrothermal fluid" carries no specific genetic implication but generally refers to any hot aqueous solution, typically with temperatures ranging from *ca.* 50 °C to over 500 °C, containing solutes that may precipitate when changes occur in the solution's properties, such as variations in pH, temperature, pressure, redox state, or salinity (Pirajno, 2009; Audétat and Edmonds, 2020). The Earth's crust serves as a major reservoir for hydrothermal fluids of diverse origins, including magmatic, metamorphic, sedimentary or meteoric sources (e.g., Robb, 2020) (Fig. I.2). Magmatic fluids encompass those directly exsolved from melts during cooling and crystallisation, as well as fluids derived from these primary magmatic fluids through processes such as boiling and phase separation. Additionally, external fluids from various sources – metamorphic, sedimentary, meteoric, or a combination of these – often invade magmatic-hydrothermal systems during their evolution. These systems thus exhibit considerable complexity, primarily due to the significant diversity of fluids involved, their variability throughout the system's evolution, and the timing of fluid influx and circulation. Chemical and isotopic analyses, combined with dating of different hydrothermal episodes, provide valuable insights into the chronology of hydrothermal circulations, the origin and evolution of mineralising fluids, the source of ore-forming elements, the temperature of mineralised systems, and the mechanisms of mineral deposition (e.g., Burnard and Polya, 2004; Legros et al., 2019; Ballouard et al., 2020a; Launay et al., 2021).

Three critical elements are fundamental to the formation of a mineralised magmatic-hydrothermal system: the presence of fluids, sources of heat and metals (Fig. I.3). In numerous

genesis models, the intrusive body is recognised not only as the heat source responsible for generating convective fluid circulation in and around the intrusion, but also as the principal source of metals (e.g., Robb, 2020). The transfer of metals from melts or rocks to fluids depends on their solubility, which is controlled by fluid properties (e.g., pH, salinity, redox potential) and T-P conditions within the system at any given moment (Fig. I.3). The formation of aqueous metal complexes with ions ligands significantly enhances metals transfer and further transport in solution. Complex ions consist in "charged species in which a metal ion is joined by co-ordinate covalent bonds to neutral molecules and/or negative ions" (Masterton et al., 1981). Sulphides ($HS^-$ and $H_2S$) and chlorides ($Cl^-$) represent the two main complexing ligands encountered in hydrothermal fluids and are responsible for the transport and redistribution of significant amounts of metals (Pirajno, 2009; Heinrich and Candela, 2014; Audétat and Edmonds, 2020). Other volatiles, such as fluorine ($F^-$), along with non-volatile ionic species like hydroxide ($OH^-$) and carbonate ($CO_3^{2-}$), also serve as common complexing ligand for metals. Many ore-forming metals form stable complexes with chlorine, indicating that fluid salinity plays a dominant role in controlling the efficiency of metal extraction from magma (Yardley, 2005). Temperature represents another controlling factor, as these complexes typically exhibit increased stability with rising temperatures (Yardley, 2005). Consequently, mineralising fluids commonly consist of high-temperature, saline fluids, and numerous studies have suggested the exsolution of magmatic volatile phase (MVP) as an efficient mechanism for metals extraction from melts (e.g., Hulsbosch et al., 2016; Harlaux et al., 2017; Legros et al., 2019; Michaud and Pichavant, 2020; Li et al., 2021).

Beyond the chemical processes that govern the transfer of metals from melts and rocks to hydrothermal fluids, structural features such as faults and fractures, along with the petrophysical characteristics of rocks (i.e., porosity and permeability), critically influence metal transport (e.g., Ingebritsen et al., 2010; Launay et al., 2019; Codeço et al., 2022). The petrological properties of both the intrusive body and surrounding rocks might then promote the creation of preferential pathways that focus fluid flows, ultimately affecting the mineralisation geometry (Fig. I.3).

Following their transfer from melts and rocks to hydrothermal fluids and their further transport, the deposition of metals is influenced by various physical and/or chemical processes. Mixing dynamics between magmatic and oxidised meteoric fluids have been recognised as a key mechanism triggering cassiterite ($SnO_2$) precipitation (Witt, 1988; Heinrich, 1990; Audétat et al., 1998; Karimzadeh Somarin and Ashley, 2004; Fekete et al., 2016; Liu et al., 2020; Chen et al., 2023; Peng et al., 2023a), although simple cooling of the ore-forming fluid has been proposed as an effective alternative mechanism (Liu et al., 2023). Both processes result in more oxidised mineralising fluids, promoting the transition from $Sn^{2+}$ to $Sn^{4+}$. In addition to mixing dynamics or temperature variations, other well-established deposition mechanisms include fluid-rock

interactions and pressure drops within the system, which may trigger the boiling of mineralising fluids (e.g., Ni et al., 2022). Boiling of mineralising fluids occurs when hot fluids are subjected to low pressures, such as during their ascent or fracturing events, which typically lead to mineral deposition in discharge zones (Fig. I.3). It causes the initial fluid to separate into a high-salinity aqueous phase and a low-salinity, low-density vapour phase, promoting the partitioning of elements between the two. Each element displays a distinct affinity for one of the phases: elements such as Na, K, Fe, Mn, Zn, Rb, Cs, Ag, Sn, Pb, W, and Tl tend to preferentially fractionate in the chloride-rich aqueous phase, whereas elements like Cu, B, Li, As (± S, Ag, La) are more likely to concentrate within the vapour phase (e.g., Heinrich et al., 1999; Audétat et al., 2000a; Harlaux et al., 2017). Other critical parameters for achieving economic metals concentrations include the circulation of substantial fluid volumes over relatively short time periods, as well-documented in porphyry systems described in section 1.2.1 (e.g., Weis et al., 2012; Mercer et al., 2015; Chelle-Michou et al., 2017; Li et al., 2017; Cernuschi et al., 2018).

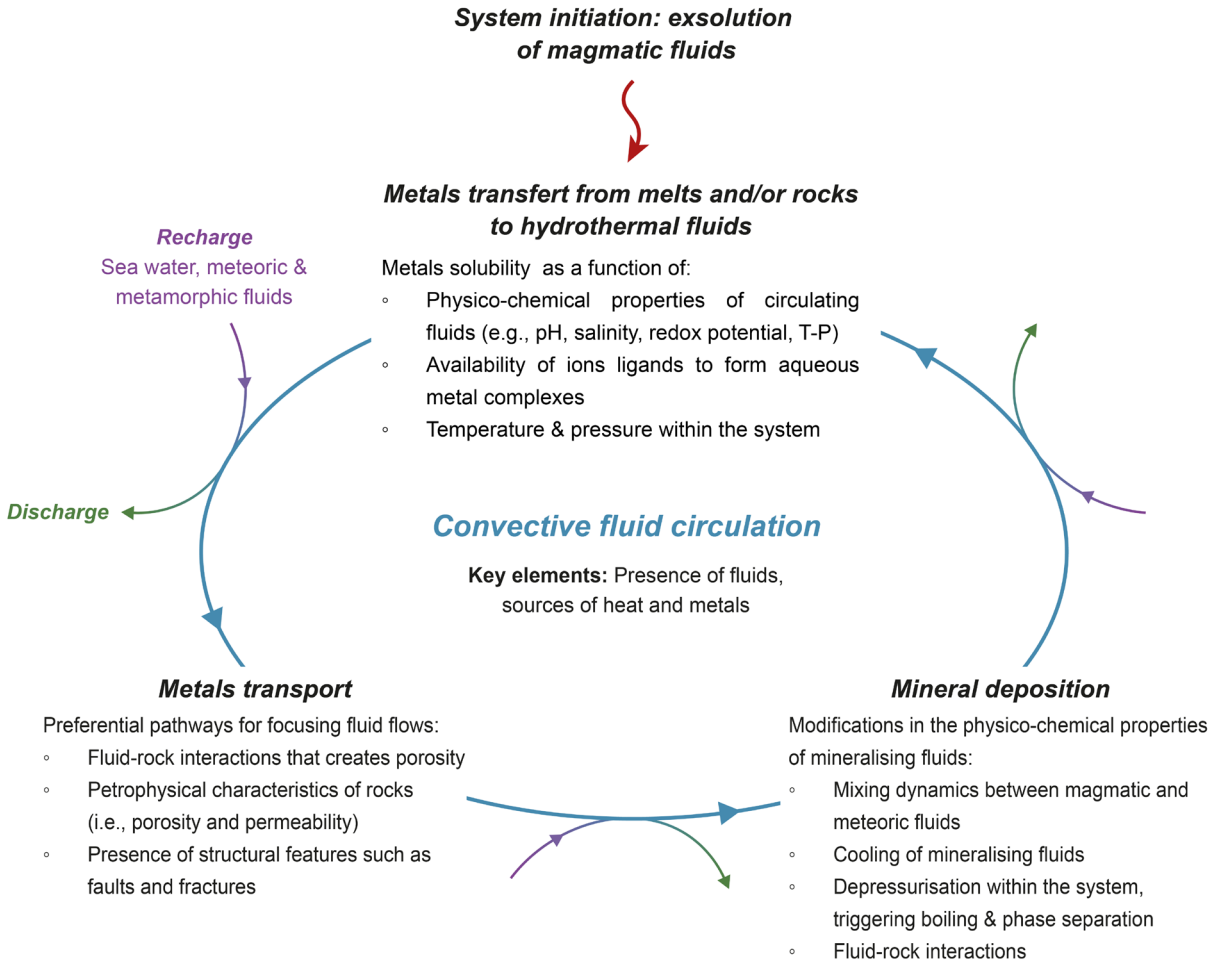



*Figure I.3. Simplified conceptual diagram of the major elements and processes involved in the development mineralised magmatic-hydrothermal systems*

## 1.2. Examples of mineralised magmatic-hydrothermal systems

### *1.2.1 Porphyry-epithermal systems*

Porphyry systems represent major global reserves of copper (~ 80 %) and molybdenum (~ 95 %), as well as gold, rhenium, and to a lesser extent, Ag, Pd, Te, Se, Bi, Zn, and Pb (Sillitoe, 2010; Sun et al., 2015). Due to the nature of their mineralisation, they are commonly referred to as "Cu ± Mo ± Au porphyry systems" or more simply "porphyry copper systems". These systems develop in association with calc-alkaline magmatism, essentially above active subduction zones at convergent plate boundaries (Sillitoe, 1972; Richards, 2003) (Fig. I.4), although some minor occurrences have also been documented in post-subduction and collisional tectonic settings (e.g., Richards, 2009). Notable examples are found in the Andes Cordillera, which hosts three of the world's largest Cu-Mo porphyry deposits formed between the late Miocene and early Pliocene: El Teniente, Río Blanco-Los Bronces, and Los Pelambres-El Pachón (Chile; Klemm et al., 2007).

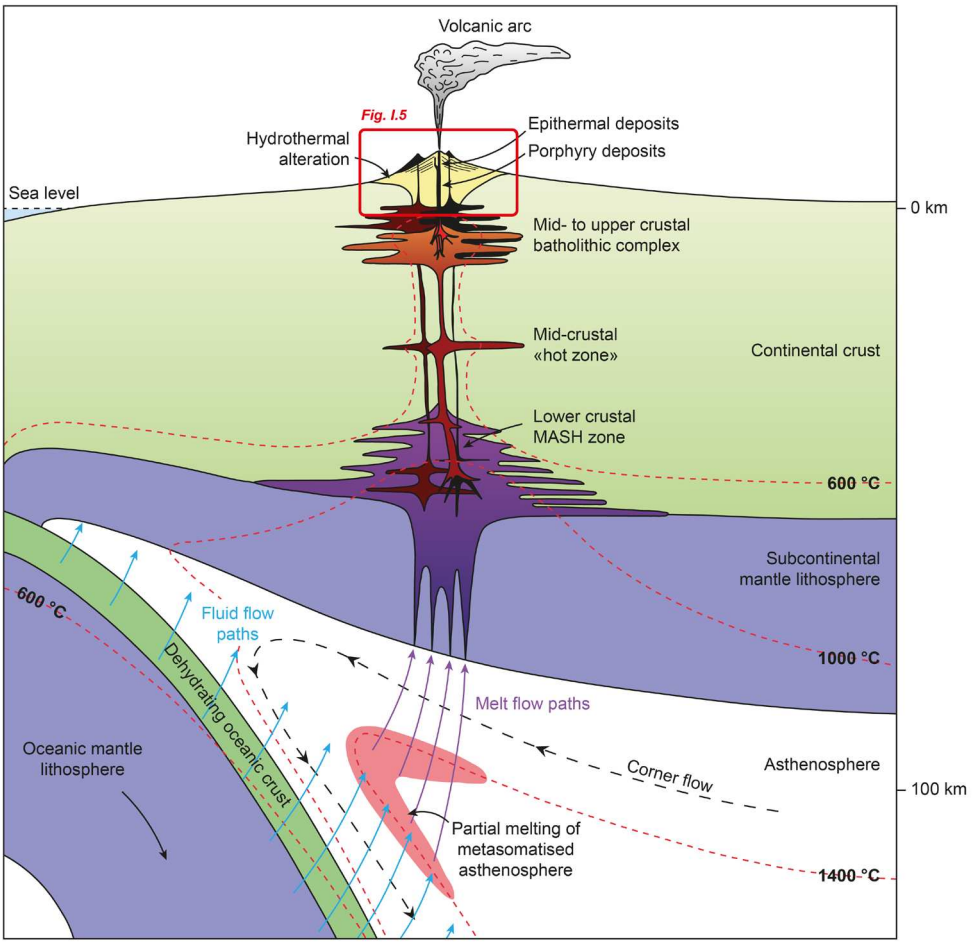



*Figure I.4. Cross section of a typical continental subduction zone and arc magmatic system, highlighting the key steps that lead to (or hinder) porphyry ore formation (modified from Richards, 2022). "MASH" refers to the Melting, Assimilation, Storage, and Homogenisation model (Hildreth and Moorbath, 1988).*

The formation of porphyry systems is a complex process governed not only by geodynamic and physicochemical conditions, but also by factors such as magmatic evolution, the flux and

duration of magmatic and hydrothermal activity, crustal architecture, volatile exsolution – all of which collectively determine the size, grade, and accessibility of porphyry copper deposits (Richards, 2022; Virmond et al., 2024). It is initiated with the production of fertile magmas as a result of metasomatic alteration, oxidation, and partial melting of the asthenospheric mantle above the downgoing oceanic lithosphere (Fig. I.4). Such magmas are typically hydrous, moderately oxidised, basaltic in composition, and enriched in incompatible elements, particularly sulphur (Sun et al., 2015; Richards, 2022). They are preferentially generated during the relatively late evolution of magmatic arcs, within stable subduction zones characterised by moderate dip (~ 30 to 45°) and oblique convergence (Richards, 2022 and references therein). The basaltic magma flux is then transformed into intermediate composition, calc-alkaline (andesitic) magmas through MASH (Melting, Assimilation, Storage, Homogenisation) processes. The MASH model posits that mantle-derived basaltic magmas are too dense to pass through the continental crust without hydraulic pressure (Walker, 1989). These magmas accumulate at the Moho, where their latent heat of crystallisation is transferred to crustal rocks, leading to their partial melting (Fig. I.4). Within the MASH zone, basaltic magmas evolve through fractional crystallisation and mix with felsic crustal magmas, producing hybrid magmas of intermediate composition and leaving ultramafic to mafic cumulates in the lower crust (Hildreth and Moorbath, 1988).

The lower density of andesitic magmas allow them to ascend within the crust, where they accumulate in magma chambers at mid- to upper-crustal levels (~ 5–10 km depth; Fig. I.4) (e.g., Herzberg et al., 1983; Richards and Porter, 2005). This second level of accumulation forms large batholiths, which serve as the parent intrusions of porphyry systems. The progressive crystallisation of andesitic magmas leads to the exsolution of lower density bubbly magma and fluids. Their ascent within the overlying brittle rocks is channelled along narrow cylindrical or elliptical structures ($\leqslant$ 1 km wide), rising to the apex of the batholith and forming zones known as "cupolas". These are characterised by a complex superposition of dikes, granite stocks, breccia pipes, hydrothermal alteration, veins and stockworks typically formed at depths ranging from 1.5 to 4 km (Singer et al., 2008; Sillitoe, 2010) (Fig. I.5).

The formation of porphyry ore deposits requires the release of a significant volume of magmatic-hydrothermal fluids along these vertical structures over a relatively short period ($\leqslant$100,000 years; e.g., Arribas Jr et al., 1995; Shinohara and Hedenquist, 1997; Von Quadt et al., 2011; Weis et al., 2012; Mercer et al., 2015; Chelle-Michou et al., 2017; Li et al., 2017; Cernuschi et al., 2018) compared to the longevity of the parent batholith, which typically spans one to several million years (Matzel et al., 2006; Miller et al., 2007; Schaltegger et al., 2009; Paterson et al., 2011; Fiannacca et al., 2017). This implies the existence of a sudden mechanism for rapid and focused fluid exsolution. External triggers, such as sudden magma chamber depressurisation or seismic shaking, have been proposed to explain the significant devolatilisation

of large magma chambers (Richards, 2018). The explosive release of fluids at depth leads to the formation of preferential flow paths, initially marked by the development of breccia pipes and diatremes (Fig. I.5). These permeable structures are subsequently intruded by more slowly flowing bubbly magmas that crystallise as dykes or stocks, but also serve as pathways for metal-rich, magmatic fluids exsolved from the batholith (Sillitoe, 2010) (Fig. I.5).

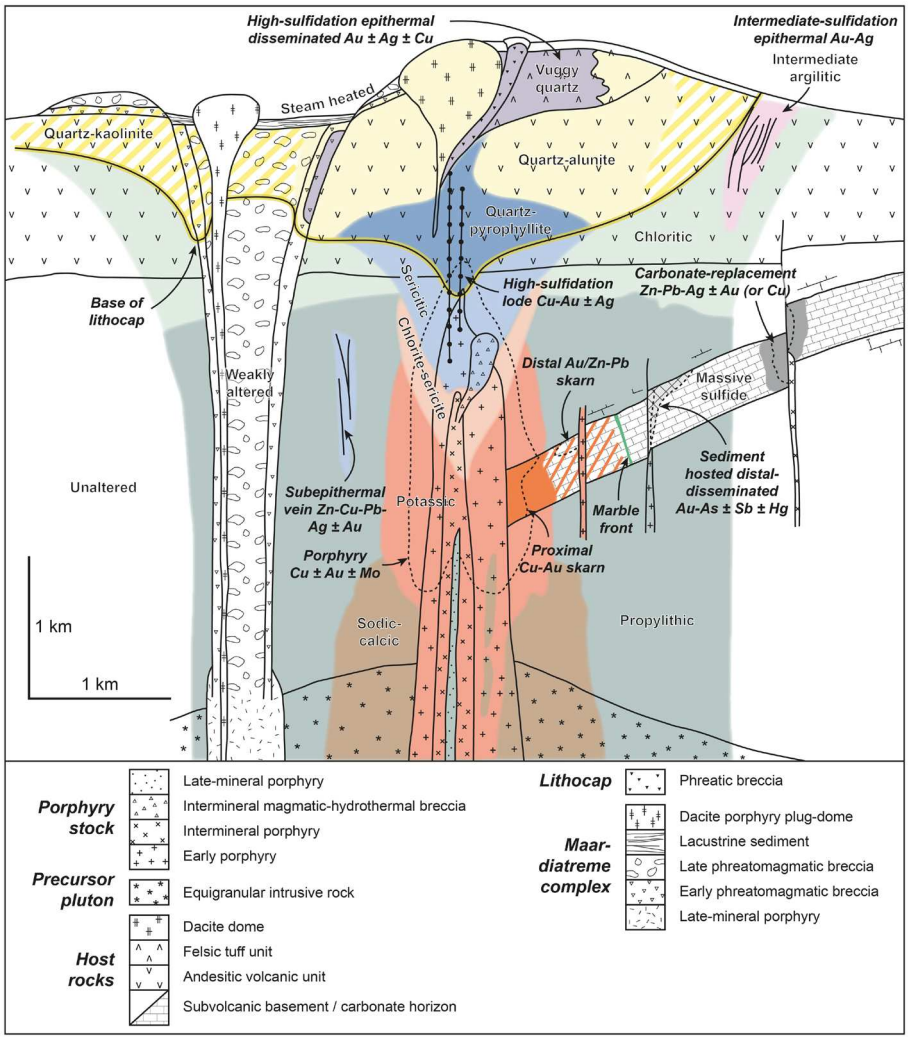



*Figure I.5. Schematic model of a telescoped porphyry Cu system showing spatial relationships between a central multiphase porphyry stock and its host rocks, as well as the generalised alteration-mineralisation zoning pattern (modified from Sillitoe, 2010).*

The convective circulation of these magmatic fluids around porphyry intrusions at temperatures ranging from over 700°C to below 250°C results in the alteration of significant volumes of rocks (10 to over 100 $km^3$) and the formation of mainly vein-type mineralisation (Sillitoe, 2010). Disseminated mineralisation may also occur within adjacent rocks, depending on their nature. The resulting alteration halo exhibits pronounced vertical and lateral zoning, reflecting both the progressive cooling of the system and the distance from the central intrusive stock (Sillitoe, 2010) (Fig. I.5). Porphyry systems are generally associated with a vertical alteration sequence from potassic at the base to chlorite-sericite, sericitic, and finally advanced

argillic at the lithocap. More distal specific alterations include propylitic alteration at depth and chloritic alteration in more superficial zones.

From 700 to 550 °C, magmatic fluids initiate potassic alteration, which constitutes the first phase of mineralisation and continues down to temperatures of *ca.* 350 °C (Sillitoe, 2010). This stage is associated with intense hydraulic fracturing processes, leading to the formation of quartz and Cu-Fe sulphide veins. Since porphyry deposits typically form at depths not exceeding 4 km, magmatic fluids typically circulate as two coexisting and immiscible phases: a predominant low-density, low-salinity vapour phase and a high-salinity liquid phase (Fournier, 1999). This two-phase fluid may have been directly exsolved from the silicate melt (Shinohara, 1994), although it more commonly forms through the phase separation of an initially homogeneous magmatic fluid (e.g., Henley and McNabb, 1978; Burnham, 1979a; Cline and Bodnar, 1991; Webster, 1992; Bodnar, 1995; Cline, 1995). Due to its lower density, the vapour phase separates from the high-salinity phase, migrates to the surface, and generates advanced argillic alteration in the lithocap. During the protracted potassic alteration, external fluids, mainly of meteoric origin, are also mobilised by the intrusions heat. Their circulation around the system induces peripheral propylitic alteration of the host rocks (Fig. I.5). The cooling of magmatic fluids upon contact with the host rocks and their dilution by mixing with meteoric fluids are considered to be key processes for the precipitation of Zn, Pb, Ag, and Mn (Hemley and Hunt, 1992).

As the parent magma chamber cools and crystallises, heat and fluid fluxes decrease within porphyry intrusions (Dilles, 1987; Shinohara and Hedenquist, 1997). At temperatures between 350 and 250 °C, exsolved fluids consist in single-phase, low to moderate salinity fluids (5–20 wt% NaCl eq; Shinohara and Hedenquist, 1997; Hedenquist et al., 1998). Their circulation within the system is controlled by pre-existing vein networks, faults, and permeable zones. This stage leads to the progressive development of chlorite-sericite and sericitic alterations, maintains advanced argillic alteration, and results in significant Cu and Au mineralisation in the overlying lithocaps (Fig. I.5). The cooling of the system causes a progressive deepening and superposition of alterations, locally redistributing copper within the deposit: sericitic alteration therefore partially overlies chlorite-sericite and potassic alteration zones, whereas potassic alteration zones are commonly partially to completely overprint by chlorite-sericite alteration.

Porphyry copper systems are connected in the subsurface to lower temperature ($<$ 300 °C) convective circulations dominated by meteoric fluids, which result in Au $\pm$ Ag $\pm$ Cu mineralisation (Figs. I.4 and I.5). These circulations are controlled by the high thermal gradient associated with the porphyry intrusions. Porphyry-epithermal deposits can consequently be divided into two zones: the deeper part of the system typically corresponds to Cu $\pm$ Mo $\pm$ Au porphyry mineralisation formed from the circulation of high-temperature ($\sim$ 250 to 700 °C) fluids exsolved from calc-alkaline magma, whereas the more superficial part commonly hosts

intermediate to high-sulfidation epithermal Au ± Ag ± Cu deposits originating from lower temperature (< 300 °C) circulation of a mixture between magmatic and meteoric fluids (Sillitoe, 2010; Richards, 2014).

### *1.2.2. Sn-W granite-related systems*

Tin and tungsten granite-related mineralisation constitutes the world's main resource for Sn and W. Their genesis is typically spatially associated with the emplacement of felsic magmas within the upper continental crust (~ 2–4 km) in late- to post-orogenic settings (Jébrak and Marcoux, 2008) (Fig. I.6). These intrusions consist in highly evolved magmas characterised by a significant enrichment in Sn, W, Be, Cs, F, B, Li, Rb, Ta, and U, and a pronounced depletion in Fe, Ti, Mg, Ca, Sr, Eu, Ba, and Zr (e.g., Stussi, 1989; Breiter et al., 2005; Lehmann, 2006). Over the years, a wide variety of Sn-W deposit types has been recognised, including greisen, quartz veins, skarn, and less commonly porphyry-type occurrences and pegmatites (Romer and Kroner, 2016). Their formation is influenced by multiple factors, notably the source and magmatic evolution of the granitic magmas, emplacement depth, the nature of the host rocks, local structural controls on melt and fluid pathways, and the evolution of fluids during late-stage magmatic processes or hydrothermal interaction between fluids and the host rocks.

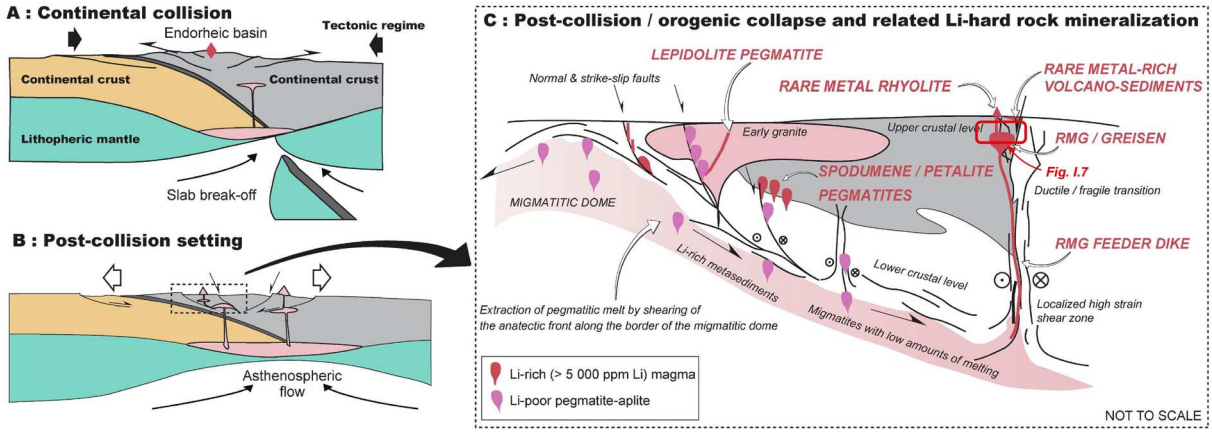



*Figure I.6 Continental collision (A) transitioning to a post-collision setting (B), which is conducive to the development of Sn-W greisen systems (modified from Gourcerol et al., 2019).*

Among Sn-W peri-granitic mineralisation, vein and greisen systems have been widely studied and are often referred to as Sn-W granite cupolas. Significant resources are found in several key metallogenic provinces, including Southeast China, the Southeast Asian belt, the Central Andean belt, the East Australian belt, the Mesoproterozoic Karagwe-Ankole belt, and the European Variscan belt (Ni et al., 2022). The Nanling region in southern China and the Variscan belt in Europe are particularly notable for their substantial contributions to global Sn and W production in recent decades. Well-known examples of Sn-W systems from these regions include the world-class Maoping and Piaotang W-Sn deposits from the Jiangxi province, China (e.g., Legros et al., 2018; Legros et al., 2019), the Cínovec (Zinnwald) granite cupola in the eastern segment of the

Krušné Hory/Erzgebirge, Czech Republic/Germany (e.g., Breiter et al., 2017), and the W-Sn(-Cu) Panasqueira ore deposit in the Central Iberian Zone, Portugal (e.g., Marignac et al., 2020; Launay et al., 2021; Fig. I.7). For instance, the Panasqueira mine has been active for *ca.* 130 years, producing a total of 76,000 metric tons of tungsten since 1934, thus making it the second largest W mine in Europe (Ni et al., 2022).

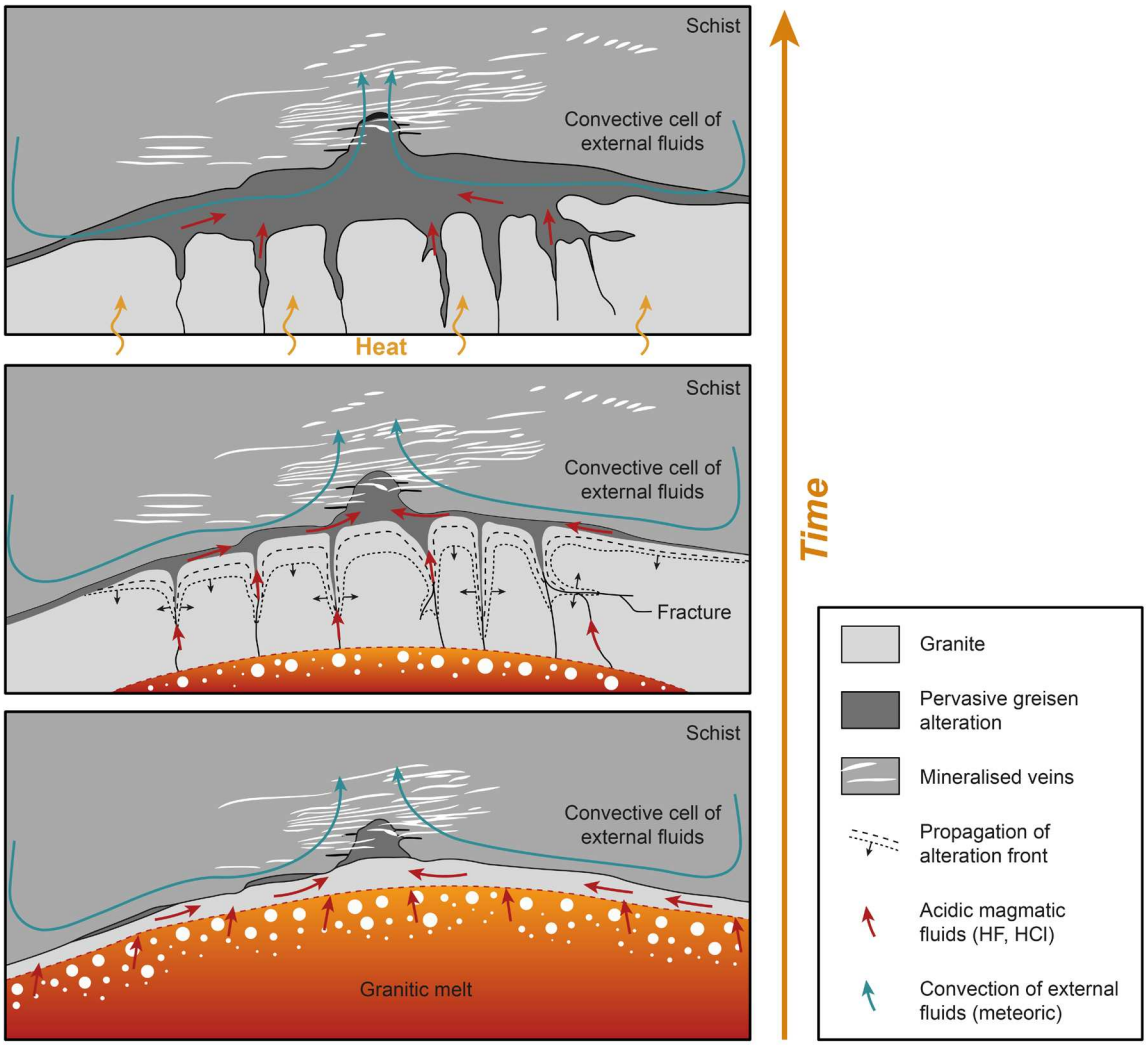



*Figure I.7. Conceptual time evolution of fluid circulation and greisen formation associated with granite crystallisation and cooling at Panasqueira, Portugal (modified from Launay et al., 2021).*

The term "cupola" is derived from the geometry of the mineralisation, which is focused at the apex of the felsic intrusion and characterised by the superposition of pervasive greisen alteration and quartz veins (Jébrak and Marcoux, 2008) (Fig. I.7). Mineralisation generally comprises wolframite ($(Fe,Mn)WO_4$) and cassiterite ($SnO_2$), which not only precipitate within centimetre- to metre-scale quartz veins, generally characterised by high grade and low tonnage, but also occur as dissemination in low-grade high-tonnage greisenised zones (e.g., Taylor, 1979; Lehmann, 1990; Mlynarczyk et al., 2003). The ultimate geometry of Sn-W mineralisation strongly depends on the structural environment, permeability conditions, and the ratio between lithostatic pressure and

fluid pressure resulting from magma degassing (Pollard et al., 1988; Jébrak and Marcoux, 2008; Launay et al., 2019).

Magmatic and hydrothermal processes are considered to play a crucial role in the genesis of Sn-W mineralisation within and around peraluminous granitic plutons (e.g., Burnham, 1979a; Candela, 1997; Audétat et al., 2000b; Xi et al., 2007; Legros et al., 2019; Ni et al., 2022). Despite the close temporal and spatial relationship existing between Sn-W vein and greisen deposits and felsic magmas, their genetic link remains debated (e.g., Marignac and Cathelineau, 2009; Ni et al., 2022 and references therein). Most genesis models recognise evolved granites as the primary source of metals in these systems, whereas metasedimentary host-rocks seem to have a more limited influence on the metal budget (e.g., Harlaux et al., 2018). However, the nature and origin of ore-forming fluids appear to be variable. Models typically involve the circulation of (i) high-salinity magmatic fluids exsolved from the granitic magma during its cooling and crystallisation (e.g., Reyf, 1997; Audétat et al., 2000b; Harlaux et al., 2018a; Korges et al., 2018; Launay et al., 2021), and/or (ii) external fluids of surficial or deep-seated origin, such as metamorphic, meteoric or mantle-derived fluids, characterised by variable volatile content and salinity, and equilibrated to varying degrees with the intrusion and its meta-sedimentary wall rocks (e.g., Smith et al., 1996; Bebout et al., 1999; Polya et al., 2000; Burnard and Polya, 2004; Minghai et al., 2007; Van Daele et al., 2018; Legros et al., 2019; Cathelineau et al., 2020) (Fig. I.7).

Oxygen fugacity ($fO_2$) and fluid acidity ($m_{HCl,aq}$) are known to have a profound influence on $SnO_2$ solubility in Cl-F-bearing magmatic fluids, with cassiterite precipitation ($Sn^{2+} \rightarrow Sn^{4+}$ transition) being favoured under oxidised and low-acidity conditions (Taylor and Wall, 1993). In Sn-W magmatic-hydrothermal ore systems, mixing dynamics between magmatic and oxidised meteoric fluids have been suggested by many authors as a key mechanism triggering cassiterite precipitation (Witt, 1988; Heinrich, 1990; Audétat et al., 1998; Karimzadeh Somarin and Ashley, 2004; Fekete et al., 2016; Liu et al., 2020; Harlaux et al., 2021; Chen et al., 2023; Peng et al., 2023a) (Fig. I.7). However, Liu et al. (2023) recently questioned the necessity of oxidising agents for cassiterite precipitation based on thermodynamic modeling, proposing that simple cooling can result in more oxidised mineralising fluids (e.g., transition from QFM to HM mineral buffers). Similarly, tungsten solubility in hydrothermal fluids depends on various parameters, and is mainly influenced by temperature, salinity, pH, oxygen fugacity and the activity of cationic precipitants (Fe, Mn) (Wood and Samson, 2000; Wang X.-S. et al., 2019). Several processes leading to physicochemical modifications of the ore-forming fluids and subsequent wolframite precipitation in quartz veins have been highlighted over the years. Fluid boiling following sudden depressurisation, fluid immiscibility, fluid–rock interactions, and simple cooling represent the most prevailing mechanisms responsible for large-scale wolframite precipitation, whereas meteoric water incursion does not appear to be effective (Ni et al., 2022 and references therein).

### 1.3. Greisen and albitic alterations: key metasomatic processes in granitic systems

The type and intensity of alteration can vary widely among magmatic-hydrothermal systems – ranging from potassic, propylitic, chlorite-sericite, sericitic and advanced argillic alterations typical of porphyry and epithermal systems, as discussed above, to greisenisation processes in Sn-W systems. In PRMGs and LCT pegmatites, greisen and albitic alterations are particularly prevalent, significantly influencing their mineralogical and geochemical evolution.

Greisenisation, as defined by Shcherba (1970), refers to a high-temperature, post-magmatic alteration of rocks involving volatile-rich fluids, and associated with the cooling of granitic intrusions. The development of greisen systems is typically associated with the intrusion, at upper crustal levels (~ 3 to 5 km), of felsic and highly differentiated granitic melts, strongly enriched in volatiles, fluxing and lithophile elements (e.g., Li, F, B, Be, Nb, Ta, Sn, W, U, and Mo) (Pirajno, 1992; Černý et al., 2005). The complex late- to post-magmatic metasomatic processes involved during greisenisation result in significant mineralogical, chemical and textural changes in both the intrusion itself and the surrounding rocks. This alteration predominantly affects the apical part of the intrusion (Fig. I.8), known as the "granitic cupola", as previously mentioned for Sn-W greisen and vein mineralisation (section 1.2.2).

An alternative definition of greisenisation, based on mineralogical characterisation, was proposed by Burt (1981). He described greisenisation as "hydrothermally altered granitic rock composed of a mixture of quartz and mica (typically lithian), with varying amounts of topaz, tourmaline, fluorite, or other minerals rich in fluorine (F) or boron (B)". The term "greisen" itself is derived from Cornish mining terminology, designating a coarse-grained assemblage primarily of quartz-muscovite replacing igneous minerals of the granite, with varying amounts of other distinctive minerals, including topaz, tourmaline, fluorite, oxide minerals (cassiterite, wolframite, hematite), scheelite, sulphides of Fe, Cu, Mo, Bi, and Cu-Bi-Pb sulphosalts (Pirajno, 2009).

The physicochemical processes involved in greisenisation are not yet fully understood, although some systematics have been highlighted over the years. The earliest stage of greisen alteration is generally associated with Na-feldspathisation or albitisation, resulting from the enrichment of the residual melt in Na and F and the exsolution of hyper-alkaline magmatic fluids (Pollard, 1983). The circulation of these fluids throughout the granitic intrusion is accompanied by replacement reactions of K-feldspar and Ca-bearing plagioclase into albite (Table I.1). Due to the progressive decrease in the alkali/$H^+$ ratio of the system during albitisation, Na metasomatism is commonly followed by acidic alteration, which induces the destabilisation of K-feldspar, plagioclase (including albite) and biotite and their replacement by quartz and muscovite (i.e. greisenisation; Table I.1). Greisen-forming reactions release silica, which precipitates to form granular quartz aggregates, quartz flooding, and veins (i.e., silicification). Although albitisation typically precedes greisenisation, the latter process releases $Na^+$ (and $K^+$) back into the fluids,

thereby increasing the alkali/$H^+$ ratio once more. Consequently, a second generation of albitite, formed as a result of greisenisation, is commonly described (e.g., Štemprok, 1987; Schwartz and Surjono, 1990; Pirajno, 2009; Launay et al., 2019). Greisenisation and albitisation thus constitute a self-sustaining chemical system, which can result in multiple successive generations of albitite and greisen (Ballouard et al., 2020a).

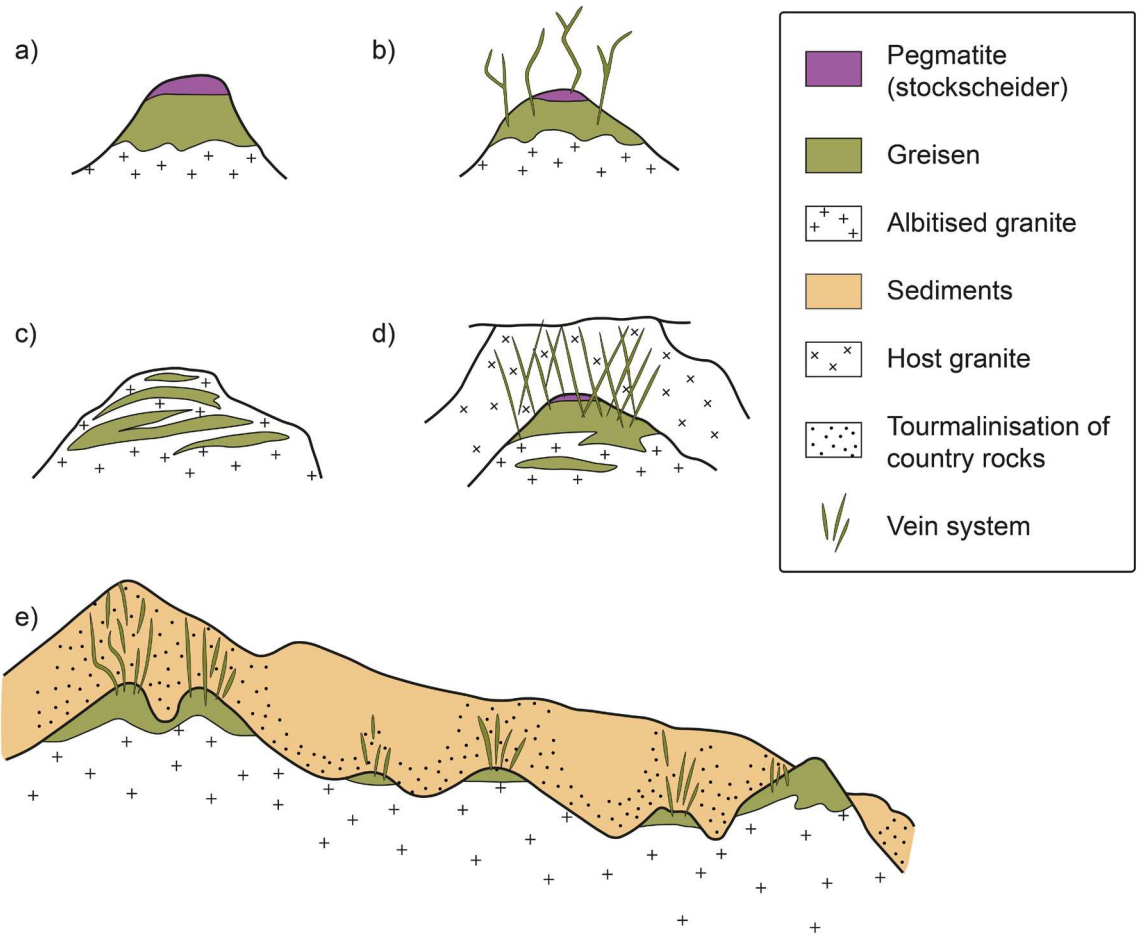



*Figure I.8. Representation of morphological types of greisen systems (modified from Pirajno, 2009). Greisen systems typically range between two end-members: (i) closed systems or endogreisens, where fluid circulation remains within the granite, leading to pervasive alteration, as illustrated in figures a and c; (ii) open systems or exogreisens, where fracturing of the overlying host rocks channels fluids beyond the intrusion. Most greisen systems lie between these extremes, combining pervasive alteration with structures such as veins, pipes, lodes, and breccias that extend into the surrounding rocks, as illustrated in figures b, d and e.*

Greisenisation might be further complicated in mineralised systems, in which there is introduction of B, F, and Li into the fluids due to the destabilisation of minerals bearing these elements (Burt, 1981; Pollard et al., 1987). For instance, in F-rich systems, the increase in the $H_2O$ activity during cooling of greisenising fluids result in the destabilisation of topaz and feldspars, releasing HF and triggering the precipitation of quartz and muscovite. Metals released into the fluid phase through destabilisation of igneous minerals would form complexes with F, enabling their subsequent transport upward within the evolving system. The nature of secondary

minerals precipitating in association with the typical greisen-related quartz-muscovite assemblage depends thus on the chemistry of the initial granitic intrusion. F-rich systems manifest the precipitation of fluorite and/or topaz, as well as Li-rich micas (e.g. lepidolite or zinnwaldite), whereas B-rich greisen systems are distinguished by abundant tourmaline.

*Table I.1. Summary of the main replacement reactions occurring during greisenisation and albitisation (Pirajno, 1992; Launay et al., 2019; Ballouard et al., 2020a)*

| | |
|---|---|
| ***Greisenisation*** | |
| (R1) | $3\,KAlSi_3O_8 + 2\,H^+_{aq} = KAl_3Si_3O_{10}(OH)_2 + 6\,SiO_2 + 2\,K^+_{aq}$<br>K-feldspar + acidic aqueous phase = muscovite + quartz + K-rich aqueous phase |
| (R2) | $3\,NaAlSi_3O_8 + 2\,H^+_{aq} + K^+_{aq} = KAl_3Si_3O_{10}(OH)_2 + 6\,SiO_2 + 3\,Na^+_{aq}$<br>Albite + acidic and K-rich aqueous phase = muscovite + quartz + Na-rich aqueous phase |
| (R3) | $3\,CaAl_2Si_2O_8 + 4\,H^+_{aq} + 2\,K^+_{aq} = 2\,KAl_3Si_3O_{10}(OH)_2 + 3\,Ca^{2+}_{aq}$<br>Anorthite + acidic and K-rich aqueous phase = muscovite + Ca-rich aqueous phase |
| (R4) | $3\,KFe_3AlSi_3O_{10}(OH)_2 + 2\,H^+_{aq} = KAl_3Si_3O_{10}(OH)_2 + 6\,SiO_2 + 3\,Fe_3O_4 + 2\,K^+_{aq} + 3\,H_{2\,aq}$<br>Biotite + acidic aqueous phase = muscovite + quartz + Fe-oxide mineral + K-rich aqueous phase |
| ***Albitisation*** | |
| (R5) | $KAlSi_3O_8 + Na^+_{aq} = NaAlSi_3O_8 + K^+_{aq}$<br>K-feldspar + Na-rich aqueous phase = albite + K-rich aqueous phase |
| (R6) | $CaAl_2Si_2O_8 + 4\,SiO_2 + 2\,Na^+_{aq} = 2\,NaAlSi_3O_8 + Ca^{2+}_{aq}$<br>Anorthite + quartz + Na-rich aqueous phase = albite + Ca-rich aqueous phase |

Hydrothermal fluids involved during greisen alteration are presumed to be acidic and moderately saline (*ca.* 3–10 wt% NaCl eq) magmatic fluids circulating at temperatures of 200–500 °C and pressures ranging from 50 to 250 MPa (e.g., Burt, 1981; Štemprok, 1987; Shepherd et al., 1985; Taylor, 1988; Schwartz and Surjono, 1990; Halter et al., 1998; Dobeš, 2005; Monnier et al., 2020). According to Štemprok (1987), greisenising fluids are believed to originate from the deeper parts of the granitic intrusion, thereby accounting for the typical presence of greisen zones intersecting the latest magmatic units as fracture networks. Furthermore, the contribution of external fluids, especially of meteoric origin, has been highlighted in many systems (e.g., Witt, 1988; Cuney et al., 1992 ; Bettencourt et al., 2005), and are presumed to play a major role in ore deposition, especially in triggering cassiterite precipitation (see section 1.2.2 on Sn-W granite-related systems).

The geometry of greisen systems presents two end-members: (i) a closed system or endogreisen, where the circulation of greisenising fluids is contained within the granitic mass, mostly leading to pervasive alteration; (ii) an open system or exogreisen, characterised by fracturing of the overlying host rocks, which channels fluids outside the intrusion (Pirajno, 2009; Černý et al., 2005). Most greisen systems exhibit characteristics that fall between these two end-

members, often showing a combination of pervasive alteration with structures such as veins, pipes, lodes, and breccias that extend into the surrounding rocks (Fig. I.8). The ultimate geometry of greisen systems, and consequently the location of mineralisation, depends on numerous parameters, including regional constraints, stress regimes generated by magma emplacement and crystallisation, the creation of porosity and permeability, as well as the intrusion depth and geometry (e.g., Černý et al., 2005; Eldursi et al., 2009; Launay et al., 2019, 2021). Replacement reactions involved during greisenisation and albitisation lead to a progressive increase in porosity and permeability, which further enhances both process and causes the local development of large greisens at the tops of plutons (Launay et al., 2019, 2021). The creation of permeability facilitates magmatic fluids exsolution, which tend to concentrate at the apical part of the intrusion, generating overpressure and subsequent fracturing. In the strict sense, the term "greisen" refers to a zone enriched in muscovite and characterised by significant porosity, whereas quartz-rich greisens formed following the filling of porosity by subsequent circulation of fluids enriched in silica.

## 2. Peraluminous rare-metal granites

### 2.1. Definition and classification of rare-metal granites

Rare elements, commonly referred to as rare metals, encompass high field strength elements (HFSE) such as Nb, Ta, W and Zr; the rare earth elements (REE) along with Y; large elements like Cs and Sn; as well as small and low-valence elements such as Li and Be (Ballouard et al., 2020a). Due to their size and/or charge, these elements do not readily incorporate into most common rock-forming minerals, exhibiting incompatible behaviour that promotes their concentration in silicate melts through processes like small degrees of partial melting or high degrees of fractional crystallisation (Pollard, 1995; Linnen and Cuney, 2005).

Rare-metal granites (RMGs) result from the crystallisation of highly evolved magmas within the upper continental crust (UCC) across diverse geological settings. The geodynamic context, especially the nature of the magma source, strongly influences their chemical and mineralogical characteristics. Several classifications have been proposed in the literature, with some identifying up to eight distinct RMGs types (Beus, 1982). Linnen and Cuney (2005) present a simplified classification based on specific geochemical and mineralogical features, categorising RMGs into three main types: (i) peralkaline (PLK-RMGs); (ii) metaluminous to low-phosphorus peraluminous (PLP-RMGs); and (iii) high-phosphorus peraluminous (PHP-RMGs) (Fig. I.9).

**(i)** **Peralkaline RMGs** are defined by alumina saturation index (ASI) and A/NK values both below 1. The ASI, also referred to as A/CNK, represents the molar ratio of $Al_2O_3$ to [CaO+$Na_2O$+$K_2O$], while A/NK corresponds to the molar ratio of $Al_2O_3$ to [$Na_2O$+$K_2O$]. PLK-RMGs are characterised by significant concentrations of F, REEs, Y, Zr, and Nb, with

typically high Nb/Ta and Zr/Hf ratios. They also exhibit enrichment in Th, Sn, Be, Rb, Fe, and U, while Li is present to a lesser extent, ranging from hundreds to several thousand ppm. Their notable enrichment in Zr and Th distinguishes them from other RMGs. Moreover, PLK-RMGs display low phosphorus contents. They typically occur in anorogenic tectonic settings and are widely acknowledged to derive from low-degree melting of metasomatised mantle or juvenile crust, followed by extreme fractional crystallisation. Disseminated mineralisation of Zr (zircon, zirconosilicates), Nb (pyrochlore), and REEs (fluorcarbonates) are commonly observed.

(ii) **Metaluminous (A/NK > 1 and A/CNK < 1) to low-phosphorus peraluminous (A/CNK > 1) RMGs** are enriched in REEs, Y, Zr, Hf, Th, and Pb. Their chondrite-normalised REE patterns are generally flat, with a pronounced negative Eu anomaly. The Nb/Ta and Zr/Hf ratios are relatively low, particularly in comparison to those observed in PLK-RMGs. These RMGs can form in both anorogenic and orogenic contexts, typically through the melting of an igneous protolith, and can thus be associated with I- and A-type granites (White and Chappell, 1977). They are commonly classified as high-K calc-alkaline rocks and are believed to originate from the melting of intermediate to mafic rocks, with varying contributions from pelitic material. The disseminated mineralisation they host essentially consists of columbite-group minerals (Nb-Ta), cassiterite (Sn), with zinnwaldite (Li-Fe) being also commonly encountered.

(iii) **High-phosphorus peraluminous RMGs (A/CNK > 1.15)** exhibit highly distinctive geochemical signatures, most notably extreme enrichment in volatile and fluxing elements (F, Li, P and/or B), which lowers the granite's solidus temperatures, decreases magma viscosity, and facilitates magma ascent (Bartels et al., 2011, 2013). They are also distinguished by extremely low concentrations of REEs, comparable to chondritic abundances, as well as low contents of Y, Zr, Hf, Th, Sc, and Pb. In contrast, they exhibit high contents of Cs and Rb, along with variable enrichments of Sn, W, Nb, Ta, and Be. Their Zr/Hf and Nb/Ta ratios are generally extremely low. As PHP-RMGs form through the partial melting of dominantly metasedimentary protoliths, they can be associated with S-type granites as described by White and Chappell (1977), and more precisely large, strongly peraluminous, muscovite-biotite-bearing leucogranites. Disseminated mineralisation of Sn, Nb, Ta, and Li is commonly present in PHP-RMGs, occurring as columbite-group minerals (Nb-Ta), pyrochlore-group minerals (Nb-Ta-U), cassiterite (Sn), lepidolite (Li), and lithium-rich phosphates from the amblygonite-montebrasite solid solution. This mineralisation is primarily thought to derive from purely magmatic processes (e.g., Kovalenko et al., 1970; Groves and McCarthy, 1978; Pichavant, 2022), yet processes leading to metal enrichment and deposition in peraluminous rare-metal granites are still debated and further discussed in section 2.2 (Part I).

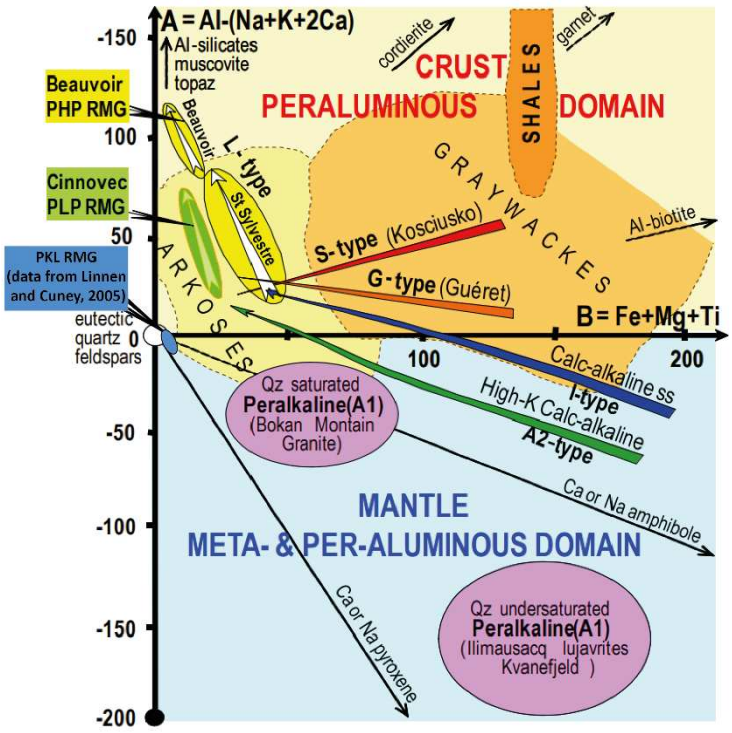



*Figure I.9. Mineralogical-chemical diagram for the classification of major types of magmas: Alumina saturation index (A) versus differentiation index (B) (modified from Cuney, 2014 & Cuney and Marignac, 2015).*

Peraluminous rare-metal magmatism manifests in diverse forms depending on geological and tectonic environments, occurring both as plutonic bodies such as rare-metal granites and pegmatites, and as volcanic to subvolcanic equivalents like rhyolites, macusanites, or ongonites. PRMGs are referred to by numerous terms in the literature, including tin granites, topaz granites, topaz-lepidolite-albite granites, zinnwaldite granites, and Li-F granites. They formed during various geological periods, typically as the final magmatic units emplaced during late-orogenic granitic magmatism (Kovalenko et al., 1970; Linnen, 1998; Linnen and Cuney, 2005) and are documented across the globe. Non-exhaustive examples include the Proterozoic Kymi topaz-bearing stock in Finland (Haapala and Lukkari, 2005), the Neoproterozoic Abu Dabbab RMG in Egypt (Zoheir et al., 2020), the Cambrian Tin-Amzi granite in Algeria (Kesraoui and Nedjari, 2002), and RMGs of the Limu district in China that were emplaced from the Jurassic to early Cretaceous (Belkasmi et al., 2000; Zhu et al., 2001; Peng et al., 2023a). In Western Europe, the late evolution of the Variscan orogeny is characterised by a significant phase of rare-metal magmatism, exemplified by the emplacement at the end of the Carboniferous of the Beauvoir RMG (France, Cuney et al., 1992), the Argemela RMG (Portugal, Michaud and Pichavant, 2020), and the Cínovec/Zinnwald Sn-W-Li deposit (Czech Republic/Germany, Breiter et al., 2017).

Traditional models propose that pegmatites form through extreme magmatic fractionation of pluton-sized batches of granitic magma, leading to pegmatite fields that extend around a central

parent granitic body (Černý, 1991; Černý and Ercit, 2005; London, 2014). Rare-metal pegmatites (RMPs) represent a specific group of pegmatites characterised by elevated concentrations of alkali and HFSE, as well as B and P. The primary distinction between granites and pegmatites is textural, reflecting different cooling regimes and processes at their emplacement depth, rather than differences in origin or magma source. Nevertheless, this distinction has resulted in contrasting classification schemes, with RMPs commonly classified into LCT-type, NYF-type, and mixed-type pegmatites (Černý and Ercit, 2005; Černý et al., 2012). Lithium-cesium-tantalum (LCT) pegmatites display a chemical composition similar to highly peraluminous RMGs, characterised by extreme enrichment mostly in lithophile metals and halogens (e.g., Li, F, Ta, Nb, Sn, W, and Be; Černý and Ercit, 2005; Černý et al., 2012). The genetic relation between peraluminous RMGs (S-type or evolved I-type) and LCT pegmatites being well-established (e.g., London, 2005), the following discussion encompasses both rare-metal deposits.

### 2.2. Genesis models for highly evolved peraluminous rare-metal deposits

Historically, the geological processes involved in the formation of highly evolved peraluminous granites and pegmatites, and more broadly rare-metal granites and pegmatites (RMGPs), have been subject of debate, particularly regarding the relative contribution of magmatic *vs.* post-magmatic or hydrothermal processes. Teuscher (1936) first suggested that the pervasive alteration of an original biotite granite by co-magmatic hydrothermal fluids resulted in the formation of a topaz- and Li-micas-bearing granite in the western Erzgebirge. This theory gained limited acceptance, whereas the albitisation model proposed by Beus et al. (1962) in the Lake Baikal region (Russia) became a central concept in discussions on granite-related mineralisation for decades. They posited that sodium, transported by hydrothermal fluids from the root zones of plutons to their apical parts, would transform the primary oligoclase and portions of K-feldspar into albite. The genesis of RMGs was then believed to derive from the upward movement of post-magmatic fluids leaching metals from the deeper parts of the intrusion and concentrating them in the apical zone (Beus et al., 1962; Beus and Zalashkova, 1964; Zalashkova and Sitnin, 1967; Hu, 1984). In contrast to this metasomatic hypothesis, many authors maintained that the observed characteristics of rare-metal deposits could entirely derive from purely magmatic processes, such as partial melting and fractional crystallisation, with only limited redistribution during late- to post-magmatic fluid-rock interactions (Kovalenko et al., 1970; Kovalenko and Kovalenko, 1976; Groves and McCarthy, 1978). This model is supported by the occurrence of hypabyssal to volcanic analogues of rare-metal granitic plutons (Kovalenko and Kovalenko, 1976; Pichavant et al., 1987a, 1988; Raimbault and Burnol, 1998), melt inclusion studies on peraluminous pegmatites (Webster et al., 1997; Thomas and Webster, 2000), and experimental research (Linnen and Cuney, 2005; Pichavant, 2022). Additionally, a recent study demonstrated that Li-F-rich RMGPs could form from the melting of felsic meta-igneous rocks, followed by

magmatic differentiation, highlighting the importance of crustal recycling processes (Ballouard et al., 2023).

Beyond the key role of magmatic processes in metal enrichment and deposition within RMGPs (e.g., Pichavant, 2022; Ballouard et al., 2023), it has also long been recognised that metasomatism, expressed as albitisation and greisenisation, typically affects rare-metal deposits, resulting in significant mineralogical and geochemical modifications of the ore-bearing mineral assemblage (e.g., Černý, 1986; Schwartz and Surjono, 1990; Schwartz, 1992). Metasomatic processes typically involve the circulation of a magmatic volatile phase (MVP), commonly referred to as magmatic fluids. These fluids, exsolved from the melt during its cooling and crystallisation, may exist in various forms, including a supercritical fluid, low-density aqueous vapour, high-density and salinity liquid (potentially hypersaline), or vapour coexisting with liquid (e.g., Burnham, 1979b; Russell et al., 1995; Candela, 1997; Webster et al., 2009). Albitisation is thought to be driven by interactions between highly fluxed melts or solute-rich MVP and crystals under near-solidus conditions, where the metasomatic medium may significantly participate in the transport and concentration of metals such as Li, Nb, and Ta (e.g., Badanina et al., 2004; Müller et al., 2018b; Kaeter et al., 2018; Ballouard et al., 2020a; Pfister et al., 2023). Greisenisation is typically associated with the circulation of acidic and moderately saline magmatic fluids (*ca.* 3–10 wt.% NaCl eq) at temperatures between 200–500 °C (e.g., Burt, 1981; Štemprok, 1987; Shepherd et al., 1985; Taylor, 1988; Schwartz and Surjono, 1990; Halter et al., 1998; Dobeš, 2005; Monnier et al., 2020), although external fluids, especially meteoric water, have also been proposed as contributing agents in several systems (e.g., Witt, 1988; Cuney et al., 1992; Bettencourt et al., 2005). The temporal and genetic connection between greisen alteration and hydrothermal Sn-W mineralisation under sub-solidus conditions is well established (e.g., Breiter et al., 2017; Monnier et al., 2020, 2021; Launay et al., 2021). Furthermore, in rare cases, interactions between the melt and external fluids have been suggested as essential to trigger metal precipitation (London et al., 1996; Linnen et al., 2019; McNeil et al., 2020). Recent research proposed a substantial contribution from external fluids to the Fe and Mn content of columbite-group minerals (Linnen et al., 2019). In the case of the Beauvoir PRMG, fluid circulation of meteoric origin at supra-solidus conditions was suspected to influence the crystallisation of columbite- and pyrochlore-group minerals, particularly in the most evolved magmatic unit (Ohnenstetter and Piantone, 1988; Fouillac and Rossi, 1991).

To summarise, even though highly evolved melts have been recognised as the primary source of metals, purely magmatic models appear incomplete without considering the significant role of magmatic fluid exsolution (or hydrosaline melt immiscibility), along with subsequent fluid-rock interactions (e.g., Raimbault et al., 1995; Thomas et al., 2011; Badanina et al., 2015; Ballouard et al., 2016, 2020a; Araujo et al., 2023; Pfister et al., 2023; Putzolu et al., 2024), and to a lesser

extent, interactions between melt and external fluids (Fouillac and Rossi, 1991; London et al., 1996; Linnen et al., 2019; McNeil et al., 2020), in the genesis of RMGPs.

### 2.3. PRMGs geometry, emplacement and textural features

Peraluminous rare-metal granites consist of relatively small intrusions, with volumes generally not exceeding a few cubic kilometres, and are typically emplaced at shallow depths within the continental crust (around 1–3 km deep; Müller et al., 2002a; Linnen and Cuney, 2005). Their geometry is variable, with occurrences as isolated, elongated, sub-vertical intrusions such as the Beauvoir granite (Cuney et al., 1992), dykes like the Richemont (Raimbault and Burnol, 1998) and Tréguennec (Chauris, 1988) dykes, or granite sheets, as documented in certain parts of the Montebras granite (Aubert, 1969). Research on the structural factors influencing the emplacement, mechanical properties, and characteristic geometries of PRMGs remains relatively limited, with studies such as that of the Beauvoir granite (Cuney and Autran, 1987), the Panasqueira deposit (Jacques et al., 2018) and the Argemela mineralised area (Michaud et al., 2020) being notable exceptions. Given the unique chemistry of PRMGs, characterised by high levels of fluxing elements, these magmas are expected to exhibit both low intrusion temperatures and anomalously fluid-like behaviour. Such properties may influence the emplacement mechanisms and lead to distinctive geometries across RMGs. In the case of the Beauvoir granite, the study of magmatic layering provides evidence for the formation of a pull-apart structure resulting from sinistral shearing oriented N060°, facilitating magma ascent within the upper continental crust (Jacquot and Gagny, 1985; Gagny and Jacquot, 1987). The Beauvoir intrusion is interpreted as the result of the stacking of successive magma batches, filling the space generated by the pull-apart opening with a predominantly northward-directed flow (Bouchez et al., 1987; Jacquot, 1987; Jacquot and Gagny, 1987). Detailed descriptions of the main magmatic units are provided in section 3.3.

Several specific textural features can be observed in PRMGs. One prominent feature is a specific facies known as "stockscheider," which typically occurs at the upper contact of PRMGs with surrounding host rocks (Jarchovský, 1962; Linnen and Cuney, 2005). This border facies is defined by unidirectional crystallisation textures (UST), where minerals grow perpendicular to the contact plane. These textures are typically composed of pegmatitic, or "plumose" feldspars that extend downward from the roof of the final granite injection into an aplitic matrix. The development of stockscheider reflects the effects of magma interactions with the cooler surrounding rocks and the accumulation of exsolved volatiles at the top of the intrusion, both of which influence crystallisation processes (e.g., Breiter et al., 2005). Another notable texture observed in PRMGs is the occurrence of "snowball" quartz phenocrysts (Schwartz, 1992; Müller and Seltmann, 1999). These phenocrysts contains small albite crystals, and less commonly lepidolite, arranged concentrically along their growth planes. This texture is thought to result

from crystallisation within a fluid-enriched, residual environment (Müller and Seltmann, 1999; Müller et al., 2002a; Wang X.-R. et al., 2019).

## 3. The Beauvoir PRMG in the European Variscan belt

### 3.1. The Variscan orogeny

The Variscan belt, also referred to as the Hercynian belt, is a segment of a broader orogenic system extending over more than 10,000 km from Middle America to Eastern Europe, known as the Ouachita-Alleghanian-Variscan orogen (Matte, 1991; Nance and Linnemann, 2008). This orogen developed during the Paleozoic through the collision between the major paleocontinents Gondwana to the south and Laurussia (i.e., Laurentia-Baltica-Avalonia) to the north, along with several intervening microcontinents of peri- (or north-) Gondwanan origin, such as Armorica, Saxo-Thuringia, Barrandia and Brunia in Western and Central Europe (Matte, 1991; Robardet, 2002; Nance and Linnemann, 2008; Kroner and Romer, 2013) (Fig. I.10). It ultimately resulted in the formation of the Pangea supercontinent (Tait et al., 2000; Nance and Linnemann, 2008). The tectonic drifting and accretion of the distinct continental domains were linked to the opening and closing of several oceanic basins, including the Iapetus, Rheic, and Middle European Oceans and the Tornquist Sea (Vanderhaeghe et al., 2020) (Fig. I.10). However, the precise number of oceanic sutures, their locations, and the initial dimensions of the associated basins remain debated (Vanderhaeghe et al., 2020).

Due to its central role in the formation of the Ouachita-Alleghanian-Variscan orogen and the assembly of Pangea, the Rheic Ocean is recognised as one of the most important oceans of the Paleozoic (e.g., Nance and Linnemann, 2008). Its opening, initiated in the Early Ordovician (*ca.* 490-480 Ma), followed an extended period of rifting and was marked by the separation of several Neoproterozoic arc terranes from the northern margin of Gondwana (Nance et al., 2009). The microcontinental terranes that separated (e.g., Avalonia, Ganderia, Carolinia, Meguma) were largely the same terranes that had accreted to Gondwana's northern margin during the Late Neoproterozoic, leading Murphy et al. (2006) to suggest that this separation occurred along a former Neoproterozoic suture.

The opening of the Rheic Ocean closely followed the onset of subduction of the older Iapetus Ocean during the Cambrian (*ca.* 510 Ma; Van Staal et al., 1998). Forces driving the fast spreading of the Rheic Ocean were then attributed either to slab pull from the northward subducting Iapetus Ocean (Murphy et al., 2006) or to roll-back of a southward subducting slab beneath the Gondwana margin (Martínez Catalán et al., 2009). From the Cambrian to the Silurian, subduction of the Iapetus Ocean is associated with the northward drifting of Avalonia-Carolinia towards Baltica and Laurentia. Small continental blocks typically designated as "peri-Gondwanan" (e.g., Avalonia, Ganderia, and Meguma) were progressively accreted to Laurentia,

leading to the formation of an expanded continent known as "composite Laurentia" (Waldron et al., 2022). Avalonia and Baltica were also amalgamated along the Thor Suture in the Late Ordovician, in connection with the closure of the Tornquist Sea (Torsvik and Rehnström, 2003) (Fig. I.10). By the Silurian, the Rheic Ocean had expanded to over 4,000 km, while the closure of the Iapetus Ocean led to the accretion of "composite Laurentia" and Baltica, resulting in the formation of the Appalachian Mountains in North America and the Caledonian Mountains in Scotland and Scandinavia (e.g., Nance and Linnemann, 2008). The Early Devonian marked the onset of the Rheic Ocean's closure, as it began subducting beneath both Baltica and the northwestern margin of Gondwana. By the Mississippian, the closure of the Rheic Ocean was largely complete with the collision of Gondwana and Laurussia, a process that persisted into the Early Permian (Nance and Linnemann, 2008).

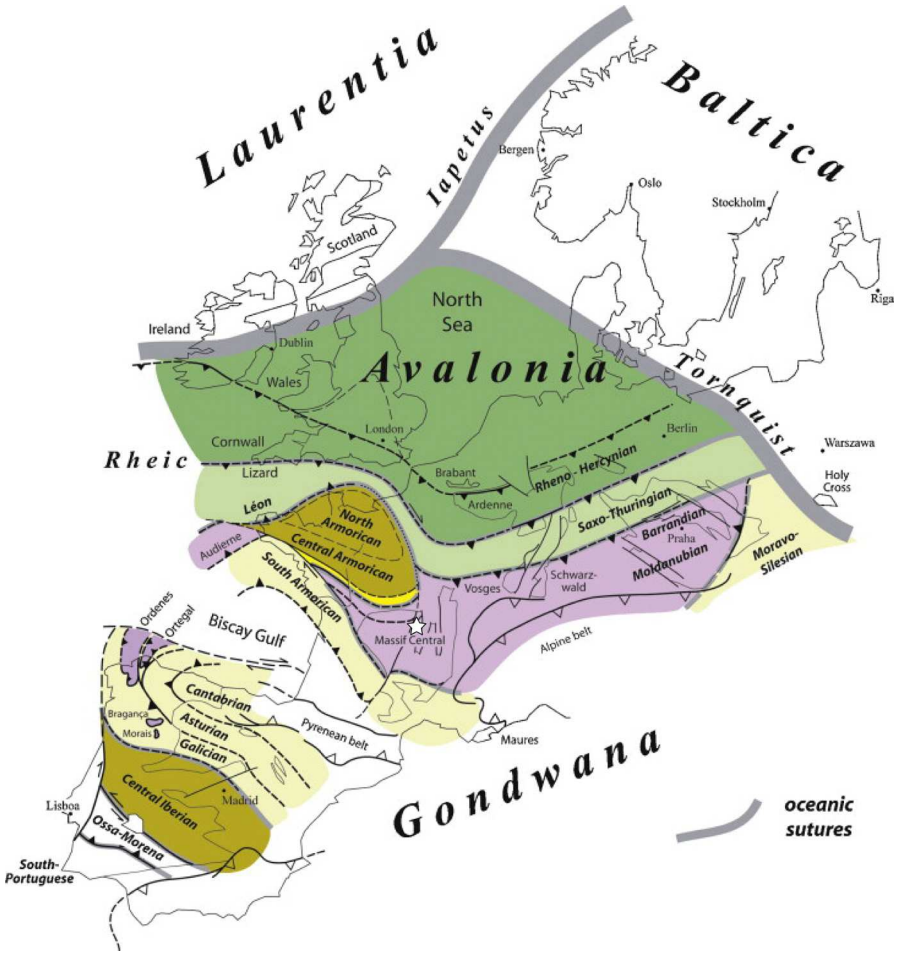



*Figure I.10. Localisation of major domains involved in the Variscan orogeny in Western Europe (modified from Ballèvre et al., 2009). Various colours are used to address nomenclature issues and to highlight potential correlations between certain zones. The location of the Echassières granitic complex is indicated by the white star.*

Spanning from the Late Devonian to the Early Carboniferous (*ca.* 380 to 290 Ma; Matte, 1986; Ballèvre et al., 2014), the Variscan orogeny represents the European manifestation of the evolution of the Pangea supercontinent. It primarily resulted from the tectonic accretion of the Avalonia and Armorica ribbon-shaped continental terranes, following the subduction of the Rheic

Ocean (Vanderhaeghe et al., 2020) (Fig. I.10). The consequent orogenic belt extends from the Iberian Peninsula in the west, through France, Germany, Czech Republic, and into Poland and the Balkans, reaching as far as North Africa. In Western and Central Europe, the closure of a third ocean, in addition to the Iapetus and Rheic Oceans, played a significant role in the Variscan orogeny. This ocean – or the associated suture – has been referred to by various names in the literature (Ballèvre et al., 2013). It has been called the Galicia-Massif Central Ocean (Matte, 1986, 1991), the Medio-European Ocean (Faure et al., 1997), the Galicia-Brittany Suture (Matte, 2001), and the Galicia-Brittany-Massif Central Suture (Matte, 2007). The Medio-European Ocean opened in the Early Ordovician, separating the Armorica-Barrandia continental block from the northern margin of Gondwana (Fig. I.10), and began to close in the Late Silurian due to the northward subduction of the Gondwana margin. In the Devonian, Armorica was then bounded by subducting zones with opposite vergence, leading to the formation of the Variscan belt, whose front progressed from the hinterland to the foreland throughout the Carboniferous (e.g., Vanderhaeghe et al., 2020). Consequently, the Variscan orogeny is characterised by three oceanic sutures: (i) the Iapetus-Tornquist suture north of Avalonia, (ii) the Rheic suture between Avalonia and Armorica, and the Middle European suture between Armorica and Gondwana (Vanderhaeghe et al., 2020) (Fig. I.10).

### 3.2. Regional geology of the French Massif Central

The French Massif Central (FMC) belongs to the internal zone of the Variscan belt, referred to as the "Moldanubian" zone (Lardeaux et al., 2014), and represents one of the most prominent exposures of this orogen in Western Europe (Fig. I.11). It consists of a reworked crustal domain, originally formed along the northern margin of Gondwana (Faure et al., 2009; Melleton et al., 2010), and is characterised by (Vanderhaeghe et al., 2020):

(i) A stack of low- to high-grade metamorphic nappes, essentially emplaced through top-to-the-south thrusting from the Devonian to the Carboniferous;
(ii) Late Devonian to Late Carboniferous plutonic rocks;
(iii) Late Devonian to Carboniferous volcanic and sedimentary rocks, including carbonates and clastic rocks, which underwent low-temperature, low-pressure (LT-LP) metamorphism;
(iv) Unconformable Late Carboniferous to Permian detrital sediments.

The Sillon Houiller fault divides the FMC into western and eastern parts (e.g., Arthaud et al., 1966; Vanderhaeghe et al., 2020). This fault crosscuts a set of NW-SE to NNW-SSE trending dextral shear zones, which are particularly well-developed in the western part of the FMC and connect with the South Armorican shear zone (Lerouge and Quenardel, 1988; Gébelin et al., 2007).

### *3.2.1. Structuration*

The FMC structure is predominantly defined by a south-verging metamorphic nappe pile, emplaced diachronously from the Devonian to the Early Carboniferous, and synchronous with Barovian metamorphism (Ledru et al., 1989; Faure et al., 2009). It was segmented during the Late Carboniferous by ductile and brittle strike-slip shear zones and detachments accommodating late-orogenic extension (Malavieille et al., 1990; Faure, 1995; Gardien et al., 1997). From south to north and from depth to surface, four major tectonic units have been recognised (Vanderhaeghe et al., 2020 and references therein):

***(i)*** ***The Para-Autochthonous Unit (PAU)***, essentially composed of metasedimentary rocks (mica schists, metagreywackes, and quartzites), which experienced pervasive Carboniferous low-grade metamorphism from the greenschist to amphibolite facies;

***(ii)*** ***The Lower Gneiss Unit (LGU)***, made of mica schists, paragneisses, and felsic orthogneisses, with minor mafic and carbonate rocks. The LGU was affected by greenschist to amphibolite facies metamorphism, and was intruded by alkaline porphyritic granitoids from the Cambrian to the Early Ordovician;

***(iii)*** ***The Middle Allochthonous Unit (MAU)***, identified in the Limousin region, mainly consisting of mica schists associated with an ophiolitic assemblage similar to the "Leptynite-Amphibolite Complex" (LAC) described in the Upper Gneiss Unit (see below). This assemblage is characterised by relics of eclogite facies metamorphism;

***(iv)*** ***The Upper Gneiss Unit (UGU)***, composed of garnet- and cordierite-bearing diatexites, associated with metatexites derived from ortho- and paragneisses containing relics of granulite facies mineral parageneses. The UGU is also characterised by a bimodal Ordovician (487–478 Ma) association of mafic to ultramafic and felsic rocks known as the ''Leptynite-Amphibolite Complex'' (Pin and Lancelot, 1982; Briand et al., 1991).

To the south, the metamorphic units of the PAU overlie unmetamorphosed sedimentary rocks of the external zone, which is structured by a fold-and-thrust belt and a foreland basin (Faure et al., 2009). The four major tectonic units of the FMC – the UGU, MAU, LGU, and PAU – are overlain by low-grade metamorphic allochthonous units, also referred to as Metamorphic Upper Units (MUU) (Vanderhaeghe et al., 2020). These units have limited lateral extent and include the Brévenne and Somme units located in the northeast of the FMC, which are unconformably overlain by the volcano-sedimentary rocks of the ''Tuffs anthracifères'' series, as well as the Thiviers-Payzac and Génis units located in the South Limousin (Faure et al., 2009). The ''Tuffs anthracifères'' series is coeval with the fold-and-thrust belt, thus supporting the north-south propagation of tectonic events throughout the entire FMC (Faure et al., 2009).

### *3.2.2. Tectono-metamorphic evolution*

The tectono-metamorphic evolution of the FMC is characterised by a succession of six major episodes (D0 to D5), leading to the emplacement of the distinct nappes (Faure et al., 2009). The earliest D0 event coincides with high- to ultra-high-pressure metamorphism during the Devonian (~390–360 Ma; Lotout et al., 2020), for which the associated structures are still poorly understood. The D1 episode mainly affected the UGU. It is characterised by the migmatisation and exhumation of high-pressure (HP) rocks around 360–352 Ma, with the flat-lying migmatitic foliation exhibiting a NE-SW trending stretching lineation associated with top-to-the-SW shearing (Lotout et al., 2020). The D2 episode, involved top-to-the-NW shearing, synchronous with Barrovian medium-pressure, medium-temperature (MP-MT) metamorphism dated between 360 and 350 Ma (Maluski and Monié, 1988; Costa, 1989, 1992). This episode corresponds to the main event of nappe stacking. A top-to-the-south ductile shearing event occurred during the Visean D3 event, only recognised in the southern part of the FMC. In the northern FMC, the Visean deformation occurred under brittle conditions. Notably, the NW–SE stretching, associated with dyke emplacement in the "Tuffs Anthracifères" series, is interpreted to result from the onset of syn-orogenic extension. The two final episodes, D4 and D5, involve the establishment of syn- and late-orogenic extensional tectonic regimes from ca. 320 to 300 Ma and are contemporaneous with Buchan low-pressure high-temperature metamorphism. The D4 episode, widespread in the entire FMC, is controlled by NW-SE-trending extension, whereas D5 is associated with a maximum stretching direction trending NNE–SSW. Those Late Carboniferous events were associated with large-scale crustal detachments, generation of anatectic domes (i.e. the Velay and Montagne Noire gneiss domes) and formation of detrital coal-basins (Malavieille et al., 1990; Faure et al., 2009; Vanderhaeghe et al., 2020).

### *3.2.3. Magmatic history*

The formation of the French Variscan belt is also related to the development of several phases of pre- to late-orogenic magmatism (Cuney and Marignac, 2015; Laurent et al., 2017a; Vanderhaeghe et al., 2020) (Fig. I.11):

#### *3.2.4.i. Cambrian to Ordovician pre-orogenic magmatism*

Pre-orogenic magmatism is associated with the emplacement of plutonic and volcano-sedimentary rocks, predominantly felsic and peraluminous in composition (Lotout et al., 2017; Couzinié et al., 2022; García-Arias et al., 2024). These rocks were later metamorphosed and are now essentially found as orthogneisses. U-Pb zircon dating of these orthogneisses has established their intrusions ages as ranging between 521 ± 7 and 446 ± 6 Ma (Melleton et al., 2010; Lotout et al., 2017; Couzinié et al., 2022). This predominantly crust-derived Cambro-Ordovician magmatic event followed the opening of a series of rifts that led to the hyperextension of the Gondwana margin. During the Early Ordovician, the separation of Avalonia and Armorica from the Gondwana supercontinent led to the opening of the Rheic and Mid-European Oceans. Within

the FMC, Early Ordovician magmatism is also recognised in the UGU as the "Leptynite-Amphibolite Complex" (i.e., bimodal association of mafic and felsic volcanic rocks, as described in section 3.2.2).

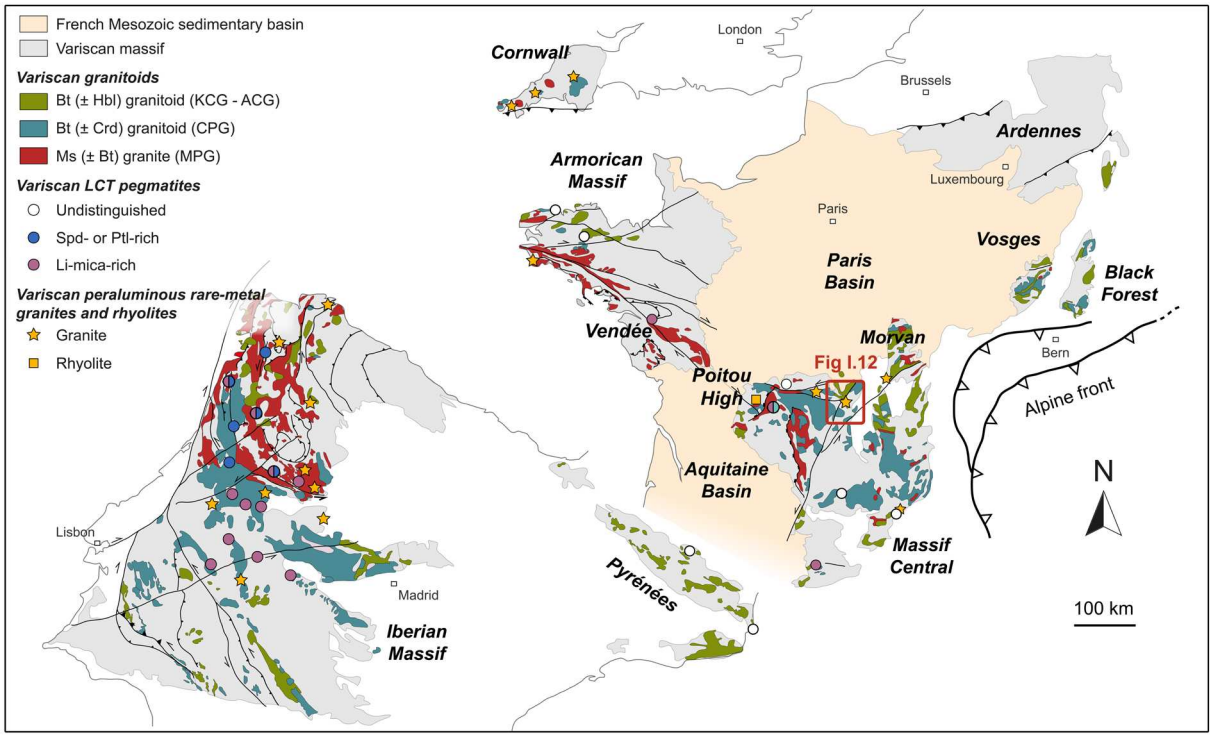



*Figure I.11. Schematic representation of the western European Variscan belt illustrating the main terranes and showing Variscan granitoids, as well as LCT pegmatites, rare-metal granites and rhyolites (modified from Ballouard et al., 2024). The granitoids typology is from Barbarin (1999). MPG: muscovite-bearing peraluminous granites; CPG: cordierite-bearing peraluminous granitoids; KCG: K-rich and K-feldspar porphyritic calc-alkaline granitoids. ACG: amphibole-rich calc-alkaline granitoids. Mineral abbreviations according to Warr (2021).*

#### *3.2.4.ii. Late Devonian to Carboniferous magmatism*

Within the FMC, the magmatic activity related to the Variscan orogeny took place over *ca.* 70 to 80 Ma, as recorded by plutonic and minor volcanic rocks. This event is characterised by a remarkable diversity in both petrological types and geochemical signatures (Vanderhaeghe et al., 2020). Mostly based on the classification of Barbarin (1999), five main plutonic rock types have been distinguished (Fig. I.11):

***(i) Calc-alkaline granitoids equivalent to the amphibole-rich calc-alkaline granitoids (ACG) of Barbarin (1999)***: They emplaced from Late Devonian to Early Carboniferous (*ca.* 370–355 Ma) and are found in association with calc-alkaline volcanic rocks in the Somme units in the Morvan (NE Massif Central; Pin et al., 1982; Delfour, 1989), to the south of the Armorican Massif (Eifelian-Givetian basaltic pillow lavas from the Meilleraie series), and along the "tonalitic line" extending from western Limousin to Vendée (Shaw et al., 1993; Bertrand et al., 2001; Cuney et al., 2001; Berger et al., 2024) (Fig. I.11). The formation of these rocks imply active margin magmatism at the Devonian-Carboniferous transition.

***(ii) Peraluminous granites and leucogranites equivalent to the muscovite-bearing peraluminous granites (MPG) of Barbarin (1999)***: They correspond to muscovite or muscovite + biotite bearing granites *sensu-stricto* and notable examples include the St-Sylvestre, Millevaches, and St-Mathieu intrusions emplaced in the Limousin (NW Massif Central) between 335 and 325 Ma (Cuney and Marignac, 2015). They resulted from the melting of metasediments at temperatures below 850 °C (water present- or muscovite breakdown) (Gardien et al., 1995; Villaros et al., 2018) and might represent the initial melt extracted from a partially molten source at the onset of partial melting (Vanderhaeghe et al., 2020).

***(iii) Peraluminous granites to granodiorites equivalent to the cordierite-bearing peraluminous granitoids (CPG) of Barbarin (1999)***: These peraluminous intrusions primarily resulted from the relatively hot (≥ 850 °C, biotite breakdown) melting of a crustal felsic source (ortho or paragneisses) (Gardien et al., 1995; Barbey et al., 1999; Villaros et al., 2018), with a possible contribution from mafic lower-crustal material (Downes and Duthou, 1988; Downes et al., 1997). They notably emplaced from *ca.* 360 to 350 Ma within the northern part of the FMC (Duthou, 1978; Duthou et al., 1984; Cuney et al., 2001) and from *ca.* 335 to 325 Ma in the southern part (Cuney and Marignac, 2015; Laurent et al., 2017a). The Stephanian (*ca.* 303 to 299 Ma, Upper Carboniferous) is characterised by the formation of the cordierite granite and migmatites of the Velay dome, as well as the emplacement of acidic tuffs, ash layers, and, to a lesser extent, alkaline basalts interlayers within the terrigenous formations of the coal basins (Bruguier et al., 2003).

***(iv) High-K sub-alkaline granitoids equivalent to the K-feldspar porphyritic calc-alkaline granitoids (KCG) of Barbarin (1999)***: They correspond to porphyritic granites to granodiorites, typically amphibole-bearing and containing abundant accessory minerals, including apatite and titanite. The rocks also feature micro-granular mafic enclaves and are commonly associated with intermediate plutonic rocks such as diorites, tonalites, and monzodiorites, which exhibit similar "vaugneritic" compositions, suggesting a possible petrogenetic link (Moyen et al., 2017). The genesis of KCG has been proposed to result either from interactions between CPG/MPG rocks and vaugnerites (described below) or from significant differentiation of the latter (Laurent et al., 2017a).

***(v) Mg-K-rich (monzo)diorites and syenites:*** In addition to granites and migmatites, mafic, potassic plutonic rocks also emplaced during the Variscan orogeny, locally known as "vaugnerites" (Michon, 1987; Sabatier, 1991). Vaugnerites vary from diorite to syenite compositions and are characterised by minerals such as amphibole, biotite, clinopyroxene, plagioclase, with occasional orthopyroxene, K-feldspar, and quartz (Sabatier, 1991). Geochemically enriched in K, large-ion lithophile elements (LILE), and light rare earth elements (LREE), these mafic to intermediate rocks likely originated from partial melting of a mantle source enriched by crustal components, probably during an earlier subduction phase (Rapp et al., 2010; Couzinié et al., 2014, 2016). Isotopic similarities (Sr, Nd, Hf) between

vaugnerites and the crust-derived granites within the FMC further imply that the crustal contribution in vaugnerite formation is locally derived (Williamson et al., 1992; Couzinié et al., 2016; Moyen et al., 2017).

In the FMC, evidence suggests coeval melting of crustal and mantle sources, with a spatial arrangement of plutons displaying progressively younger emplacement ages toward the south (Laurent et al., 2017a; Vanderhaeghe et al., 2020). This southward age progression is thought to result from the gradual southward delamination of the lithospheric mantle, potentially driven by lithospheric rollback after continental subduction or by "retro-delamination" linked to the retreat of a south-verging subduction zone.

#### *3.2.4.iii. Late Carboniferous peraluminous rare-metal magmatism*

From 325 to 310 Ma, the axial part of the Variscan belt underwent lithospheric extension, resulting in crustal melting and extensive granitic magmatism (e.g., Vanderhaeghe et al., 2020; Schulmann et al., 2022). The end of this event at *ca.* 315–310 Ma is marked by peraluminous rare-metal magmatism, characterised by the emplacement small, highly differentiated granitic intrusions enriched in rare metals (e.g., Beauvoir granite; Cuney et al., 1992; Raimbault et al., 1995), LCT pegmatites (e.g., Chèdeville pegmatite field; Raimbault, 1998; Deveaud et al., 2013, 2015), and rhyolitic dykes (e.g., Richemont rhyolite; Raimbault and Burnol, 1998). The extreme rare-metal enrichment observed in these rocks is dominantly considered as a primary magmatic feature (e.g., Linnen and Cuney, 2005; Pichavant, 2022), although magmatic-hydrothermal processes, such as fluid-melt immiscibility and alkali metasomatism, may impact metal enrichment and distribution at the end of the crystallisation (e.g., Badanina et al., 2004; Kaeter et al., 2018; Ballouard et al., 2020a; Pfister et al., 2023). Greisen alteration typically also contributes as a subsolidus process that redistributes rare metals, potentially resulting in hydrothermal Sn and/or W mineralisation (e.g., Monnier et al., 2020; Launay et al., 2021). The origin of rare-metal granites and pegmatites (RMGPs) remains primarily linked to magmatic processes, either through extreme differentiation of less evolved peraluminous felsic magmas, producing residual silicate melts (Černý et al., 2005; Hulsbosch et al., 2014; Roda-Robles et al., 2018; London, 2018), or through low-degree melting of potentially enriched crustal sources (Stewart, 1978; Müller et al., 2017; Knoll et al., 2018, 2023; Konzett et al., 2018; Gourcerol et al., 2019; Ballouard et al., 2023). Two main pathways to produce enriched protoliths have been recognised: (i) rare metals such as Sn, W, or Li may be enriched in siliciclastic sedimentary protoliths through weathering prior to tectonic stacking in collisional orogens (Romer and Kroner, 2015, 2016); (ii) polycyclic evolution associated with re-melting of granites followed by magmatic differentiation may ultimately generate fertile meta-igneous protoliths (Černý, 1989; Ballouard et al., 2023). An alternative model posits that F-, LILE-, rare metal-rich granitic melts may derive from the percolation of F-, LILE-, rare metal-rich fluids released during the dehydration

of the lower crust induced by granulite-facies metamorphism, potentially promoting partial melting at intermediate crustal levels (Cuney and Barbey, 2014). Finally, the breakdown of biotite at temperatures above 800 °C appears crucial for the genesis of RMGPs melts (e.g., Michaud et al., 2021; Kunz et al., 2022).

### *3.2.4. Focus on the Sioule metamorphic series*

In the northern part of the FMC, the stack of the UGU, LGU, and PAU constitutes the Sioule series, which represents a typical example of inverted metamorphic sequence formed during the Variscan orogeny (Grolier, 1971) (Fig. I.12). This series is bounded to the west and to the south by sinistral (Sillon Houiller fault) and dextral (Sainte-Christine fault) Carboniferous shear zones, respectively (Fig. I.12). Its eastern boundary is defined by the normal fault system of the Oligocene Limagne and Ebreuil grabens (Fig. I.12). Additionally, the Sioule metamorphic series is structured by two major antiforms, in the centre of which the PAU mica schists crop out.

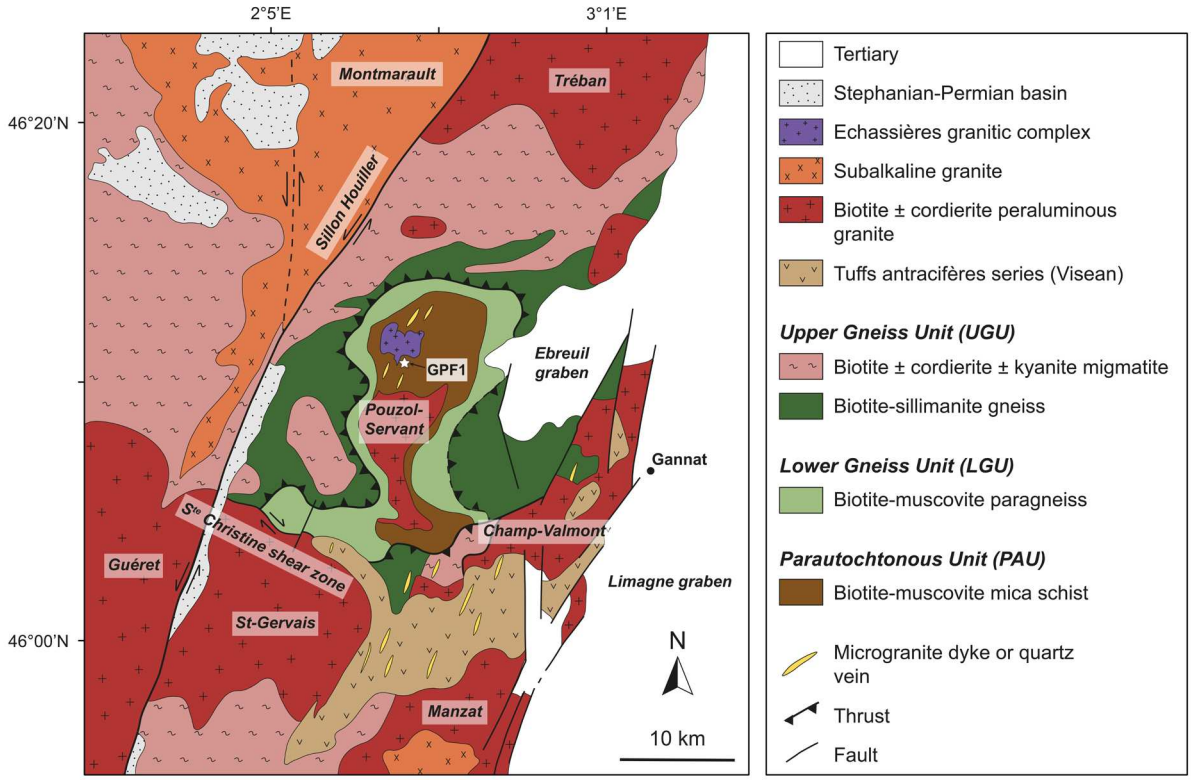



*Figure I.12. Simplified geological context of the Echassières granitic complex in the northern part of the French Massif Central (FMC) (modified from Cuney et al. (1992) and Harlaux et al. (2017)). The location of the GPF1 deep drillhole that crosscuts the Beauvoir PRMG is indicated by the white star.*

The three lithostructural units identified within the Sioule metamorphic series are composed as follows: the UGU comprises cordierite migmatites and biotite-sillimanite gneisses; the LGU consists of biotite-muscovite paragneisses; and the PAU is composed of biotite-muscovite mica schists, with local occurrences of staurolite. The series has undergone at least three of the major tectonic-metamorphic episodes recorded at the scale of the FMC (Faure et al., 2009; Schulz, 2009;

Do Couto et al., 2015) including: (i) a high pressure $D_0$ event, during which the UGU experienced high- to ultra-high-pressure eclogite-granulite-facies metamorphism, as recorded elsewhere in the FMC between 390 and 360 Ma (Lotout et al., 2020; De Hoÿm de Marien et al., 2023); (ii) a $D_1$ event characterised by top-to-the-SW shearing synchronous with migmatisation and exhumation of the UGU and LGU units; and (iii) a medium-pressure medium-temperature $D_2$ event associated with top-to-the-NW shearing. The D1 and D2 events, which have been related to nappe stacking, preceded the unconformable deposition of the "Tuffs anthracifères" series around 335 Ma, which consists of weakly deformed and metamorphosed terrigenous sedimentary and felsic volcanic rocks (Bruguier et al., 1998; Do Couto et al., 2015).

The Sioule series was intruded by several granitic plutons, notably, the Pouzol-Servant porphyritic granite in the southern antiform, dated at 330 ± 9 Ma (whole rock Sr-Nd dating; Pin, 1991), and the Echassières granitic complex in the northern antiform, which will be discussed in the following section (Fig. I.12).

### 3.3. The Echassières granitic complex

The Echassières granitic complex is a circular intrusive body, 3 km in diameter, emplaced within the Sioule metamorphic series during a major N20° shortening event at the end of the Carboniferous (Gagny et al., 1984; Gagny and Jacquot, 1987; Feybesse, 1985; Blès et al., 1989) (Fig. I.13a). It outcrops over an area of approximately 40 $km^2$ and gravimetric data indicate a thickness of *ca.* 3–4 km, leading to an estimated total volume of about 65 $km^3$ (Vigneresse, 1987). The Echassières complex developed through the intrusion of at least three distinct granitic units (Cuney et al., 1992; Raimbault et al., 1995), listed from the oldest to the youngest: (i) the inferred La Bosse granite, concealed at depth and thought to be at the origin of an early quartz-wolframite vein system that crosscuts the PAU mica schists, known as the La Bosse stockwork; (ii) the Colettes granite, a cordierite-bearing two-mica porphyritic granite; and (iii) the Beauvoir granite, a highly evolved albite-lepidolite-topaz leucogranite (Fig. I.13a).

The Beauvoir granite is a small intrusive body that outcrops over approximately 0.10 $km^2$, with an estimated minimum volume of 0.21 $km^3$ (Raimbault et al., 1995) (Fig. I.13b). This volume estimate is consistent with the 3D model developed by the French mining company Imerys, based on 120 drillholes realised from 1969 to 2017 (Imerys Ceramics France, 2020). The Beauvoir granite was emplaced during the late-orogenic extensional stage of the Variscan orogeny, around 315–310 Ma (Rb-Sr on whole rock; Duthou and Pin, 1987; Ar-Ar on lepidolite; Cheilletz et al., 1992, and U-Pb on columbite-group minerals; Melleton et al., 2015). It is recognised as one of the best studied examples worldwide of peraluminous high-phosphorus rare-metal granite (PHP-RMG; Cuney et al., 1992). The Beauvoir PRMG is notably enriched in fluxing and lithophile elements (Li, P, F, Rb, Cs, Be, Nb, Ta, Sn, W, U), particularly in its apical part (Raimbault et al., 1995), and shares many characteristics with rare-element pegmatites of

the LCT (Lithium-Cesium-Tantalum) family (Raimbault, 1998; Černý and Ercit, 2005). For example, concentrations of Li, Sn, and Ta range from 0.1 to 1 wt.%, 0.02 to 0.4 wt.%, and 40 to 500 ppm, respectively, which significantly exceed the typical values for the bulk upper continental crust (24 ppm for Li; 2.1 ppm for Sn; and 0.9 ppm for Ta; Rudnick and Gao, 2003).

Crystallisation experiments indicate that the melts forming the Beauvoir PRMG crystallised under pressures of 100 to 300 MPa at very low temperatures (below 670 °C), with an estimated solidus near 550 °C, which is characteristic of flux-rich granitic melts (Pichavant et al., 1987a; Pichavant, 2022). The main magmatic minerals in the Beauvoir crystallisation sequence include albite, quartz, K-feldspar, and Li-Fe-micas, transitioning from zinnwaldite to lepidolite compositions with increasing differentiation, along with accessory minerals such as cassiterite (Sn) (generation I; see section 4.1 for the description of generation II), topaz (F), apatite (F), amblygonite-group minerals (Li-F), herderite (Be-F), zircon, columbite-group minerals (Nb-Ta), pyrochlore-group minerals (Nb-Ta-U), and uraninite (U) (Pichavant et al., 1987a; Rossi et al., 1987; Johan et al., 1988; Cuney et al., 1992; Raimbault et al., 1995; Pichavant, 2022).

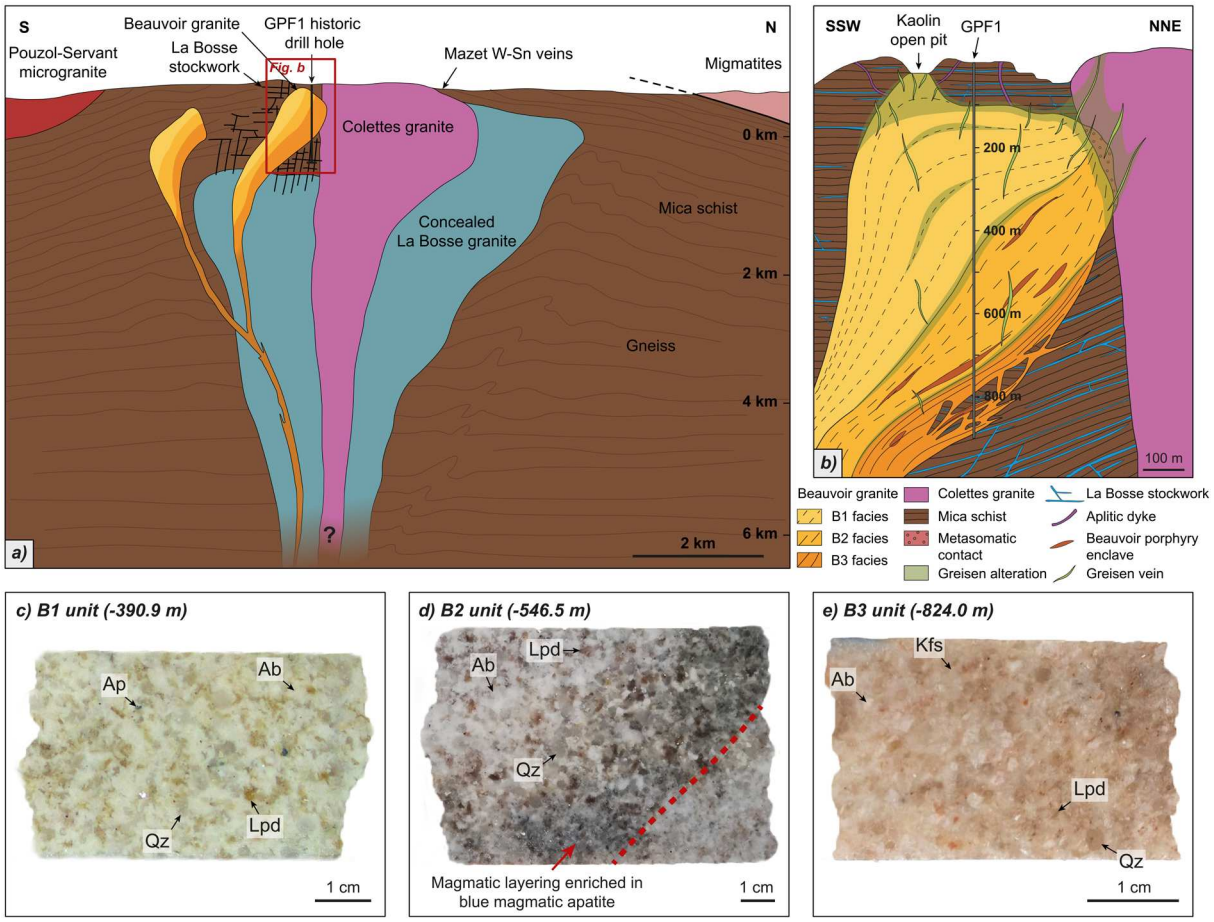



*Figure I.13. (a) Interpretative cross-section of the Echassières granitic complex based on geological data and gravimetric modeling (modified from Cuney and Autran, 1987); (b) Interpretative cross-section of the Beauvoir PRMG representing the vertical magmatic internal zoning composed by the three successive units B1, B2, and B3 (modified from Cuney et al. (1992) and Monnier et al. (2018)); (c) to (e) Macroscopic photographs of typical samples from the B1, B2, and B3 units, respectively. Abbreviations follow the IMA conventions compiled by Warr (2021).*

Following the drilling of a *ca.* 900m deep drillhole (GPF1) in 1985 as part of the "Géologie Profonde de la France" (GPF) drilling program, extensive studies have contributed to a comprehensive understanding of the Beauvoir magmatic-hydrothermal system (Cuney and Autran, 1987). These studies encompass structural analysis, petrographic and geochemical characterisation, determination of the emplacement age, identification of successive hydrothermal parageneses, as well as the establishment of a relative chronology of fluid circulations through the investigation of fluid inclusions. Petrographic and structural studies have revealed a vertical zonation within the Beauvoir PRMG, leading to the identification of three main magmatic units that are inferred to have successively intruded the parautochthonous mica schists of the Sioule metamorphic series (Bouchez et al., 1987; Gagny, 1987; Jacquot and Gagny, 1987; Monier et al., 1987; Rossi et al., 1987) (Fig. I.13). The transitions between these three units are characterised by metric zones exhibiting alternating layers rich in albite and lepidolite, along with variations in grain size (Jacquot, 1987). Within each unit, lepidolite layering is also observed and interpreted as magmatic (Bouchez et al., 1987; Jacquot, 1987).

These magmatic units are designated as the B1 (~ 100–450 m depth in GPF1), B2 (~ 450–750 m), and B3 (~ 750–880 m) facies, with the B1 unit believed to represent the final and most differentiated magma batch (Figs. I.13b and c). The magmatic paragenesis evolves across these three units, with the proportion of accessory minerals (topaz, cassiterite, Li-Be phosphates, columbite- and pyrochlore-group minerals) tending to increase with increasing differentiation (i.e., from B3 to B1). A similar trend is observed for the abundance of albite, while the proportions of quartz and K-feldspar progressively decrease from B3 to B1, with Li-micas evolving from zinnwaldite to lepidolite. A recent study has suggested a more complex sequence, composed of 18 sub-units distributed across four units (B1, B1', B2, and B3), which incrementally intruded the host mica schists (Esteves et al., 2024a, b). Finally, a fourth unit, characterised by its porphyritic texture and referred to as the "Beauvoir porphyry enclave," has been encountered within the B2 and B3 units, occurring either as dykes or enclaves (e.g., Cuney et al., 1992; Monnier et al., 2018). Its chemical characteristics closely resemble those of the Colettes granite, indicating a potential genetic connection (e.g., Raimbault and Azencott, 1987; Monnier et al., 2018).

## 4. The expression of the Beauvoir magmatic-hydrothermal system

The magmatic-hydrothermal to hydrothermal evolution of the Beauvoir PRMG is complex and marked by multiple episodes of fluid circulation. This evolution can be divided into four major stages (Merceron et al., 1992; Cuney et al., 1992; Monnier et al., 2019) (Fig. I.14):

**(i) Early hydrothermal stage (200–550 °C)**: Driven by heat from the intrusion, this stage primarily resulted in the formation of vertical quartz veins and greisen alteration affecting both the

Beauvoir intrusion and its surrounding rocks (i.e., Colettes granite, La Bosse stockwork, and host mica schists);

**(ii to iv) Three late hydrothermal stages**: These involved fluid circulation genetically and temporally disconnected from the emplacement of the Beauvoir PRMG. The first two late hydrothermal stages were characterised by the development of sub-vertical quartz veins, respectively accompanied by **fluorite mineralisation (< 250 °C)** and **illite-smectite precipitation (100–200 °C)**, while the third and final stage involved widespread supergene **kaolinisation (≤ 50 °C)**, mainly affecting the apical part of the Beauvoir intrusion and coinciding with low-temperature phosphate precipitation, particularly crandallite-group minerals.

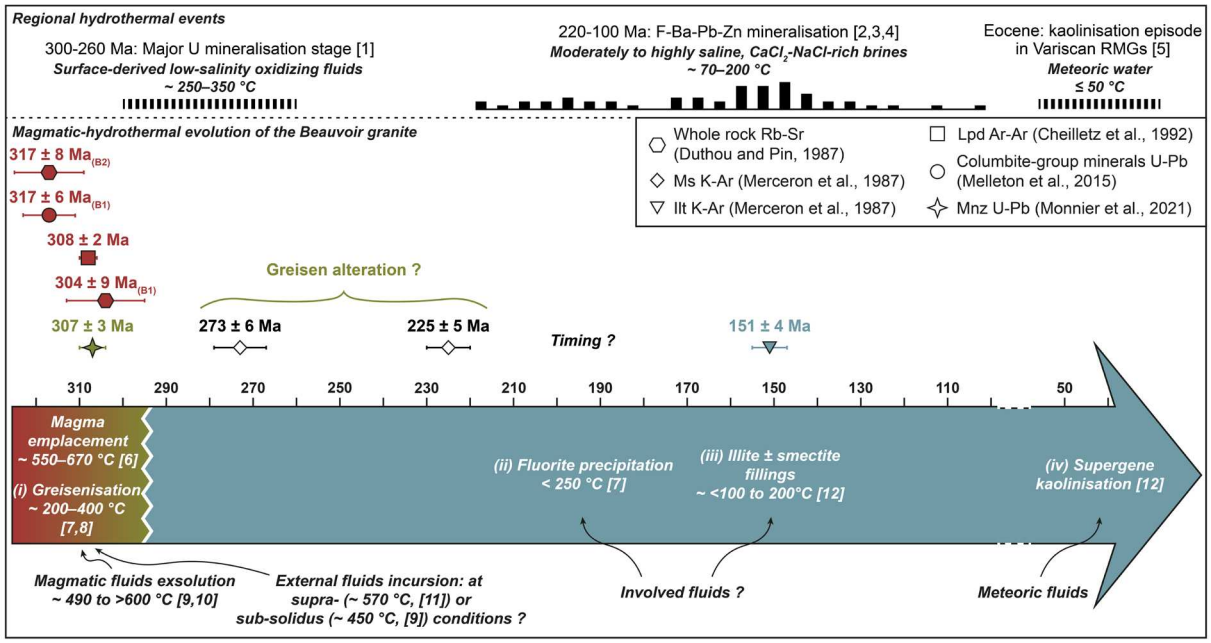



*Figure I.14. Chronology of the different magmatic and hydrothermal events (i to iv) that occurred in the Beauvoir PRMG between 315 Ma and the Eocene in parallel with the main regional hydrothermal events. All ages are reported with uncertainties at the 2-sigma level. Ages obtained by Rb-Sr dating of whole rock samples from the B1 and B2 units (Duthou and Pin, 1987) were recalculated using the $^{87}$Rb decay constant of Villa et al. (2015). The F-Ba-Pb-Zn mineralisation event is from a compilation of geochronological data for the FMC and adjacent regions (i.e., Poitou High, Morvan and Vendée). The histogram represents only central ages, disregarding associated uncertainties. [1] Ballouard et al. (2017) and references therein; [2] Cathelineau et al. (2012) and references therein; [3] Gigoux (2015) and references therein; [4] Bouat et al. (2023); [14] Gaudin et al. (2015) and references therein; [6] Pichavant (2022); [7] Merceron et al. (1992); [8] Monnier et al. (2020); [9] Aïssa et al. (1987); [10] Harlaux et al. (2017); [11] Fouillac and Rossi (1991); [12] Merceron et al. (1987).*

## 4.1. Early hydrothermal stage

### *4.1.1. Comprehensive overview*

The early hydrothermal stage can also be referred to as the magmatic-hydrothermal transition. This transition represents a continuous evolution, during the cooling of the granitic melt, from an initial purely magmatic system dominated by crystal-melt interactions, to a system governed by interactions between crystals, melt, and fluid phases, ultimately progressing into a

purely hydrothermal system characterised by fluid-rock interactions (Halter and Webster, 2004; Audétat and Edmonds, 2020). Therefore, the term "early hydrothermal stage" encompasses both the magmatic and early hydrothermal stages described by Merceron et al. (1992), as well as the early orthomagmatic and greisenisation stages detailed by Monnier et al. (2022).

The initiation of this stage involved the exsolution of hot ($\geqslant$490 °C) magmatic fluids from the Beauvoir melts during crystallisation, referred to as L1 fluids (Aïssa et al., 1987) (Figs. I.14 and I.15). Early circulation of these magmatic fluids primarily led to acidic, F-rich alteration (i.e., topazification), predominantly localised in the contact zones between the granite and the host mica schists (Cuney et al., 1992; Monnier et al., 2020). L1 magmatic fluids concentrated in the shallowest B1 unit, creating overpressure that was rapidly released through fracturing (Aïssa et al., 1987; Cuney et al., 1992). The system transitioned then from an initial lithostatic pressure regime to a hydrostatic pressure regime. It induced the emplacement of sub-vertical, centimetric quartz veins (Merceron et al., 1987, 1992), as well as the phase separation of primary magmatic fluids (L1) into a high-salinity brine (L2) and a low- to moderate-salinity vapour (V2) (Aïssa et al., 1987; Harlaux et al., 2017) (Fig. I.15). Both primary (L1) and secondary (L2, V2) magmatic fluids evolved over time through cooling and mixing with externally-derived fluids, such as meteoric or metamorphic fluids (Aïssa et al., 1987; Cuney et al., 1992; Monnier et al., 2020). These fluid circulations were responsible for greisenisation of the Beauvoir intrusion and surrounding rocks, which represents the most extensive alteration during the early hydrothermal stage) (Fig. I.15).

Greisen alteration is presumed to be temporally and genetically linked to the emplacement of the Beauvoir intrusion around 310–315 Ma (Duthou and Pin, 1987; Cheilletz et al., 1992; Melleton et al., 2015), as evidenced by the age of 307 ± 3 Ma obtained from U-Pb dating of greisen-related monazite within the Echassières complex (Monnier et al., 2021) (Fig. I.14). However, K-Ar dating of muscovite suggests younger ages (273 ± 6 Ma for pervasive alteration and 225 ± 5 Ma for greisen veins; Merceron et al., 1987), introducing some uncertainty, although the earlier hypothesis remains the most plausible (Cuney et al., 1992; Monnier et al., 2020). Greisenisation was most intense at the apical part of the Beauvoir PRMG but was also observed at depth, particularly in the transition zones between the three magmatic units (B1, B2, B3; Merceron et al., 1992). The process involved the pervasive replacement of igneous minerals, predominantly feldspar (± quartz and lepidolite), by a quartz-muscovite assemblage, often accompanied by the precipitation of secondary minerals such as apatite, topaz, cassiterite (generation II; see section 3.3 for the description of generation I), columbite- and pyrochlore-group minerals, as well as the formation of millimetric quartz-muscovite veins (Merceron et al., 1987; Monnier et al., 2018, 2019) (Fig. I.16).

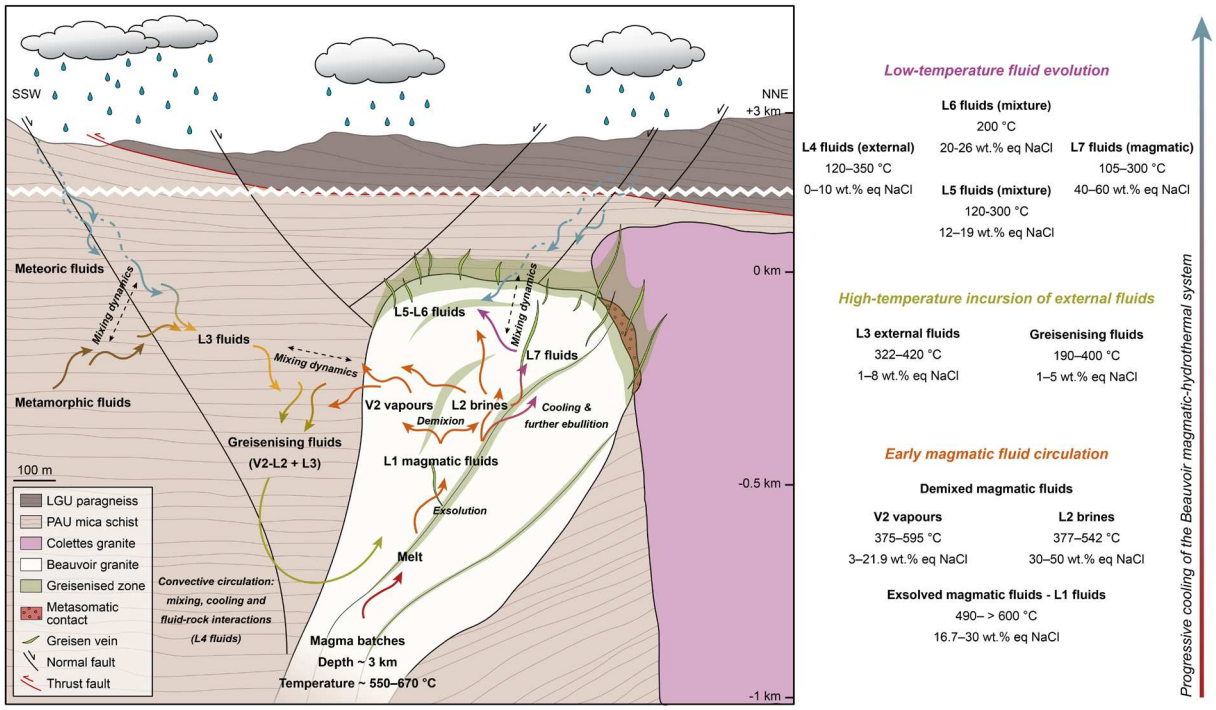



*Figure I.15. Conceptual model illustrating fluid circulation during the early hydrothermal stage in the Beauvoir granite and highlighting the physico-chemical evolution of the involved fluids (adapted from Aïssa et al., 1987). Temperature and salinity data are derived from the fluid inclusion studies of Aïssa et al. (1987); Harlaux et al. (2017); Monnier et al. (2020). Mean paleoelevation in the Limousin region during the Late Carboniferous was estimated by Dusséaux et al. (2021).*

As greisen-forming fluids progressively cooled, they induced the sequential crystallisation of muscovite, pyrophyllite, donbassite, tosudite, and minor early kaolinite (Kln I), occurring both as veinlets fillings and pervasive alteration (Merceron et al., 1987, 1992). Within veinlets, these minerals are typically associated with small quartz crystals (10–50 µm), which generally contain few fluid inclusions. Kaolinite (Kln I) primarily forms as a replacement of K-feldspar and albite, while donbassite completely replaces feldspar and partially replaces lepidolite and secondary muscovite. Tosudite typically substitutes feldpar and muscovite. Donbassite and tosudite are lithium-rich minerals, with average $Li_2O$ contents of 1.6 % and 0.7 %, respectively (Merceron et al., 1988). The crystallisation of these minerals thus requires relative Li-enrichment in the greisenising fluids, likely derived from the alteration of lepidolite and Li-rich phosphates (amblygonite-montebrasite) within the Beauvoir PRMG. Greisenising fluids periodically invaded the host mica schists, leading to the precipitation of secondary topaz and cassiterite (Monnier et al., 2019, 2020), as well as the formation of phengite-biotite, chlorite-illite, and kaolinite alteration at temperatures ranging from 400 to 150 °C (Merceron et al., 1992). Furthermore, greisen alteration is presumed to have resulted in the minor precipitation of cassiterite, columbite-tantalite, and wolframite (type c) within quartz veins in the vicinity of the Colettes and Beauvoir granites (Monnier et al., 2019, 2020).

Sodic (albitisation) and potassic alterations were also observed, albeit to a lesser extent, and are thought to result from the circulation of highly saline magmatic brine L2 (Monnier et al.,

2018). During greisenisation, the release of $Na^+$ and $K^+$ into the aqueous solution increased the alkali/$H^+$ ratio, potentially promoting alkali metasomatism (e.g., Štemprok, 1987; Pirajno, 2009; Ballouard et al., 2020a). Conversely, alkali metasomatism may contribute to greisenisation by gradually lowering the alkali/$H^+$ ratio. Thus, both greisen and alkali alterations observed in the Beauvoir PRMG may have been driven by the same fluids, with the replacement reactions forming a self-sustaining chemical system that could lead to multiple successive generations of albitite and greisen (e.g., Ballouard et al., 2020a).

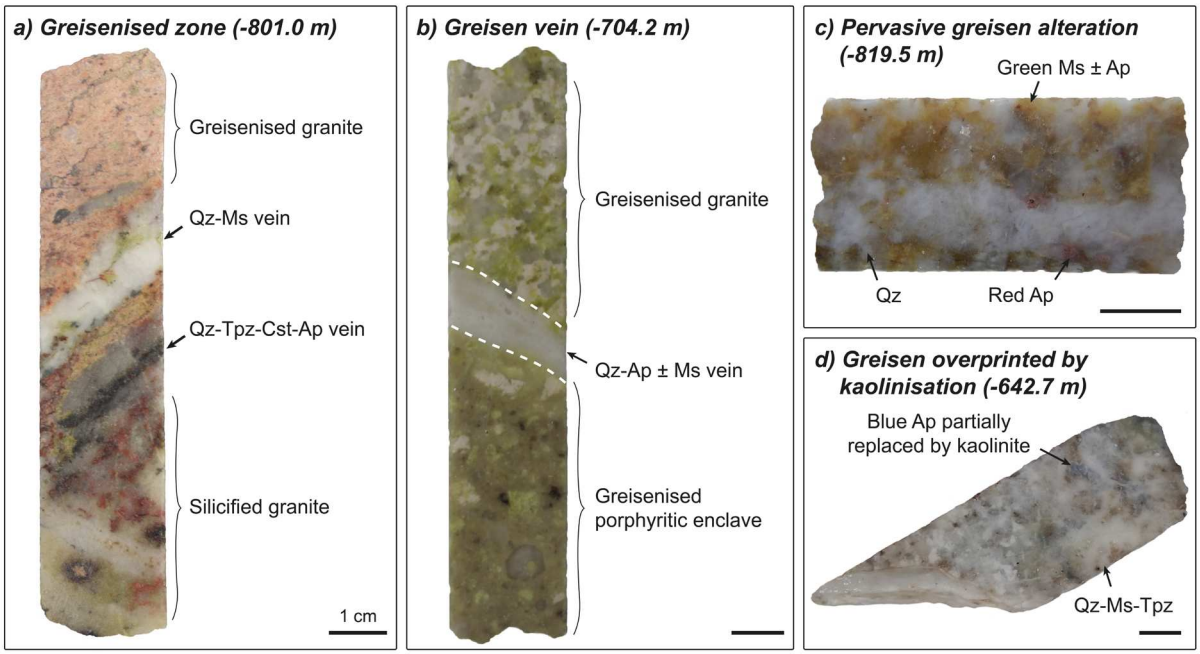



*Figure I.16. Selected macrophotographs of early hydrothermal alterations within the Beauvoir PRMG: (a) Quartz-topaz-cassiterite-apatite vein crosscutting the greisenised Beauvoir granite; (b) Quartz-apatite vein at the contact between the greisenised Beauvoir and porphyritic granites; (c) Greisenised Beauvoir granite; (d) Greisenised Beauvoir granite partially overprinted by kaolinisation. Abbreviations follow the IMA conventions compiled by Warr (2021). The scale below each photograph represents 1 cm.*

### *4.1.2. Detailed dynamics and evolution of fluid circulation*

Fluid inclusions (FIs) are microscopic pockets of fluid trapped within minerals that serve as direct records of past fluid circulation. Typically ranging in size from a few to several tens of micrometres, fluid inclusions preserve a snapshot of the physico-chemical conditions (such as temperature, pressure, salinity, and composition) of the fluids at the time of their entrapment. They therefore represent valuable tools in petrology and geochemistry, providing crucial insights into the genesis and evolution of mineral deposits, as well as the fluid pathways involved in ore formation (Roedder, 1984; Shepherd et al., 1985).

Fluid inclusions within magmatic and hydrothermal minerals of the Beauvoir PRMG have been extensively studied, particularly to elucidate fluid dynamics and the evolution of the fluids' physico-chemical properties during the early hydrothermal stage (Aïssa, 1987; Aïssa et al., 1987; Harlaux et al., 2017; Monnier et al., 2020). Three main phases of fluid circulation have been

highlighted, involving eight distinct fluid types (Aïssa et al., 1987; Cuney et al., 1992) (Fig. I.15; Table I.2):

#### *4.1.2.i. Early magmatic fluid circulation*

Three types of high-temperature magmatic fluid inclusions have been identified in igneous quartz and topaz from the B1 unit of the Beauvoir PRMG, designated as L1, L2, and V2 (Aïssa et al., 1987; Harlaux et al., 2017) (Fig. I.15). The exsolution of L1 fluids from the Beauvoir melts during cooling and crystallisation marked the onset of the magmatic-hydrothermal transition, and L1 fluids therefore represent primary magmatic fluids. At room temperature, L1-type fluid inclusions are multiphase (liquid + vapour + solid), with the aqueous phase being dominant (Table I.2). The solid phase consists of small cubic solids (< 5 µm), identified as halite and potentially sylvite (Harlaux et al., 2017). L1-type FIs exhibit irregular shapes, with sizes ranging from 10 to 23 µm. They occur as clusters in igneous quartz and topaz, exclusively within the B1 unit (Aïssa et al., 1987; Harlaux et al., 2017). Although L1-type FIs are mainly aqueous, their vapour phase contains traces of low-density volatiles, with $CO_2$ (10–66 mol%) and $N_2$ (20–82 mol%) as the dominant components, along with minor amounts of $CH_4$ (0.3–22 mol%) (Harlaux et al., 2017; Table I.2). They are characterised by homogenisation temperatures varying from 490 to over 600 °C, and salinities ranging from *ca.* 17 to 30 wt% NaC eq (Figs. I.15 and I.17; Table I.2). Their high Na content is accompanied by very high contents in Sn, Cs, and K, as well as significant concentrations in Mn, Fe, Rb, Li, and W (Harlaux et al., 2017) (Fig. I.18; Table I.3). Minor elements include Nb, Ta, and Sr. The Na/Li and Na/K ratios range from 6.2 to 24 and 2.5 to 4.6, respectively. The elevated Na/K ratios (≥ 1) are characteristic of magmatic fluids that have equilibrated with a granitic melt (Rankin et al., 1992; Audétat et al., 2000a, b), whereas the low Na/Li ratios (⩽5) suggest a Li-rich magma source for the fluid (Cathelineau et al., 1994). Preliminary LIBS analyses of L1-type FIs in topaz from the Beauvoir granite revealed Na/Li ratios around 1–3 (Fabre et al., 2001), indicating that the earliest magmatic fluid might have been even more enriched in lithium. This is consistent with the composition of Li-micas in the Beauvoir granite, which represent a relatively late-stage phase in the granite's crystallisation sequence (Pichavant et al., 1987a; Pichavant, 2022). These Li-micas exhibit complex zoning, transitioning from Li-muscovite cores to zinnwaldite rims, and external lepidolite overgrowths, the latter presumed to result from the early magmatic-hydrothermal transition (Monier et al., 1987). The increasing lithium content in the Li-micas may therefore have recorded the exsolution of the early Li-rich magmatic fluid (L1) from the Beauvoir melts (Harlaux et al., 2017).

The exsolution of L1 magmatic brines induced fluid overpressure in the apical part of the intrusion, triggering hydraulic fracturing and a transition from lithostatic to hydrostatic pressure conditions (Aïssa et al., 1987). This decompression caused the boiling of the L1 primary magmatic fluids between 400 and 520 °C, resulting in phase separation into: (i) a low-density, low- to

moderate-salinity vapour phase (3–21.9 wt% NaCl eq), designated as V2, and (ii) a high-salinity liquid phase (30–50 wt% NaCl eq), referred to as L2 (Aïssa et al., 1987; Harlaux et al., 2017) (Figs. I.15 and I.17). L2-type fluid inclusions are multiphase (L+V+S), with a dominant liquid phase, and typically contain at least two solids, including halite and possibly sylvite (Table I.2). In contrast, V2-type fluid inclusions are vapour-dominant and rarely contain solids. Similar to L1-type FIs, L2- and V2-type FIs are mostly aqueous, with trace volatiles present in the vapour phase (i.e., $CO_2$, $N_2$ and $CH_4$; Table I.2). Though L2- and V2-type FIs were mostly trapped in independent clusters in magmatic quartz and topaz from the B1 unit exclusively, their occasional co-occurrence within the same assemblage supports contemporaneity (Aïssa, 1987; Aïssa et al., 1987). As with L1 fluids, their circulation appears to be confined to the B1 unit, with temperatures ranging from approximately 375 to 595 °C (Fig. I.17). L2-type FIs exhibit the highest concentrations of most elements compared to L1- and V2-type FIs (Harlaux et al., 2017) (Fig. I.18; Table I.3). During boiling, elements such as Na, K, Mn, Rb, Sn, Cs, and W preferentially partition into the brine, whereas only Mg and Li favour the vapour phase (Harlaux et al., 2017). This partitioning behaviour, with most elements enriched in the Cl-rich aqueous phase, has also been noted in similar systems, such as the Mole granite in Australia (Audétat et al., 2000a).

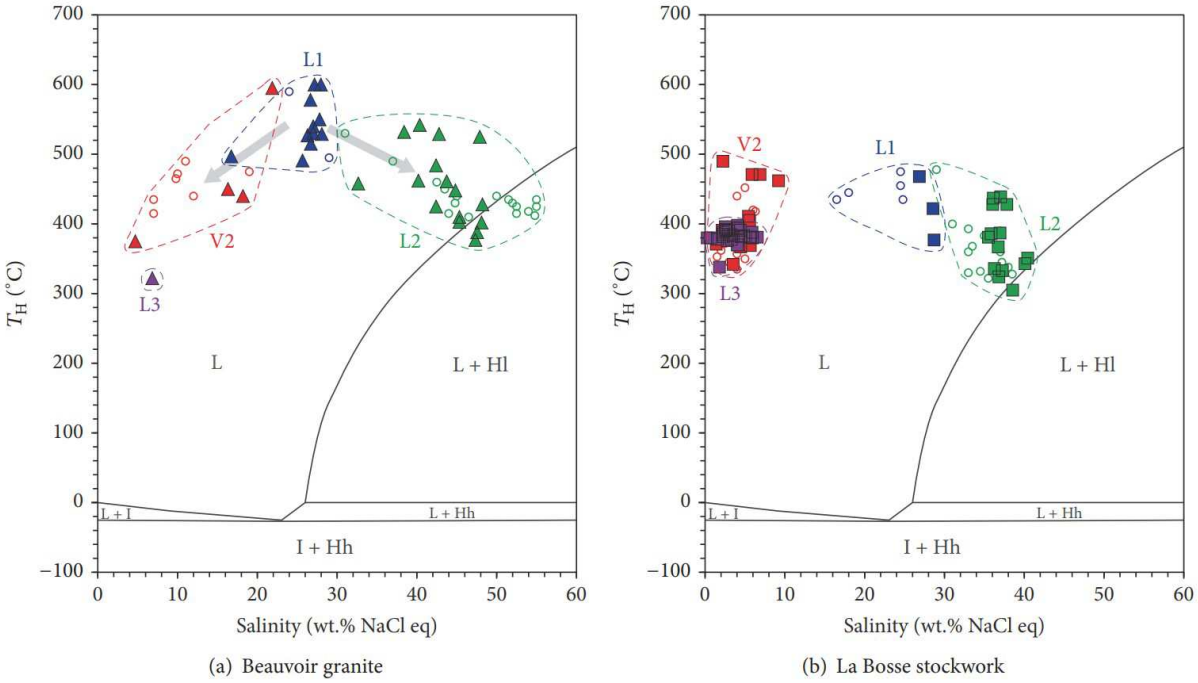



*Figure I.17. Diagram showing salinity versus homogenisation temperature $T_H$ for different generations of fluid inclusions in the Beauvoir granite (a) and the La Bosse stockwork (b) (from Harlaux et al., 2017). Filled symbols represent data from Harlaux et al. (2017), while open circles indicate data from Aïssa et al. (1987). Phase equilibrium curves for the pure $H_2O$-NaCl system (Bodnar, 2003) are reported for reference. L = liquid; Hl = halite; Hh = hydrohalite; I = ice.*

A remarkable analogy between the signature of magmatic fluid inclusions (L1, L2, and V2) in the B1 unit of the Beauvoir PRMG and certain fluid inclusions found in the La Bosse

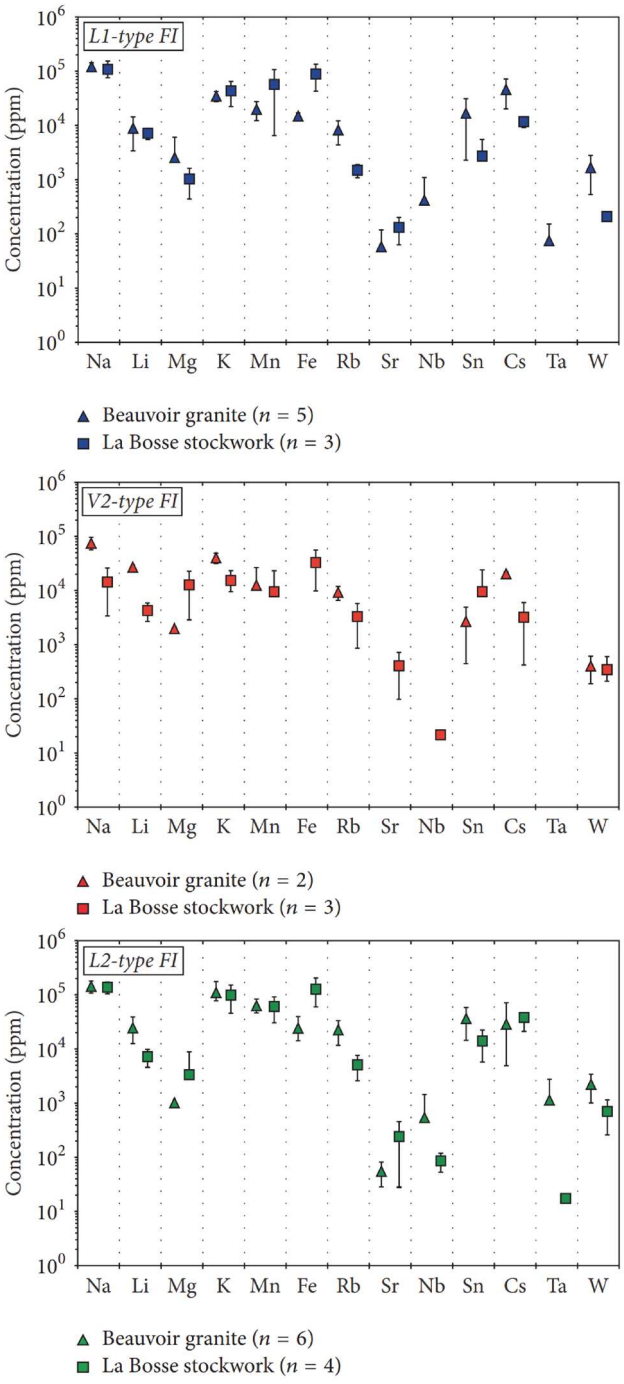



*Figure I.18. Major and trace element concentrations in L1-, V2-, and L2-type fluid inclusions from the Beauvoir granite and La Bosse stockwork, determined by LA-ICP-MS analysis (from Harlaux et al., 2017). Data points represent average concentrations for each fluid inclusion assemblage, with error bars indicating the corresponding standard deviations.*

stockwork was highlighted by Harlaux et al. (2017), suggesting the circulation of Beauvoir magmatic fluids within the stockwork (Figs. I.17 and I.18). Fluid inclusions from the La Bosse stockwork show a decrease in homogenisation temperatures by 60–120 °C and in salinities by 3–10 wt% NaCl eq compared to those in the Beauvoir granite (Fig. I.17). These observations were interpreted as evidence of cooling and thermal equilibration of the fluids surrounding the granitic body, coupled with potential mixing between magmatic fluids and externally derived low-salinity fluids. Despite some disparities, the chemical signature of magmatic fluids from the Beauvoir granite remains preserved in FIs from the stockwork. These disparities primarily include enrichments in Mn, Fe, and Sr, alongside depletions in Mg, Rb, Cs, Nb, Ta, Li, and Sn, which were attributed to fluid-rock interactions with the host mica schists (Fig. I.18). However, this analogy is challenged by the findings of Monnier et al. (2020), as they observed very limited overprinting of the La Bosse quartz veins by the Beauvoir greisen fluids. They proposed that the fluids observed in the stockwork by Harlaux et al. (2017) may instead reflect the signature of a distinct magma responsible for an earlier topazification episode predating the emplacement of the Beauvoir melts.

#### *4.1.2.ii. High-temperature incursion of external fluids*

The L3 fluids were involved in the early convective circulation of external fluids, which affected not only the entire granitic body but also the La Bosse stockwork and host mica schists (Aïssa et al., 1987; Cuney et al., 1992) (Fig. I.15). These post-magmatic fluids likely consist of a

mixture of metamorphic, magmatic and meteoric fluids, the meteoric contribution presumed to be dominant. L3-type fluid inclusions are biphasic (L+V), exhibit highly variable volumetric fraction of the vapour phase ($R_v$ ~ 40–100 %), regular shapes, and range in size from 10 to 40 µm (Aïssa et al., 1987; Harlaux et al., 2017) (Table I.2). They have been observed as clusters, isolated inclusions, or trails along fractures in igneous quartz and topaz throughout the entire Beauvoir intrusion. No clear spatial relationships with other fluid inclusion types have been identified, except for associations with L4-type FIs described below (Aïssa, 1987; Aïssa et al., 1987; Harlaux et al., 2017). L3-type fluid inclusions are characterised by low salinities (1–8 wt% NaCl eq) and homogenisation temperatures ranging from 322 to 420 °C, occurring in either the liquid or vapour phase.

The circulation of L3 external fluids is thought to have driven widespread greisen alteration of the Beauvoir granite and surrounding rocks (Cuney et al., 1992; Monnier et al., 2020) (Fig. I.15). Evidence of mixing with L2 magmatic brines suggests that L3 fluids infiltrated the magmatic-hydrothermal system while L2 fluid circulation was still ongoing. The incursion of L3 fluids therefore likely occurred under sub-solidus conditions at temperatures of *ca.* 400–450 °C (Cuney et al., 1992). However, oxygen isotopic signatures of magmatic minerals within the Beauvoir PRMG suggest earlier incursion of low $\delta^{18}O$ external fluids – primarily of meteoric origin – under supra-solidus conditions, interacting with melts at approximately 570 ± 50°C (Fouillac et al., 1987; Fouillac and Rossi, 1991). These fluid-melt interactions are believed to have influenced the crystallisation of ore-bearing minerals, particularly columbite- and pyrochlore-group minerals in the most evolved B1 unit (Ohnenstetter and Piantone, 1988; Fouillac and Rossi, 1991; Raimbault et al., 1995). The exact timing of meteoric fluid infiltration into the Beauvoir magmatic-hydrothermal system appears therefore poorly constrained, although numerical modelling suggests that meteoric fluid incorporation into the melts is unlikely (e.g., Weis et al., 2012).

#### *4.1.2.iii. Low-temperature fluid evolution*

Following the initial incursion of external fluids into the Beauvoir magmatic-hydrothermal system, multiple fluid generations circulated at lower temperatures, four of which were identified by Aïssa et al. (1987) as L4, L5, L6, and L7 (Fig. I.15). No clear chronological sequence has been established between these fluid types.

L4-type fluid inclusions are biphasic, with a low volumetric fraction of the vapour phase ($R_v$ ~ 2–20 %) and highly variable shapes and sizes (Table I.2). They are found along fractures or as clusters in magmatic quartz and topaz from all three magmatic units of the Beauvoir PRMG, frequently coexisting with L3-type FIs. They exhibit low-salinities (0–10 wt% NaCl eq), similar to L3-type FIs, but have lower homogenisation temperatures ranging from 120 to 350 °C. L4

fluids are interpreted as the cooler successors of L3 fluids, reflecting the continued evolution of the Beauvoir magmatic-hydrothermal system during its gradual cooling (Fig. I.15).

L5- and L6-type fluid inclusions are biphasic, with low volumetric fractions of the vapour phase ($R_v$ ~ 2–20%) and sizes reaching up to 80 µm (Table I.2). Both occur as trails in magmatic quartz from the B1 unit exclusively. L5-type FIs display moderate salinities (12–19 wt% NaCl eq) and homogenise at temperatures between 120 and 300°C. They are relatively uncommon, except at 207.9 m depth along the GPF1 drillhole. L6-type fluid inclusions are slightly more saline (20–26 wt% NaCl eq) and typically homogenise around 200 °C, except at 339.8 m in GPF1, where temperatures range from 130 to 420 °C. The exclusive occurrence of L5- and L6-type FIs in B1 quartz, together with their distinct physico-chemical properties, suggest that they formed from a variable mixture of early or late high-salinity brines (i.e., L1, L2 or L7) and external aqueous fluids (i.e., L3 or L4) (Fig. I.15).

L7-type fluid inclusions are multiphase (L+V+S), with highly variable volumetric fractions of the vapour phase and two to nine solids (Table I.2). They are extremely saline Na-K brines (40–60 wt% NaCl eq) that homogenise at an average temperature that decreases from depth (225 °C at 379.5 m depth along GPF1) to the surface (180 °C at 98.38 m). These fluids are found exclusively in magmatic quartz from the B1 unit and are thought to have formed through the cooling and boiling evolution of early magmatic brines L1 and L2 (Fig. I.15). The data display significant salinity dispersion but a relatively narrow range of homogenisation temperatures. This configuration is characteristic of fluids saturated with salts and undergoing boiling, with the salinity variations likely resulting from the heterogeneous trapping of salt crystals (halite ± sylvite) of varying sizes within the fluid inclusions (Aïssa et al., 1987).

*Table I.2. Synthesis of petrographic observations, microthermometric and Raman spectrometry results for the different fluid inclusion types identified in the Beauvoir granite, based on the studies of [1] Aïssa et al. (1987); [2] Aïssa (1987); [3] Harlaux et al. (2017); and [4] Monnier et al. (2020). All FI types are presumed to have been trapped during the early hydrothermal stage. FIA: fluid inclusion assemblage; $R_V$: volumetric fraction of the vapour phase contained within the FI; $T_e$: first visible melting of the solidified aqueous phase during heating; $T_m$ice: final melting of the solidified aqueous phase; $T_d$Hh, $T_d$H & $T_d$Slv: final dissolution temperatures of hydrohalite, halite and sylvite, respectively; and $T_H$: total homogenisation temperature that occurs either to the liquid (L), vapour (V), or critical phase (C). Mineral abbreviations follow the IMA conventions compiled by Warr (2021).*

| Type | Facies | Host mineral | FIA type | Size (µm) | Shape | Phases | Rv (%) | Solids identification | $T_e$ | $T_m$ice | $T_d$Hhl | $T_d$Hl | $T_d$Syl | $T_H$ | Salinity (wt% NaCl eq) | Gas composition (mol%) | | | Refs |
|---|---|---|---|---|---|---|---|---|---|---|---|---|---|---|---|---|---|---|---|
| | | | | | | | | | | | | | | | | $CO_2$ | $N_2$ | $CH_4$ | |
| ***L1*** | B1 | Magmatic Qz & Tpz | Clusters or unspecified | 10–23 | Irregular | L+V+S | 20–60 | N ≥ 1<br>Hl ± Syl, Cst | -78;<br>-56 | -39.9;<br>-12.8 | -48.7;<br>-44 | 275;<br>300 | – | 490;<br>>600 (L) | 16.7–30 | 10–66 | 20–82 | 0–22 | [1,2,3] |
| ***L2*** | B1 | Magmatic Qz & Tpz | Clusters or unspecified<br>Occasionally coexisting with V2 | 10–35 | Irregular to regular | L+V+S | 20–40 | N > 2<br>Hl ± Syl | -77; -52 | -39.9;<br>-1.6 | – | 215;<br>407 | – | 377;<br>542 (L) | 30–50 | 52 | 34 | 13 | [1,2,3] |
| ***V2*** | B1 | Magmatic Qz & Tpz | Clusters, trails or unspecified<br>Occasionally coexisting with L2 | 12–24 | Irregular to negative crystal | L+V(±S) | 80–90 | N = 0–2<br>Possibly Hl | -72 | -19.3 | – | 300 | – | 375;<br>595 (V, L or C) | 3–21.9 | 58–60 | 32–35 | 7–8 | [1,2,3] |
| ***L3*** | All units | Magmatic Qz & Tpz | Clusters, isolated or trails<br>Frequently coexisting with L4 | 10–40 | Regular | L+V(±S) | Highly variable<br>40–100 | N = 0–1 | -61 | -5; -1 | – | – | – | 322;<br>420<br>(L or V) | 1–8 | – | – | – | [1,2,3] |
| ***Greisen fluids*** | All units | Greisen-related Qz (vein & disseminated) | Mostly in growth bands, primary | < 1–20 | Irregular to oval/rectangular | L+V(±S) | 20–90 | N = 0 | *Ca.* -21 | -10; 0 | – | – | – | 190;<br>400 | 1–5 | – | – | – | [3] |
| ***L4*** | All units | Magmatic Qz & Tpz | Trails in fractures or clusters<br>Frequently coexisting with L3 | Up to 80 | Irregular to regular | L+V(±S) | 2–20 | N = 0–1 | – | -6.5; 0 | – | – | – | 120;<br>350 (L) | 0–10 | – | – | – | [1,2] |
| ***L5*** | B1 | Magmatic Qz | Trails | Up to 80 | Irregular to regular | L+V(±S) | 2–20 | N = 0–1 | < -35 | – | > 20 | – | – | 120;<br>300 (L) | 12–19 | – | – | – | [1,2] |
| ***L6*** | B1 | Magmatic Qz | Trails | Up to 80 | Irregular | L+V(±S) | 2–20 | N = 0–1 | < -35 | – | > 0 | – | – | 200;<br>300 (L) | 20–26 | – | – | – | [1,2] |
| ***L7*** | B1 | Magmatic Qz | Unspecified | – | – | L+V+S | Highly variable | N = 2–9 | – | – | – | 250;<br>550 | 50; 100 | 105;<br>300 (L) | 40–60 | – | – | – | [1,2] |

*Table I.3. Chemical composition ranges for magmatic fluid inclusions hosted in magmatic quartz and topaz from the Beauvoir PRMG, as determined by LA-ICP-MS (from Harlaux et al., 2017). "Bld" refers to values below the detection limit.*

| | L1-type (n = 5) | L2-type (n = 6) | V2-type (n = 2) |
|---|---|---|---|
| ***Concentrations (ppm)*** | | | |
| **Na** | 103,500–110,600 | 158,200–189,700 | 71,600–86,200 |
| **Li** | 4,450–17,960 | 7,370–51,310 | 25,440–28,480 |
| **Mg** | bld–4770 | bld–1010 | bld–1980 |
| **K** | 32,300–41,720 | 65,350–128,000 | 33,850–46,200 |
| **Ca** | bld | bld | bld |
| **Mn** | 8,930–29,300 | 44,550–86,500 | 2,640–22,400 |
| **Fe** | bld–16,800 | bld–41,800 | bld |
| **Rb** | 1,380–9,330 | 14,950–44,100 | 7,360–11,100 |
| **Sr** | bld–130 | bld–84 | bld |
| **Nb** | bld–1,450 | bld–1,590 | bld |
| **Sn** | 1,170–38,450 | 14,300–75,000 | 1,100–4,270 |
| **Cs** | 22,200–75,650 | 23,700–42,150 | 19,100–21,600 |
| **Ta** | 18–180 | bld–2,280 | bld |
| **W** | bld–2,970 | bld–4,250 | 250–550 |
| ***Mass ratios*** | | | |
| **Na/Li** | 6.2–24 | 3–23 | *Ca.* 3 |
| **Na/K** | 2.5–4.6 | 1.5–2.6 | *Ca.* 2 |

#### *4.1.3. Fluid circulation involved in extensive greisenisation of the Beauvoir PRMG*

Within the Beauvoir PRMG, greisenisation resulted from the prolonged circulation of relatively low-salinity fluids (1–5 wt% NaCl eq), which progressively cooled from 400 to 190 °C without significant changes in fluid chemistry (Monnier et al., 2018, 2020) (Fig. I.15; Table I.2). Based on alteration paragenesis, these greisen-forming fluids are further believed to have exhibited low pH, very low concentrations of Mg and Fe, and high contents in Li, Na, and K (Merceron et al., 1992). They are inferred to derive from the boiling of exsolved magmatic fluids, leading to the formation of coexisting brine and vapour (Monnier et al., 2020). However, greisenising fluids exhibit homogenisation temperatures and salinities similar to those of the L3 fluids described by Aïssa et al. (1987) (Table I.2). The L3 fluids were interpreted as external fluids, mostly of meteoric origin, that mixed with magmatic fluids at relatively high temperatures (*ca.* 400–450 °C), with the meteoric signature becoming progressively dominant (Aïssa et al., 1987; Cuney et al., 1992) (Fig. I.15). Cuney et al. (1992) associated the circulation of the L3 fluids to greisen processes and tin leaching. This raises an ambiguity regarding the origin of greisenising fluids in the Beauvoir PRMG, leaving open the question of whether they are primarily magmatic in nature or significantly influenced by meteoric contributions.

Greisen alteration involved several stages (Monnier et al., 2020; Fig. I.19):

(i) Greisen alteration initiated at relatively high temperatures (*ca.* 400 °C), with pervasive alteration predominantly affecting the Beauvoir PRMG under lithostatic pressure conditions (Fig. I.19b).

(ii) Subsequently, a significant fracturing event, induced by regional shear slip constraints (Gagny and Jacquot, 1987) and increasing fluid pressure, connected greisenising fluids to the surface. This led to rapid pressure release and flashing of the fluids (i.e., intense boiling followed by an instantaneous transformation into vapour).

(iii) Pressure quickly stabilised around hydrostatic values, marking a phase of intense greisen activity at temperatures of *ca.* 250–280 °C (Fig. I.19c). This phase involved pervasive alteration of the granite, along with vein formation and reactivation in the host rock (e.g., Mazet veins), driven by local pressure variations.

(iv) At lower temperatures (≤ 230 °C), pervasive alteration appeared to be ineffective, and fluid flow became concentrated in veins both within the granite (greisen veins) and in the surrounding rocks (e.g., Suchot and Nades veins) (Fig. I.19d).

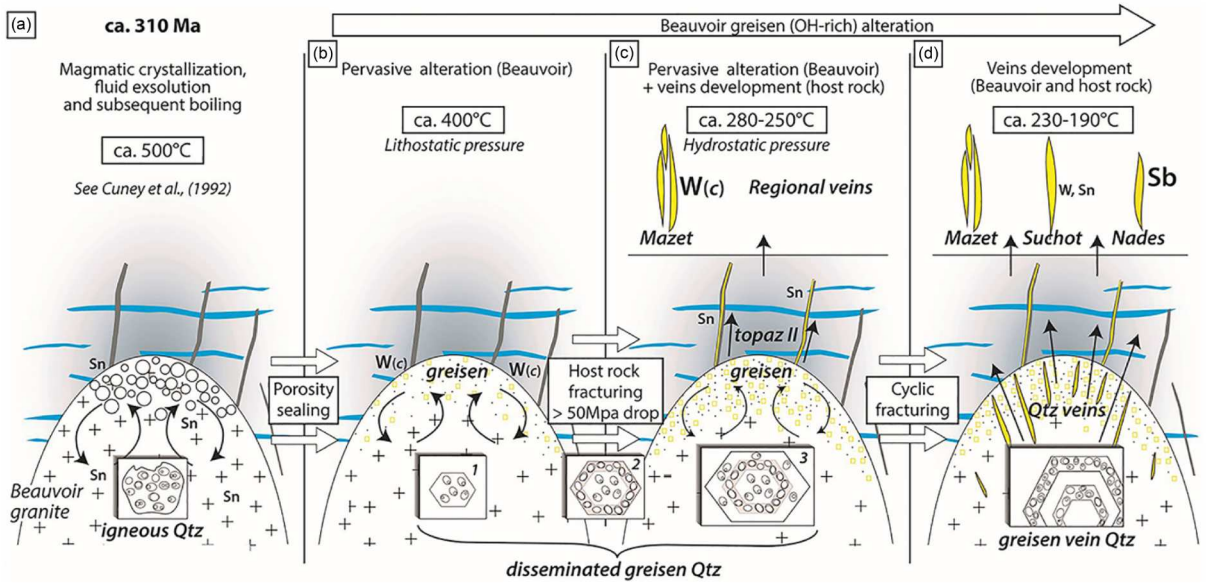



*Figure I.19. Conceptual model deciphering the evolution of OH-rich greisen alteration in the Beauvoir magmatic-hydrothermal system (from Monnier et al., 2020). High-temperature alteration is pervasive, while lower-temperature stages are characterised by fracturing and vein formation. (a) Exsolution of L1 magmatic brine at the onset of the magmatic-hydrothermal transition, followed by fracturing and boiling, resulting in phase separation into L2 brine and V2 low-salinity fluid. (b) Initiation of pervasive greisen alteration of the Beauvoir granite by V2 low-salinity fluids under lithostatic pressure. Only few fractures occur in the host mica schist and fluids remained essentially within the granitic cupola. At the end of this stage, intense fracturing connected for a second time the Beauvoir system to the surface, resulting in important pressure drops and subsequent vaporisation of the greisen fluid. (c) Continued greisen alteration with fracturing, reactivation of pre-Beauvoir topaz veins, and W-enriched quartz vein formation during localised depressurisation. (d) Final alteration stage restricted to quartz vein selvages, marked by efficient fluid transport and widespread quartz vein development within and outside the granite.*

The greisen-forming system has been shown to exhibit a cyclic behaviour, characterised by successive fracturing/sealing phases (Monnier et al., 2020). During fracturing, sharp pressure drops drastically reduced minerals solubility in the greisenising fluids, leading to the massive precipitation of minerals such as quartz and muscovite. This rapid mineral deposition sealed the porosity (e.g., Launay et al., 2019), reducing permeability and increasing fluid pressure, thus triggering a new fracture-seal cycle. Occurring along the fluid's cooling path, this process was marked by successive boiling – which concentrated metals in the fluid – and subsequent flashing – which initiated their precipitation. The fracturing/sealing cyclic mechanism is presumed to have ultimately led to wolframite mineralisation within veins developed around the Beauvoir PRMG, particularly in the Mazet veins (Monnier et al., 2020) (Figs. I.19c, d).

### 4.2. Late hydrothermal stages

Three distinct late hydrothermal stages have been recognised based on detailed petrographic and mineralogical investigations within the Beauvoir PRMG and are interpreted to derive from the circulation of external fluids (e.g., meteoric, metamorphic fluids, or basinal brines) through the cooled granitic body (Merceron et al., 1987, 1992) (Figs. I.14 and I.20). These stages include: (i) fluorite mineralisation, (ii) illite ± smectite vein fillings and pervasive alteration, and (iii) widespread supergene kaolinisation.

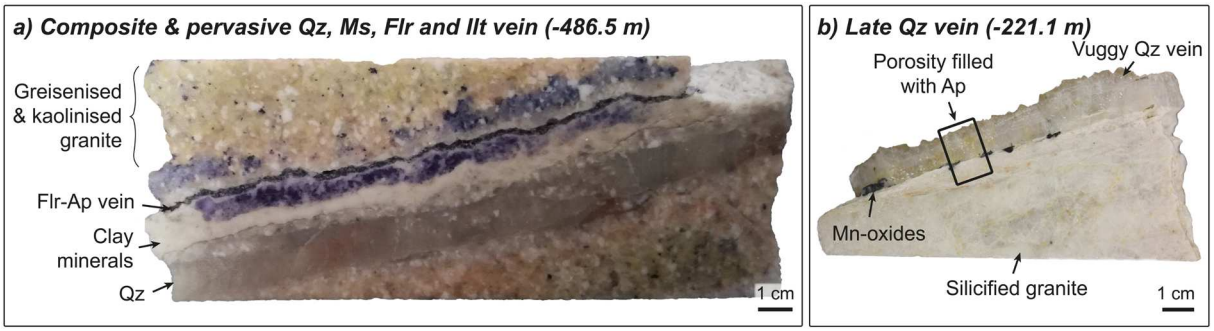



*Figure I.20. Selected macrophotographs of late hydrothermal alterations within the Beauvoir PRMG: (a) Composite quartz-fluorite-clay mineral-apatite vein crosscutting the Beauvoir granite showing signs of both greisenisation and kaolinisation. Purple fluorite precipitated during the first late hydrothermal stage (i). The vein was reactivated during the second late hydrothermal stage (ii), as evidenced by illite fillings; (b) Vuggy quartz vein exhibiting Mn-oxides as fillings along the selvedge and late hydrothermal apatite having precipitated in the vein porosity, representative or the third late hydrothermal stage (iii; kaolinisation). Abbreviations follow the IMA conventions compiled by Warr (2021).*

Fluorite is found in association with quartz in sub-vertical veins, within intergranular secondary porosity, or as a replacement of igneous minerals, particularly albite (Merceron et al., 1987) (Fig. I.20a). Its REE chemistry remains consistent across the 427.3 m and 624.7 m depth range in the GPF1 drillhole, exhibiting low REE contents ($\Sigma$REE ~ 1.3–7.6 ppm) and LREE depletion relative to MREE and HREE ($La_N/Yb_N$ ~ 5.5–27) (Raimbault, 1988; Raimbault et al., 1995). Similar REE patterns were observed in other French fluorite deposits (e.g., Marchand et al., 1976; Touray et al., 1981). Based on these observations, a single fluid, likely of external origin,

circulating at temperatures not exceeding 250 °C (as inferred from thermodynamic calculations; Merceron et al., 1992), has been proposed as responsible for fluorite precipitation in the Beauvoir PRMG. Although the exact timing of fluid circulation and the origin of these fluids remain poorly constrained, fluorite mineralisation seems to clearly postdate greisen alteration. Previous authors have proposed that this late hydrothermal stage in the Beauvoir PRMG may be linked to a widespread hydrothermal event that affected Western Europe, leading to the formation of extensive veins and stratiform F-Ba-Pb-Zn ore deposits (Merceron et al., 1987; Raimbault, 1988) (Fig. I.14). The genesis of these hydrothermal deposits occurred over an extensive period spanning from the Early Jurassic to the Early Cretaceous (approximately 210–100 Ma; Joseph et al., 1973; Baubron et al., 1980; Davaine, 1980; Soule de Lafont and Lhegu, 1980; Nigon, 1988; Sizaret et al., 2009; Boiron et al., 2010; Cathelineau et al., 2012; Gigoux et al., 2015; Bouat et al., 2023; Lenoir et al., 2023). The available geochronological data for the FMC, the Morvan, Vendée, and Poitou regions highlight a well-documented period of F mineralisation from *ca.* 165 to 140 Ma.

Illite and mixed-layer illite/smectite minerals co-precipitated with quartz as vein fillings, as well as replacement of igneous albite within the Beauvoir PRMG (Merceron et al., 1987, 1992) (Fig. I.20a). These minerals are commonly associated with non-crystalline iron oxides and goethite, which form as weathering products in reactivated fractures, likely during the supergene kaolinisation phase. Both illite and mixed-layer illite/smectite minerals are enriched in Mg and Fe, and illite exhibits a relatively heavy oxygen isotopic signature, with a single $\delta^{18}O$ value of 12.3 ‰ (Merceron et al., 1987). This particular chemistry has been interpreted as reflecting the circulation of meteoric fluids, partially reequilibrated with the country rocks, at temperatures ranging from 100 to 200 °C. This late hydrothermal event occurred at 151 ± 4 Ma, during the Upper Jurassic, as determined by K-Ar dating of illite (Merceron et al., 1987) (Fig. I.14).

The final late hydrothermal stage involved supergene kaolinisation, which affected the Beauvoir PRMG from the Eocene to Oligocene (Merceron et al., 1987; Charoy et al., 2003; Monnier et al., 2019) (Fig. I.14). Kaolinisation of other Variscan RMGs has been attributed to the circulation of meteoric fluids at low temperatures ($\leqslant$50 °C; Gaudin et al., 2015), a weathering process that likely also occurred in the Beauvoir PRMG. Kaolinisation has been particularly intense at the apical part of the Beauvoir intrusion and overprints previous greisen alteration (Fig. I.16d). Kaolinite replaces greisen-related muscovite and igneous feldspar, and apatite is also systematically altered either into kaolinite or crandallite-group minerals. Accessory minerals include Mn-oxides, W-rich goethite, crandallite-group minerals, and illite/smectite clays, which commonly co-precipitate with quartz in late brecciated veins exhibiting multiple reactivation events (Monnier et al., 2019) (Fig. I.20b). Two generations of kaolinite have been identified: a minor early phase (Kln I) precipitating at the end of the early hydrothermal stage, and a second, more significant phase resulting from the supergene alteration event (Kln II).

## 5. Key questions and research strategy

Peraluminous rare-metal granites, and more widely RMGs, represent unique magmatic-hydrothermal systems, characterised by an intricate interplay between magmatic and hydrothermal processes. Among these, the Beauvoir granite is one of the most thoroughly studied examples worldwide, owing to the *Geology of Deep France* (GPF) program initiated in 1982, which included the deep GPF1 drillhole at the Échassières site in 1985 (Cuney and Autran, 1987). This program facilitated extensive research, providing a comprehensive understanding of the Beauvoir magmatic-hydrothermal system that developed following the magma emplacement (Aïssa et al., 1987; Fouillac et al., 1987; Merceron et al., 1987, 1992; Fouillac and Rossi, 1991; Cuney et al., 1992; Charoy et al., 2003; Harlaux et al., 2017; Monnier et al., 2020). Involved fluid circulation notably resulted in widespread greisenisation (Aïssa et al., 1987; Merceron et al., 1992; Cuney et al., 1992; Monnier et al., 2020) and induced hydrothermal mobility of rare metals (Harlaux et al., 2017), thereby influencing their multi-scale distribution. Several key questions regarding the evolution of the Beauvoir magmatic-hydrothermal system remain nonetheless unanswered and are outlined below:

### a. What is the precise timing of fluid circulation episodes?

As detailed in section 4 of Part I, the Beauvoir magmatic-hydrothermal system experienced multiple episodes of fluid circulation, the absolute timing of which remains debated. Greisen alteration is thought to be genetically and temporally connected to the emplacement of the Beauvoir melts around 310–315 Ma (Cuney et al., 1992; Monnier et al., 2020), a hypothesis supported by U-Pb dating of greisen-related monazite from the Echassières complex, which yielded an age of 307 ± 3 Ma (Monnier et al., 2021). Conversely, K-Ar dating of muscovite suggested significantly younger ages of 273 ± 6 Ma for pervasive alteration and 225 ± 5 Ma for the development of greisen veins (Merceron et al., 1987). These discrepancies pose challenges to existing interpretations, particularly considering the cooling timeframe of approximately $10^4$ years, inferred from the small size (~0.21 $km^3$) of the Beauvoir intrusion (~ 0.21 $km^3$; Raimbault et al., 1995) and its shallow emplacement (~ 3 km; Cuney et al., 1992) (e.g., Coulson et al., 2002; Ingebritsen et al., 2010; Andersen and Weis, 2020). Beyond early greisen alteration, the Beauvoir granite was affected by three main late hydrothermal episodes, likely driven by tectonic and thermal processes around the cooled granitic body (Merceron et al., 1987, 1992). These episodes have poor constraints, both in terms of their impact on metal endowment and their precise timing.

Apatite represents a ubiquitous accessory mineral precipitating throughout the supra- and sub-solidus evolution of the Beauvoir PRMG (Aubert, 1969; Wang, 1988; Johan et al., 1988; Cuney et al., 1992; Monnier et al., 2019). It is also commonly found in a variety of igneous and ore-forming systems and incorporates many elements in its structure, notably U and Pb, making

it an ideal candidate for constraining the timing of mineralising melt- and fluid-related processes. To refine the understanding of the Beauvoir magmatic-hydrothermal system, U-Pb geochronology of the distinct magmatic and hydrothermal apatite generations has therefore been performed using laser ablation–inductively coupled plasma–mass spectrometry (LA-ICP-MS). This work was carried out in collaboration with Oscar Laurent and Loïs Monnier (Géosciences Environnement Toulouse, GET) as part of Yanis Khebabza's Master 2 research project.

**b. What is the origin of involved fluids and how did it evolve over time?**

Fluid circulation in the Beauvoir PRMG appears to have involved contributions from multiple origins, including magmatic, metamorphic and meteoric fluids (Aïssa et al., 1987; Fouillac et al., 1987; Fouillac and Rossi, 1991; Merceron et al., 1992; Cuney et al., 1992; Monnier et al., 2020). Fluid inclusion study has notably inferred the exsolution of magmatic fluids, followed by the progressive incursion of external fluids into the magmatic-hydrothermal system, the precise nature of these fluids and their implication during the greisenisation process still debated (Aïssa et al., 1987; Cuney et al., 1992; Monnier et al., 2020). While early hydrothermal fluid circulation ceased as the intrusion cooling, late fluids invaded the pluton during several episodes (Merceron et al., 1987, 1992). Although these late fluids likely derived from external sources, the details on their precise origin, composition, and the mechanisms driving their circulation into the system remain poorly understood.

As mentioned above, apatite is capable of incorporating a wide range of major and trace elements, including REEs, Y, Mn, Fe, Sr, Pb, Na, and the actinides U and Th (as substitutes for Ca); small, highly charged ions such as Si, S, As, and V (replacing P); and halogens (F, Cl, Br, and I) in the anion site (Pan and Fleet, 2002). Apatite is highly sensible to melt or fluid-induced textural and geochemical modifications across a broad range of pressures and temperatures (Harlov, 2015). As such, its unique chemistry provides a powerful tool for tracing the origin and composition of hydrothermal fluids and deciphering fluid-rock interactions (e.g., Harlov, 2015; Kusebauch et al., 2015a, 2015b; Ballouard et al., 2018; Pochon et al., 2018; Andersson et al., 2019; Melfou et al., 2023). In the context of the same collaboration with Oscar Laurent and Loïs Monnier (GET), undertaken as part of Yanis Khebabza's Master 2 research project, the distinct magmatic and hydrothermal apatite generations were characterised *in-situ* for their major and trace elements, as well as their oxygen isotopic compositions, aiming to unravel the evolution of the origin and chemistry of fluids circulating within the Beauvoir magmatic-hydrothermal system. Greisen-related quartz and cassiterite were also analysed *in-situ* for their O isotopic signatures to further constrain the origin and temperature of ore-bearing fluids in the Beauvoir PRMG.

**c. What are the exact nature and consequences of fluid-melt and fluid-fluid interactions during the magmatic-hydrothermal transition?**

Numerous studies have emphasised the role of magmatic fluids (or hydrosaline melts) exsolution and subsequent fluid-rock interactions in the genesis of rare-metal deposits, thereby identifying the magmatic-hydrothermal transition as a pivotal stage (e.g., Thomas et al., 2011; Badanina et al., 2015; Ballouard et al., 2016, 2020a; Araujo et al., 2023; Pfister et al., 2023; Putzolu et al., 2024). In the Beauvoir granite, this transition involved the exsolution of magmatic fluids, their subsequent boiling and mixing with external fluids, resulting in a system increasingly dominated by non-magmatic fluids (Aïssa et al., 1987). Based on oxygen isotopic signatures of igneous minerals, some authors have proposed that external fluids – likely meteoric in origin – infiltrated the Beauvoir system at the magmatic stage. These fluids are hypothesised to have played a significant role in the precipitation of metal-bearing minerals, particularly columbite- and pyrochlore-group minerals within the highly evolved B1 unit (Fouillac et al., 1987; Ohnenstetter and Piantone, 1987; Fouillac and Rossi, 1991). However, this hypothesis remains contested, leaving the exact processes governing the magmatic-hydrothermal transition unresolved.

Quartz, often described as a versatile archival mineral due to its sensitivity to the geochemical environment, provides a valuable record of magmatic-hydrothermal systems. As one of the earliest minerals to crystallise from the Beauvoir melts (Pichavant, 2022) and hosting numerous generations of fluid inclusions (Aïssa et al., 1987), magmatic quartz potentially preserved a detailed history of the physico-chemical processes involved during the magmatic-hydrothermal transition. Quartz and its associated fluid inclusions were characterised petrographically, and quartz was further analysed for its trace element content and oxygen isotopic composition.

**d. To what extent did fluids contribute to metal mobility as the system cooled?**

Following the onset of fluid circulation, a complex magmatic-hydrothermal system developed, primarily resulting in the widespread greisen alteration of the Beauvoir intrusion (Aïssa et al., 1987; Cuney et al., 1992). Petrographic and geochemical evidence suggested a significant impact on the distribution of metals, notably the leaching and mobilisation of lithium toward the surrounding country rocks. This interpretation has been further supported by the analysis of magmatic fluid inclusions, which reveal substantial hydrothermal mobility of metals (Harlaux et al., 2017). However, magmatic fluids constitute only a fraction of the total fluids that influenced the Beauvoir granite, and the evolution of metal transport during the cooling of the system remains incompletely understood.

To address this question, the composition of the distinct FI types identified within magmatic quartz (Aïssa et al., 1987) were analysed by microthermometry, Raman spectrometry and LA-

ICP-MS, aiming to deduce the pressure-temperature conditions of fluid entrapment, as well as their salinity and detailed composition in terms of gases, major elements, and trace elements. A particular focus was placed on determining the partition coefficients of metals between the earliest magmatic fluids and those that evolved through cooling and boiling, as well as understanding the impact of mixing with non-magmatic fluids on the redistribution of metals at the scale of the granitic stock.

# PART II

# Unravelling the magmatic and hydrothermal evolution of rare-metal granites through apatite geochemistry and geochronology: the Variscan Beauvoir granite (French Massif Central)

---

Published paper: Rocher O., Ballouard C., Richard A., Monnier L., Carr P., Laurent O., Khebabza Y., Lecomte A., Bouden N., Villeneuve J., Barré B., Fullenwarth P., Leisen M. and Mercadier J. (2024) Unravelling the magmatic and hydrothermal evolution of rare-metal granites through apatite geochemistry and geochronology: The Variscan Beauvoir granite (French Massif Central). *Chemical Geology* **670**, 122400, https://doi.org/10.1016/j.chemgeo.2024.122400

## 1. Introduction

### *Version française*

La compréhension détaillée des évolutions magmatique, magmatique-hydrothermale et hydrothermale des gisements granitiques à métaux rares, tels que le granite de Beauvoir, se heurte souvent à l'absence de traceurs géochimiques adaptés pour reconstituer les processus complexes mis en jeu. Les micas du granite de Beauvoir, par exemple, ont largement été étudiés pour leur composition en éléments majeurs et traces, permettant d'éclairer le comportement des métaux depuis le stade magmatique jusqu'aux circulations hydrothermales de haute température (Monier et al., 1987; Monnier et al., 2022). Toutefois, ces minéraux n'étant pas stables tout au long de l'évolution du système, leur utilisation pour obtenir des données isotopiques *in-situ* essentielles à la contrainte des âges et des sources des circulations fluides hydrothermales reste limitée. Par ailleurs, d'autres minéraux couramment utilisés comme traceurs, notamment le zircon et la monazite, sont rares dans ces systèmes, et les zircons présentent souvent un fort degré de métamictisation.

L'apatite [$Ca_5(PO_4)_3(OH,Cl,F)$], en revanche, constitue un minéral accessoire commun dans les systèmes ignés et minéralisateurs, connu pour sa sensibilité aux processus magmatiques et hydrothermaux, ces derniers induisant des modifications texturales et chimiques sur une large gamme de pressions et de températures (Harlov, 2015). Ce minéral peut incorporer une grande variété d'éléments majeurs et traces dans sa structure, notamment les terres rares (REE), le Y, Mn, Fe, Sr, Pb, Na, ainsi que les actinides U et Th remplaçant le Ca; ou encore des ions comme le Si, S, As et V substituant au P; et les halogènes (F, Cl, Br, I) occupant le site anionique (Pan and Fleet, 2002). La cristallisation ou l'altération de l'apatite peut être datée *in-situ* grâce au système U-Pb (Chew and Spikings, 2015) et les analyses isotopiques haute résolution (O, Cl, Sr et Nd) fournissent des informations clés sur la source et les conditions physico-chimiques des fluides ou magmas minéralisateurs (e.g., Decrée et al., 2020; Cao et al., 2021; Melfou et al., 2023).Grâce à sa chimie unique, l'apatite s'avère ainsi être un outil précieux pour étudier l'évolution des suites ignées (e.g., Sha and Chappell, 1999; Belousova et al., 2002; Laurent et al., 2017b; Zhang et al., 2020; Xu et al., 2024), l'origine et la composition des fluides hydrothermaux, les interactions fluide-roche, ainsi que pour établir la chronologie des processus hydrothermaux (e.g., Harlov, 2015; Kusebauch et al., 2015a, 2015b; Ballouard et al., 2018; Pochon et al., 2018; Andersson et al., 2019; Melfou et al., 2023).

La présence d'apatite a largement été documentée dans de nombreux gisements à métaux rares associés au magmatisme granitique peralumineux, comme le gisement à Sn-W de Panasqueira au Portugal (e.g., Marignac et al., 2020), le stock granitique à Li-Sn-W-Nb-Ta de Podlesí en République Tchèque (e.g., Breiter et al., 2005) et la pegmatite LCT de Szklary en

Pologne (e.g., Szuszkiewicz et al., 2018). Les travaux antérieurs sur les plutons peralumineux à métaux rares se sont principalement concentrés sur les processus pétrogénétiques, notamment la différenciation magmatique ou le mélange entre magmas (Broska et al., 2004; Hsieh et al., 2008; Chu et al., 2009; Roda-Robles et al., 2022). L'utilisation de l'apatite pour reconstituer l'histoire hydrothermale de ces systèmes reste quant-à-elle limitée. La géochronologie de l'apatite a notamment permis de contraindre l'âge des minéralisations magmatique-hydrothermales primaires en étain dans l'Erzgebirge en Allemagne (Romer et al., 2007), et de fournir des éléments essentiels à la construction du modèle métallogénique du système minéralisé de Panasqueira (Launay et al., 2021; Jaranowski et al., 2021). Plus récemment, l'étude de l'apatite dans le granite peralumineux à métaux rares pauvre en phosphore de Qianlishan (Sud de la Chine) a confirmé son potentiel pour retracer les évolutions magmatique et métasomatique de ces systèmes (Zhang et al., 2024). Au sein du granite de Beauvoir, l'apatite est particulièrement abondante en raison de sa forte teneur en phosphore, en faisant un minéral clé pour mieux comprendre son évolution magmatique et hydrothermale qui reste à ce jour encore fragmentée.

Cette étude combine l'analyse *in-situ* de la chimie élémentaire, de la composition des isotopes de l'oxygène et la géochronologie U-Pb de l'apatite afin de reconstituer l'évolution magmatique et hydrothermale du système de Beauvoir, replacée dans le contexte géodynamique du Massif central. Plus précisément, l'apatite est utilisée comme proxy pour (i) contraindre la chronologie des circulations fluides au sein de l'intrusion de Beauvoir et leur relation avec la cristallisation du magma ; (ii) retracer l'origine des fluides successifs, leur dynamique de mélange, leurs conditions physico-chimiques et leurs interactions avec les roches encaissantes ; et (iii) comprendre l'impact de ces circulations fluides sur l'enrichissement en métaux rares et les mécanismes de cristallisation des minéraux porteurs de ces métaux dans le granite de Beauvoir.

### *English version*

The circulation of hydrothermal fluids in the Earth's crust is known to play a key role in mineralisation processes, sometimes leading to remarkable metal concentrations, both in terms of metal grade and volume. Mineralised hydrothermal systems can be associated with magma emplacement, and are then designated as ore-forming magmatic-hydrothermal systems. They are found in many geodynamic environments, encompassing continental as well as oceanic domains. Porphyry and greisen-related Sn-W ore deposits represent well-known examples of ore-forming magmatic-hydrothermal systems and result from the intrusion in the upper continental crust of intermediate to felsic magmas (Robb, 2020). In those two systems, fluid circulation within and around the intrusive bodies is proven to be a key element to metal enrichment and controls the spatial distribution of the mineralisation (e.g., Dilles, 1987; Audétat et al., 2000b; Burnard and Polya, 2004; Sillitoe, 2010; Lecumberri-Sanchez et al., 2017; Legros et al., 2019). This relation

between hydrothermalism and metal deposition seems to be less obvious for rare-metal granites and pegmatites, although they are emplaced in similar geologic settings.

Highly peraluminous rare-metal granites (PRMGs; Linnen and Cuney, 2005) as well as lithium-cesium-tantalum (LCT) pegmatites (Černý and Ercit, 2005) are characterised by extreme enrichment mostly in lithophile metals and halogens (e.g., Li, F, Ta, Nb, Sn, W, and Be), with concentrations exceeding those of the bulk upper continental crust by several order of magnitude (Tischendorf, 1977; Romer and Pichavant, 2020). They result from the crystallisation of highly evolved magmas and typically represent the final magmatic units emplaced during late-orogenic granitic magmatism (Kovalenko et al., 1970; Linnen, 1998; Linnen and Cuney, 2005). The primary mineralisation they host, such as Li aluminosilicates along with Nb-Ta-Sn oxide minerals, is disseminated throughout the intrusive body, and magmatic processes, such as partial melting and fractional crystallisation, play a key role for metal enrichment and deposition (e.g., Raimbault et al., 1995; Pichavant, 2022; Ballouard et al., 2023). However, it has also been long recognised that metasomatism, commonly designated as albitisation and greisenisation, generally affects highly evolved peraluminous granites and pegmatites and may lead to significant mineralogical and geochemical modifications of the ore-bearing mineral assemblage (e.g., Černý, 1986; Schwartz, 1992). Both metasomatic processes typically involve the circulation of a magmatic volatile phase (MVP), also referred to as magmatic fluids, which corresponds to either a supercritical fluid, low-density aqueous vapor, higher density and salinity liquid (possibly hypersaline), or vapor coexisting with liquid exsolved from the melt during its cooling and crystallisation (e.g., Burnham, 1979b; Russell et al., 1995; Candela, 1997; Webster et al., 2009). Albitisation was suggested to be related to the interactions between highly fluxed melt or solute-rich magmatic volatile phase (i.e., MVP) and crystals at near-solidus conditions and the metasomatic media can significantly participate to the transport and concentrations of metals such as Li, Nb and Ta (e.g., Badanina et al., 2004; Müller et al., 2018b; Kaeter et al., 2018; Ballouard et al., 2020a; Pfister et al., 2023). Greisenisation is presumed to mainly involve acidic and moderately saline (*ca.* 3–10 wt.% NaCl eq) magmatic fluids circulating at temperatures of 200-500 °C (e.g., Burt, 1981; Štemprok, 1987; Shepherd et al., 1985; Taylor, 1988; Schwartz and Surjono, 1990; Halter et al., 1998; Dobeš, 2005; Monnier et al., 2020), although the contribution of external fluids, especially of meteoric origin, has been highlighted in many systems (e.g., Witt, 1988; Cuney et al., 1992; Bettencourt et al., 2005). The relationship between greisen alteration and hydrothermal Sn and/or W mineralisation at subsolidus conditions is well documented (e.g., Monnier et al., 2020; Launay et al., 2021) and in some cases, the interactions between melt and external fluids equilibrated with the host-rocks was proposed as a key process to trigger the supra-solidus precipation of metal-bearing phases such as Nb-Ta oxide minerals (Fouillac and Rossi, 1991; London et al., 1996; Linnen et al., 2019; McNeil et al., 2020). Therefore, deciphering and quantifying the impact of exsolved magmatic fluids as well as external fluids, during and

after the magmatic-hydrothermal transition, is essential to fully explain the formation of rare metal granite deposits.

The Beauvoir granite is located in the northern part of the French Massif Central (FMC) of the European Variscan belt and represents one of the best studied examples worldwide of peraluminous high-phosphorus rare-metal granite (PHP-RMG; Cuney et al., 1992). It is characterised by disseminated Sn-Li-Ta-Nb-Be mineralisation, which is broadly considered to initially derive from magmatic processes (Pichavant et al., 1987b; Raimbault et al., 1995; Pichavant, 2022). The importance of fluids in metal deposition has been clearly highlighted (Fouillac et al., 1987; Fouillac and Rossi, 1991; Charoy et al., 2003) with a complex magmatic-hydrothermal system developed following the emplacement of the intrusion that resulted in widespread greisenisation (Aïssa et al., 1987; Merceron et al., 1992; Cuney et al., 1992; Monnier et al., 2020) and hydrothermal mobility of rare metals (Harlaux et al., 2017). However, some key elements of its evolution remain rather poorly constrained, such as the role of external fluids in the greisenisation processes (Cuney et al., 1992; Monnier et al., 2020, 2021). The nature, conditions and timing of circulation of these external fluids, of potential diverse origins, are also debated (Fouillac et al., 1987; Fouillac and Rossi, 1991; Cuney et al., 1992). Furthermore, tectonic and thermal processes leading to the circulation of late fluids throughout the cooled granitic body, their impact on metal endowment, as well as the precise absolute chronology of these events, has not been fully elucidated yet (Merceron et al., 1987, 1992).

The difficulty of precisely deciphering the magmatic, magmatic-hydrothermal and hydrothermal evolutions of rare-metal deposits, like the Beauvoir granite system, arises from the scarcity of minerals representing suitable geochemical proxies to track back these processes. For example, micas from the Beauvoir PRMG have been extensively studied for both major and trace elemental compositions, providing insights into metal behavior from the magmatic to high-temperature hydrothermal stages (Monier et al., 1987; Monnier et al., 2022). However, micas are not stable throughout the global evolution of such system and *in-situ* isotopic data providing direct age and source constraints for hydrothermal fluid circulation are missing. Other traditional tracer minerals, like zircon and monazite, cannot be used as they are rare, and scarce zircon shows a high degree of metamictisation.

Apatite [$Ca_5(PO_4)_3(OH,Cl,F)$] is a common accessory mineral in many igneous and ore-forming systems, sensitive to melt or fluid-induced textural and geochemical changes over a wide range of pressures and temperatures (Harlov, 2015). Apatite can incorporate many major and trace elements in its structure, the most common being REE, Y, Mn, Fe, Sr, Pb , Na and the actinides U and Th substituting for Ca; small, highly charged ions such as Si, S, As and V replacing P; and the halogens (F, Cl, Br and I) in the anion site (Pan and Fleet, 2002). Because of this specific chemistry, apatite has been used for several years to decipher the evolution of

igneous suites (e.g., Sha and Chappell, 1999; Belousova et al., 2002; Laurent et al., 2017b; Zhang et al., 2020; Xu et al., 2024), the origin and composition of hydrothermal fluids, fluid-rock interactions and constrain the timing of hydrothermal processes (e.g., Harlov, 2015; Kusebauch et al., 2015a, 2015b; Ballouard et al., 2018; Pochon et al., 2018; Andersson et al., 2019; Melfou et al., 2023). Additionnaly, apatite crystallisation or alteration can be dated in-situ notably using the U-Pb system (Chew and Spikings, 2015) and high resolution O, Cl, Sr, Nd isotope systematics (e.g., Decrée et al., 2020; Cao et al., 2021; Melfou et al., 2023) can provide crucial information regarding the source and physico-chemical conditions of mineralising melts or fluids.

Apatite occurrences have been well-documented in numerous rare metal deposits related to peraluminous granite magmatism, including the Panasqueira Sn-W deposit (Portugal; e.g., Marignac et al., 2020), the Podlesí Li-Sn-W-Nb-Ta granite stock (Czech Republic; e.g., Breiter et al., 2005), and the Szklary LCT pegmatite (Poland; e.g., Szuszkiewicz et al., 2018). Previous studies of apatite within PRMGs and LCT pegmatites mainly investigated petrogenetic processes, such as magmatic differentiation or magma mixing (Broska et al., 2004; Hsieh et al., 2008; Chu et al., 2009; Roda-Robles et al., 2022). Few studies used apatite to assess the hydrothermal history of these systems. Apatite geochronology has been employed to constrain the timing of primary magmatic-hydrothermal Sn mineralisation in the Erzgebirge (Germany; Romer et al., 2007), and also provided key constraints on establishing the metallogenic model for the Panasqueira ore system (Launay et al., 2021; Jaranowski et al., 2021). A recent study of apatite from the Mesozoic Qianlishan low-phosphorus PRMG (South China) supported its usefulness as a tracer of magmatic and metasomatic evolution (Zhang et al., 2024). The textural and geochemical record of the magmatic to hydrothermal evolution of PRMG systems such as the Beauvoir deposit remains fragmented, whereas apatite is a ubiquitous mineral crystallising from the supra- to sub-solidus stages in PRMGs due to the high-phosphorous content.

In this study, we couple in-situ determination of apatite chemistry, oxygen isotope systematics and U-Pb geochronology to unravel the magmatic and hydrothermal evolution of the Beauvoir system within the geodynamic evolution of the FMC. More specifically, we use apatite as a proxy to (i) constrain the timing of fluid circulations within the Beauvoir intrusion and relative to igneous crystallisation; (ii) trace the origin of successive fluids, the mixing dynamics, the physico-chemical conditions and fluid-rock interactions and (iii) decipher their implications regarding the metal endowment and crystallisation mechanism of rare metal-bearing minerals in the Beauvoir PRMG.

## 2. Geological setting

### 2.1. Regional geology

The FMC belongs to the internal zone of the European Variscan belt (Fig. II.1a), which results from the main collision between the supercontinents Gondwana to the south and Laurussia to the north (Matte, 1991; Robardet, 2002). Spanning from the Late Devonian to the Early Carboniferous (*ca.* 380 to 290 Ma; Matte, 1986; Ballèvre et al., 2014), this orogenic event ultimately led to the formation of Pangea (Tait et al., 2000).

The structure of the FMC essentially consists of a metamorphic nappe stack, composed of four main tectonic units, developed diachronously during the Devonian to Early Carboniferous and intruded by granitic magmas from *ca.* 360 to 295 Ma (Vanderhaeghe et al., 2020 and references therein). From north to south and from top to bottom, these tectonic units are: the Upper Gneiss Unit (UGU), the Middle Allochthonous Unit (MAU) identified in the Limousin, the Lower Gneiss Unit (LGU) and the Parautochtonous Unit (PAU). In the northern part of the FMC, in the region of Echassières, the stack of the UGU, LGU and PAU forms the Sioule series, an inverted metamorphic sequence (Grolier, 1971) (Fig. II.1b). This series is bounded to the west and to the south, respectively, by sinistral and dextral Carboniferous shear zones (i.e., the Sillon Houiller and Sainte-Christine faults, respectively) and underwent at least three significant tectonic-metamorphic episodes (Faure et al., 2009; Schulz, 2009; Do Couto et al., 2015) including: (i) a high pressure $D_0$ event, during which the UGU experienced high- to ultra-high-pressure eclogite-granulite-facies metamorphism recorded elsewhere in the FMC between 390 and 360 Ma (Lotout et al., 2020; De Hoÿm de Marien et al., 2023); (ii) a $D_1$ event, characterised by a top-to-the-SW shearing synchronous with migmatisation and exhumation of the UGU and LGU units; and (iii) a medium pressure-medium temperature $D_2$ event, associated with a top-to-the-NW shearing. $D_1$ and $D_2$ events are thought to have been postdated by the unconformable deposition at *ca.* 330 Ma of the "Tuffs anthracifères" series consisting of weakly deformed and metamorphosed terrigenous sedimentary and felsic volcanic rocks (Bruguier et al., 1998; Do Couto et al., 2015). The Sioule metamorphic series is structured by two major antiforms, in the centre of which the PAU mica schists crop out. They are intruded by two granitic plutons: the Pouzol-Servant porphyritic granite in the southern antiform and the Echassières granitic complex in the northern antiform (Fig. II.1b).

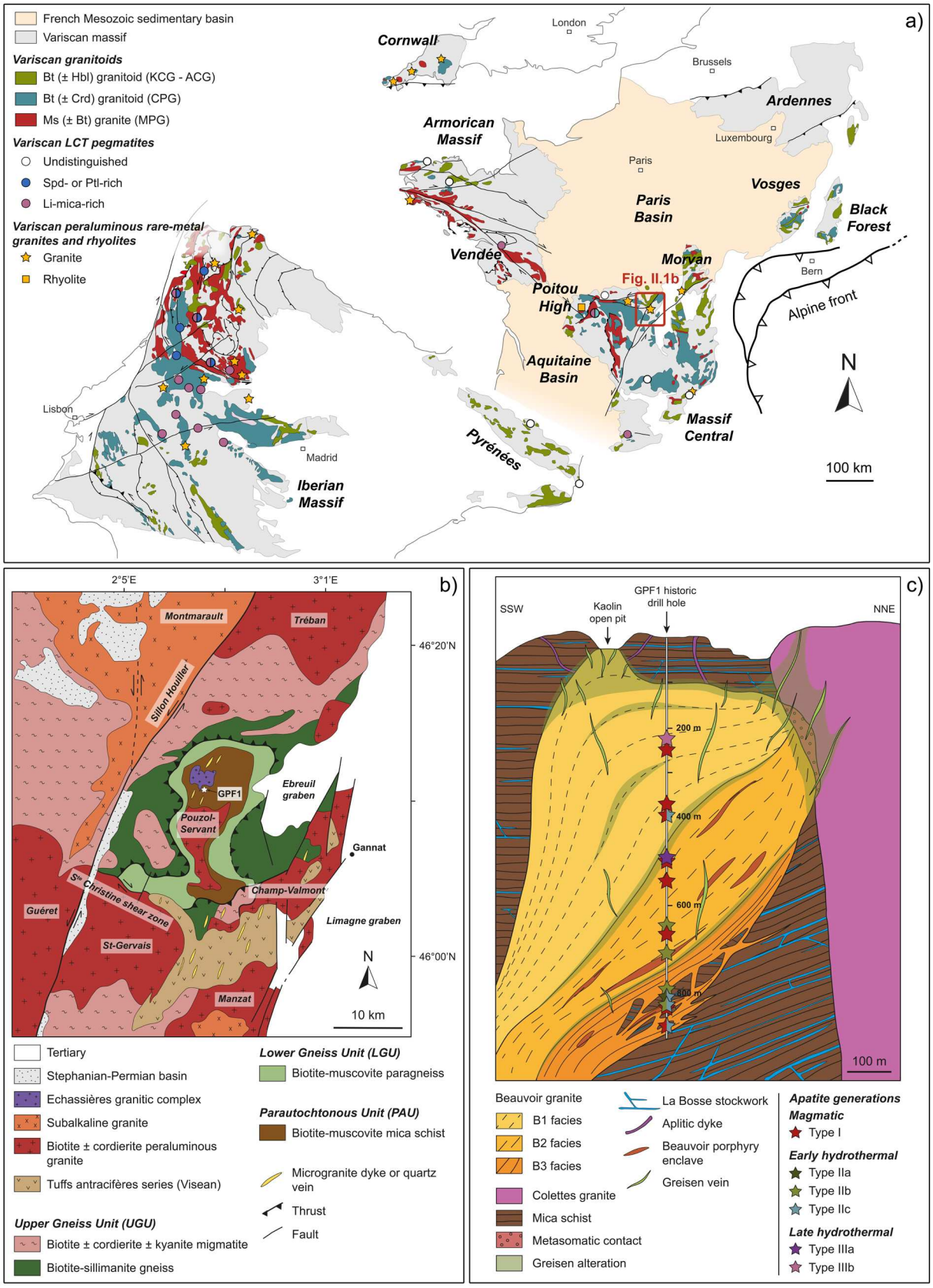



*Figure II.1. (a) Schematic representation of the western European Variscan belt representing the main terranes and showing Variscan granitoids, as well as LCT pegmatites, rare-metal granites and rhyolites (modified from Ballouard et al. (2024)). The granitoids typology is from Barbarin (1999). MPG: muscovite-bearing peraluminous granites; CPG: cordierite-bearing peraluminous granitoids; KCG: K-rich and K-feldspar porphyritic calc-alkaline granitoids. ACG:*

*amphibole-rich calc-alkaline granitoids. Mineral abbreviations according to Warr (2021). (b) Simplified geological context of the Echassières granitic complex in the northern part of the French Massif Central (FMC) (modified from Cuney et al. (1992) and Harlaux et al. (2017)). The location of the GPF1 deep drillhole that crosscuts the Beauvoir PRMG is indicated by the white star. (c) Interpretative cross-section of the Beauvoir PRMG representing the vertical magmatic internal zoning composed by the three successive units B1, B2, and B3 (modified from Cuney et al. (1992) and Monnier et al. (2018)). The location of the studied samples is shown together with the classification of the encountered apatite generations (section 4.1).*

### 2.2. The Echassières granitic complex

The Echassières granitic complex is a circular intrusive body, 3 km in diameter, emplaced during a major N20° shortening episode at the end of the Carboniferous (Gagny et al., 1984; Gagny and Jacquot, 1987; Feybesse, 1985; Blès et al., 1989). It results from the intrusion of at least three granitic units (Cuney et al., 1992; Raimbault et al., 1995) (Fig. II.1c): (i) the inferred La Bosse granite, concealed at depth and possibly at the origin of a quartz-wolframite vein system, the La Bosse stockwork, developed within the PAU mica schists; (ii) the Colettes granite, a cordierite-bearing two-mica porphyritic granite; and (iii) the Beauvoir granite, a highly evolved albite-lepidolite-topaz leucogranite hosting disseminated Sn-Li-Ta-Nb-Be mineralisation.

The Beauvoir PRMG was emplaced during the Variscan late-orogenic extensional stage at *ca.* 310–315 Ma (Rb-Sr on whole rock; Duthou and Pin, 1987; Ar-Ar on lepidolite; Cheilletz et al., 1992, and U-Pb on columbite-group minerals; Melleton et al., 2015). It has been studied by many authors, in particular following the drilling of a *ca.* 900m deep drillhole (GPF1) in 1985 as part of the "Géologie Profonde de la France" (GPF) drilling program (Cuney and Autran, 1987). Petrographic and structural studies highlighted a vertical zonation within the granite, leading to the proposal of three main magmatic units that were inferred to have successively intruded the parautochthonous mica schists of the Sioule metamorphic series (Bouchez et al., 1987; Gagny, 1987; Jacquot and Gagny, 1987; Monier et al., 1987; Rossi et al., 1987). These units are designated as the B1 (~ 100–450 m depth in GPF1), B2 (~ 450–750 m) and B3 (~ 750–880 m) facies, with the B1 unit thought to represent the final and most differentiated magma batch (Fig. II.1c). A recent study revealed a more complex sequence composed of 18 sub-units distributed across 4 units (i.e., B1, B1', B2 and B3), which incrementally intruded the host mica schists (Esteves et al., 2024a). A last facies, distinguished by its porphyritic texture and referred to as "Beauvoir porphyry enclave", has been encountered within the B2 and B3 units, either as dykes or enclaves (e.g., Cuney et al., 1992; Monnier et al., 2018). Its chemical characteristics closely resemble those of the Colettes granite, indicating a possible genetic connection (Raimbault and Azencott, 1987; Monnier et al., 2018).

The Beauvoir PRMG exhibits a remarkable enrichment in fluxing and litophile elements (Li, P, F, Rb, Cs, Be, Nb, Ta, Sn, W, U), especially at its apical part (Raimbault et al., 1995), and therefore shares many characteristics with rare-element pegmatites of the LCT family (Raimbault, 1998; Černý and Ercit, 2005). For instance, the concentrations in Li, Sn, and Ta

respectively vary from 0.1 to 1 wt.%, 0.02 to 0.4 wt.%, and 40 to 500 ppm, values that largely exceed those of the bulk upper continental crust (24 ppm for Li; 2.1 ppm for Sn; and 0.9 ppm for Ta; Rudnick and Gao, 2003). Crystallisation experiments have demonstrated that the melts that formed the Beauvoir PRMG crystallised under pressures of 100 to 300 MPa at very low temperatures (below 670 °C) with solidus estimated to be near 550 °C, a common characteristic of flux-rich granitic melts (Pichavant et al., 1987a; Pichavant, 2022). Albite, quartz, K-feldspar and Li-F-micas, with zinnwaldite to lepidolite compositions, represent the major magmatic minerals of the Beauvoir crystallisation sequence, along with cassiterite (Sn; generation I), topaz (F), apatite (F), amblygonite-group minerals (Li-F), herderite (Be-F), zircon, columbite-group minerals (Nb-Ta), pyrochlore-group minerals (Nb-Ta-U), and uraninite (U) as accessories (Pichavant et al., 1987a; Rossi et al., 1987; Johan et al., 1988; Cuney et al., 1992; Raimbault et al., 1995; Pichavant, 2022) (Fig. II.2). This magmatic paragenesis evolves across the three magmatic units (i.e., B1, B2 and B3). The proportion of accessory minerals tends to increase from the B3 unit to the most evolved B1 unit. A similar trend is observed for the abundance of albite, whereas the proportions of quartz and K-feldspar progressively decrease from the B3 to the B1 unit, with Li-micas transitioning from zinnwaldite to lepidolite.

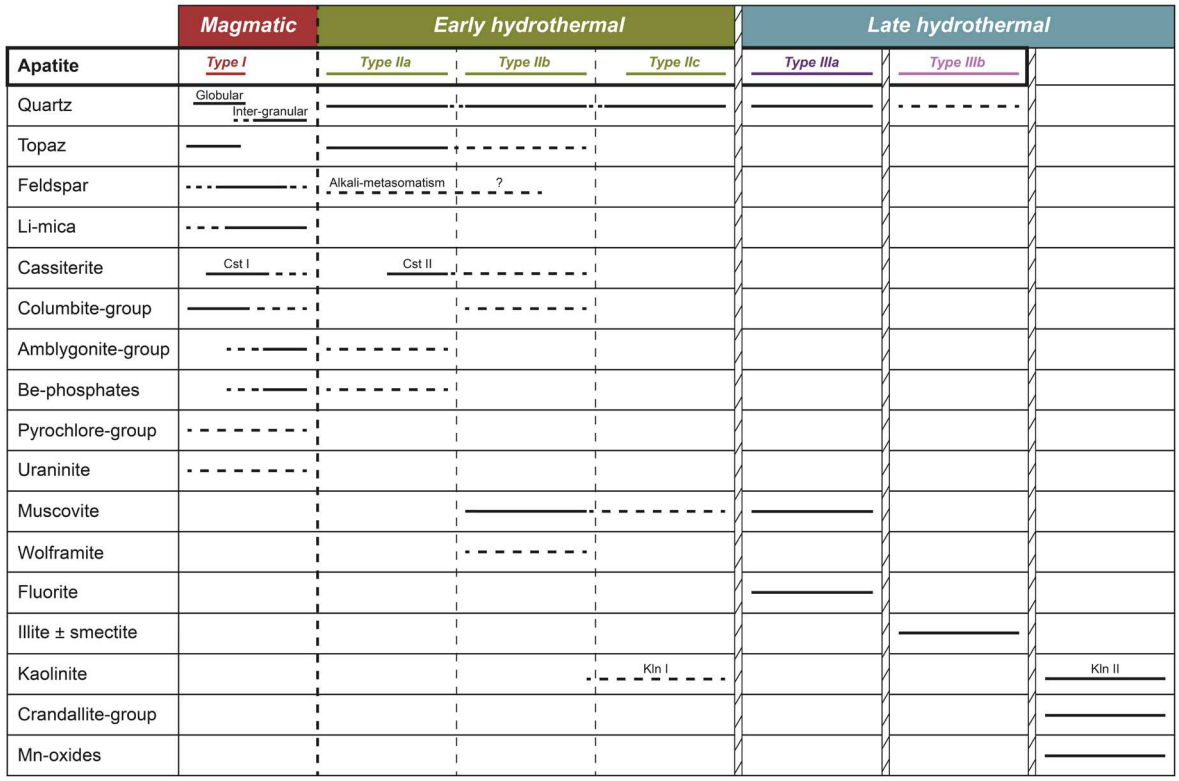



*Figure II.2. Paragenetic synthesis of magmatic and hydrothermal mineralogical associations of the Beauvoir system. The hatched areas indicate a temporal and genetic disconnection of events during the early and late hydrothermal evolution of the Beauvoir PRMG. Magmatic paragenesis is based on Pichavant et al. (1987a), Rossi et al. (1987), Johan et al. (1988), Cuney et al. (1992), Raimbault et al. (1995), and Pichavant (2022). The early hydrothermal paragenesis relies on the studies of Merceron et al. (1987, 1992) and Monnier et al. (2018, 2019). The late hydrothermal paragenesis draws from the descriptions of Merceron et al. (1987, 1992). See sections 2.4 and 4 for details on the different apatite generations. Abbreviations follow the IMA conventions compiled by Warr (2021).*

### 2.3. The Beauvoir magmatic-hydrothermal system

The magmatic-hydrothermal to hydrothermal evolution of the Beauvoir PRMG is complex and characterised by multiple fluid circulation episodes. Four major stages can be recognised (Cuney et al., 1992; Merceron et al., 1992; Monnier et al., 2019): (i) the early hydrothermal stage (200–550 °C), driven by the intrusion heat, mostly led to the development of vertical quartz veins, as well as the greisen alteration of both the intrusion and the surrounding rocks (i.e., the Colettes granite, La Bosse stockwork and host mica schists); (ii to iv) three late hydrothermal stages were associated to fluid circulation genetically and temporally disconnected from the Beauvoir PRMG emplacement. The first two late hydrothermal stages are respectively characterised by the development of sub-vertical quartz veins associated with fluorite (< 250 °C) and illite-smectite (100–200 °C) precipitation, while the third and final stage resulted in widespread supergene kaolinisation (⩽50 °C), essentially affecting the apical part of the Beauvoir intrusion and coeval with low-temperature phosphate precipitation (i.e., crandallite-group minerals) (Fig. II.2).

The early hydrothermal stage can also be designated as a magmatic-hydrothermal transition. This transition consists of a continuous evolution, throughout cooling of the granitic melt, from an initially purely magmatic system dominated by crystal-melt interactions to a system dominated by crystal-melt-fluid phase interactions, that finally results in a purely hydrothermal system associated to fluid-rock interactions (Halter and Webster, 2004; Audétat and Edmonds, 2020). The term "early hydrothermal stage" thus includes the magmatic and early hydrothermal stages described by Merceron et al. (1992) and the early orthomagmatic and greisenisation stages as detailed by Monnier et al. (2022). It has been initiated by the exsolution of hot (> 490 °C) magmatic fluids from the Beauvoir melts during crystallisation. The early circulation of these magmatic fluids (i.e. L1 fluids described by Aïssa et al. (1987)) primarily led to acidic F-rich alteration, predominantly occurring in the contact zones between the granite and the host mica schists (Cuney et al., 1992; Monnier et al., 2020). Magmatic fluids concentrated in the shallowest B1 unit, generating an overpressure abruptly released by fracturing (Aïssa et al., 1987; Cuney et al., 1992) that induced the emplacement of sub-vertical, centimetric quartz veins (Merceron et al., 1987, 1992), as well as the phase separation of primary magmatic fluids (L1) into a high-salinity brine (L2) and a low- to moderate-salinity vapour (V2) (Aïssa et al., 1987; Harlaux et al., 2017). Primary (L1) and secondary (L2 and V2) magmatic fluids progressively evolved by cooling and mixing with fluids of external origin (e.g., meteoric or metamorphic fluids; Aïssa et al., 1987; Cuney et al., 1992; Monnier et al., 2020). These fluid circulations were responsible for the widespread greisenisation of the Beauvoir intrusion and adjacent rocks. Greisen-alteration thus seems temporally and genetically linked to the Beauvoir intrusion emplacement dated at *ca.* 310–315 Ma (Duthou and Pin, 1987; Cheilletz et al., 1992; Melleton et al., 2015), as suggested by the age of 307 ± 3 Ma obtained through U-Pb dating of greisen alteration-related monazite

within the Echassières complex (Monnier et al., 2021). Greisenisation has been particularly intense at the apical part of the Beauvoir PRMG but is also encountered at depth, essentially at the transition zones between the three magmatic units (i.e., B1, B2 and B3; Merceron et al., 1992). It involved the pervasive replacement of igneous minerals, mainly feldspar (± quartz and lepidolite), by a quartz-muscovite assemblage, commonly associated with the precipitation of other secondary minerals, such as apatite, topaz, cassiterite (generation II), columbite- and pyrochlore-group minerals, as well as the formation of millimetric quartz-muscovite veins (Merceron et al., 1987; Monnier et al., 2018, 2019) (Fig. II.2) The progressive cooling of greisen-forming fluids is thought to be associated with successive crystallisation of muscovite, pyrophyllite, donbassite, tosudite and minor early kaolinite (Kln I on Fig. II.2) (Merceron et al., 1987, 1992). Sodic (i.e., albitisation) and potassic alterations were also observed to a lesser extent and were proposed to derive from the circulation of the highly saline magmatic brine L2 (Monnier et al., 2018). During greisenisation, $Na^+$ and $K^+$ are released into the aqueous solution, increasing the alkali/$H^+$ ratio and potentially triggering alkali-metasomatism (e.g., Štemprok, 1987; Pirajno, 2009; Ballouard et al., 2020a). In constrast, alkali-metasomatim may induce greisenisation by progressively decreasing the alkali/$H^+$ ratio of the system. Therefore, the greisen and alkali alterations encountered in the Beauvoir PRMG might have been driven by the same fluids, as the associated replacement reactions form a self-sustaining chemical system, potentially leading to multiple successive generations of albitite and greisen (e.g., Ballouard et al., 2020a).

The three distinct late hydrothermal stages are interpreted to derive from the circulation of external fluids (i.e. meteoric, metamorphic fluids or basinal brines) throughout the cooled granitic body (Merceron et al., 1992), and consist in: (i) fluorite mineralisation, (ii) illite ± smectite vein fillings, and (iii) widespread supergene kaolinisation. Fluorite occurs in association with quartz in sub-vertical veins or in inter-granular secondary porosity, as well as a replacement of igneous minerals, in particular albite (Merceron et al., 1987). Fluorite precipitation seems to clearly postdate greisen alteration and to be related to the circulation of external fluids; however its timing and the origin of involved fluids remain poorly constrained (Merceron et al., 1987; Raimbault, 1988). The precipitation of illite results from hydrothermal fluid circulation at temperatures of *ca.* 200 °C during the Upper Jurassic (151 ± 4 Ma obtained by K-Ar dating of illite; Merceron et al., 1987). It is followed by the precipitation of illite/smectite mixed-layer minerals as vein-filling materials. Finally, supergene kaolinisation occured during the last alteration event of the Beauvoir PRMG (Eocene to Oligocene; Merceron et al., 1987; Charoy et al., 2003; Monnier et al., 2019). Kaolinisation has been particularly intense at the apical part of the intrusion, and mostly overprints greisen alteration. Kaolinite is found as replacement of greisen-related muscovite and igneous feldspar, and apatite is systematically altered either into kaolinite or crandalite-group minerals. Accessory Mn-oxides, W-rich goethite, crandalite-group minerals, and illite/smectite mixed layer clays commonly accompany kaolinite precipitation.

These minerals also co-precipitated with quartz in late brecciated veins exhibiting evidence of multiple reactivation episodes (Monnier et al., 2019). Two generations of kaolinite have then been identified, the first and minor one (Kln I on Fig. II.2) precipitating at the end of the early hydrothermal stage, and the second one resulting from the supergene alteration event (Kln II in Fig. II.2).

### 2.4. Apatite occurrences in the Beauvoir PRMG

Three apatite generations were previously described within the Beauvoir PRMG (Aubert, 1969; Wang, 1988; Johan et al., 1988; Cuney et al., 1992; Monnier et al., 2019).

Apatite I, also referred to as apatite A by Wang (1988), represents an accessory mineral found throughout the entire intrusive complex, with a lesser occurrence in the B1 unit. It is characterised by a green to blue natural colour, and forms euhedral to subhedral crystals included in or closely associated with igneous topaz. Based on this textural relation, apatite I has been interpreted as an early crystallising mineral in the magmatic sequence (Wang, 1988; Johan et al., 1988; Cuney et al., 1992). Apatite I exhibits high MnO contents, decreasing from the B3 and B2 units (2–7 wt.%) to the B1 unit (< 1 wt.%) (Wang, 1988).

Apatite II forms colourless to green subhedral to anhedral grains, typically replacing apatite I and albite within the three magmatic units (Aubert, 1969; Wang, 1988; Johan et al., 1988). Although it essentially co-precipitates with quartz, muscovite and topaz, apatite II is locally associated with fluorite. Its precipitation is thought to derive from the extensive greisenisation affecting the Beauvoir PRMG, as well as the surrounding rocks.

Finally, a third apatite population (apatite III) has been described by Cuney et al. (1992) and Charoy et al. (2003). It forms a rim on crandallite-group minerals, more particularly goyazite, and mainly differs from apatite I and II by its significant SrO content, reaching up to 1.5 wt.%. The precipitation of crandallite-group minerals in the Beauvoir PRMG was presumed to result from the low-temperature destabilisation of albite and lepidolite during the Oligocene continental extension, responsible for the opening of the Limagne graben (Charoy et al., 2003).

## 3. Material and methods

### 3.1. Sampling strategy

As described in section 2, the evolution of the Beauvoir PRMG is characterised by three main supra- and sub-solidus stages: (i) magmatic, (ii) early hydrothermal and (iii) late hydrothermal stages. Sixteen samples were collected along the GPF1 historic drillhole to ensure the best representativity possible of each stage within the three magmatic units (i.e. B1, B2, and B3; Fig. II.1c; Table II.1). Eight samples of granite with little to no visible alteration were selected as reference for the magmatic stage: three from B1, four from B2, and one from B3. The early

hydrothermal stage was investigated through eight samples. Among these, five samples were chosen to represent the different degrees of pervasive greisen alteration in the Beauvoir PRMG (390.9, 642.7, 789.7, 819.5 and 862.0 m), two samples displayed veins formed by early and greisen-related fluid circulation (704.2 and 801.0 m), and one sample represented greisen alteration of the pre-existing La Bosse stockwork (816.5 m). Finally, two samples were analysed for the late hydrothermal stages, respectively from the B1 (221.1 m) and B2 (486.5 m) units. A pair of thin and thick sections (30 µm and 150–200 µm, respectively) was prepared for each sample to provide equivalent areas for petrographic study and analytical data acquisition.

Previous studies suggested the contribution of external fluids potentially reequilibrated with the country rocks during the development of the Beauvoir magmatic-hydrothermal system (section 2.3; Fouillac and Rossi, 1991; Merceron et al., 1992; Charoy et al., 2003). For comparison with apatite compositions, and to trace external fluid contribution, we investigated the bulk geochemical compositions of representative metasedimentary rock samples from the Sioule series, which represent the country rocks of the Echassières magmatic complex. The location and a brief description of the samples are provided in Table II.A9 (Appendix II.A4).

### 3.2. Imaging and analytical methods

Details about analytical protocols are provided along with data in Appendix II.A1 and are briefly summarised here.

The mineralogy, textural relationships and chemical zoning of apatite grains were investigated using optical microscopy, cathodoluminescence (CL) imaging with an OPEA Cathodyne connected to a Nikon Eclipse LV100 microscope, micro-XRF chemical mapping along with backscattered electron (BSE) imaging using a TESCAN VEGA3 Scanning Electron Microscope (SEM) at GeoRessources (Nancy, France). Higher resolution chemical maps along with quantitative major and minor element compositions of apatite were obtained by electron microprobe analyses (EPMA) at GeoRessources using natural and synthetic standards. The structural formulae of the distinct apatite generations were calculated based on 12.5 oxygen atoms per formula unit (apfu). Whole-rock geochemical analyses of metasedimentary rocks from the Sioule series were performed at the SARM (Nancy, France).

Measurements of oxygen isotopic composition and halogen concentrations (F, Cl, Br and I) of apatite were performed by ion microprobe (SIMS) at the CRPG (Nancy, France). Analyses were performed close to EPMA spots by focusing a primary $Cs^+$ ion beam on a raster area of ~15x15 and 5x5 µm for oxygen isotope and halogen compositions, respectively. Conditions similar to those of Decrée et al. (2020) were used for O isotope measurements. Correction of instrumental mass fractionation (IMF) was conducted by analysing the Durango fluorapatite reference material ($\delta^{18}O$ = 9.4 ‰; Trotter et al., 2008). The $^{18}O/^{16}O$ ratios are expressed as $\delta^{18}O$ values

and are normalised to the Vienna Standard Mean Ocean Water (VSMOW) composition ($^{18}O/^{16}O$ = 0.0020052; Baertschi, 1976) with long-term reproductibility (2s) varying from 0.08 to 0.20 ‰. Halogen concentration analysis protocol follows that of Melfou et al. (2023). Halogen compositions were again determined relative to the Durango fluorapatite standard with detection limits of 6.6 x $10^{-5}$ ppm for F, 1.3 x $10^{-4}$ ppm for Cl, 3.8 x $10^{-3}$ ppm for Br, and 7.9 x $10^{-4}$ ppm for I. Relative standard deviations are (RSD, 1s) of 2.99 % for F, 0.45 % for Cl, 6.00 % for Br, and 1.19 % for I.

Trace element concentrations and U-Pb isotope compositions of apatite were determined by LA-ICP-MS at Géosciences Environnement Toulouse (GET, France) and GeoRessources laboratories, and similar analytical protocols were used in both laboratories. Laser ablation for trace element analyses were performed with a constant spot size of 30 µm. For trace element analyses, the NIST SRM 610 glass was used as primary reference material for the correction of mass bias and instrumental drift (Jochum et al., 2011). The NIST SRM 612 glass (Jochum et al., 2011) and the Durango apatite were used as secondary control materials. Trace elements concentrations determined for the Durango apatite mostly fall within the range of reported values (note that this apatite is not homogenous in most elements; Table II.A6 in Appendix II.A4). The signal on $^{43}Ca$ within apatite was used as the internal standard, assuming a stoichiometric Ca content of 39.74 wt.%. For U-Pb analyses, isotope ratios were initially determined using the NIST SRM 610 glass again as a primary reference material for the correction of mass bias and instrumental drift. Matrix-corrected ratios were then determined by an average fractionation factor calculated for multiple apatite reference materials employed throughout the study, including Madagascar (Thomson et al., 2012), McClure Mountain (Schoene and Bowring, 2006), Durango (McDowell et al., 2005) and Duluth apatite (Schmitz et al., 2003). U-Pb ages presented in this study are lower intercept ages calculated in $^{238}U/^{206}Pb$ vs. $^{207}Pb/^{206}Pb$ Tera-Wasserburg diagrams with IsoplotR (Vermeesch, 2018) and errors are quoted at the 2-sigma level. Despite similar analytical protocols, systematic bias of U–Pb isotope compositions and ages will exist between both laboratories. We estimate the interlaboratory reproducibility to be ± 1.0 % relative from the dispersion of apatite reference material lower intercept ages obtained during this study (Fig. II.A1 in Appendix II.A1). This uncertainty is added in quadrature to any lower intercept date. The resulting total uncertainty is referred to in the following sections and indicated in brackets on Figs. II.11 and II.A2 (Appendix II.A2).

*Table II.1. Summary of samples and apatite characteristics. All samples derive from the GPF1 historic drillhole. Abbreviations follow the IMA conventions compiled by Warr (2021), with the exception of AGM: amblygonite-group minerals; CGM: columbite-group minerals; CdlGM: crandallite-group minerals PGM: pyrochlore-group minerals; M: magmatic mineral; EH: early hydrothermal mineral; LH: late hydrothermal mineral.*

| Generation | Type | Facies | Depth (m) | Sample description | Mineral association | Apatite main petrographic features |
|---|---|---|---|---|---|---|
| **Magmatic** | **I** | Beauvoir – B1 | 247,0 | Granite with little to no visible alteration | **M:** Quartz, albite, K-feldspar, lepidolite/zinnwaldite, topaz, apatite, AGM ± CGM, PGM, cassiterite, zircon | Anhedral to euhedral blue to green apatite closely associated with igneous topaz and commonly containing inclusions of zircon and CGM |
| | | | 368.7 | | | |
| | | | 390.9 | | | |
| | | Beauvoir – B2 | 495.3 | | | |
| | | | 546.5 | | | |
| | | | 660.4 | | | |
| | | | 862,0 | | | |
| | | Beauvoir – B3 | 824.0 | | | |
| **Early hydrothermal** | **IIc** | Beauvoir – B1 | 390.9 | Slightly greisenised granite | **M:** Quartz, albite, K-feldspar, lepidolite, topaz, apatite, AGM ± CGM, PGM, cassiterite, zircon<br>**EH:** Apatite ± muscovite | Anhedral apatite replacing igneous AGM |
| | **IIb** | Beauvoir – B2 | 642.7 | Greisenised Beauvoir granite overprinted by kaolinite | **M:** Quartz, lepidolite, albite ± cassiterite, CGM<br>**EH:** Quartz, muscovite, topaz, apatite<br>**LH:** Kaolinite | Anhedral grains partially replaced by a kaolinite |
| | **IIb** | Beauvoir – B2 | 704.2 | Vein at the contact between the greisenised Beauvoir and porphyric granites | **EH:** Quartz, apatite ± muscovite | Fringes of sub-euhedral to euhedral apatite mainly growing sub-perpendicular to the strike of the quartz vein |
| | **IIb** | Beauvoir – B3 | 789.7 | Beauvoir granite showing traces of oxidative late alteration | **M:** Quartz, albite, K-feldspar, zinnwaldite, topaz, apatite, AGM ± CGM, PGM, cassiterite, zircon<br>**EH:** Apatite ± muscovite<br>**LH:** CdlGM, kaolinite, Fe-oxides | Anhedral apatite replacing igneous minerals, in particular albite, in turn partially replaced by CdlGM |
| | **IIa and IIc** | Beauvoir – B3 | 801.0 | Polyphase vein at the contact between the Beauvoir granite and a mica schist enclave | **EH:** Quartz, topaz, cassiterite, lepidolite, muscovite, apatite<br>**LH:** CdlGM, Sr-sulfide | **IIa:** Sub-euhedral apatite co-precipitating with quartz, topaz and cassiterite<br>**IIb:** Anhedral apatite co-precipitating with Ms and partially replaced by CdlGM associated to Sr-sulfide |
| | **IIb** | Pre-existing La Bosse stockwork | 816.5 | Disseminated greisen in a stockwork enclave | **EH:** Topaz, muscovite, quartz, apatite ± wolframite, rutile, monazite | Subhedral to euhedral apatite commonly containing monazite inclusions |
| | **IIb and IIc** | Beauvoir – B3 | 819.5 | Greisenised Beauvoir granite | **M:** Quartz, zinnwaldite, Be-phosphates<br>**EH:** Quartz, muscovite, apatite | **IIb:** Anhedral apatite found in replacement of zinnwaldite and co-crystallising with a Qz-Ms assemblage<br>**IIc:** Anhedral red apatite replacing Be-phosphates |
| | **IIc** | Beauvoir – B2 | 862.0 | Slightly greisenised granite | **M:** Quartz, albite, K-feldspar, zinnwaldite, topaz, apatite, AGM ± CGM, PGM, cassiterite, zircon<br>**EH:** Apatite ± muscovite | Anhedral to subhedral apatite co-precipitating with Ms and replacing igneous minerals such as albite |
| **Late hydrothermal** | **IIIa** | Beauvoir – B2 | 486.5 | Polyphase pervasive vein | **LH:** Fluorite, quartz, muscovite, apatite, illite | Subhedral to euhedral apatite precipitating at the edge of the fluorite vein |
| | **IIIb** | Beauvoir – B1 | 221.1 | Vuggy quartz vein with Mn-oxides at the selvedges | / | Aggregates of small euhedral apatite grains precipitating in the vein porosity |

# 4. Results

## 4.1. Apatite petrography

Three major apatite generations were identified (Table II.1; Figs. II.2, II.3, II.4, II.5): (i) Magmatic apatite (type I) interpreted to have crystallised from the granitic melt; (ii) Early hydrothermal apatite (types IIa, IIb and IIc) which formed through fluid circulation associated with greisen alteration and directly related to the emplacement and cooling of the Beauvoir granite body; (iii) Late hydrothermal apatite (types IIIa and IIIb) that precipitated following fluid circulations thought to be genetically and temporally disconnected from the granite emplacement.

### *4.1.1. Magmatic apatite*

Magmatic apatite (type I) is widespread in unaltered to weakly altered granite samples throughout the entire intrusive complex, with a relatively lower abundance in the B1 unit in comparison to the B2 and B3 units. Its natural colour varies from dark green to deep blue, being mostly dark green in the B1 unit and deep blue in the B2 and B3 units (Figs. II.3a-c, II.4b). This colour diversity between magmatic units was already outlined by Wang (1988). Apatite I forms euhedral to subhedral grains co-crystallising with typical magmatic minerals as defined by phase equilibria experiments of the Beauvoir PRMG (e.g., Pichavant et al., 1987a; Pichavant, 2022), in particular topaz but also Li-micas, albite, quartz and K-feldspar. In addition to a close textural relationship with igneous topaz (Fig. II.4a), apatite I commonly hosts inclusions of zircon and columbite-group minerals (Figs. II.4e, h). This is consistent with previous petrographic observations of the Beauvoir PRMG supporting its magmatic origin (Rossi et al., 1987; Johan et al., 1988; Wang, 1988). Within the three magmatic units, local accumulations of Li-mica flakes define layering interpreted as magmatic fabrics (Bouchez et al., 1987; Jacquot, 1987) and exhibiting enrichment in magmatic topaz and apatite, as observed in the B2 unit (Figs. II.3b, II.4a). Magmatic apatite shows a yellow-greenish CL signal, which is generally brighter and more greenish in the B1 unit compared to the B2 and B3 units (Figs. II.4c, d, f, g, i). In some cases, it is characterised by a growth zoning, evolving from a dark greenish to yellowish colour in the core to a relatively brighter rim, whereas irregular patches with a brighter yellowish CL signal generally cross-cut this zoning and probably correspond to alteration zones (Figs. II.4c, d, f, g, i). All observations collectively confirm the magmatic origin of apatite I and indicate that it may be an early crystallising mineral, contemporaneous with magmatic topaz, within the magmatic paragenetic sequence.

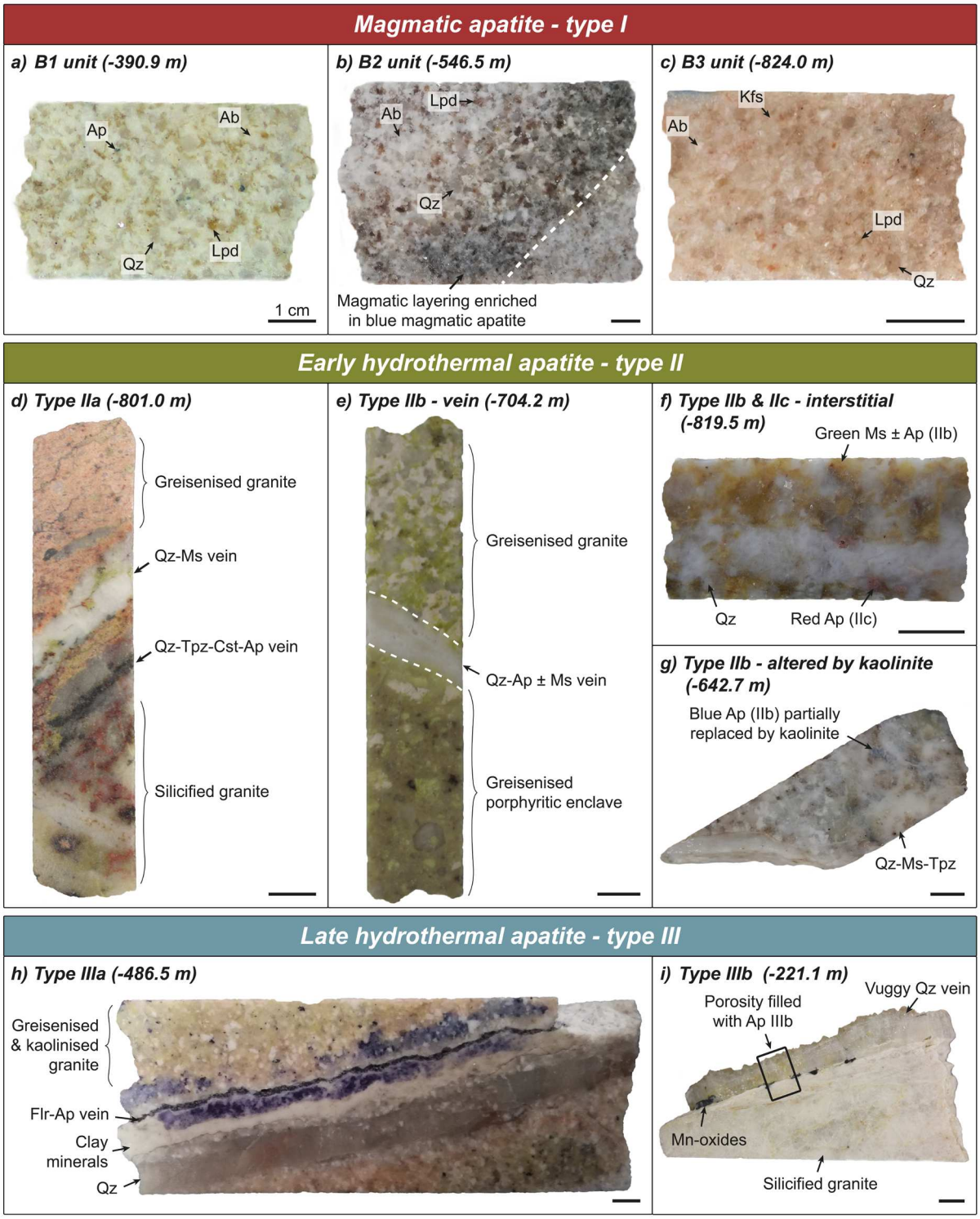



*Figure II.3. Selected macrophotographs of investigated samples grouped by hosted apatite type: (a) to (c) Beauvoir granite from the B1, B2 and B3 units, respectively; (d) Quartz-topaz-cassiterite-apatite (type IIa) vein crosscutting the greisenised Beauvoir granite; (e) Quartz-apatite (type IIb) vein at the contact between the greisenised Beauvoir and porphyritic granites; (f) Greisenised Beauvoir granite with interstitial type IIb and IIc apatite; (g) Greisenised Beauvoir granite with apatite IIb partially overprinted by kaolinisation; (h) Composite quartz-fluorite-clay mineral-apatite (type IIIa) vein crosscutting the Beauvoir granite showing signs of both greisenisation and kaolinisation; (i) Vuggy quartz vein exhibiting Mn-oxides as fillings along the selvedges and late hydrothermal apatite (type IIIb) having precipitated in the vein porosity. Abbreviations follow the IMA conventions compiled by Warr (2021). The scale below each photograph represents 1 cm.*

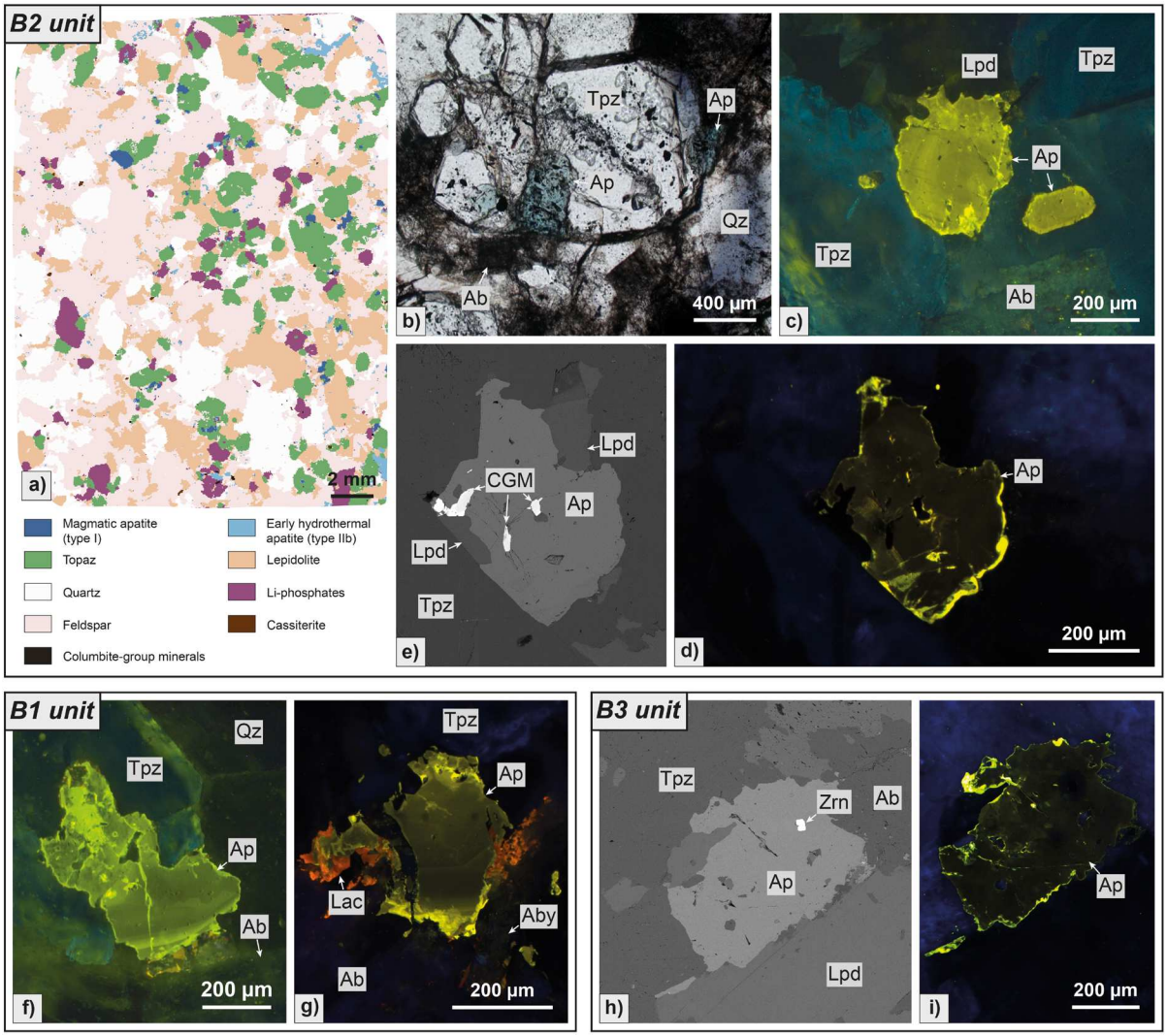



*Figure II.4. Petrographic characteristics of magmatic apatite (type I) within the three magmatic units of the Beauvoir PRMG (i.e., B1, B2 and B3). (a) µ-XRF mineralogical map of a typical thin section from the B2 unit (-546.5 m) showing the close spatial relation between magmatic apatite (type I) and topaz, as well as the partial replacement of igneous feldspar and lepidolite by apatite IIb; (b) Thick section microphotograph (plane-polarised light) of blue apatite I; (c-d) CL images of apatite I in the B2 unit; (e) BSE image of apatite I containing inclusions of columbite-group minerals in the B2 unit; (f-g) CL images of apatite I in the B1 unit; (h-i) BSE and CL image of apatite I containing a zircon inclusion in the B3 unit. Abbreviations follow the IMA conventions compiled by Warr (2021), with the exception of CGM: columbite-group minerals.*

#### *4.1.2. Early hydrothermal apatite*

The early hydrothermal stage resulted in the precipitation of an apatite population (type II) occurring in silicified or greisenised Beauvoir granite and pre-existing La Bosse stockwork, in association with mineral assemblages typical of the Beauvoir early hydrothermal event. Apatite II shows heterogeneous distribution, paragenetic context, textural and CL characteristics, leading to the definition of different subtypes (i.e., apatite IIa, IIb, and IIc).

Apatite IIa has been found in association with topaz, quartz and cassiterite within a hydrothermal vein near a contact between the altered Beauvoir granite and the host mica schist in the B3 unit (Fig. II.3d). It shows a complex CL texture characterised by dark primary areas

partially replaced by brighter secondary zones (Fig. II.5b). Cassiterite seems to have preferentially precipitated within these bright-CL secondary zones or at the transition between dark- and bright-CL zones (Figs. II.5a, b).

Apatite IIb precipitated with quartz ± muscovite, topaz and accessory wolframite and columbite-group minerals (Figs. II.5c, e, g, i), which is a typical mineralogical assemblage of greisen alteration (Pirajno, 2009; Monnier et al., 2019). Apatite IIb is colourless to light blue and has been found as replacement of igneous minerals (Figs. II.3f, II.5c, II.5e), in particular feldspar and Li-micas, as well as within quartz ± muscovite veins (Figs. II.3e, II.5g). As previously mentioned, kaolinisation commonly overprints greisen-altered areas, and apatite systematically shows signs of alteration (Charoy et al., 2003; Monnier et al., 2019). This is the case in samples 642.7 and 789.7, where apatite IIb is partially replaced by kaolinite and crandalite-group minerals, in particular goyazite ($SrAl_3(PO_4)_2(OH)_5(H2O)$) (Fig. II.5i). Three sub-sets of occurrences of apatite IIb can then be distinguished based on petrographic observations: (i) pervasive greisen alteration (samples 816.5 and 819.5); (ii) greisen vein (sample 704.2); and (iii) greisen alteration overprinted by kaolinite (samples 642.7, 789.7 and 801.0).

The greisen vein selected for further investigation was observed at the contact between the Beauvoir PRMG and a porphyritic enclave, both of which have been intensively greisenised (Fig. II.3e). It shows fringes of sub-euhedral to euhedral apatite, which grew sub-perpendicular to the strike of the quartz vein (Fig. II.5g).

The CL signature of apatite IIb is characterised by a brighter and more greenish colour than magmatic apatite found in the B2 and B3 units but is similar to the CL signal of magmatic apatite from the B1 unit (Figs. II.5d, f, h, j). Apatite IIb commonly exhibits altered zones, especially in the sample 816.5, and brighter altered areas contain small (*ca.* <5 µm) monazite inclusions (Figs. II.5c, d). This characteristic suggests that the apatite grains underwent metasomatism, possibly leading to the leaching of LREE from apatite lattice and precipitation of secondary monazite (e.g., Harlov, 2015).

Apatite IIc forms anhedral grains replacing Li- and Be-phosphates (i.e., amblygonite-group minerals and herderite, respectively), and greisen-related minerals (i.e., quartz, muscovite and topaz) (Fig. II.5k). It shows a CL signature varying from a greenish colour similar to apatite IIb, yet darker, to a distinctive orange colour, especially when it occurs as a replacement of Be-phosphates (Fig. II.5l). In that case, apatite IIc also differs from apatite IIb by a red to orange natural colour (Fig. II.3f).

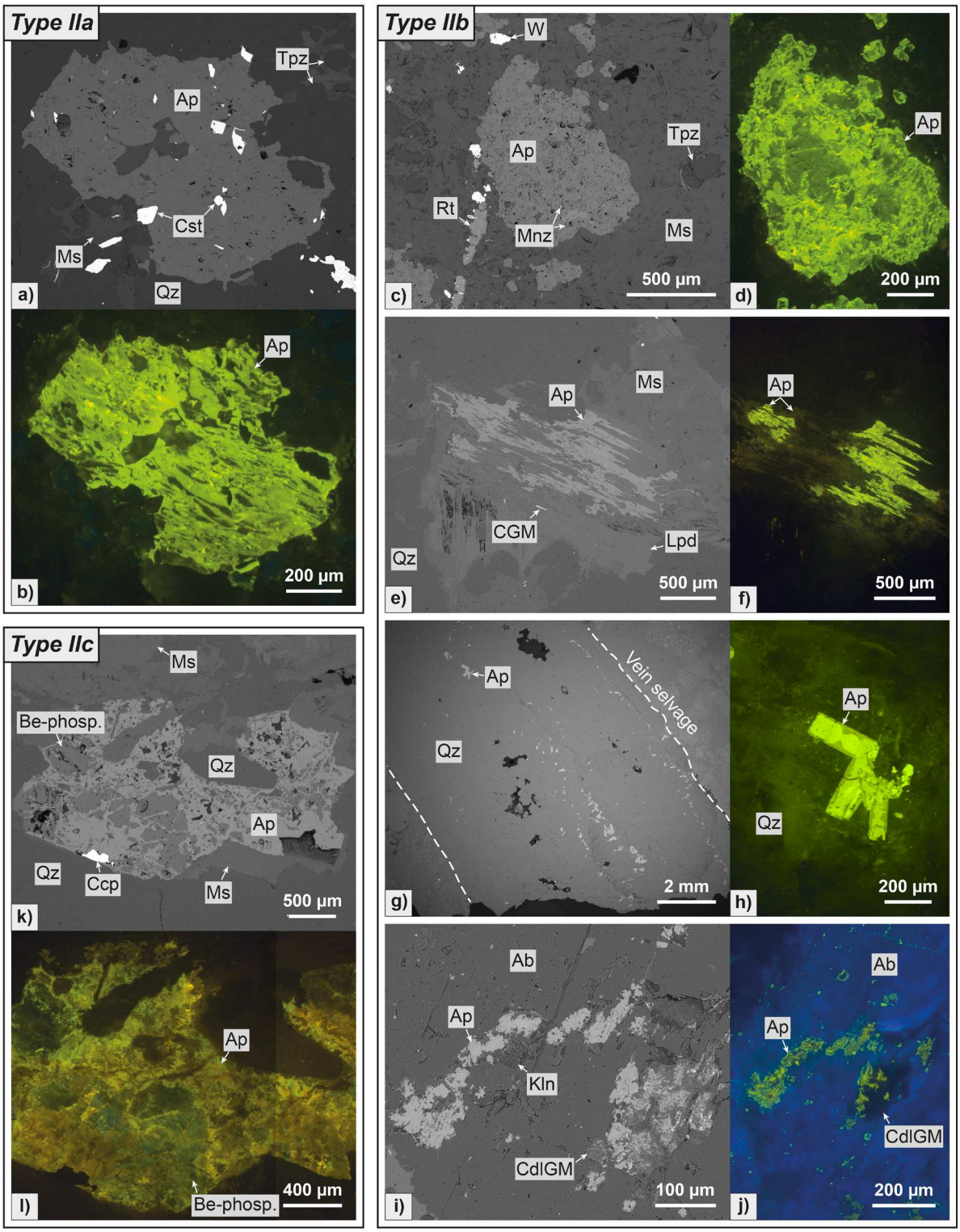



*Figure II.5. Petrographic characteristics of early hydrothermal apatite (type II) within the Beauvoir PRMG and host mica schists. (a-b) BSE and CL images of apatite IIa in the B3 unit. Apatite IIa exhibits a complex CL texture characterised by dark primary areas partially overprinted by brighter zones. Cassiterite seems to have preferentially precipitated within bright-CL secondary zones or at the transition between dark- and bright-CL zones. (c-d) BSE and CL images of a greisenised mica schist enclave. Apatite IIb exhibits metasomatism, revealed by the patchy CL texture and the presence of monazite inclusions. (e-f) BSE and CL images of apatite IIb replacing magmatic lepidolite in the B3 unit. (g-h) BSE image of an apatite IIb-bearing greisen vein crosscutting the B2 unit and CL image of hosted apatite. Sub-euhedral to euhedral apatite IIb mainly grew sub-perpendicular to the strike of the quartz vein. (i-j) BSE and CL images of apatite IIb partially replaced by kaolinite and crandallite-group minerals in the B3 unit. (k-l) BSE and CL images of apatite IIc replacing Be-phosphates in the B3 unit. Abbreviations follow the IMA conventions compiled by Warr (2021), with the exception of CdlGM: crandallite-group minerals, and CGM: columbite-group minerals.*

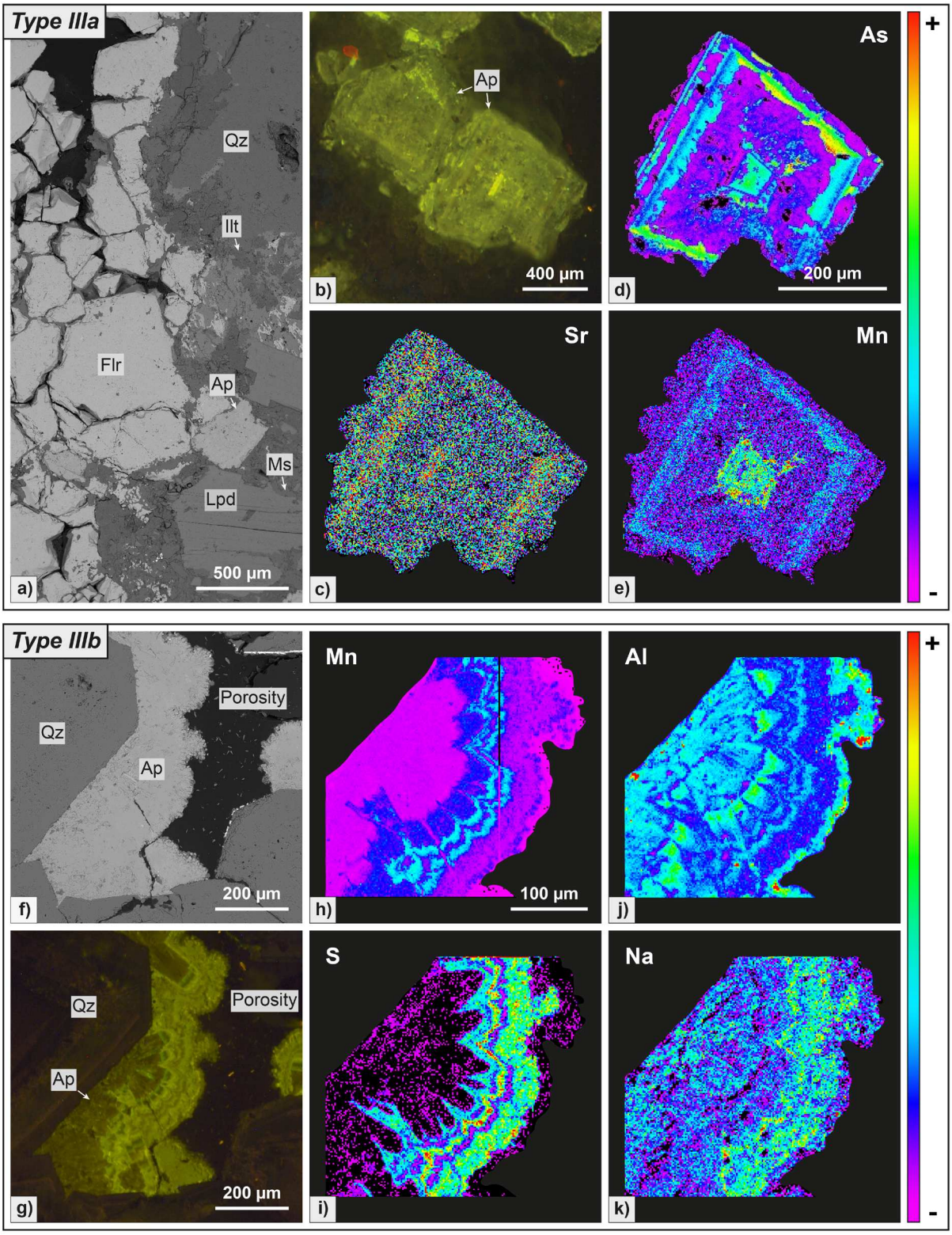



*Figure II.6. Petrographic characteristics of late hydrothermal apatite (type III) within the Beauvoir PRMG. (a) BSE image highlighting the close spatial relation between apatite IIIa and fluorite; (b) CL image of apatite IIIa showing a discrete oscillatory zonation; (c-e) WDX element mapping of apatite IIIa revealing As, Sr and Mn relative distribution within the grain; (f-g) BSE and CL images of apatite IIIb forming colloform aggregates precipitating in the porosity of a vuggy quartz vein; (h-k) WDX mapping of Mn, Al, S and Na distributions in apatite IIIb. Abbreviations follow the IMA conventions compiled by Warr (2021).*

#### *4.1.3. Late hydrothermal apatite*

Apatite IIIa was observed within a composite and pervasive quartz, muscovite, fluorite and illite vein (Fig. II.3h). Igneous lepidolite and a greisen-related quartz-muscovite assemblage are partially replaced by illite (Fig. II.6a), which is one of the typical late hydrothermal alteration minerals in the Beauvoir PRMG. Apatite IIIa forms subhedral to euhedral crystals precipitating in close spatial relation with fluorite (Fig. II.6a). It shows more yellowish colour but less luminescence in CL images than apatite II (especially apatite IIb) and exhibits growth zoning (Fig. II.6b).

Apatite IIIb forms colloform aggregates in the porosity of a vuggy quartz vein exhibiting a Mn-oxides selvedge (Fig. II.6f). As apatite IIIa, its CL signature is less luminescent but more yellowish than apatite II varying from a dark core to a brighter rim (Fig. II.6g).

### 4.2. Halogens

All apatite occurrences have relatively low Cl content, below 1100 ppm, while most of them show F content above 3.0 wt.% (first quartile value). The vast majority of apatite generations encountered within the Beauvoir PRMG are therefore fluorapatite, with minor (< 1% of measured compositions) hydroxyapatite identified in the brightest secondary zones of apatite IIa, where the calculated $H_2O$ content reaches up to 1.6 wt.%. Bromine and iodine can substitute for F on the anion site, albeit as trace constituents (Pan and Fleet, 2002; Kusebauch et al., 2015a). Bromine and I contents are low, yet always well above detection limits, and range from 0.2 to 47.2 ppm and from 0.01 to 4.99 ppm, respectively.

### 4.3. Major and minor elements

$P_2O_5$ and CaO contents of all apatite generations fall into relatively wide ranges, respectively varying from 36.4 to 44.4 wt.% and 48.7 to 58.6 wt.% respectively, revealing significant substitution on Ca and P sites. Manganese also appears as a major constituent, ranging in concentrations from below the detection limit (i.e., < 0.1 wt.%) to *ca.* 6.5 wt.% MnO. Systematic variations in MnO contents include: (i) as previously emphasised by Wang (1988), apatite I concentrations globally correlate with depth, the average contents decreasing from 5.6 to 4.3 and 1.6 wt.% from the B3, B2 and B1 units, respectively. Such a magmatic differentiation trend, whereby Mn concentration decreases with increasing differentiation without significant changes in Sr and S contents (Fig. II.7), differs distinctly from the early hydrothermal apatite II evolution trend, whereby Mn depletion is associated with Sr enrichment; (ii) an overall decrease in MnO content is also observed over time, i.e., from apatite I (mean ~ 3.7 wt.%) to apatite II and III (mean ~ 1.7 wt.% and 0.4 wt.%, respectively).

Apatite I is characterised by high MnO content (Fig. II.7), low to moderate $Na_2O$, $SiO_2$ and FeO concentrations reaching up to 0.7, 0.2 and 0.6 wt.%, respectively. The chemistry of apatite II

reveals a three-step trend (Fig. II.7) evolving from: (i) a composition similar to magmatic apatite, dominated by high MnO and low to moderate FeO concentrations. This particular chemistry is associated with dark-CL primary zones of apatite IIa (MnO ~ 2.7–4.8 wt.% and FeO < 0.9 wt.%; Fig. II.4b); (ii) a composition differing by a significant Sr enrichment, locally noticeable within the bright-CL secondary zones of apatite IIa (SrO < 0.8 wt.%) and clearly characteristic of apatite IIb. Strontium in apatite IIb reaches up to 4.7 wt.% SrO (mean ~ 1.15 wt.%), with the exception of apatite IIb overprinted by kaolinisation, where Sr was rarely detected through EPMA (< 0.5 wt.%). This SrO enrichment is accompanied by low to moderate FeO contents (< 1.1 wt.%); and finally (iii) a composition characterised by relatively high $Na_2O$ and $SO_3$ concentrations, that are generally above the detection limit and reach up to 1.4 and 4.1 wt.%, respectively. This is the case in apatite IIb overprinted by kaolinisation and apatite IIc. The simultaneous enrichment in S and Na can be attributed to the following co-substitution on the Ca and P sites (Pan and Fleet, 2002):

$$SO_4^{2-} + Na^{+} \leftrightarrow PO_4^{3-} + Ca^{2+}$$

A significant $Al_2O_3$ enrichment is also observed in most early hydrothermal apatite sub-generations, especially in apatite IIb overprinted by kaolinisation, with $Al_2O_3$ values up to 3.5 wt.%.

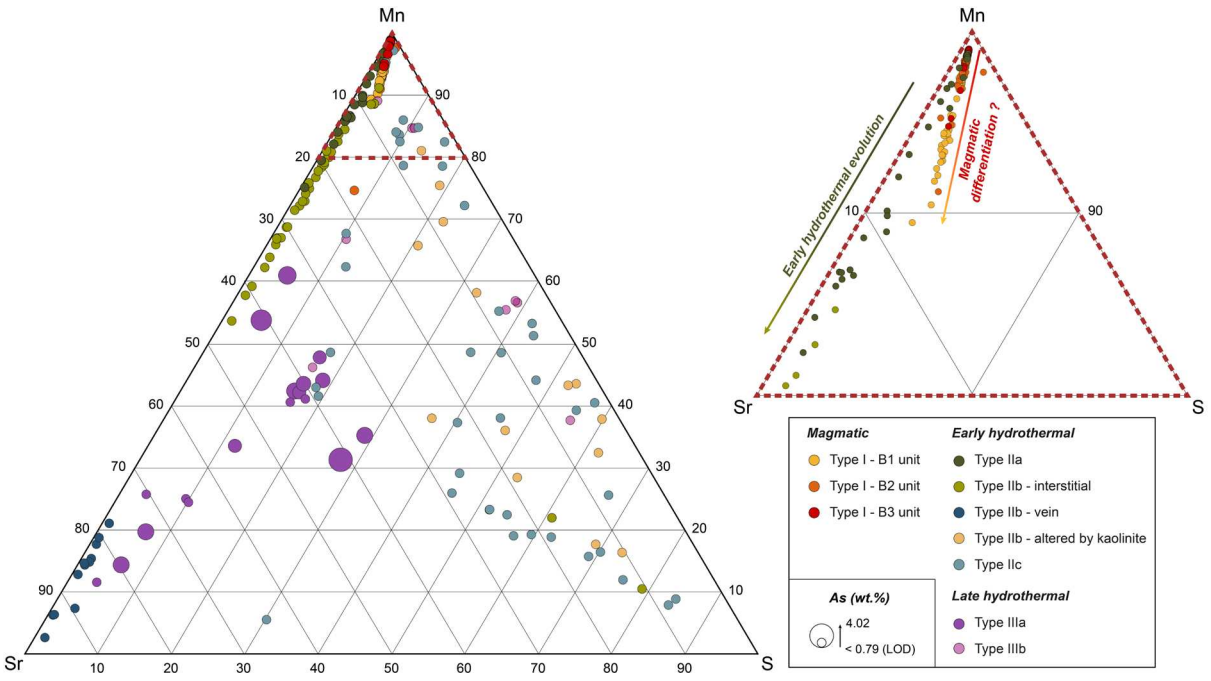


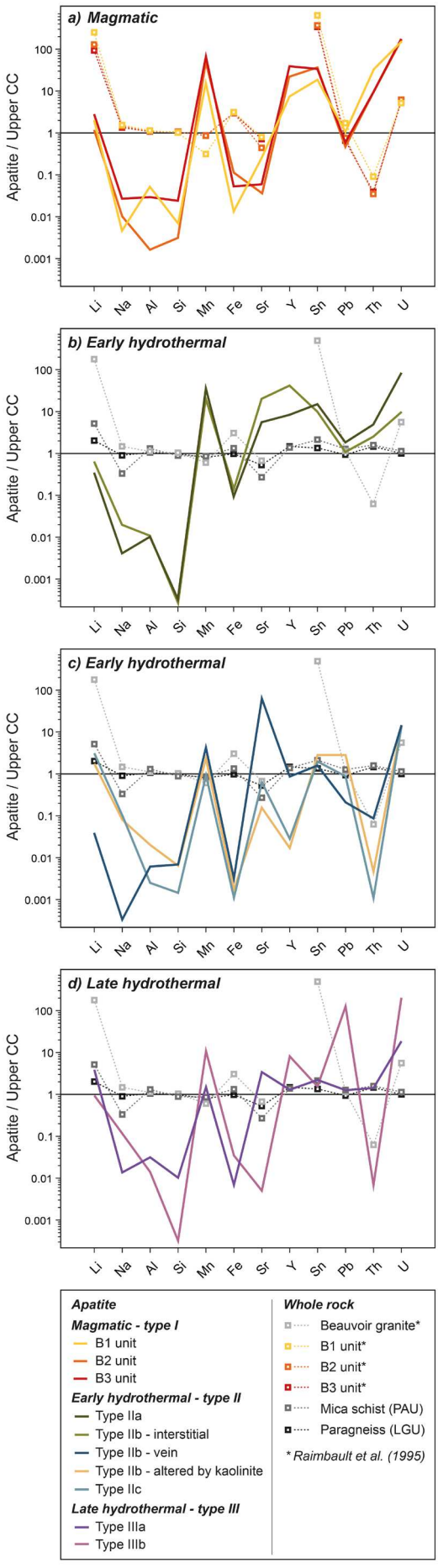

*Figure II.7. Sr, S and Mn ternary plot with indication on the As content (circle size) in apatite generations from the Beauvoir PRMG. Magmatic apatite is characterised by an enrichment in Mn. Early hydrothermal apatite varies from Mn-enriched (type IIa), to Sr-rich (type IIb) and S-rich (type IIb altered by kaolinite and type IIc), whereas late hydrothermal apatite is As-enriched for apatite IIIa and S-enriched for apatite IIIb. Data are from EPMA. When an element was not detected at an analysis spot, half of the detection limit was assigned as the concentration.*

Apatite IIIa predominantly differs from the other apatite generations by a relatively important enrichment in As with $As_2O_3$ concentrations ranging from 0.4 to 5.3 wt.% (mean ~ 1.8 wt.%). The oscillatory zonation highlighted by CL imaging correlates with modifications of the major element chemistry; slightly brighter zones are enriched in As, Mn and Sr and depleted in P compared to the darker areas (Figs. II.6c-e). Apatite IIIb exhibits low to moderate $SO_3$ (<0.1–1.6 wt.%; mean ~ 0.5 wt.%) and $Na_2O$ (0.2–0.6 wt.%; mean ~ 0.4 wt.%) concentrations. Similarly to apatite IIb overprinted by kaolinisation, it is also relatively enriched in Al, with $Al_2O_3$ content varying from below the detection limit to 1.1 wt.% (mean ~ 0.4 wt.%). Apatite IIIb CL luminescence correlates with systematic variations in those elements, the brighter areas being enriched in S, Na and depleted in Al and Mn compared to the darker areas (Figs. II.6h-k).

### 4.4. Trace elements

Apatite generations are associated with distinct trace elements and REE signatures (Figs. II.8, II.9). Apatite I shows similar trace elements distributions within the three magmatic units, but Sn, Y and total REE concentrations display an overall decreasing trend from the deepest B3 to intermediate B2 and shallowest B1 unit (Figs. II.8a, II.9a, II.9b). Chondrite-normalised REE patterns of apatite I display LREE enrichment ($La_N/Yb_N$ ~ 2.8–35.7), as well as a strong to moderate negative Eu anomaly (Eu/Eu* ~ 0.01–0.75) (Fig. II.9a). Similar features characterise the whole rock REE patterns of the unaltered Beauvoir PRMG (Fig. II.9a) (Raimbault et al., 1995). Additionally, apatite I exhibits irregular REE distributions consisting in four curved segments (La-Nd, Pm-Gd, Gd-Ho, and Er-Lu) (Fig. II.9a), and designated as lanthanide tetrad effect (Masuda et al., 1987; Bau, 1996; Irber, 1999). The tetrad effect degree ($TE_{1-3}$) can be quantified for each magmatic unit following Irber (1999), and ranges from 1.05 to 1.73. As estimated $TE_{1-3}$ values essentially exceed 1.1, the tetrad effect degree for magmatic apatite is considered significant (Irber, 1999). Some distinctions are noticeable in the apatite REE patterns of the three magmatic units (Figs. II.9a, d). An overall depletion in REEs associated with an increase in $La_N/Yb_N$ is observed from the B3 ($\Sigma$REE ~ 590–5420 ppm; $La_N/Yb_N$ ~ 2.8–7.7), to the B2 ($\Sigma$REE ~ 490–3230 ppm; $La_N/Yb_N$ ~ 3.5–8.7), and finally the B1 unit ($\Sigma$REE ~ 160–1580 ppm; $La_N/Yb_N$ ~ 7.5–35.7). The Eu anomaly is also more pronounced in the B3 and B2 units, exhibiting very similar Eu/Eu* ratios ranging from less than 0.01 to 0.47, in contrast to the B1 unit where the Eu/Eu* ratios vary from 0.27 to 0.75 (Fig. II.9a).

Based on the distribution of trace elements in apatite II, two main groups can be identified. The first group, comprising apatite IIa and interstitial apatite IIb, exhibits trace element and REE patterns broadly comparable to those of apatite I, although they are characterised by a distinctive positive Eu anomaly (Eu/Eu* ~ 1.5–5.7; Fig. II.9b) and show slightly lower Li, Sn, Th and U concentrations, as well as higher Sr contents (Fig. II.8b). The second group includes apatite IIb overprinted by kaolinisation and apatite IIc. By contrast, this group is associated with




a relative enrichment in Li, and is depleted in Y, Sn and Th (Fig. II.8c). Apatite II from this group is REE-depleted, with total REE content not exceeding 50 ppm (Fig. II.9d). REE distributions are characterised by LREE depletion, MREE enrichment, and no distinct Eu anomaly ($0.02 \leqslant La_N/Yb_N < 2.4$) (Fig. II.9b). Flat HREE signatures are also observed for apatite IIc, whereas the REE spectra of apatite IIb overprinted by kaolinisation display a more irregular pattern. Those characteristics resemble the whole rock distribution of the kaolinised granite (Fig. II.9c). Apatite IIb found within a quartz vein shows an intermediate trace element distribution between the two groups of early hydrothermal crystals, with REE chondrite-normalised spectra similar to the second group (Fig. II.9b) but a Sr enrichment similar to the first group (Figs. II.8b, c).

Late hydrothermal apatite III comprises some of the most Li-enriched (up to 230 ppm) apatite generations in the Beauvoir PRMG (Fig. II.8d). They have variable total REE contents between 2 and 130 ppm, and are globally depleted in REE compared to apatite I (Fig. II.9d). Their REE distribution is mainly characterised by a LREE depletion compared to MREE and HREE ($La_N/Yb_N$ ~ 0.06–0.51), and again resembles the whole rock REE pattern of the kaolinised granite (Fig. II.9c). Apatite IIIa has modest negative Eu anomaly ($Eu/Eu^*$ ~ 0.38–0.71) and its composition notably stands out due to strong Pb enrichment (Fig. II.8d).

*Figure II.8. Trace elements distribution normalised to the upper continental crust (CC) (Rudnick and Gao, 2003) for the distinct apatite generations from the Beauvoir PRMG. Whole rock trace elements distributions for the Beauvoir granite (Raimbault et al., 1995), the Sioule mica schist and paragneiss (Table II.A9 in Appendix II.A4) are plotted as references. PAU: Parautochtonous Unit; LGU: Lower Gneiss Unit.*

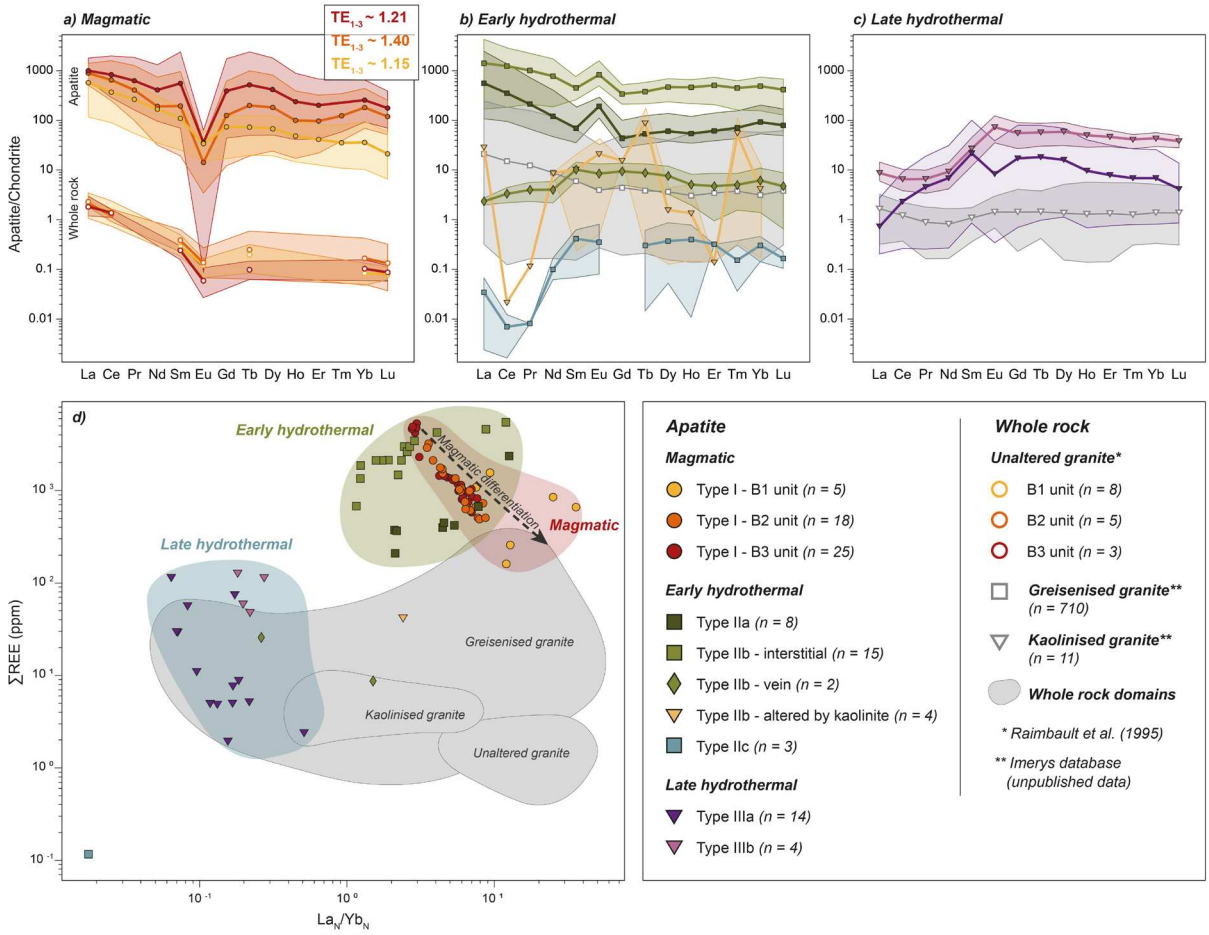



*Figure II.9. REE compositions of the different apatite generations from the Beauvoir PRMG: (a-c) Chondrite-normalised REE patterns (Boynton, 1984). The degree of the tetrad effect ($TE_{1-3}$) was estimated for magmatic apatite following Irber (1999). (d) Total REE content as a function of the $La_N/Yb_N$ ratio within apatite. Whole-rock compositions of samples of unaltered granite (Raimbault et al., 1995) greisenised granite and kaolinised granite (unpublished Imerys database) from the Beauvoir intrusion are shown for comparison.*

### 4.5. Oxygen isotopes

Disregarding the altered zones of the grains, apatite I shows a wide range of O isotopic composition throughout the entire intrusive complex, with $\delta^{18}O$ values varying from 2.0 to 15.8 ‰ (Fig. II.10a). This pronounced scatter is predominantly attributed to apatite I analysed in the B1 unit (2.0–15.8 ‰; mean ~ 5.8 ± 0.4 ‰, 2s), whereas less variable $\delta^{18}O$ values are obtained for the B2 (3.9–9.9 ‰; mean ~ 6.1 ± 0.3 ‰) and B3 units (6.3–8.5 ‰; mean ~ 7.7 ± 0.3 ‰). In terms of mean $\delta^{18}O$ values, an overall decrease is observed from the deepest B3 unit (mean ~ 7.7 ± 0.3 ‰) to the intermediate B2 unit (mean ~ 6.1 ± 0.3 ‰) and the shallowest B1 unit (mean ~ 5.8 ± 0.4 ‰; Fig. II.10a). Intra-grain variation range in apatite I increases from the B3 unit (*ca.* 1 ‰), to the B2 (0.5–3 ‰) and B1 (4–6 ‰) units. In the B1 unit only, a systematic core to rim trend is noticeable, with brighter-CL magmatic growth rims (Figs. II.4f, g) commonly exhibiting heavier O isotopic signatures compared to cores ($\delta^{18}O_{rim}$ values up to 3 ‰ higher).

The $\delta^{18}O$ values of altered zones observed in apatite I fall into a wide range of -3.7 to 8.3 ‰ in the B1 unit and of -14.8 to 12.2 ‰ in the B2 unit. A single value of 5.2 ± 0.3 ‰ has been obtained for an altered domain of apatite I from the B3 unit. Altered zones (mean ~ 3.7 ± 0.4 ‰ and 4.9 ± 0.3 ‰ for the B1 and B2 units, respectively) overall show lower $\delta^{18}O$ values compared to unaltered magmatic micro-domains.

Apatite II is associated with significantly scattered O isotopic compositions, ranging from -6.7 to 7.5 ‰ for apatite IIa, -8.8 to 13.4 ‰ for apatite IIb, and -7.5 to 12.5 ‰ for apatite IIc (Figs. II.10b, c). Among all analysed apatite IIb, two apparent end-members can be distinguished: (i) the quartz-apatite greisen vein (sample 704.2), for which $\delta^{18}O$ fall into a narrow negative range of -3.3 to -1.0 ‰ (mean ~ -2.1 ± 0.2 ‰); (ii) the greisen-altered zones, with apatite being partially replaced by kaolinite and crandallite-groupe minerals (samples 642.7, 789.7 and 801.0), in which the O isotopic signature of apatite is notably heavier (-1.2 to 13.4 ‰; mean ~ 10.8 ± 0.2 ‰). The two other samples (i.e., 816.5 and 819.5) are representative of pervasive greisen alteration and exhibit significant scatter in O isotopic compositions between these two end-members, their $\delta^{18}O$ values ranging from -3.7 to 8.6 ‰ (mean ~ 5.3 ± 0.2 ‰) and from -8.8 to 12.7 ‰ (mean~ -0.8 ± 0.2 ‰), respectively.

A noticeable systematics exists between O isotopic signature, elemental chemistry and apatite CL-signal, when the grain distinctly exhibits darker-CL primary replaced by brighter-CL secondary zones, as it is the case for apatite IIa (Fig. II.5b) and apatite IIb from sample 816.5 (Fig. II.5d). The darker-CL primary zones tend to exhibit heavier O isotopic signatures, higher Mn and total REE contents and lower Sr concentrations than the brighter-CL micro-domains. For instance, dark-CL primary areas within apatite IIa exhibit O isotopic compositions of 2.7 to 7.5 ‰ (mean ~ 5.9 ± 0.2 ‰), average MnO and Sn concentrations of 4.1 wt.% and 43 ppm, respectively, an average REE total content of 870 ppm and SrO content essentially below the detection limit (i.e., < 0.1 wt.%). In contrast, bright-CL secondary areas are characterised by a distinctly lighter O isotopic signature, with $\delta^{18}O$ values ranging from -6.7 to 3.7 ‰ (mean ~ -3.5 ± 0.3 ‰), lower MnO (mean ~ 3.0 wt.%), Sn (mean ~ 3 ppm) and total REE (mean ~ 320 ppm) concentrations and a higher SrO (mean ~ 0.3 wt.%) content (see sections 5.1 and 5.4 for further discussion).

The O isotopic signature of apatite III is typically heavy (Fig. II.10d). Apatite IIIa shows scattered $\delta^{18}O$ values ranging from 3.4 to 14.4 ‰ (mean ~ 9.2 ± 0.2 ‰), while apatite IIIb has the heaviest O isotopic signature, with $\delta^{18}O$ values varying between 13.6 and 17.0 ‰ (mean ~ 15.6 ± 0.2 ‰).

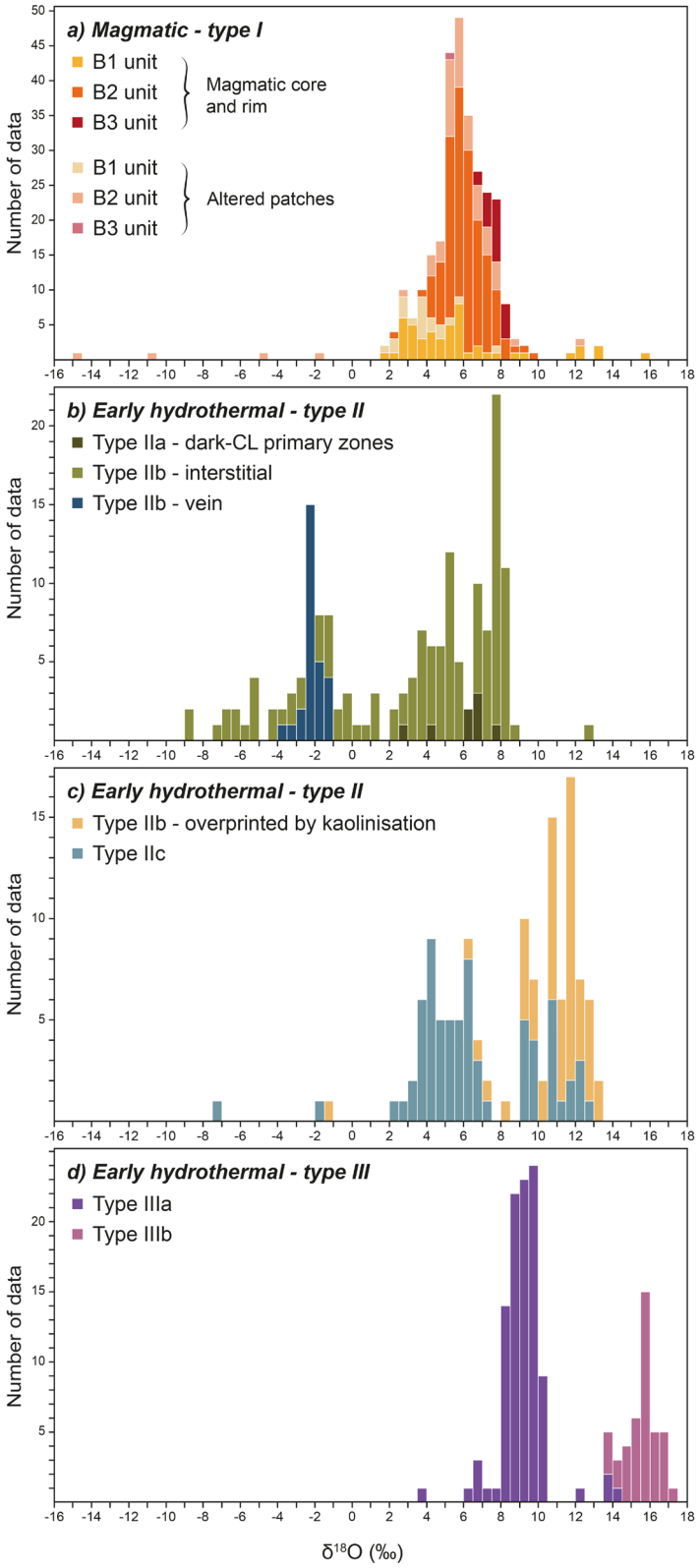



*Figure II.10. O isotopic composition of the distinct apatite generations from the Beauvoir PRMG system: (a) Magmatic generation; (b-c) Early hydrothermal generations; (d) Late hydrothermal generations.*

### 4.6. U-Pb geochronology

Tera-Wasserburg diagrams for the main supra- and sub-solidus stages (i.e., magmatic, early hydrothermal and late hydrothermal stages) are presented in Figure II.11, and additional plots for the distinct magmatic and early hydrothermal apatite sub-generations are presented in Figure II.A2 (Appendix II.A2). The U content of the different apatite generations from the Beauvoir PRMG shows a wide range, from less than 1 ppm to *ca.* 1000 ppm. Apatite I is relatively enriched in U (*ca.* 140–790 ppm) compared to typical apatite from other felsic igneous rocks (*ca.* 1–100 ppm; O'Sullivan et al., 2020). Apatite II shows lower U concentrations (*ca.* 0.04–140 ppm), except for the dark-CL primary zones of apatite IIa and for apatite IIb overprinted by kaolinisation, which yield similar values to apatite I. Moderate to high U concentrations characterise apatite III, with U content reaching up to *ca.* 1000 ppm in apatite IIIb.

Apatite I from the B1, B2 and B3 units plot relatively close to the concordia curve in the Tera-Wasserburg diagram due to their high U and relatively low initial Pb contents (Fig. II.11a). Lower intercept dates of 315.0 ± 6.8 Ma (n = 16; MSWD = 1.7), 312.0 ± 18.3 Ma (n = 23; MSWD = 1.2) and 313.6 ± 5.0 Ma (n = 22; MSWD = 1.3) obtained for the B1, B2 and B3 units, respectively, are identical within uncertainty (Figs. II.A2a-c in Appendix II.A2). Apatite I from the B1 unit is characterised by the highest $^{207}Pb/^{206}Pb$ and lowest $^{238}U/^{206}Pb$ ratios, reflecting a relative enrichment in initial Pb (Fig. II.A2a). The combination of all data for magmatic apatite define a lower intercept date of 314.6 ± 4.7 Ma (n = 61; MSWD = 2.2) and the discordia line returns an initial $^{207}Pb/^{206}Pb_{(i)}$ ratio of 0.80 ± 0.02, reasonably close to the model isotopic composition of terrestrial lead at 310 Ma (i.e.,$^{207}Pb/^{206}Pb_{(310\ Ma)}$ ~ 0.86; Stacey and Kramers, 1975) (Fig. II.11a).

Three subsets can be distinguished within the early hydrothermal generation (i.e., apatite IIa, IIb and IIc). Data from apatite IIa yield a lower intercept date of 314.3 ± 5.5 Ma (n = 27; MSWD = 4.0) and a $^{207}Pb/^{206}Pb_{(i)}$ composition of 0.83 ± 0.01, which is similar to the common Pb value defined by magmatic apatite (Fig. II.11b). A significant spread along the discordia is observed, with bright-CL secondary zones enriched in common Pb compared to the darker-CL primary zones. Three samples have been analysed for apatite IIb, and represent: (i) pervasive greisen alteration, (ii) vein formation during the greisenisation episode, and (iii) greisen-alteration overprinted by kaolinisation. Data from apatite IIb associated with pervasive alteration define a relatively well-constrained isochron with a lower intercept date of 315.8 ± 7.2 Ma (n = 54; $^{207}Pb/^{206}Pb_{(i)}$ = 0.85 ± 0.01; MSWD = 2; Fig. II.A2d in Appendix II.A2), whereas U-Pb analyses of apatite from the greisen-related vein result in an imprecise date of 301.0 ± 20.2 Ma (n = 35; $^{207}Pb/^{206}Pb_{(i)}$ = 0.84 ± 0.01; MSWD = 2.3; Fig. II.A2e in Appendix II.A2). Two clusters in the Tera-Wasserburg plot can be identified from the analysis of apatite IIb overprinted by

kaolinisation, especially differing by their U content (Fig. II.A2f in Appendix II.A2). No date can be unambiguously assigned on the basis of these data, given that the two clusters are sharply separated and appear to belong to distinct discordia trends. As all apatite IIb, except for apatite IIb overprinted by kaolinisation, produce similar U-Pb dates and $^{207}Pb/^{206}Pb_{(i)}$ compositions within uncertainty, this subset is presumed to have precipitated over a relatively short period of time. Therefore, all data, except for apatite IIb overprinted by kaolinisation, were pooled to obtain an overall date of 311.7 ± 8.1 Ma, with a $^{207}Pb/^{206}Pb_{(i)}$ ratio of 0.85 ± 0.004 (n = 90; MSWD = 3.2) (Fig. II.11c). Due to the lack of exploitable signals, no date could be obtained for apatite IIc.

Finally, U-Pb data from the two late hydrothermal generations yield distinct dates of 268.3 ± 20.4 Ma (n = 59; MSWD = 4.6) for fluorite-related apatite (apatite IIIa; Fig. II.11d) and of 148.5 ± 26.6 Ma (n = 20; MSWD = 1.5) for colloform apatite occurring in the porosity of a quartz vein with a Mn-oxide selvedge (apatite IIIb; Fig. II.11e). While both apatite subsets show a dominant common Pb proportion of total Pb, which results in imprecise dates, they are still significantly younger than the Beauvoir PRMG.

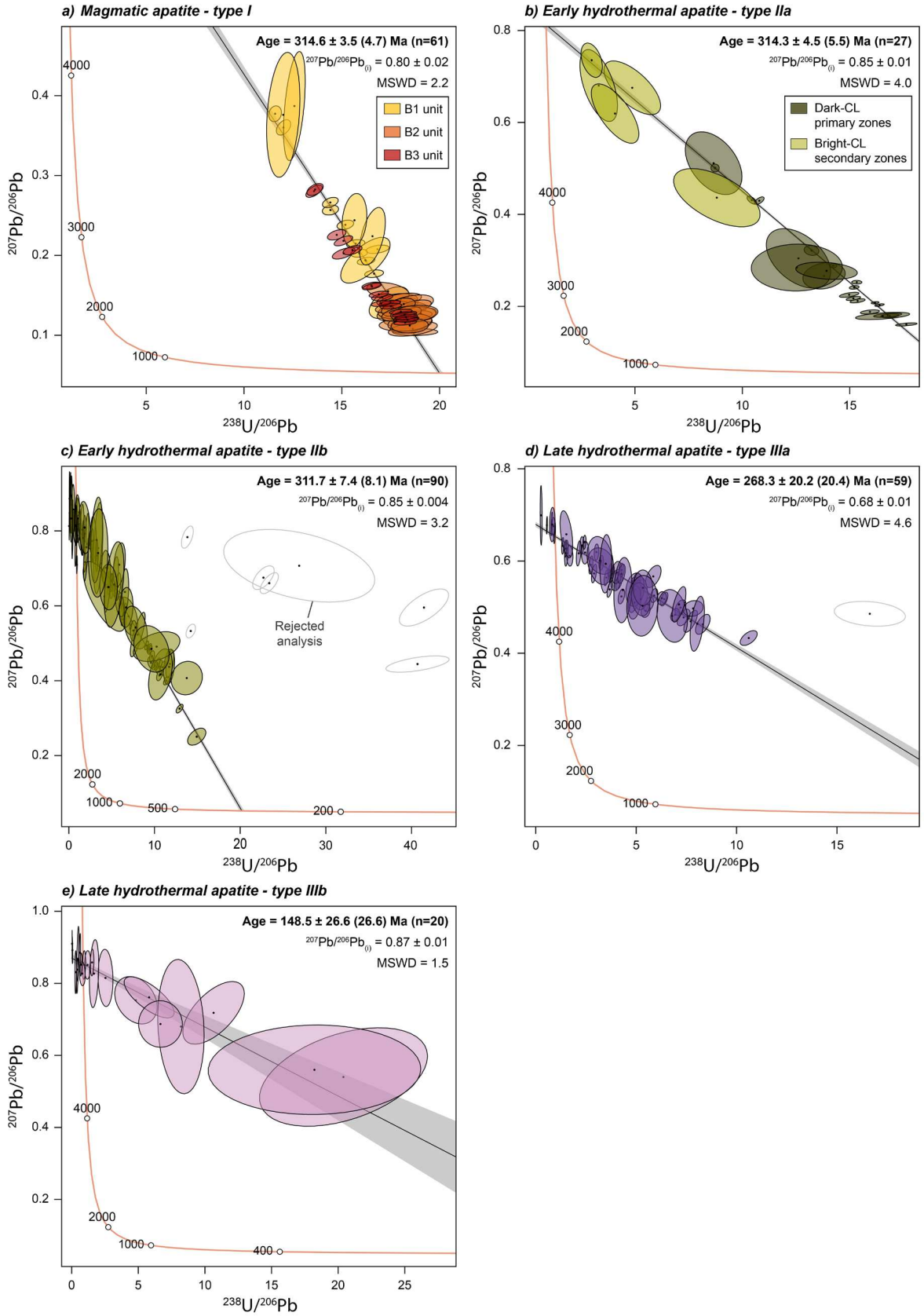



*Figure II.11. Tera-Wasserburg diagrams for the different apatite generations from the Beauvoir PRMG. (a) Magmatic apatite; (b-c) Early hydrothermal apatite – types IIa and IIb, respectively; (d-e) Late hydrothermal apatite – types IIIa and IIIb, respectively. Ellipses and age uncertainties are reported at the 2-sigma level. The first uncertainty indicated corresponds to the analytical uncertainty with overdispersion, whilst the second one in brackets takes into account interlaboratory reproducibility (± 1 %).*

## 5. Discussion

### 5.1. Timing of magmatic and hydrothermal episodes for the Beauvoir PRMG

The Beauvoir PRGM is marked by four major apatite generations, which are respectively characteristic of the magmatic, early hydrothermal and the two late hydrothermal stages. Based on textural evidence, apatite I is related to the crystallisation of the Beauvoir magmas and represents an early mineral within the magmatic paragenetic sequence (section 4.1; Fig. II.2). Analyses of apatite I from the three main magmatic units together yield an age of 314.6 ± 4.7 Ma (Fig. II.11a). Considering the magmatic origin of apatite I, this date likely represents the crystallisation age of the Beauvoir PRMG, which is consistent with previous studies that suggested emplacement ages identical within uncertainties, i.e., 304 ± 9 Ma and 317 ± 8 Ma by Rb-Sr dating of whole rock samples from the B1 and B2 units, respectively (Duthou and Pin, 1987; ages recalculated with the $^{87}$Rb decay constant of Villa et al., 2015), 308 ± 2 Ma by $^{40}$Ar-$^{39}$Ar dating of lepidolite (Cheilletz et al., 1992) and 317 ± 8 Ma by applying the U-Pb method on columbite-group minerals from the B1 unit (Melleton et al., 2015) (Fig. II.12). From 325 to 310 Ma, the axial part of the Variscan belt experienced lithospheric extension, leading to crustal melting and widespread granitic magmatism (e.g., Vanderhaeghe et al., 2020; Schulmann et al., 2022). The emplacement of the Beauvoir PRMG at *ca.* 315–310 Ma marks the end of this event. In the FMC, it is contemporaneous with the emplacement of other PRMGs and pegmatites, as well as peraluminous leucogranite-related W±Sn hydrothermal deposits, within transcurrent or extensional tectonic structures (Cuney et al., 2002; Bouchot et al., 2005; Melleton et al., 2015; Harlaux et al., 2018b; Carr et al., 2021; Monnier et al., 2021).

Early hydrothermal apatite II and late hydrothermal apatite III generally display intergrowth textures with hydrothermal assemblages and occur as pervasively distributed alteration minerals, or are found within veins. Those characteristics supports their precipitation from hydrothermal fluids. The early hydrothermal generation is associated with quartz ± muscovite ± topaz ± cassiterite and is characteristic of greisen alteration (Monnier et al., 2019) (Fig. II.2). The complex and irregular textures in early hydrothermal apatite observed in CL (Figs. II.5b, d, f, j) suggest dissolution-reprecipitation processes during metasomatic alteration. In some apatite II occurrences, grains distinctly exhibit darker-CL primary replaced by brighter-CL secondary zones, which correlate with systematic changes in elemental and O-isotopic compositions (section 4.5). Consequently, the overprint of the initial chemistry appears predominantly restricted to brighter-CL altered zones, whereas the darker-CL unaltered zones potentially preserve the signature from the primary fluid circulation. This modification in apatite chemistry is also reflected in the U-Pb data, as the altered zones are typically characterised by higher proportion of initial Pb relative to radiogenic Pb compared to primary zones. (e.g., Fig. II.11b for apatite IIa). Yet, for most samples, U-Pb analyses from the altered and unaltered zones lie

along the same trend between initial and radiogenic Pb, indicating that they formed within a timespan shorter than the obtained uncertainties (2s = 5.5 and 8.1 Ma for apatite IIa and IIb, respectively). Considering that the Beauvoir magmatic-hydrothermal system probably cooled over a time scale of the order of *ca.* $10^4$ years due to the small size of the intrusion (~ 0.21 $km^3$; Raimbault et al., 1995) and its shallow emplacement (~ 3 km; Cuney et al., 1992) (e.g., Coulson et al., 2002; Ingebritsen et al., 2010; Andersen and Weis, 2020), apatite U-Pb dating does not allow to assert that metasomatic processes recorded in most early hydrothermal apatite (apatite II) are temporally linked to greisen alteration. However, petrographic observations support a genetic link between the precipitation of apatite II and greisenisation. The textural and compositional variability observed in early hydrothermal apatite likely results from changes in greisenising fluids properties (e.g., temperature, composition), leading to destabilisation and (re-)crystallisation of apatite.

The two main ages determined for the early hydrothermal stage (i.e., 314.3 ± 5.5 Ma for apatite IIa and 311.7 ± 8.1 Ma for apatite IIb; Fig. II.12) are consistent with a preliminary age of 307 ± 3 Ma for the greisenisation event related to the Beauvoir PRMG emplacement, obtained by U-Pb dating of monazite from the alteration halo of a quartz vein formed from greisen-related fluids within the Echassières complex (Monnier et al., 2021). These ages are indistinguishable within uncertainty from those of magmatic apatite and, conversely, significantly older than the Permian-Triassic estimate derived from K-Ar dating of muscovite (273 ± 6 Ma for pervasive greisen alteration and 225 ± 5 Ma for the formation of greisen-related veins; Merceron et al., 1987) (Fig. II.12). Therefore, our new geochronological results support a strong temporal and genetic relation between greisen alteration and Beauvoir PRMG magma emplacement, as proposed by many authors for the Beauvoir PRMG (e.g., Cuney et al., 1992; Monnier et al., 2020). Such temporal relationship between granite intrusion and greisen alteration has been documented for other similar systems (e.g., Breiter et al., 2017; Launay et al., 2021).

To date, there is limited data available to constrain the timing of the fluorite mineralisation episode within the Beauvoir intrusion. An external origin of mineralising fluids has been emphasised based on fluorite REE patterns (Raimbault, 1988). Previous authors also suggested that a conceivable origin may lie in the widespread hydrothermal event affecting western Europe and resulting in the formation of large veins and stratiform F-Ba-Pb-Zn ore deposits (Merceron et al., 1987; Raimbault, 1988). Although the genesis of these hydrothermal deposits occurred over an extensive period spanning from the Early Jurassic to the Early Cretaceous (*ca.* 210–100 Ma; Joseph et al., 1973; Baubron et al., 1980; Soule de Lafont and Lhegu, 1980; Davaine, 1980; Nigon, 1988; Sizaret et al., 2009; Boiron et al., 2010; Cathelineau et al., 2012; Gigoux et al., 2015; Lenoir et al., 2023), the geochronological data available for the FMC, the Morvan, Vendée and Poitou regions (Fig. II.1a) emphasises a well-documented F mineralisation period between *ca.* 165 and

140 Ma (Fig. II.12). A similar observation has been made by Burisch et al. (2022) on a broader scale, highlighting a major F deposition episode between *ca.* 185 and 140 Ma when taking into account most of Europe's major fluorite provinces. Considering the close textural relation between fluorite and apatite IIIa in the Beauvoir PRMG, fluorite precipitation likely occurred around 268.3 ± 20.4 Ma (Fig. II.12). Despite the large uncertainty of this age, it significantly contrasts with previous assumptions suggesting a Liassic mineralisation event. Nevertheless, it supports its temporal dissociation with the magma emplacement and related early hydrothermal stage (*ca.* 305–315 Ma) (Fig. II.12), thus necessitating the involvement of external (non-magmatic-hydrothermal) fluid circulation.

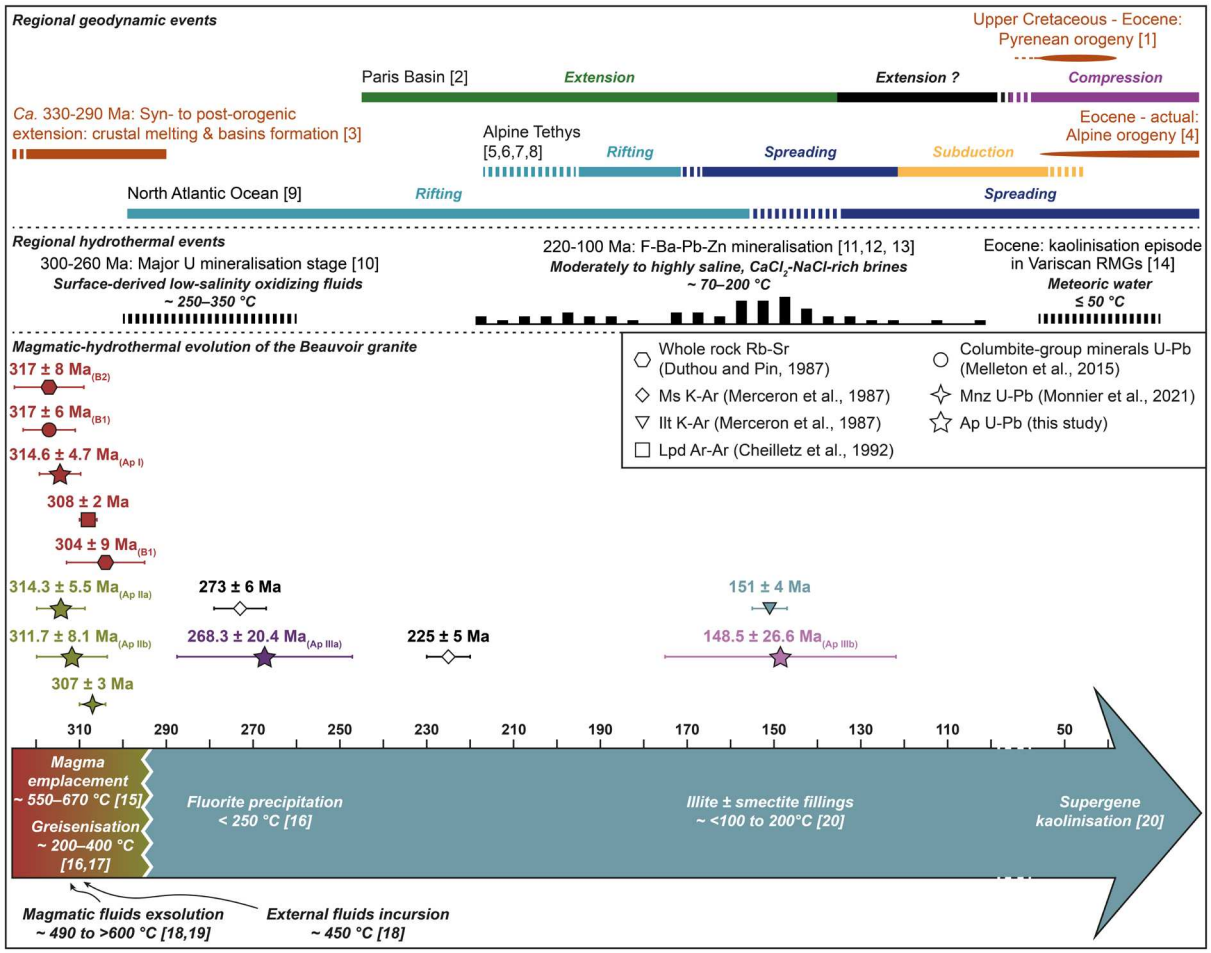



*Figure II.12. Chronology of the different magmatic and hydrothermal events that occurred in the Beauvoir PRMG between 315 Ma and the Eocene in parallel with the main regional geodynamic and hydrothermal events. All ages are reported with uncertainties at the 2-sigma level. Ages obtained by Rb-Sr dating of whole rock samples from the B1 and B2 units (Duthou and Pin, 1987) were recalculated using the $^{87}$Rb decay constant of Villa et al. (2015). The F-Ba-Pb-Zn mineralisation event is from a compilation of geochronological data for the FMC and adjacent regions (i.e., Poitou High, Morvan and Vendée). The histogram represents only central ages, disregarding associated uncertainties. [1] Rosenbaum et al. (2002); [2] Guillocheau et al. (2000); [3] Vanderhaeghe et al. (2020); [4] Ford and Lickorish (2004); [5] Stampfli et al. (2002); [6] Handy et al. (2010); [7] Bellahsen et al. (2014); [8] Van Hinsbergen et al. (2020); [9] Angrand and Mouthereau (2021); [10] Ballouard et al. (2017) and referencess therein; [11] Cathelineau et al. (2012) and referencess therein; [12] Gigoux (2015) and referencess therein; [13]Bouat et al. (2023); [14] Gaudin et al. (2015) and referencess therein; [15] Pichavant (2022); [16] Merceron et al. (1992); [17] Monnier et al. (2020) ; [18] Aïssa et al. (1987); [19] Harlaux et al. (2017); [20] Merceron et al. (1987).*

The Variscan belt (e.g., Bohemian Massif, Black Forest, Massif Central and Armorican Massif) is characterised by important hydrothermal uranium mineralisation, mostly deposited between 300 and 260 Ma (e.g., Wendt et al., 1979; Carl et al., 1983; Eikenberg, 1988; Cathelineau et al., 1990; Hofmann and Eikenberg, 1991; Kříbek et al., 2009; Velichkin and Vlasov, 2011; Ballouard et al., 2018) (Fig. II.12). The mobilisation of U from fertile peraluminous leucogranites, syntectonically emplaced along extensional faults or strike-slip shear zones during the late Carboniferous, derives from sub-solidus alteration via surface-derived low-salinity oxidising fluids, with possible contribution of Permian basin-derived fluids, at temperatures ranging from *ca.* 250 to 350 °C (e.g., Cathelineau, 1982; Turpin et al., 1990b; Barsukov et al., 2006; Kříbek et al., 2009; Dolníček et al., 2014; Ballouard et al., 2017; Dusséaux et al., 2022). Rare occurrences of U-rich fluorite, also referred to as antozonite, have been documented in late Carboniferous to Permian U deposits, such as the Retail mineralised vein (Vendée; Ruhlmann et al., 1980), the Ecarpière deposit (Vendée; Sarcia et al., 1958), or the Bauzot mineralisation (Burgundy; Carrat, 1956). Fluorine mineralisation recognised within the Beauvoir intrusion is proposed to be related to this widespread hydrothermal event, thus recording brittle reactivation of Variscan shear zones during the Permian post-orogenic evolution (e.g., Cathelineau et al., 1990; Ballouard et al., 2017, 2018).

No clear intergrowth texture has been observed between apatite IIIb and other minerals. However, precipitation of colloform apatite IIIb in the porosity of a vuggy quartz vein exhibiting a Mn-oxides selvedge suggests a late precipitation, Fe- and Mn-oxides being thought to derive from weathering during the late hydrothermal evolution of the Beauvoir PRMG (Merceron et al., 1987, 1992; Monnier et al., 2019). Supergene kaolinisation, known to affect Variscan RMGs during the Eocene (e.g., Estéoule-Choux, 1967; Gaudin et al., 2015), represents the last pervasive alteration episode of the Beauvoir PRMG (Merceron et al., 1987). The main P-bearing mineral precipitating during supergene kaolinisation of the Beauvoir PRMG consists of crandallite-group minerals typically replacing greisen-related apatite (Figs. II.5i, j; Monnier et al., 2019), thus precipitation of apatite IIIb most likely predates this event. Apatite IIIb yields a lower intercept age of 148.5 ± 26.6 Ma, which, albeit imprecise, overlaps the precipitation age of illite within the Beauvoir PRMG estimated at 151 ± 4 Ma (K-Ar on illite; Merceron et al., 1987) (Fig. II.12). As previously mentioned, F-Ba-Pb-Zn ore deposits formed across Western Europe from the Jurassic to Lower Cretaceous period, with a well-documented mineralisation event occurring between *ca.* 140 and 165 Ma in the FMC and adjacent regions (i.e., Poitou, Morvan and Vendée). At this time, metals from the Variscan metamorphic rocks and granites were leached by basinal brines and redeposited below or above the unconformity between basement and Liassic sediments. The circulation of such fluids at temperatures up to 200 °C, was notably conducive to illite precipitation (e.g., Cathelineau et al., 2012), and likely resulted from far-field deformation during the Tethys-Atlantic-Caribbean rift evolution (Burisch et al., 2022) and the onset of the opening of the Bay of Biscay (Bouat et al., 2023). The precipitation of apatite IIIb and illite within the

Beauvoir PRMG suggests that the Sioule region might have been partially covered by the Paris basin sediments at the end of the Jurassic and fluid infiltrations during reactivation of ancient basement faults may reflect the influence of the Pangea breakup on the FMC.

### 5.2. Apatite as a proxy for magmatic evolution in PRMG systems

Cathodoluminescence imaging of magmatic apatite from the Beauvoir PRMG commonly reveals growth zoning, as well as resorption textures, and distinctly secondary zones resulting from dissolution-reprecipitation processes, possibly related to the greisen alteration event (Figs. II.4c, d, f, g, i). The greenish blue colour of magmatic apatite reflects high Mn content (Ribeiro et al., 2005) (Figs. II.3a-c, II.4b), which is a distinctive feature of apatite crystallising from highly evolved peraluminous melts (e.g., Sha and Chappell, 1999; Belousova et al., 2002; Broska et al., 2004; Roda-Robles et al., 2022). The decreasing proportion of magmatic apatite from the B2 and B3 units to the B1 unit is proposed to derive from the higher degree of magmatic evolution of the latter, P being preferentially concentrated into feldspars with increasing differentiation (London, 1992). Another possible explanation is the higher abundance of amblygonite-group minerals scavenging P from the melt in the B1 unit compared to the B2 and B3 units (Raimbault et al., 1995).

Considering the typical plots proposed to identify the parent rock type from apatite chemistry (e.g., Sha and Chappell, 1999; Belousova et al., 2002; O'Sullivan et al., 2020), magmatic apatite from the B2 and B3 units exhibit partial overlap with the "S-type granites" field as depicted on the Sr/Y vs ΣLREE biplot proposed by O'Sullivan et al. (2020) (Fig. II.13). The remaining data points from these two units, as well as magmatic apatite from the B1 unit, fall within the fields corresponding to apatite from leucosomes/partial melts from high-grade metamorphic rocks and low-grade metamorphic/metasomatic rocks. Given that the Beauvoir PRMG exhibits a chemistry that is highly distinct from typical S-type granites, it is very likely that the chemistry of its magmatic apatite is also unique, which may account for the observed discrepancy from the "S-type granites" field. This is supported by the particular composition of igneous apatite from highly differentiated peraluminous granites and Li-rich pegmatites from the Variscan Iberian Massif (Spain; Merino Martínez, 2014; Roda-Robles et al., 2022) and Nb-Ta-(Li-Be-Cs) pegmatites from the Mufushan Complex rare-metal ore field (South China; Madayipu et al., 2024), exhibiting similar to even higher Sr/Y and lower LREE content compared to magmatic apatite in the Beauvoir PRMG. As illustrated in Figure II.13 and also in Figure II.9d, the transition from the less evolved B3 unit to the intermediate B2 unit, and most differentiated B1 unit is associated with an overall depletion in REE and an increase in the $La_N/Yb_N$ as well as Sr/Y ratios. This evolution could be ascribed to magmatic differentiation processes for PRMGs, as REE typically behave compatibly in low-temperature peraluminous magmas (e.g., Montel, 1993).

The chondrite-normalised REE distribution of magmatic apatite from the Beauvoir PRMG also slightly differs from typical patterns of apatite from S-type granites or other highly differentiated leucogranites (e.g., Sha and Chappell, 1999; Hsieh et al., 2008; Chu et al., 2009; Belousova et al., 2002; Roda-Robles et al., 2022). As previously described, apatite I is associated with a systematic LREE enrichment, a strong to moderate negative Eu anomaly (Eu/Eu* ~ 0.01–0.75), and a slight depletion in Nd only observed in the B2 and B3 units (Fig. II.9a). REE patterns of apatite from typical S-type granites from the Lachlan Fold Belt, exhibiting upward convex profiles, pronounced negative Eu anomaly and frequent Nd depletion, resemble those of magmatic apatite from the Beauvoir PRMG (Sha and Chappell, 1999). However, apatite from those S-type granites differ from Beauvoir PRMG's apatite by a significant LREE depletion that has been ascribed to the crystallisation of monazite, which tends to reach saturation earlier than apatite in reduced and peraluminous magmas (Sha and Chappell, 1999). Due to the high concentration in fluxing elements, such as F and Li, within the Beauvoir melts, monazite saturation was likely not achieved (Raimbault et al., 1995). This could account for the LREE-enriched feature observed in both the whole-rock and igneous apatite REE patterns of the Beauvoir PRMG (Fig. II.9a).

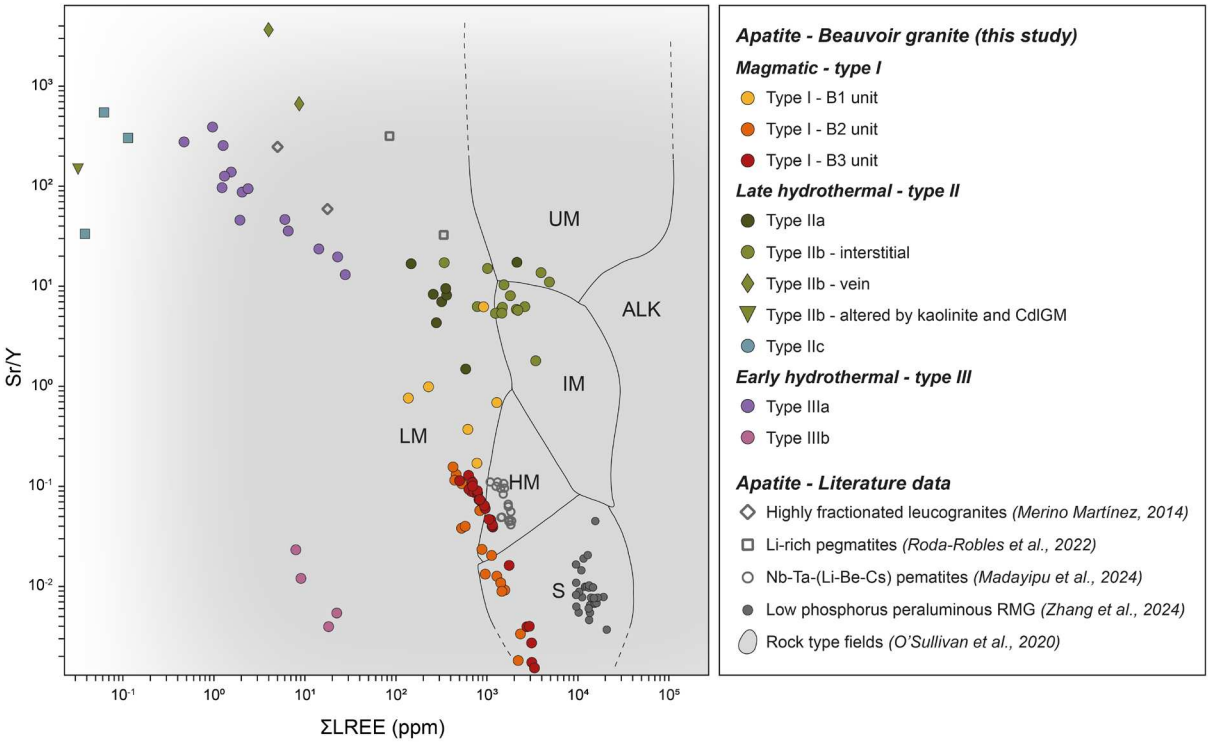



*Figure II.13. Discriminant Sr/Y vs ∑LREE plot after O'Sullivan et al. (2020) to decipher the nature of the parent rock from apatite chemistry. Abbreviations for groups: ALK = alkali-rich igneous rocks; IM = mafic I-type granitoids and mafic igneous rocks; LM = low- and medium-grade metamorphic and metasomatic; HM = partial-melts/leucosomes/high-grade metamorphic; S = S-type granitoids and high aluminium saturation index (ASI) 'felsic' I-types; UM = ultramafic rocks including carbonatites, lherzolites and pyroxenites.*

As expected for highly peraluminous granites, apatite I displays a pronounced negative Eu anomaly, its amplitude decreasing from the least differentiated B3 unit and intermediate B2 unit to the most evolved B1 units. As $Eu^{3+}$ is much closer to $Ca^{2+}$ in ionic radius than $Eu^{2+}$ at the two Ca non-equivalent sites in apatite, $Eu^{3+}$ is preferentially incorporated in apatite structure compared to $Eu^{2+}$ that is concentrated into feldspars (e.g., Budzinski and Tischendorf, 1989; Sha and Chappell, 1999). The partition coefficient of Eu between apatite and melt is thought to increase with increasing oxygen fugacity ($fO_2$), decreasing melt aluminosity and $Eu^{2+}/Eu^{3+}$ ratio (Sha and Chappell, 1999). Therefore, the relative Eu enrichment observed with increasing differentiation may derive from the increase of oxidation degree characterising the transition from the B3 and B2 units to the B1 unit within the Beauvoir PRMG, which was interpreted by Cuney et al. (1992) and Pichavant (2022) as a primary magmatic feature.

Moreover, magmatic apatite exhibits an important tetrad effect, with estimated tetrad effect degrees ($TE_{1\text{-}3}$) ranging from 1.05 to 1.73 and mostly exceeding the significance threshold of 1.1 (Fig. II.9a; Irber, 1999). This feature is commonly observed in highly evolved granites and associated metasomatic rocks. It has also been documented in melt inclusions (Peretyazhko and Savina, 2010) and minerals, such as zircon (Yang et al., 2014), columbite-group minerals (Badanina et al., 2015) and apatite (Chu et al., 2009; Roda-Robles et al., 2022). Although some recent studies suggested that the tetrad effect could be inherited from monazite and xenotime fractionation (Duc-Tin and Keppler, 2015; Shuai et al., 2021), it has been widely attributed to the selective complexation of REE by F or Cl during metasomatism, or fluid and melt exsolution (e.g., Bau, 1996; Irber, 1999; Jahn et al., 2001; Veksler et al., 2005; Monecke et al., 2007; Peretyazhko and Savina, 2010; Dostal et al., 2015; Ballouard et al., 2020b). As monazite and xenotime likely did not reach saturation from the Beauvoir melts (Raimbault et al., 1995), the pronounced tetrad effect observed in magmatic apatite REE distribution could reflect the exsolution of F-rich and Cl-rich magmatic fluids during magma crystallisation, which has been emphasised by the study of fluid inclusions (Aïssa et al., 1987).

From these data, apatite I has essentially preserved its original magmatic signature, but its chemistry also reveals signs of metasomatic overprint, in particular its O isotopic signature (Fig. II.10a). In the absence of O isotopic data for apatite from other strongly fractionated highly peraluminous rocks, we suggest comparing the bulk rock $\delta^{18}O$ values of other Variscan peraluminous leucogranites and the Richemont rhyolitic dyke, which represents the subvolcanic equivalent of the Beauvoir PRMG, with the calculated oxygen isotopic composition of the Beauvoir melts. The latter can be estimated from $\delta^{18}O$ data obtained for magmatic apatite using the crystal-melt temperature-dependent fractionation factor of Zhao and Zheng (2003) for rhyolitic melt. For a crystallisation temperature of *ca.* 670 to 550 °C (emcompassing liquidus to solidus temperatures determined by Pichavant, 2022), the oxygen isotopic fractionation between

apatite and the parent melt is limited ($\Delta^{18}O_{apatite\text{-}melt}$ ~ -1.3 to -1.0 ‰; Zhao and Zheng, 2003). For unaltered zones of magmatic apatite, $\delta^{18}O$ values for the corresponding Beauvoir melts range from 7.3 to 9.8 ‰ (median ~ 8.9 ‰), 4.9 to 11.2 ‰ (median ~ 7.2 ‰), and 3.0 to 17.1 ‰ (median ~ 6.4 ‰) for the B3, B2 and B1 units, respectively. More than half of these estimates are significantly lower than the bulk rock $\delta^{18}O$ compositions of other Variscan peraluminous granites, which are typically above 11 ‰ when their magmatic signature is preserved (~ 10.7–13.6 ‰; Bernard-Griffiths et al., 1985; Turpin et al., 1990a; Tartèse and Boulvais, 2010; Ballouard et al., 2017), and are also below the single whole-rock $\delta^{18}O$ ratio of 9.0 ‰ obtained for the Richemont rhyolitic dyke (Raimbault and Burnol, 1998). Such discrepancy possibly indicates a partial reequilibration of apatite O isotopic compositions with external hydrothermal fluids, resulting in relatively low and highly variable $\delta^{18}O$ ratios. This O isotopic exchange might have been more intense towards the surface (i.e., from the B3 to B2 and B1 units), thus explaining the observed variability between magmatic apatite from the distinct units. Relatively low $\delta^{18}O$ values have been reported for other igneous minerals within the Beauvoir PRMG, including quartz, feldspar and lepidolite, and were interpreted to record meteoric water incursion at supra-solidus conditions and subsequent melt-fluid interactions (Fouillac et al., 1987; Fouillac and Rossi, 1991). Such hypothesis cannot be fully excluded and could explain the light isotope signature of magmatic apatite from the Beauvoir PRMG. However, apatite is sensitive to metasomatism (Harlov, 2015) and a subsolidus isotopic reequilibration with hydrothermal fluids remains plausible.

Overall, although the oxygen isotope signature of magmatic apatite was possibly partially reequilibrated during supra- to sub-solidus alteration, we argue that its elemental composition, at least its content of immobile elements (e.g., REEs and Y), was mostly preserved, thereby recording the evolution of the Beauvoir granitic melts. A comparable finding was observed in magmatic apatite from the Black Mountain porphyry deposit (Philippines; Cao et al., 2021). In this case, hydrothermal alteration resulted in modifications to the CL characteristics, fluid-mobile element concentrations (including Cl, Mg, Fe, Sr, Pb), and Sr-O isotope signatures of apatite, whereas other components (REE, Y, U, Th, and Zr) and the Nd isotope composition were preserved. Although Mn is generally considered as fluid-mobile, its concentration in magmatic apatite (Fig. II.7) decreases from the B3 to B1 unit, mimicking Mn bulk rock concentrations, which could be ascribed to magmatic differentiation processes (Raimbault et al., 1995).

### 5.3. Apatite as a proxy to trace nature and dynamics of hydrothermal systems in PRMGs

The isotopic and elemental chemistry of apatite are currently considered as valuable tools in deciphering hydrothermal evolution in diverse geological environments, particularly in ore-forming systems (e.g., Seo et al., 2015; Bouzari et al., 2016; Mao et al., 2016; Ballouard et al., 2018; Cave et al., 2018; Pochon et al., 2018; Andersson et al., 2019; Melfou et al., 2023). For

example, the $\delta^{18}O$ value in apatite is derived from the parent fluid and governed by temperature-dependent fractionation (Zheng, 1996), making the apatite O isotopic signature a recorder of fluid origin. The halogen (i.e., F, Cl, Br, and I) composition of apatite is also distinctive, as major terrestrial fluid reservoirs exhibit characteristic halogen chemistry generally preserved through most ore-forming processes (Lecumberri-Sanchez and Bodnar, 2018 and references therein). Although the anion site in apatite is dominated by F, Cl and OH, additional trace elements are typically incorporated, including Br and I (Pan and Fleet, 2002), with possible minor fractionation between Br and I during apatite precipitation (Andersson et al., 2019). The Br/I ratio of apatite could thus be used as a proxy for the Br/I ratio of the melts and hydrothermal fluids, providing insights into their origin.

O isotopic composition, major and trace elements content in the successive hydrothermal apatite generations of PRMGs, as exemplified by the Beauvoir case study, is a powerful approach to decipher the complex hydrothermal history that affected such type of magmatic system through time. Dark-CL primary micro-domains of apatite IIa (Fig. II.5b) are characterised by significant MnO and Sn concentrations (2.7–4.8 wt.% and 24–65 ppm, respectively). Their REE distribution also shares similarities with magmatic apatite (i.e., comparable total REE concentrations and LREE enrichment), yet differing by a distinctive positive Eu anomaly (Fig. II.9b). The latter may reflect the destabilisation of igneous feldspars during greisen alteration, which preferentially incorporate Eu in felsic magmas (Sha and Chappell, 1999). These dark primary micro-domains also exhibit Br/I molar ratios varying between 2.6 and 15.9, which largely overlap the range observed for apatite I (1.1–39.1), and fall in the range of fluids exsolved from S-type intrusions (3–20; Andersson et al., 2019) (Fig. II.15). Furthermore, the co-precipitation of apatite IIa with cassiterite (generation II) in a vein highlights significant transport of Sn by hydrothermal fluids (Figs. II.2, II.5a). All of these characteristics combined suggest that apatite IIa primarily precipitated from hot and saline magmatic fluids, capable of transporting a significant amount of metals including Sn and REE (e.g., Candela, 1995; Bai and Van Groos, 1999; Audétat et al., 2008; Pirajno, 2009; Audétat and Edmonds, 2020). Dark primary micro-domains most likely recorded the circulation at high temperature (*ca.* 490 to $>$ 600 °C) of magmatic fluids exsolved from the Beauvoir melts (Aïssa et al., 1987; Harlaux et al., 2017), which are proven to be relatively enriched in Sn (*ca.* 1000–40,000 ppm; Harlaux et al., 2017) (Fig. II.14). At such elevated temperatures, oxygen isotopic fractionation between fluids and apatite is minor (i.e., $\Delta^{18}O_{apatite\text{-}fluid} \sim$ -0.1 to -0.5 ‰; Zheng, 1996). The $\delta^{18}O$ value of dark primary zones in apatite IIa varying between 2.7 and 7.5 ‰, the O isotopic composition estimated for the parent fluid (i.e., 2.8–8.0 ‰) essentially falls in the expected range for magmatic fluids (i.e., 5.5–9.5 ‰; Sheppard, 1986). The lowest $\delta^{18}O$ values probably derive from metasomatic alteration of apatite IIa, resulting in precipitation of the bright secondary micro-domains (Fig. II.5b).

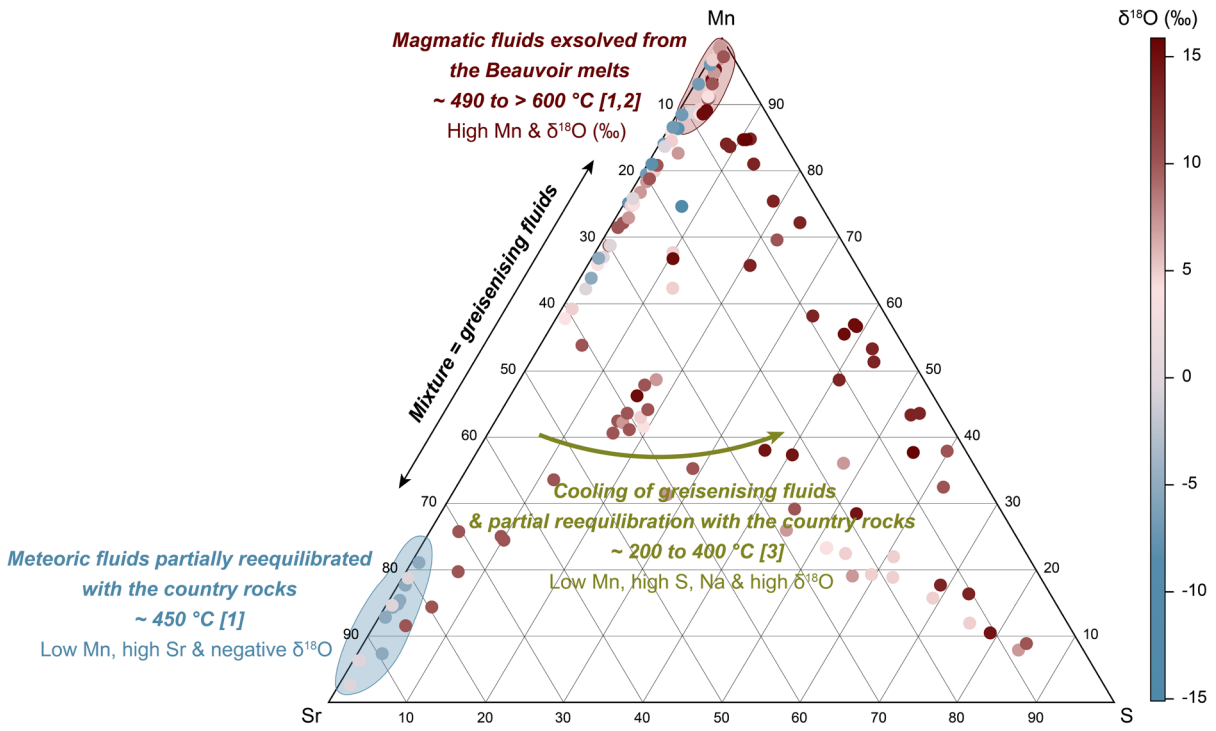



*Figure II.14. Mn, Sr & S ternary diagram showing the geochemical evolution of hydrothermal apatite from the Beauvoir PRMG with colour scale representing $\delta^{18}O$ values. Data are from EPMA. When an element was not detected at an analysis spot, half of the detection limit was assigned as the concentration. Detailed trends between Sr and S content and O isotopic signature of apatite are illustrated on Figure II.A3 (Appendices). The early evolution of the Beauvoir magmatic-hydrothermal system is associated with mixing dynamics between isotopically heavy Mn-rich magmatic fluids and isotopically light oxidised Sr-rich meteoric fluids, partially reequilibrated with mica schist and paragneiss country rocks, at relatively high temperature. Progressive cooling and oxidation of the system concomitant with an increase of meteoric fluid contribution and degree of fluid-host-rock interaction led to an increase of $\delta^{18}O$ along with Mn depletion and S ± Na enrichment in apatite. The enrichement in S indicates partial reequilibration of the fluids with the counstry rocks. [1] Aïssa et al. (1987); [2] Harlaux et al. (2017); [3] Monnier et al. (2020).*

Apatite IIb exhibits heterogeneous O isotopic (Fig. II.10) and elemental signatures (Figs. II.7, II.8, II.9), with a trend between two end-members, excluding apatite IIb overprinted by kaolinisation (Fig. II.14). The first end-member corresponds to magmatic fluids, as identified through the chemistry of apatite IIa. The second end-member, essentially represented by the analysed quartz-apatite vein, displays low MnO and high SrO contents (<0.1–1.0 wt.% and 1.0–4.7 wt.%, respectively), negative $\delta^{18}O$ values (-3.3 to -1.0 ‰) and a significantly different REE distribution from that of apatite IIa (i.e., MREE enrichment, with low $La_N/Yb_N$ ratios, flat HREE signatures, and no distinct Eu anomaly). The following information can be deduced from these observations:

- Due to the preferentially incorporation of $Mn^{2+}$ over $Mn^{3+}$ and $Mn^{4+}$ in apatite from direct substitution with $Ca^{2+}$, Mn content in apatite not only depends on magma or fluid compositions, but also on oxygen fugacity ($fO_2$) within the system (e.g., Belousova et al. 2002). Within the Beauvoir PRMG, apatite Mn content progressively decreases over time,

with the magmatic generation exhibiting significantly higher Mn concentrations compared to the early and late hydrothermal generations (MnO ~ 3.7 wt.%, 1.7 wt.% and 0.4 wt.%, respectively). Manganese depletion upon alteration has been documented in apatite from U deposit-related leucogranites of the Variscan belt and interpreted to reflect an interaction with oxidised meteoric hydrothermal fluids at subsolidus conditions (e.g., Ballouard et al., 2018).

- Strontium behaves compatibly during peraluminous magma differentiation, due to feldspar fractionation. Consequently, differentiated granitic intrusions typically exhibit very low whole-rock Sr contents. Experimental work has confirmed that Sr should have been depleted in the Beauvoir residual melts upon crystallisation (Pichavant, 2022). Despite its strongly differentiated nature, the Beauvoir PRMG is paradoxically rich in Sr, with whole-rock concentrations reaching up to 1000 ppm (Raimbault et al., 1995). To explain this unexpected particularity, Charoy et al. (2003) suggested the introduction of external Sr at the magmatic-hydrothermal transition by meteoric fluids partially equilibrated with the host mica schist. This high temperature hydrothermal event is presumed to have significantly affected both the chemistry and mineralogy of the Beauvoir PRMG, notably by inducing the recrystallisation of primary feldspars in albite (Pichavant et al., 1987a; Charoy et al., 2003; Pichavant, 2022). However, since the host mica schist is relatively Sr-poor (34–144 ppm, Table II.A9 in Appendix II.A4), the Sr-enrichment observed in the Beauvoir PRMG may more likely originate from the leaching of the structurally overlying (Fig. II.1b) and Sr-richer paragneiss units (112–259 ppm Sr; Fig. II.8) by meteoric fluids. This incursion of Sr-rich meteoric fluids may also account for the Sr enrichment observed in apatite IIb (up to 4.7 wt.% SrO; mean ~ 1.15 wt.%), except in cases where apatite IIb has been overprinted by kaolinisation.
- Oxygen isotopic fractionation between fluids and apatite is minor at high temperature (e.g., $\Delta^{18}O_{apatite\text{-}fluid}$ = -0.5 ‰ at 600 °C; Zheng, 1996). At temperatures lower than 480 °C, $\delta^{18}O$ values of the parent fluid are shown to be systematically lower than those of apatite (i.e., $\Delta^{18}O_{apatite\text{-}fluid} > 0$; Zheng, 1996). Consequently, the negative $\delta^{18}O$ values of several apatite IIb imply an equilibrium fluid with even more negative $\delta^{18}O$, strengthening the interpretation of a meteoric origin (Sheppard, 1986).
- This second end-member finally displays low total REE concentrations (<26 ppm), MREE enrichment compared to LREE and HREE, with low $La_N/Yb_N$ ratios (0.26–1.50), flat HREE profiles, and no distinct Eu anomaly. These characteristics are typically associated with a decrease in pH, temperature and fluid salinity, along with an increase in $fO_2$, which tend to result in an increased speciation of LREE within the fluid as highly stable and soluble chloride complexes, inhibiting their incorporation into apatite (e.g.,

Krneta et al., 2017). LREE depletion in apatite could also result from the co-precipitation of LREE-rich minerals, such as secondary monazite, as observed in Figure II.5c.

All these features indicate the influx of external fluids, mostly of meteoric origin, which underwent partial chemical equilibration and likely oxygen isotopic exchange with the country rocks during the greisenisation episode at *ca.* 310–315 Ma. At this period, the infiltration of meteoric fluids in the upper continental crust through strike-slip and detachment shear zones was previously highlighted in the Limousin region (north-western FMC) (Dusséaux et al., 2021). The distribution of apatite IIb data between the two end-members suggests mixing dynamics between magmatic and meteoric fluids (Fig. II.14). Incursion of external fluids, concomitant with magmatic fluid circulation within the Beauvoir PRMG at high temperatures equal or above 400 °C, was previously emphasised by the study of fluid inclusions (Aïssa et al., 1987; Harlaux et al., 2017), and confirmed based on O isotope analyses by Fouillac et al. (1987) and Fouillac and Rossi (1991).

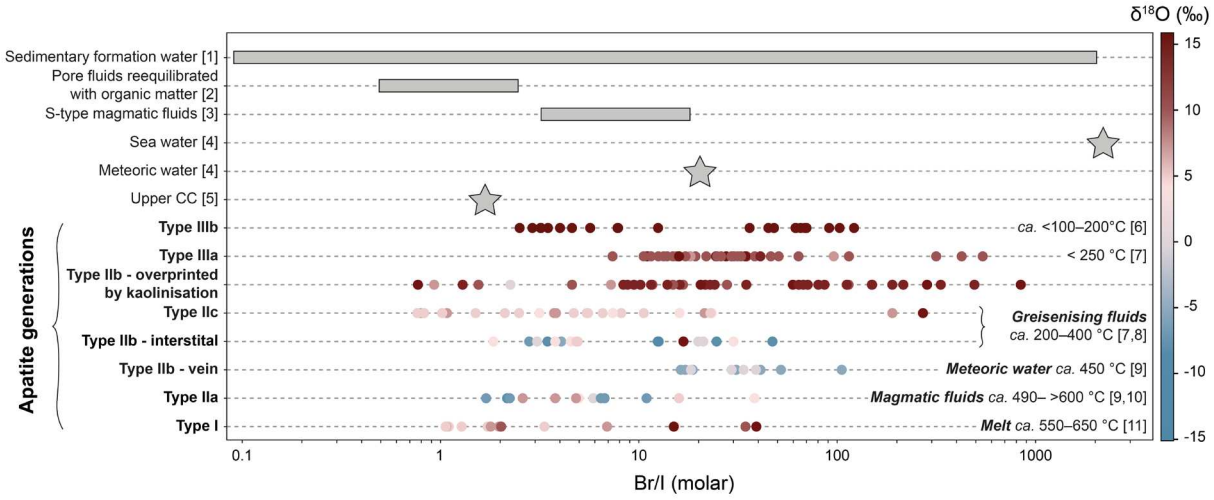



*Figure II.15. Br/I molar ratios of the distinct apatite generations within the Beauvoir PRMG with colour scale representing $\delta^{18}O$ values. Data for the upper continental crust, meteoric water, sea water, S-type magmatic fluids, pore fluids reequilibrated with organic matter and sedimentary formation water are plotted as reference. [1] Worden (1996); [2] Kendrick et al. (2011); [3] Andersson et al. (2019); [4] Worden (2018); [5] Webster et al. (2018); [6] Merceron et al. (1987); [7] Merceron et al. (1992); [8] Monnier et al. (2020); [9] Aïssa et al. (1987); [10] Harlaux et al. (2017); [11] Pichavant (2022).*

Greisen-alteration affecting RMGs is proposed to be mainly caused by the circulation of magmatic, acidic fluids, exhibiting low to moderate salinities (up to 10 wt.% NaCl eq) and a broad range of circulation temperatures (*ca.* 200 to 500 °C; e.g., Burt, 1981; Štemprok, 1987; Shepherd et al., 1985; Taylor, 1988; Schwartz and Surjono, 1990; Halter et al., 1998; Dobeš, 2005; Monnier et al., 2020). Mixing of magmatic fluids with fluids of external origin, in particular meteoric water, has however been emphasised in many ore-forming systems. This is for example the case for the Piaotang W-Sn deposit (Jiangxi, China), where meteoric fluids infiltrated the Piaotang granite from the earliest stages of its hydrothermal evolution (Legros et al., 2016, 2018

and references therein). Moreover, in the Cornubian Batholith (SW England), fluids of meteoric origin mixed with acidic and B-(Fe-Sn)-saturated magmatic-hydrothermal fluids and were responsible for muscovitisation (Putzolu et al., 2024). In the Beauvoir PRMG, meteoric fluid incursion is proposed to have been facilitated by fracture formation during greisenisation, and could have contributed to the progressive cooling of greisenising fluids from *ca.* 400 °C to 190 °C (Monnier et al., 2020).

Further evolution of the early hydrothermal fluid circulation, as recorded by apatite IIb overprinted by kaolinisation and apatite IIc, is characterised by a more pronounced depletion in MnO (<0.1–4.3 wt.%), an enrichment in $SO_3$, $Na_2O$, and, to a lesser extent, $Al_2O_3$ (<0.1–4.1 wt.%, <0.05–1.4 wt.% and <0.05–3.5 wt.%, respectively), along with heavier O isotopic signatures (mean~ 8.2 ± 0.2 ‰) and highly variable Br/I ratios (~ 0.8–842) (Figs. II.14, II.15 and II.A3b in Appendix II.A3). The S enrichment of the involved fluids most likely derives from similar processes to Sr enrichment, i.e., interactions with surrounding mica schist or paragneiss. Incorporation of the high-valence oxidised $S^{6+}$ into the apatite structure also indicates that the hydrothermal system was relatively oxidising (i.e., high $fO_2$; e.g., Mao et al., 2016; Wang et al., 2022). The observed increase in Na content is probably a result of the co-substitution of S with Na to maintain charge balance (Pan and Fleet, 2002). The heavier O isotopic signature may originate from the combination of: (i) low-temperature fluid circulation inducing important oxygen isotope fractionation between fluids and apatite, and (ii) isotopic reequilibration of fluids with the host mica schists/paragneisses. While partial reequilibration of meteoric fluids with organic matter during their circulation within the country rocks may explain the relatively low Br/I ratios observed (*ca.* < 30) (Kendrick et al., 2011), another hypothesis could be the involvement of low Br/I sedimentary formation water (Worden, 1996) (Fig. II.15). The first hypothesis seems more conceivable, as the Sioule region was likely not covered by a sedimentary basin at *ca.* 310–315 Ma. Higher Br/I ratios are mostly observed for apatite IIb overprinted by kaolinisation, and may result from a major contribution of high Br/I sedimentary formation water, possibly deriving from Mesozoic basins, and/or seawater (Worden, 1996) (Fig. II.15). In summary, the early hydrothermal stage is initially dominated by the circulation of magmatic fluids, which mixed at high temperature (⩾400 °C) with meteoric fluids partially reequilibrated with the host-rocks (Fig. II.14). Meteoric fluids became progressively predominant (and cooler), inducing an increase in $fO_2$, and a subsequent decrease in Mn content and increase in S content and $\delta^{18}O$ in apatite II (Figs. II.14 and II.A3b in Appendix II.A3).

Two late hydrothermal events are temporally disconnected from the intrusion of the Beauvoir PRMG and result from the circulation of external fluids related to the regional tectonics. Apatite IIIa co-precipitated with fluorite at *ca.* 270 Ma and is essentially characterised by high $As_2O_3$ concentrations (0.4–5.3 wt.%) (Fig. II.7), variable Br/I ratios (7–542; Fig. II.15), a

relatively heavy O isotope signature ($\delta^{18}O$ ~ 3.4–14.4 ‰) (Fig. II.10h), as well as a LREE depletion compared to MREE and HREE ($La_N/Yb_N$ ~ 0.06–0.51), and a moderate negative Eu anomaly (Eu/Eu* ~ 0.38–0.71) (Fig. II.9c). The high As content of apatite IIIa reflects a high $fO_2$ within the system, as apatite preferentially incorporates its high-valence oxidised state (i.e., $As^{5+}$) (e.g., Mao et al., 2016; Wang et al., 2022). Arsenic mobilisation from minerals depends on many parameters, including fluids temperature, pH and redox conditions (Smedley and Kinniburgh, 2002). Oxidising conditions will trigger As release from sulphide species, such as arsenopyrite (FeAsS) and arsenian pyrite ($Fe(S,As)_2$). Elevated As concentrations between 130 and 170 ppm, likely hosted in sulphide minerals, were measured for the Sioule mica schists (Table II.A9 in Appendix II.A4) and hydrothermal alteration of such rocks at oxidised conditions could have liberated significant amount of this metal. Although Br/I ratios predominantly fall within the range of magmatic fluids, some values reach up to *ca.* 542. This may reflect halogen introduction from an external source, and more precisely, the possible circulation of sedimentary formation water derived from the overlying Permian basins (Fig. II.15; Worden, 1996). Uraniferous deposits from the European Variscan belt were emplaced following the circulation of surface-derived oxidising aqueous fluids able to leach U from uranium oxides in the leucogranites (e.g., Cathelineau, 1982; Turpin et al., 1990b; Barsukov et al., 2006; Kříbek et al., 2009; Dolníček et al., 2014; Ballouard et al., 2017; Dusséaux et al., 2022) and As-rich apatite, dated at *ca.* 290 Ma, was found in a U-mineralised episyenite from a leucogranitic massif of the Variscan Armorican Massif (Ballouard et al., 2018). The circulation of such oxidised fluids within the Echassières complex may have mobilised As from the Sioule mica schists, and the F component of fluorite could directly originate from the destabilisation of F-rich igneous minerals such as lepidolite, topaz (and apatite) during interaction with hydrothermal fluids, without the need for external input of F.

Finally, the last hydrothermal stage affecting the Beauvoir PRMG, as identified in this study, led to the precipitation of apatite IIIb. Apatite IIIb exhibits a similar chemistry to the apatite characterising the end of the early hydrothermal stage, i.e., enrichment in $SO_3$, $Na_2O$ and $Al_2O_3$ (<0.1–16 wt.%, 0.2–0.6 wt.% and <0.05–1.10 wt.%, respectively) (Fig. II.7), LREE depletion compared to MREE and HREE (Fig. II.9c), as well as the heaviest O isotopic signature (~ 13.6–17.0 ‰) (Fig. II.10d). Therefore, the corresponding hydrothermal event likely originated from external fluid circulation at relatively low temperature in an oxidising environment. Apatite IIIb precipitation appears contemporaneous to illite precipitation in the Beauvoir PRMG (Fig. II.12), and involved fluids that might have circulated at temperatures of *ca.* 200 °C (Merceron et al., 1987). As discussed in section 5.1, the precipitation of apatite IIIb may be linked to the widespread hydrothermal event affecting Western Europe from *ca.* 210 to 100 Ma, leading to the genesis of F-Ba-Pb-Zn mineralisation (Fig. II.12). F-Ba (Pb–Zn) vein-type deposits have been attributed to the circulation of moderately to highly saline, $CaCl_2$-NaCl-rich brines derived from

seawater and/or meteoric water at temperatures ranging from 70 to 200 °C (Sizaret et al., 2004; Boiron et al., 2010; Sánchez et al., 2010). Assuming negligible fluid-apatite fractionation, the variable Br/I ratios observed for apatite IIIb, ranging from *ca.* 3 to 122 (Fig. II.15), are consistent with such fluid origins.

### 5.4. Apatite as a window into mineralising processes within PRMGs

The decrease of Eu anomaly from the B3 to B1 unit (Fig. II.9a) has important metallogenic implications as it confirms an increase in oxygen fugacity conditions during Beauvoir granitic magma differentiations previously recognised, based on the decrease in the $Fe^{3+}/Fe^{2+}$ ratio of Li-micas from the B3 to the B1 (Cuney et al., 1992) and crystallisation experiments (Pichavant, 2022). Crystallisation experiments were carried out on powder samples from the Beauvoir B1 and B2 units and demonstrated that, to achieve the mineralogical and geochemical characteristics of the Beauvoir PRMG, the melts crystallised under unexpectedly oxidising conditions compared to the reduced conditions typically characterising highly peraluminous granitic magmas (Pichavant, 2022). Oxygen fugacity has been shown to have a dramatic influence on $SnO_2$ solubility in granitic melts, with cassiterite crystallisation ($Sn^{2+} \rightarrow Sn^{4+}$ transition) being favoured under oxidised conditions (Linnen et al., 1996; Bhalla et al., 2005; Pichavant, 2022). Therefore, in the Beauvoir PRMG, magmatic oxidation concomitant with increasing differentiation may have enhanced cassiterite crystallisation at the magmatic stage notably in the B1 unit (Cst I; Fig. II.2). The causes of such oxididation remain unclear. It may reflect the "self-oxidation" of the melt due to the exsolution of $HF^-$ as a vapour component (Pichavant et al., 2016). However, open-system mechanisms including the impact of external fluids still deserves to be evaluated in the context of the Beauvoir PRMG, considering that the oxygen isotope analyses of igneous minerals including quartz, lepidolite (Fouillac et al., 1987; Fouillac and Rossi, 1991) and magmatic apatite (this study) suggest incursion of oxidised meteoric fluids at high temperatures and possibly suprasolidus conditions.

Vein apatite IIa is characterised by a complex CL texture, featuring bright secondary zones replacing dark primary areas (Fig. II.16a). It represents the only hydrothermal apatite subset within the Beauvoir PRMG that notably co-precipitates with rare metal-bearing minerals, in this instance cassiterite (Fig. II.16b). Apatite IIb has also been found in association with wolframite within greisen-altered quartz veins of the La Bosse stockwork (Fig. II.5c; Table II.1; Monnier et al., 2019).

The two distinct textural micro-domains of apatite IIa differ by specific elemental and O isotopic chemistries, as illustrated on Figures II.16c and d. The dark-CL primary zones show high Mn and low Sr contents, as well as relatively heavy O isotopic signatures. In contrast, bright-CL secondary zones exhibit lower Mn but higher Sr concentrations and negative $\delta^{18}O$ values. While the characteristics of dark-CL primary zones can be attributed to their precipitation from

magmatic fluids exsolved from the melt, the precipitation of bright-CL secondary zones is unambiguously related to the circulation of meteoric fluids (section 5.3). Another interesting discrepancy between both micro-domains is their Sn concentrations, which are relatively higher in dark-CL primary zones compared to secondary ones (*ca.* 23–65 ppm and 0–3 ppm, respectively; Fig. II.16c). This observation is consistent with the significant Sn content of magmatic fluids emphasised through the study of fluid inclusions (*ca.* 1000–40,000 ppm; Harlaux et al., 2017).

In Cl-F-bearing magmatic fluids, $SnO_2$ solubility decreases with increasing oxygen fugacity ($fO_2$) and decreasing fluid acidity ($m_{HCl,aq}$) (Taylor and Wall, 1993). The early incursion of meteoric fluids highlighted in apatite IIa and their mixing with magmatic fluids would thus likely trigger cassiterite precipitation (Cst II; Fig. II.2). This process could explain the preferential localisation of cassiterite within the luminescent secondary zones or at the transition between dark- and bright-CL zones (Fig. II.16b).

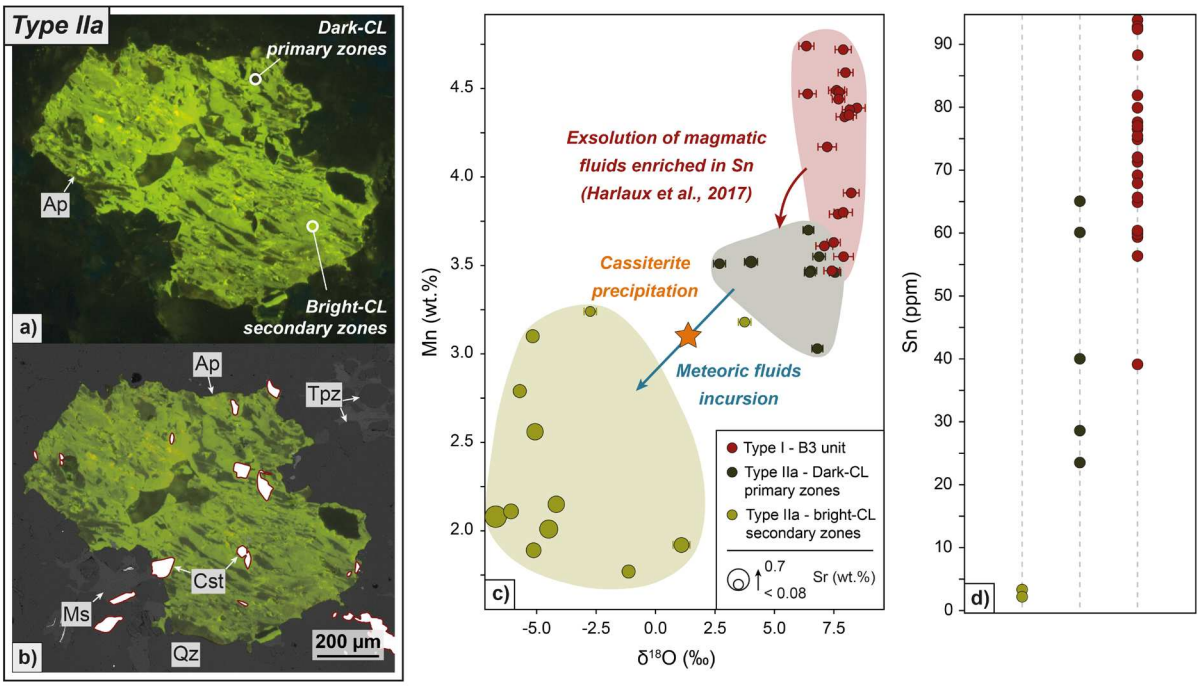



*Figure II.16. Chemistry of CL textural micro-domains in early hydrothermal apatite IIa: (a) CL image highlighting dark primary and bright secondary zones; (b) Superposition of CL and BSE images highlighting cassiterite preferential precipitation in bright-CL secondary zones or at the transition between dark- and bright-CL zones; (c) Oxygen isotopic signature plotted against Mn content in apatite, with the size of the data points representing the Sr content; (d) Sn contents of the two distinct micro-domains of apatite IIa. The composition of magmatic apatite I from the B3 unit of the Beauvoir PRMG is shown in (c) and (d) for comparison.*

Mixing dynamics between magmatic and meteoric fluids thus appear to have significant implications for the precipitation of metals, particularly Sn, during the hydrothermal stage within the Beauvoir PRMG. Although the necessity of oxidising agents for cassiterite precipitation was questioned by Liu et al. (2023), the prominent role of meteoric water influx in the crystallisation

of cassiterite is well-established in Sn(-W) hydrothermal deposits associated with granite intrusions (Witt, 1988; Heinrich, 1990; Audétat et al., 1998; Karimzadeh Somarin and Ashley, 2004; Fekete et al., 2016; Liu et al., 2020; Chen et al., 2023; Peng et al., 2023). Therefore, although the majority of Sn mineralisation derives from Sn saturation at the magmatic stage, leading to the crystallisation of cassiterite I, meteoric water influx also appears to be inherent to the hydrothermal ore-forming processes (Cst II) of the Beauvoir PRMG, and could probably play a major role in other PRMGs.

The majority of current genetic models proposed for PRMGs, and more broadly RMGs, involve closed systems of iso-composition dominated by purely magmatic processes (e.g., Kovalenko et al., 1970; Groves and McCarthy, 1978; Raimbault et al., 1995; Pichavant, 2022). Yet, some studies highlighted the necessity to consider the exsolution of magmatic fluids (or hydrosaline melt) and subsequent fluid-rock interactions to fully explain the formation of rare-metal deposits (e.g., Thomas et al., 2011; Badanina et al., 2015; Ballouard et al., 2016, 2020a; Araujo et al., 2023; Pfister et al., 2023; Putzolu et al., 2024), and in some rare cases, the interactions between melt and external fluids to trigger metal precipitation (London et al., 1996; Linnen et al., 2019; McNeil et al., 2020). Beyond the already well-established role of meteoric fluids in Sn precipitation, some authors have suggested a significant contribution of external fluids to the Fe and Mn content of columbite-group minerals (Linnen et al., 2019). In the Beauvoir PRMG, the crystallisation of columbite- and pyrochlore-group minerals is thought to have been influenced by fluid circulation of meteoric origin, especially in the most evolved B1 unit (Ohnenstetter and Piantone, 1988; Fouillac and Rossi, 1991). Therefore, RMGs genesis involving open systems, potentially characterised by interactions between melts and external fluids, seems to require more serious consideration.

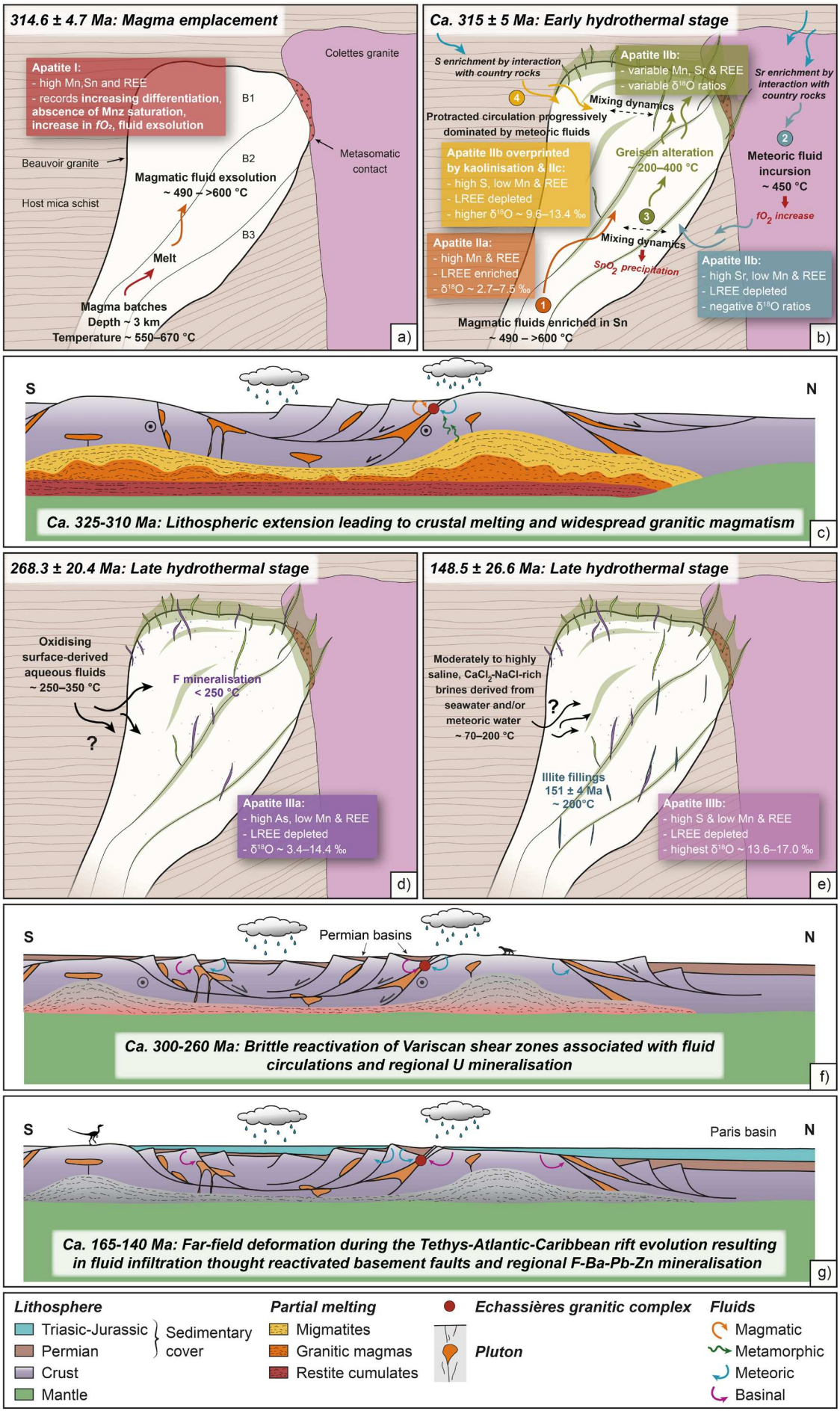
## 6. Summary and conclusions

The study of apatite within the Beauvoir PRMG unravel a complex and polyphased magmatic-hydrothermal system (Fig. II.17):

- Magmatic apatite (apatite I) formed at $314.6 \pm 4.7$ Ma, consistent with previous estimations based on other geochronometers. The LREE enrichment observed reflects the absence of monazite saturation during crystallisation, while the decrease in the Eu anomaly amplitude may record the increase in $fO_2$ from the root to the apical zone of the granite upon differentiation, which may have facilitated the crystallisation of the predominant cassiterite generation (i.e., cassiterite I) at supra-solidus conditions. The exsolution of magmatic fluids also affected the signature of magmatic apatite, especially from the deeper facies, by inducing a pronounced tetrad effect in its REE patterns.

- The exsolution of magmatic fluids, evidenced by apatite I and IIa, initiated the early hydrothermal stage at 314.3 ± 5.5 Ma. It is characterised by magmatic fluid exsolution followed by mixing dynamics between magmatic and meteoric fluids during greisenisation, which contributed to a gradual decrease in temperature and further increase in $fO_2$ of the system (Mn-depleted apatite reaching negative $\delta^{18}O$ values). Meteoric fluids were partially reequilibrated with the country rocks, resulting in a progressive introduction of Sr and S within the Beauvoir PRMG. Apatite chemistry shows that meteoric fluids play an important role in greisenisation processes within the Beauvoir PRMG. The early incursion of meteoric fluids most likely resulted in a sudden shift in redox conditions towards a more oxidising environment, triggering precipitation of cassiterite from magmatic fluids. Further constraining the timing and temperature conditions of meteoric fluid incursion in the Beauvoir magmatic-hydrothermal system is crucial, as it might have major implications for understanding the crystallisation mechanism of rare metal-bearing minerals in PRMG environments.
- Two later hydrothermal events, post-dating granite emplacement at *ca.* 310–315 Ma and the circulation of magmatic-hydrothermal fluids, have been identified from apatite U-Pb ages and chemical characteristics, providing insights in the influence of regional tectonic events on the evolution of the Beauvoir PRMG. The first event took place at 268.3 ± 20.4 Ma (Permian-Triassic). It resulted in fluorite mineralisation in the Beauvoir PRMG, and is possibly related to Europe-wide post-orogenic extension-related circulation of basin- and surface-derived oxidising fluids that mobilised U from fertile Variscan leucogranites between 300 and 260 Ma. The second event, dated at 148.5 ± 26.6 Ma (Jurassic-Cretaceous), is proposed to be linked to widespread extension-related F-Ba-Pb-Zn mineralisation affecting Western Europe from *ca.* 210 to 100 Ma.

As demonstrated in several studies, apatite represents a powerful mineral to decipher magmatic and hydrothermal processes within various environments, and this study showcases its usefulness in granite-related rare metal deposits. The PHP-RMGs typified by the Beauvoir granite are specifically marked by high P concentrations which favour apatite crystallisation throughout most of its magmatic and hydrothermal evolution. As such, studying the distinct apatite generations in such context thus provides major insights for the magmatic and hydrothermal processes that have affected them through geological history and controlled their metal endowment.




*(Caption on the next page)*

*Figure II.17. Simplified cross-sections illustrating a schematic evolution of the Beauvoir magmatic-hydrothermal system, as revealed by apatite chemistry and U-Pb geochronology, along with corresponding regional geodynamic events: (a-c) Magmatic to early hydrothermal evolution and (d-g) Late hydrothermal evolution. Crustal scale cross-sections (c-f-g) are modified from Monnier et al., (2021). The age mentioned in Figure b corresponds to the overlap of ages obtained for apatite IIa and IIb (i.e., 314.3 ± 5.5 Ma and 311.7 ± 8.1 Ma, respectively). Temperatures of fluid circulations and greisen alteration within the Beauvoir PRGM (a-b-d-e) are from Aïssa et al. (1987); Merceron et al. (1987, 1992); Harlaux et al. (2017); Monnier et al. (2020); Pichavant (2022).*

# PART III

## Insights of quartz into mechanisms influencing the magmatic-hydrothermal transition

## 1. Introduction

### *Version française*

L'étude de l'apatite dans le granite de Beauvoir met en lumière une évolution magmatique et hydrothermale complexe et polyphasée, caractérisée par une succession de quatre phases majeures (Partie II; Rocher et al., 2024). Cette évolution englobe un stade magmatique, un stade hydrothermal précoce correspondant à la transition magmatique-hydrothermale, ainsi qu'au moins deux événements épisodes hydrothermaux tardifs, non magmatiques, induits par des événements tectoniques régionaux.

La transition magmatique-hydrothermale occupe une place centrale dans cette évolution. Dans le granite de Beauvoir, comme dans les granites à métaux rares de façon générale, cette transition est initiée par l'exsolution de fluides magmatiques et, parfois, de magmas résiduels enrichis en volatils, dans le système (e.g., Aïssa et al., 1987; Badanina et al., 2004; Kaeter et al., 2018; Ballouard et al., 2020a; Pfister et al., 2023). Ces processus d'exsolution engendrent des interactions complexes – et souvent peu comprises – entre liquides silicatés et fluides. L'étude des inclusions fluides dans le granite de Beauvoir a permis d'identifier plusieurs générations de fluides magmatiques (Aïssa et al., 1987), présentant des enrichissements significatifs en métaux rares, tels que Li, Sn, Nb et Ta ($10^2$–$10^4$ ppm; Harlaux et al., 2017). Ces circulations fluides de haute température (~ 400– >600 °C) ont très probablement joué un rôle essential – bien que peu contraint à ce jour – dans la distribution des métaux, du stade supra-solidus jusqu'à l'évolution sub-solidus du système.

Par ailleurs, l'infiltration de fluides externes, possiblement d'origine météorique, a également été mise en évidence par l'analyse des inclusions fluides (Aïssa et al., 1987; Cuney et al., 1992). Certains travaux suggèrent que ces fluides météoriques se seraient infiltrés à des conditions sub-solidus (≥ 450 °C; Cuney et al., 1992), tandis que d'autres interprètent la composition isotopique de l'oxygène ($\delta^{18}O$) de certains minéraux magmatiques tels que le quartz, la topaze, la lépidolite et le feldspath, comme reflétant des interactions supra-solidus entre le liquide silicaté et des fluides météoriques à des températures d'environ 570 ± 50 °C (Fouillac et al., 1987; Fouillac et Rossi, 1991). Ces fluides météoriques auraient largement participé à l'altération sub-solidus de type greisen, qui a significativement remobilisé les métaux au sein de l'intrusion, et a notamment entraîné le lessivage de l'étain et du lithium vers les micaschistes encaissants (Cuney et al., 1992). La greisenisation est communément associée à la circulation de fluides magmatiques acides et modérément salés (~ 3–10 %pds eq NaCl), à des températures comprises entre 200 et 500 °C (e.g., Burt, 1981; Štemprok, 1987; Shepherd et al., 1985; Taylor, 1988; Schwartz et Surjono, 1990; Halter et al., 1998a; Dobeš, 2005), bien que la contribution de fluides externes d'origine météorique ait toutefois été documentée au sein de certains systèmes (e.g., Witt, 1988; Cuney et al., 1992; Bettencourt et al., 2005). Au sein de l'intrusion de Beauvoir, l'étude de Monnier et al.

(2020) soutient que les fluides greisenisants ont une origine magmatique, soulevant ainsi des incertitudes concernant la nature exacte de ces fluides et le timing de l'incursion des fluides externes. Contraindre ce timing apparaît crucial pour la compréhension de la mobilité hydrothermale des métaux, les fluides météoriques entraînant communément la précipitation de la cassitérite ($SnO_2$) au sein des systèmes de greisen à Sn-W (Witt, 1988; Heinrich, 1990; Audétat et al., 1998; Karimzadeh Somarin et Ashley, 2004; Fekete et al., 2016; Liu et al., 2020; Chen et al., 2023; Peng et al., 2023a).

Cette partie repose essentiellement sur la caractérisation pétrographique, l'analyse *in-situ* des éléments traces et des isotopes de l'oxygène dans le quartz magmatique du granite de Beauvoir, ainsi que l'analyse par microthermométrie, spectrométrie Raman, et LA-ICP-MS des inclusions fluides piégées, qui illustrent l'évolution des fluides magmatiques à travers des processus d'ébullition, de refroidissement et de dilution par des fluides externes (Aïssa et al., 1987; Cuney et al., 1992). Cette analyse est enrichie par l'étude des isotopes de l'oxygène dans la cassitérite magmatique, le quartz et la cassitérite de greisen. L'ensemble de ces analyses vise à: (i) contraindre les conditions physico-chimiques du système au cours de la transition magmatique-hydrothermale ; (ii) enrichir la chronologie relative des circulations fluides déjà existante ; (iii) étudier les interactions fluide-liquide silicaté et fluide-fluide, et leur influence sur la distribution des métaux ; et (iv) tracer l'évolution de la nature et de la chimie des fluides mis en jeu tout au long de la transition magmatique-hydrothermale, apportant des informations cruciales sur la mobilité hydrothermale des métaux.

### *English version*

The study of apatite within the Beauvoir PRMG deciphers a complex and polyphased magmatic and hydrothermal evolution, characterised by a sequence of four major phases, encompassing the magmatic stage, the early hydrothermal stage corresponding to the magmatic-hydrothermal transition, and two late, non-magmatic, hydrothermal stages driven by regional tectonic processes (Part II; Rocher et al., 2024).

The magmatic-hydrothermal transition plays a central role in this evolution. In the Beauvoir PRMG, and more widely in rare-metal granite deposits, this transition is initiated by the exsolution of magmatic fluids and, eventually, of volatile-rich residual melts within the system (e.g., Aïssa et al., 1987; Badanina et al., 2004; Kaeter et al., 2018; Ballouard et al., 2020a; Pfister et al., 2023). These exsolution processes result in complex and often poorly understood interactions between melts and fluids. Fluid inclusion studies in the Beauvoir PRMG have identified multiple generations of magmatic fluids (Aïssa et al., 1987), enriched in rare metals such as Li, Sn, Nb, and Ta ($10^2$–$10^4$ ppm; Harlaux et al., 2017). These high-temperature fluid circulations (*ca.* 400 to >600 °C) likely played a significant, although still unclear, role in metal distribution, from the supra-solidus to the sub-solidus evolution of the system.

Moreover, the infiltration of external fluids, possibly of meteoric origin, has also been deciphered from fluid inclusion analyses (Aïssa et al., 1987; Cuney et al., 1992). Some studies suggest that meteoric fluids infiltrated the system under sub-solidus conditions (≥ 450 °C; Cuney et al., 1992), while others interpret the oxygen isotope composition ($\delta^{18}O$) of magmatic minerals, such as quartz, topaz, lepidolite, and feldspar, as reflecting supra-solidus interactions between the Beauvoir melts and meteoric fluids at temperatures around 570 ± 50 °C (Fouillac et al., 1987; Fouillac and Rossi, 1991). Meteoric fluids may have significantly contributed to sub-solidus greisenisation, which remobilised metals within the intrusion and notably led to the leaching of Sn and Li into the surrounding mica schists (Cuney et al., 1992). Greisenisation is commonly associated with the circulation of acidic, moderately saline magmatic fluids (*ca.* 3–10 wt% NaCl eq) at temperatures between 200 and 500 °C (e.g., Burt, 1981; Štemprok, 1987; Shepherd et al., 1985; Taylor, 1988; Schwartz and Surjono, 1990; Halter et al., 1998a; Dobeš, 2005), although the contribution of external meteoric fluids has also been documented in some systems (e.g., Witt, 1988; Cuney et al., 1992; Bettencourt et al., 2005). Within the Beauvoir intrusion, Monnier et al. (2020) support a magmatic origin for the greisenising fluids, raising uncertainties regarding the exact nature of these fluids and the timing of external fluid incursion. Constraining the timing of this infiltration is critical for understanding the hydrothermal mobility of metals, as meteoric fluids notably typically lead to the precipitation of cassiterite ($SnO_2$) in Sn-W greisen systems (Witt, 1988; Heinrich, 1990; Audétat et al., 1998; Karimzadeh Somarin and Ashley, 2004; Fekete et al., 2016; Liu et al., 2020; Chen et al., 2023; Peng et al., 2023a).

This study is primarily based on petrographic characterisation, *in-situ* trace element and oxygen isotope analysis of magmatic quartz from the Beauvoir granite, as well as the analysis through microthermometry, Raman spectroscopy, and LA-ICP-MS of trapped fluid inclusions, the latter retracing the evolution of magmatic fluids through processes of boiling, cooling, and dilution by external fluids (Aïssa et al., 1987; Cuney et al., 1992). This work is further enriched by the study of oxygen isotopes in magmatic cassiterite, and greisen-related quartz and cassiterite. These analyses provide valuable insights, particularly by utilising the quartz-cassiterite oxygen thermometer to constrain the crystallisation temperatures of these minerals, as well as the oxygen isotopic composition of the parent magma or fluid. Together, these methods offer a comprehensive framework for: (i) constraining the physicochemical conditions of the system during the magmatic-hydrothermal transition; (ii) enriching the existing relative chronology of fluid circulations; (iii) unravelling the melt-fluid and fluid-fluid interactions, and their influence on metal distribution; and (iv) tracing the evolution of the nature and chemistry of the fluids involved throughout the magmatic-hydrothermal transition, shedding light on the hydrothermal mobility of metals.

## 2. Petrographic insights into melt and fluid evolution

### 2.1. Material and methods

#### *2.1.1. Studied material*

Five granite samples with little to no visible alteration were selected along the GPF1 historic drillhole to ensure optimal representation of the three distinct magmatic units of the Beauvoir PRMG (i.e. B1, B2, and B3) (Fig. III.1). Two samples were collected from the B1 unit (379.0 and 390.9 m depth in GPF1), two from the B2 unit (546.5 and 862.0 m) and one from the B3 unit (824.0 m). For each sample, a pair of thin and thick sections (30 µm and 150–200 µm thick, respectively) was prepared, ensuring equivalent areas for petrographic study and analytical data acquisition. These samples, along with their petrographic characteristics described in this section, form the foundation for the analyses and discussions presented in sections 3 and 4 (Part III).

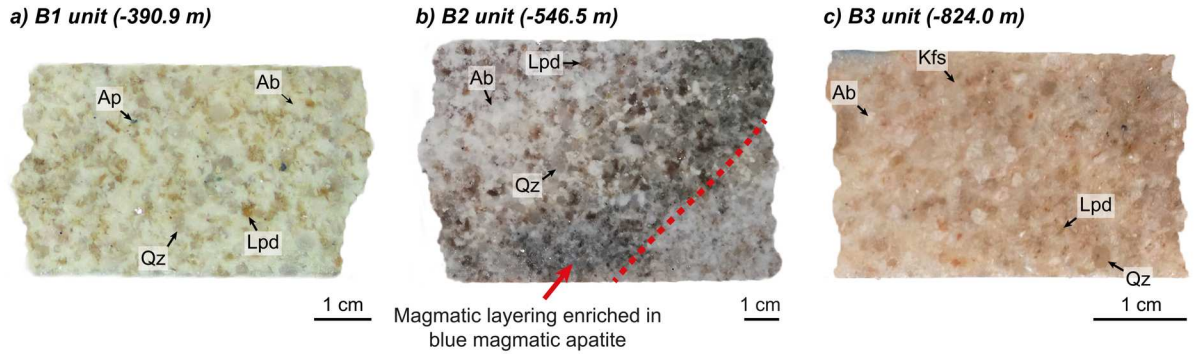



*Figure III.1. Macrophotographs of characterised Beauvoir granite samples, showing minimal to no visible alteration: (a) B1 unit, (b) B2 unit, and (c) B3 unit. Abbreviations follow the IMA conventions compiled by Warr (2021).*

#### *2.1.2. Quartz petrography and element mapping*

Petrographic observations were conducted using optical microscopy at GeoRessources laboratory (Nancy, France) and scanning electron microscopy cathodoluminescence (SEM-CL) at the Centre de Recherches Pétrographiques et Géochimiques (CRPG, Nancy, France). CL imaging was performed on a JEOL JXA 8230 electron microprobe equipped with a panchromatic CL detector, applying an accelerating voltage of 20 kV and a beam current of 100 nA. The pixel resolution ranged from 2 to 5 µm, depending on grain size, with a dwell time of 10 ms per pixel. Since the CL detector is panchromatic, the observed colours do not reflect the true luminescence colours of quartz crystals, although the signal intensities can still be compared qualitatively. This CL study revealed potential intra-granular growth patterns within magmatic quartz grains, offering a deeper understanding of the paragenetic context of the studied fluid inclusion assemblages. The colours have been filtered and adjusted to optimise the visualisation of zonation within quartz.

Furthermore, Wavelength Dispersive X-ray (WDX) element mapping was conducted on magmatic quartz from the B1 unit to measure Al, P, Sn, and Ti distributions. Operating

conditions included an accelerating voltage of 15 kV and a beam current of 100 nA. A pixel resolution of 5 µm was used, with a counting time of 50 ms per pixel.

#### *2.1.3. Fluid inclusion petrography*

Previous studies have investigated fluid inclusions (FIs) within magmatic quartz and topaz from the Beauvoir granite (Aïssa et al., 1987; Harlaux et al., 2017), leading to the identification of eight distinct types of fluid inclusions. Building on this context, our study focused on magmatic quartz, which hosts the full range of these FI types. Due to the more limited diversity of elements that can be incorporated into its crystal lattice, quartz has a simpler chemical composition than topaz, facilitating the processing of LA-ICP-MS data.

Observations of fluid inclusions within magmatic quartz from the Beauvoir granite were conducted at room temperature on double-polished thick sections (150–200 µm) under transmitted light using a Zeiss Axio Imager.A1m microscope (GeoRessources laboratory). The petrographic characterisation of FIs followed criteria established by Roedder (1984), to identify fluid inclusion assemblages (FIAs) corresponding to the eight previously described types (Aïssa et al., 1987). This assemblage-based approach ensures the simultaneous trapping of fluid inclusions within a single set, allowing for reliable data on the origin and evolution of fluids while minimising the risk of analysing FIs that may have been altered by decrepitation or re-equilibration processes.

Solid phases within FIs were identified through Raman spectrometry. Analyses were conducted at room temperature with a Horiba Jobin-Yvon LabRAM 300 spectrometer equipped with a 1,800 gr $mm^{-1}$ grating and an Olympus BX40 microscope at GeoRessources laboratory. A laser Cobolt Fandango DPL with a 514.75 nm wavelength and a maximum output power of 300 mW was employed as the excitation source. At the sample surface, the laser beam had a diameter of approximately 1 µm. To optimise the signal-to-noise ratio (S/N), both the acquisition time and the number of accumulations were carefully adjusted during data collection. After obtaining the spectrum of the solid phase within the FI, a reference spectrum of the host mineral was acquired and subtracted to isolate the spectrum of the inclusion's solid phase. Identification of the solid phases was then carried out either using the Crystal Sleuth software (Laetsch and Downs, 2006) or by comparing the characteristic spectral peaks to reference spectra from the literature.

### 2.2. Results

#### *2.2.1. Quartz petrography*

Magmatic quartz studied within the three magmatic units of the Beauvoir PRMG crystallised with the typical assemblage described by numerous authors, essentially composed of albite, K-feldspar, and Li-Fe-micas (lepidolite-zinnwaldite solid solution), with accessory minerals such as cassiterite, topaz, apatite, amblygonite-group minerals, herderite, zircon, columbite-group

minerals, pyrochlore-group minerals, and uraninite (Pichavant et al., 1987a; Rossi et al., 1987; Johan et al., 1988; Cuney et al., 1992; Raimbault et al., 1995; Monnier et al., 2018; Pichavant, 2022) (Figs. III.1, III.2, III.3, III.4 and Table III.1).

Magmatic quartz varies in size from approximately 500 µm to several millimetres. In the B1 unit, quartz crystals exhibit continuous growth between matrix minerals, characterised by ramified grain boundaries that penetrate the matrix (Fig. III.2). These crystals host euhedral albite inclusions, concentrically arranged with their long axis parallel to growth borders, forming "snowball" textures, a distinctive feature of highly evolved rare-metal granites (Schwartz, 1992; Müller and Seltmann, 1999) (Figs. III.2b, f). Small cassiterite inclusions (*ca.* 20–100 µm) are also occasionally observed (Figs. III.2b, f). In contrast, magmatic quartz from the B2 and B3 units is globular to euhedral (Figs. III.3 and III.4). Quartz phenocrysts contains fewer albite inclusions, which lack the characteristic alignment described in the B1 unit, and no cassiterite inclusions were noted. Rare Li-Fe-micas inclusions occur sporadically in quartz from all three magmatic units (Figs. III.2f and III.3d). Additionally, small topaz grains (*ca.* 1–20 µm) crystallised at mineral joins and along cleavages of lepidolite and albite, as notably documented by Johan et al. (1988) and Cuney et al. (1992). Minerals observed at the contact with magmatic quartz predominantly include the major phases crystallised in the Beauvoir PRMG, namely albite, K-feldspar, and lepidolite, with lesser amounts of cassiterite (Figs. III.2, III.3, III.4 and Table III.1).

*Table III.1. Main minerals observed at the contact with magmatic quartz and as inclusions within magmatic quartz in the three units of the Beauvoir PRMG. xx: frequent, x: scarce and –: absent. Abbreviations follow the IMA conventions compiled by Warr (2021).*

| | Minerals at the contact | | | | | Mineral inclusions | | |
|---|---|---|---|---|---|---|---|---|
| | Ab | Kfs | Lpd | Cst | Tpz at grain joins | Ab | Lpd | Cst |
| B1 | xx | – | xx | x | xx | xx | x | x |
| B2 | xx | xx | xx | x | xx | x | x | – |
| B3 | xx | xx | x–xx | x | xx | x | x | – |

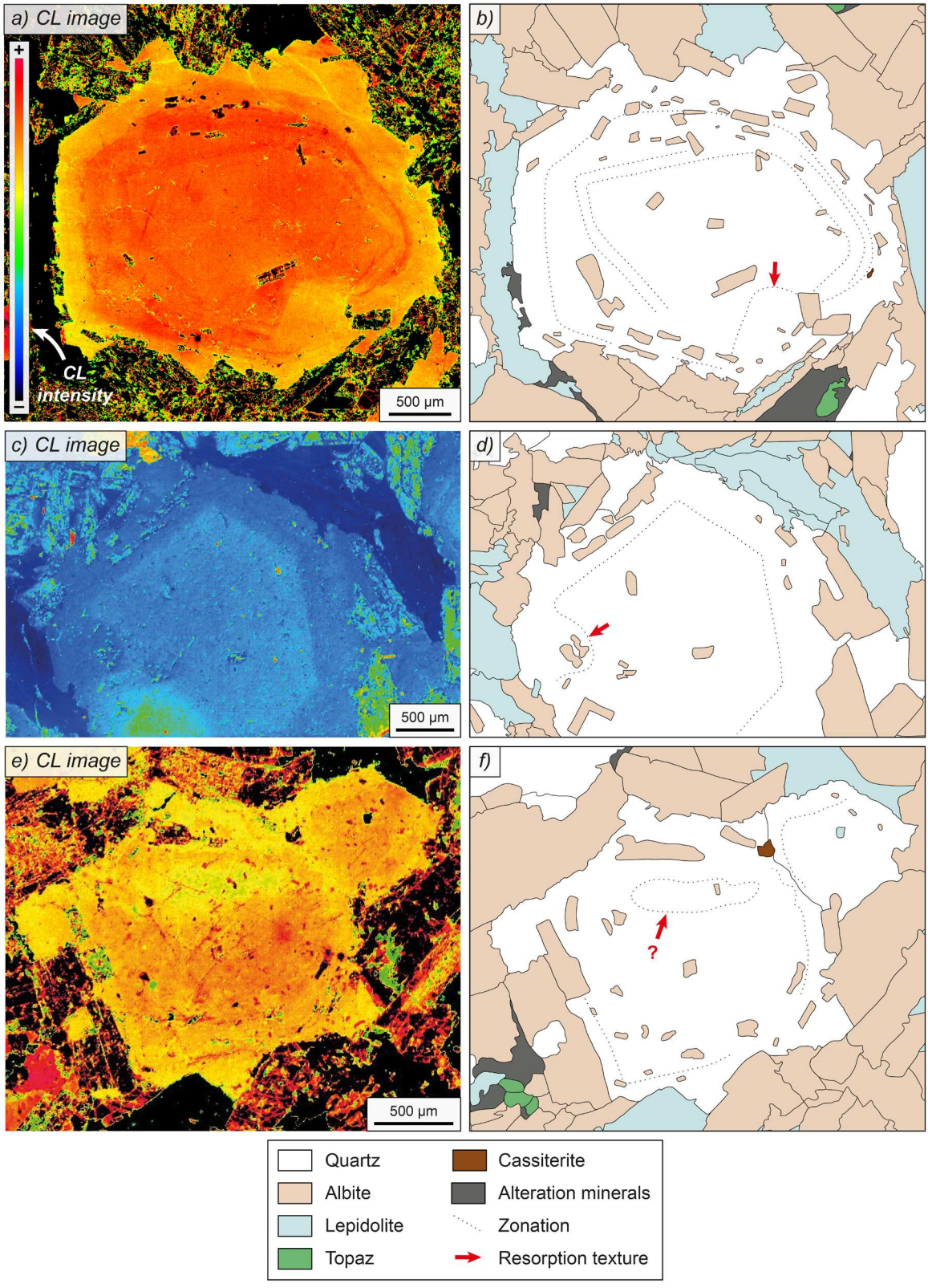



*Figure III.2. Petrographic characteristics of magmatic quartz within the B1 unit. Three main CL textures are identified: (a-b) alternating thin growth bands, several to tens of microns thick, characteristic of oscillatory zoning; (c-d) a sub-euhedral to euhedral core surrounded by a less-luminescent rim, and (e-f) a gradual transition in the CL signal from core to rim. Magmatic zonation is occasionally disrupted by resorption textures, indicated by red arrows. Albite inclusions, concentrically arranged parallel to growth borders, define "snowball" textures, particularly visible in (b) and (f). Occasional small cassiterite inclusions (ca. 20–100 µm) are observed in (b) and (f). The colour scale representing CL intensity in (a) is consistent across all CL images.*

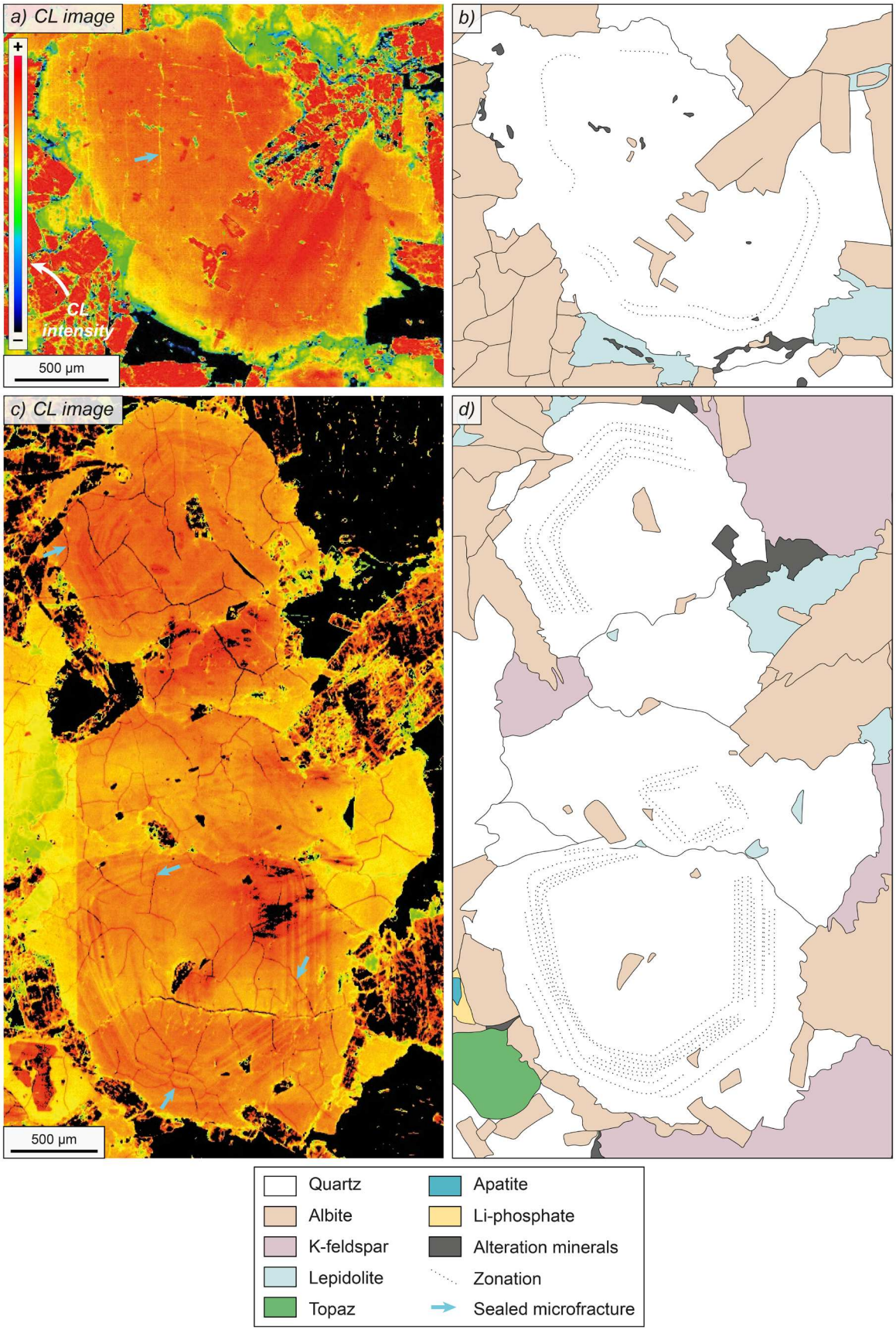



*Figure III.3. Petrographic characteristics of magmatic quartz within the B2 unit. Two main CL textures are shown: (a-b) a gradual transition in CL intensity from the core to a less-luminescent rim; and (c-d) alternating thin growth bands, several to tens of microns thick, characteristic of oscillatory zoning. Magmatic zonation is occasionally crosscut by dissolution-reprecipitation textures along fractures, particularly visible in (c). Albite inclusions are scarce and do not define "snowball" textures. The colour scale representing CL intensity in (a) is consistent across all CL images.*

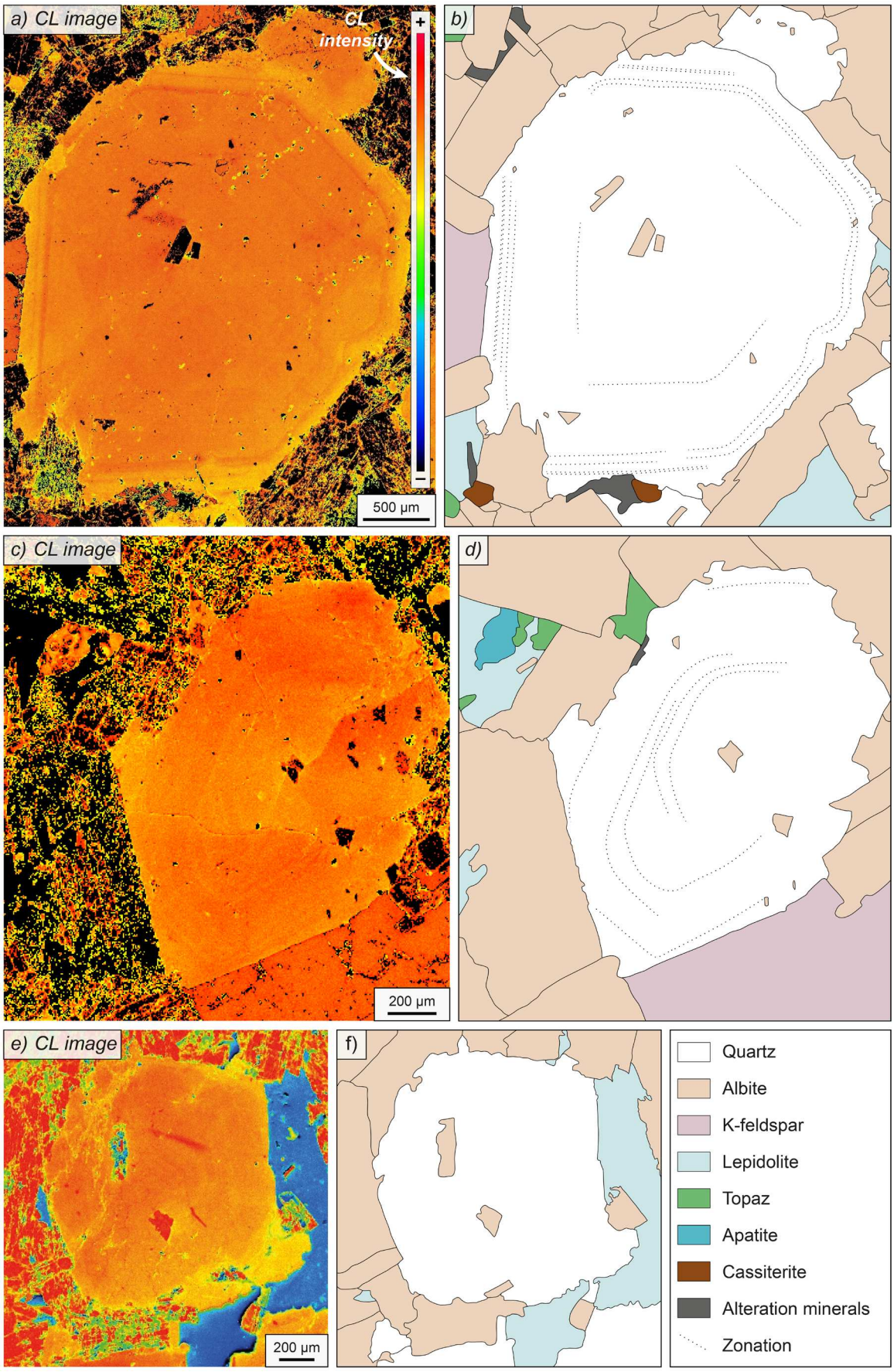



*Figure III.4. Petrographic characteristics of magmatic quartz within the B3 unit. Two main CL textures are identified: (a-d) alternating thin growth bands, several to tens of microns thick, characteristic of oscillatory zoning; and (e-f) a gradual transition in CL intensity from the core to a less-luminescent rim. Albite inclusions are scarce and do not define "snowball" textures. The colour scale representing CL intensity in (a) is consistent across all CL images.*

Magmatic quartz predominantly exhibit heterogeneous CL signatures, characterised by growth bands and, to a lesser extent, resorption and dissolution-reprecipitation textures. Three dominant magmatic textures are consistently identified across all three units (Figs. III.2, III.3, III.4 and Figs. III.A1, III.A2, III.A3 in Appendices): (i) alternating thin growth bands, several to tens of microns thick, characteristic of oscillatory zoning; (ii) sub-euhedral to euhedral core surrounded by a distinct less-luminescent rim; and (iii) gradual decrease in the CL intensity from the crystal core to its outer rim. Magmatic zonation is occasionally disrupted by resorption textures in magmatic quartz from the B1 unit (Figs. III.2a-d), and by dissolution-reprecipitation textures along fractures, particularly in the sample collected from the B2 unit at 546.5 m along the GPF1 drillhole (Fig. III.3). No clear relationship is observed between the CL signal and the occurrence of albite inclusion bands in magmatic quartz from the B1 unit. Albite tends to show heterogeneous CL signal, likely indicative of alteration (Figs. III.2, III.3 and III.4).

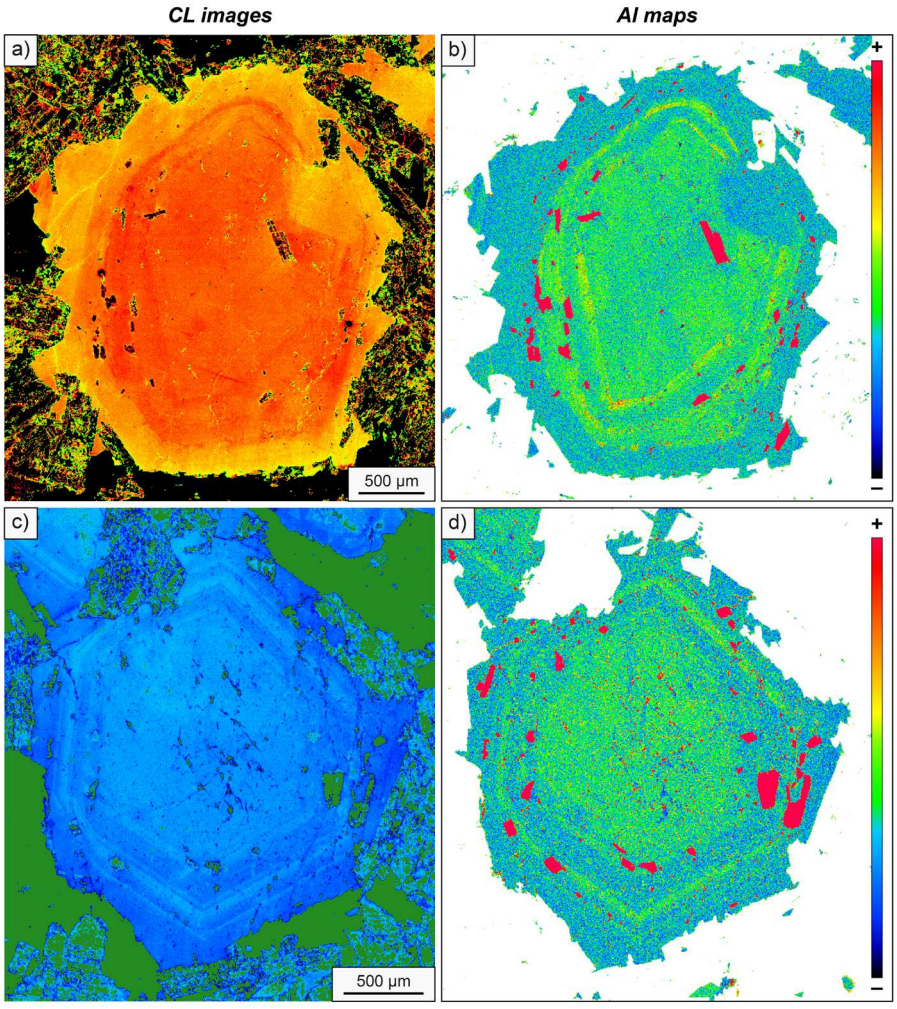



*Figure III.5. CL images and associated WDX element maps of aluminium in magmatic quartz crystals from the B1 unit of the Beauvoir PRMG reveal a strong correlation between Al distribution and CL textures, thereby highlighting the influence of trace element content on the observed luminescence patterns.*

Although CL activation in quartz is primarily influenced by intrinsic lattice defects (Götze et al., 2021), correlations with trace elements content have also been documented, both in hydrothermal (e.g., Penniston-Dorland, 2001; Landtwing and Pettke, 2005) and magmatic quartz (e.g., Watt et al., 1997; Müller et al., 2000, 2002b, 2003; Götze et al., 2004; Yuguchi et al., 2020). As expected from the low trace element concentrations reported in magmatic quartz from the Beauvoir granite (Monnier et al., 2018), only Al was detected through elemental mapping using electron microprobe. In the B1 unit, Al distribution strongly correlates with the CL signal (Fig. III.5). However, this correlation could not be verified in quartz from the B2 and B3 units, as no elemental mapping was performed.

#### *2.2.2. Fluid inclusion petrography*

As detailed in section 4.1.2 of Part I and further mentioned in section 2.1.3 of Part III, previous fluid inclusion studies in the Beauvoir granite identified eight distinct FI types within magmatic quartz (Aïssa et al., 1987; Harlaux et al., 2017), designated as L1, L2, L3, L4, L5, L6, L7 and V2. In the present study, all these FI types were described and analysed, with the exception of L1-type FIs (Figs. III.6, III.7 and III.8). This particular FI type was initially identified exclusively in magmatic topaz from the B1 unit by Aïssa et al. (1987), and later characterised in magmatic quartz from the same unit using LA-ICP-MS analysis by Harlaux et al. (2017). L1-type FIs appear to be scarce in magmatic quartz and were not observed during this investigation.

***L2-type fluid inclusions:*** These are exclusively observed in magmatic quartz from the B1 unit, where they occur in various assemblage types, including clusters, pseudo-secondary and secondary planes (Fig. III.6c), as well as primary FIs aligned along growth planes (Fig. III.6e). Melt inclusions have been identified on a single occasion within the same growth plane as an L2-V2 assemblage (Fig. III.6d). L2-type FIs exhibit diverse morphologies, ranging from negative crystal to irregular shapes, which remain relatively consistent within individual assemblages. They range in size from a few microns to *ca.* 30 µm. At room temperature, these FIs are multiphase (liquid + vapour + solids), containing at least one and up to nine solid phases. Halite is systematically present among the solid phases, with sylvite potentially included as well. The liquid phase is dominant, with the volumetric fraction of the vapour phase ($R_V$) typically ranging from 20 to 40 µm (mean ~ 30 %).

***V2-type fluid inclusions:*** Like L2-type FIs, V2-type FIs are exclusively encountered in magmatic quartz from the B1 unit, occurring in diverse assemblage types, including clusters, pseudo-secondary and secondary planes (Fig. III.6b), as well as primary FIs aligned along growth planes (Fig. III.6e). V2 and L2-type FIs occasionally coexist in the same assemblage, particularly when aligned along growth planes, suggesting their contemporaneity (Fig. III.6e). V2-type FIs exhibit regular oval to negative crystal shapes and range in size from *ca.* 1 to 25 µm. At room

temperature, V2-type FIs are two- to multiphase (liquid + vapour ± solids), with the vapour phase being dominant ($R_V$ ~ 70–90 %). One of the solids phase typically present displays elongated shapes resembling mica needles (Fig. III.9). This assumption is supported by Raman spectrometry, which detected the presence of the OH group at a wavelength of *ca.* 3600 $cm^{-1}$ in the mineral structure (Fig. III.9b). Based on the observed peak at low wavelengths, the hydroxyl-bearing mineral likely is likely muscovite or trilithionite (Fig. III.9a). However, obtaining further detailed information on the nature of the white mica is challenging using Raman spectrometry, as the associated low-wavelength signal of phyllosilicates is generally weak (Wang et al., 2015). Additional analysis would be valuable to determine whether the nature of the white mica varies between FIs located in the crystal core and those at the rim. Albite crystals were also identified in two instances.

***L3-L4-type fluid inclusions:*** L3- and L4-type FIs have been previously reported to frequently coexist within the same assemblages and to share similar petrographic features, salinities, and continuous homogenisation temperature ranges (Aïssa et al., 1987). To simplify classification and discussion, these two FI types are addressed collectively in this study.

L3-L4-type FIs have been observed in magmatic quartz from the three main magmatic units of the Beauvoir granite, where they occur as pseudo-secondary to secondary trails (Figs. III.6h, III.7 and III.8). They generally exhibit highly regular to irregular shapes, with sizes ranging from a few microns to approximately 20 µm. While most of these inclusions are biphasic (liquid + vapour), some contain up to three solid phases, often elongated and needle-like in shape, potentially corresponding to muscovite or phengite as identified through Raman spectrometry. The volumetric fraction of the vapour phase ($R_V$) is highly variable, ranging from 20 to 80 %, with either the liquid or the vapour phase being dominant. Notably, liquid-dominant and vapour-dominant FIs appear to occur in separate FIs with distinct orientations within the quartz crystal.

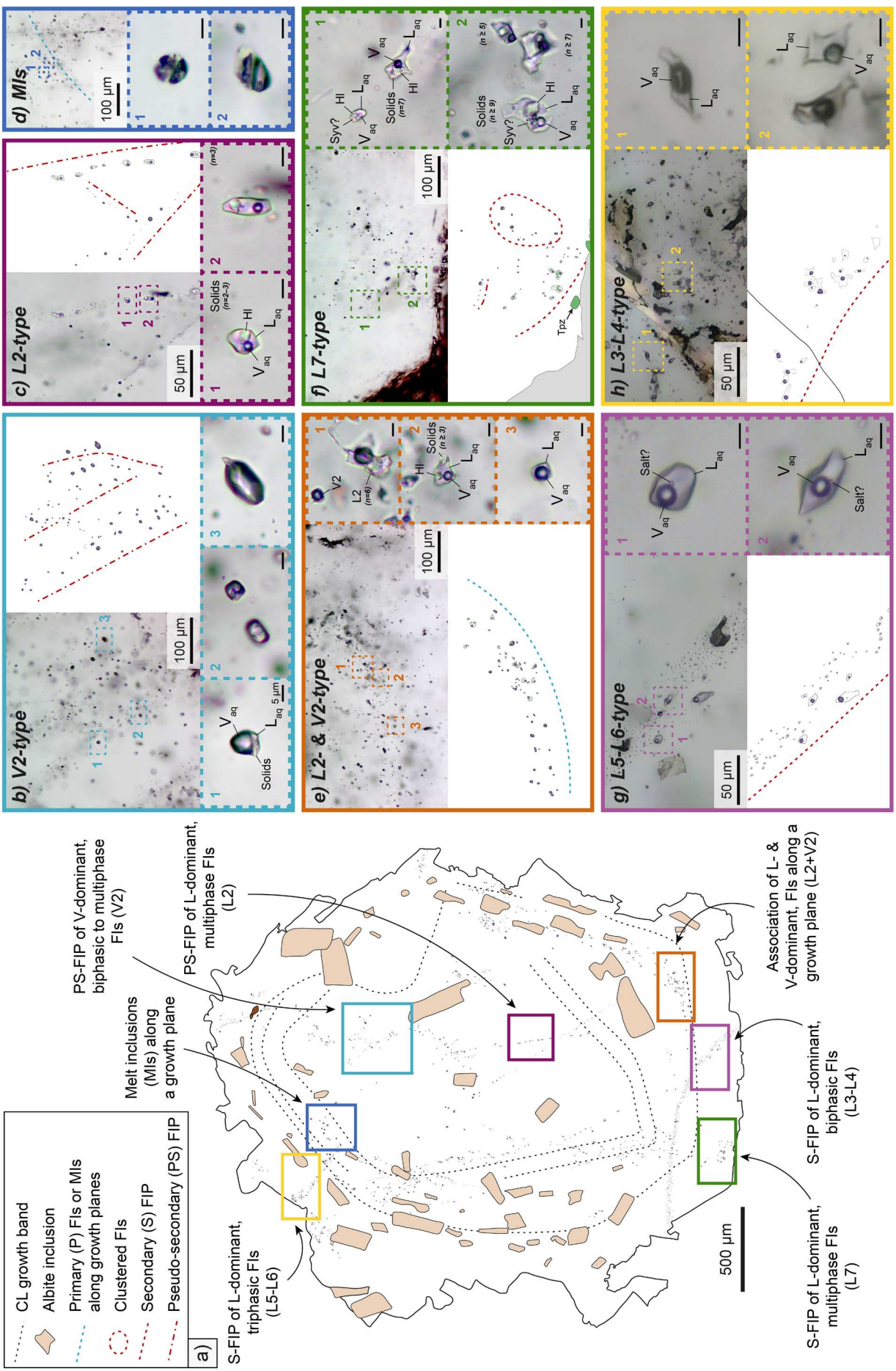



*Figure III.6. Petrography of melt and fluid inclusion assemblages (FIAs) in magmatic quartz from the B1 unit (-379.0 m) of the Beauvoir PRMG. All FIs described in this study (i.e., L2, V2, L3-L4, L5-L6 and L7) were identified. Zooms show representative FIs within each FIA and the associated scale bar represents 5 µm. (a) Schematic representation of FIAs in relation to crystal borders and CL zoning. (b) Pseudo-secondary fluid inclusion plane (FIP) of V2-type FIs, restricted to the crystal core. (c) Pseudo-secondary FIP of L2-type FIs, limited to the crystal core. (d) Melt inclusions (MIs) along a growth plane. (e) Co-occurrence of L2- and V2-type FIs along a growth plane revealed by CL imaging. (f) Secondary FIP of L7-type FIs at the crystal rim. (g) Secondary FIP of L5-L6-type FIs. (h) Secondary FIP of L3-L4-type FIs.*

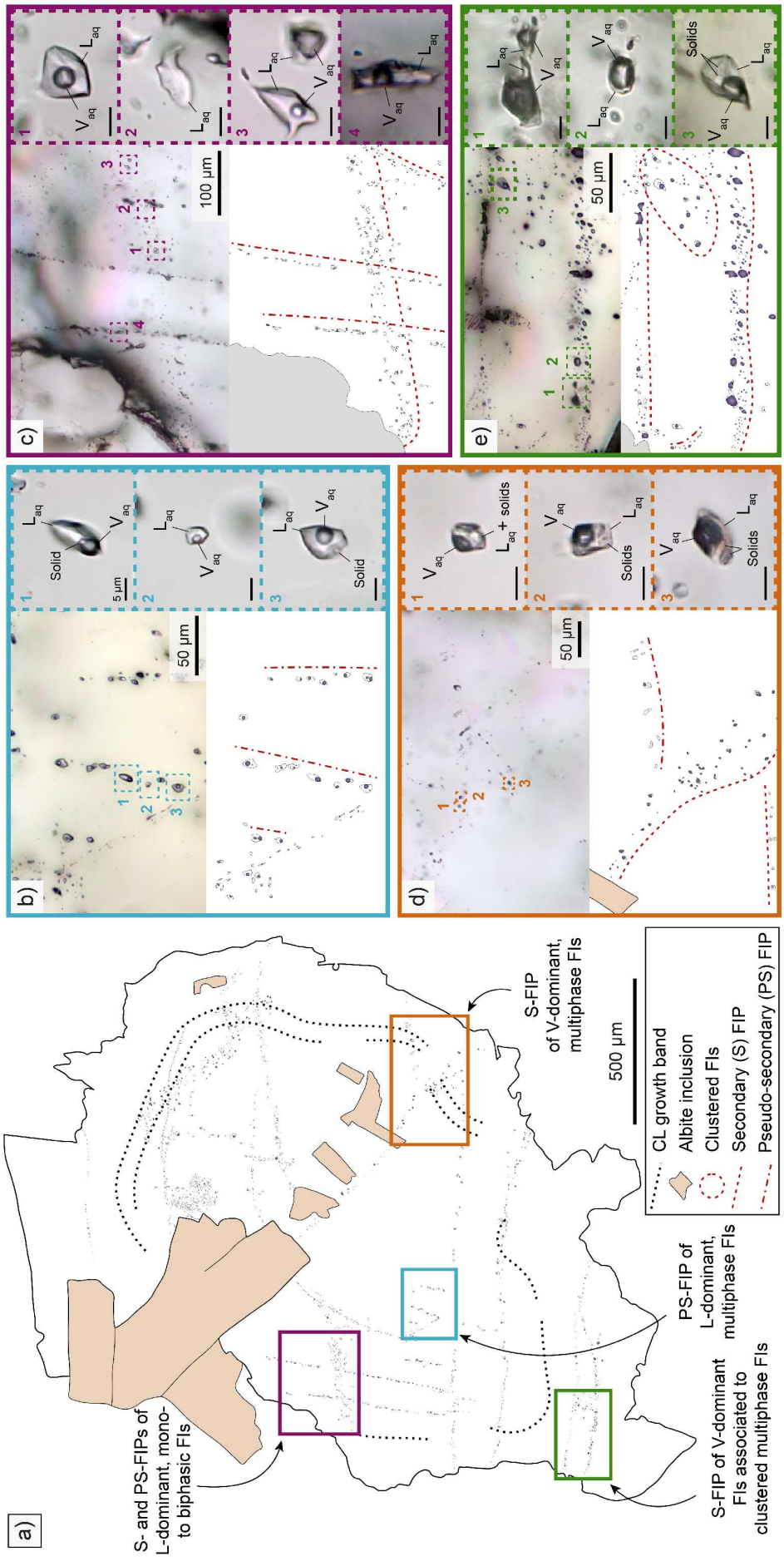



*Figure III.7. Petrography of fluid inclusion assemblages (FIAs) in magmatic quartz from the B2 unit (-546.5 m) of the Beauvoir PRMG. Only L3-L4-type FIs are present in this unit and illustrated in this figure. Zooms show representative FIs within each FIA and the associated scale bar represents 5 µm. (a) Schematic representation of FIAs in relation to crystal borders and cathodoluminescence zoning. (b) Pseudo-secondary fluid inclusion plane (FIP) of liquid-dominant, multiphase ($L_{aq}+V_{aq}+S$) FIs. (c) Secondary and pseudo-secondary FIPs of mono- to biphasic ($L_{aq}\pm V_{aq}$) FIs. (d) Secondary FIP of vapour-dominant, multiphase ($L_{aq}+V_{aq}+S$) FIs. (e) Secondary FIP of vapour-dominant, biphasic ($L_{aq}+V_{aq}$) FIs associated to clustered multiphase ($L_{aq}+V_{aq}+S$) FIs.*

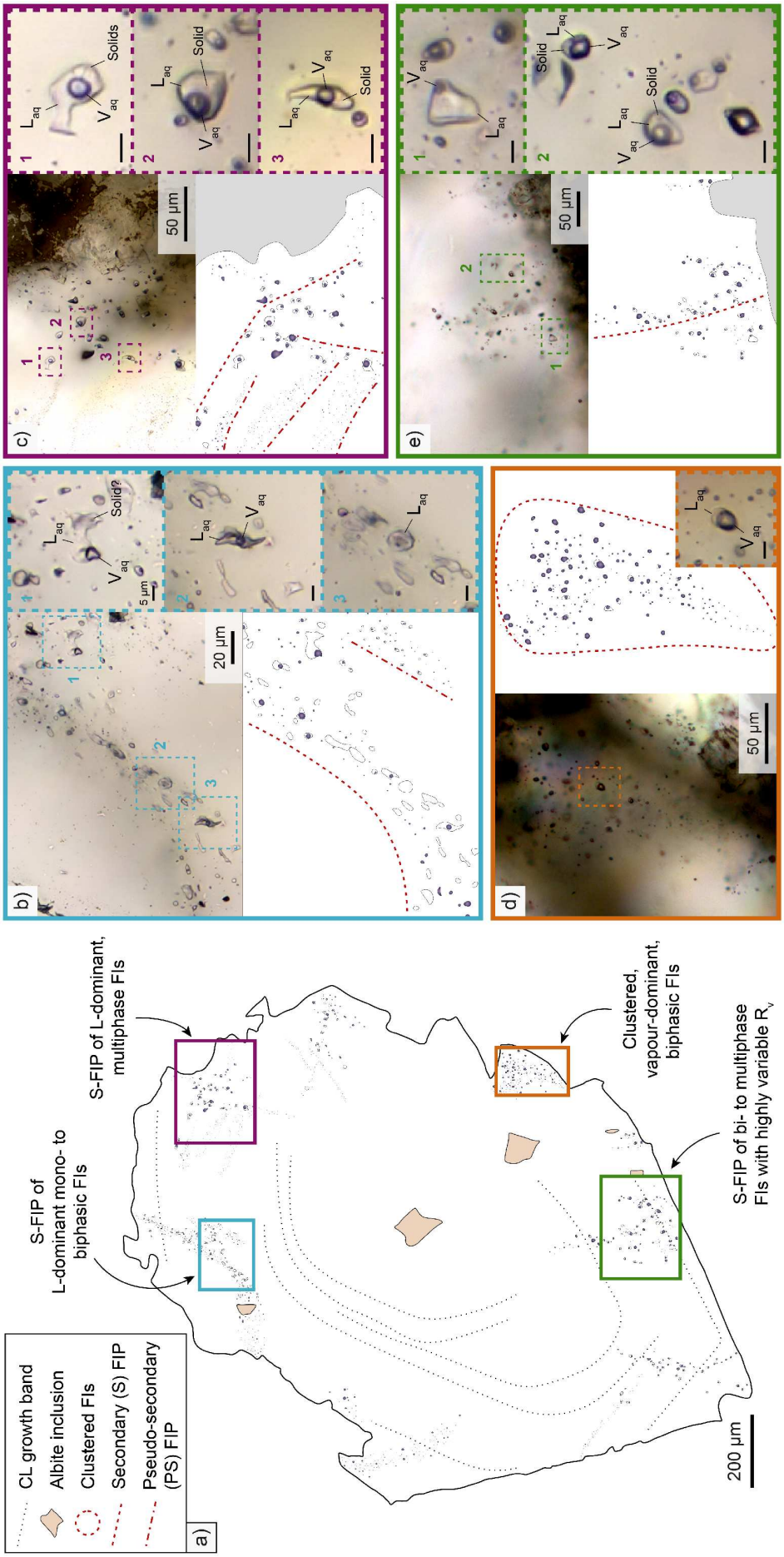



*Figure III.8. Petrography of fluid inclusion assemblages (FIAs) in magmatic quartz from the B3 unit (-824.0 m) of the Beauvoir PRMG. Only L3-L4-type FIs are observed in quartz from this unit. Zooms show representative FIs within each FIA and the associated scale bar represents 5 µm. (a) Schematic representation of FIAs relative to crystal borders and cathodoluminescence zoning. (b) Secondary fluid inclusion plane (FIP) with one-phase liquid ($L_{aq}$) to two-phase liquid ($L_{aq}$) + vapour ($V_{aq+}$) aqueous FIs, exhibiting irregular shapes. (c) Secondary FIP with multiphase ($L_{aq}+V_{aq}+$solid) FIs containing unidentified rounded solids and elongated phyllosilicates. (d) Cluster of vapour-dominant, biphasic ($L_{aq}+V_{aq}$) FIs. (e) Secondary FIP of bi- to multiphase ($L_{aq}+V_{aq}\pm S$) FIs with highly variable volumetric fraction of the vapour phase ($R_v$).*

***L5-L6-type fluid inclusions:*** L5- and L6-type FIs have been previously shown to share similar petrographic features, homogenisation temperatures, and slightly distinct salinities (*ca.* 12–19 and 20–26 wt% NaCl eq, respectively) (Aïssa et al., 1987). Based on these similarities and their coexistence within the same assemblages – although seemingly infrequent – these two FI types are discussed together in this study.

Unlike L3-L4-type FIs, but similar to L2- and V2-type FIs, L5-L6-type FIs are exclusively observed in magmatic quartz from the B1 unit of the Beauvoir granite (Fig. III.6g). Within this unit, they occur as pseudo-secondary to secondary trails. These FIs are characterised by regular to slightly irregular shapes, with sizes reaching up to approximately 16 µm. L5-L6-type FIs are predominantly triphasic (liquid + vapour + solid), with the liquid phase being dominant (Rv ~ 20–50 %, mean ~ 40 %). They typically contain a single solid phase that could not be conclusively identified via Raman spectrometry. The lack of a detectable Raman signal is consistent with the properties of halite or sylvite, both of which are plausible candidates for this solid phase.

***L7-type fluid inclusions:*** L7-type FIs are also exclusive to magmatic quartz from the B1 unit of the Beauvoir granite. These FIs are present in pseudo-secondary to secondary trails, as well as in clusters that may represent primary assemblages (Fig. III.6f). These FIs exhibit a range of morphologies, from regular to irregular shapes, with sizes reaching up to 30 µm. L7-type FIs are multiphase, with the liquid phase being dominant ($R_V$ ~ 20–35 %). They contain between two and nine solid phases, among which halite is consistently identified as a cubic solid, frequently accompanied by sylvite and metallic sulphides.

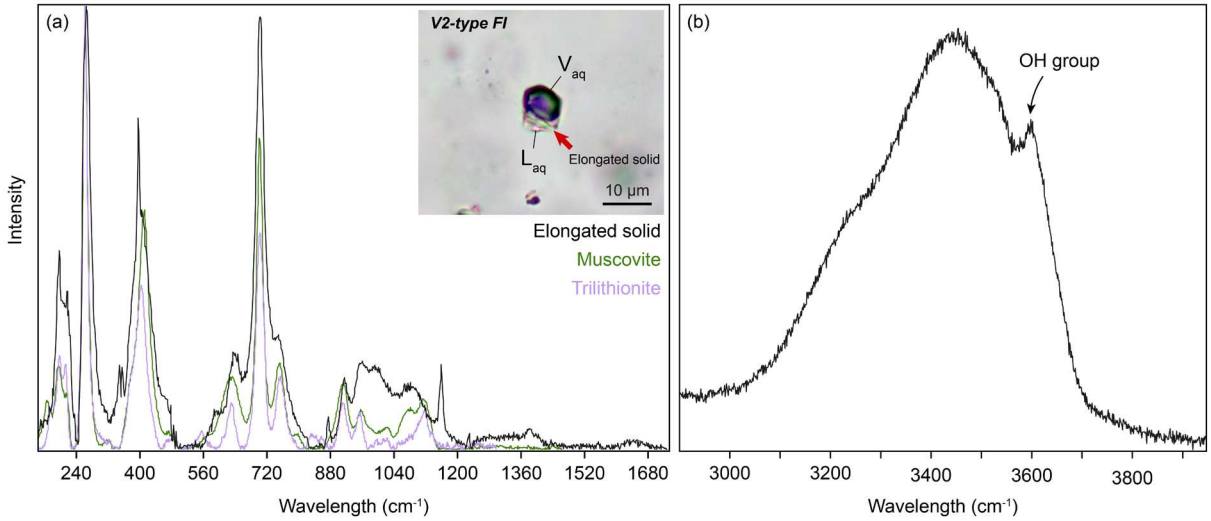



*Figure III.9. Raman spectrometry identification of elongated, needle-shaped solids present in V2-type fluid inclusions hosted in magmatic quartz from the B1 unit of the Beauvoir PRMG: (a) Low-wavelength spectrum compared to reference spectra of muscovite and trilithionite (Crystal Sleuth database). (b) High-wavelength spectrum highlighting the presence of OH groups in the mineral structure.*

### 2.3. Preliminary discussion and conclusions: snowball-textured quartz as a marker of extensive devolatilisation in the Beauvoir PRMG

If magmatic quartz and associated fluid inclusions from the B2 and B3 units of the Beauvoir granite appear similar, the most evolved B1 unit exhibit distinctive features, most notably the presence of snowball textures (Fig. III.2). Such textures are characteristic of rare-metal granites with strongly peraluminous composition (e.g., Schwartz, 1992). They have been documented in several peraluminous granite systems, including the Podlesí granite (Czech Republic; Müller and Seltmann, 1999), the Argemela stock (Portugal; Breiter et al., 2022), the Yichun rare-metal deposit (China; Wu et al., 2018), and were also previously identified in the Beauvoir PRMG (Johan et al., 1988).

The origin of snowball-textured quartz has been widely discussed, with metasomatic (e.g., Beus et al., 1962; Sonyushkin et al., 1991), magmatic (e.g., Kovalenko, 1977; Yin et al., 1995; Poutiainen and Scherbakova, 1998) and magmatic-hydrothermal (e.g., Müller and Seltmann, 1999; Müller et al., 2002a) processes proposed. A magmatic origin has been supported by the absence of replacement textures and the presence of melt inclusions in snowball quartz crystals (e.g., Kovalenko, 1977; Yin et al., 1995; Poutiainen and Scherbakova, 1998; Zhu et al., 2001). Some authors suggested that snowball quartz crystallises during the early stage of magma evolution from a volatile-undersaturated melt, capturing coexisting albite crystals during growth (Poutiainen and Scherbakova, 1998). However, a purely magmatic origin is unlikely, as significant evidence points to the involvement of magmatic fluids during the late stages of crystallisation, notably the co-existence of low- and high-salinity fluid and melt inclusions (e.g., Müller and Seltmann, 1999; Müller et al., 2000, 2002a, 2009; Breiter et al., 2005; Wang D. et al., 2019). In the most differentiated units, the late stage of magma evolution is characterised by a highly evolved, fluid-saturated, residual melt, in which early quartz phenocrysts resorb as a result of the exsolution of highly reactive magmatic fluids and late-magmatic snowball quartz is presumed to crystallise from a highly fluxed residual melt at temperatures below 600 °C. Magma devolatilisation appears therefore to be key to creating the disequilibrium conditions, volatile enrichment, nearly non-convecting crystal-mush, and rapid crystallisation rates typically associated with snowball quartz textures. This assumption is notably supported by the coexistence of fluid and melt inclusions in quartz crystals (e.g., Wang D. et al., 2019).

In the Beauvoir PRMG, the exsolution of magmatic fluids during snowball quartz growth in the B1 unit is evidenced by the trapping of L2- and V2-type primary fluid inclusions along growth planes (Fig. III.6e). These fluid inclusions are absent from the less evolved B2 and B3 units (Figs. III.7 and III.8), where snowball quartz is also not encountered (Figs. III.3 and III.4). Petrographic and microthermometric characterisation has identified these fluids as magmatic in origin (Aïssa et al., 1987; Cuney et al., 1992). In this study, melt inclusions were observed on a

single occasion within the same growth plane as a L2-V2 assemblage (Fig. 6d). Their presence in the B1 and B2 units has also been reported in earlier work (Kovalenko et al., 1998). Melt inclusions in the B1 unit were described as coexisting with multiphase FIs, containing at least one salt crystal and homogenising at temperatures of *ca.* 290–335 °C (Kovalenko et al., 1998), consistent with the characteristics of L7-type magmatic FIs (Aïssa et al., 1987). Snowball-textured quartz in the B1 unit seems therefore to have recorded extreme crystallisation conditions involving a volatile-rich residual melt, consistent with the magmatic-hydrothermal model proposed by several authors (e.g., Müller and Seltmann, 1999; Müller et al., 2000, 2002a, 2009; Breiter et al., 2005; Wang D. et al., 2019) (Fig. III.10).

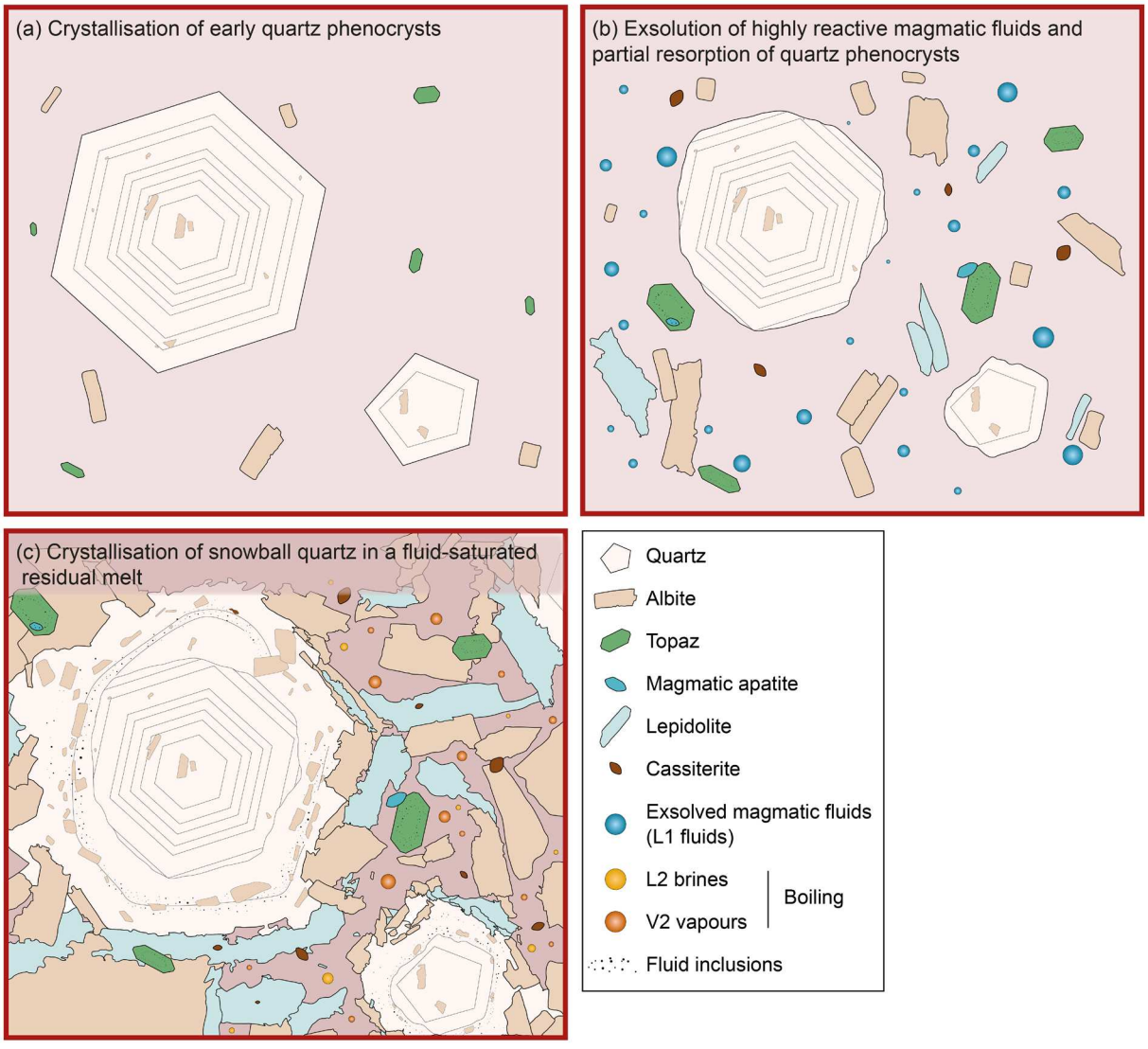



*Figure III.10. Conceptual model of the formation of snowball quartz in the B1 unit of the Beauvoir PRMG. (a) Crystallisation of early quartz phenocrysts preserved in the less evolved B2 and B3 units. (b) Exsolution of highly reactive magmatic fluids causing the partial resorption of quartz phenocrysts in the B1 unit. (c) Crystallisation of snowball-textured quartz from a fluid-saturated residual melt.*

This volatile-rich crystallisation environment may account for the abrupt compositional variation observed in Li-Fe-micas associated with the crystallisation of Li-enriched overgrowth

around magmatic lepidolite, which has been predominantly documented in the B1 unit (Monier et al., 1987). The magmatic-hydrothermal transition in the Beauvoir PRMG thereby appears to have played a critical role not only in the potential resorption of early quartz phenocrysts and the crystallisation of snowball-textured quartz, but also in influencing the crystallisation of other magmatic, metal-bearing minerals. This transition is widely recognised as a key process in the formation of rare-metal deposits (e.g., Thomas et al., 2011; Badanina et al., 2015; Ballouard et al., 2016, 2020a; Araujo et al., 2023; Pfister et al., 2023; Putzolu et al., 2024), yet its impacts remain insufficiently understood. To refine our understanding of involved mechanisms, we propose to further characterise magmatic quartz and its trapped FIs in the Beauvoir PRMG.

## 3. Fluid inclusions as archives of fluid dynamics and metal mobility

In magmatic-hydrothermal systems, fluid inclusions constitute precious archives of fluid circulation, from the exsolution of magmatic fluids at high temperatures to lower temperature metasomatic processes (e.g., Legros et al., 2019; Audétat et al., 2000b). Magmatic quartz from the Beauvoir PRMG hosts a wide variety of fluid inclusions (Aïssa et al., 1987; Harlaux et al., 2017; this study). The diversity of fluid inclusion types, along with their salinity and elemental compositions, suggests complex interactions between exsolved magmatic fluids and external fluids, likely affecting hydrothermal rare-metal mobility. Further tracing the physico-chemical evolution of fluids in the Beauvoir magmatic-hydrothermal system is key to reconstruct fluid dynamics, their interplay with the melts, as well as the mechanisms governing metal transport and deposition from supra- to sub-solidus stages. This section presents a detailed investigation of fluid inclusions hosted in magmatic quartz from the Beauvoir PRMG through microthermometry, Raman spectrometry and LA-ICP-MS analyses.

### 3.1. Material and methods

The fluid inclusions (FIs) analysed in this section were previously described in section 2.2.2 (Part III) as part of the petrographic study, along with magmatic quartz in which they are hosted.

#### *3.1.1. Microthermometry*

Microthermometric analyses of selected fluid inclusion assemblages (FIAs) were conducted on a Linkam THMS600 heating-cooling stage both at GeoRessources (Nancy, France) and at ETH Zürich (ETHZ, Switzerland). This system is connected to an Olympus BX51 microscope at GeoRessources and a Leitz optical microscope at ETHZ. It permits measurements in a temperature range from -196 °C to 600 °C and is equipped with a cooling circuit for measurements above 200 °C. Calibration was performed during each analytical session. In both laboratories, the thermocouple was calibrated at low temperature (i.e., $T < 0$ °C) against the triple point of $CO_2$ (-56.6 °C) using natural and synthetic $H_2O$-$CO_2$ fluid inclusions, and of pure water (0.0 °C) using

$H_2O$ synthetic capillaries. High-temperature calibration was notably based on the homogenisation temperature of a natural aqueous fluid inclusion (165.9 °C) at GeoRessources, and the critical point of pure water (374.1 °C) at ETHZ. Measurement accuracy varies from ± 0.1 °C at low temperatures to better than ± 2 °C at high temperatures.

The following phase transition temperatures were measured: the eutectic temperature ($T_e$) indicating the first visible melting of the solidified aqueous phase during heating; the ice-melting temperature ($T_m$ice) corresponding to the final melting of the solidified aqueous phase; the final dissolution temperatures of hydrohalite ($T_d$Hh), halite ($T_d$Hl) and sylvite ($T_d$Syv); and the total homogenisation temperature ($T_H$) which occurs either to the liquid (L) or vapour phase (V). The commonly used term "eutectic temperature" ($T_e$) is retained here; however, for rigorous accuracy, it should more appropriately be referred to as the "temperature of first visible melting," as observing the precise initiation of melting is often challenging at such small scales.

Fluid inclusions were initially investigated at high temperature to prioritise low-temperature analysis on well-preserved fluid inclusions. Due to the sensitivity of host quartz grains to temperature increases, a progressive step-heating procedure was implemented to minimise fracturing and subsequent decrepitation of fluid inclusions. The heating rates were adjusted based on the temperature range as follows: 20 °C/min from room temperature to 400 °C, 10 °C/min from 400 °C to 500 °C, and 5°C/min for temperatures exceeding 500 °C. Precise measurements of phase transition temperatures ($T_d$Syv, $T_d$Hl, $T_H$) were obtained using a heating rate of 1 °C/min when the temperature was around the phase transition points. Analyses at temperatures exceeding 500 °C were limited due to the high decrepitation ratio.

Petrographic features of fluid inclusions after microthermometric analysis at high temperature were compared with their initial characteristics to assess any leakage or changes in the shape and volume of the vapour phase. Subsequently, selected fluid inclusions were analysed during cooling/freezing experiments. Fluid inclusions were firstly overcooled to approximately -150 °C to completely freeze the liquid and vapour phases. The temperatures of phase transitions ($T_e$, $T_m$ice, and $T_d$Hh) were then measured during progressive reheating at a rate of 0.5°C/min.

#### *3.1.2. Raman spectrometry*

Raman spectrometry was employed to analyse fluid inclusions, specifically to determine the salinity of the aqueous phase, identify solid phases (as detailed in section 2 of Part III), and assess the trace gas content in the vapour phase. Raman spectra were acquired at room temperature using a Horiba Jobin-Yvon LabRAM 300 spectrometer equipped with a 1,800 gr $mm^{-1}$ grating and an Olympus BX40 microscope, located at GeoRessources laboratory. Excitation was provided by a laser Cobolt Fandango DPL operating at 514.75 nm with an output power of 300 mW. The laser beam diameter at sample surface was approximately 1 µm. The signal-to-noise ratio (N/S) was optimised by adjusting the acquisition time and accumulation number. For example, a total

of 10 acquisitions of 15 seconds each were typically accumulated during the analysis of the vapour phase composition to yield satisfactory spectra (i.e., N/S <<1). The trace gas content of the vapour phase was determined using an in-house calibration based on gas mixtures of known composition. Results are expressed in mol% relative to the volatile phase, with an estimated uncertainty of a few mol%, although the precise uncertainty of the final results remains undetermined at this stage. Salinity of the aqueous phase present in fluid inclusions was estimated following the method described by Caumon et al. (2013) and is reported in wt.% NaCl eq, with a median measurement uncertainty of ± 0.7 wt.% NaCl eq (2s).

### *3.1.3. Laser ablation – inductively coupled plasma – mass spectrometry*

#### *3.1.3.i. Acquisition procedure*

After conducting petrographic characterisation of the FIAs, determining phase transition temperatures, and identifying some of the trapped solids, the chemical composition of individual fluid inclusions was analysed by LA-ICP-MS at ETH Zürich. FI microanalyses were performed using a GeoLas (Coherent) laser ablation system (193 nm ArF excimer laser) coupled to a quadrupole ICP-MS (Perkin Elmer Nexion 2000 DRC) (Günther et al., 1997, 1998; Heinrich et al., 2003). The laser energy density was set to 15–30 J.cm$^{-2}$, with a constant repetition rate of 10 Hz. To minimise mechanical stress on the mineral surface and reduce the risk of explosive opening of FIs, as well as to ensure representative sampling of the bulk composition of the heterogeneous FIs, an iris aperture was progressively and manually opened during analysis from *ca.* 3–5 µm up to a maximum of 40 µm, depending on the size of the FI (Günther et al., 1998; Guillong and Heinrich, 2007). The entire content of the FI, including daughter crystals, liquid and vapour phases, was removed from the cell as an aerosol by a constant He flux (1 L.min$^{-1}$), then mixed with make-up gas (Ar, *ca.* 1 L.min$^{-1}$), and homogenised by flushing through a squid device before introduction into the plasma torch. Prior to each analytical session, the LA-ICP-MS system was optimised using NIST SRM 610 glass to ensure maximum sensitivity while maintaining a Th/U ratio close to 1.0 and a ThO/Th ratio below 0.5 %. Two external reference materials – NIST SRM 610 glass (Jochum et al., 2011) and a natural scapolite (Sca17; Seo et al., 2011) – were analysed twice at both the beginning and end of each set of twelve FIs. The isotopes measured during analysis included $^{7}$Li, $^{9}$Be, $^{23}$Na, $^{24}$Mg, $^{29}$Si, $^{39}$K, $^{43}$Ca, $^{55}$Mn, $^{57}$Fe, $^{63}$Cu, $^{66}$Zn, $^{121}$Sb, $^{140}$Ce, and $^{238}$U with a dwell time of 2 ms; $^{31}$P, $^{79}$Br, $^{85}$Rb, $^{88}$Sr, and $^{208}$Pb with a dwell time of 5 ms; and $^{35}$Cl, $^{75}$As, $^{93}$Nb, $^{118}$Sn, $^{133}$Cs, $^{181}$Ta, and $^{182}$W with a dwell time of 10 ms.

#### *3.1.3.ii. Data reduction*

The raw data were processed using SILLS (Signal Integration for Laboratory Laser Systems) software package, developed in MATLAB® and specifically designed for reducing data and calculating concentrations of transient LA-ICP-MS signals (Guillong et al., 2008). Due to the variability in the major cations detected across different fluid inclusion types, a uniform data processing proved unsuitable. Consequently, two distinct approaches were employed depending

on whether potassium was detected or not: (i) for FIs associated with a significant K signal, the $H_2O$-NaCl-KCl ternary system was used to provide a more accurate salinity estimate reflecting the fluid's actual composition; (ii) for FIs without detectable K (i.e., typically low-salinity FIs), salinity was estimated in the $H_2O$-NaCl binary system.

For the entire dataset, the mass-balance approach implemented in SILLS was dismissed due to significant uncertainties associated with empirical mass-balance equations, particularly the difficulty in accurately estimating the weighting factor (Allan et al., 2005). Furthermore, the charge-balance approach was also disregarded, as not all major cations were detected in each analysis. Instead, an internal standardisation based on the sodium concentration (ppm) in fluid inclusions proved to be the most robust method for generating a consistent final dataset. Given the significant lithium concentrations in magmatic quartz from the Beauvoir granite (40–160 ppm; Monnier et al., 2018), the matrix contribution was systematically subtracted from the Li signal to isolate the fluid inclusion content during final data processing. The two approaches detailed below differ only in the methodology used to estimate salinity, employing either the ternary $H_2O$-NaCl-KCl system or the binary $H_2O$-NaCl system (Fig. III.11).

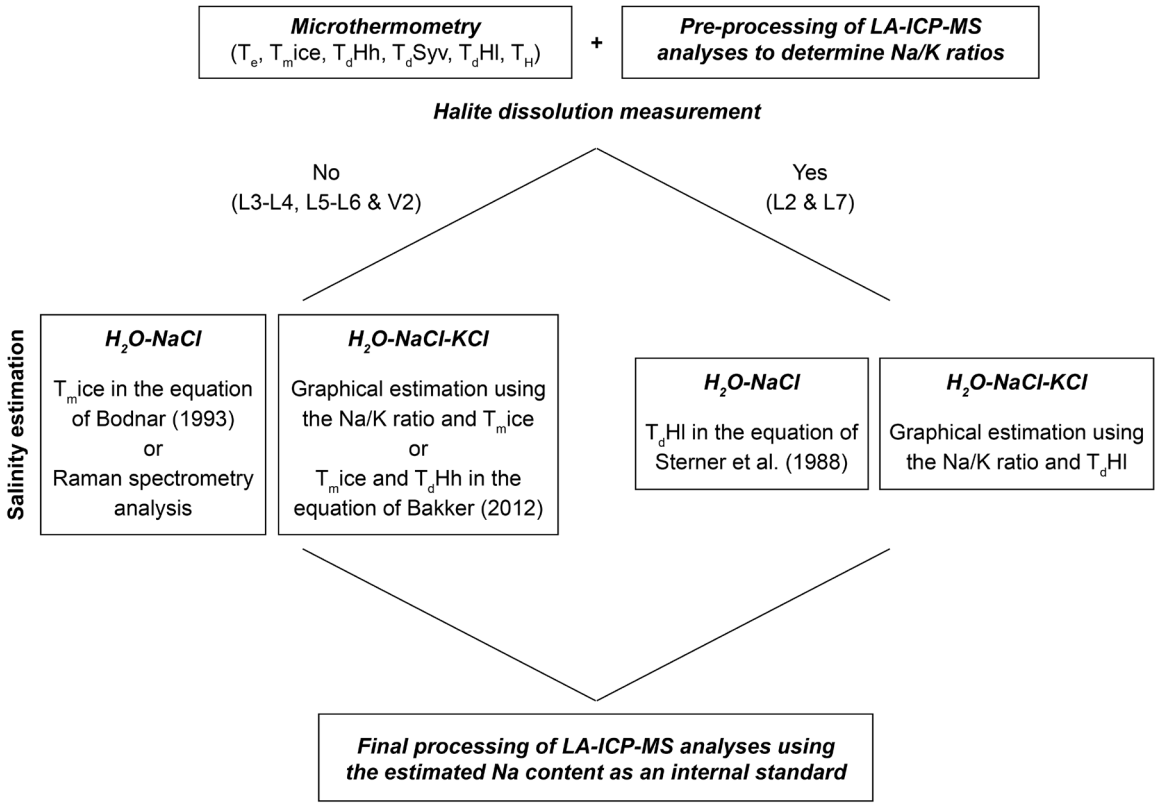



*Figure III.11. Synthetic description of approaches used to process fluid inclusion LA-ICP-MS spectra and estimate salinity in the binary $H_2O$-NaCl system and ternary $H_2O$-NaCl-KCl system.*

(i) The first approach was applied to L2, and L7-type fluid inclusions, as K was detected in over 90 % of cases. In L7-type FIs, sylvite was almost always present as a daughter mineral alongside halite, while in L2-type FIs, sylvite was also present, though to a lesser extent.

However, the dissolution of sylvite was observed in only a few cases during microthermometric analysis, preventing the direct use of equations, which requires both halite and sylvite dissolution temperatures to determine salinity (Sterner et al., 1992; Bakker, 2012). To address this limitation, an initial processing of the LA-ICP-MS data was performed using SILLS to extract Na/K ratios from each signal. $NaCl_{eq}$ and $KCl_{eq}$ contents were then estimated in the $H_2O$-NaCl-KCl ternary diagram using both the Na/K ratio obtained from LA-ICP-MS data and halite dissolution temperature measured by microthermometry (Bodnar et al., 1989; Bodnar, 2003). The Na concentration associated with each FI was determined by converting the $NaCl_{eq}$ salinity obtained from the ternary diagram into Na values as follows:

$$Na\ (ppm) = NaCl\ (wt\%) \times \frac{22.99}{58.44} \times 10^5$$

Subsequently, a second and final step of data processing was carried out in SILLS to determine absolute concentrations for each analysed element. For all elements except halogens, LA-ICP-MS raw data were reduced using NIST SRM 610 glass (Jochum et al., 2011) as the primary external reference material, and natural scapolite Sca17 (Seo et al., 2011) as a secondary control material, with the Na content of the fluid inclusion serving as the internal standard. For halogens, the raw data were reduced using natural scapolite Sca17 as the primary external reference, and NIST SRM 610 glass as a secondary control material, with the Na content of the fluid inclusion also serving as the internal standard. Trace elements concentrations determined for Sca17 (Si, K, Ca, Mn, Fe and Rb) deviated by less than 10 % from reported values, except for Li, which differed by approximately 21 % from the reference value (Seo et al., 2011; Table III.A4 in Appendix III.A3). Halogens concentrations obtained for NIST SRM 610 glass (Br and Cl) deviated by *ca.* 10 % for Br and by more than 200 % for Cl compared to reported values (Jochum et al., 2011; Table III.A5 in Appendix III.A3).

(ii) The second approach was applied to L3, L4, L5 and L6-type fluid inclusions. Potassium was not detected in approximately 40 % of the analyses for L5 and L6-type FIs, and around 80 % of the analyses for L3 and L4-type FIs. When K was detected, the first approach was employed: initial processing in SILLS to extract Na/K ratios, followed by salinity estimation in the $H_2O$-NaCl-KCl ternary system using the Na/K ratio and the ice melting temperature (as these FIs did not contain halite as a daughter mineral), and a subsequent step involving reprocessing the data in SILLS using the Na concentration as an internal standard.

In cases where K was not detected, the binary $H_2O$-NaCl system was considered, and salinity was directly estimated from the ice melting temperature (Bodnar, 1993). The resulting $NaCl_{eq}$ salinity was then converted to Na concentration, which was used as an internal standard during signal processing in SILLS. To quantify the variation in absolute concentrations between the $H_2O$-NaCl and $H_2O$-NaCl-KCl systems, all signals with significant potassium

concentrations were processed in both systems. In all figures, the symbology distinguishes between data processed using the $H_2O$-NaCl binary system from the $H_2O$-NaCl-KCl ternary system.

*3.1.3.iii. Data cleaning and exclusion criteria*

To ensure a clean and reliable dataset, only spectra of sufficient quality were retained. Ablation quality was assessed through real-time qualitative observations of video images from the ablation cell and signal from the mass spectrometer. The reliability of LA-ICP-MS analyses was further evaluated during data reduction. Spectra associated with the explosive opening of fluid inclusions were excluded from elemental quantification, as such events likely result in biased sampling of FI content by the mass spectrometer. Following quantification, outliers in element-to-salinity ratios were identified within each FI type using the interquartile range (IQR), with values exceeding 1.5 times the IQR above Q3 or below Q1 flagged for further scrutiny. Each associated spectrum was individually examined, which could lead to its exclusion, retention, adjustments to the selected signal for the fluid inclusion, or the removal of isolated spikes in SILLS, typically linked to minor explosive ablation. Exclusion of spectra associated with outliers was rare and applied only when signals were too weak, when elemental signals attributed to the fluid inclusion showed poor correlation, or when multiple FIs were ablated simultaneously, making it difficult to isolate the target FI.

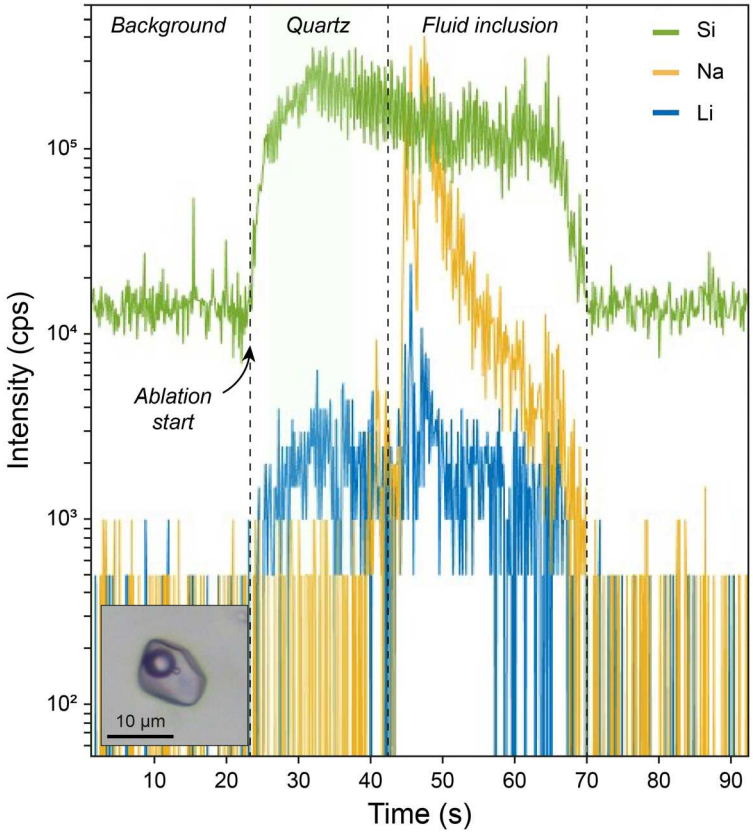



*Figure III.12. Example of Li and Na spectra obtained by LA-ICP-MS for a L5-L6-type fluid inclusion hosted in magmatic quartz from the B1 unit of the Beauvoir PRMG.*

Furthermore, because correcting the Li signal for contributions from the matrix is a complex process, this correction was applied only to fluid inclusions for which the Li signal distinctly stood out from the quartz background (Fig. III.12).

### 3.2. Results

#### *3.2.1. Microthermometry*

***L2-type fluid inclusions:*** Together with L7-type FIs, L2-type fluid inclusions exhibit the lowest eutectic temperatures in the Beauvoir granite, typically ranging from -75 to -49 °C (mean ~ -63 ± 5 °C), with one recorded value of -36 °C significantly higher than -50 °C (Fig. III.13a). The ice melting temperatures are relatively low, varying between -42.7 and -20.8 °C (mean ~ -28.7 ± 0.1 °C). Metastable hydrohalite dissolution was observed in approximately 40 % of the analysed FIs, with $T_dHh$ ranging from *ca.* 5 to 16 °C (mean ~ 12 ± 1 °C). L2-type FIs homogenise into the liquid phase, and $T_H$ predominantly range from 308 to over 500 °C (Fig. III.13b). Due to high decrepitation rates, fluid inclusions that homogenised above 500 °C were not analysed. Reported homogenisation temperatures rarely correspond to complete homogenisation of the fluid inclusions, as some solid phases persist. For more than 80 % of the high-temperature analyses (n = 29/35), the disappearance of the vapour phase followed halite dissolution, which occurred over a temperature range from approximately 217 to 502 °C (mean ~ 268 ± 1 °C) (Fig. III.14). Finally, sylvite dissolution temperatures were measured at two instances, at temperatures of 58 and 88 ± 2 °C, respectively.

***V2-type fluid inclusions:*** Due to the high volumetric fraction of the vapour phase characterising V2-type FIs, the liquid phase is poorly visible, and microthermometric measurements were challenging. Only twelve fluid inclusions were analysed, exhibiting low eutectic temperatures ranging from -69 to -29 °C (mean ~ -49 ± 5 °C), slightly higher than those observed in L2-type fluid inclusions (Fig. III.13c). The ice melting temperature is relatively low, varying between -23 and -6 °C (mean ~ -16 ± 1 °C). Finally, homogenisation occurs in the vapour phase at high temperatures ranging from *ca.* 500 °C to over 540 °C (Fig. III.13d). Analyses were not conducted beyond these temperatures to preserve fluid inclusions from decrepitation.

***L3-L4-type fluid inclusions:*** L3-L4-type fluid inclusions are characterised by eutectic temperatures ranging from approximately -63 to -12 °C (mean ~ -45 ± 5 °C), relatively high ice melting temperatures between -3.8 and -0.2 °C (mean ~ -1.4 ± 0.1 °C), and homogenisation predominantly into the liquid phase over a temperature range of *ca.* 137 °C to >350 °C (Figs. III.13e, f). A single analysed FI showed homogenisation in the vapour phase at a temperature exceeding 320 °C. As described in section 2.2.2 of Part III, L3-L4-type FIs exhibit highly variable vapour-phase volumetric fraction ($R_V$ ~ 20–80 %). To facilitate microthermometric analyses, only FIs with vapour fractions below 60 % were selected, likely explaining the consistent observation of homogenisation via vapour-phase disappearance, in

contrast to the liquid or vapour homogenisation reported by Aïssa et al. (1987). Our data suggest a potential trend, with eutectic temperatures progressively decreasing from the B1 to B2 and B3 units, whereas homogenisation temperatures tend to increase. Variations in ice melting temperatures are less clear, though they may show a slight decrease from the B1 to B2 and B3 units. Additional data are needed to confirm or not these observations.

***L5-L6-type fluid inclusions:*** L5-L6-type fluid inclusions share similarities with L3-L4-type FIs, exhibiting relatively low eutectic temperatures, ranging from -63 to -27 °C (mean ~ -43 ± 5 °C), and homogenisation temperatures to the liquid phase between 172 and 331 °C (mean ~ 253 ± 1 °C; Figs. III.13g, h). However, the disappearance of the vapour phase did not signify complete homogenisation of the fluid inclusions, as a solid phase remained present. This solid was identified as a potential salt crystal, which dissolution temperature was not recorded. L5-L6-type FIs are further characterised by lower ice melting temperatures ($T_m$ice), ranging from *ca.* -17.6 to -6.7 °C (mean ~ -13.4 ± 0.1 °C), reflecting higher salinities compared to L3-L4-type FIs (Fig. III.13g). Hydrohalite dissolution was observed in 30 % of analysed FIs (n = 9/31), with an average dissolution temperature of -22.2 ± 0.1 °C.

***L7-type fluid inclusions:*** L7-type fluid inclusions are characterised by particularly low eutectic and ice melting temperatures, ranging from -72 to -46 °C (mean ~ -59 ± 5 °C) and from -34.9 to -24.3 °C (mean ~ -26.4 ± 0.1 °C), respectively (Fig. III.13i). Metastable hydrohalite dissolution was observed in more than 50 % of analysed fluid inclusions (n = 11/20) at temperatures varying between *ca.* 10 and 20 °C (mean ~ 14 ± 1 °C). The aqueous content of L7-type FIs homogenises via vapour-phase disappearance over a wide temperature range, from *ca.* 108 to 354 °C (mean ~ 262 ± 1°C; Fig. III.13j). However, in contrast to L2-type FIs, this transition rarely corresponds to complete homogenisation of the fluid inclusion, as several solid phases, including halite, persist and dissolve at higher temperatures (Fig. III.14). Halite dissolution was consistently observed between 153 °C and over 360 °C, while sylvite dissolution was noted in only four FIs, at temperatures ranging from *ca.* 60 to 80 °C. Due to high decrepitation rates, inclusions homogenising above 360 °C were not analysed, resulting in a dataset that might predominantly reflect the lower-salinity range of L7-type fluid inclusions (Sterner et al., 1988) (section 3.2.3).

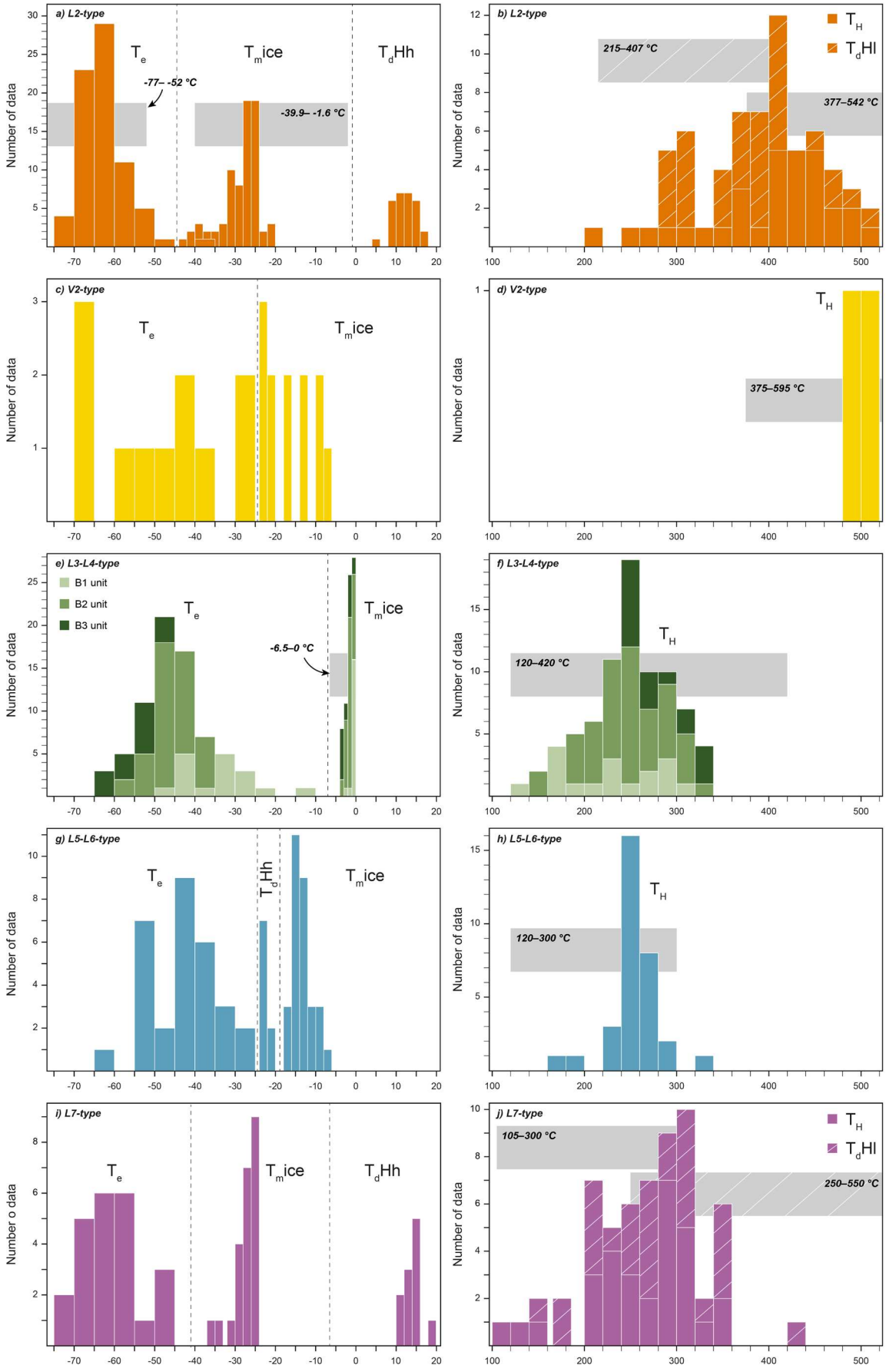



*Figure III.13. Transition phase temperatures ($T_e$, $T_m$ice, $T_d$Hh, $T_d$Hl and $T_H$) of fluid inclusions in magmatic quartz from the Beauvoir PRMG, determined through microthermometry: (a-b) L2-type, (c-d) V2-type, (e-f) L3-L4-type, (g-h) L5-L6-type, and (i-j) L7-type. Shaded ranges in the background represent data from Aïssa et al. (1987) and Harlaux et al. (2017).*

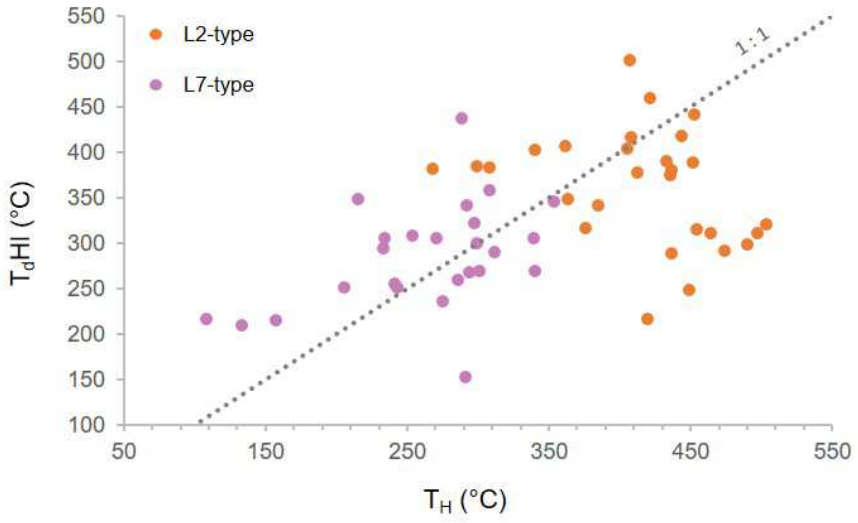



*Figure III.14. Halite dissolution temperature ($T_dHl$) versus homogenisation temperature ($T_H$) for L2- and L7-type fluid inclusions in the Beauvoir PRMG. In L2-type FIs, homogenisation predominantly occurred after halite dissolution, whereas in L7-type FIs, halite dissolution more commonly took place after the disappearance of the vapour phase.*

### *3.2.2. Trace gas content relative to the vapour phase*

Fluid inclusions encountered in the Beauvoir PRMG are predominantly aqueous, though some volatiles may be present as trace components in the low-density vapour phase. The trace gas content in the vapour phase has been determined for L2-, V2- and L7-type FIs in magmatic quartz from the B1 unit (Fig. III.15; Table III.2).

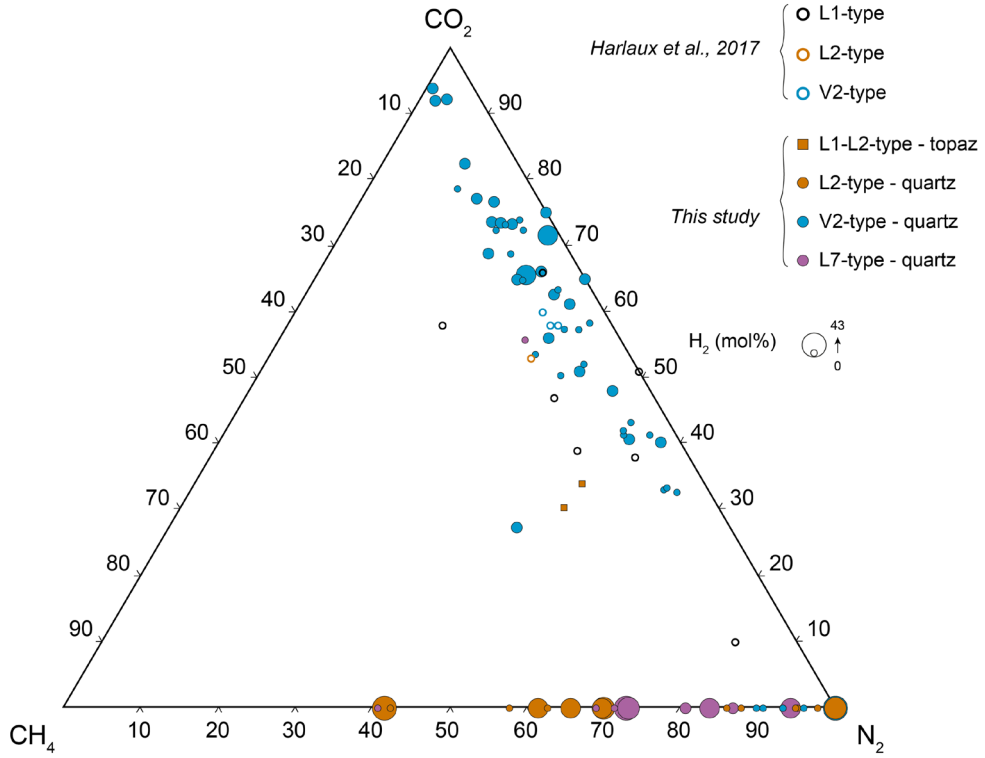



*Figure III.15. $CO_2$-$CH_4$-$N_2$ ternary diagram illustrating the trace gas content of fluid inclusions in the Beauvoir PRMG, with $H_2$ content represented by feature size, as determined by Raman spectrometry. Data from Harlaux et al. (2017) on similar fluid inclusions in magmatic quartz and topaz are reported for comparison.*

*Table III.2. Synthesis of microthermometric and Raman spectrometry results for the different fluid inclusion types analysed in magmatic quartz from the Beauvoir PRMG. The classification follows Aïssa et al. (1987). $T_e$: first visible melting of the solidified aqueous phase during heating; $T_m$ice: final melting of the solidified aqueous phase; $T_d$Hh, $T_d$H & $T_d$Slv: final dissolution temperatures of hydrohalite, halite and sylvite, respectively; and $T_H$: total homogenisation temperature that occurs either to the liquid (L) or vapour phase (V). Values in italic represent average temperatures and median trace contents relative to the vapour phase. The first number of measurements (n) for each fluid inclusion type indicates the total number of fluid inclusions analysed through microthermometry (sometimes just at high or low temperatures), and the second corresponds to Raman analyses.*

| FI type | Microthermometric measurement (°C) | | | | | | Gas composition (mol%) | | | |
|---|---|---|---|---|---|---|---|---|---|---|
| | $T_e$ | $T_m$ice | $T_d$Hh | $T_d$Syl | $T_d$Hl | $T_H$ | $CO_2$ | $N_2$ | $CH_4$ | $H_2$ |
| L2 *(n = 74; 16)* | -75; -36<br>*(-63 ± 5)* | -42.7; -20.8<br>*(-28.7 ± 0.1)* | 5; 16<br>*(12 ± 1)* | 58; 88 | 217; 502<br>*(268 ± 1)* | 268; >500 (L) | 0 | 28; 98<br>*(64)* | 0; 58<br>*(20)* | 0; 42<br>*(0)* |
| V2 *(n = 11; 50)* | -69; -29<br>*(-49 ± 5)* | -23; -6<br>*(-16 ± 1)* | – | – | – | 500; >540 (V) | 0; 92<br>*(61)* | 1; 96<br>*(34)* | 0; 27<br>*(6)* | 0;43<br>*(0)* |
| L3-L4 *(n = 83)* | -63; -12<br>*(-45 ± 5)* | -3.8; -0.2<br>*(-1.4 ± 0.1)* | – | – | – | 137; >350 (L) | – | – | – | – |
| L5-L6 *(n = 37)* | -63; -27<br>*(-43 ± 5)* | -17.6; -6.7<br>*(-13.4 ± 0.1)* | -23.3; -20.4<br>*(-22.2 ± 0.1)* | – | – | 172; 331<br>*(253 ± 1)* | – | – | – | – |
| L7 *(n = 38; 11)* | -72; -46<br>*(-59 ± 5)* | -34.9; -24.3<br>*(-26.4 ± 0.1)* | 10; 20<br>*(14 ± 1)* | 60; 80 | 153; >360 | 108; 354<br>*(262 ± 1)* | 0; 56<br>*(0)* | 32; 89<br>*(69)* | 0; 59<br>*(19)* | 0; 43<br>*(4)* |

***L2-type fluid inclusions:*** L2-type FIs contain traces of $N_2$ (28–98 mol%), along with variable amounts of $H_2$ (0–42 mol%) and $CH_4$ (0–58 mol%). Notably, $CO_2$ has not been detected, contrasting with the value of *ca.* 34 mol% previously reported for L2-type FIs (Harlaux et al., 2017). However, analyses of L1-L2-type FIs in magmatic topaz from the B1 unit yield trace gas compositions comparable to the value obtained by Harlaux et al. (2017), with approximately 30–34 mol% $CO_2$, 50 mol% $N_2$, and 16–20 mol% $CH_4$ (Fig. III.15).

***V2-type fluid inclusions:*** The aqueous vapour phase of V2-type FIs typically contains a majority of $CO_2$ (median ~ 61 mol%), with variable proportions of $N_2$ (1–96 mol%), $CH_4$ (0–27 mol%), and $H_2$ (0–43 mol%). These results largely align with trace gas compositions reported by Harlaux et al. (2017) (58–60 mol% $CO_2$, 32–35 mol% $N_2$, and 7–8 mol% $CH_4$).

***L7-type fluid inclusions:*** Finally, L7-type FIs exhibit trace gas compositions resembling those of L2-type FIs, dominated by $N_2$ (32–89 mol%), with varying amounts of $H_2$ (0–43 mol%) and $CH_4$ (0–59 mol%). A single L7-type FI display a significant $CO_2$ content of approximately 56 mol%.

### *3.2.3. Salinity calculations*

As detailed in section 3.1.3.ii of the methodology, salinity can be estimated within two distinct chemical systems depending on the major cations detected: the binary $H_2O$-NaCl system or the ternary $H_2O$-NaCl-KCl system (Figs. III.11, III.16 and III.17 and Table III.3).

#### *3.2.3.i. Absence of halite*

In the absence of halite within FIs, salinity in the $H_2O$-NaCl system is calculated using the equation from Bodnar (1993), based on the ice melting temperature (denoted as T, in °C):

$$NaCl_{eq} = 0.00 + 1.78T - 0.0442T^2 + 0.000557T^3$$

An additional method for estimating salinity in the $H_2O$-NaCl system, in the absence of salt crystals, involves Raman spectrometry analysis. This approach was particularly advantageous for V2-type fluid inclusions, which are characterised by significant volumetric fractions of the vapour phase ($R_V$ ~ 70–90 %), making microthermometric measurements challenging. Raman analysis was also performed to a lesser extend to characterise the salinity of the vapour-dominant L3-L4-type FIs.

When potassium is detected via LA-ICP-MS analysis, salinity in the $H_2O$-NaCl-KCl system is estimated by plotting the Na/K ratio and ice melting temperature in the ternary phase diagram (Fig. III.11). Alternatively, hydrohalite dissolution temperature have been measured for seven L5-L6-type FIs. The ice melting and hydrohalite dissolution temperatures can directly yield $NaCl_{eq}$ and $KCl_{eq}$ values without relying on graphical interpolation (Bakker, 2012).

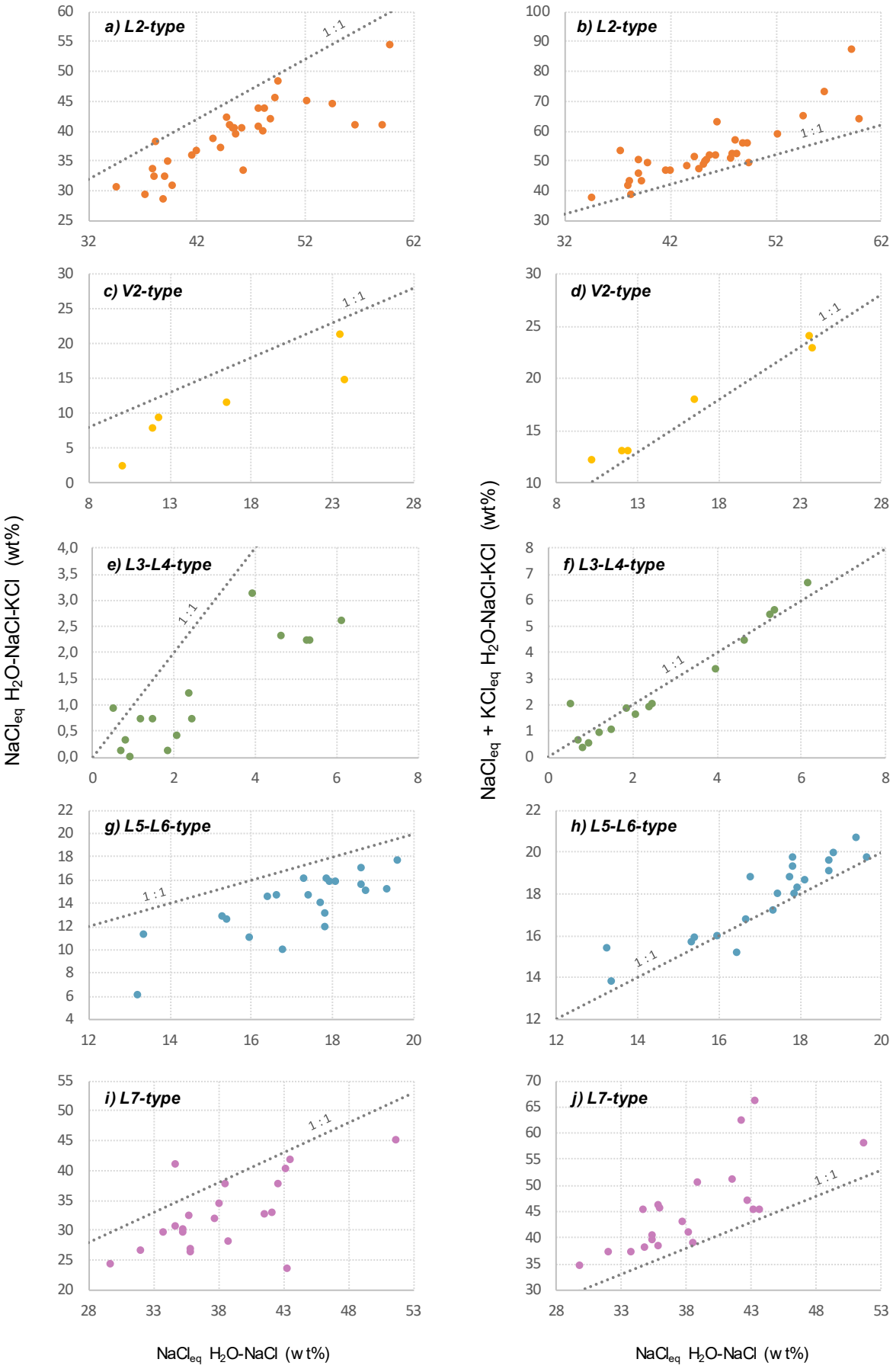
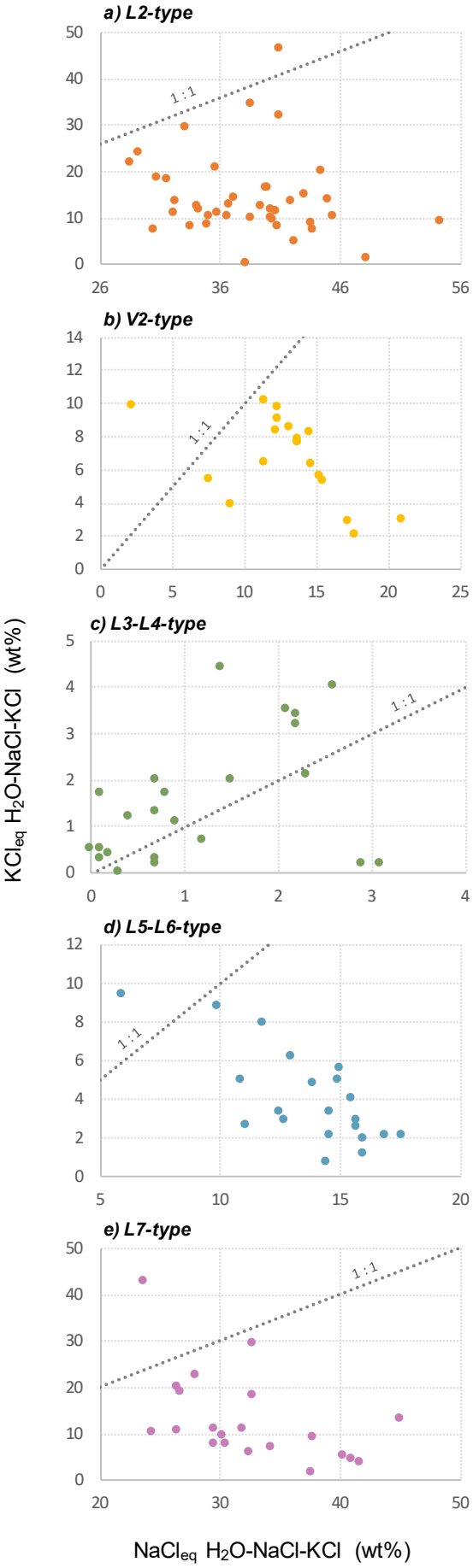



*Figure III.16. Comparison of salinities obtained in the binary $H_2O$-NaCl system and the ternary $H_2O$-NaCl-KCl system for L2-type (a-b), V2-type (c-d), L3-L4-type (e-f), L5-L6-type (g-h), and L7-type (i-j) fluid inclusions.*




***V2-type fluid inclusions:*** Raman spectrometry yields salinities ranging from *ca.* 4.9 to 34.4 wt% NaCl eq (mean ~ 19.2 wt% NaCl eq; n=57), which largely align with the the 3–22 wt% NaCl eq range reported by Aïssa et al. (1987) and Harlaux et al. (2017). These values are also consistent with the salinities of *ca.* 10.2 to 24.5 wt% NaCl eq directly calculated from $T_m$ice using the equation proposed by Bodnar (1993) (Figs. III.16c-d). Salinities derived from microthermometry and those obtained through Raman spectrometry can be different by up to 23 wt% NaCl eq for a single FI, yet no systematic variation is observed between both methods. LA-ICP-MS analysis of V2-type FIs indicates Na/K ratios of 0.2 to 9.7 (median ~ 1.7, n=88) and salinities estimated in the $H_2O$-NaCl-KCl system vary between *ca.* 6.2 and 23.9 wt% total (NaCl + KCl) eq (Figs. III.16c-d and III.17b).

***L3-L4-type fluid inclusions:*** In the $H_2O$-NaCl system, L3-L4-type FIs exhibit salinities ranging from 0.4 to 6.2 wt% NaCl eq (mean ~ 2.5 wt% NaCl eq, n=73), consistent with the 0–10 wt% NaCl eq range reported by Aïssa et al. (1987) (Figs. III.16e-f). LA-ICP-MS data indicate Na/K ratios ranging from 0.1 to 8.6 (median ~ 0.5, n=38), suggesting a dominance of KCl over NaCl (Fig. III.17c). Salinities derived graphically from the $H_2O$-NaCl-KCl ternary diagram are comparable and vary between 0.3 and 6.6 wt% total (NaCl + KCl) eq (mean ~ 2.7 wt% total eq, n=23) (Fig. III.16f).

*Figure III.17. Comparison of $NaCl_{eq}$ and $KCl_{eq}$ contents estimated graphically using Na/K ratios and microthermometric measurements ($T_m$ice or $T_d$Hl) in the ternary phase diagram.*

Vapour-dominant L3-L4-type FIs are characterised by salinities ranging from *ca.* 2.6 to 8.7 wt% NaCl eq, as determined in the $H_2O$-NaCl system by Raman spectrometry. These estimates are consistent with those derived from microthermometry data.

***L5-L6-type fluid inclusions:*** In the $H_2O$-NaCl system, salinities of L5-L6-type FIs vary between 10.0 and 20.8 wt% NaCl eq (mean ~ 17.1 wt% NaCl eq, n=31), consistent with the 12–26 wt% NaCl eq range reported by Aïssa et al. (1987) (Figs. III.16g-h). LA-ICP-MS analysis reveals Na/K ratios between 1.3 and 14.7 (median ~ 5.0, n=25). Total salinities estimated in the $H_2O$-NaCl-KCl system range from 13.7 to 20.6 wt% total (NaCl + KCl) eq (mean ~ 17.8 wt% total eq, n=21). Sodium chloride accounts for the majority of salts (5.9–17.6 wt% NaCl eq), while potassium chloride content varies from 0.7 to 9.4 wt% KCl eq (Fig. III.17d).

Estimates derived from ice melting and hydrohalite dissolution temperatures are similar, ranging from 15.6 to 20.2 wt% total eq (Bakker, 2012). These values deviate by no more than 0.6 wt% total eq from those estimated in the binary $H_2O$-NaCl system and by up to 1.5 wt% total eq from graphical estimates in the ternary $H_2O$-NaCl-KCl system. While total salinities are similar between the two systems, Na content is consistently higher in the binary $H_2O$-NaCl system.

*3.2.3.ii. Presence of halite*

For halite-bearing fluid inclusions, salinity in the $H_2O$-NaCl system is determined using the halite dissolution temperature, applying the equation from Sterner et al. (1988):

$$NaCl_{eq} = 26.242 + 0.4928T + 1.42T^2 - 0.223T^3 + 0.04129T^4 + 0.006295T^5 - 0.001967T^6 + 0.0001112T^7$$

$$where\ T(°C) = \frac{T_dHl(°C)}{100}\ and\ 0.1\ °C \leq T_dHl \leq 801°C)$$

When potassium is detected via LA-ICP-MS analysis, salinity in the $H_2O$-NaCl-KCl system is estimated by plotting the Na/K ratio and the halite dissolution temperature on the ternary phase diagram (Fig. III.11).

***L2-type fluid inclusions:*** L2-type FIs show salinities varying between 32.8 and 60.0 wt% NaCl eq (mean ~ 44.7 wt% NaCl eq; n=37), as estimated from $T_dHl$ in the $H_2O$-NaCl binary system (Sterner et al., 1988) (Figs. III.16a-b). These values are largely consistent with the 30–50 wt% NaCl eq range reported by Aïssa et al. (1987) and Harlaux et al. (2017).

Potassium was detected in over 90 % of analyses, yielding Na/K ratios ranging from 1.4 to 10.8 (median ~4.3, n=50). Higher total salinities ($NaCl_{eq}$ + $KCl_{eq}$) of *ca.* 37.7–87.7 wt% total eq (mean ~ 53.1 wt% total eq; n=37) are obtained in the $H_2O$-NaCl-KCl ternary system, which deviate by approximately 0 to 28 wt% from estimates in the binary system (Fig. III.16b). $NaCl_{eq}$

values (*ca.* 28.6–54.3 wt% NaCl eq) are generally lower in the ternary system than in the binary system, with discrepancies ranging from 0.1 to 18.2 wt% NaCl eq (Fig. III.16a).

Most salinity values do not exceed 62.7 wt% total eq, with the exception of a single extreme value of 87.7 wt% total eq. This outlier appears abnormally high and should therefore be interpreted with caution. Two major sources of uncertainty in salinity estimates are found in the potential accidental trapping of halite within fluid inclusions and post-entrapment modifications. Such FIs, originally formed from a NaCl-saturated fluid, could artificially increase measured salinity and lead to an overestimation of solute concentrations. This effect is particularly relevant for FIs where the halite dissolution temperature ($T_dHl$) exceeds the total homogenisation temperature ($T_H$), indicating that the FI salinity may not represent the salinity of the initial fluid (e.g., Audétat, 2023). However, this specific criterion does not apply to the fluid inclusion associated with the extreme salinity value of 87.7 wt% total eq. While this extremum value is retained in the figures and interpretations that follow, it is acknowledged as a potential source of variability in the dataset.

*Table III.3. Summary of salinity estimates in the $H_2O$-NaCl binary system and the $H_2O$-NaCl-KCl ternary system. Salinities in the binary system are derived either from microthermometric measurements ($T_m$ice or $T_d$Hl) (1) or from Raman spectrometry analysis (2). Salinities in the ternary system are determined graphically using Na/K ratios and $T_m$ice or $T_d$Hl. Values between brackets and in italics are medians.*

| FI type | Salinity in $H_2O$-NaCl system | | Salinity in $H_2O$-NaCl-KCl system | | | Na/K ratios from LA-ICP-MS analysis |
|---|---|---|---|---|---|---|
| | [NaCl] (1) wt% eq | [NaCl] (2) wt% eq | [NaCl] wt% | [KCl] wt % | Total salinity [NaCl + KCl] | |
| L2 | 32.8–60.0 | – | 28.6–54.3 | 0.1–46.2 | 37.7–87.7 | 1.4–10.8 *(4.3)* |
| V2 | 10.2–24.5 | 4.9–34.4 | 2.2–21.0 | 2.0–10.1 | 6.2–23.9 | 0.2–9.7 *(1.7)* |
| L3-L4 | 0.4–6.2 | 2.6–8.7 | 0.0–3.1 | 0.0–4.4 | 0.3–6.6 | 0.1–8.6 *(0.5)* |
| L5-L6 | 10.0–20.8 | – | 5.9–17.6 | 0.7–9.4 | 13.7–20.6 | 1.3–14.7 *(5.0)* |
| L7 | 29.8–51.7 | – | 23.6–45.0 | 1.4–42.6 | 34.6–66.2 | 1.8–13.8 *(4.1)* |

***L7-type fluid inclusions:*** In the $H_2O$-NaCl binary system, L7-type FIs are characterised by salinities ranging from *ca.* 29.8 to 51.7 wt% NaCl eq, with most values slightly below the 40–60 wt% NaCl eq range reported by Aïssa et al. (1987) (Figs. III.16c-d). Due to high decrepitation rates, halite dissolution measurements beyond 360 °C were largely unattainable, limiting data for highly saline inclusions (> 40 wt% NaCl eq) characteristic of L7 fluids (Aïssa et al., 1987).

Potassium was detected in over 90 % of L7-type FIs, allowing for graphical salinity estimation in the $H_2O$-NaCl-KCl ternary diagram using Na/K ratios (median ~ 4.1; n=33) and halite dissolution temperatures. Total salinities ($NaCl_{eq}$ + $KCl_{eq}$) range from *ca.* 34.6 to 66.2 wt% total eq, aligning more closely with the previously reported range of *ca.* 40–60 wt% NaCl eq (Aïssa et

al., 1987) (Fig. III.16d). This consistency likely results from the consideration of the H₂O-NaCl-KCl system in their salinity calculations. While total salinities are consistently higher – by 0.4 to 22.9 wt% total eq – than those estimated in the binary system, $NaCl_{eq}$ values are generally lower in the ternary system (*ca.* 23.6–45.0 wt% NaCl eq) compared to the binary H₂O-NaCl system (*ca.* 29.8–51.7 wt% NaCl eq) (Figs. III.16c-d).

#### *3.2.4. Assessment of compositional variations between processing methods*

The absolute quantification of fluid inclusion compositions was performed in SILLS using the Na concentration (in ppm) as the internal standard, which was estimated either in the binary H₂O-NaCl system or the ternary H₂O-NaCl-KCl system. Na concentrations are found to be almost systematically higher when evaluated in the binary system (Fig. III.16; section 3.2.3), which consequently impacts the concentrations of other elements. It is therefore crucial to assess the influence of using one system versus the other on the final results. To achieve this, the difference in concentration estimated in the ternary system relative to the binary system was calculated using the following equation (Table III.4):

$$Percentage\ difference = \frac{X_{H2O-NaCl} - X_{H2O-NaCl-KCl}}{X_{H2O-NaCl}} \times 100$$

where $X_{H2O-NaCl}$ and $X_{H2O-NaCl-KCl}$ represent the concentrations of the chemical element $X$ in the H₂O-NaCl and H₂O-NaCl-KCl systems, respectively.

As expected, concentrations are almost systematically higher when estimated in the binary H₂O-NaCl system (Table III.4; Fig. III.18). The majority of the percentage differences calculated between the concentrations are below 90 % in absolute value, indicating that concentrations in the ternary system remain sufficiently close to those in the binary system to be considered of the same order of magnitude. For each element, a systematic increase in percentage differences is observed as salinity decreases (Table III.4). Percentage differences are highest for L3-L4-type FIs, which are associated with the lowest salinities, and lowest for L2- and L7-type FIs, corresponding to the highest-salinity FIs. Intermediate percentage differences and salinities characterise V2- and L5-L6-type FIs. The observed increase in the discrepancy between results derived from the binary and ternary systems could be attributed to the following factors: (i) low-salinity fluid inclusions may contain a higher proportion of salt as KCl rather than NaCl compared to other FI types, leading to greater overestimation of Na concentrations in the binary H₂O-NaCl system relative to the ternary H₂O-NaCl-KCl system; and/or (ii) the low salinity characteristic of L3-L4-type fluid inclusions inherently results in weaker Na signals, reducing the precision of Na/K ratio estimation – a critical parameter for determining salinity in the ternary H₂O-NaCl-KCl system. Conversely, in the binary H₂O-NaCl system, salinity is directly calculated from microthermometric data, likely ensuring a high level of accuracy given that Na was the major cation detected by LA-ICP-MS.

*Table III.4. Percentage differences of elemental concentrations estimated in the $H_2O$-NaCl and $H_2O$-NaCl-KCl systems for fluid inclusions (number of data points are between brackets and in italics). The $NaCl_{H_2O\text{-}NaCl}$ ranges derive from microthermometry data.*

| [$NaCl_{H2O\text{-}NaCl}$] (wt% eq) | L2-type | V2-type | L3-L4-type | L5-L6-type | L7-type |
|---|---|---|---|---|---|
| | 32.8–60.0 | 10.2–24.5 | 0.4–6.2 | 10.0–20.8 | 29.8–51.7 |
| Li | 21 *(17)* | 33 *(25)* | 20 *(1)* | 24 *(11)* | 12 *(10)* |
| Be | 12 *(22)* | 27 *(23)* | 67 *(5)* | 19 *(9)* | 14 *(15)* |
| Na | 15 *(51)* | 30 *(57)* | 58 *(16)* | 20 *(25)* | 14 *(33)* |
| Mg | 13 *(19)* | 29 *(14)* | 51 *(6)* | 21 *(9)* | 15 *(13)* |
| P | 16 *(7)* | 34 *(4)* | 66 *(2)* | 21 *(1)* | 14 *(3)* |
| Cl | 15 *(50)* | 28 *(15)* | 52 *(6)* | 19 *(22)* | 14 *(33)* |
| K | 16 *(50)* | 29 *(35)* | 58 *(16)* | 20 *(25)* | 14 *(33)* |
| Ca | – | 25 *(1)* | – | – | 10 *(1)* |
| Mn | 15 *(51)* | 27 *(26)* | 45 *(5)* | 21 *(23)* | 14 *(33)* |
| Fe | 15 *(18)* | 29 *(3)* | – | 33 *(1)* | 16 *(11)* |
| Cu | 17 *(16)* | 32 *(13)* | – | 15 *(3)* | 13 *(22)* |
| Zn | 15 *(49)* | 27 *(17)* | 52 *(5)* | 19 *(24)* | 14 *(33)* |
| As | 15 *(27)* | 30 *(31)* | 52 *(3)* | 22 *(1)* | 14 *(12)* |
| Br | – | – | – | – | 15 *(5)* |
| Rb | 15 *(51)* | 30 *(57)* | 59 *(11)* | 20 *(25)* | 14 *(33)* |
| Sr | 16 *(32)* | 29 *(12)* | 20 *(1)* | 16 *(11)* | 13 *(18)* |
| Nb | 17 *(13)* | 31 *(24)* | 58 *(1)* | 26 *(6)* | 12 *(2)* |
| Sn | 15 *(45)* | 30 *(55)* | 60 *(4)* | 25 *(12)* | 14 *(26)* |
| Sb | 16 *(26)* | 33 *(23)* | 64 *(1)* | 18 *(5)* | 15 *(12)* |
| Cs | 16 *(57)* | 30 *(57)* | 58 *(16)* | 20 *(25)* | 14 *(33)* |
| Ce | 17 *(14)* | 34 *(10)* | – | 33 *(2)* | 17 *(2)* |
| Ta | 17 *(23)* | 31 *(35)* | 54 *(8)* | 31 *(9)* | 14 *(6)* |
| W | 16 *(38)* | 30 *(35)* | 68 *(9)* | 25 *(13)* | 14 *(19)* |
| Pb | 15 *(51)* | 30 *(55)* | 55 *(5)* | 20 *(25)* | 14 *(33)* |
| U | 14 *(19)* | 28 *(23)* | 53 *(7)* | 26 *(11)* | 12 *(18)* |

Subsequently, the concentrations reported for L3-L4-type fluid inclusions will be those estimated in the binary $H_2O$-NaCl system. This decision is justified by the less intense signals generally observed, introducing imprecision in salinity estimation – and consequently the concentrations of analysed elements – in the ternary $H_2O$-NaCl-KCl system. For L2- and L7-type fluid inclusions, concentrations will be reported using the ternary $H_2O$-NaCl-KCl system, as potassium was detected in more than 90 % of analyses. Finally, for V2- and L5-L6-type fluid inclusions, the reported data will be mixed, depending on whether potassium was detected during LA-ICP-MS analysis and the availability of microthermometry data for graphical estimation of salinity in the ternary diagram. For practical reasons, many of the salinity data for V2-type FIs were obtained via Raman spectrometry (sections 3.2.1 and 3.2.3).

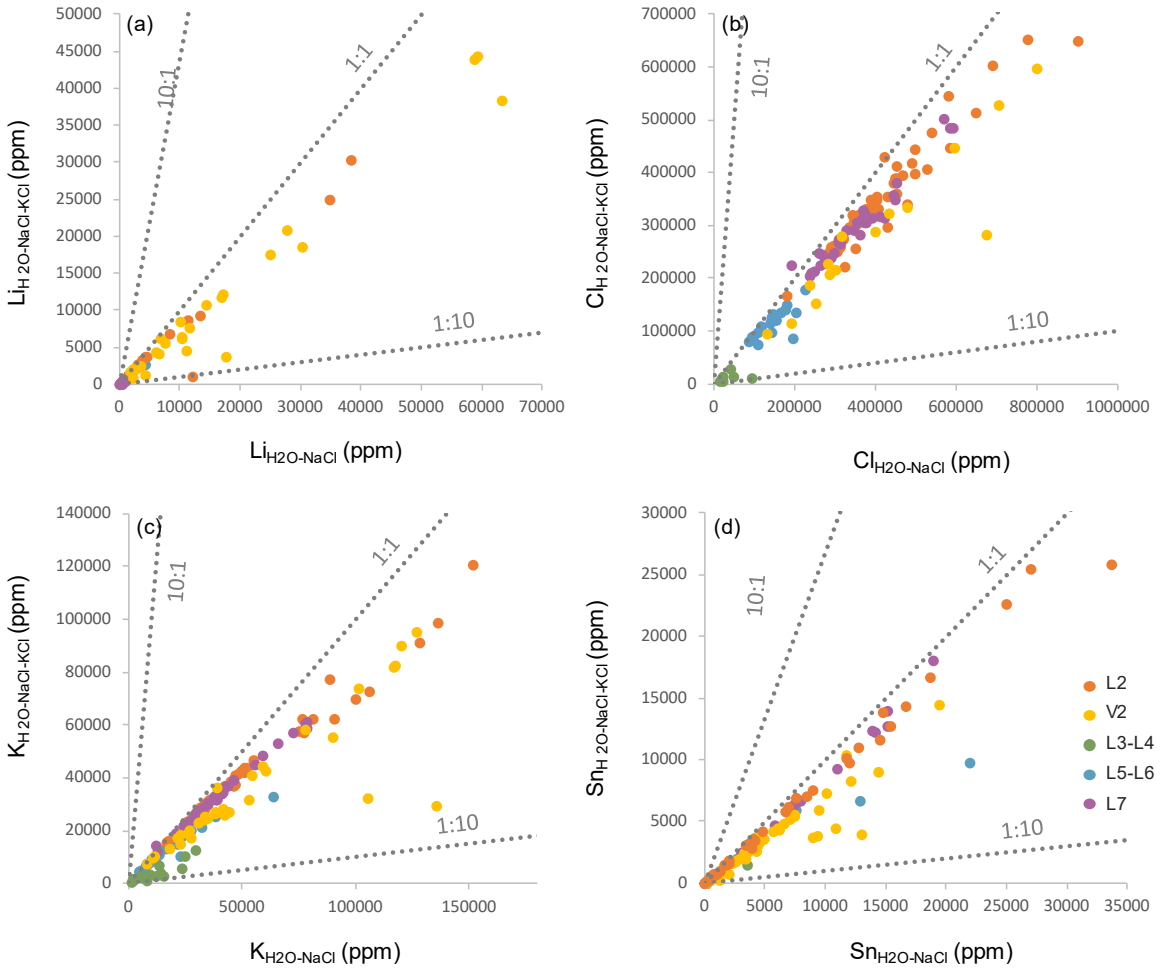



*Figure III.18. Comparison of Li, Cl, K and Sn concentrations deriving from the binary $H_2O$-NaCl system and ternary $H_2O$-NaCl-KCl system for fluid inclusions hosted in magmatic quartz from the Beauvoir PRMG.*

### *3.2.5. Chemical composition of fluid inclusions in the Beauvoir PRMG*

All values reported here derive from a rigorous verification of LA-ICP-MS spectra, ensuring that any variability or outliers observed within the data are genuine. Each analysed element was detected in at least one type of fluid inclusion. Br and Ca were the least frequently detected elements (< 5 % of analyses), followed by P, Fe, and Ce (< 20 % of analyses). A detailed summary of the elements detected for each FI type, along with the proportion of analyses in which they were identified and the corresponding limits of detection, is provided in Table III.5.

#### *3.2.5.i. Chemical composition of the distinct FI types*

***L2-type fluid inclusions:*** These FIs are characterised by very high concentrations of Na (115,300–213,600 ppm), Cl (167,500–652,600 ppm), K (15,100–120,800 ppm), Mn (5,400–119,000 ppm), Fe (8,100–53,100 ppm), Zn (1,100–65,200 ppm) and Cs (6,300–113,900 ppm), and high concentrations of Li (690–9,300 ppm), P (4,400–12,200 ppm), Rb (2,500–18,800 ppm), and Sn (20–34,900 ppm) (Fig. III.19a). Moderate concentrations of Be (40–7,700 ppm), Mg (20–2,900 ppm), Cu (210–4,200 ppm), As (90–1,200 ppm), W (20–2,200 ppm), and Pb (40–7,400 ppm) are observed. In contrast, concentrations of Sr (10–320 ppm), Nb (10–90 ppm), Sb (60–470 ppm),

Ce (1–30 ppm), Ta (1–110 ppm), and U (1–30 ppm) are relatively low. Br and Ca were not detected. The concentrations reported in this study are mostly consistent with previously published data for L2-type FIs (Harlaux et al., 2017), although slightly lower values are observed in the present dataset. These discrepancies likely derive from systematic biases introduced by methodological variations. Specifically, the use of slightly lower Na content estimates as internal standards for absolute quantification in SILLS (Fig. III.19a) and the subtraction of the matrix contribution to the Li signal – an adjustment not applied by Harlaux et al. (2017) – are probable factors contributing to the reduced concentrations observed in this study. To minimise the influence of these methodological biases, comparing element-to-Na ratios provides a more robust approach than relying on absolute concentrations (Fig. III.20).

Na/K ratios range from 1.4 to 10.8, with an median value of 4.3, consistent with – although generally higher than – the Na/K ratios of *ca.* 1.5–2.6 previously reported from L2-type fluid inclusions in the Beauvoir PRMG (Harlaux et al., 2017) (Fig. III.21a). Na/Li ratios exhibit a wide range from *ca.* 12.7 to 208.1, with a median value of *ca.* 64.1, significantly higher than the previously reported ratios (*ca.* 3–23; Harlaux et al., 2017) (Fig. III.21b). Nb/Ta ratios vary between 0.5 and 4.1 (median ~ 1.3) (Fig. III.21c).

***V2-type fluid inclusions:*** V2-type FIs show very high concentrations of Na (8,700–165,200 ppm), Cl (95,200–935,300 ppm), K (7,100–314,300 ppm), Fe (19,000–74,400 ppm), and Cs (2,200–123,700 ppm), as well as high concentrations of Li (1,300–104,800 ppm), P (5,400–39,100 ppm), Mn (790–35,400 ppm), and Zn (1,200–93,500 ppm) (Fig. III.19b). Moderate concentrations are observed for Be (110–8,700 ppm), Mg (120–32,800 ppm), Cu (110–3,800 ppm), As (120–3,400 ppm), Rb (210–60,200 ppm), Sn (70–16,000 ppm), Sb (30–1,300 ppm), and Pb (10–5,100 ppm). Lower amounts are detected for Sr (4–320 ppm), Nb (10–630 ppm), Ce (2–60 ppm), Ta (2–530 ppm), W (10–1,400 ppm), and U (1–100 ppm). A single Ca concentration of *ca.* 1,890,600 ppm was measured, while Br was not detected.

Some Cl concentrations in V2-type FIs are anomalously high, exceeding even those measured in the higher-salinity L2-type FIs (Figs. III.19a-b). These values are challenging to reconcile with the expected salinity or type of the fluid inclusions, and may indicate potential analytical limitations. The relatively weak signal from V2-type vapour-dominant FIs, combined with the inherent difficulty of analysing anions such as Cl via LA–ICP–MS – arising from their high first ionisation potentials, which are close to the ionisation energy of the Ar plasma source (Seo et al., 2011) – could contribute to unreliable Cl quantification in these FIs.

Similarly to L2-type FIs, the concentrations obtained for V2-type FIs are generally consistent with those reported by Harlaux et al. (2017). Minor discrepancies are observed, which likely derive from: (i) the difference in the number of data points between both studies, and (ii) the

same methodological factors identified for L2-type FIs, namely the use of slightly lower Na concentrations as internal standards during quantification and the subtraction of the matrix contribution from the Li signal of the fluid inclusion.

*Table III.5. Summary of elements detected in fluid inclusions hosted in magmatic quartz from the Beauvoir PRMG by LA-ICP-MS, indicating the percentage of analyses in which each element was identified for each FI type, along with the corresponding median limit of detection (LOD) for each element. N.d. = not detected.*

| | Element detection percentage | | | | | Median LOD (ppm) |
|---|---|---|---|---|---|---|
| | L2-type *N = 51* | V2-type *N = 90* | L3-L4-type *N = 65* | L5-L6-type *N = 37* | L7-type *N= 33* | |
| Li | 29 | 30 | 31 | 30 | 30 | 2 |
| Be | 43 | 34 | 43 | 43 | 48 | 1,927 |
| Na | 100 | 100 | 100 | 100 | 100 | 731 |
| Mg | 37 | 31 | 25 | 49 | 39 | 166 |
| P | 14 | 7 | 12 | 11 | 9 | 13,558 |
| Cl | 98 | 29 | 26 | 73 | 100 | 127,820 |
| K | 98 | 59 | 58 | 70 | 100 | 9,177 |
| Ca | n.d. | 1 | 2 | n.d. | 3 | 660,337 |
| Mn | 100 | 46 | 11 | 89 | 100 | 1,012 |
| Fe | 35 | 7 | n.d. | 3 | 33 | 34,537 |
| Cu | 31 | 24 | 15 | 22 | 67 | 654 |
| Zn | 96 | 33 | 14 | 97 | 100 | 2,312 |
| As | 53 | 43 | 28 | 3 | 36 | 542 |
| Br | n.d. | n.d. | n.d. | n.d. | 15 | 22,735 |
| Rb | 100 | 98 | 83 | 100 | 100 | 58 |
| Sr | 63 | 19 | 11 | 43 | 55 | 47 |
| Nb | 25 | 36 | 31 | 16 | 6 | 37 |
| Sn | 88 | 92 | 45 | 46 | 79 | 100 |
| Sb | 51 | 43 | 14 | 14 | 36 | 175 |
| Cs | 100 | 100 | 100 | 100 | 100 | 17 |
| Ce | 27 | 16 | 6 | 8 | 6 | 34 |
| Ta | 45 | 56 | 66 | 35 | 18 | 6 |
| W | 75 | 52 | 63 | 51 | 58 | 38 |
| Pb | 100 | 93 | 20 | 100 | 100 | 23 |
| U | 37 | 38 | 40 | 43 | 55 | 19 |

Na/K ratios range from 0.2 to 9.7, comparable to those of L2-type fluid inclusions, but are generally lower, as indicated by a median Na/K ratio of 1.7 (Fig. III.21a). These values align with the two Na/K ratios of 1.9 and 2.1 previously determined for V2-type FIs in the Beauvoir PRMG (Harlaux et al., 2017). Na/Li ratios, also generally lower than those of L2-type FIs, vary from *ca.* 0.6 to 84.7, with a median value of 4.6 (Fig. III.21b). These ratios are consistent with the Na/Li ratios of 2.8 and 3.0 previously documented for V2-type FIs, though slightly higher

(Harlaux et al., 2017). Nb/Ta ratios closely resemble those of L2-type FIs, ranging between *ca.* 0.4 and 4.9, with a median of 1.2 (Fig. III.21c).

***L3-L4-type fluid inclusions:*** These FIs exhibit very high concentrations of Na (1,800–24,200 ppm), P (2,000–27,300 ppm), Cl (14,200–426,500 ppm), and K (1,100–225,600 ppm), along with high concentrations of Li (300–43,700 ppm), and Cs (20–526,700 ppm) (Fig. III.19c). Moderate concentrations of Be (10–5,200 ppm), Mn (130–8,600 ppm), Cu (180–1,300 ppm), Zn (100–1,600 ppm), As (90–119,600 ppm), Rb (70–23,600 ppm), and Sn (40–3,600 ppm) are determined. Relatively low concentrations are also observed for Mg (8–3,800 ppm), Sr (30–320 ppm), Nb (10–920 ppm), Sb (70–580 ppm), Ce (10–70 ppm), Ta (1–2,100 ppm), W (10–1,300 ppm), Pb (10–180 ppm), and U (1–50) ppm. A single Ca concentration of *ca.* 211,900 ppm could be determined, while Br and Fe were not detected.

Na/K ratios range from *ca.* 0.1 to 8.6, with a median value of 0.5, which is lower than medians obtained for L2- and V2-type FIs (4.3 and 1.7, respectively) (Fig. III.21a). The lower Na/K values tend to be associated with anomalously high total salinities in L3-L4-type fluid inclusions and should therefore be interpreted with caution. A possible explanation for these elevated salinities in both L3-L4- and V2-type fluid inclusions is discussed in section 3.3.2.iii (Part III). Na/Li ratios, ranging from *ca.* 0.4 to 48.3 (median ~ 2.9), lower than those of L2- and V2-type FIs (64.1 and 4.6, respectively) (Fig. III.21b). Nb/Ta ratios closely resemble those of L2- and V2-type FIs, varying between 0.1 and 4.4 (median ~ 1.2) (Fig. III.21c).

***L5-L6-type fluid inclusions:*** They have very high concentrations of Na (23,200–81,600 ppm), Cl (73,300–261,500 ppm), and K (4,300–32,900 ppm), along with relatively high concentrations of P (7,700–27,900 ppm), Mn (250–18,800 ppm), Zn (1,600–12,300 ppm), and Cs (3,200–21,500 ppm) (Fig. III.19d). Moderate concentrations are observed for Li (10–2,800 ppm), Cu (40–2,000 ppm), Rb (280–36,100 ppm), Sn (2–11,500 ppm), and Pb (70–1,900 ppm), and low concentrations are also determined for Be (30–510 ppm), Mg (10–1,900 ppm), Sr (10–140 ppm), Nb (10–200 ppm), Sb (20–180 ppm), Ce (10–40 ppm), Ta (4–820 ppm), W (4–1,000 ppm), and U (1–30 ppm). Single values for Fe and As content of 6,700 ppm and 530 ppm could be obtained, while Ca and Br were not detected.

Na/K ratios range from 1.3 to 14.7, with a median value of *ca.* 5.0. These ratios are comparable to those of L2-type FIs (*ca.* 1.4–10.8, median ~ 4.3) (Fig. III.21a). Na/Li ratios vary over a wide range of *ca.* 14.5 to 8,470 (median ~ 159), and are mostly higher than for all other FI types in the Beauvoir PRMG, except L7-type FIs (median ~ 348; see below) (Fig. III.21b). Nb/Ta ratios appear slightly lower than for L2-, V2, and L3-L4-type FIs, ranging from *ca.* 0.2 to 2.0 (median ~ 0.8) (Fig. III.21c).

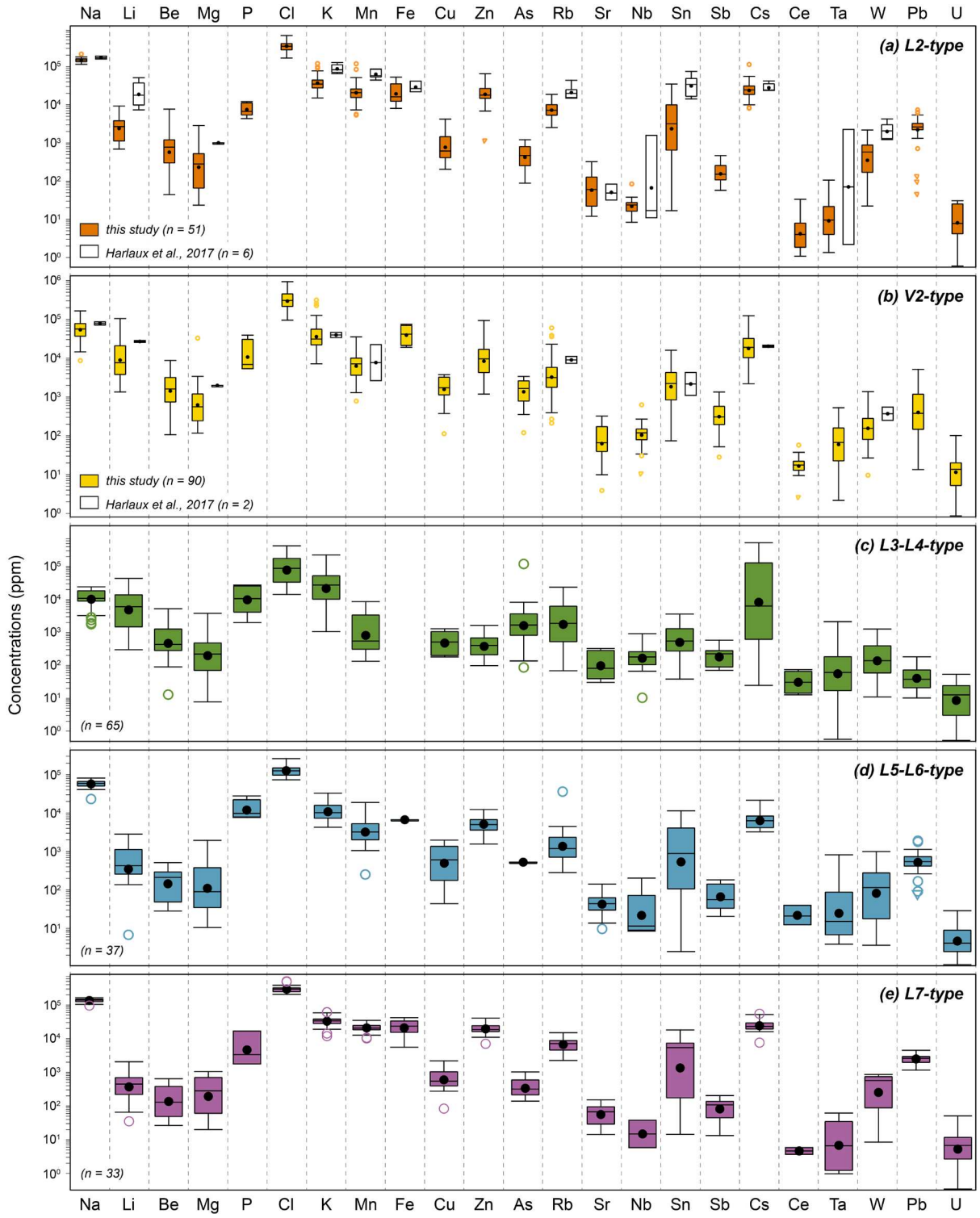



*Figure III.19. Major, minor and trace element contents of L2-, V2- , L3-L4-, L5-L6-, and L7-type fluid inclusions hosted in magmatic quartz from the Beauvoir granite. Coloured circular features represent outliers and triangular features indicate far outliers. Outliers are defined as values exceeding 1.5 times the interquartile range (IQR = Q3–Q1) from the box, while far outliers exceed 3 times the IQR. Previously published data for L2- and V2-type fluid inclusions hosted in magmatic quartz and topaz are shown in white boxplots (Harlaux et al., 2017). The number of data points indicated (n) represents the total number of analyses for each FI type; however, not all elements were detected in every analysis. Detection percentages for each element are specified in Table III.5.*

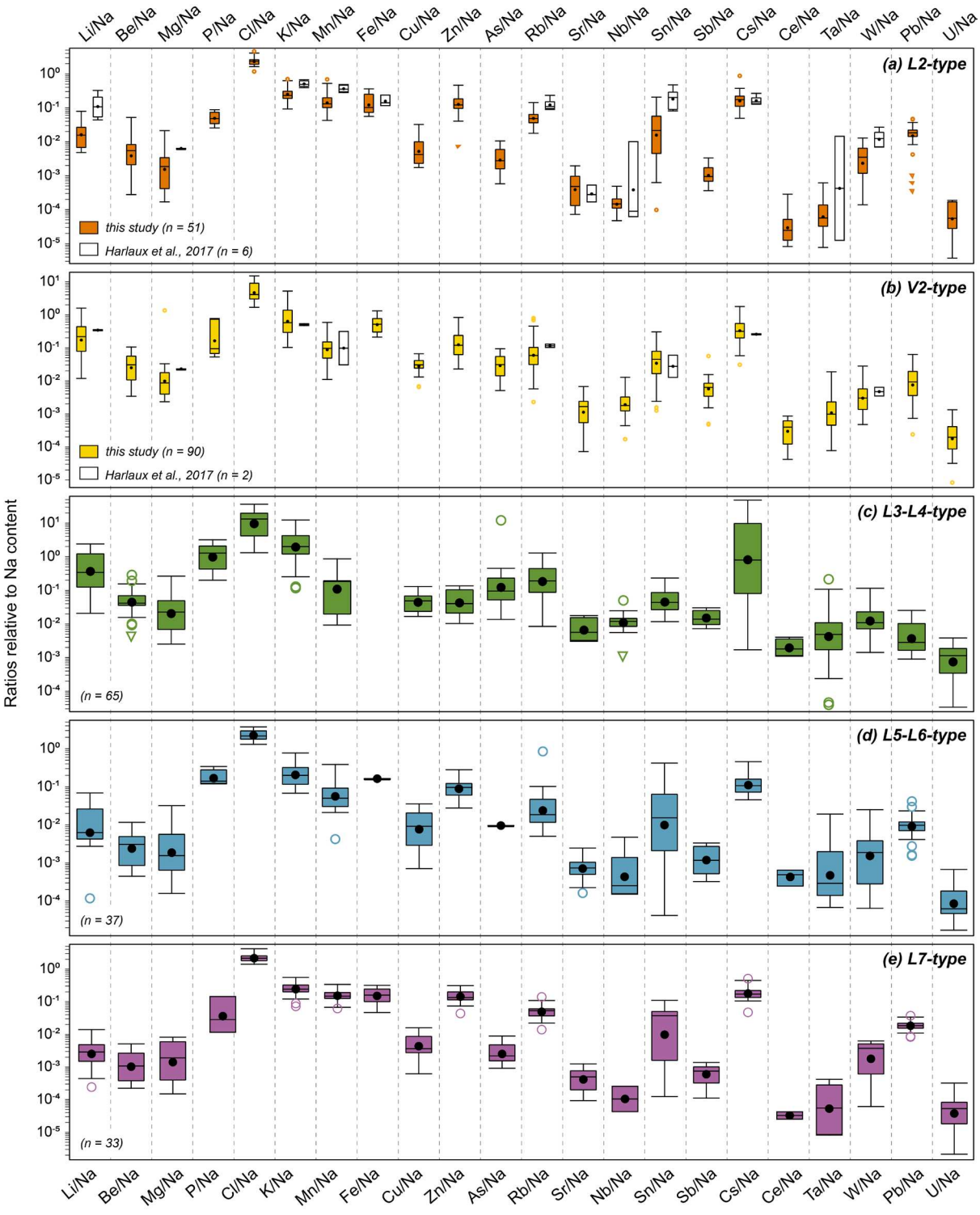



*Figure III.20. Boxplots illustrating the major, minor, and trace element contents normalised to Na concentrations for L2-, V2-, L3-L4-, L5-L6-, and L7-type fluid inclusions hosted in magmatic quartz from the Beauvoir granite. Coloured circular markers denote outliers, while triangular markers indicate far outliers. Outliers are defined as values exceeding 1.5 times the interquartile range (IQR = Q3–Q1), whereas far outliers exceed 3 times the IQR. Previously published data for L2- and V2-type fluid inclusions hosted in magmatic quartz and topaz are represented by white boxplots (Harlaux et al., 2017). The total number of analyses (n) for each FI type is indicated, though not all elements were detected in every analysis. Detection percentages for individual elements are provided in Table III.5.*

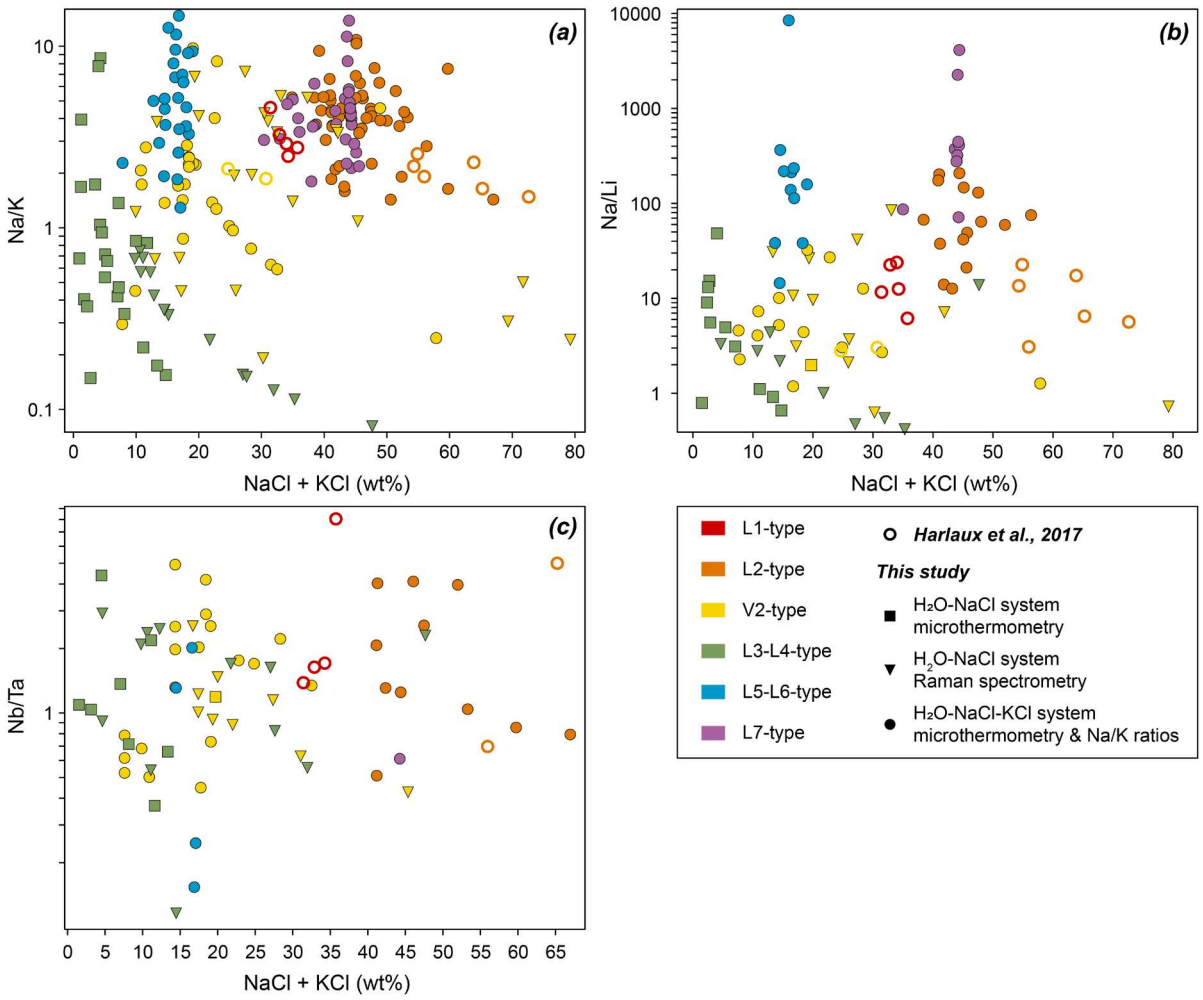



*Figure III.21. (a) Na/K vs. total salinity (NaCl + KCl), (b) Na/Li vs. total salinity, and (c) Nb/Ta vs. total salinity for fluid inclusions hosted in magmatic quartz from the Beauvoir PRMG. Symbols indicate the chemical system used for salinity estimation: either the H₂O-NaCl binary system (determined via microthermometry or Raman spectrometry) or the H₂O-NaCl-KCl ternary system (estimated using microthermometry data and Na/K ratios). Previously published data for L1-, L2- and V2-type fluid inclusions hosted in magmatic quartz and topaz are included for comparison (Harlaux et al., 2017).*

***L7-type fluid inclusions:*** These FIs are characterised very high concentrations of Na (96,000–164,000 ppm), Cl (206,600–503,700 ppm), K (11,900–61,100 ppm), Mn (10,200–34,900 ppm), Fe (5,500–42,000 ppm), Zn (7,000–40,600 ppm) and Cs (7,600–54,600 ppm), along with high concentrations of Rb (2,200–15,000 ppm), and Sn (10–18,100 ppm) (Fig. III.19e). Moderate concentrations are obtained for Li (40–2,100 ppm), P (1,800–16,700 ppm), Cu (80–2,200 ppm), W (10–860 ppm), and Pb (1,200–4,500 ppm), while concentrations of Be (30–640 ppm), Mg (20–1,100 ppm), As (140–1,000 ppm), Sr (10–150 ppm), Nb (6–40 ppm), Sb (10–200 ppm), Ce (4–6 ppm), Ta (1–60 ppm), and U (<1–50 ppm) are lower. A single Ca concentration of *ca.* 49,400 ppm could be determined, lower than those obtained for L3-L4-type (211,900 ppm) and V2-type (1,890,600 ppm) FIs. L7-type FIs represent the only type for which Br was detected, with concentrations ranging from 3,200–11,500 ppm (n = 5).

Na/K ratios range from *ca.* 1.8 to 13.8, with a median value of 4.1 (Fig. III.21a). These values closely resemble those of L2- (1.4–10.8, median ~ 4.3) and L5-L6-type FIs (1.3–14.7, median ~ 5.0). Na/Li ratios are the highest among FI types from the Beauvoir PRMG, varying between 71 and 4,126 (median ~ 348) (Fig. III.21b). A single Nb/Ta ratio of 0.6 has been determined, consistent with ratios characterising the other FI types (Fig. III.21c). Finally, Br/Cl ratios vary between 0.015 and 0.054.

#### *3.2.5.ii. Comparison of absolute concentrations across FI types*

The distinct FI types analysed in magmatic quartz from the Beauvoir PRMG exhibit broadly similar compositional patterns, with consistent relative enrichments and depletions observed across most elements (Fig. III.19). However, while the same elements tend to be enriched or depleted across FI types, the absolute concentrations generally differ between FI types, often correlating with salinity (Fig. III.22).

As expected, Cl concentrations increase with increasing total salinity (NaCl + KCl), with L2-, V2-, and L7-type FIs displaying higher Cl content (median ~ 342,600, 307,200, and 292,400 ppm, respectively) compared to L3-L4- and L5-L6-type FIs (median ~ 88,400 and 125,600 ppm) (Fig. III.22e). Similar positive correlations with salinity are observed for Mn, Zn, Rb, Cs, and Pb concentrations (Figs. III.22g, j, l, q, u). K, Sn, and W concentrations also show a general correlation with NaCl-KCl content, although data exhibit considerable dispersion around this trend (Figs. III.22f, o, t). The dispersion of Sn concentrations along the positive correlation with NaCl-KCl content is particularly pronounced for L2-, L5-L6-, and L7-type FIs. Such variability in Sn content was also reported in L1-type FIs (Harlaux et al., 2017). Median K concentrations remain of the same order of magnitude across FI types, ranging from approximately 10,000 to 35,000 ppm (Fig. III.22f). Broader dispersion of K concentrations is observed in L3-L4-type FIs, possibly due to weaker signals associated with these fluid inclusions, leading to reduced analytical precision. As K concentrations show minimal variation among FI types, systematic differences in Na/K ratios primarily reflect variations in Na concentrations (Fig. III.21a). For P and Fe, trends are challenging to discern due to limited data and low concentrations (Figs. III.22d, h). Nonetheless, Fe is primarily detected in high-temperature L2 and V2 fluids, as well as in the slightly cooler but highly saline L7 fluids.

In contrast, Nb, and Ce tend to show opposite trends, with concentrations seeming to decrease as total salinity increases (Figs. III.22n, r). Median Ta concentrations also tend to decrease with increasing salinity (Fig. III.22s), resulting in similar Nb/Ta ratios across all FI types (Fig. III.21c). Although no clear systematic in Li content emerges from the data, moderate- to low-salinity FIs, specifically V2 and L3-L4-type FIs, exhibit the highest Li concentrations (median ~ 7,600 and 6,000 ppm, respectively), which are an order of magnitude higher than those in L5-

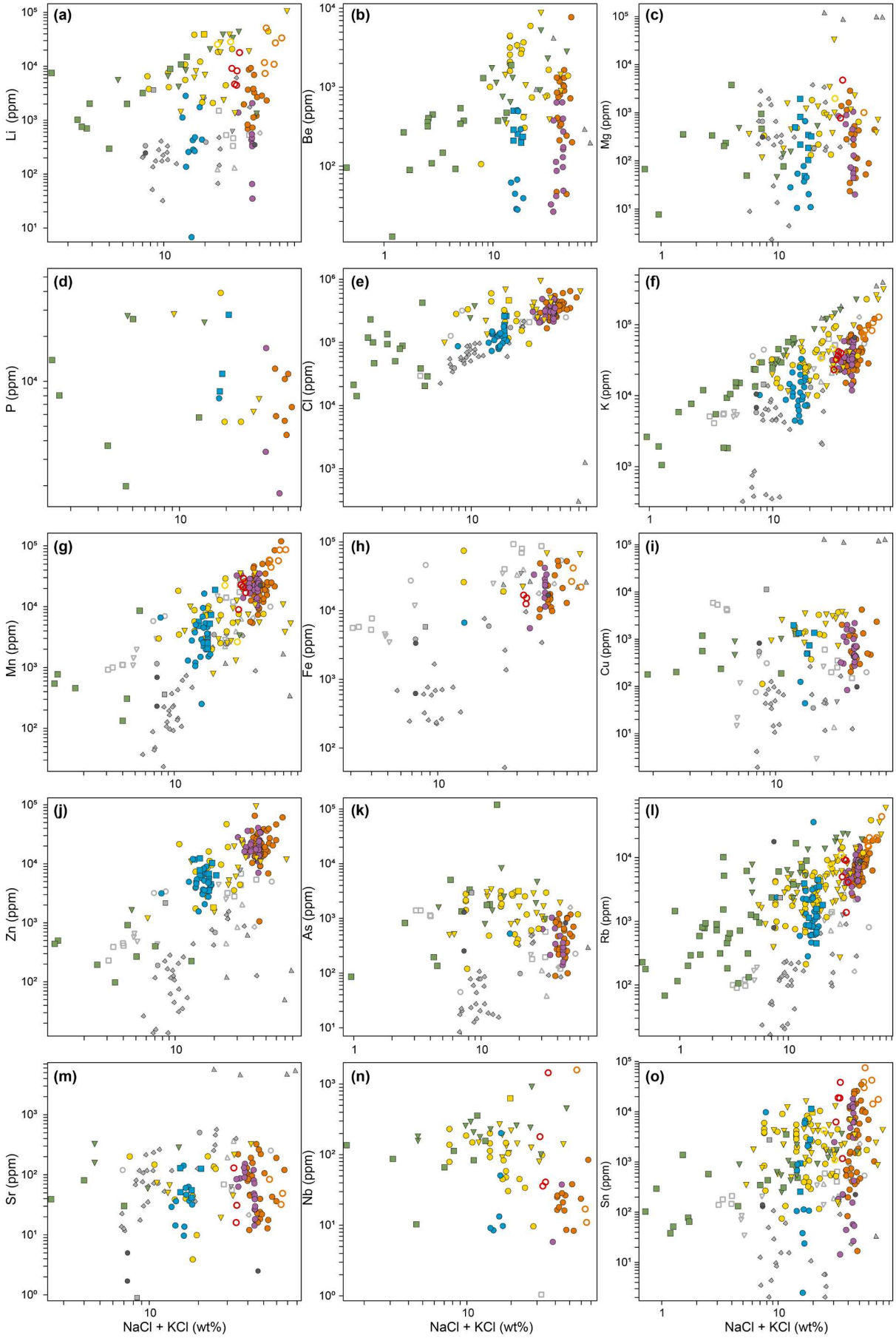
L6 and L7 FIs (median ~ 430 and 450 ppm, respectively) (Fig. III.22a). High-temperature, high-salinity L2 fluids display intermediate Li concentrations (median ~ 2,700 ppm).

Concentrations of Mg, Sr, Sb, and U are generally of the same order of magnitude across all FI types (Figs. III.22c, m, p, v). However, it is noteworthy that Sr and Sb tend to be less frequently detected as the salinity and homogenisation temperature of fluid inclusions decrease (Table III.5). Mg and Sb concentrations are typically in the range of hundreds of ppm, median Sr concentrations are below 100 ppm, and U concentrations are very low, rarely exceeding 50 ppm.

#### *3.2.5.iii. Comparison of element-to-Cl ratios across FI types*

Possible biases may have been introduced during the reconstruction of fluid inclusion compositions using SILLS, primarily due to the choice of the chemical system for salinity estimation, which is subsequently used as an internal standard during processing (sections 3.1.3 and 3.2.4). As a result, absolute concentrations should be interpreted with caution, and in many cases, comparing ratios across different FI types provides a more reliable basis for interpretation. Elements-to-Cl ratios were selected for this discussion, as Na is not the only cation significantly contributing to the fluid salinity (Fig. III.23).

Many element-to-Cl ratios are mostly comparable across FI types, including Mg/Cl, P/Cl, K/Cl, Mn/Cl, Fe/Cl, Cu/Cl Zn/Cl, Sr/Cl, Sb/Cl, Pb/Cl, and U/Cl. Cs/Cl ratios appear to decrease with decreasing salinity, whereas the higher Nb/Cl ratios are associated to the low-salinity L3-L4-type FIs. Significant variability in Sn/Cl and W/Cl is observed within L2, L5-L6, and L7-type FIs.


(a)
Li (ppm)
(b)
Be (ppm)
(c)
Mg (ppm)
(d)
P (ppm)
(e)
Cl (ppm)
(f)
K (ppm)
(g)
Mn (ppm)
(h)
Fe (ppm)
(i)
Cu (ppm)
(j)
Zn (ppm)
(k)
As (ppm)
(l)
Rb (ppm)
(m)
Sr (ppm)
(n)
Nb (ppm)
(o)
Sn (ppm)
NaCl + KCl (wt%)
NaCl + KCl (wt%)
NaCl + KCl (wt%)

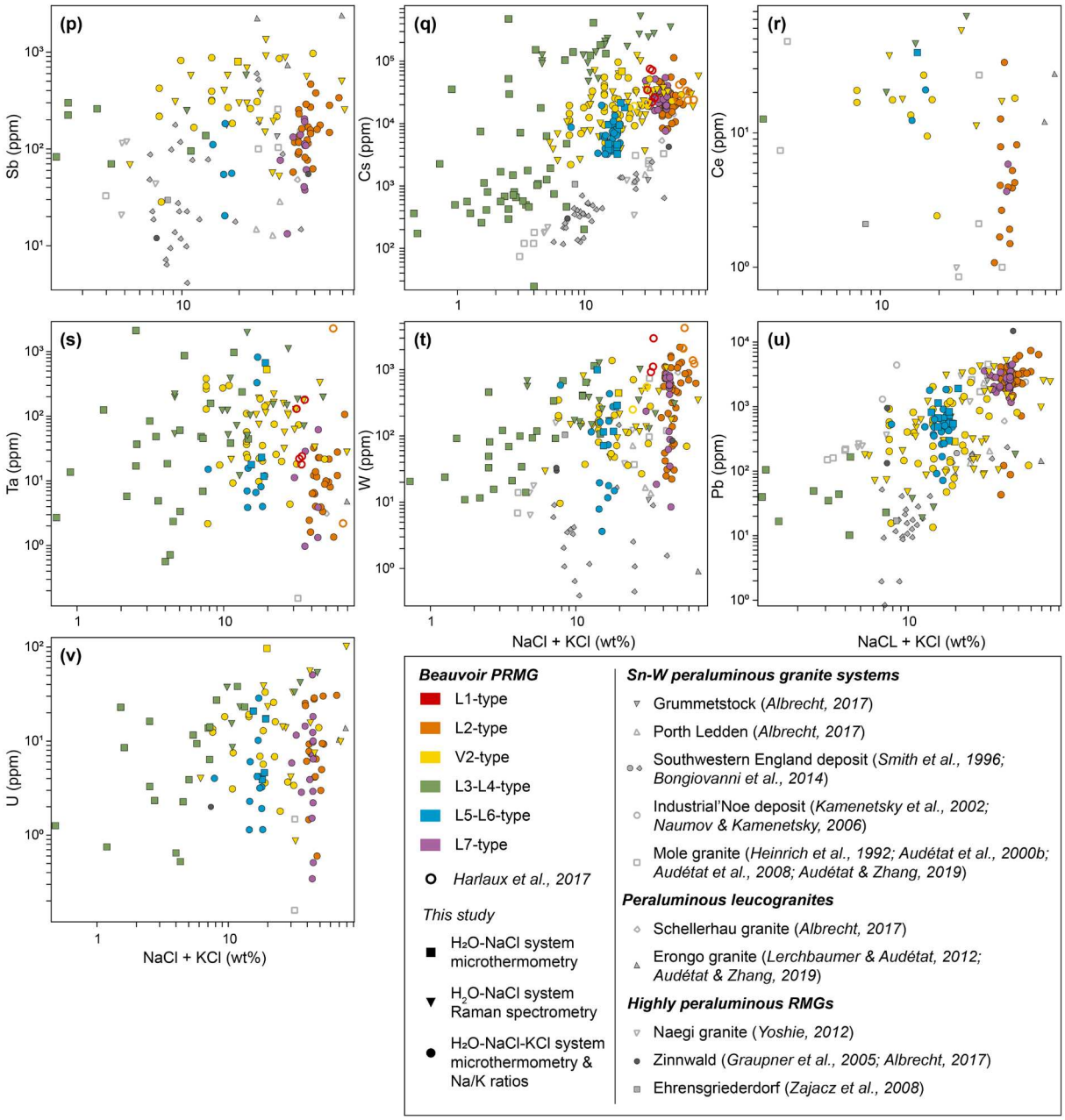
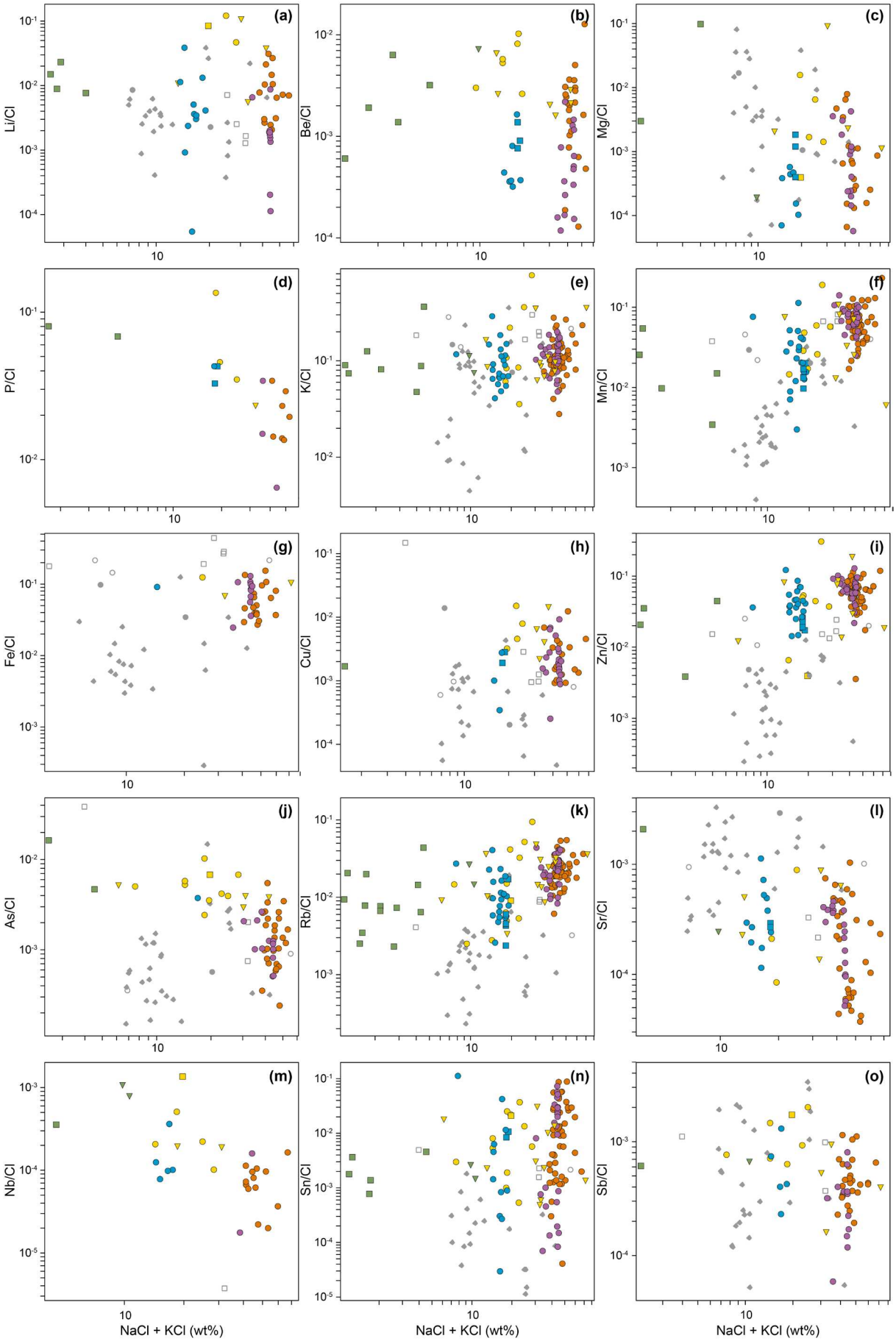



*Figure III.22. Evolution of concentrations in function of total salinity (NaCl + KCl) for the distinct fluid inclusion types hosted in magmatic quartz from the Beauvoir PRMG. Symbols for the Beauvoir PRMG indicate the chemical system used for salinity estimation: either the $H_2O$-NaCl binary system (determined via microthermometry or Raman spectrometry) or the $H_2O$-NaCl-KCl ternary system (estimated using microthermometry data and Na/K ratios). Previously published data for L1-, L2- and V2-type fluid inclusions hosted in magmatic quartz and topaz are included for comparison (Harlaux et al., 2017), as well as data for Sn-W peraluminous systems (Heinrich et al., 1992; Smith et al., 1996; Audétat et al., 2000b; Kamenetsky et al., 2002; Naumov and Kamenetsky, 2006; Audétat et al., 2008; Albrecht, 2017; Audétat and Zhang, 2019; Bongiovanni et al., 2024), peraluminous leucogranites (Lerchbaumer and Audétat, 2012; Albrecht, 2017; Audétat and Zhang, 2019),and highly peraluminous rare-metal granites (Graupner et al., 2005; Zajacz et al., 2008; Yoshie, 2012; Albrecht, 2017).*


(a)
Li/Cl
(b)
Be/Cl
(c)
Mg/Cl
(d)
P/Cl
(e)
K/Cl
(f)
Mn/Cl
(g)
Fe/Cl
(h)
Cu/Cl
(i)
Zn/Cl
(j)
As/Cl
(k)
Rb/Cl
(l)
Sr/Cl
(m)
Nb/Cl
(n)
Sn/Cl
(o)
Sb/Cl
NaCl + KCl (wt%)
NaCl + KCl (wt%)
NaCl + KCl (wt%)

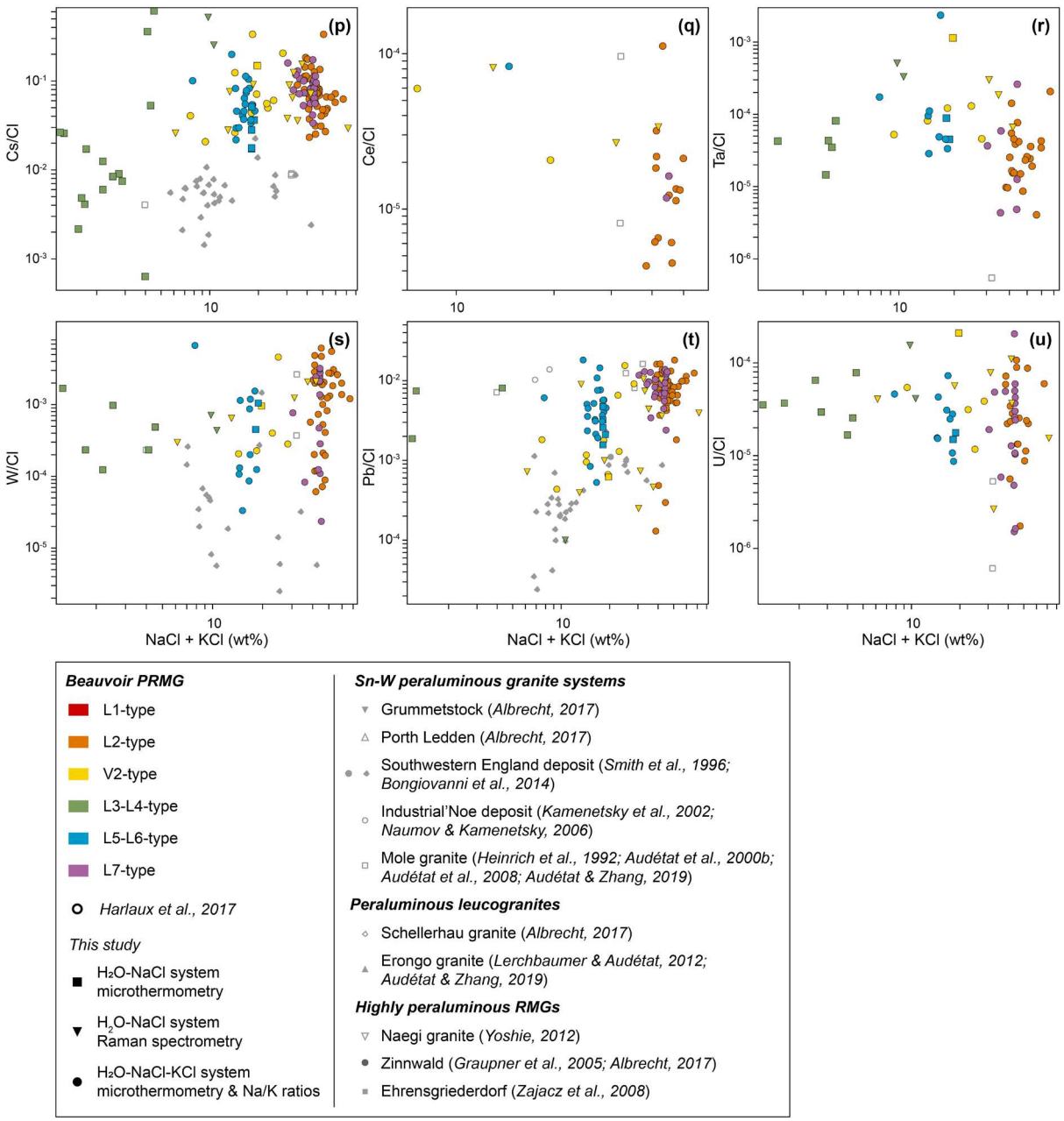



*Figure III.23. Evolution of element-to-Cl ratios in function of total salinity (NaCl + KCl) for the distinct fluid inclusion types hosted in magmatic quartz from the Beauvoir PRMG. Symbols indicate the chemical system used for salinity estimation: either the $H_2O$-NaCl binary system (determined via microthermometry or Raman spectrometry) or the $H_2O$-NaCl-KCl ternary system (estimated using microthermometry data and Na/K ratios). Previously published data for L1-, L2- and V2-type fluid inclusions hosted in magmatic quartz and topaz are included for comparison (Harlaux et al., 2017), as well as data for Sn-W peraluminous systems (Heinrich et al., 1992; Smith et al., 1996; Audétat et al., 2000b; Kamenetsky et al., 2002; Naumov and Kamenetsky, 2006; Audétat et al., 2008; Albrecht, 2017; Audétat and Zhang, 2019; Bongiovanni et al., 2024), peraluminous leucogranites (Lerchbaumer and Audétat, 2012; Albrecht, 2017; Audétat and Zhang, 2019),and highly peraluminous rare-metal granites (Graupner et al., 2005; Zajacz et al., 2008; Yoshie, 2012; Albrecht, 2017).*

## 3.3. Preliminary discussion and conclusions

### *3.3.1. Magmatic nature of high-temperature fluids in the Beauvoir PRMG*

Petrographic observations and microthermometric measurements suggest that multiple generations of magmatic fluids circulated through the B1 unit of the Beauvoir PRMG (Aïssa et al., 1987). Although not observed in the present study, L1 fluids have been previously documented as magmatic fluids exsolved from the Beauvoir melts (Aïssa et al., 1987). Their composition, determined via LA-ICP-MS analysis, reveals a multi-cation nature, high Na/K ratios ($\geq 1$), and relatively low Na/Li ratios ($\leq 5$), consistent with their exsolution from a highly evolved, Li-rich melt (Harlaux et al., 2017). These fluids are characterised by salinities of *ca.* 17 to 30 wt% NaCl eq (Aïssa et al., 1987; Harlaux et al., 2017) (Fig. III.24), significantly exceeding the salinities typically observed in one-phase, magmatic fluids exsolved in felsic systems mineralised in Mo, Cu, Sn-W, or Li-Nb-Ta-W-Zr-Hf (e.g., O'Reilly et al., 1997; Linnen, 1998; Audétat et al., 2000b, 2008). However, similar elevated salinities are commonly reported in highly peraluminous rare-metal granites, particularly in pegmatitic environments, such as the East Kemptville tin deposit (Nova Scotia, Canada, Halter et al., 1998b; Kontak et al., 2001) and the mineralised pegmatites from the Damara belt (Namibia; Ashworth et al., 2018). In the Beauvoir PRMG, these high salinities seem to have facilitated the partitioning of Sn and other Cl-complexing elements in favour of the exsolved fluid phase (Harlaux et al., 2017). The salinity of the single-phase fluid exsolved from intermediate-composition magmas has been shown to increase with progressive crystallisation at pressures below *ca.* 1.3 kbar (Cline and Bodnar, 1991; Audétat et al., 2008). Furthermore, the exsolution of magmatic fluids during the late stages of crystallisation of a felsic melt typically produces higher-salinity fluids, the F-rich composition of the melt enhancing both $H_2O$ and Cl solubility in felsic systems (e.g., Holtz et al., 1993; Webster, 1997). These findings suggest that the relatively high salinity of the primary magmatic fluids in the Beauvoir PRMG reflects a relatively late-stage exsolution from the melt, consistent with its F-rich nature (Cuney et al., 1992; Raimbault et al., 1995).

Following fluid saturation, phase separation of L1 fluids formed a low- to moderate-salinity vapour phase V2 (*ca.* 2–22 wt% NaCl eq) and a high-salinity liquid phase L2 (*ca.* 30–55 wt% NaCl eq) (Aïssa et al., 1987; Harlaux et al., 2017; this study) (Fig. III.24). This boiling process occurred at supra-solidus conditions, as evidenced by the coexistence of L2- and V2-type FIs as primary fluid inclusions aligned along a growth plane in magmatic quartz from the B1 unit (section 2 of Part III). Fluid inclusions analysed within this growth band show homogenisation temperatures ranging from *ca.* 420 to >500 °C (n = 4) for L2-type FIs and from 500 to >530 °C (n = 4) for V2-type FIs, closely approaching the estimated solidus temperature of the Beauvoir melts at approximately 550 °C (Pichavant et al., 1987a; Pichavant, 2022). In addition to their high homogenisation temperatures, which range from 310 to 595 °C when considering all existing data (Aïssa et al., 1987; Harlaux et al., 2017; this study) (Figs. III.13b and d), these fluids are

characterised by very low eutectic temperatures, primarily varying between -80 and -50 °C (Figs. III.13a and c). Such low eutectic temperatures were previously interpreted for L1-type FIs as indicative of high Li content (Harlaux et al., 2017). Consistent with this interpretation, L2- and V2-type FIs contain 690–9,300 ppm and 1,300–104,800 ppm of Li, respectively (Fig. III.19a-b). These concentrations exceed by one to two order of magnitude most Li values reported for Sn-W peraluminous granite systems and similar highly peraluminous rare-metal granites (data compiled from Yardley, 2005; Audétat, 2019; Bongiovanni et al., 2024) (Fig. III.22a). V2-type FIs exhibit relatively high salinities (2–22 wt% NaCl eq; Aïssa et al., 1987; Harlaux et al., 2017; this study) compared to the salinities expected for vapours derived from boiling at temperatures of *ca.* 400–550 °C and pressures of 200–700 bars in the binary $H_2O$-NaCl system, which typically range from 1 to 3 wt% NaCl eq (e.g., Bodnar, 2003; Driesner, 2007; Driesner and Heinrich, 2007). The elevated salinity of the magmatic vapour phase in the Beauvoir PRMG may result from phase separation occurring near critical conditions, a hypothesis supported by the observation of homogenisation in the vapour, liquid, or critical phase for V2-type fluid inclusions (Aïssa, 1987; Aïssa et al., 1987).

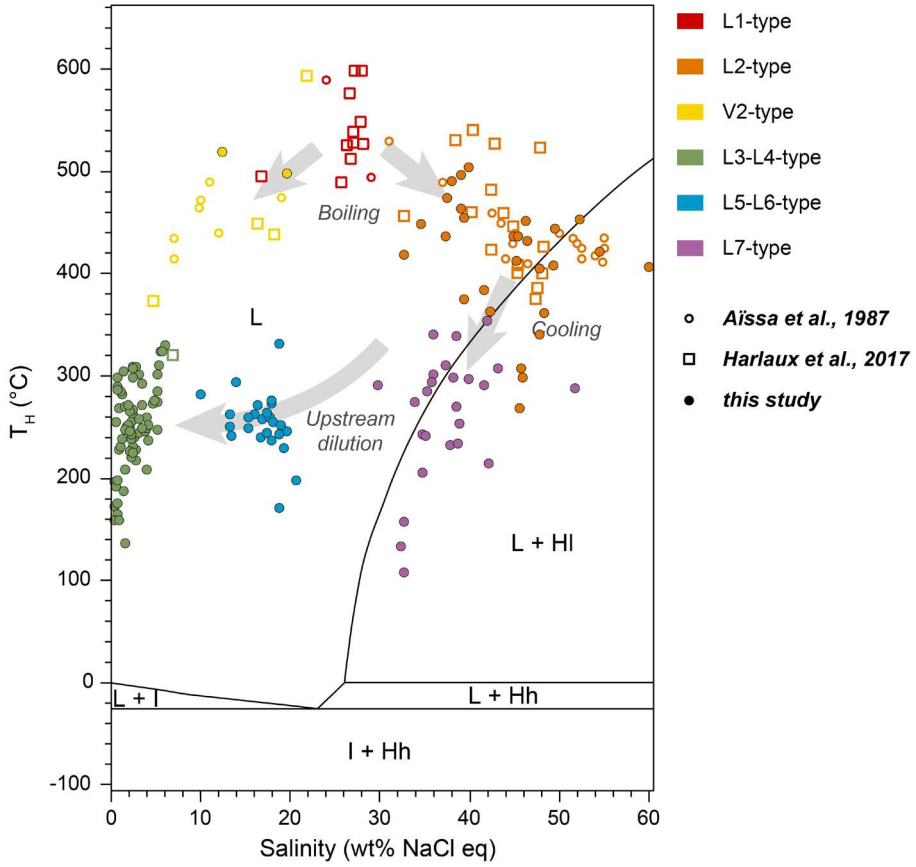



*Figure III.24. Salinity versus homogenisation temperature ($T_H$) for the distinct fluid inclusion types recognised in the Beauvoir PRMG. Salinity has been estimated in the $H_2O$-NaCl system from microthermometric measurements and phase equilibrium curved for this system are reported from Bodnar (2003). I = ice, L = liquid, Hl = halite, Hh = hydrohalite. The reported salinity values should be considered as approximate estimates, as potassium is also an important cation in these fluids.*

### *3.3.2. Insights into magmatic-hydrothermal processes derived from fluid inclusions*

#### *3.3.2.i. Element partitioning during high-temperature phase separation*

As early phase separation of the initial magmatic fluid (L1) occurred at temperatures of *ca.* 400–520 °C, elements were partitioned between the coexisting vapour (V2) and brine (L2) phases (Harlaux et al., 2017). Partitioning coefficients were estimated using four distinct datasets (Fig. III.25): (i) data from Harlaux et al. (2017); (ii) the boiling assemblage of coexisting L2- and V2-type fluid inclusions (FIs) observed along a growth plane in magmatic quartz (Fig. III.6e); (iii) all L2- and V2-type FI data obtained in this study; and (iv) data for L2-type FIs relative to a subset of V2-type FIs with salinities ≤ 10 wt% $(NaCl+KCl)_{eq}$.

Calculations based on data from the boiling assemblage are considered more precise and reliable, as the L2- and V2-type FIs in this context are presumed to have formed contemporaneously. However, it is important to note that vapour-like fluids typically ascend, whereas brines tend to remain stationary or migrate downward to deeper levels (Henley and McNabb, 1978). Numerical models of magmatic-hydrothermal systems that account for dynamic changes in permeability demonstrate that brines do not ascend under lithostatic conditions and tend to sink as permeability increases within the system (Weis, 2012, 2014; Weis et al., 2012; Scott et al., 2017). Consequently, while the boiling assemblage provides a more reliable basis for estimating partition coefficients, it may not exclusively represent contemporaneous vapour and brine phases. Partitioning coefficients have been calculated on larger datasets for comparison. In dataset (iv), the decision to focus only on V2-type FIs with salinities ≤ 10 wt% $(NaCl+KCl)_{eq}$ aimed to fit with a more a conventional scenario, as moderate-salinity vapours produced through phase separation are relatively unusual, as discussed in section 3.3.1 (Part III).

Harlaux et al. (2017) reported a preferential partitioning of most elements (Na, K, Mn, Rb, Sn, Cs, and W) into the L2 brine, whereas only Mg and Li were found to preferentially enrich the V2 vapour. In this study, a larger uncertainty is considered for partition coefficients, estimated using the following formula:

$$\sigma = R \times \sqrt{\frac{\sigma_V{}^2}{V} + \frac{\sigma_L{}^2}{L}}$$

where L and V are the mean concentrations of an element in the L2- and V2-type FIs, respectively, R is the ratio of these mean concentrations (V/L), and $\sigma_L$ and $\sigma_V$ are the standard deviations associated with concentrations from L2- and V2-type FIs, respectively. This broader estimation of the error bars confirms the accuracy of previous conclusions for most elements from Harlaux et al. (2017) data (Fig. III.25). However, for Li, the increased uncertainty makes it difficult to conclude on its behaviour during phase separation only based on this previous dataset.

Focusing on the boiling assemblage identified in the B1 unit, several elements appear to preferentially partition into the V2 vapour phase, including Li, Be, Fe, Cu, Zn, Sr, Nb, Ce, Ta (Fig. III.25). These findings neither confirm nor contradict previous work on the Beauvoir PRMG, as these elements were not analysed or detected, with the exception of Li (Harlaux et al., 2017). K exhibits a slight enrichment in the vapour relative to the brine, which contrasts with previous observations. Conversely, Na, Mn, and Pb show preferential partitioning into the L2 brine. For elements such as Mg, P, As, Rb, Sn, Sb, Cs, W, and U, no definitive conclusions can be drawn due to overlapping error bars with the 1:1 partitioning ratio. When considering the complete dataset, similar conclusions emerge: Li, Be, Mg, K, Cu, Sr, Nb, Ce, Ta, and U show a preferential partitioning into the vapour phase, whereas Na, Mn, W, and Pb exhibit a stronger affinity for the brine. When exclusively focusing on V2-type FIs with salinities ≤ 10 wt% $(NaCl+KCl)_{eq}$, vapour/brine partitioning is essentially comparable, with a significant affinity of Na, Mn, Rb, Cs, W and Pb for the brine, whereas P, Nb, Ce, Ta partition into the vapour phase.

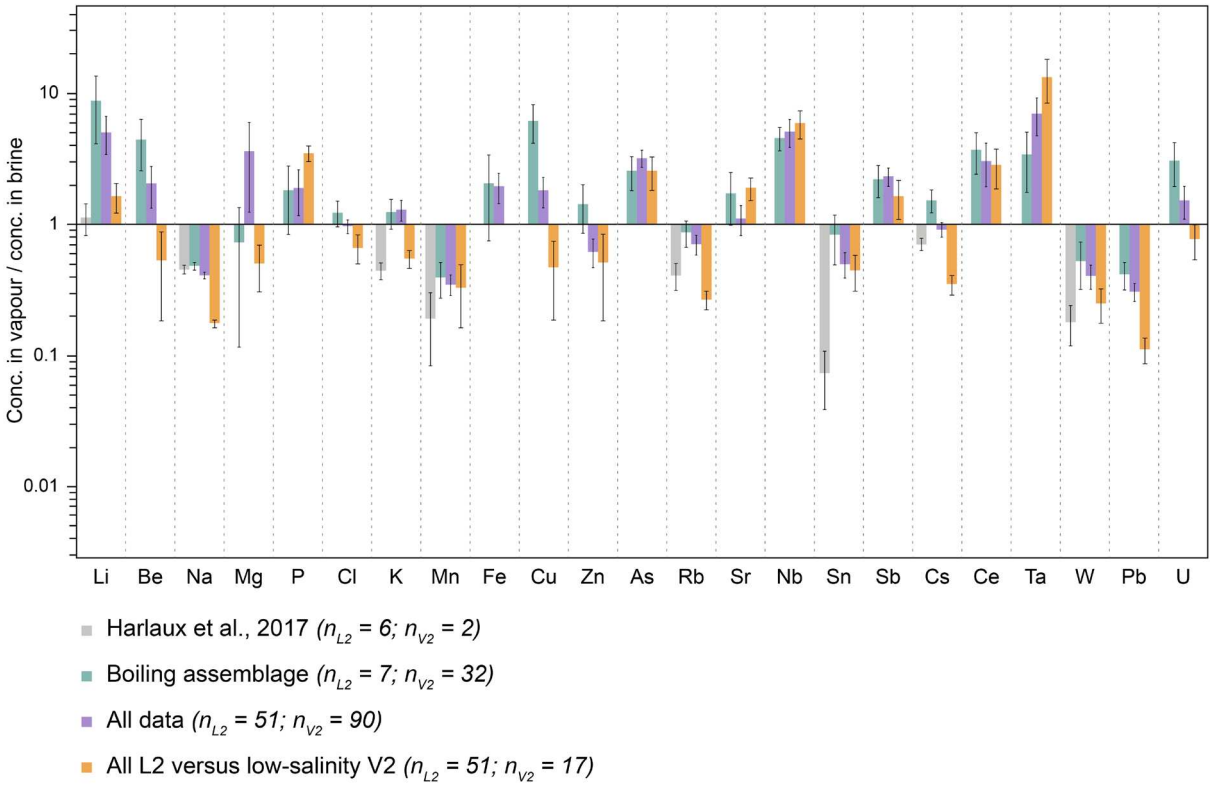



*Figure III.25. Partition coefficients between the L2 brine and V2 vapour formed through phase separation of the initial L1 magmatic fluids in the Beauvoir PRMG. The calculations are based on: (i) data from Harlaux et al. (2017); (ii) the boiling assemblage of coexisting L2- and V2-type fluid inclusions (FIs) identified along a growth plane in magmatic quartz (Fig. III.6d); (iii) all data for L2- and V2-type FIs obtained in this study; and (iv) data for L2-type FIs relative to data for V2-type FIs with salinities ≤ 10 wt% $(NaCl+KCl)_{eq}$. Error bars are estimated using the formula: $\sigma = R \times \sqrt{\frac{\sigma_V{}^2}{V} + \frac{\sigma_L{}^2}{L}}$, where L and V are the mean concentrations of an element in the L2- and V2-type FIs, respectively, R is the ratio of these mean concentrations (V/L), and $\sigma_L$ and $\sigma_V$ are the standard deviations associated with L2- and V2-type FIs, respectively.*

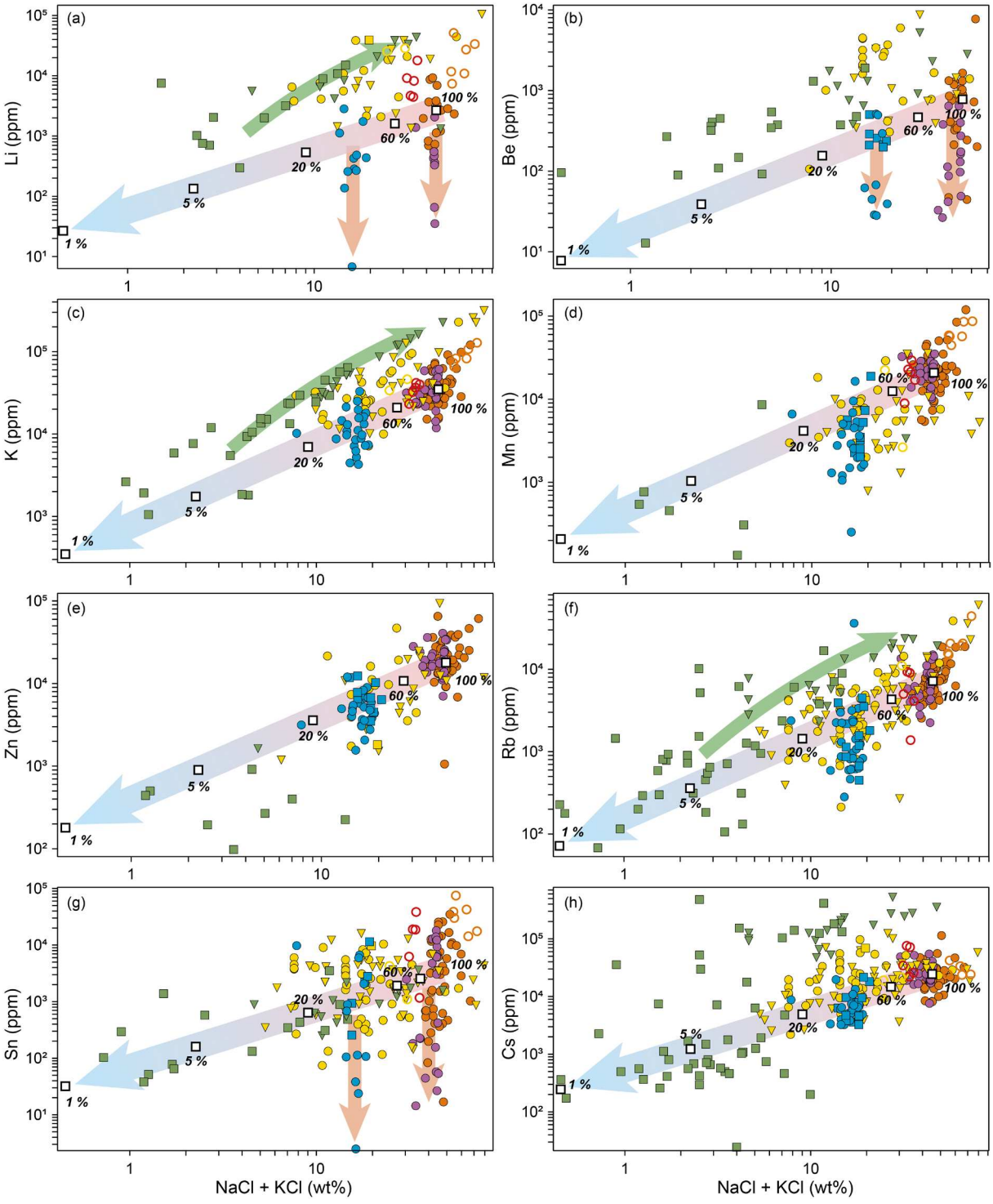
The partitioning behaviour of elements during phase separation in high-temperature magmatic-hydrothermal systems has been the subject of many studies (e.g., Heinrich et al., 1992, 1999; Audétat et al., 2000a, 2008; Audétat and Pettke, 2003; Foustoukos and Seyfried, 2007; Audétat, 2019). Lithium and As have been shown to preferentially partition into the vapour phase, whereas Na, K, Mn, Fe, Zn, Rb, Cs, W, Pb have a preferential affinity for the coexisting Cl-bearing liquid phase. The preferential partitioning of Cu in the vapour phase has also been suggested in some studies (Heinrich et al., 1999; Audétat et al., 2000a), although the high vapour/brine partition coefficients determined on natural boiling assemblages have been later considered as an artefact resulting from post entrapment diffusion of Cu into the vapour-dominated fluid inclusion (Lerchbaumer and Audétat, 2012; Seo and Heinrich, 2013). In the Beauvoir PRMG, the relative enrichment of Li in the vapour with the relative depletion in Na, Mn, and Pb are consistent with other experimental studies. However, enrichments of K, Fe, Zn in the vapour phase contrasts with their expected behaviour, which could be explained by the unconventional moderate salinity of V2-type FIs. Finally, Nb and Ta are known to form stable complexes with fluorine and their hydrothermal mobility is significantly enhanced in acid, F-rich fluids circulating at moderate to high temperatures (e.g., Webster, 1990; Zaraisky et al., 2010; Timofeev et al., 2015; Akinfiev et al., 2020; Liu et al., 2024; Hu et al., 2024). Their enrichment in the V2 magmatic vapour may indicate a higher fluorine content in the vapour phase relative to the L2 brine (Fig. III.25). While partition coefficients for fluorine during phase separation in magmatic-hydrothermal systems remain poorly constrained, fluid/melt partition coefficients for fluorine in felsic systems are relatively low, typically below 1 (Webster and Holloway, 1990; Xiaolin et al., 1998; Cassidy et al., 2022). Moreover, Webster and Holloway (1990) shown that fluid/melt partitioning for F is influenced by diverse parameters including F concentration of the melt. As previously discussed by Cuney et al. (1992) for the Beauvoir PRMG, a F content of *ca.* 4 wt% for the melt – a value likely reached in the Beauvoir system, taking into account the F loss, and later confirmed by the analyses of melt inclusions from the B1 unit (Kovalenko et al., 1998) – would yield a partitioning coefficient of *ca.* 0.5 (Webster and Holloway (1990), resulting in a F concentration of *ca.* 2 wt% for the magmatic fluids in equilibrium. Such F enrichment in magmatic fluids aligns with the observed topaz alteration in the La Bosse stockwork, which has been attributed to the percolation of fluids originating from the Beauvoir melts (Cuney et al., 1992; Monnier et al., 2020). The experimental study of Webster (1990) further supports the possible F-rich nature of magmatic fluids related to F-rich melts by demonstrating that fluorine preferentially partitions into aqueous fluids over $CO_2$-rich fluids and that F enrichment in silicate melts can significantly influence fluid composition during magma evolution. Despite the unexpectedly high concentrations of Nb, Ta, and Li, particularly in the vapour phase and to a lesser extent in the brine, these values appear therefore consistent with the exceptionally F-rich nature of the Beauvoir system.

*3.3.2.ii. Dilution of magmatic fluids by low-salinity fluids?*

In the Beauvoir PRMG, magmatic quartz hosts a diversity of FI types, exhibiting a broad yet fragmented range of salinities from 0.5 and 60 wt% $(NaCl+KCl)_{eq}$ and homogenisation temperatures spanning from *ca.* 110 °C to over 600 °C (Aïssa et al., 1987; Harlaux et al., 2017; this study) (Fig. III.24). The distinction between early magmatic fluids (L1, L2, and V2) and later magmatic to hydrothermal fluids (L3-L4, L5-L6, and L7) is evidenced by their respective salinity and homogenisation temperature ranges (Aïssa et al., 1987). However, despite detailed petrographic characterisation of fluid inclusion assemblages and careful consideration of their relationship to quartz zonation, establishing a complete relative chronology among the later magmatic to hydrothermal fluids remains challenging. This difficulty arises from the occurrence of L3-L4, L5-L6, and L7 inclusions in secondary to pseudo-secondary trails, the lack of observable crosscutting relationships and the similarity of homogenisation temperatures. Nonetheless, a plausible origin for these fluids has been proposed by Aïssa et al. (1987): L7 fluids likely resulted from the cooling and further boiling of L2 brines, L3-L4 fluids are interpreted as external fluids, and L5-L6 fluids are mixtures between magmatic (L1, L2 and L7) and external end-members (Figs. III.24 and III.26).

The trace element chemistry of fluids from the Beauvoir magmatic-hydrothermal system is characterised by a concomitant decrease of salinity, non-precipitating elements such as K, Mn, Zn, Rb, Cs, and Pb, and a rough decrease in Be, W and Sn concentrations (Fig. III.26). No clear trend can be identified for Sr, Nb, Ta, U, whose concentrations in the L2 magmatic brines and V2 magmatic vapours are already relatively low (Figs. III.22m, n, s, v). A positive correlation between salinity and trace element contents may reflect a low-pressure magmatic fractionation trend (Audétat, 2019); however, in this case, the lowest salinity fluids should represent the earliest fluids and therefore have the highest homogenisation temperatures. In the Beauvoir PRMG, the observed trend likely records the dilution of magmatic fluids by low-salinity external fluids, an evolution previously emphasised through FI petrography and microthermometry (Aïssa et al., 1987; Cuney et al., 1992) (Fig. III.24). The incursion of external fluids has been similarly highlighted in other magmatic-hydrothermal systems, such as the Mole granite (Audétat et al., 1998) and the Cornubian batholith (Bongiovanni et al., 2024). Mixing dynamics between magmatic and external fluids in the Beauvoir system are thought to primarily involve magmatic brines (L1, L2, and L7), with magmatic vapours (V2) being excluded from this process (Aïssa et al., 1987; Cuney et al., 1992). When excluding the V2 vapours, the decrease in salinity and element concentrations in not continuous across FI types (Fig. III.26). This fragmented trend suggests that dilution may not have occurred *in-situ*, at the depths where the samples were collected (379.0 and 390.9 m depth along GPF1 drillhole), but instead, upstream. The dilution of magmatic brines by external fluids at the apex of the Beauvoir intrusion appears consistent

with numeric models presented by Weis (2012), which propose the development of meteoric fluid convection cells at the upper levels of magmatic-hydrothermal systems.




*(Figure continued on the next page)*

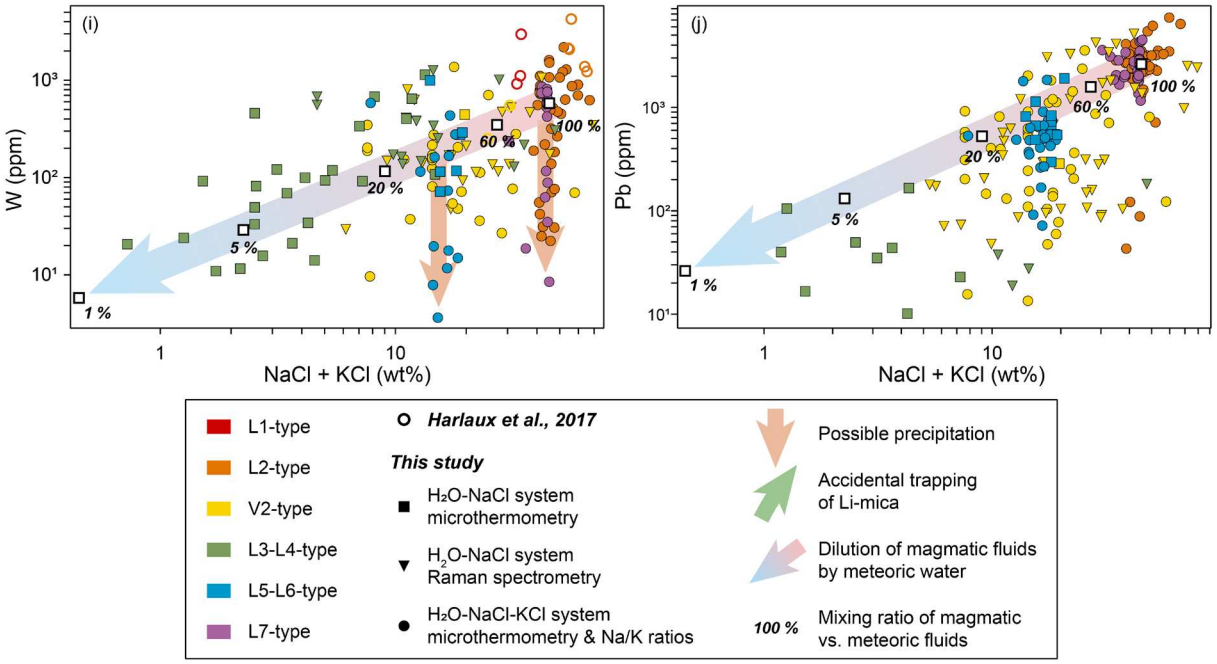



*Figure III.26. Concentrations of representative elements vs. total salinity (NaCl + KCl) for the distinct FI types hosted in magmatic quartz from the Beauvoir PRMG, showing three main trends (i.e., possible precipitation, accidental trapping of Li-mica and dilution of magmatic fluids by meteoric water). The envelope associated with the mixing trend represents the ideal concentration estimated by mixing between the median concentration of L2-type FIs and pure water. It is likely that V2-type fluid inclusions were minimally affected by this dilution process.*

Although the origin of low-salinity fluids invading the Beauvoir magmatic-hydrothermal system was not fully constrained, previous studies suggested a mixture of magmatic, metamorphic, and meteoric fluids, with a dominant meteoric contribution (Aïssa et al., 1987; Cuney et al., 1992). Meteoric fluids were hypothesised to infiltrate the Beauvoir melts under supra-solidus conditions, leading to a decrease in the oxygen isotopic composition of magmatic minerals from depth to the surface (Fouillac et al., 1987; Fouillac and Rossi, 1991). The elemental and oxygen isotopic chemistry of the early hydrothermal apatite generation (type II) also supports a gradual infiltration of oxidising meteoric fluids within the system, but under near-solidus conditions (Part II; Rocher et al., 2024). The dilution trends observed in FI data for elements such as Be, K, Mn, Zn, Rb, Sn, Cs, W, and Pb further suggest that the mixture of external fluids with magmatic fluids approached the composition of pure water (Fig. III.26). The dispersion in the compositions is likely a result of fluid-rock interactions and the accidental trapping of minerals (section 3.3.2.iii of Part III) or precipitation processes (section 3.3.2.iv of Part III). Based on these lines of evidence, the low-salinity external fluids responsible for diluting magmatic fluids are most likely of meteoric origin and its contribution within the Beauvoir magmatic-hydrothermal system may have reached up to *ca.* 95 %. The absence of low-salinity L3-L4-type FIs in primary assemblages within magmatic quartz (Aïssa et al., 1987; Harlaux et al., 2017; this study) combined with early hydrothermal apatite geochemistry, suggests that the incursion of meteoric fluids occurred under sub-solidus conditions. This interpretation contrasts

with the supra-solidus infiltration hypothesis proposed by Fouillac et al. (1987) and Fouillac and Rossi (1991).

*3.3.2.iii. Possible evidence of accidental trapping of Li-micas?*

Lithium concentrations exhibit a complex distribution among FI types, likely reflecting the superposition of at least boiling and dilution effects. Interestingly, the highest Li concentrations, observed in V2- and L3-L4-type FIs, correlate with elevated concentrations of K and Rb, elements that are key constituents of mica (Figs. III.26 and III.27). In the case of V2-type FIs, their occurrence as primary fluid inclusions within magmatic quartz suggests that these magmatic vapours circulated under supra-solidus conditions (Fig. III.6e; section 2.2.2 of Part III). The extreme Li concentrations in V2-type FIs may be attributed to the accidental trapping of Li-micas crystallising from the residual melt, whose presence within V2-type FIs was inferred by Raman spectrometry (section 2.2.2 of Part III).

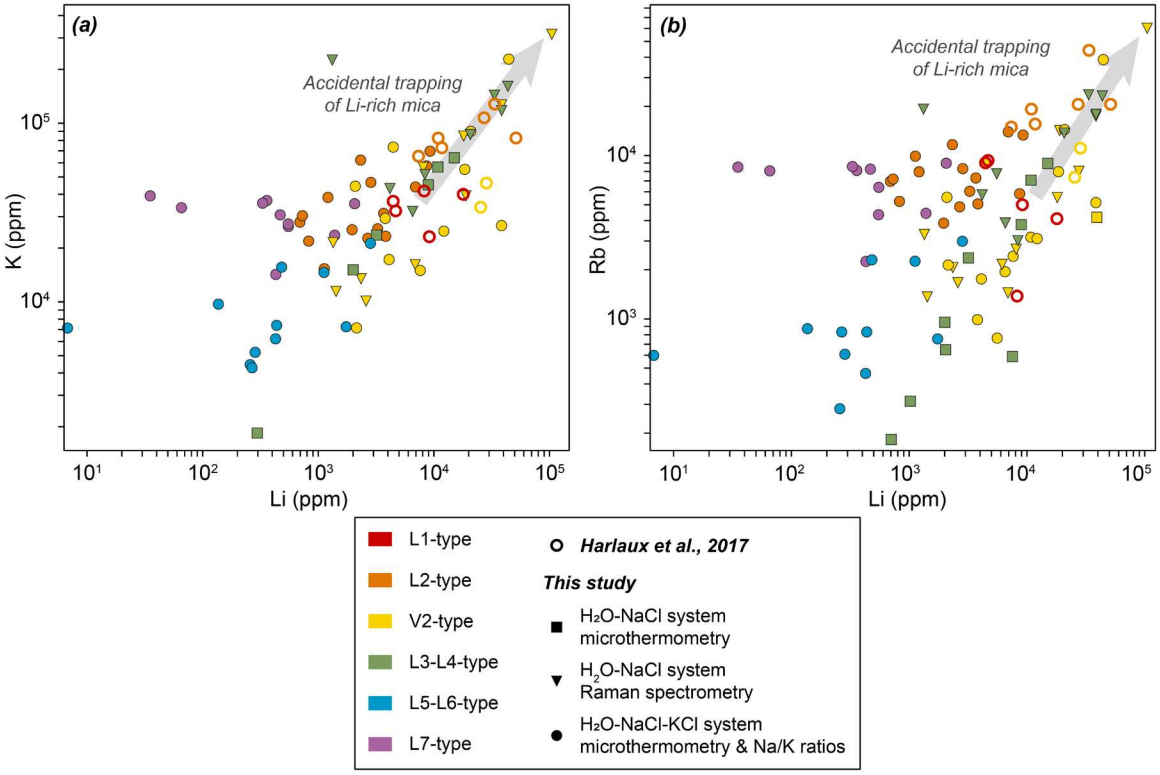



*Figure III.27. Biplots of K vs. Li (a) and Rb vs. Li (b) for the distinct FI types hosted in magmatic quartz from the Beauvoir PRMG. Symbols indicate the chemical system used for salinity estimation: either the H₂O-NaCl binary system (determined via microthermometry or Raman spectrometry) or the H₂O-NaCl-KCl ternary system (estimated using microthermometry data and Na/K ratios). The highest Li concentrations, observed in V2- and L3-L4-type fluid inclusions, appear to correlate with elevated K and Rb concentrations. Previously published data for L1-, L2-, and V2-type fluid inclusions are included for comparison (Harlaux et al., 2017).*

The circulation of L3-L4 fluids was responsible for extensive greisen alteration of the Beauvoir PRMG and its surrounding rocks (Cuney et al., 1992; Monnier et al., 2020). Greisen alteration is characterised by the pervasive replacement of igneous minerals, primarily feldspar (± quartz and lepidolite), with a typical quartz-muscovite assemblage, commonly associated with the

precipitation of other secondary minerals (e.g., apatite, topaz, cassiterite, columbite- and pyrochlore-group minerals), as well as by the formation of millimetric quartz-muscovite veins (Merceron et al., 1987; Monnier et al., 2018, 2019). Similar to V2-type FIs, the presence of trapped mica within L3-L4-type FIs has been confirmed through Raman spectrometry. These micas could likely originate from the sub-solidus entrapment of either altered igneous Li-mica or greisen-related muscovite.

While many elements tend to become depleted with increasing dilution of the Beauvoir magmatic fluids, relatively high As concentrations are observed in the L3-L4 low-salinity fluids (Fig. III.22k). As discussed in relation to late hydrothermal apatite associated with F-mineralisation in the Beauvoir PRMG (type IIIa; Part II), arsenic may be liberated from sulphide species, such as arsenopyrite (FeAsS) and arsenian pyrite ($Fe(S,As)_2$), under oxidising conditions (Smedley and Kinniburgh, 2002). The Sioule mica schists, into which the Beauvoir PRMG intruded, are characterised by elevated As concentrations ranging from 130 and 170 ppm, likely hosted within sulphide minerals (whole rock data in Table II.A9 of Appendix II.A4). Hydrothermal alteration of these rocks under oxidised conditions could have released significant amount of arsenic into the L3-L4 fluids. Alternatively, the high variability in As content and the anomalously high arsenic concentrations of approximately 120,000 ppm may be better explained by accidental trapping of As-bearing mineral inclusions within the L3-L4-type FIs, resulting from the alteration of mica schist enclaves present within the Beauvoir PRMG.

#### *3.3.2.iv. Processes triggering ore-bearing minerals precipitation?*

Significant variability, spanning up to three orders of magnitude, is observed for Li, Be, Sn, and W concentrations within individual FI types. This is particularly evident in L2, L5-L6 and L7 fluids, where such variability occurs without notable changes in fluid salinity, suggesting possible precipitation trends rather than dilution effects (Fig. III.26). In the Beauvoir PRMG, these rare-metals are hosted in ore-bearing minerals, including lepidolite (Li-W), Li- and Be-phosphates, cassiterite (Sn), and columbite-group minerals (Nb-Ta-W) (Cuney et al., 1992). A substantial spread in Sn content has also been reported in L1-type FIs, attributed to the heterogeneous trapping of cassiterite nano-inclusions rather than $SnO_2$ oversaturation of the magmatic fluid (Harlaux et al., 2017). This section explores additional processes that may account for the variability in rare-metal content within the Beauvoir magmatic-hydrothermal fluids.

Although fluid mixing between magmatic and meteoric fluids is widely recognised as a key mechanism triggering cassiterite precipitation in Sn(-W) granite-related deposits (Witt, 1988; Heinrich, 1990; Audétat et al., 1998; Karimzadeh Somarin and Ashley, 2004; Fekete et al., 2016; Liu et al., 2020; Chen et al., 2023; Peng et al., 2023a), other processes, such as phase separation, fluid-rock interaction, and simple cooling, have also been proposed (e.g., Heinrich, 1990; Ni et al.,

2022; Liu et al., 2023). The high-salinity L2 and L7 fluid generations are thought to result from fluid immiscibility during boiling of magmatic fluids in the B1 unit (Aïssa et al., 1987; Cuney et al., 1992). Vapour separation from L2 and L7 brines may have triggered Sn and other rare-metal precipitation, accounting for the observed decrease in their concentrations in FI data.

Furthermore, $SnO_2$ solubility in Cl-F-bearing magmatic fluids is known to decrease with both decreasing fluid acidity ($m_{HCl,aq}$) and increasing oxygen fugacity ($fO_2$) (Taylor and Wall, 1993). Progressive degassing of silicate melts has been shown to increase oxygen fugacity by up to two log units in sulphur-free magmas (Burgisser and Scaillet, 2007). In hydrous, F-bearing leucogranitic and pegmatitic magmas, the impact of devolatilisation on their oxidation state has been further explored by Pichavant et al. (2016). They introduced the concept of "self-oxidation" to explain the oxidising conditions necessary for muscovite crystallisation. This mechanism involves the dissociation of $H_2O$ during the gradual loss of volatiles in volatile-rich melts, leading to the production of HF as a gas phase and an increase in the concentration of oxygen anions in the melt. The reaction is as follows:

$$\underset{melt/gas}{H_2O} + \underset{melt}{2F^{2-}} = \underset{gas}{2HF} + \underset{melt}{O^{2-}}$$

The loss of hydrogen as HF gas decreases the cation-to-oxygen ratio in the melt, thereby increasing its oxidation state. This hypothesis aligns with the evidence of increasing $fO_2$ during the differentiation of the Beauvoir granitic magma, as indicated by the decrease in the $Fe^{3+}/Fe^{2+}$ ratio of Li-micas from the B3 to B1 units (Cuney et al., 1992) and corroborated by crystallisation experiments (Pichavant, 2022). While earlier hypotheses involving interaction of the melts with oxidising meteoric fluids (Fouillac et al., 1987; Fouillac and Rossi, 1991) face significant physical limitations (e.g., Weis et al., 2012), the influence of degassing from the B1 F-rich melt on cassiterite precipitation from magmatic brines appears plausible. This is supported by the exclusive presence of magmatic fluid inclusions within the B1 unit, which suggests significant devolatilisation of the B1 melt compared to the B2 and B3 melts (Aïssa et al., 1987). Interestingly, cassiterite inclusions within magmatic quartz are observed only in the B1 unit, sometimes in close association with magmatic fluid inclusions in primary growth planes (Figs. III.6d-e; section 2 of Part III). This spatial association reinforces the idea that processes related to melt degassing and fluid immiscibility in the B1 unit played a critical role in Sn precipitation under supra-solidus conditions (and possibly other metals). Finally, Li variability in magmatic fluid inclusions (L2- and L7-type) may derive from the formation of Li-richer overgrowths around magmatic lepidolite, which was proposed to precipitate from Li-rich magmatic fluids (Monier et al., 1987).

The variability in rare-metal concentrations observed in L5-L6-type FIs likely reflects a slightly different process, as these fluids are not associated with boiling evidence and represent

intermediate fluids between magmatic high-salinity and external low-salinity end-members (section 3.3.2.ii of Part III). As previously noted, $SnO_2$ saturation in Cl-F-bearing magmatic fluids is promoted by decreasing fluid acidity ($m_{HCl,aq}$) and increasing oxygen fugacity ($fO_2$) (Taylor and Wall, 1993). During the circulation of L5-L6 fluids within the Beauvoir magmatic-hydrothermal system, the progressive infiltration of external low-salinity fluids may have shifted the redox conditions toward more oxidised states. This hypothesis readily accounts for the observed decrease in Sn concentrations in L5-L6-type FIs. However, it provides a less straightforward explanation for the precipitation of Li, Be, and W, which could instead result from fluid cooling or fluid-rock interactions.

## 4. Trace elements and oxygen isotopes in quartz as tracers of the magmatic-hydrothermal evolution

The petrographic characterisation of fluid inclusions hosted in magmatic quartz from the B1 unit of the Beauvoir PRMG reveals the presence of primary FI assemblages, reflecting significant devolatilisation of the melt (Aïssa, 1987; this study). This finding sharply contrasts with the less evolved B2 and B3 units, where magmatic quartz lacks primary FIs. While devolatilisation processes have been proposed as a key mechanism for the formation of snowball-textured quartz in the B1 unit (section 2.3 of Part III), it is likely that they also influenced the crystallisation of the B1 melt in other ways. The critical role of fluid dynamics during the magmatic-hydrothermal stage in the formation of rare-metal granite deposits has long been emphasised, yet it remains frequently underestimated in genetic models. (e.g., Badanina et al., 2004; Müller et al., 2018b; Kaeter et al., 2018; Ballouard et al., 2020a; Pfister et al., 2023). This section explores the trace element and oxygen isotopic signatures of magmatic quartz to unravel the fluid-melt interactions that may have influenced the crystallisation of the Beauvoir magmas.

### 4.1. Material and methods

#### *4.1.1. Laser ablation – inductively coupled plasma – mass spectrometry*

Similar to the analysis of FI compositions discussed in section 2 of Part III, the trace element content of magmatic quartz was analysed by LA-ICP-MS at ETH Zürich (ETHZ, Switzerland), using a GeoLas (Coherent) laser ablation system (193 nm ArF excimer laser) coupled to a quadrupole ICP-MS (Perkin Elmer Nexion 2000 DRC) (Günther et al., 1997, 1998; Heinrich et al., 2003). Laser ablation was performed with a constant repetition rate of 10 Hz and laser energy densities of 15–20 J.cm$^{-2}$. Each analysis included a 30-second background acquisition period prior to ablation, which lasted approximately 35 s and was followed by a 40-second cell washout. To mitigate quartz explosion during ablation, an iris aperture was progressively and manually opened from ~3–5 µm to 40 µm during the analysis (Guillong and Heinrich, 2007), with the ablation spots positioned over or near the SIMS spots. The ablation aerosol was removed from the cell by constant He flux (1 L.min$^{-1}$), then mixed with make-up gas (Ar, *ca.* 1 L min$^{-1}$) and homogenised

via a squid device before introduction into the plasma torch. Before each analytical session, the LA-ICP-MS system was optimised using NIST SRM 610 glass to maximise sensitivity while maintaining a Th/U ratio close to 1.0 and a ThO/Th ratio below 0.5 %. Following the analytical setup implemented by Monnier et al. (2018) for the Beauvoir granite, all quartz crystals were analysed for the following isotopes: $^{7}$Li, $^{9}$Be, $^{11}$B, $^{23}$Na, $^{27}$Al, $^{49}$Ti, $^{72}$Ge, $^{85}$Rb, $^{88}$Sr, $^{93}$Nb, $^{118}$Sn, $^{121}$Sb, $^{181}$Ta, and $^{184}$W. Dwell times for individual elements are provided in Table III.A6 in Appendix III.A4.

LA-ICP-MS transient signals were processed with Iolite v4 software using the "Trace element" data reduction scheme (Paton et al., 2011). All ablation spectra were carefully inspected for anomalous peaks, which could indicate the presence of fluid or mineral inclusions. The NIST SRM 610 glass (Jochum et al., 2011) and quartz standard BGS-Q1 (Audétat et al., 2015) were analysed twice before and after groups of maximum 24 unknowns analyses. NIST SRM 610 glass served as the primary external reference material for correcting mass bias and instrumental drift, while the signal of $Si^{29}$ within quartz was used as the internal standard, assuming a stoichiometric Si content of 46.74 wt.%. The BGS-Q1 natural quartz crystal from Shandong province (China) was used as a secondary control material to verify the accuracy and reliability of the measurements. The measured concentrations for Li, Ti, and Al deviated by no more than 5 % from reported values (Audétat et al., 2015). The average limit of detection (LOD) for each element was estimated following the method of Longerich et al. (1997) and is provided in Table III.A7 in Appendix III.A4.

#### *4.1.2. Secondary ion mass spectrometry (SIMS)*

Similar to the O isotope analysis of apatite detailed in Part II, *in-situ* oxygen isotope microanalysis of quartz and cassiterite was performed at the CRPG using a Cameca IMS 1270-E7 large geometry ion microprobe (SIMS). Analysis spots were carefully positioned to best assess the distinct micro-domain identified through CL imaging. Each analysis involved the following steps: (i) a 120-second background noise measurement of the Faraday collectors for subsequent calculation of internal error, (ii) 90 s of pre-sputtering the target area in the quartz grain with a 20x20 µm raster beam to remove the gold coating and minimise surface contamination, (iii) sputtering of the quartz to generate a secondary ion beam, (iv) acceleration of the negative secondary $^{16,18}$O ions at 10 kV and automatic mass centering in the deflector contrast and field apertures, and (v) collection of 30 to 40 cycles of $^{16}$O and $^{18}$O signals. During step (iii), a primary $Cs^{+}$ ion beam with an intensity of 2 nA and a bombardment energy of 10 kV was focused on a 10x10 µm raster area to sputter oxygen ions from the quartz. Charge build-up at the sample surface was compensated by a normal-incident electron gun (NEG) beam. Following the mass centering on $^{16}$O isotope (step (iv)), measurements were conducted on Faraday collectors in multicollection mode, with an integration time ranging from 150 to 200 s (30 to 40 cycles of *ca.*

5 s). The mass resolution was set to 5000 M/ΔM, and the energy slit was opened to 30 eV.

Instrumental mass fractionation (IMF) corrections were performed by analysing matrix-matched reference materials, specifically the Bresil and Sonar 2 quartz, or the Yongde cassiterite (Li et al., 2022). Analytical precision was evaluated by calculating the internal error (or internal precision, 2SE) and external error (reproducibility, 2SD), both of which depend on the secondary ion beam intensity and integration time. The internal error on $\delta^{18}O$ was systematically below 0.30 ‰ (2SE) for both quartz and cassiterite, with an average value of approximately 0.08 ‰ and 0.15 ‰, respectively. The long-term external error (2SD) was assessed through multiple analyses of the two matrix-matched standards for quartz and varied from *ca.* 0.12 ‰ to 0.42 ‰, reflecting changes in the analytical conditions, particularly integration time. For cassiterite, repeated measurements of the Yongde cassiterite yielded a long-term external error of *ca.* 0.14 ‰. The total analytical uncertainty, reported as the quadratic sum of the internal error and the external error of the reference material, ranges from 0.24 ‰ to 0.46 ‰ (mean ~ 0.30 ‰) for quartz and from 0.12 to 0.61 ‰ (mean ~ 0.32 ‰) for cassiterite. The $^{18}O/^{16}O$ ratios are expressed as $\delta^{18}O$ values and normalised to the Vienna Standard Mean Ocean Water (VSMOW) composition ($^{18}O/^{16}O$ = 0.0020052; Baertschi, 1976), as outlined in the following equation:

$$\delta^{18}O_{measured}\ (‰) = \left[\frac{^{18}O}{^{16}O}_{measured} \div \frac{^{18}O}{^{16}O}_{VSMOW} - 1\right] \times 1000$$

## 4.2. Results

### *4.2.1. Quartz trace elements*

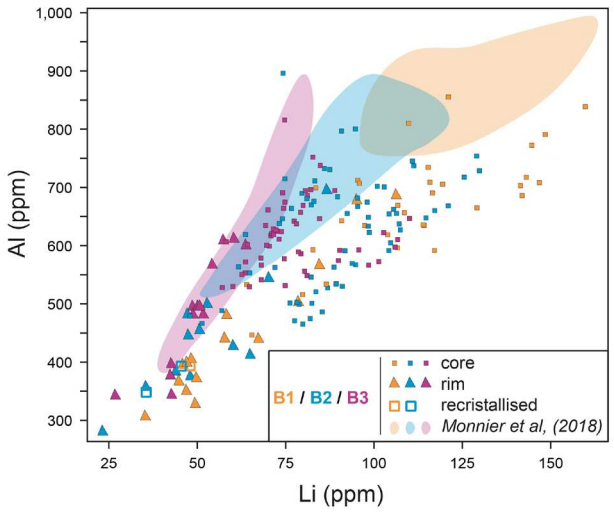



*Figure III.28. Al vs. Li diagram showing a rough positive correlation between the two elements. In all three magmatic units, Li and Al contents tend to decrease near grain boundaries.*

Among the analysed elements, only Li and Al were consistently detected, whereas Na was below the detection limit in *ca.* 60 % of measurements, Rb in 85 %, and Ti and B in 10 %. Ta and W were detected in less than 1 % of analyses, and all other elements (i.e., Be, Ge, Sr, Nb, Sn, Sb) were not detected.

Lithium and Al contents range from approximately 20 to 160 ppm and 285 to 900 ppm, respectively, across the three magmatic units. Those concentration ranges are globally consistent with the values previously reported by Monnier et al. (2018), with *ca.* 40–160 ppm Li and 400–1000 ppm Al, albeit slightly lower for Al (Fig. III.28).

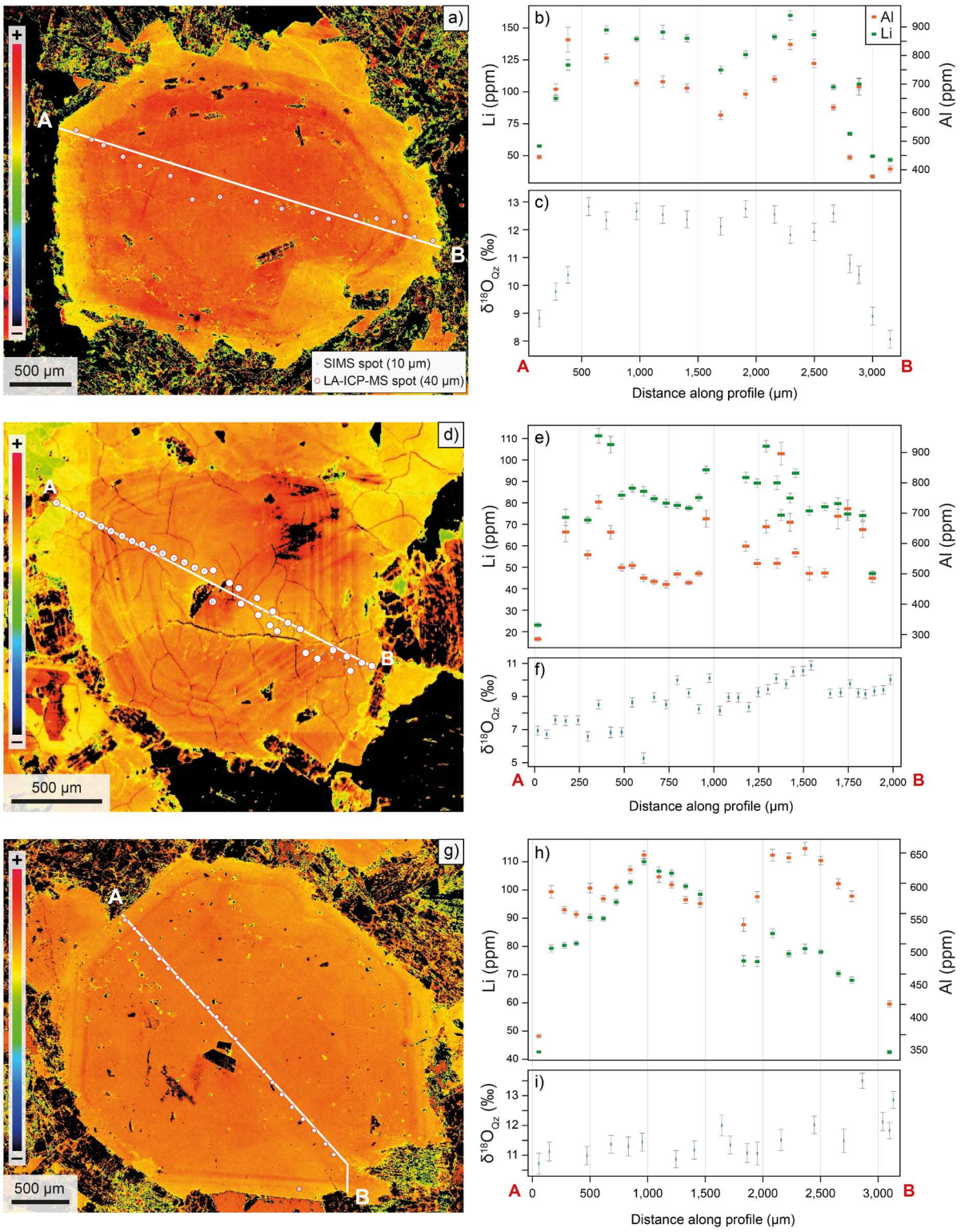



*Figure III.29. SEM-CL images of magmatic quartz associated with Al and Li concentrations and $\delta^{18}O$ ratios along profiles A-B for the B1 (a-c), B2 (d-f) and B3 (g-i) units. The data for the B2 unit correspond to a quartz phenocryst exhibiting numerous microfractures, whereas quartz from the B1 and B3 units remains unaltered. The feature width reflects the size of the SIMS and LA-ICP-MS analytical spots.*

A rough correlation between Li and Al is observed (Figs. III.28 and III.29), likely reflecting the coupled substitution of $Si^{4+}$ by $Al^{3+}$ and $Li^{+}$ in quartz (e.g., Weil, 1984; Götze et al., 2004). Magmatic quartz from the three units overlap in terms of compositions. However, it is noteworthy that, for all three units, the lowest Al and Li contents are consistently found at the grain boundaries and in recrystallised zones, with an intra-grain variability ranging from *ca.* 30 to 110 ppm (mean ~ 65 ppm) (Figs. III.28 and III.29). Only considering data from quartz cores, a global increase of Al and Li concentrations can be seen from the B3 (~ 80 ppm Li and 620 ppm Al) to B1 (~ 110 ppm Li and 670 ppm Al), through B2 unit (~ 95 ppm Li and 625 ppm Al) (Fig. III.28). Such trend was previously attributed to magmatic differentiation by Monnier et al. (2018). The new dataset further highlights a core-to-rim trend partially hindering the early magmatic differentiation record, explaining the compositional overlap between the units not observed by Monnier et al. (2018).

Magmatic quartz from the Beauvoir granite also exhibit moderate Na concentrations ranging from *ca.* 2 to 145 ppm, low concentrations of B (4–14 ppm), Ti (3–6 ppm), Rb (1–16 ppm), and very low Ta and W concentrations both below 1 ppm. Magmatic quartz from the B3 unit is less rich in Rb (< 2 ppm) compared to the B1 and B2 units, whereas it is relatively enriched in B (mean ~ 6 ppm) and Ti (mean ~ 6 ppm).

#### *4.2.2. Quartz and cassiterite oxygen isotopes*

Magmatic quartz exhibits a wide range of O isotopic compositions throughout the Beauvoir intrusive complex, with $\delta^{18}O$ values varying from -4.9 to 14.3 ‰ (Figs. III.30a-c). This pronounced scatter is predominantly associated with magmatic quartz from the B1 and B2 units, which show $\delta^{18}O$ ratios ranging from 2.1 to 14.3 ‰ (mean ~ 8.8 ± 0.3 ‰) and -4.9 to 14.3 ‰ (mean ~ 8.8 ± 0.3 ‰), respectively (Figs. III.30a-b). In contrast, quartz from the B3 unit display a narrower range of $\delta^{18}O$ values (10.7–13.5 ‰; mean ~ 11.6 ± 0.3 ‰), with limited intra-grain variability (*ca.* 0.8–2.8 ‰) and no systematic core-to-rim disparity (Fig. III.30c).

In the B1 unit, the observed scatter appears to result from a systematic, progressive decrease in $\delta^{18}O$ ratios of *ca.* 4.8–7.8 ‰ from the core to the rim, a trend clearly identified in seven out of eight of the analysed grains (Figs. III.29c and III.30a). A single $\delta^{18}O$ value of 9.6 ± 0.3 ‰ was recorded in recrystallised zones within quartz, which does not introduce additional intra-granular variability. As detailed in section 2 of Part III, quartz from the B1 unit contains sparse cassiterite inclusions. Analysis of three such grains reveals that cassiterite inclusions are located towards the rims, where the oxygen isotopic composition of quartz is declining ($\delta^{18}O_{Qz}$ ~ 5.5–8.9 ‰) (Fig. III.31).

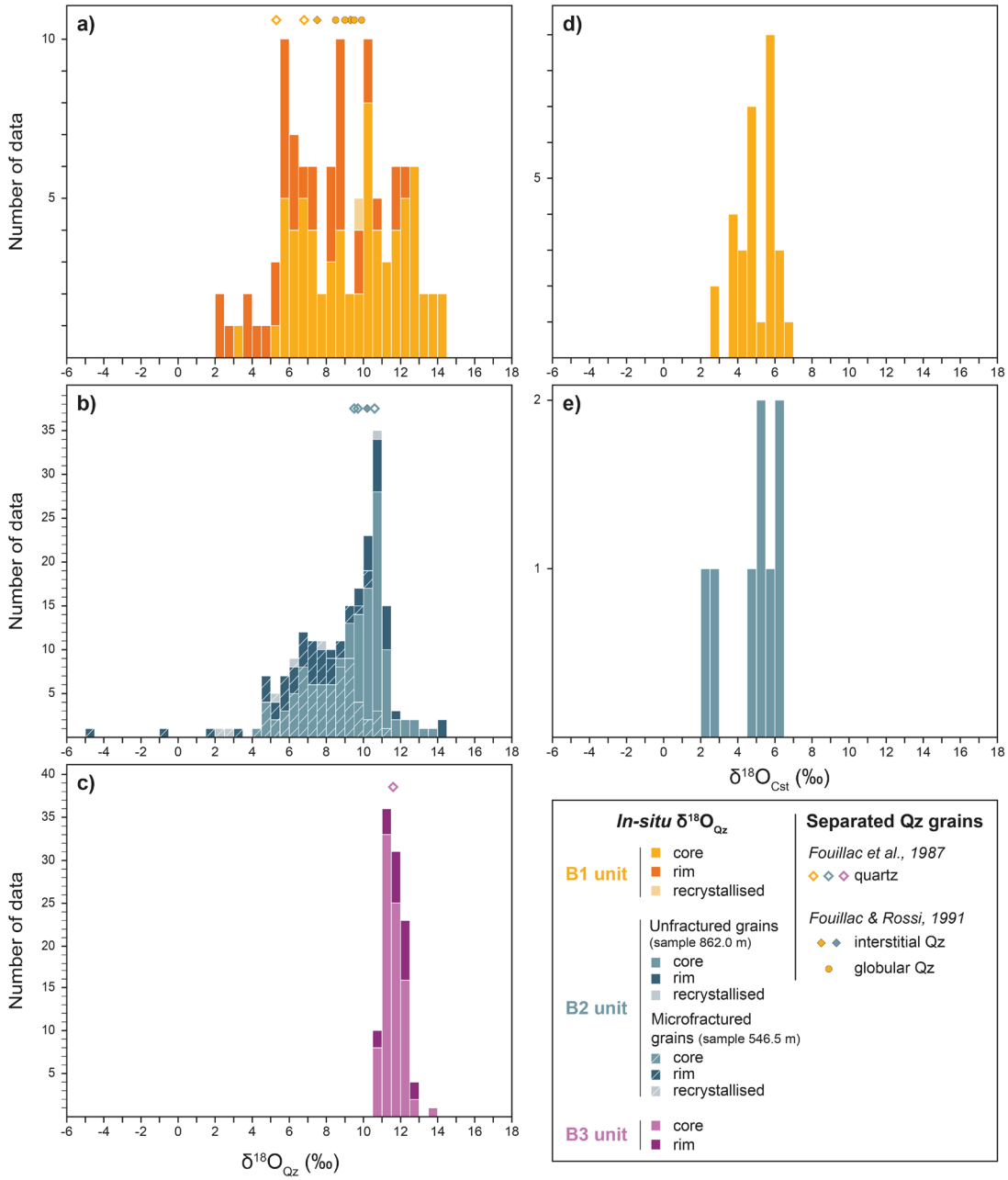



*Figure III.30. Oxygen isotopic compositions of magmatic quartz (a-c) and cassiterite (d-e). For quartz, colours associated with each units differentiate between core, rim, and recrystallised zones, whereas no such distinction is made for cassiterite. For comparison, $\delta^{18}O$ ratios of separated quartz grains reported by Fouillac et al. (1987) and Fouillac and Rossi (1991) are also shown. The uncertainties on these ratios are approximately 0.2 ‰ (Fouillac and Rossi, 1991), smaller than the size of the plotted features.*

The observed core-to-rim trend is a distinctive feature of quartz from the B1 unit, whereas $\delta^{18}O$ variability in the B2 unit primarily reflects intra-granular differences without a discernible pattern (Fig. III.29f). The $\delta^{18}O$ values range from 1.1 to 14.3 ‰ even when excluding recrystallised zones (Fig. III.30b). This variability is less pronounced in magmatic quartz from the sample collected at 862.0 m along the GPF1 drillhole (intra-grain variability ~ 1.1–3.7 ‰) compared to the sample from 546.5 m depth (~ 3.1–14.3 ‰) (Fig. III.30b). The latter is

characterised by numerous microfractures (see section 2.2.1 of Part III for petrographic details), with the observed variability primarily occurring in non-recrystallised zones along fractures. Similar to magmatic quartz in the B1 unit, recrystallised zones in the B2 unit (Fig. III.A2b in Appendix III.A1) do not generate greater intra-grain variability, with $\delta^{18}O$ ratios ranging from 2.9 to 7.4 ‰.

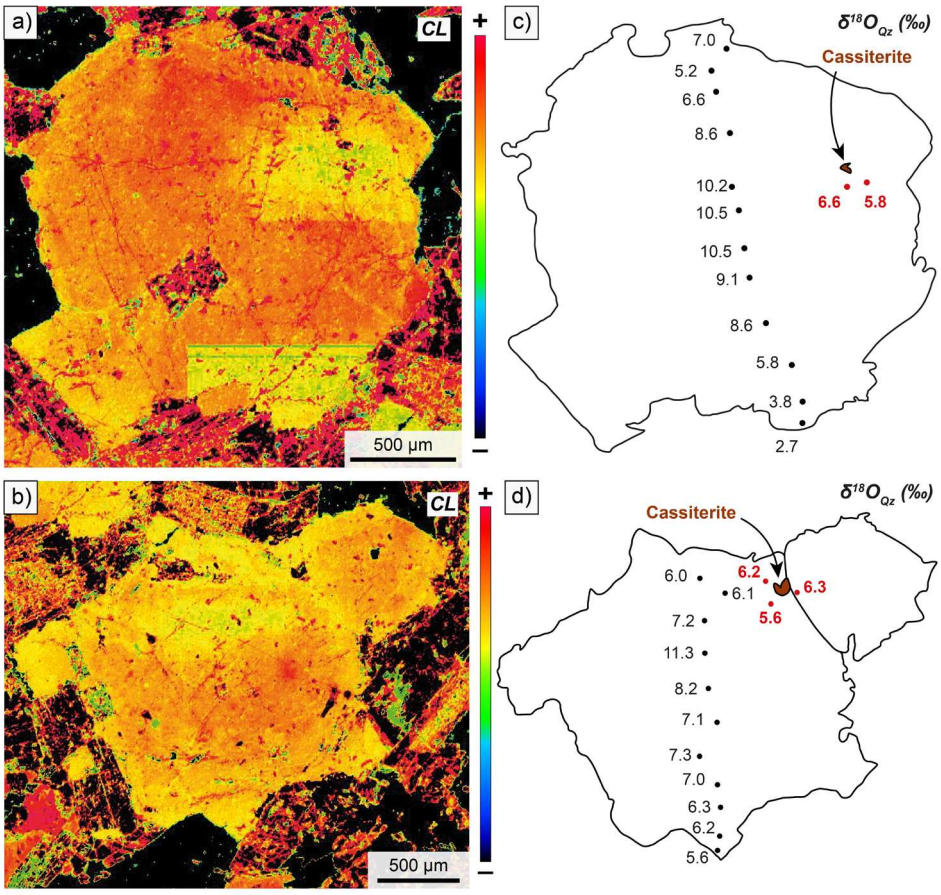



*Figure III.31. Cathodoluminescence images of quartz grains from the B1 unit (a-b) and associated $\delta^{18}O$ profiles across grains (c-d). Cassiterite inclusions occur in low- $\delta^{18}O$ quartz rims.*

Magmatic quartz from all three units exhibits comparable maximum $\delta^{18}O$ values; however, the B3 unit is distinguished by a higher mean $\delta^{18}O$ ratio (*ca.* 11.6 ± 0.3 ‰) compared to the B1 and B2 units, which share similar average $\delta^{18}O$ ratios of *ca.* 8.8 ± 0.3 ‰. Our *in-situ* analyses show slight discrepancies with previous O isotopic data obtained on separated quartz grains from the Beauvoir PRMG, which suggested a progressive decrease in $\delta^{18}O$ values from the B3 to B2 and B1 units (11.6 ‰, 9.5–10.6 ‰ and 5.3–9.9 ‰, respectively; Fouillac et al., 1987; Fouillac and Rossi, 1991) (Figs. III.30a-c). The mean $\delta^{18}O$ ratios from *in-situ* analyses and those from separated quartz grains show strong consistency for the B1 (mean ~ 8.8 ± 0.3 ‰ vs. 8.2 ± 0.2 ‰) and B3 (11.6 ± 0.3 ‰ vs. 11.6 ± 0.2 ‰) units. However, a discrepancy is observed in the B2 unit (8.8 ± 0.3 ‰ vs. 10.0 ± 0.2 ‰), essentially due to analyses of grains with numerous microfractures. When data from microfractured quartz crystals are excluded, the mean $\delta^{18}O$ value

for the B2 unit increases to 10.7 ± 0.3 ‰, aligning well with values obtained from separated quartz grains (10.0 ± 0.2 ‰; Fouillac et al., 1987; Fouillac and Rossi, 1991).

The oxygen isotopic composition of cassiterite was analysed in the B1 and B2 units, with a focus on crystals exhibiting close textural relationships with quartz (Figs. III.31 and III.32). This proved to be challenging, as such relationships are rare. Moreover, when cassiterite inclusions are present within quartz of the B1 unit, they are typically very small in size (*ca.* 20–100 µm) (Fig. III.31). Cassiterite from both units show comparable $\delta^{18}O$ ranges, varying from 2.6 to 6.9 ‰ (mean ~ 4.9 ± 0.3 ‰) in the B1 unit and from 2.4 to 6.4 ‰ (mean ~ 4.8 ± 0.3 ‰) in the B2 unit (Figs. III.30d-e). Variability in $\delta^{18}O_{Cst}$ ratios is observed at the grain scale, with intra-grain variations of *ca.* 1.0 to 4.0 ‰, depending on grain size.

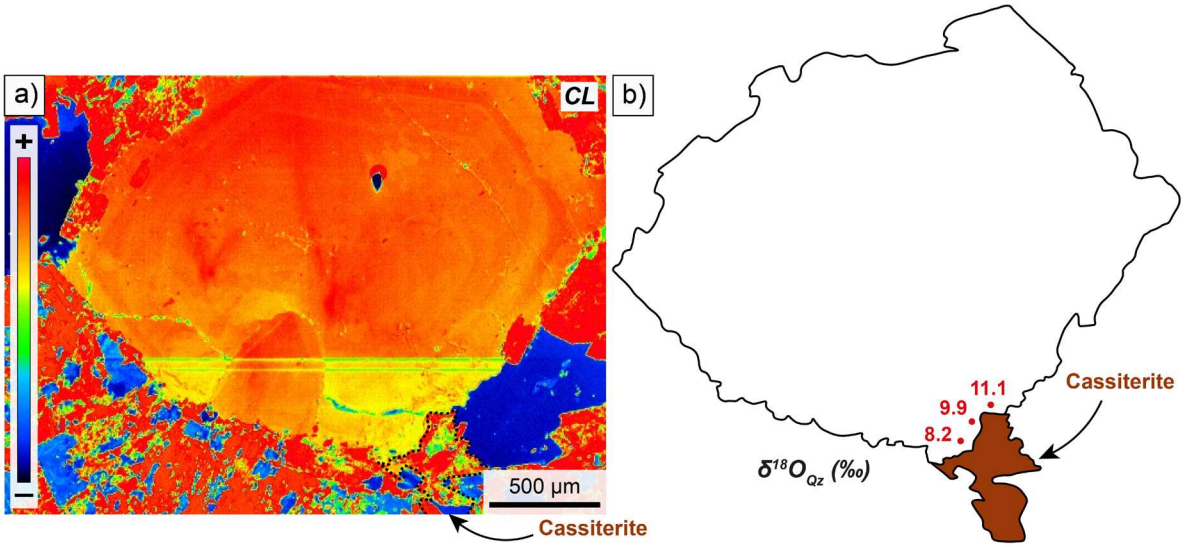



*Figure III.32. Cathodoluminescence image of magmatic quartz from the B2 unit (a) and associated $\delta^{18}O$ ratios of quartz at its contact with cassiterite (b).*

### 4.3. Preliminary discussion and conclusions

#### *4.3.1. Al and Li incorporation in magmatic quartz of the Beauvoir PRMG: influence of melt composition, partitioning behaviour, and co-crystallising phases*

Due to its highly stable atomic structure of Si-O bonds, combined with the small ionic radius and high valence of $Si^{4+}$, quartz incorporates only limited amounts of other elements into its crystal lattice. Aluminium represents the most common trace element found in quartz, likely reflecting the similarity in ionic radii between $Si^{4+}$ and $Al^{3+}$ (e.g., Dennen, 1966; Weil, 1984, 1993). The substitution of $Si^{4+}$ by $Al^{3+}$ is typically charge-balanced by cations occupying interstitial lattice sites. These charge-balancing cations predominantly include alkali ions such as $Li^{+}$, $Na^{+}$, $K^{+}$ and $H^{+}$, but may also include other ions such as those of Cu, Ag, Al, Fe, Ti, Co, Cr, Ni (Weil, 1984, 1993).

Enrichments in Al and rare elements like Li in quartz are characteristic of highly evolved, flux-rich magmas crystallising at low temperatures (e.g., Götze et al., 2004; Breiter and Müller, 2009; Breiter et al., 2013; Müller et al., 2018a; Michaud and Pichavant, 2020). This is particularly evident in quartz from the Beauvoir PRMG, which exhibits Al and Li concentrations ranging from *ca.* 285 to 990 ppm and 20 to 160 ppm, respectively (Monnier et al., 2018; this study). These concentrations are comparable to those reported for the Macusani Tuffs, representing extrusive equivalents of two-mica leucogranites and PRMGs, whose quartz phenocrysts feature Al concentrations of *ca.* 210–890 ppm and Li concentrations of *ca.* 50–200 ppm (Pichavant et al., 2024). The incorporation of Al and Li in quartz is controlled by multiple factors, including melt composition and notably Li-Al abundance, elemental partitioning between different mineral phases, and the pressure-temperature conditions of the system (e.g., Breiter et al., 2017; Müller et al., 2018a). The relationship between Al content in quartz and the aluminium saturation index of the melt (ASI) remains debated (Breiter and Müller, 2009). Nonetheless, in the Beauvoir PRMG, the three magmatic units differ in their peraluminous character, the ASI progressively increasing from the B3 to B2 and B1 units in relation with magmatic differentiation (e.g., Cuney et al., 1992; Raimbault et al., 1995). This differentiation trend, observed at the whole-rock scale, is consistent with increases in Li and Al concentrations in quartz cores across these units (Fig. III.28).

Monnier et al. (2018) previously highlighted such trend; however, this study emphasises an additional feature: a decrease in Li content at the rims of quartz crystals (Figs. III.28 and III.29). Within the Beauvoir PRMG, Li-bearing minerals such as lepidolite and, to a lesser extent, Li-phosphates, represent the primary hosts of Li at the magmatic stage (e.g., Cuney et al., 1992). The initiation of lepidolite crystallisation, which preferentially scavenges Li from the melt relative to quartz, is a conceivable cause for the observed Li depletion in quartz rims.

Both the differentiation trend highlighted from data in quartz cores and the Li depletion in rims align with crystallisation experiments of the Beauvoir PRMG, which identified quartz as an early phase to crystallise from the melt, preceding lepidolite formation (Pichavant et al., 1987a; Pichavant, 2022). These observations, together with petrographic observations detailed in section 2 (Part III), support a preservation of the initial magmatic signature of quartz crystals with early-magmatic cores and late-magmatic rims, as opposed to a sub-solidus metasomatic origin.

#### *4.3.2. Temperature estimation of quartz crystallisation*

##### *4.3.2.i. TitaniQ geothermobarometry*

Beyond the $[AlO4]^0$ centre, Ti, Ge and Fe commonly occur as trace-element crystallographic defects in quartz (Weil, 1984, 1993). The incorporation of Ti into quartz is influenced by its activity in the melt ($a_{TiO2}$), as well as by pressure, and most notably, temperature. Several empirical laws describing the behaviour of $TiO_2$ in quartz have been proposed (e.g., Wark and

Watson, 2006; Thomas et al., 2010; Huang and Audétat, 2012). While the Ti-in-quartz thermobarometer has proven to be a powerful tool for estimating quartz formation temperatures in felsic and intermediate igneous systems and has been successfully applied to quartz with low Ti contents (< 10 ppm) in some studies (Mao et al., 2017; Müller et al., 2018a; Ashworth et al., 2020; Pfister et al., 2024), its use in such cases has also raised challenges, occasionally yielding unrealistically high-pressure and low-temperature estimates for quartz crystallisation (Huang and Audétat, 2012; Breiter et al., 2012; Monnier et al., 2018; Wang D. et al., 2019).

The enrichment in Al and rare elements in quartz crystallising at low temperatures from highly evolved, flux-rich magmas is typically associated with significant titanium depletion (e.g., Götze et al., 2004; Breiter and Müller, 2009; Breiter et al., 2013; Müller et al., 2018a; Michaud and Pichavant, 2020). Quartz from the Beauvoir PRMG exhibits low Ti concentrations (< 0.7 to 17 ppm; Monnier et al., 2018; this study), resulting in the calculation of unrealistically low crystallisation temperatures for the Beauvoir melts by Monnier et al. (2018) (370–500 °C for the B2-B3 units and 350–450 °C for the B1 unit) under the assumptions of a pressure of 1 kbar and $a_{TiO2}$ values ranging from 0.2 to 1 (Fig. III.33a). In this study, the Ti concentrations of magmatic quartz are slightly lower than those previously reported for the Beauvoir PRMG (Monnier et al., 2018), and the influence on temperature estimates is briefly discussed in this section.

Two parameters are required to apply the TitaniQ method: accurate estimate of pressure and $a_{TiO2}$. In the Beauvoir PRMG, no Fe-Ti oxide appears to have crystallised at the magmatic stage and only secondary rutile has been observed (e.g., Monier et al., 1987; Cuney et al., 1992). As $TiO_2$ saturation was likely not reached, $a_{TiO2}$ was below 1.0 during the Beauvoir magmas emplacement (Ghiorso and Gualda, 2013). Moreover, a crystallisation pressure of approximately 0.8 kbar was estimated from the study of fluid inclusions hosted in magmatic quartz and topaz (Aïssa et al., 1987). Assuming a crystallisation pressure of 1kbar and $a_{TiO2}$ values varying between 0.2 and 1, temperatures calculated from the TitaniQ thermometer (Thomas et al., 2010) range from *ca.* 320 to 440 °C and 350 to 460 °C for the B2 and B3 units, respectively (Fig. III.33a). These temperatures are even lower than those reported by Monnier et al. (2018) and are inconsistent with the estimated crystallisation temperature range of *ca.* 670 to 550 °C for the Beauvoir melts, which encompasses liquidus to solidus temperatures (Pichavant, 2022).

If a crystallisation temperature of *ca.* 600 °C is assumed for magmatic quartz (Pichavant, 2022), with $a_{TiO2}$ still varying between 0.2 and 1, the corresponding pressures estimated using the TitaniQ barometer are unrealistically high, ranging from *ca.* 9 to 18 kbar for the B2 unit and 8 to 16 kbar for the B3 unit, even when considering an uncertainty of at least ± 1.2 kbar resulting from a temperature uncertainty of ± 25 °C (Fig. III.33b; Thomas et al., 2010). Therefore, as previously highlighted for the Beauvoir PRMG (Monnier et al., 2018) and similar systems (Huang

and Audétat, 2012; Breiter et al., 2012; Wang D. et al., 2019), the TitaniQ thermobarometer appears to be unreliable for quartz from PRMGs characterised by low Ti concentrations.

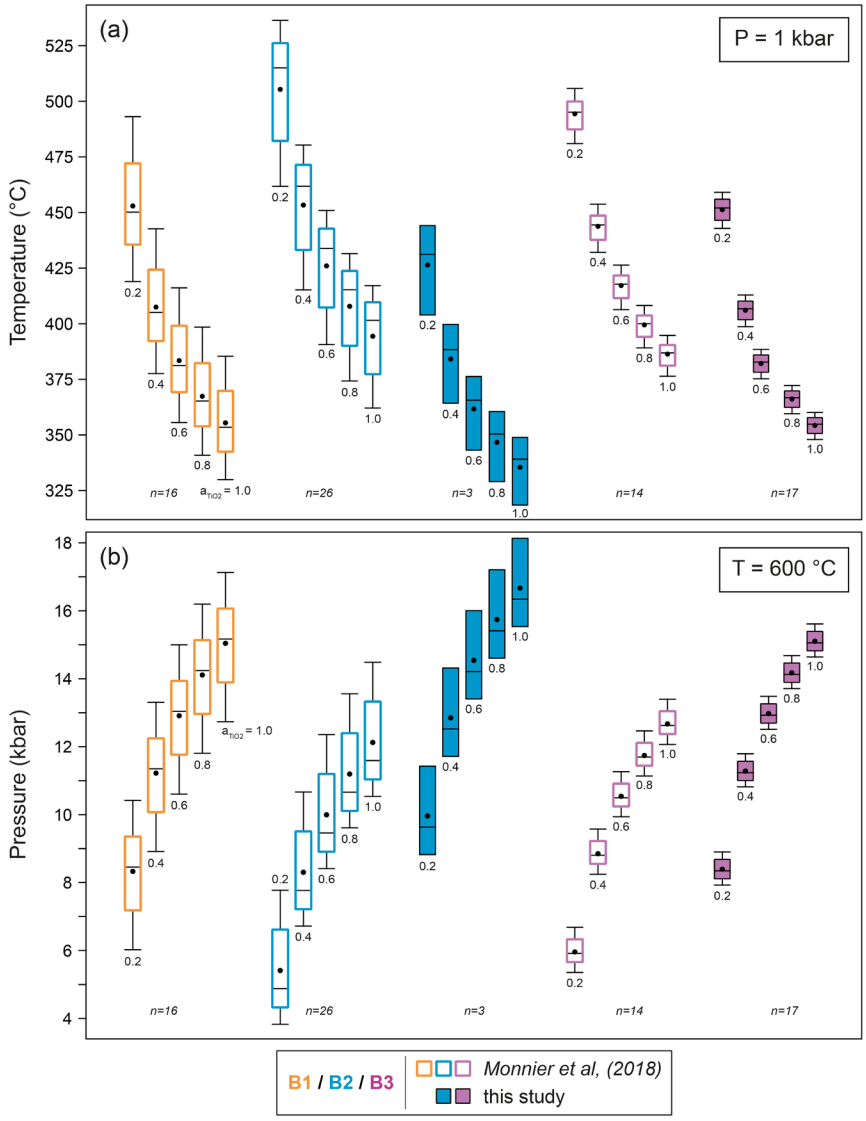



*Figure III.33. Temperatures (a) and pressures (b) of quartz crystallisation estimated using the TitaniQ thermobarometer (Thomas et al., 2010). Several values of $TiO_2$ activity ($a_{TiO2}$) have been considered, ranging from 0.2 and 1.*

#### *4.3.2.ii. Oxygen thermometry*

The partitioning of oxygen stable isotopes between two minerals represents a unique case of element partitioning characterised by pressure insensitivity due to the negligible molar volume change associated with isotope exchange reactions (e.g., Bottinga and Javoy, 1973; Clayton, 1981; Zheng, 1996). Oxygen isotopic thermometry relies on the assumption that coexisting minerals formed in isotopic equilibrium and that isotopic exchange was negligible after mineral precipitation. The fractionation of $\delta^{18}O$ between mineral pairs is primarily temperature-dependent and numerous models for this equilibrium have been developed based on theoretical calculations, experimental and empirical calibrations. The relationship between isotopic fractionation and temperature is defined as:

$$\Delta_{A-B} = \delta^{18}O_A - \delta^{18}O_B \cong 1000 \ln \alpha_{A-B}$$

$$\text{with } 1000 \ln \alpha_{A-B} = \frac{A}{T^2} + \frac{B}{T} + C$$

Determining equations for the temperature-dependent oxygen isotope fractionation coefficients between minerals, melts, and fluids is crucial for accurately reconstructing temperature conditions in geological systems (e.g., Bottinga and Javoy, 1973; Clayton, 1981; Zheng, 1996), deciphering fluid-rock interactions, and understanding magmatic, metamorphic, and hydrothermal processes (e.g., Taylor and Epstein, 1962; Zhao and Zheng, 2003; Wei and Zhao, 2022). Several computational and experimental studies have focused on estimating the oxygen isotope fractionation coefficients between quartz and cassiterite (Zheng, 1991; Zhang et al., 1994; Hu et al., 2005; Polyakov et al., 2005; Li et al., 2022), with the most recent establishing a theoretical relationship through Density Functional Theory (DFT) calculations. This equation has been shown to be in remarkable agreement with the studies of Hu et al. (2005) and Polyakov et al. (2005), likely reflecting advances in both computing and experimental methods over recent decades. It has been applied to Sn-W magmatic-hydrothermal deposits from various mineralised districts in China, associated with well-documented independent constraints on temperature (e.g., mineral paragenesis or fluid inclusion temperatures), confirming its validity for magmatic-hydrothermal systems over a temperature range of 300 to 600 °C. The oxygen isotope fractionation between quartz and cassiterite ($\Delta^{18}O_{quartz\text{-}cassiterite}$) has been demonstrated to be highly sensitive to temperature, establishing quartz-cassiterite as an excellent mineral pair for oxygen isotope thermometry (Li et al., 2022). The following theoretical equation has been proposed to estimate the temperature of isotope equilibrium between both minerals and has been applied to magmatic quartz and cassiterite data from the Beauvoir granite:

$$T\,(°C) = 2427 \times (\delta^{18}O_{Qz} - \delta^{18}O_{Cst})^{-0.4326} - 492.4$$

As mentioned in section 4.2.2 (Part III), obtaining paired oxygen isotope data for quartz and cassiterite with strong textural constraints indicating co-crystallisation proved to be challenging. In the B1 unit, cassiterite is locally observed as an inclusion within quartz (Fig. III.31). As illustrated in Figure III.31, quartz in contact with cassiterite exhibits $\delta^{18}O$ ratios ranging from 5.6 to 6.3 ‰, while cassiterite shows values of 5.9 and 6.9 ± 0.3 ‰. The temperature calculation, based on the lowest $\delta^{18}O_{Cst}$ ratio and a mean $\delta^{18}O$ ratio of 6.1 ± 0.3 ‰ for quartz, yields an unrealistic value of 4290 ± 10 °C, whereas no temperature estimate could be obtained from the second $\delta^{18}O_{Cst}$ ratio (Li et al., 2022). However, a more coherent temperature range of approximately 500 to 900 °C (mean = 675 ± 100 °C, n = 30) is obtained using the mean isotopic composition of relatively high $\delta^{18}O$ quartz cores from the B1 unit (10.5 ± 0.3 ‰) (Fig. III.34). It should be noted that this mean $\delta^{18}O_{Qz}$ value is derived from a restricted zone of the quartz cores, specifically where the $\delta^{18}O$ values are both highest and most stable, prior to their decrease

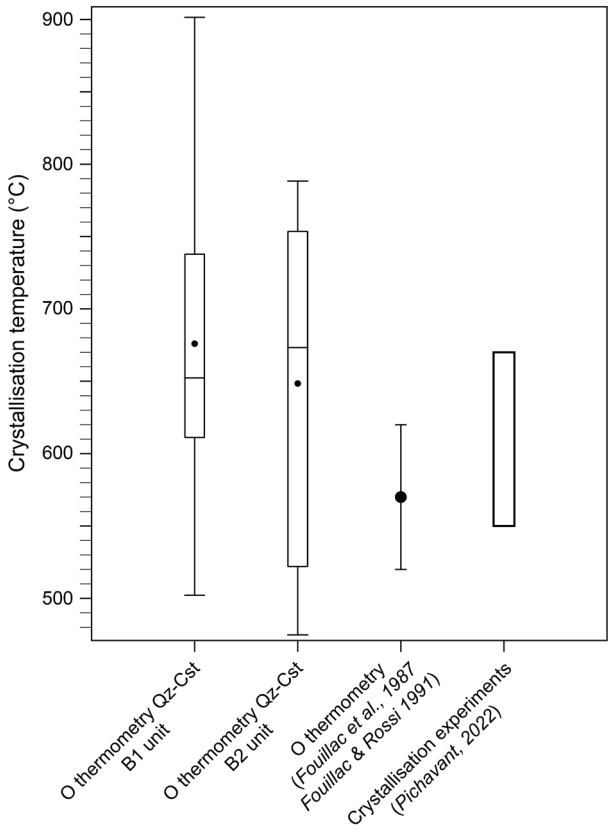



*Figure III.34. Summary of crystallisation temperatures obtained through oxygen thermometry on magmatic minerals (Fouillac et al., 1987; Fouillac and Rossi, 1991; this study) and crystallisation experiments (Pichavant, 2022). The error calculation on the average temperature is calculated by the addition of the one sigma error on individual temperatures (± 5 °C for a ± 0.3 ‰ (2σ) uncertainty on $\delta^{18}O$ ratios; Li et al., 2022) and group standard deviation.*

toward the rims (Fig. III.29c). Although the absence of clear textural evidence for co-crystallisation between quartz and cassiterite means that the isotopic equilibrium temperature estimates cannot be considered fully robust, this approach can be justified. Indeed, there are constraints on the magmatic origin of both minerals (Johan et al., 1988; Cuney et al., 1992; Pichavant, 2022), the crystallisation temperature range of the Beauvoir melts relatively narrow (*ca.* 670–550 °C; Pichavant, 2022), and variations in isotopic fractionation between the melt and minerals at high temperatures is relatively small (e.g., Zhao and Zheng, 2003).

In the B2 unit, as in the B1 unit, co-crystallisation textures between quartz and cassiterite are rare and were observed in only one instance (Fig. III.32). Three $\delta^{18}O$ ratios were obtained for quartz at the contact with cassiterite, ranging from 8.2 to 11.1 ‰. Considering a mean $\delta^{18}O_{Qz}$ ratio of 9.8 ± 0.3 ‰ and the range of $\delta^{18}O$ ratios for the co-crystallising cassiterite, temperatures of O isotopic equilibrium are estimated between *ca.* 530 and 940 °C (mean = 750 ± 150 °C, n = 8) (Li et al., 2022). As quartz from the B2 unit does not show core-to-rim variations, using the mean $\delta^{18}O_{Qz}$ ratio based on all data from this sample (10.7 ± 0.3 ‰, n = 94) appears to provide a better estimate of the mean quartz value to apply in the equation. In this case, the estimated temperatures are slightly lower, ranging from 475 to 790 °C (mean = 650 ± 115 °C, n = 8), which is more consistent with the crystallisation temperature range for the Beauvoir melts (*ca.* 670–550 °C; Pichavant, 2022) (Fig. III.34).

Applying oxygen thermometry appears thus challenging when textural constraints on co-crystallisation between minerals are weak. However, relatively consistent temperatures were obtained for the quartz-cassiterite pair in the Beauvoir PRMG (675 ± 100 °C and 650 ± 115 °C for the B1 and B2 units, respectively), which are comparable to the oxygen isotopic equilibrium temperature of 570 ± 50 °C derived from other mineral pairs (Fouillac et al., 1987; Fouillac and Rossi, 1991) (Fig. III.34).

### *4.3.3. Initial O isotopic signature of the melt and implications for its source*

The O isotopic signature of minerals and whole rock has long been recognised as a powerful tool for deciphering the source of magmas (Taylor, 1968, 1978). Due to the significantly slower diffusion rate of oxygen in quartz compared to feldspars and other granitic minerals (Giletti et al., 1978; Yund et al., 1978; Giletti and Yund, 1984; Elphick et al., 1986), quartz tends to preserve its original oxygen isotopic signature more effectively. In the Beauvoir PRMG, CL imaging of magmatic quartz revealed minimal evidence of dissolution-reprecipitation textures, indicating that quartz was only slightly affected by alteration processes such as albitisation and greisenisation (section 2 of Part III). Consequently, compared to apatite (see Part II), quartz appears to be a more reliable proxy for the initial oxygen isotopic composition of the parent melt.

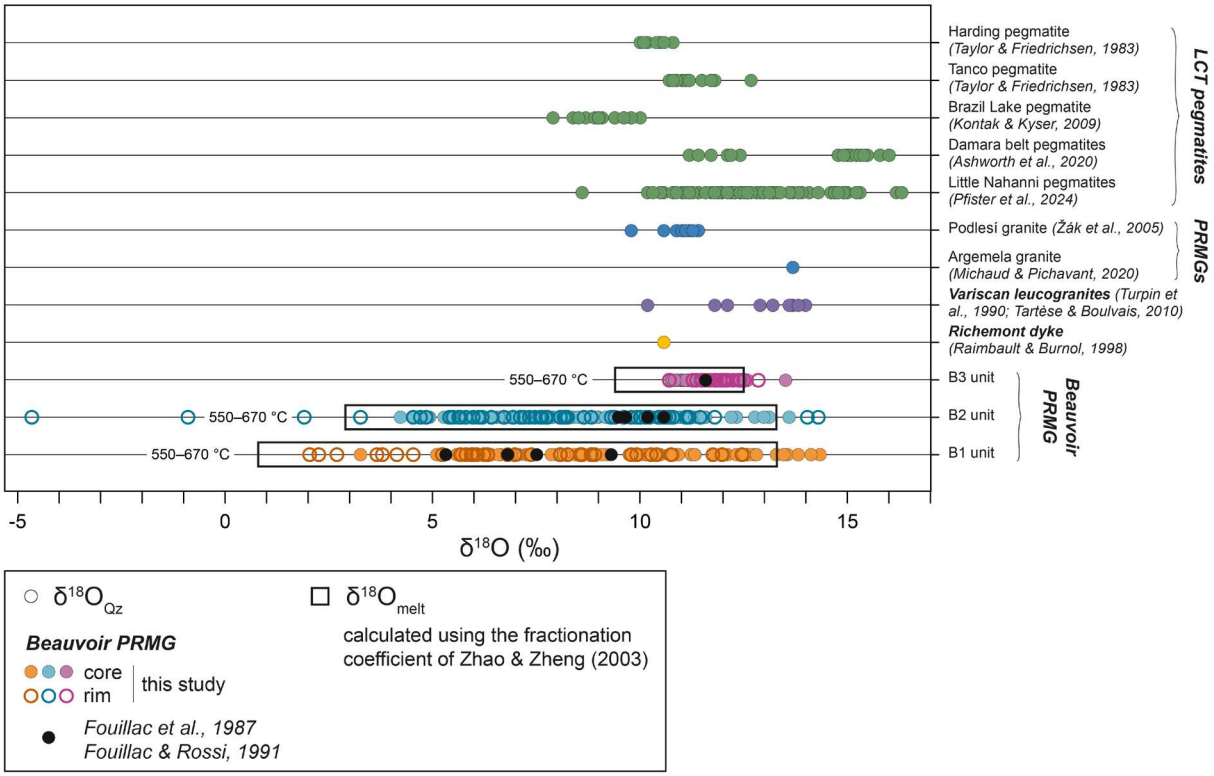



*Figure III.35. Oxygen isotopic composition of quartz from the three magmatic units of the Beauvoir PRMG (excluding recrystallised zones within grains) (Fouillac et al., 1987; Fouillac and Rossi, 1991; this study) in comparison with values reported for other PRMGs (Žák et al., 2005; Michaud and Pichavant, 2020), LCT pegmatites (Taylor and Friedrichsen, 1983; Kontak and Kyser, 2009; Ashworth et al., 2020; Pfister et al., 2024), Variscan peraluminous leucogranites (Turpin et al., 1990b; Tartèse and Boulvais, 2010) and the Richemont rhyolitic dyke (Raimbault and Burnol, 1998). The $\delta^{18}O$ ratios of the Beauvoir melts were estimated using the crystal-melt temperature-dependent fractionation factor proposed by Zhao and Zheng (2003) for rhyolitic melt and a crystallisation temperature of ca. 670 to 550 °C (Pichavant, 2022). The four lowest $\delta^{18}O$ ratios observed for quartz in the B2 unit were excluded from this calculation.*

The significant dispersion of data for quartz in the B1 and B2 units, excluding recrystallised zones, is unusual when considering a single granitic magma reservoir (e.g., Taylor, 1968; Taylor et al., 1979; Taylor and Sheppard, 1986) (Fig. III.35). Similar dispersion in quartz O isotopic composition has been observed in other similar rare-metal granite deposits, such as the Cretaceous Little Nahanni LCT pegmatites (Canada), where the spread has been attributed to

supra-solidus melt-wall rocks interactions, further superimposed by sub-solidus fluid-rock interactions (Pfister et al., 2024). In the Beauvoir PRMG, the potential processes responsible for these variations are discussed in section 4.3.4. Conversely, quartz from the B3 unit exhibits a relatively narrow range of $\delta^{18}O$ ratios, consistent with those reported for other PRMGs (Žák et al., 2005; Michaud and Pichavant, 2020), LCT pegmatites (Taylor and Friedrichsen, 1983; Kontak and Kyser, 2009; Ashworth et al., 2020), Variscan peraluminous leucogranites (Turpin et al., 1990b; Tartèse and Boulvais, 2010) and the Richemont rhyolitic dyke (Raimbault and Burnol, 1998) (Fig. III.35), the latter representing the subvolcanic equivalent of the Beauvoir PRMG. Therefore, the O isotopic signature of quartz from the B3 unit seems to be the most reliable indicator of the initial magma signature.

Using the crystal-melt temperature-dependent fractionation factor proposed by Zhao and Zheng (2003) for rhyolitic melt, the oxygen isotopic composition of the Beauvoir melts can be estimated. For crystallisation temperatures of *ca.* 670 to 550 °C, which encompasses liquidus to solidus temperatures (Pichavant, 2022), the oxygen isotopic fractionation between quartz and the parent melt is relatively small ($\Delta^{18}O_{quartz\text{-}melt}$ ~ 1.0 to 1.3 ‰; Zhao and Zheng, 2003). The calculated $\delta^{18}O$ values for the Beauvoir melts range from 9.4 to 12.5 ‰ for the B3 unit, whereas broader ranges of 0.8–13.3 ‰ and 2.9–13.3 ‰ are observed for the B1 and B2 units, respectively (Fig. III.35). The relatively high $\delta^{18}O$ values of the B3 melt are consistent with a crustal source (e.g., O'Neil et al., 1977; O'Neil and Chappell, 1977; Taylor et al., 1979; Chappell and White, 1992; Eiler, 2001).

### *4.3.4. Processes resulting in $\delta^{18}O$ variation in magmatic quartz*

As outlined in section 4.3.3, the $\delta^{18}O$ ratios in quartz from the B1 and B2 units exhibit a high degree of dispersion, including instances of low $\delta^{18}O$ values, both of which are inconsistent with crystallisation from a single crustal-derived magma under equilibrium conditions (e.g., Taylor, 1968; Taylor et al., 1979; Taylor and Sheppard, 1986) (Fig. III.35). Three main features associated with this dispersion emerge from the data (Figs. III.29 and III.30): (i) an overall decrease in $\delta^{18}O$ ratios from the less evolved B3 unit to the B2 and B1 units; (ii) a core-to-rim decrease in $\delta^{18}O$ ratios in quartz from the B1 unit; and (iii) significant, heterogeneous intra-granular variations of $\delta^{18}O$ ratios within quartz from the B2 unit. The processes considered plausible to explain these variations in magmatic quartz are explored below.

#### *4.3.4.i. Sub-solidus alteration and re-equilibration*

Although quartz is generally resistant to sub-solidus alteration and re-equilibration, its initial oxygen isotopic signature can occasionally appear shifted. This phenomenon been documented, for example, in the Cretaceous Little Nahanni LCT pegmatites (Canada), where fluid-rock interactions partially overprinted the original signature of the melt (Pfister et al., 2024). In the Beauvoir PRMG, significant intra-granular variability in some quartz grains from the B2 unit,

including negative $\delta^{18}O$ values, suggests the involvement of meteoric fluids during sub-solidus processes (Sheppard, 1986). The relatively low $\delta^{18}O$ values occur heterogeneously along $\delta^{18}O$ profiles, not limited to grain rims (Fig. III.29f), and are restricted to grains with microfractures crosscutting magmatic oscillatory zoning (Fig. III.30b; see section 2.2.1 of Part III for additional petrographic details). The microfractures, healed by quartz precipitation and detectable only through CL imaging, likely acted as pathways for fluid flow, promoting hydrothermal exchange (Valley and Graham, 1996). The localised and partial lowering of $\delta^{18}O$ values in quartz grains from the B2 unit could therefore be attributed to oxygen isotopic re-equilibration with meteoric fluids circulating along micro-scale fractures.

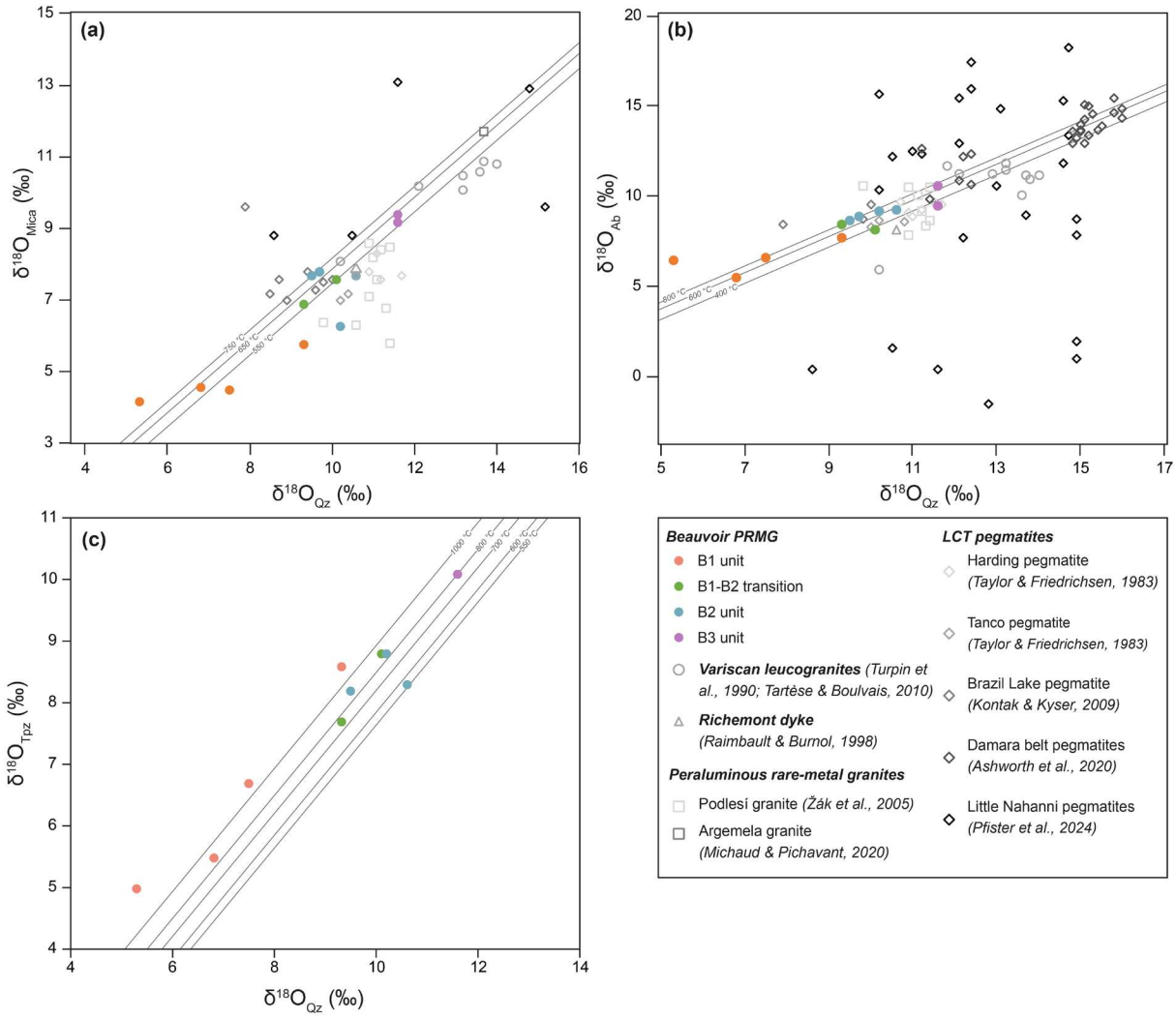



*Figure III.36. (a) $\delta^{18}O$ values of mica versus quartz, (b) albite versus quartz, and (c) topaz versus quartz for the Beauvoir PRMG (Fouillac et al., 1987; Fouillac and Rossi, 1991). O isotopic compositions of minerals from other PRMGs (Žák et al., 2005; Michaud and Pichavant, 2020), LCT pegmatites (Taylor and Friedrichsen, 1983; Kontak and Kyser, 2009; Ashworth et al., 2020; Pfister et al., 2024), Variscan peraluminous leucogranites (Turpin et al., 1990b; Tartèse and Boulvais, 2010) and the Richemont rhyolitic dyke (Raimbault and Burnol, 1998) are reported for comparison. The O isotopic equilibrium lines are calculated using temperature-dependent fractionation factors from Zheng (1993a) for quartz-albite, Zheng (1993b) for quartz-topaz, and Vho et al. (2019) for quartz-muscovite.*

Previous studies have proposed that meteoric fluid infiltration could also explain the progressive decrease in O isotopic compositions of separated magmatic minerals—including quartz, albite, lepidolite, and topaz – from the B3 to B2 and B1 units (Fouillac et al., 1987; Fouillac and Rossi, 1991) (Fig. III.36). These minerals were interpreted to be in isotopic equilibrium at temperatures of 570 ± 50 °C, suggesting that meteoric fluids interacted with the melt under supra-solidus conditions (Fig. III.36). However, due to the complexity and questionable plausibility of meteoric fluid infiltration into a melt (e.g., Weis et al., 2012), this hypothesis was later abandoned in favour of isotopic disequilibrium among the analysed minerals, ascribed to sub-solidus alteration that progressively intensified from the deeper B3 to the shallower B1 unit (Cuney et al., 1992).

While meteoric fluid infiltration under supra-solidus conditions remains unlikely, separated minerals analysed from the Beauvoir PRMG show limited dispersion along isotopic equilibrium lines at supra-solidus temperatures, suggesting isotopic equilibrium (Fig. III.36). This is particularly evident when compared to data from Variscan peraluminous leucogranites (Turpin et al., 1990b; Tartèse and Boulvais, 2010), the Richemont dyke (Raimbault and Burnol, 1998), and other examples of PRMGs (Žák et al., 2005; Michaud and Pichavant, 2020) and LCT pegmatites (Taylor and Friedrichsen, 1983; Kontak and Kyser, 2009; Ashworth et al., 2020; Pfister et al., 2024), which generally exhibit similar dispersions. As previously noted, the only case where significant dispersion along equilibrium lines has been observed – far exceeding that of Beauvoir – is the Cretaceous Little Nahanni LCT pegmatites, attributed to sub-solidus fluid-rock interactions (Pfister et al., 2024) (Fig. III.36). In the Beauvoir PRMG, the analysis of separated minerals inherently provides weaker textural constraints compared to *in-situ* analyses, which may contribute to the observed dispersion of isotopic data along equilibrium lines at supra-solidus temperatures (Fig. III.36). Moreover, the two samples analysed from the B2 unit in this study, located respectively above and below the B3 sample along the GPF1 drillhole, exhibit $\delta^{18}O$ values lower than quartz from the B3 unit (Fig. III.37). This observation does not support the hypothesis of progressively stronger sub-solidus alteration toward the granite's apex but instead indicates a progressive decrease in $\delta^{18}O$ values with increasing differentiation.

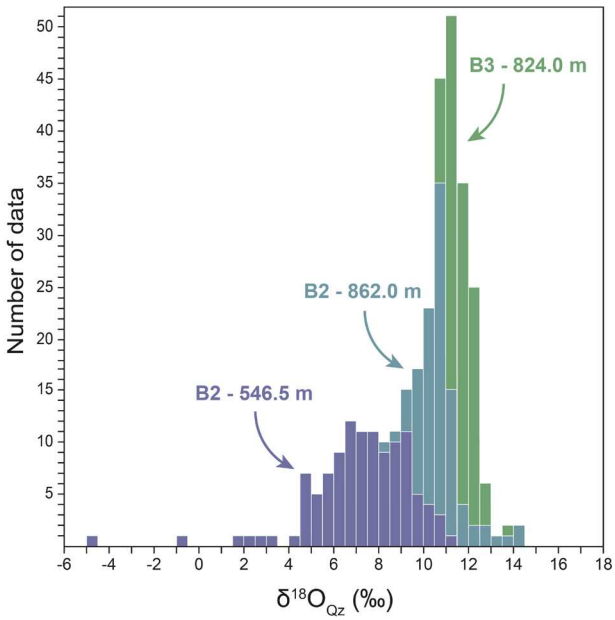



*Figure III.37. $\delta^{18}O_{Qz}$ values for the two samples analysed from the B2 unit, positioned respectively above and below the B3 sample along the GPF1 drillhole.*

We propose that meteoric fluid infiltration occurred under sub-solidus conditions and accounts for the intra-grain $\delta^{18}O$ variations in microfractured quartz from the B2 unit. However, this process would neither explain (i) the decrease in $\delta^{18}O$ ratios between units, as data mostly align along equilibrium lines at supra-solidus temperatures and $\delta^{18}O$ values decrease with increasing differentiation rather than toward the surface, or (ii) the core-to-rim $\delta^{18}O$ trend observed in quartz from the B1 unit, based on the absence of pronounced dissolution-reprecipitation textures and microfractures in quartz and the presence of primary melt and magmatic fluid inclusions in the quartz rims. Both O isotopic features are more likely to reflect primary oxygen isotopic variations established during the magmatic stage.

#### *4.3.4.ii. Temperature-dependent isotopic fractionation*

Oxygen isotopic fractionation between minerals and the parent melt is primarily temperature-dependent (e.g., Zhao and Zheng, 2003). Along the crystallisation path of the Beauvoir melts, temperature is inferred to decrease from *ca.* 670 to 550 °C (Pichavant, 2022). At these relatively high temperatures, O isotopic fractionation between quartz and the parent melt is limited and varies from 1.0 ‰ ($\Delta^{18}O_{quartz\text{-}melt}$) at 670 °C to 1.3 ‰ at 550 °C (e.g., Zhao and Zheng, 2003; Bucholz et al., 2017). This fractionation variation of 0.3 ‰ between the liquidus and solidus temperatures is much smaller than the dispersion observed in the $\delta^{18}O$ ratios of quartz from the B1 unit, which range from 2.1 to 14.3 ‰ (Figs. III.30 and III.35).

#### *4.3.4.iii. Magmatic system involving multiple $\delta^{18}O$ reservoirs*

Oxygen isotopic zonation in igneous quartz, such as that observed in the Beauvoir B1 unit, has not been documented in other rare-metal granites or rhyolites (e.g., Raimbault and Burnol, 1998; Michaud and Pichavant, 2020). However, comparable features have been described in magmatic quartz from certain high-silica volcanic rocks, where they are commonly attributed to open-system processes such as the assimilation of low-$\delta^{18}O$ hydrothermally altered host rocks or melt-melt mixing (e.g., Bindeman and Valley, 2002; Budd et al., 2017). The mica schists surrounding the Beauvoir granite exhibit relatively high $\delta^{18}O$ values, ranging from 9.4 to 11.5 ‰ (Fouillac et al., 1987). If assimilation of these rocks had significantly influenced the late crystallisation of the B1 melt, it would be expected to produce $\delta^{18}O$-enriched quartz rims relative to the core, contrary to the observed O isotopic trend. Furthermore, the low liquidus temperature of the Beauvoir melts, experimentally constrained at approximately 670 °C (Pichavant, 2022), suggests that substantial assimilation of host rocks is unlikely, a conclusion further reinforced by the absence of textural evidence for such a process.

Recent petrographic and geochemical investigations of Esteves et al. (2024b) revealed the open-system nature of the Beauvoir magmatic system, which was emplaced as a series of distinct sub-units, each resulting from the stacking and amalgamation of multiple sills (Esteves et al., 2024b). This complex emplacement history, marked by episodic recharge and internal

differentiation, resulted in the inflation of individual sills. Within the B1 unit, interactions between late-stage low-$\delta^{18}O$ melts and the original high-$\delta^{18}O$ melt may offer a conceivable explanation for the observed O isotopic zonation in magmatic quartz, and is further discussed in section 1 of Part IV.

#### *4.3.4.iv. Oxygen isotopic fractionation in relation with devolatilisation processes*

A last hypothesis to explain the core-to-rim decrease in $\delta^{18}O$ ratios characterising magmatic quartz from the B1 unit involves intense devolatilisation processes likely occurring during the late stage of magma crystallisation. The existence of these processes are evidenced by the development of snowball textures and the presence of primary melt and magmatic fluid inclusions at quartz rims (section 2 of Part III). The exsolution of a vapour phase from silicate melts has been recognised as a key factor influencing the hydrogen isotopic composition of granitic rocks, often leading to a pronounced decrease in whole-rock $\delta D$ values (e.g., Taylor et al., 1983; Nabelek et al., 1983). In contrast, oxygen isotope composition generally remains stable during devolatilisation processes. However, certain observations suggest that devolatilisation may influence O isotopic fractionation, a possibility further explored in section 1 of Part IV.

## 5. High-temperature magmatic fluid circulation in the Beauvoir PRMG

Two key processes governing the hydrothermal mobility of rare metals, particularly Sn, under supra- to sub-solidus conditions have been identified through the characterisation of apatite generations (Part II) and fluids inclusions in magmatic quartz (section 3 of Part III) from the Beauvoir PRMG: (i) phase separation of magmatic fluids, and (ii) mixing dynamics between magmatic and meteoric fluids. Both mechanisms involve metals transport by magmatic fluids, released through melt devolatilisation during the magmatic stage. Beyond initiating metal hydrothermal mobility, devolatilisation and subsequent boiling of magmatic fluids might also have influenced the crystallisation of magmatic quartz, as recorded by its oxygen isotopic composition (section 4 of Part III).

In this section, we aim to further characterise the physico-chemical properties of magmatic fluids in the Beauvoir PRMG by examining the oxygen isotopic composition of minerals precipitating from these fluids. Apatite chemistry suggests that magmatic fluids exsolved from the melts and responsible for high-temperature alteration were rapidly mixed with meteoric fluids during greisenisation, with magmatic fluid signatures preserved only in apatite precipitated within quartz-cassiterite greisen veins (Part II). Quartz-cassiterite greisen thus appears to represent the highest-temperature alteration within the Beauvoir magmatic-hydrothermal system, closely associated with magmatic fluid circulation. The relationship between tin transport and magmatic fluid circulation was already highlighted by a previous fluid inclusion study in the Beauvoir PRMG (Harlaux et al., 2017), and is well-documented in analogous greisen systems,

such as the Panasqueira W-Sn(-Cu) deposit (Portugal; Launay et al., 2021), the granite-related W-Sn deposits from the Jiangxi province (China; Legros et al., 2019), or the Yankee Lode tin deposit (Australia; Audétat et al., 1998).

Quartz ($SiO_2$) and cassiterite ($SnO_2$), both suitable for oxygen isotope analysis, were selected as the primary targets of this study. A detailed petrographic characterisation was conducted to confirm their co-precipitation. Once established, the isotopic data can be used to estimate the precipitation temperature of these minerals which in turn enables the reconstruction of the oxygen isotope composition of the fluid. This approach further provides robust constraints on the mechanisms driving the magmatic-hydrothermal transition in the Beauvoir granite.

## 5.1. Material and methods

### *5.1.1. Studied material*

Two samples were selected to represent quartz-cassiterite greisen alteration in the Beauvoir PRMG. The first sample was collected from a depth of 801.0 m along the historic GPF1 drillhole, whereas the second sample corresponds to a quartz-cassiterite vein that crosscuts the altered Beauvoir granite in the quarry (sample collected by Matthieu Harlaux as part of his PhD research, referred to as ECH14-17).

### *5.1.2. Scanning electron microscope (SEM) and cathodoluminescence (CL) imaging*

Petrographic observations were carried out through optical microscopy, scanning electron microscopy (SEM) and cathodoluminescence (CL) at the Centre de Recherches Pétrographiques et Géochimiques (CRPG, Nancy, France). Scanning electron microscopy cathodoluminescence imaging (SEM-CL) of the high-temperature greisen-related quartz and cassiterite was realised using two type of CL detector. Similar to magmatic quartz (section 2 of Part III), CL imaging was partly conducted on a JEOL JXA 8230 electron microprobe equipped with a panchromatic CL detector, using the same analytical parameters (i.e., an accelerating voltage of 20 kV and a beam current of 100 nA). Pixel resolution varied between 2 and 5 µm, depending on the grain size, with a dwell time of 10 ms per pixel. Additional CL imaging was performed on a JEOL 6510 SEM equipped with a tungsten filament and a Gatan CL detector. The acceleration voltage and beam current were set at 20 kV and 17 nA, respectively. For both instruments, observed colours do not represent the true luminescence colours of the imaged minerals; however, signal intensities can still be compared qualitatively.

### *5.1.3. Micro-XRF chemical mapping*

Micro-X-Ray Fluorescence (µ-XRF) analysis was performed on a thick section from the drillhole sample using a Bruker M4 Tornado µ-XRF benchtop spectrometer at GeoRessources (Nancy, France). The M4 Tornado device is equipped with a 30 W Rh-anode X-ray source, operating at 50 kV and 400 µA. The primary X-ray beam is focused onto a 20 µm spot on the sample surface using polycapillary optics. Two XFlash silicon drift energy dispersive X-ray

detectors (SSD-EDS), with an energy resolution not exceeding 145 eV, are positioned on each side of the primary X-ray source. X-ray maps were acquired with a dwell time of 12 ms per pixel and a point spacing of 25 µm. Elemental maps for individual atomic species were processed using an in-house Python routine.

#### *5.1.4. Secondary ion mass spectrometry (SIMS)*

*In-situ* oxygen isotopic composition of greisen-related quartz and cassiterite was measured at the CRPG, following the same analytical procedure as described for magmatic quartz and cassiterite in section 4 of Part III. Analytical precision was assessed by calculating the internal error (or internal precision, 2SE) and external error (reproducibility, 2SD), both dependent on the secondary ion beam intensity and integration time. The internal error (2SE) on $\delta^{18}O$ did not exceed 0.31 ‰ for quartz (mean ~ 0.07 ‰) and 0.26 ‰ for cassiterite (mean ~ 0.14 ‰). The long-term external error (2SD) was evaluated through multiple analyses of the distinct matrix-matched standards, yielding values of approximately 0.12 ‰ for quartz and ranging from 0.04 to 0.12 ‰ for cassiterite. Finally, the reported analytical uncertainty, which corresponds to the quadratic sum of the internal error and of the reference material external error, ranges from 0.25 ‰ to 0.66 ‰ (mean ~ 0.28 ‰) for quartz, and from 0.20 to 0.49 ‰ (mean ~ 0.29 ‰) for cassiterite.

### 5.2. Results

#### *5.2.1. Petrography*

##### *5.2.1.i. Drill core sample*

The drill core sample corresponds to a polyphase greisen band located near the contact between the greisenised Beauvoir granite and a mica schist enclave (Fig. III.38a). The granite is also crosscut by a geodic quartz vein oriented parallel to the greisen band, and whose porosity is primarily infilled by rosette-like muscovite. The pervasive greisen band replaces the igneous minerals of the granite with an early hydrothermal assemblage consisting of quartz, topaz, apatite (type IIa, as described in Part II), and cassiterite (Figs. III.38b-c). This first hydrothermal assemblage was subsequently overprinted by a secondary assemblage of quartz, muscovite and apatite (type IIc, as detailed in Part II), likely precipitated during the late stage of the greisenisation process. The host granite exhibits extensive alteration characterised by both topazification and muscovitisation. The selvedge of the greisen band is strongly topazified, whereas those of the geodic quartz vein are predominantly muscovitised (Fig. III.38b).

Quartz in the greisen band forms an equidimensional mosaic of subhedral to anhedral grains, with sizes of one micron to several hundreds of microns (Figs. III.38c, d, f). Its CL signal exhibits either gradual core-to-rim zoning with discernible but not sharply defined growth bands, or heterogeneous patchy textures intersected by more-luminescent fractures filled with quartz.

Higher CL intensities observed at grain boundaries are potentially attributed to the accumulation of point defects and dislocations (e.g., Götze et al., 2013) (Fig. III.38d).

Cassiterite is subhedral to euhedral, varying in size from a few tens of microns to *ca.* 200 µm (Fig. III.38c). It occurs as isolated crystals or aggregates and is frequently included within early hydrothermal apatite (type IIa), but rarely in quartz. The CL signature of cassiterite is characterised by potential oscillatory zoning (Figs. III.38e, g, h).

#### *5.2.1.ii. Quarry sample*

The quarry sample was collected from a sub-vertical greisen structure oriented N060°, crosscutting the Beauvoir granite, which exhibits both kaolinisation and greisenisation alterations (Fig. III.39a). Its contact with the Beauvoir granite is diffuse. The greisen structure comprises two distinct domains: (i) quartz-muscovite ± topaz greisen with a partially preserved granitic texture; and (ii) quartz-cassiterite ± lepidolite zones characterised by more massive textures (Fig. III.39b). The contact between these two domains is gradational and enriched with disseminated cassiterite.

Quartz from the quartz-cassiterite greisen occurs as subhedral to globular grains, ranging in size from several hundred microns to *ca.* 1–2 mm (Fig. III.39c). The larger grains tend to be elongated and display a preferred orientation. The CL signature of quartz is essentially characterised by internal wavy growth zoning (Figs. III.39d-e), some more-luminescent quartz being also observed as fracture or veinlet filling (Figs. III.39f-g).

Cassiterite is present as aggregates of anhedral to subhedral grains, typically 100–400 µm in size. CL imaging reveals two cassiterite generations: (i) an earlier generation, appearing in blue to green tones, characterised by growth bands and occasional vermicular textures of cassiterite radially oriented toward the grain border; and (ii) a later generation, identified by orange colours, precipitated as fracture fillings within the earlier cassiterite (Figs. III.39f-g).

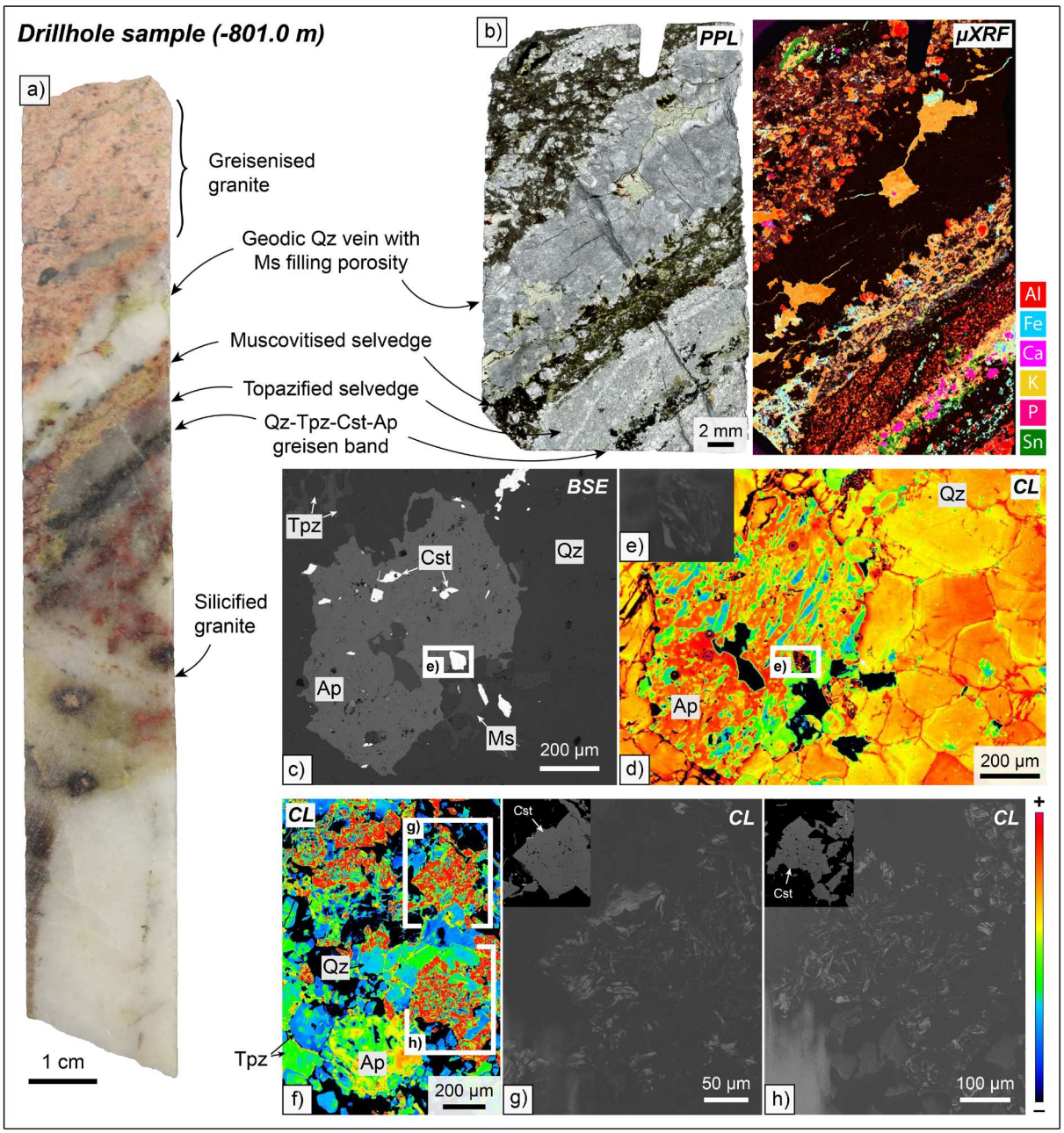



*Figure III.38. Petrographic characteristics of the greisen band from the drill core sample collected at 801 m depth along the historic GPF1 drillhole (B3 unit): (a) Macrophotograph of the sample characterised by a quartz-topaz-cassiterite-apatite greisen band subparallel to a geodic quartz vein, both crosscutting the greisenised Beauvoir granite. (b) Scan of the thick section under plane-polarised light (PPL) and corresponding µ-XRF elemental map showing the distribution of Al, Fe, Ca, K, P, and Sn. (c-d) Backscattered electron (BSE, c) and cathodoluminescence (CL, d) images of the early hydrothermal assemblage (Qz-Tpz-Ap-Cst) with interstitial secondary muscovite. In (d), quartz displays gradual core-to-rim zoning with discernible, though not sharply defined, growth bands. (e) CL image of cassiterite showing oscillatory zoning. (f) CL image highlighting heterogeneous patchy textures in quartz intersected by more-luminescent fractures filled with quartz. (g-h) CL images of cassiterite displaying potential oscillatory zoning. Abbreviations follow the IMA conventions compiled by Warr (2021).*

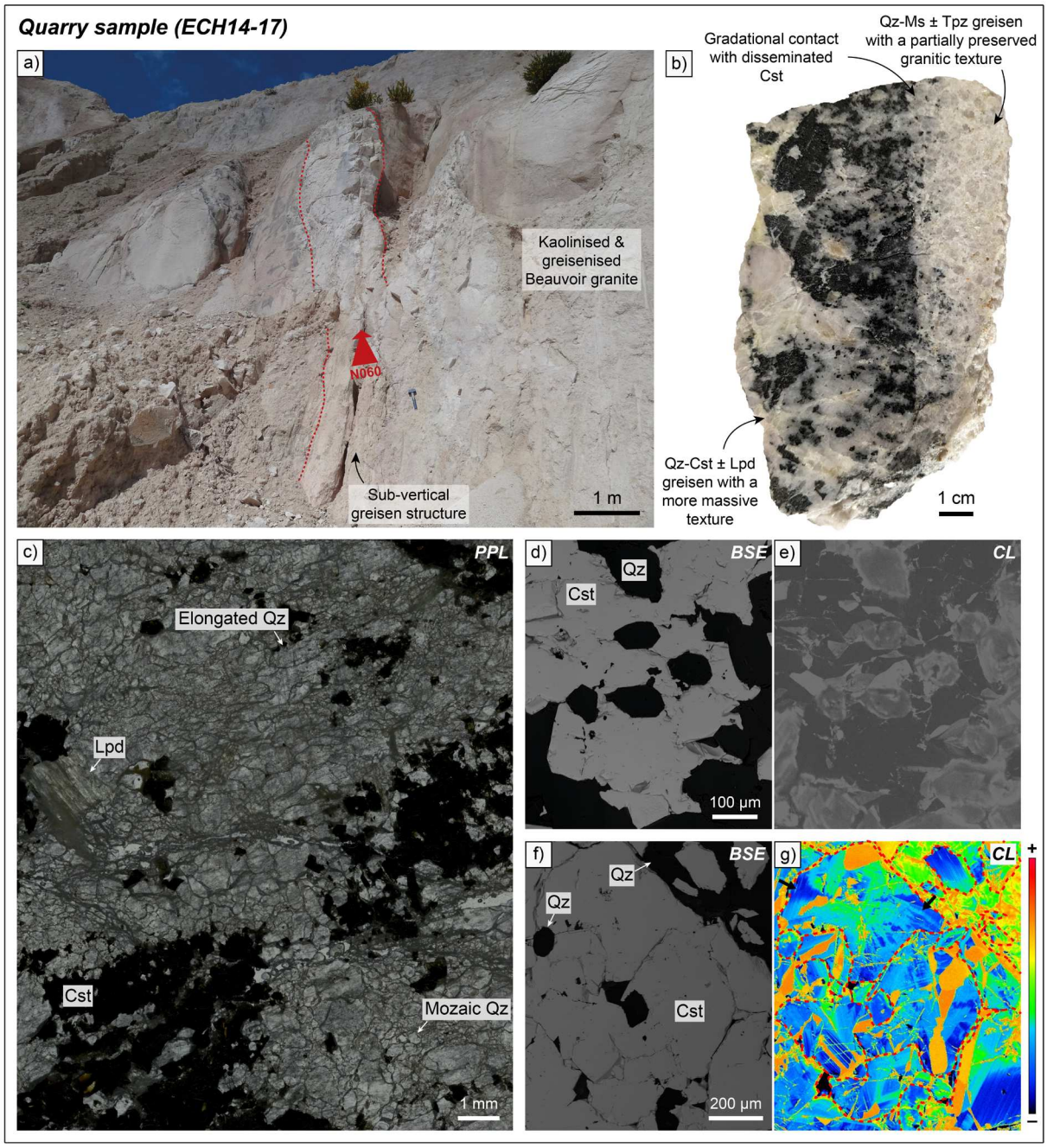



*Figure III.39. Petrographic characteristics of quartz-cassiterite greisen collected from the Beauvoir quarry: (a) Field photograph showing the contact between the subvertical greisen structure, oriented N060°, and the altered Beauvoir granite (Photo credit: Matthieu Harlaux, 2014). (b) Macrophotograph of the greisen characterised by two domains: (i) quartz-muscovite ± topaz greisen with a partially preserved granitic texture, and (ii) quartz-cassiterite ± lepidolite zones exhibiting more massive textures. (c) Scan of a thick section of massive Qz-Cst ± Lpd greisen under plane-polarised light (PPL), showing two quartz habits: a mosaic of subhedral to globular grains and elongated grains. (d-e and f-g) BSE and CL images of the cassiterite-quartz assemblage. Cl image in (e) shows wavy growth zoning in quartz grains. CL image in (g) highlights two quartz generations: (i) an earlier, less-luminescent globular quartz with wavy growth zoning, as seen in (e); and (ii) a later, more-luminescent quartz filling veinlets. Two cassiterite generations are also observed in (g): (i) an earlier generation, appearing in blue to green tones, characterised by growth bands and sector zoning (black arrows); and (ii) a later generation, identified by orange colours, precipitated as fracture fillings within the earlier cassiterite. Dashed lines in (g) outline grain boundaries, making the quartz and cassiterite generations more clearly visible. Abbreviations follow the IMA conventions compiled by Warr (2021).*

*5.2.1.iii. Fluid inclusion observations in the quarry sample*

As stated at the beginning of this section, our focus is on characterising minerals likely precipitated from magmatic fluids in the Beauvoir granite. The petrographic study of fluid inclusions (FIs) serves as a valuable tool to confirm the nature of the fluids involved in the formation of quartz-cassiterite greisen, particularly given that the distinct fluid generations in the Beauvoir granite have been extensively characterised (Aïssa et al., 1987; Harlaux et al., 2017; Monnier et al., 2020). A brief examination of fluid inclusions was therefore conducted in quartz and cassiterite from the quarry sample, which exhibits a simpler mineralogical assemblage with a well-defined association compared to the drill core sample. However, this petrographic study does not aim to provide an exhaustive description of all trapped fluid inclusions but rather focuses on FIs that appear to be primary (Fig. III.40).

Smaller quartz grains (*ca.* < 400–500 µm) exhibit few secondary FI trails, which are considerably more abundant in larger grains. Liquid-dominant, multiphase fluid inclusions are frequently observed in quartz, occurring either within growth planes parallel to grain boundaries (Figs. III.40b', c) or as primary to pseudo-secondary clusters (Figs. III.40a', b''). These FIs exhibit various morphologies, from regular to irregular shapes, with sizes typically between *ca.* 10–20 µm. The volumetric fraction of the vapour phase ($R_V$) varies from *ca.* 20 and 40 %. Solid phases within the fluid inclusions include at least two solids, such as halite crystals, with the others remaining unidentified. Some FIs seem to contain two halite crystals (Figs. III.40b', c). These multiphase FIs are occasionally spatially associated with vapour-dominant, biphasic FIs along growth planes (Fig. III.40c).

In greisen-related cassiterite, fluid inclusions are sparse and small, making petrographic characterisation challenging. A growth plane was observed, comprising liquid-dominant, triphasic FIs (Fig. III.40d). These fluid inclusions display highly irregular shapes and range in size from less than 1 µm to *ca.* 7–8 µm. The solid phase present is likely halite.

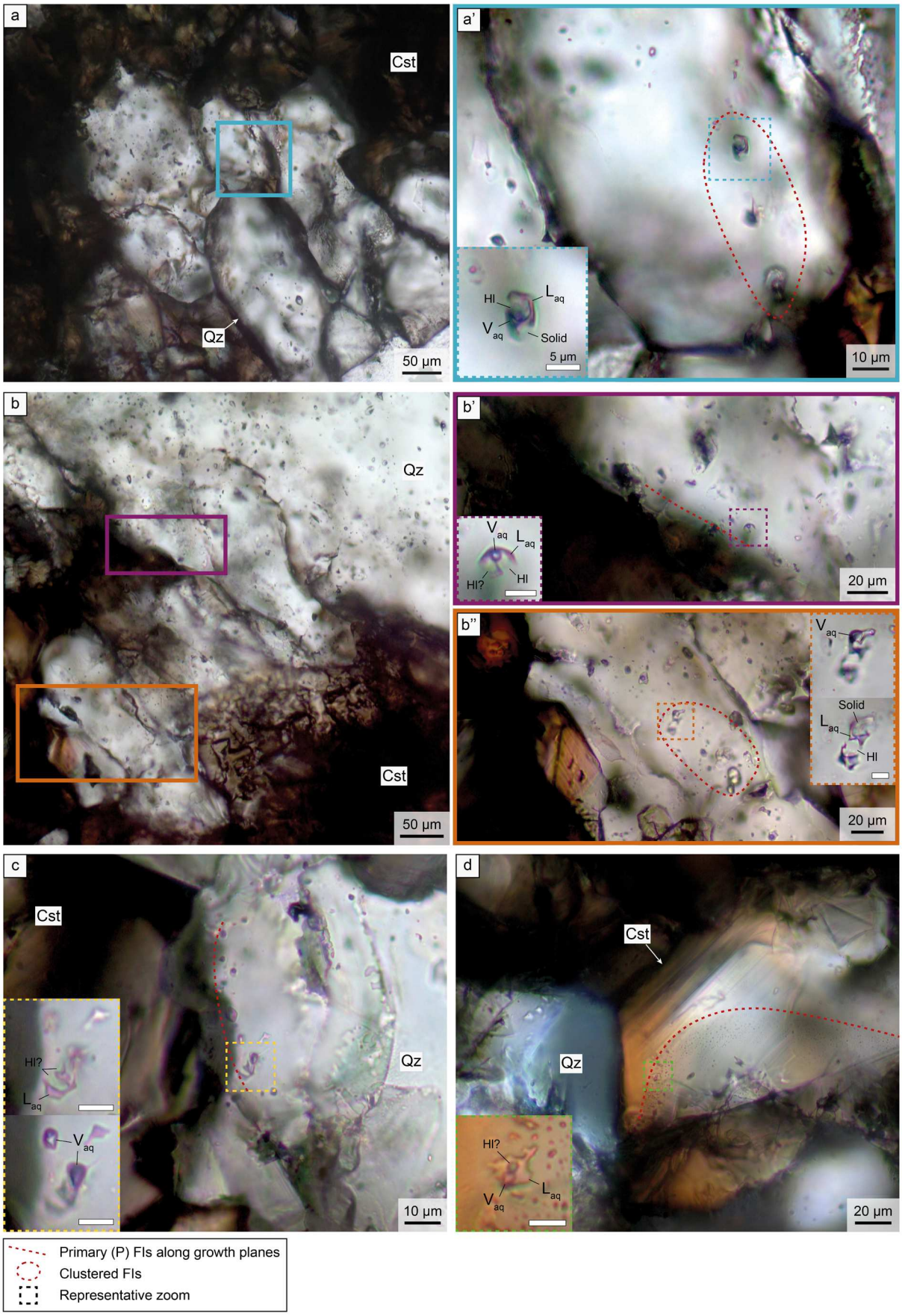



*Figure III.40. Petrography of fluid inclusions (FIs) of likely primary origin hosted in greisen-related quartz and cassiterite from the quarry sample. (Caption continued on the next page)*

*(Continued caption) (a-a') Primary or pseudo-secondary cluster of liquid-dominant, multiphase FIs. (b-b'') Liquid-dominant, multiphase FIs observed in greisen-related quartz, either as primary FIs along the grain border or in cluster. (c) Association of liquid-dominant, multiphase FIs with vapour-dominant, biphasic FIs within a growth plane along a quartz grain boundary. (d) L-dominant, triphasic FIs along growth plane in greisen-related cassiterite. The scale indicated on representative zooms correspond to 5 µm. Abbreviations follow the IMA conventions compiled by Warr (2021).*

### *5.2.2. Oxygen isotopes*

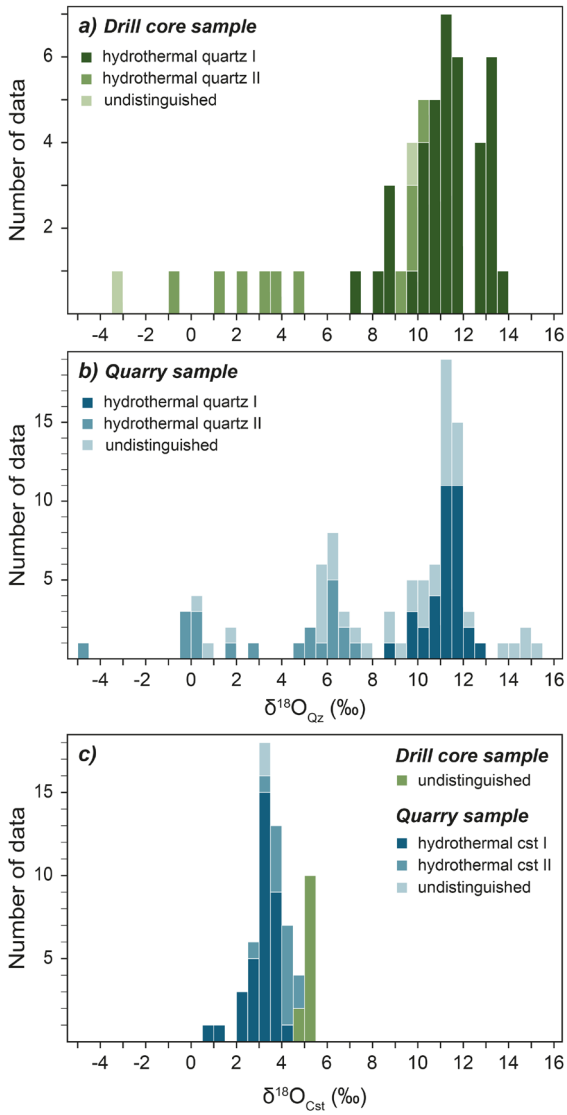



*Figure III.41. O isotopic compositions of quartz (a-b) and cassiterite (c) from the high-temperature greisen within the Beauvoir PRMG. The $\delta^{18}O$ ratios of quartz exhibit a significant spread, likely reflecting the analysis of distinct quartz generations.*

Greisen-related quartz exhibits a wide range of O isotopic compositions, consistent across both samples (Figs. III.41a-b). The $\delta^{18}O$ ratios range from -3.4 to 13.6 ‰ (mean ˜ 9.8 ± 0.3 ‰, n = 51) in the drill core sample and from -4.6 to 15.2 ‰ (mean ˜ 8.7 ± 0.3 ‰, n = 98) in the quarry sample. Two extreme values of 20.7 and 30.8 ‰ were measured in one quartz grain from the drill core; however, the analysed area was close to the thick section border, likely leading to issues such as secondary ion loss, beam instability, and reduced analytical precision. Some $\delta^{18}O$ values from this grain also showed extreme uncertainties reaching up to 31.3 ‰. The entire dataset from this grain was therefore deemed unreliable and excluded from further consideration.

Multiple generations of quartz were identified through CL imaging, with early hydrothermal quartz I frequently interspersed with secondary alteration zones (hydrothermal quartz II), manifesting as recrystallised patches or fractures fillings (Figs. III.38 and III.39). A clear distinction between measurements in early hydrothermal quartz and altered zones was possible for approximately 70 % of the analyses, the lack of true luminescence colour detection occasionally complicating this differentiation. Within this subset, quartz I typically exhibit higher $\delta^{18}O$ ratios (7.5–13.6 ‰, mean ˜ 11.2 ± 0.3 ‰) compared to altered zones (-4.6–10.1 ‰, mean ˜ 4.1 ± 0.3 ‰), particularly evidenced by the two Gaussian-like populations observed in the data from the quarry sample (Fig. III.41b). The analysis of both early greisen quartz (quartz I) and altered zones (quartz II) for O isotopes likely accounts for the significant spread in the isotopic data.

In contrast to quartz, greisen-related cassiterite exhibits a narrow range of O isotopic compositions, with $\delta^{18}O$ ratios predominantly varying between 2.1 and 5.5 ‰ (Fig. III.41c). Two lower outliers of 0.6 and 1.1 ‰ were also measured in cassiterite from the quarry sample. Cassiterite from the drill core sample displays a more homogeneous and slightly heavier O isotopic signature, although fewer data points are available. The broader $\delta^{18}O$ range observed in the quarry sample likely reflects the presence of two cassiterite generations (Fig. III.39g). The earlier hydrothermal cassiterite tends to exhibit slightly lighter O isotopic compositions (*ca.* 0.6–4.2 ‰, mean ~ 3.1 ± 0.3 ‰) compared to the later generation precipitated in fracture fillings (*ca.* 2.5–4.6 ‰, mean ~ 3.9 ± 0.3 ‰) (Fig. III.41c).

#### *5.2.3. Quartz-cassiterite oxygen isotope thermometry*

Temperatures of oxygen isotopic equilibrium between greisen-related quartz and cassiterite were estimated using the equation proposed by Li et al. (2022), as detailed for magmatic quartz and cassiterite in section 4.3.2 of Part III. For the quarry sample, the pair of $\delta^{18}O$ ratios for quartz and cassiterite used in the equation was selected from closely adjacent points in neighbouring crystals to ensure the most reliable temperature estimation (Fig. III.42a). This approach was not feasible for the drill core sample due to limited association between quartz and cassiterite. In this sample, the predominance of altered zones in quartz compared to cassiterite, combined with the considerable scatter in the quartz $\delta^{18}O$ data compared to cassiterite, suggests that quartz has been more susceptible to metasomatism following its precipitation. Consequently, the average $\delta^{18}O$ value of early hydrothermal quartz I (11.3 ± 0.3 ‰) was used to calculate equilibrium isotopic temperatures with the various cassiterite $\delta^{18}O$ values (Fig. III.42a). Most of the calculated temperatures range from approximately 460 to 670 °C, with one lower value of 365 °C derived from an outlier $\delta^{18}O$ ratio for cassiterite in the quarry sample (Figs. III.42a-b). The temperatures obtained for the quarry sample (mean = 505 ± 130 °C, 2σ), where a closer spatial correspondence between quartz and cassiterite analyses was achieved, are generally lower than those for the drill core sample (mean = 610 ± 45 °C). Details on the estimation of the uncertainty in the mean temperature for each sample are provided in Appendix III.A2.

#### *5.2.4. Estimation of the O isotopic composition of the parent fluid*

Once an equilibrium temperature for each quartz-cassiterite data pair is estimated, the oxygen isotopic composition of the fluid from which the minerals precipitated can be evaluated using temperature-dependent fractionation factors, thereby providing valuable insights into their origin. For both quartz and cassiterite, several equations are available to calculate 1000 ln α for equilibrium temperatures ranging from 365 to 670 °C. For quartz, the equation proposed by Zheng (1993) accounts for the effect of NaCl enrichment in fluids, making it particularly suitable for greisen systems, which typically involve moderately saline (*ca.* 3–10 wt% eq. NaCl) magmatic fluids (e.g., Burt, 1981; Štemprok, 1987; Shepherd et al., 1985; Taylor, 1988; Schwartz and Surjono, 1990; Halter et al., 1998a; Dobeš, 2005; Monnier et al., 2020). Additionally, the equation

of Vho et al. (2019) offers a robust alternative for the Beauvoir magmatic-hydrothermal system, having been optimised through integration of semi-empirical, experimental, and natural studies, and validated against published oxygen isotope data for quartz in selected natural samples. The $\delta^{18}O$ of the parent fluid estimated from greisen-related quartz using Zheng (1993) and Vho et al. (2019) equations are comparable ($\delta^{18}O_{fluid}$ ~ 6.9–9.4 ‰ and 7.3–10 ‰, respectively), with values derived from Vho et al. (2019) equation being slightly higher by 0.4–0.6 ‰ (Fig. III.42c). This difference is negligible, as the propagated uncertainties of ±0.3 ‰ for quartz oxygen isotope measurements and ±10 °C for equilibrium temperatures estimated for each data pair result in an overall uncertainty of approximately ±0.3 ‰ for $\delta^{18}O_{fluid}$ (see Appendix III.A2 for detailed calculations).

Li et al. (2022) suggested that cassiterite data may provide more robust estimates of fluid composition, as cassiterite-fluid fractionation is relatively insensitive to temperature, varying by less than 3 ‰ over a wide temperature range (200–800 °C), compared to a variation of 11 ‰ for quartz. Consequently, large uncertainties in temperature estimates could significantly affect the precision of $\delta^{18}O_{fluid}$ determinations from quartz data. For cassiterite, two equations appear suitable for the Beauvoir magmatic-hydrothermal system. The first, derived from the increment method, spans a temperature range of 0–1200 °C (Zheng, 1991), while the second is based on the well-established quartz-water 1000 ln α from Sharp et al. (2016), combined with the cassiterite-water fractionation coefficient refined by Li et al. (2022). Similar to quartz, these equations yield comparable results when applied to cassiterite oxygen isotope data, with fluid compositions estimated using Zheng (1991) equation being slightly higher (by 0.1–0.7 ‰) (Fig. III.42d). This difference is negligible relative to the combined uncertainty of *ca.* 0.3 ‰.

In conclusion, using the most recent studies (Vho et al., 2019; Li et al., 2022), which are based in extensive datasets and validated against natural data, the reconstructed fluid oxygen isotope signature is highly consistent whether derived from quartz ($\delta^{18}O_{fluid}$ ~ 7.3–10 ‰) or cassiterite data ($\delta^{18}O_{fluid}$ ~ 7.1–9.7 ‰) (Fig. III.42e).

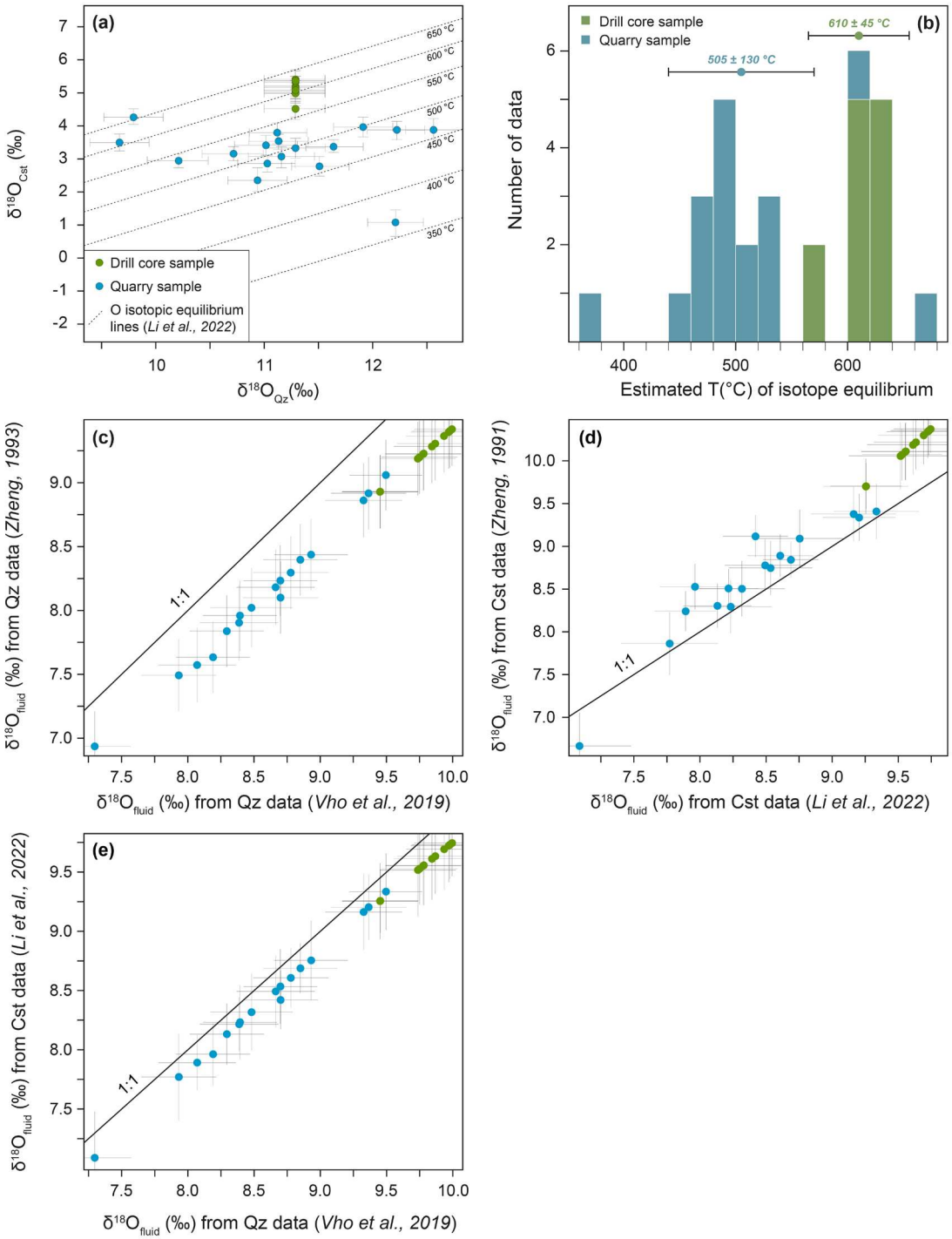



*Figure III.42. (a) Diagram showing pairs of $\delta^{18}O$ ratios for quartz and cassiterite used to estimate the temperature of O isotopic equilibrium, with equilibrium lines for temperatures ranging from 350 to 650 °C calculated using the equation proposed by Li et al. (2022): $1000 \ln \alpha_{quartz-cassiterite} = 1.259 \times 10^6/T^2 + 8.15 \times 10^3/T - 4.72$, where T is the temperature in Kelvin. Data from the quarry sample are primarily clustered around a temperature of 505 ± 130 °C, whereas data for the drill core sample suggests slightly higher temperatures around 610 ± 45 °C. (b) Distribution of estimated temperatures for O isotope equilibrium between quartz and cassiterite. (c) $\delta^{18}O$ ratios estimated for the fluid from quartz data using temperature-dependent fractionation factors from Zheng (1993) and Vho et al. (2019). (d) $\delta^{18}O$ ratios estimated for the fluid from cassiterite data using temperature-dependent fractionation factors from Zheng (1991) and Li et al. (2022). (e) Comparison of fluid $\delta^{18}O$ ratios estimated from quartz cassiterite data using temperature-dependent fractionation factors of Vho et al. (2019) and Li et al. (2022), respectively. It is important to note that the temperatures used to calculate the $\delta^{18}O_{fluid}$ ratios from quartz and cassiterite data correspond to the estimates associated with each data pair, not the average temperature calculated for each sample.*

## 5.3. Preliminary discussion and conclusions

### *5.3.1. Magmatic fluid involvement in quartz-cassiterite greisen formation*

Fluid inclusion petrography in quartz-cassiterite greisen collected in the quarry has been focused on primary assemblages and reveals the entrapment of multiphase halite-bearing FIs, occasionally associated with vapour-dominant, biphasic FIs along growth planes (Fig III.40) (section 5.2.1.iii of Part III). Petrographic features of these FI types closely resemble those of demixed magmatic fluids (L2 and V2) previously described in magmatic quartz and topaz (Aïssa et al., 1987; Harlaux et al., 2017; this study) (Figs. III.6b-e). However, they significantly differ from those of relatively low-salinity (*ca.* 1–5 wt% NaCl eq) greisenising fluids hosted in quartz from typical quartz-muscovite mineralogical assemblages (Monnier et al., 2020). The remarkable similarity to magmatic fluid inclusions supports the initial magmatic origin of greisenising fluids inferred from apatite chemistry, which was rapidly overprinted by meteoric fluids (Part II).

Further evidence for magmatic fluid involvement is provided by oxygen isotope thermometry on greisen-related quartz and cassiterite pairs, which indicates relatively high precipitation temperatures ranging from 460 to 670 °C (Figs. III.42a-b). These values exceed the *ca.* 450 °C threshold for external fluid incursion into the Beauvoir PRMG, as determined by fluid inclusion studies (Aïssa et al., 1987; Cuney et al., 1992; this study), yet align well with the circulation temperatures deciphered for magmatic fluids (Aïssa et al., 1987). Additional confirmation of the magmatic nature of these fluids comes from the reconstructed oxygen isotopic composition of the parent fluid, with $\delta^{18}O_{fluid}$ values range from 7.1 to 9.7 ‰ (Figs. III.42c-e). These ratios fall within the typical magmatic fluid range (5.5–9.5 ‰) and contrast sharply with the negative $\delta^{18}O$ values characteristic of meteoric fluids (Sheppard, 1986).

Both petrographic and oxygen isotopic evidence strongly suggest that magmatic fluid circulation played a key role in the formation of quartz-cassiterite greisen, a hypothesis coherent with the relatively high Sn concentrations characterising these fluids (median ~ 3200 ppm for L2-type FIs) (Harlaux et al., 2017; this study) (Fig. III.19). While the rapid examination of primary fluid inclusions did not allow for the identification of low-salinity FIs that could record mixing between magmatic and meteoric fluids, the coexistence of liquid-dominant halite-bearing FIs with vapour-dominant FIs suggests boiling of magmatic fluids (Fig. III.40). The separation of a magmatic vapour phase from a magmatic brine represents an efficient mechanism for metal precipitation (e.g., Heinrich, 1990; Korges et al., 2018; Ni et al., 2022) and likely played a crucial role in cassiterite precipitation, particularly in the apical greisen zones. Moreover, the liquid-dominant FIs are occasionally characterised by the trapping of two halite solids, possibly reflecting halite saturation in the circulating fluids. This process is well-documented in shallow magmatic-hydrothermal systems and may have contributed to decreasing $SnO_2$ solubility in the magmatic fluid (e.g., Lecumberri-Sanchez et al., 2015).

#### *5.3.2. Influence of boiling processes on the O isotopic composition of the vapour phase*

The accumulation within the residual crystal-mush of a low-$\delta^{18}O$ vapour phase formed through intense boiling of magmatic fluids has been proposed as a conceivable mechanism influencing the crystallisation of low-$\delta^{18}O$ quartz rims in the B1 unit (section 4.3.4.iv of Part III). As discussed in the previous section (5.3.1), quartz-cassiterite greisen appears to have precipitated from magmatic brines following the separation of a magmatic vapour phase and, therefore, likely records the oxygen isotopic composition of these brines ($\delta^{18}O_{fluid}$ ~ 7.1–9.7 ‰; Figs. III.42c-e).

Although the oxygen isotopic fractionation between coexisting magmatic brines and vapours at elevated temperatures is typically low, studies on $H_2O$-NaCl and $H_2O$-KCl salt systems have documented fractionation values reaching up to 2‰ ($\Delta^{18}O_{L\text{-}V}$) at temperatures between 350 and 600 °C (Shmulovich et al., 1999). If a similar mechanism occurred within the Beauvoir PRMG, the magmatic vapour phase would exhibit $\delta^{18}O$ values of *ca.* 5.1 to 7.7 ‰. Given the estimated crystallisation temperatures of *ca.* 550 to 670 °C for the Beauvoir melts (Pichavant et al., 2022), oxygen isotopic fractionation between quartz and magmatic vapours would have remained relatively limited, with $\Delta^{18}O_{quartz\text{-}vapour}$ ranging from 1.0 to 2.0 ‰ (Vho et al., 2019). Quartz growth from such high-temperature vapours would therefore display $\delta^{18}O$ ratios between 6.1 and 9.7 ‰, consistent with the average $\delta^{18}O$ ratio of *ca.* 7.2 ‰ recorded in quartz rims from the B1 unit (Fig. III.30a).

These observations suggest that intense boiling of magmatic fluids may have contributed to decreasing the O isotopic composition of quartz rims in the B1 unit, especially knowing that the volume of produced vapours significantly exceed that of magmatic brines in such magmatic-hydrothermal systems (e.g., Heinrich, 2007).

## 6. Conclusion

The characterisation of magmatic quartz and its associated fluid inclusions in the Beauvoir PRMG provides deeper insight into fluid circulation dynamics and metal transport during the critical magmatic-hydrothermal transition. An episode of intense devolatilisation under supra-solidus conditions appears to have strongly influenced quartz crystallisation in the B1 unit, leading to the development of snowball textures, the entrapment of numerous primary magmatic fluid inclusions, and likely impacting its oxygen isotopic signature. This devolatilisation event may have contributed to increasing oxygen fugacity during differentiation, thereby influencing the magmatic precipitation of cassiterite. Exsolved magmatic fluids show strong enrichment in rare metals, which precipitated in response to changes in oxidation state and boiling processes. As evidenced by apatite chemistry, sub-solidus evolution of the Beauvoir magmatic-hydrothermal system is characterised by mixing dynamics between magmatic and meteoric fluids, significantly reducing hydrothermal metal mobility. Ultimately, magmatic fluids accounted for only ~5 % of the fluid system.

# Part IV

# General discussion

The evolution of the Beauvoir PRMG is marked by a complex interplay of magmatic and hydrothermal processes, spanning from the emplacement of the Beauvoir melts at *ca.* 310–315 Ma (Duthou and Pin, 1987; Cheilletz et al., 1992; Melleton et al., 2015; Rocher et al., 2024) to supergene kaolinisation during the Eocene-Oligocene (Merceron et al., 1987; Charoy et al., 2003; Monnier et al., 2019). Apatite has proven to be a key mineral for deciphering the distinct magmatic and hydrothermal events that define the Beauvoir system's evolution (Part II; Rocher et al., 2024). By integrating *in-situ* elemental compositions (major, trace elements and halogens), oxygen isotopic systematics, and U-Pb geochronology of the different apatite generations, it is possible to constrain the timing of hydrothermal events identified through mineralogical studies (Merceron et al., 1987, 1992; Charoy et al., 2003; Monnier et al., 2019) and gain new insights into the chemistry and nature of the fluids involved.

Four major magmatic to hydrothermal events have been identified, encompassing magmas crystallisation, the magmatic-hydrothermal transition, and two late, non-magmatic hydrothermal events associated with regional tectonic activity (i.e., fluorite mineralisation and illite ± smectite vein fillings). The following section delves into the magmatic-hydrothermal history of the Beauvoir PRMG, which represents a pivotal stage in its evolution.

## 1. Impact of melt devolatilisation on crystallisation dynamics

The magmatic-hydrothermal transition is defined as a continuous evolution during the cooling of the granitic melt, shifting from an initially magmatic system governed by crystal-melt interactions to a more complex regime where crystal-melt-fluid interactions prevail, ultimately evolving in a purely hydrothermal system dominated by fluid-rock interactions (Halter and Webster, 2004; Audétat and Edmonds, 2020). In peraluminous rare-metal granite systems, this transition is characterised by the exsolution of magmatic fluids from volatile-saturated melts, and eventually melt-melt immiscibility processes that liberate residual, flux-rich melts within the system (e.g., Aïssa et al., 1987; Badanina et al., 2004; Kaeter et al., 2018; Ballouard et al., 2020a; Pfister et al., 2023). This section discusses the intricate interactions between melt and fluids that govern this transition, as well as the nature of involved fluids and their implications for the metal budget and mobility throughout the magmatic-hydrothermal evolution of the Beauvoir system.

In the Beauvoir PRMG, evidence of volatile saturation has been highlighted through the presence of magmatic fluid inclusions in magmatic quartz and topaz from the highly evolved B1 unit (Aïssa et al., 1987). In contrast, no magmatic fluid inclusions have been observed in the less evolved B2 and B3 units, reflecting either that magmatic fluids were predominantly concentrated in the apical part of the system (i.e., in the B1 unit) and/or that water saturation was minimally achieved in these units, if at all, possibly at the final stages of melt crystallisation. The complete lack of magmatic fluid inclusions in B2 and B3 makes it unlikely that significant amounts of

magmatic fluids were exsolved from these units. Further supporting this interpretation, the water content of melt inclusions from the B1 unit (*ca.* 3.6 wt%) is significantly lower than that of the B2 unit (6.2–7.3 wt%) (Kovalenko et al., 1998), suggesting that volatile saturation and fluid exsolution were more subdued in the B2 unit. Although the intensity of magmatic fluid exsolution was likely lower in the B2 and B3 units than in the B1 unit, evidence of devolatilisation processes is nevertheless preserved, particularly in the geochemical signature of magmatic apatite (type I) (Part II; Rocher et al., 2024). The chondrite-normalised REE distribution of apatite I is notably characterised by pronounced tetrad effect, with estimated tetrad effect degrees ($TE_{1\text{-}3}$) varying between 1.05 to 1.73 and predominantly exceeding the significance threshold of 1.1 defined by Irber (1999) (Part II; Rocher et al., 2024) (Table IV.1). Such feature is typically associated with highly evolved granites and related metasomatic rocks. Similar patterns have also been documented in melt inclusions (Peretyazhko and Savina, 2010) and various minerals, including zircon (Yang et al., 2014), columbite-group minerals (Badanina et al., 2015), and apatite (Chu et al., 2009; Roda-Robles et al., 2022). Although recent research has suggested that the fractionation of monazite and xenotime during magmatic differentiation may result in tetrad effects (Duc-Tin and Keppler, 2015; Shuai et al., 2021), it is widely attributed to the selective complexation of REE with F or Cl during metasomatism, or during fluid and melt exsolution (e.g., Bau, 1996; Irber, 1999; Jahn et al., 2001; Veksler et al., 2005; Monecke et al., 2007; Peretyazhko and Savina, 2010; Dostal et al., 2015; Ballouard et al., 2020b). The non-negligible influence of fluid exsolution on magmatic apatite chemistry, even in units where devolatilisation appears to have been less intense, emphasises the significant role of these processes in shaping the chemical composition of magmatic minerals (Table IV.1; Fig. IV.1).

A notable feature potentially inherited from the devolatilisation dynamics lies in the oxidising magmatic evolution recognised in the Beauvoir PRMG. Given its highly evolved and felsic nature, such melts would typically be strongly reduced (Sha and Chappell, 1999). However, a progressive increase in oxygen fugacity ($fO_2$) during magmatic differentiation has been highlighted by (i) a decrease in the $Fe^{3+}/Fe^{2+}$ ratio of Li-micas from the least differentiated B3 unit to the highly evolved B1 unit (Cuney et al., 1992); (ii) crystallisation experiments (Pichavant et al., 2016; Pichavant, 2022); and (iii) the decrease in the amplitude of the negative Eu anomaly observed in the REE distribution of magmatic apatite from the B3 and B2 ($Eu/Eu^* \sim 0.01$–$0.47$) to B1 ($Eu/Eu^* \sim 0.27$–$0.75$), as discussed in Part II (Rocher et al., 2024) (Table IV.1; Fig. IV.1c). The mechanisms driving this evolution remain unclear and previous hypotheses invoking interaction of the melts with oxidising meteoric fluids (Fouillac et al., 1987; Fouillac and Rossi, 1991) face significant physical constraints (e.g., Weis et al., 2012). A more plausible explanation lies in the progressive degassing of silicate melts, which has been shown to increase oxygen fugacity by up to two log units in sulfur-free magmas (Burgisser and Scaillet, 2007). For hydrous, F-bearing leucogranitic and pegmatitic magmas, Pichavant et al. (2016) introduced the concept of "self-

oxidation" to explain the oxidising evolution required for muscovite crystallisation. This mechanism involves the dissociation of $H_2O$ during progressive devolatilisation in volatile-rich melts, producing HF as a gas phase and an increase in the concentration of oxygen anions in the melt, as described by the reaction:

$$\underset{melt/gas}{H_2O} + \underset{melt}{2F^{2-}} = \underset{gas}{2HF} + \underset{melt}{O^{2-}}$$

The loss of hydrogen as HF gas reduces the cation-to-oxygen ratio in the melt, effectively increasing its oxidation state. The implications of this oxidising evolution are significant, particularly for Sn precipitation. Oxygen fugacity strongly influences $SnO_2$ solubility in granitic melts, with oxidised conditions promoting cassiterite saturation ($Sn^{2+} \rightarrow Sn^{4+}$ transition) (Linnen et al., 1996; Bhalla et al., 2005; Pichavant, 2022). Thus, beyond creating conditions favourable for muscovite stability over biotite (Pichavant et al., 2016), devolatilisation likely played a critical role in the precipitation of metals, particularly Sn (Table IV.1; Fig. IV.1c). Additional evidence of degassing-related metal precipitation is derived from fluid inclusion data from the B1 unit (Fig. III.24; section 3 of Part III). Significant variability, spanning up to three orders of magnitude, has been observed in the concentrations of Li, Be, Sn, and W within individual FI types. This variability, particularly evident in magmatic brines (L2 and L7), occurs without changes in fluid salinity, suggesting precipitation trends rather than dilution effects (Fig. III.24; section 3 of Part III). L2 and L7 brines formed through vapour separation during supra- to sub-solidus boiling stages (and subsequent cooling for L7), which may have triggered the precipitation of Sn and other rare metals, leading to a decrease in metal concentrations as observed in FI data (Heinrich, 1990; Ni et al., 2022) (Table IV.1; Figs. IV.1c-d). Interestingly, cassiterite inclusions within magmatic quartz are found exclusively in the B1 unit, occasionally in spatial association with magmatic fluid inclusions (L2 and V2) along primary growth planes (Fig. III.6; section 2 of Part III). This co-occurrence further underscores the pivotal role of melt-fluid and fluid-fluid immiscibility processes in the B1 unit in driving Sn (and potentially other metal) precipitation under supra-solidus conditions.

*Table IV.1. Summary of key arguments derived from the analysis of apatite, quartz, cassiterite, and fluid inclusions hosted in magmatic quartz, which collectively help reconstruct the supra- to sub-solidus history of the Beauvoir PRMG. The letters and associated events correspond to those presented in subsequent Figure IV.1.*

| | ***Apatite*** | | ***Quartz*** | | | ***Cassiterite*** | ***Physico-chemical evolution of he Beauvoir magmatic-hydrothermal system*** | | | | | |
|---|---|---|---|---|---|---|---|---|---|---|---|---|
| | Elemental composition | $\delta^{18}O_{Ap}$ | Petrography | $\delta^{18}O_{Qz}$ | Fluid inclusion composition | $\delta^{18}O_{Cst}$ | t | Temperature | Magma-fluid ratio | Magmatic-meteoric fluids ratio | Hydrothermal metal mobility | Redox conditions |
| ***(a) Crystallisation of early quartz phenocryts*** ***All units*** | | | Absence of magmatic FIs | | | | 314.6 ± 4.7 Ma (Ap I) | ~ 670 °C [4] | ***Deep fluids*** | | | Reduced |
| | | | | ≥ 10 ‰ | | 2.4–6.9 ‰ | | | | | | |
| ***(b) Initiation of magmatic fluid exsolution*** ***All units*** | Tetrad effects in REE distribution (Ap I) | | L1-type FIs hosted in magmatic Tpz from the B1 unit [1] | | Enrichment of Sn, Nb & W in L1 fluids compared to the bulk B1 unit [2] | | | 675 ± 100 °C* (B1) 650 ± 115 °C* (B2) ≥ 600 °C [1,2] | | | | |
| ***(c) Extensive devolatilisation causing 'self-oxidation'*** ***B1 unit*** | Decrease in the amplitude of the negative Eu anomaly (Ap I) | | Partial resorption of Qz phenocrysts Abundance of magmatic FIs in quartz | | Boiling assemblages: - Enrichment of Be, Sn & W compared to the bulk B1 unit - Sn & W in the brine (L2), Li, Be, Nb & Ta in the vapour (V2) | | | | | | ***Cst I*** ***Decrease in $fO_2$ & boiling of magmatic fluids (L2)*** | |
| ***(d) Evolution toward a highly evolved, fluid-saturated residual melt*** ***B1 unit*** | | | Snowball textures Primary growth planes of fluid (L2-V2) and melt inclusions | Progressive decrease in $\delta^{18}O_{Qz}$ down to 2.1 ‰ | | | | | | | | |
| ***(e) Initiation of greisen alteration*** ***All units - more intense at the apex*** | High Mn, Sn & REE, LREE enriched (Ap IIa) | 2.7–7.5 ‰ (Ap IIa) | Secondary planes of magmatic FIs (L2-V2-L7) | 7.5–13.6 ‰ | $\delta^{18}O_{fluid}$ ~ 7–10 ‰ | 2.1–5.5 ‰ | 314.3 ± 5.5 Ma (Ap IIa) | 505 ± 130 °C* 610 ± 45 °C* | | | ***Cst II*** | |
| ***(e) Progressive incursion of meteoric fluids*** ***All units*** | High Sr, low Mn & REE, LREE depleted (Ap IIb) | -3.3– -1.0 ‰ (Ap IIb) | Secondary planes of low- to moderate-salinity FIs (L3-L4 & L5-L6) | Overprint of $\delta^{18}O$ of magmatic Qz through diffusion along fractures ($\delta^{18}O_{Qz}$ < 0) | Dilution trend of magmatic fluids with a low-salinity external fuid | | 311.7 ± 8.1 Ma (Ap IIb) | ~ 200–450 °C [1,3] | | | ***Boiling of magmatic fluids (L2-L7) and/or decrease in $fO_2$*** | Oxidised |

SUPRA-SOLIDUS

SUB-SOLIDUS

* Temperature of oxygen isotopic equilibrium between quartz and cassiterite

Cassiterite precipitation

In the Beauvoir PRMG, the late crystallisation stage of the B1 unit thus likely occurred in a dynamic hybrid environment shaped by the interaction between residual flux-rich melt and exsolved magmatic fluids. This highly specialised setting provided ideal conditions for the development of snowball-textured quartz crystals, as detailed in section 2 of Part III (e.g., Müller and Seltmann, 1999; Müller et al., 2000, 2002a, 2009; Breiter et al., 2005; Wang D. et al., 2019) (Fig. IV.1d). The coexistence of melt inclusions and multiphase, magmatic fluid inclusions within these quartz crystals further supports this hypothesis (Kovalenko et al., 1998; this study) (Table IV.1; Fig. IV.1d). Beyond their distinctive snowball texture – absent in the B2 and B3 units – magmatic quartz from the B1 unit exhibit a unique core-to-rim trend in their oxygen isotopic composition. This trend is marked by a systematic and progressive decrease in $\delta^{18}O$ ratios from core to rim, with $\Delta_{core\text{-}rim}$ values ranging from *ca.* 4.8 to 7.8 ‰ (Fig. III.27; section 4 of Part III). Similar unexpected low O isotopic compositions have previously been documented in other magmatic minerals from the B1 unit, including topaz, lepidolite and feldspar (Fouillac et al., 1987; Fouillac and Rossi, 1991) (Fig. III.34; section 4 of Part III). They were ascribed to meteoric fluid incursion under supra-solidus conditions, the physical process of which is difficult to conceive (e.g., Weis et al., 2012). The preservation of primary growth textures in these quartz crystals appears to exclude the possibility of a post-crystallisation fluid overprint (Fig. III.2; section 2 of Part III), which would typically manifest as irregular domains indicative of fluid infiltration fronts. Processes possibly responsible for generating this primary isotopic signature are explored in detail below.

To my knowledge, oxygen isotopic zonation in igneous quartz, such as that observed in the Beauvoir B1 unit, has not been reported in other rare-metal granites or rhyolites (e.g., Raimbault and Burnol, 1998; Michaud and Pichavant, 2020). However, it was reported in magmatic quartz from some high-silica volcanic rocks, where it is often attributed to open-system processes such as the assimilation of low-$\delta^{18}O$ hydrothermally altered host rocks or melt-melt mixing (e.g., Bindeman and Valley, 2002; Budd et al., 2017). Open-system processes have also been documented in LCT pegmatites, such as the Little Nahanni Pegmatite Group in Canada (e.g., Kontak et al., 2016; Burns, 2016; Pfister et al., 2023). In this case, interactions between melt and metasedimentary country rocks were suggested to slightly increase the melt $\delta^{18}O$ composition, and sub-solidus fluid-rock interactions were invoked to explain the large spread in $\delta^{18}O$ and $\Delta$mineral values (Pfister et al., 2024). Similarly, the host mica schists of the Beauvoir granite exhibit relatively heavy O isotopic signatures, with $\delta^{18}O$ ratios varying between 9.4 and 11.5 ‰ (Fouillac et al., 1987). Consequently, their assimilation could not account for the significant core-to-rim decrease in $\delta^{18}O$ observed in magmatic quartz from the B1 unit. Moreover, the low liquidus temperature characterising the Beauvoir melts, experimentally estimated at *ca.* 670 °C (Pichavant, 2022), suggests that significant assimilation of host rocks is unlikely, and textural evidence for such process is missing.

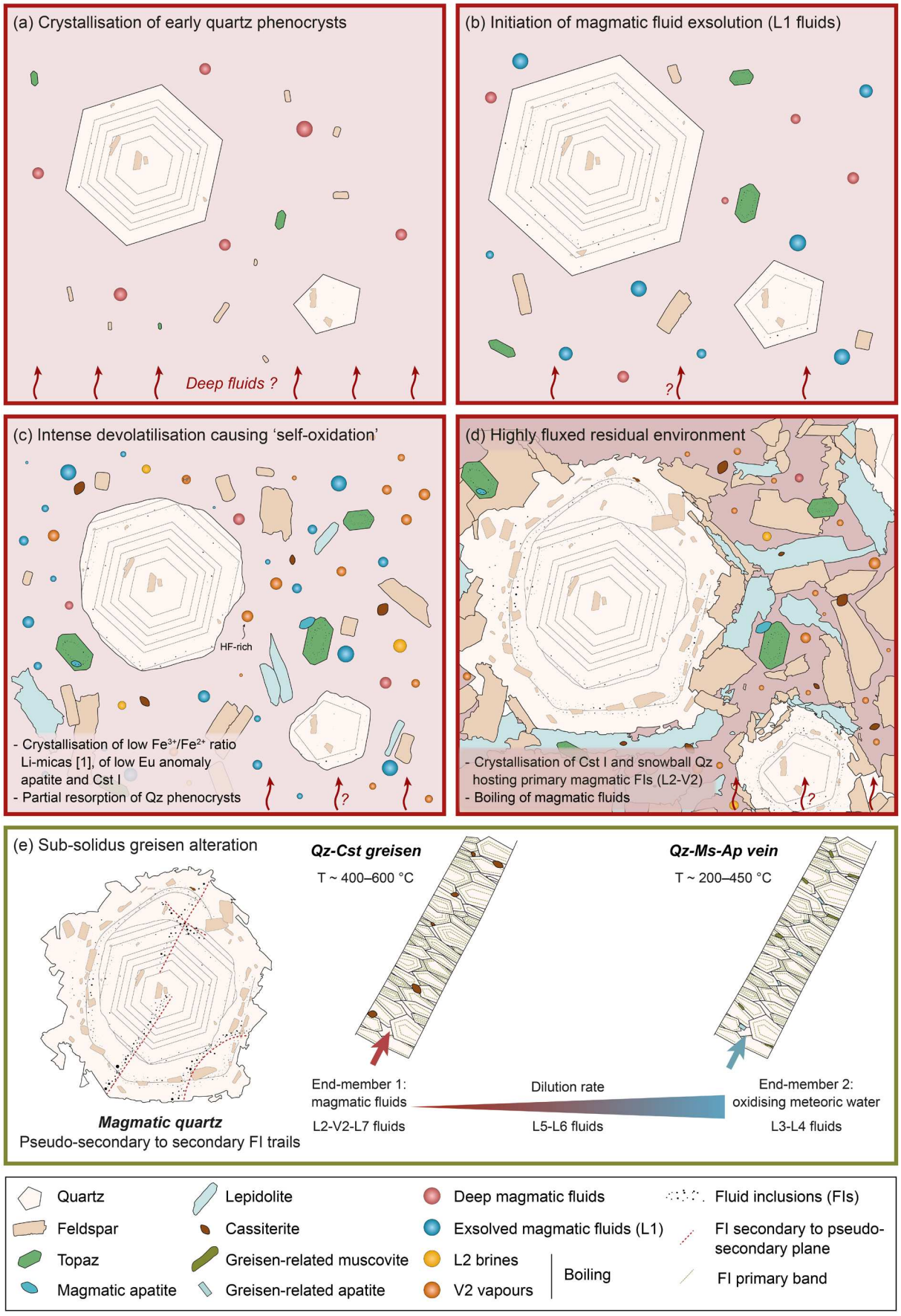



*Figure IV.1. Synthetic illustration of the magmatic-hydrothermal evolution of the Beauvoir PRMG (Caption continued on the next page)*

*(Continued caption) Figures (c-d) emphasise the specific features of magmatic-hydrothermal evolution of the B1 unit, whereas figures (a-b-e) apply to all three magmatic units. (a) Crystallisation of early quartz phenocrysts with high $\delta^{18}O$ ratios within all three magmatic units; (b) Initiation of magmatic fluid exsolution, evidenced by tetrad effects in REE distribution of magmatic apatite from the three units and the trapping of magmatic fluid inclusions (L1-type) in magmatic quartz and topaz from the B1 unit; (c) "Self-oxidation" resulting from extensive devolatilisation of the B1 melt, leading to partial resorption of quartz phenocrysts and promoting cassiterite precipitation; (d) Late-stage growth of snowball quartz in a highly fluxed residual melt; (e) Fluid dynamics driving sub-solidus greisen alteration throughout the entire intrusive body. The letters and associated events correspond to those presented in Table IV.1. [1] Cuney et al., 1992. Abbreviations follow the IMA conventions compiled by Warr (2021).*

The open-system nature of the Beauvoir magmatic system has been recently inferred from the detailed petrographic and geochemical study of Esteves et al. (2024b). These investigations reveal that the Beauvoir PRMG is structured into distinct sub-units, each formed by the stacking and amalgamation of multiple sills. These sub-units reflect a dynamic emplacement history, with successive injections of melts, often accompanied by episodes of recharge and mixing, leading to sill inflation and differentiation. Theoretically, in the B1 unit, low-$\delta^{18}O$ late-stage melts could have mixed with the original high-$\delta^{18}O$ magmatic melt, providing a plausible explanation for the relatively low-$\delta^{18}O$ rims of magmatic quartz. In such scenario, low- $\delta^{18}O$ melts could have originated at depth through the partial melting of rocks that had been hydrothermally altered by meteoric fluids at high temperatures. Both events would likely be temporally disconnected, with hydrothermal alteration predating partial the melting that generated the Beauvoir magmas. This process would be analogous to what has been documented in Yellowstone, where rhyolitic melts resulting from the melting or assimilation of hydrothermally altered material in the collapsed caldera roof were found to have low $\delta^{18}O$ signatures (e.g., Bindeman and Valley, 2002; Bindeman and Simakin, 2014; Troch et al., 2018). However, the presence of such a hydrothermally altered rock source in the deep Variscan crust remains hypothetical, and the reason for its contribution at the final stage of the Beauvoir magmatic system's evolution is even more enigmatic. Moreover, the whole-rock $\delta^{18}O$ value of 9.0 ‰ ($\delta^{18}O_{quartz}$ = 10.6 ‰) reported for the Richemont dyke – representing the sub-volcanic equivalent of the Beauvoir granite in the Limousin region – suggests that the existence of an altered meta-volcanic source (i.e. a buried volcano-sedimentary system) may not be necessary to form these highly evolved magmas (Raimbault and Burnol, 1998). Finally, some uncertainties emerge regarding the plausibility of melt-mixing processes. These doubts arise from the lack of significant variations in trace element composition, the absence of correlations between cathodoluminescence (CL) zoning patterns and $\delta^{18}O$ isotopic compositions, as well as the absence of compositional changes in exsolved magmatic fluids between quartz cores and rims (Part III).

Among the processes discussed in section 4 of Part III, one hypothesis stands out as particularly consistent with the intense melt-melt and melt-fluid immiscibility processes observed in the Beauvoir PRMG. More specifically, I suggest that the original oxygen isotope composition zoning recorded in B1 magmatic quartz relates to the same process as the one responsible for

snowball textures, and is linked to the highly fluxed character of the B1 residual melt (Table IV.1; Fig. IV.1d). The low $\delta^{18}O$ compositions recorded in other magmatic minerals from the B1 unit (Fouillac et al., 1987; Fouillac and Rossi, 1991) may also reflect the effects of late-stage fluid exsolution, resulting in the partial resorption of early-formed crystals by a highly reactive aqueous phase, followed by the crystallisation of low-$\delta^{18}O$, late-stage overgrowths in a volatile-rich residual melt. The vapour phase exsolution from melts has been shown to significantly influence the hydrogen isotopic composition of granitic rocks, resulting in significant decrease in the whole rock $\delta D$ ratio (e.g., Taylor et al., 1983; Nabelek et al., 1983). However, oxygen isotopic composition tends to remain mostly constant throughout degassing. Considering hypothetical extreme cases, where isotopic fractionation would be influenced by devolatilisation of a melt, the lighter isotope ($^{16}O$) would preferentially partition into the exsolved vapour, resulting in higher-$\delta^{18}O$ melts (Zhao and Zheng, 2003), which contrasts with the decrease in $\delta^{18}O$ ratios of magmatic quartz from the Beauvoir PRMG. Nevertheless, some evidence of pronounced oxygen isotopic fractionation between coexisting liquid and vapour, up to 2 ‰ ($^{18}O/^{16}O_{(L\text{-}V)}$), has been highlighted in $H_2O$-NaCl and $H_2O$-KCl salt systems between 350 and 600 °C (Shmulovich et al., 1999). Extreme boiling of magmatic fluids could have therefore produced a low-$\delta^{18}O$ vapour phase, which may have accumulated within the residual crystal mush, influencing the growth of quartz rims. Another plausible explanation, though not documented in the literature, is the direct production of a low-$\delta^{18}O$ highly fluxed residual melt through disequilibrium oxygen isotopic fractionation during melt-melt immiscibility. While this process remains largely unexplored, experimental studies have demonstrated that oxygen isotope fractionation in silicate melts is influenced by their degree of polymerisation, with structural changes potentially affecting $\delta^{18}O$ values (Dubinina and Borisov, 2018). While their study does not explicitly address highly fluxed residual melts – which would typically be more depolymerised than their parental magmas – their findings suggest that variations in melt polymerisation could, in principle, contribute to a depletion in $\delta^{18}O$ relative to the initial melt (Dubinina and Borisov, 2018). However, as this mechanism has yet to be tested in natural or experimental systems, its role in magmatic-hydrothermal environments remains speculative. The Beauvoir PRMG represents one of the most evolved and flux-enriched magmas worldwide, characterised by high fractionation processes (Cuney et al., 1992; Raimbault et al., 1995), significant devolatilisation (Aïssa et al., 1987; this study), and melt-melt immiscibility (Esteves et al., 2024b). This unique, highly specialised character may have facilitated disequilibrium and irreversible oxygen isotopic fractionation processes.

## 2. Meteoric fluid incursion and its role in the evolution of the Beauvoir system

In the Beauvoir PRMG, several lines of evidence point to the involvement of external fluids during its magmatic-hydrothermal evolution. Early studies proposed that meteoric fluids infiltrated the Beauvoir melts under supra-solidus conditions at temperatures of *ca.* 570 ± 50 °C,

based on the O isotopic signature of magmatic minerals (Fouillac et al., 1987; Fouillac and Rossi, 1991). The involvement of external fluids, likely of meteoric origin, has also been inferred from the study of fluid inclusions, indicating their incursion under sub-solidus conditions at temperatures of approximately 450 °C (Aïssa et al., 1987; Cuney et al., 1992). Mixing dynamics between external fluids and magmatic brines produced relatively low-salinity fluids (1–8 wt% NaCl eq; L3-type FIs), which circulated throughout the entire intrusive complex, ultimately driving widespread greisen alteration (Cuney et al., 1992). More recent work on fluid inclusions hosted in greisen-related quartz further support this hypothesis, revealing the circulation of low- to moderate-salinity fluids (1–5 wt% NaCl eq) at temperatures ranging from 400 to 190 °C (Monnier et al., 2020). However, fluid inclusion data, along with the apparent lack of changes in fluid chemistry, have led some authors to propose a magmatic origin for greisenising fluids, which would have formed through the phase separation of primary fluids exsolved from the melts (Monnier et al., 2018, 2020). Yet, phase separation of primary magmatic fluids resulted in the formation of a low- to moderate-salinity vapour phase V2 (3–21.9 wt% NaCl eq) and a high-salinity liquid phase L2 (30–50 wt% NaCl eq) (Aïssa et al., 1987; Harlaux et al., 2017), which contrast with the relatively low salinities of greisenising fluids (1–5 wt% NaCl eq; Monnier et al., 2020). If greisen alteration is unlikely related to the circulation of magmatic brines, the condensation of magmatic vapours maybe the origin of greisenising fluids. This interpretation introduces ambiguity regarding the extent to which these fluids were influenced by meteoric contributions or retained their magmatic character throughout the greisenisation process. Uncertainty also remains about the timing of external fluid incursion, whether it occurred under sub-solidus or supra-solidus conditions, adding complexity to the understanding of fluid dynamics during the Beauvoir system's evolution.

In this study, an evolutionary trend between two distinct end-members has been identified in the elemental and oxygen isotopic composition of early hydrothermal apatite (Table IV.1; Fig. IV.1e). The first end-member, exhibiting elevated MnO (2.7–4.8 wt.%) and Sn (24–65 ppm) contents, a positive Eu anomaly and $\delta^{18}O$ values between 2.7 and 7.5 ‰, is interpreted as precipitating from magmatic fluids. The second end-member, characterised by low MnO (<0.1–1.0 wt%) and high SrO (1.0–4.7 wt%) contents, negative $\delta^{18}O$ values (-3.3 to -1.0 ‰), MREE enrichment, low $La_N/Yb_N$ ratios, flat HREE patterns, and the absence of a distinct Eu anomaly, reflects the influence of oxidising meteoric fluids (Fig. II.14; Part II; Rocher et al., 2024). Meteoric fluid incursion likely began at near-solidus conditions, triggering the precipitation of hydrothermal cassiterite (Cst II) from magmatic fluids (Table IV.1; Fig. IV.1e). The analysis of fluid inclusions hosted in magmatic quartz further support this interpretation, showing evidence of dilution of magmatic fluids by meteoric water, manifested as decreases in salinity and trace element concentrations as the system evolved to lower temperatures (Fig. III.24; section 3 of Part

III). The absence of primary low-salinity fluid inclusions in magmatic quartz suggests that meteoric water incursion under sub-solidus conditions is more plausible.

Thus, the chemistry of early hydrothermal apatite (Part II) and the analysis of fluid inclusions in magmatic quartz (Part III) collectively support a significant contribution of meteoric fluids to the Beauvoir magmatic-hydrothermal system under near- to sub-solidus conditions, particularly as part of the greisenising fluid phase. These findings contrast with greisenisation processes observed in similar magmatic-hydrothermal systems, which are generally attributed to the circulation of acidic and moderately saline (*ca.* 3–10 wt% NaCl eq) magmatic fluids at temperatures of 200-500 °C (e.g., Burt, 1981; Štemprok, 1987; Shepherd et al., 1985; Taylor, 1988; Schwartz and Surjono, 1990; Halter et al., 1998; Dobeš, 2005). Nevertheless, external fluid contributions, particularly of meteoric origin, have also been documented in some instances (e.g., Witt, 1988; Cuney et al., 1992; Bettencourt et al., 2005).

Although recent thermodynamic modeling has challenged the necessity of oxidising agents for Sn precipitation (Liu et al., 2023), the role of meteoric water influx in triggering cassiterite precipitation is well-established in Sn(-W) magmatic-hydrothermal deposits (Witt, 1988; Heinrich, 1990; Audétat et al., 1998; Karimzadeh Somarin and Ashley, 2004; Fekete et al., 2016; Liu et al., 2020; Chen et al., 2023; Peng et al., 2023a). In the Beauvoir PRMG, apatite chemistry supports a similar mechanism, where magmatic-meteoric fluid mixing significantly influenced cassiterite precipitation (Rocher et al., 2024) (Table IV.1). Meteoric fluid circulation is also thought to have promoted the crystallisation of columbite- and pyrochlore-group minerals, especially within the highly differentiated B1 unit (Ohnenstetter and Piantone, 1988; Fouillac and Rossi, 1991). These observations emphasise the critical importance of open-system dynamics in the formation of PRMGs and, more broadly, RMGs, with significant implications on the mobility and distribution of metals within these systems, further discussed in the following section.

## 3. Dynamics and significance of hydrothermal mobility of metals in the Beauvoir magmatic-hydrothermal evolution

### *3.1. Characterisation of magmatic fluid metal enrichment and high-temperature metal mobility*

As previously mentioned, the Beauvoir PRMG exhibits exceptional enrichment in lithophile metals and halogens (e.g., Li, F, Ta, Nb, Sn, W, and Be) (Cuney et al., 1992; Raimbault et al., 1995), with concentrations significantly exceeding those of the bulk upper continental crust (Tischendorf, 1977; Romer and Pichavant, 2020). Previous analyses of exsolved magmatic fluids (L1-type FIs) using LA-ICP-MS have suggested notable enrichment in rare-metals compared to the whole-rock content of the most evolved B1 unit (Harlaux et al., 2017) (Fig. IV.2a). In this study, magmatic fluids derived from phase separation and cooling of primary exsolved fluids (L2,

V2, and L7) were further examined to refine constrains on metal mobility at high temperatures (*ca.* 100–600 °C; Aïssa et al., 1987; Harlaux et al., 2017; this study). Magmatic fluids show systematic enrichment in Be, Cs, Sn, and W compared to average bulk-rock composition of the evolved B1 unit, whereas Ta – and to a lesser extent, Nb – tend to be more concentrated in the whole-rock than in the fluids (Fig. IV.2). Lithium shows no consistent trend across all fluid types, with enrichment observed in the vapour phase (V2; Fig. IV.2c) but relative depletion in L2 and L7 fluids (Figs. IV.2b, d). The Li concentrations reported for L1 and L2 fluids in Harlaux et al. (2017) should be interpreted with caution due to the absence of correction for matrix contributions to the Li signal within fluid inclusions. Overall, magmatic fluids associated with the Beauvoir system are distinguished by their high concentrations in rare-metals, highlighting their importance in the transport and mobilisation of metals within the system.

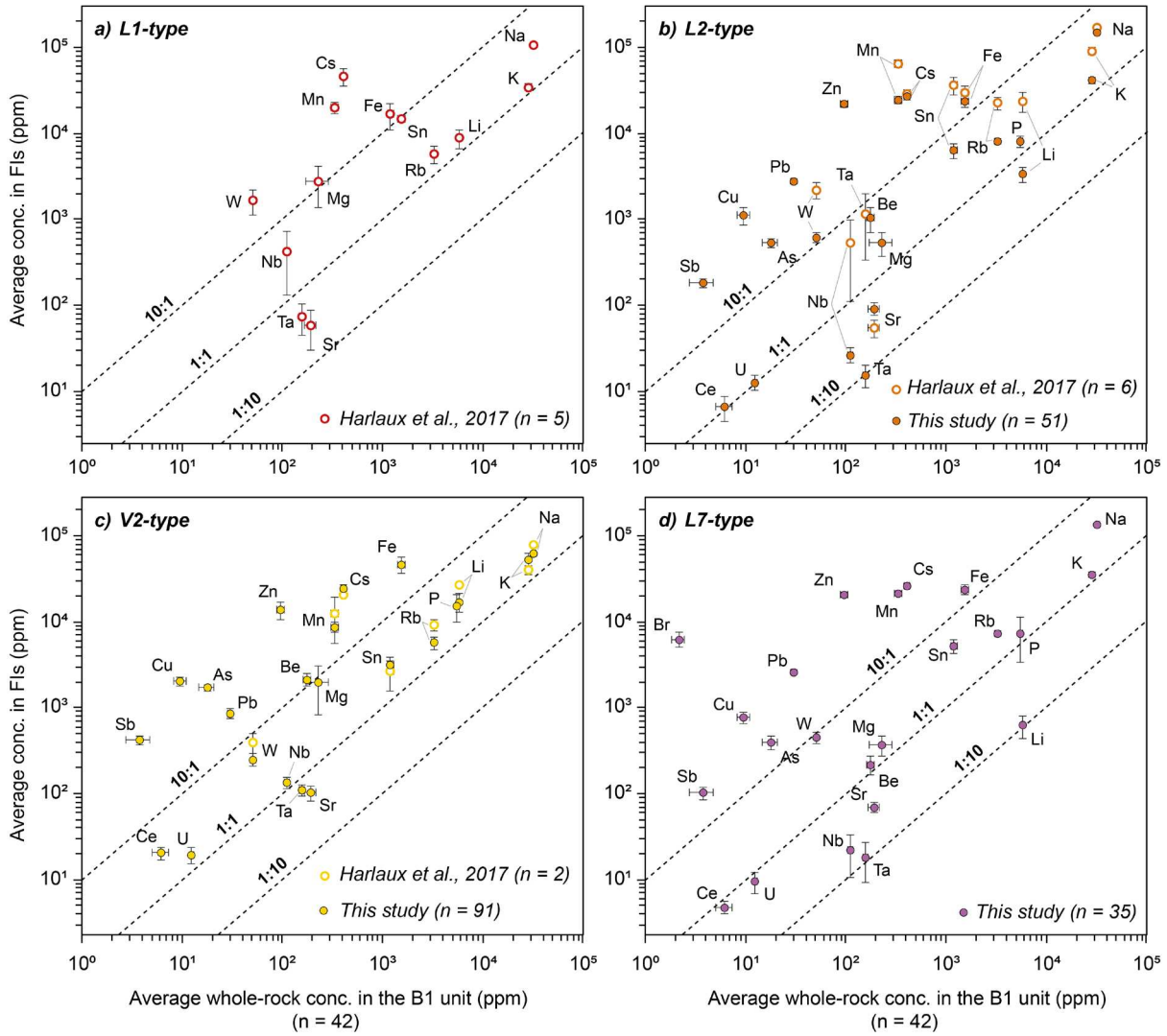



*Figure IV.2. Average concentrations for magmatic fluid inclusions (L1, L2, V2, and L7) hosted in magmatic quartz from the B1 unit of the Beauvoir PRMG versus average whole-rock concentrations of the B1 unit compiled from Burnol and Viallefond (1984); Pichavant et al. (1987a); Rossi et al. (1987); and Raimbault et al. (1995). Error bars correspond to the standard error of the average concentration, calculated as* $\sigma_{avg} = \frac{SD}{\sqrt{n}}$ *where SD is the standard deviation and n the number of data.*

### *3.2. Unveiling the complex role of vapour and brine phases in metal transport and enrichment*

As discussed in section 3 of Part III, phase separation of primary magmatic fluids (L1) led to the partitioning of elements between coexisting vapour (V2) and brine (L2) phases (Harlaux et al., 2017; this study). A strong affinity for the Cl-rich aqueous phase was observed for Na, Mn, Rb, W, Pb, and likely Sn and Zn, aligning with behaviours reported in comparable high-temperature magmatic-hydrothermal systems (e.g., Heinrich et al., 1992, 1999; Audétat et al., 2000a, 2008; Audétat and Pettke, 2003; Foustoukos and Seyfried, 2007; Audétat, 2019) (Fig. III.23 in Part III). Similarly, the preferential partitioning of Li into the vapour phase is consistent with earlier findings (Foustoukos and Seyfried, 2007). A novel observation in this study is the partitioning behaviour of Nb and Ta during fluid boiling, with both elements showing a pronounced affinity for the vapour phase – a phenomenon not documented in previous research. This may reflect a relative enrichment in F, which is known to enhance the hydrothermal mobility of Nb and Ta (e.g., Webster, 1990; Zaraisky et al., 2010; Timofeev et al., 2015; Akinfiev et al., 2020; Liu et al., 2024; Hu et al., 2024).

If unaffected by post-entrapment artefacts, as demonstrated for Cu (Lerchbaumer and Audétat, 2012; Seo and Heinrich, 2013), both the L2 brine and the V2 vapour phases may therefore represent ore-bearing fluids in the Beauvoir PRMG, likely contributing to metal enrichment in the apical zone but with distinct metallogenic roles: Sn and W are predominantly mobilised by the brine phase, whereas Li, Nb, and Ta are transported by the vapour phase. The accumulation of Ta-enriched vapour in the intrusion's apex may have contributed to its Ta enrichment, which was previously attributed solely to the ascent of Ta-rich melts during the late unmixing of an F-rich brine (Raimbault et al., 1995). The Ta enrichment, reaching up to *ca.* 50 ppm, documented at the metasomatic contact between the Beauvoir and Colettes granites (Raimbault et al., 1995) may further evidence the circulation of these vapours. This behaviour contrasts with that observed in analogous mineralised magmatic-hydrothermal systems, such as Sn-W greisen-related systems, where ore-bearing fluids are predominantly magmatic brines forming chlorine-metal complexes (e.g., Legros et al., 2019). However, the capability of vapour phases to transport ore-forming elements, particularly As, B, and Au, has also long been recognised in porphyry deposits, in which vapours tend to migrate towards the surface to form epithermal deposits (e.g., Audétat et al., 1998; Ulrich et al., 1999; Heinrich et al., 1999). A similar mechanism could be envisioned for the Beauvoir magmatic-hydrothermal system, where the migration of metal-rich vapour towards the surface may have contributed to the formation of a sub-volcanic environment enriched in Li, Nb, and Ta.

While the transport of metals in vapour phases was primarily thought to be influenced by their dry volatility (e.g., Krauskopf, 1964; Eastoe, 1982), more recent research has demonstrated the critical role of high water vapour density in enhancing the solubility and transport of metals

and other solute compounds in the vapour phase (e.g., Williams-Jones et al., 2002; Williams-Jones and Heinrich, 2005). Experimental work (e.g., Pokrovski et al., 2005, 2006a, b), as well as the study of synthetic fluid inclusions (e.g., Simon et al., 2005, 2006) have confirmed the ability of dense vapours to host substantial metal concentrations. In the Beauvoir PRMG, phase separation at near critical conditions, for which the distinction between liquid and vapour diminishes, may have facilitated the formation of dense vapour. This, combined with the high F content of the Beauvoir melts, is proposed to have greatly enhanced the vapour's capacity to transport metals, especially Li, Nb and Ta. While the brine phase undoubtedly remains important, the significantly larger volume of vapour in such systems (e.g., Heinrich, 2007) suggests a more complex interplay in metals transport between the two fluid phases than previously recognised, with the vapour potentially playing a major, yet previously underappreciated, role in shaping the metal distribution within the Beauvoir PRMG.

### *3.3. Open-system dynamics in supra-solidus magmatic-hydrothermal evolution*

Beyond potentially enriching the apical zone of the Beauvoir PRMG, the circulation of magmatic fluids (L2, V2, and L7), and to a greater extend, the mixture of magmatic and meteoric fluids forming greisenising fluids (L3-L4), led to substantial depletion of metals and other elements in the pervasively greisenised zones, with these elements being leached and redistributed into the surrounding host rocks (Aubert, 1969; Cuney et al., 1992; Harlaux et al., 2025) (Fig. IV.3a). Mica schists within the first hundred meters from the Beauvoir PRMG show notable Sn concentrations exceeding 100 ppm, likely resulting from the remobilisation of metals from the Beauvoir PRMG (Cuney et al., 1992). Further analyses also reveal elevated concentrations of Li and Sn ($\geqslant 10^2$–$10^3$ ppm) in quartz- and topaz-hosted fluid inclusions (Harlaux et al., 2017) and in mica (Monnier et al., 2022) from the La Bosse stockwork. The chemical overprint of the La Bosse stockwork by the Beauvoir magmatic-hydrothermal system is evidenced by the precipitation of (F, Li)-rich micas, cassiterite, a second generation of topaz, and a third generation of wolframite within reactivated polyphased veins (Merceron et al., 1992; Monnier et al., 2019). Concentric dispersion halos of F, Li, Sn, Be, W, As, and P have been documented over distances extending from several hundred meters to kilometres around the Beauvoir PRMG (Aubert, 1969; Cuney et al., 1992; Harlaux et al., 2025) (Figs. IV.3a-c).

The extent of alteration halos, the distribution of metal concentrations around the Beauvoir PRMG, and the concentrations of metals in circulating fluids (liquid + vapour) provide a basis for estimating the volume of fluid required to produce the observed chemical overprint. Cuney et al. (1992) previously applied a similar mass-balance approach, demonstrating that the Sn depleted from the cupola was sufficient to explain the Sn enrichment within the 130 m proximal halo in the surrounding mica schists. The Beauvoir magmatic-hydrothermal system likely caused significant chemical overprinting of the mica schists surrounding the upper part of the intrusion.

In the conceptual model, the remobilisation halo within the mica schists is approximated as a half-spherical zone centred at approximately 400 m depth along the GPF1 drillhole, comparable with the geometry proposed by Cuney et al. (1992) (Fig. IV.3d). The Beauvoir intrusion is represented by the half sphere drawn with a solid line on Figure IV.3d, with a diameter of approximately 615 m. This is enveloped by a larger half sphere, represented with a dashed line, which delineates the extent of the remobilisation halo. The diameter of this larger half sphere is not fixed and is adjusted to estimate fluid volumes required to form varying halo sizes. The volume of overprinted mica schists is determined by calculating the volume between the two half spheres (Fig. IV.3d).

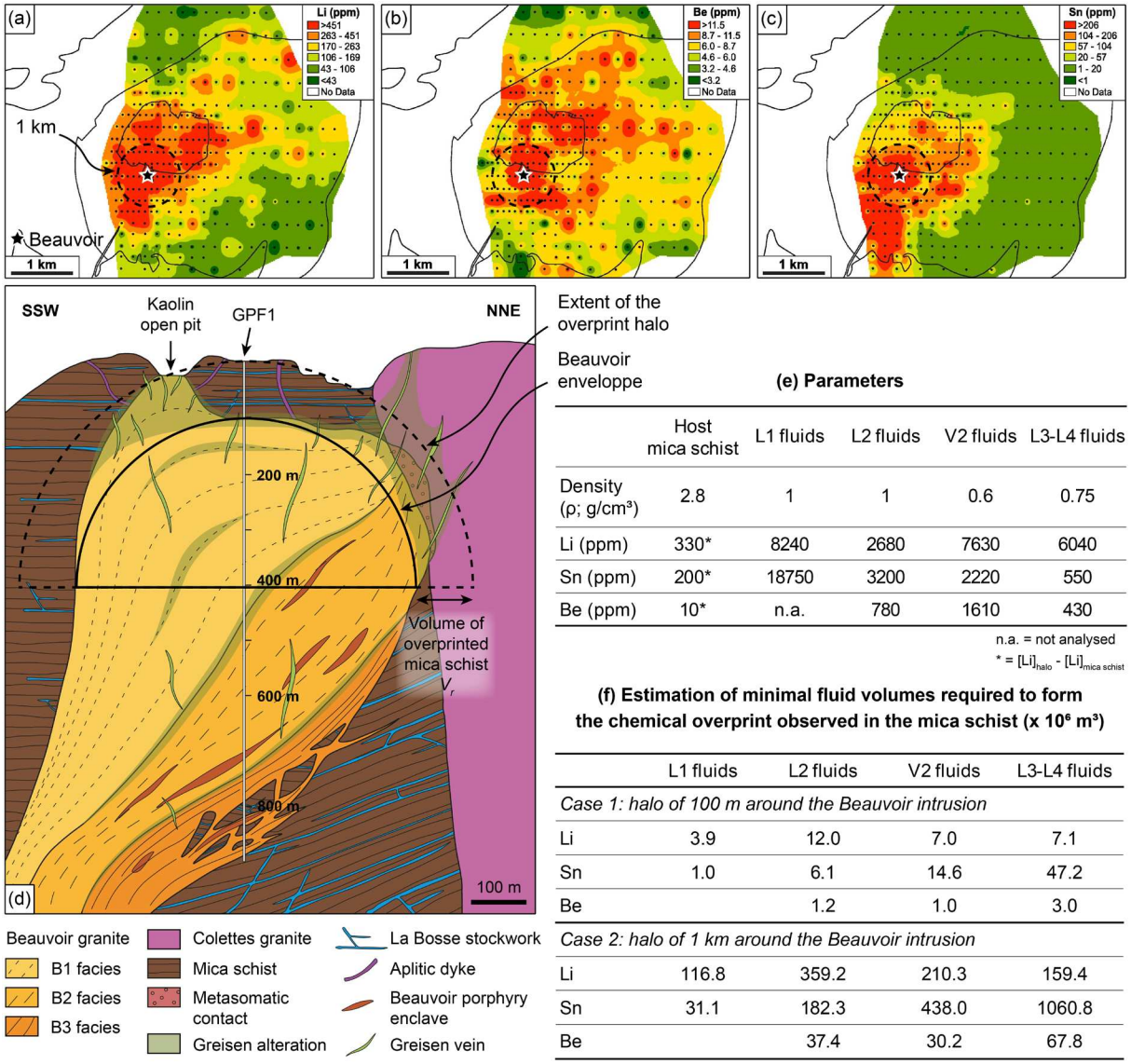
To estimate the volume of fluid required to enrich a given rock volume ($V_r$) with a target metal enrichment ($C_r$), a mass balance approach is applied. The total mass of the metal in the enriched mica schist is considered to result from both the initial metal content of the mica schist and the contribution of hydrothermal fluids derived from the Beauvoir PRMG. The average initial content of the mica schist for Li, Be, and Sn are 120 ppm, 5 ppm, and 4 ppm, respectively (Table II.A9 in Appendix II.A4). The mass balance can be expressed as:

$$V_f \times \rho_f \times C_f = V_r \times \rho_r \times C_r \quad (IV.1)$$

where $V_f$ is the fluid volume, $C_f$ is the metal concentration in the fluid, and $\rho_r$ and $\rho_f$ are the densities of the rock and fluid, respectively. By rearranging the equation, the fluid volume required is:

$$V_f = \frac{V_r \times \rho_r \times C_r}{\rho_f \times C_f} \quad (IV.2)$$

For typical mica schists, the rock density ($\rho_r$) ranges from approximately 2.75 to 2.85 g/cm$^3$, depending on the mineralogical composition and degree of metamorphism. In our model, an average value of 2.8 g/cm$^3$ is considered. The density of hydrothermal L3 fluids is relatively low, varying between 0.6 and 0.75 g/cm$^3$ (Aïssa et al., 1987) (Fig. IV.3e). Specific density estimates for magmatic fluids L1, L2, V2, and L7 are not available. However, the densities of L1, L2 and L7 brines were likely higher than those reported for L3 fluids, ranging between 0.8 and 1.2 g/cm$^3$, whereas V2 vapour density may have been slightly lower, estimated between 0.5 and 0.6 g/cm$^3$ for moderate-salinity vapours enriched in P, F, and Li (e.g., Driesner and Geiger, 2007; Liebscher, 2007; Driesner and Heinrich, 2007). For modeling purposes, a density of 1 g/cm$^3$ is assumed to provide a reasonable approximation for L1 and L2 fluids, while a density of 0.6 g/cm$^3$ is used for the V2 vapour (Fig. IV.3e).




**(e) Parameters**

| | Host mica schist | L1 fluids | L2 fluids | V2 fluids | L3-L4 fluids |
|---|---|---|---|---|---|
| Density (ρ; g/cm³) | 2.8 | 1 | 1 | 0.6 | 0.75 |
| Li (ppm) | 330* | 8240 | 2680 | 7630 | 6040 |
| Sn (ppm) | 200* | 18750 | 3200 | 2220 | 550 |
| Be (ppm) | 10* | n.a. | 780 | 1610 | 430 |

n.a. = not analysed

* = $[Li]_{halo}$ - $[Li]_{mica\ schist}$

**(f) Estimation of minimal fluid volumes required to form the chemical overprint observed in the mica schist (x $10^6$ m³)**

| | L1 fluids | L2 fluids | V2 fluids | L3-L4 fluids |
|---|---|---|---|---|
| *Case 1: halo of 100 m around the Beauvoir intrusion* | | | | |
| Li | 3.9 | 12.0 | 7.0 | 7.1 |
| Sn | 1.0 | 6.1 | 14.6 | 47.2 |
| Be | | 1.2 | 1.0 | 3.0 |
| *Case 2: halo of 1 km around the Beauvoir intrusion* | | | | |
| Li | 116.8 | 359.2 | 210.3 | 159.4 |
| Sn | 31.1 | 182.3 | 438.0 | 1060.8 |
| Be | | 37.4 | 30.2 | 67.8 |

*Figure IV.3. Mass balance approach proposed to estimate the volume of fluid required for the Beauvoir magmatic-hydrothermal system to generate the observed chemical overprint in the host mica schists, as expressed in the equation (IV.2). (a-c) Geological map and element distribution maps for Li, Be, and Sn around the Beauvoir PRMG, generated using inverse distance weighted interpolation (Harlaux et al., 2025). (d) Conceptual model of the enrichment halo surrounding the Beauvoir intrusion. The remobilisation halo in the mica schists is approximated as a half-spherical zone centred at approximately 400 m depth along the GPF1 drillhole, comparable with the geometry proposed by Cuney et al. (1992). (e) Fixed parameters include rock and fluid densities, as well as their respective Sn, Li, and Be concentrations. Fluid compositions are based on median values determined for fluid inclusions: L1 fluids from Harlaux et al. (2017), and L2, V2, and L7 fluids from this study. Enrichment values for the mica schists are calculated by subtracting the average initial metal concentration in the mica schists (Table II.A9 in Appendix II.A4) from the values estimated in the enrichment halo (Harlaux et al., 2025), and thus represent minimal estimates. (f) Fluid volumes are calculated for the distinct magmatic fluids (L1, L2, and V2) and hydrothermal fluids (L3-L4) under two scenarios: (i) a halo extending 100 m from the Beauvoir intrusion, and (ii) a halo extending 1 km from the Beauvoir intrusion.*

The estimated volume of fluid required to produce an alteration halo extending 100 m around the Beauvoir intrusion ranges from approximately $10^6$ to $10^7$ m³ (Fig. IV.3f). However, the enrichment in Li, Sn, and Be considered in the mica schists represents minimal values (Harlaux et al., 2025) (Fig. IV.3a-c). This suggests that the calculated fluid volumes are minimal estimates.

Inverse distance weighted interpolation of Li, Sn, and Be distributions reveals alteration halos significantly larger than 100 m, with elevated concentrations observed over a radius of approximately 1 km around the intrusion (Harlaux et al., 2025) (Figs. IV.3a-c). To account for such a widespread overprint, the required fluid volume is one to two order of magnitude higher, varying between approximately $10^7$ and $10^9$ $m^3$.

The Beauvoir granite is a relatively small intrusive body, outcropping over an area of approximately 0.10 $km^2$, with an estimated minimum volume of 0.21 $km^3$ or 2.1x$10^8$ $m^3$ (Raimbault et al., 1995). The study of melt inclusions yielded $H_2O$ concentrations of *ca.* 3.6 wt% and 6.2–7.3 wt% in the B1 and B2 units, respectively (Kovalenko et al., 1998). From these information, the maximal volume of fluid exsolved from the Beauvoir melts can be estimated as follows:

$$V_{fluid} = \frac{mass_{fluid}}{\rho_{fluid}} = \frac{V_{magma} \times \rho_{magma} \times C_{H2O}}{\rho_{fluid}} \quad (IV.3)$$

where $V_{magma}$ and $V_{fluid}$ are the volumes of magma and of fluid contained in the magma, respectively, $\rho_{magma}$ and $\rho_{fluid}$ are the densities of the magma and the fluid, respectively, and $C_{H2O}$ is the concentration of water in the magma. If we consider an average density of 2.3 g/cm⊠typically attributed to evolved granitic magmas enriched in volatiles, a density of 1 g/$cm^3$ for the fluid, a water content varying between 3.6 and 7.3 wt% (Kovalenko et al., 1998), and a volume of magma of 0.21 $km^3$ (Raimbault et al., 1995), the volume of fluid contained in the Beauvoir magmas ranges from approximately 1.7 to 3.5x$10^7$ $m^3$.

The percolation of exsolved magmatic fluids (L1) into the surrounding mica schists could therefore have been responsible for their relative Li and Sn enrichments observed within a 100 m zone around the intrusion, which require *ca.* 1 to 4x$10^6$ $m^3$ of L1 fluids (Figs. IV.3f and IV.4a-c). However, the volume of exsolved magmatic fluids alone was insufficient to produce the 1 km alteration halo evidenced in previous studies (Aubert, 1969; Harlaux et al., 2025). The chemistry of apatite (Part II) and the composition of fluid inclusions (Part III) suggest that the Beauvoir magmatic-hydrothermal system was progressively infiltrated by external meteoric fluids, leading to the dilution of magmatic fluids, which ultimately accounted for only 5% of the system (Fig. III.24). This mixing process resulted in the formation of L3-L4 fluids. Assuming an average volume of exsolved magmatic fluids of 2.6x$10^7$ $m^3$, representing ~5% of the total L3-L4 fluid volume (Fig. III.24; section 3.3.2 of Part III), the estimated volume of these mixed fluids would be 5.3x$10^8$ $m^3$. This implies the incorporation of 5.0x$10^8$ $m^3$ of meteoric fluids into the system. A fluid volume of 5.3x$10^8$ $m^3$ for L3-L4 fluids could account for the 1 km-wide alteration halo observed for Li and Be around the intrusion; however it remains insufficient to explain the extent of Sn enrichment. (Fig. IV.3f and IV.4a-c). Moreover, this estimated fluid volume represents a maximum value that was likely not fully reached, considering the limited fluid exsolution from

the B2 and B3 melts compared to B1 (section 1 of Part IV) and the significant release of magmatic fluids into the mica schists prior to mixing (Aubert, 1969; Cuney et al., 1992; Harlaux et al., 2025). The substantial geochemical overprint observed in the host mica schists appears unlikely to result solely from fluid circulation directly linked to the Beauvoir melts, suggesting the involvement of an additional magmatic fluid source that contributed to the system.

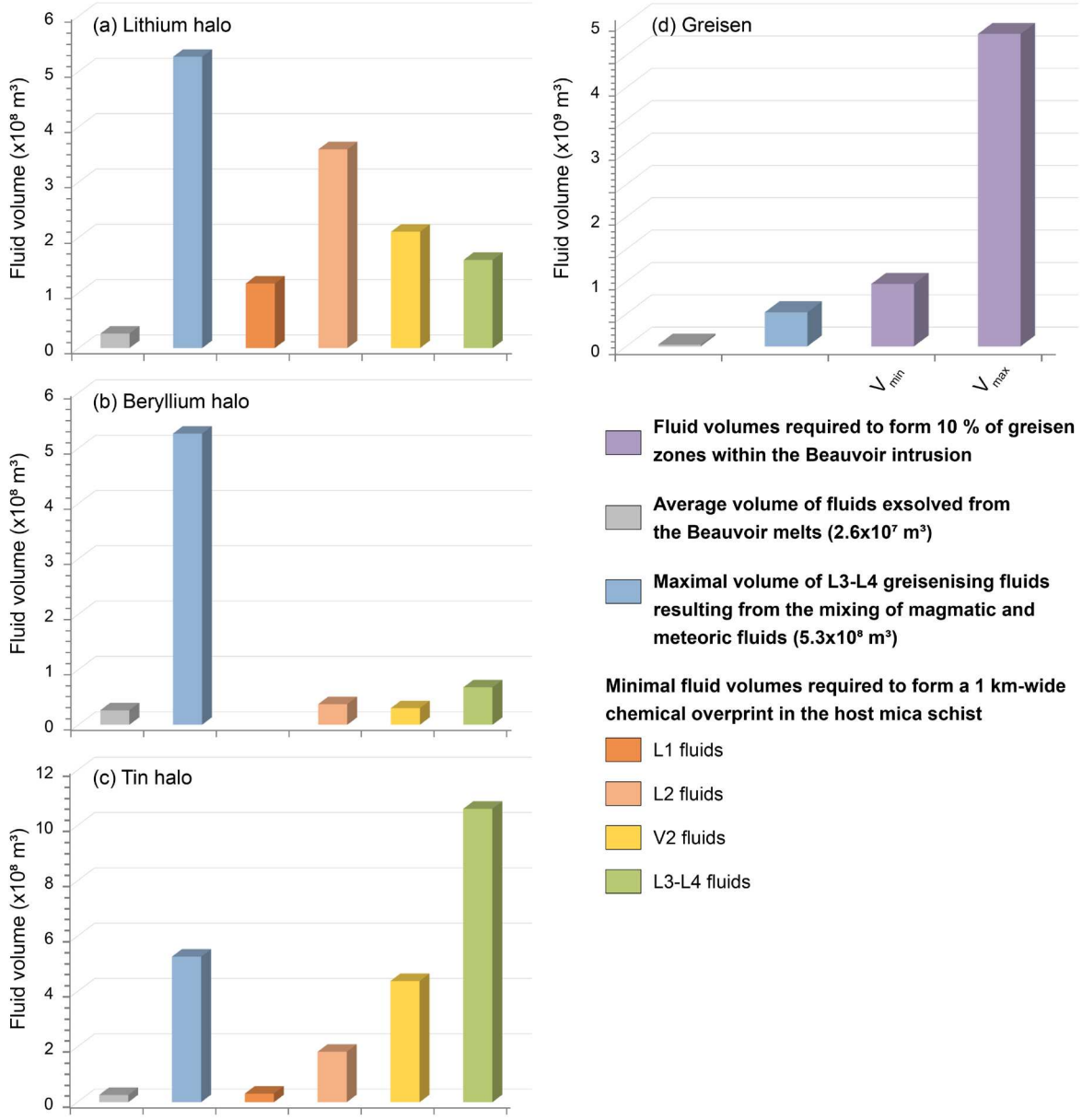



*Figure IV.4. Histogram representation of the estimated fluid volumes required for (a-c) the formation of the 1 km-wide alteration halo in the host mica schists and (d) the development of 10% greisenised zones within the Beauvoir intrusion. In each graph, the average volume of fluids exsolved from the Beauvoir melts (grey) and the maximum estimated volume of greisenising L3-L4 fluids (blue) are reported for comparison.*

The greisenised zones, which comprise approximately 10% of the total intrusion volume (i.e., 0.021 km$^3$ out of 0.21 km$^3$) (Cuney et al., 1992; Imerys database), further demonstrate that the volume of exsolved magmatic fluids alone difficultly explain the observed metasomatism. The formation of greisen typically requires high fluid-to-rock mass ratios (e.g., Pirajno, 2009; Launay et al., 2019), and the necessary fluid volume can be estimated using the following equation:

$$V_{fluid}\ required\ for\ greisen\ alteration = \frac{mass_{fluid}}{\rho_{fluid}} = \frac{a \times mass_{magma}}{\rho_{fluid}}$$

$$= \frac{a \times V_{magma} \times \rho_{magma}}{\rho_{fluid}} \quad (IV.4)$$

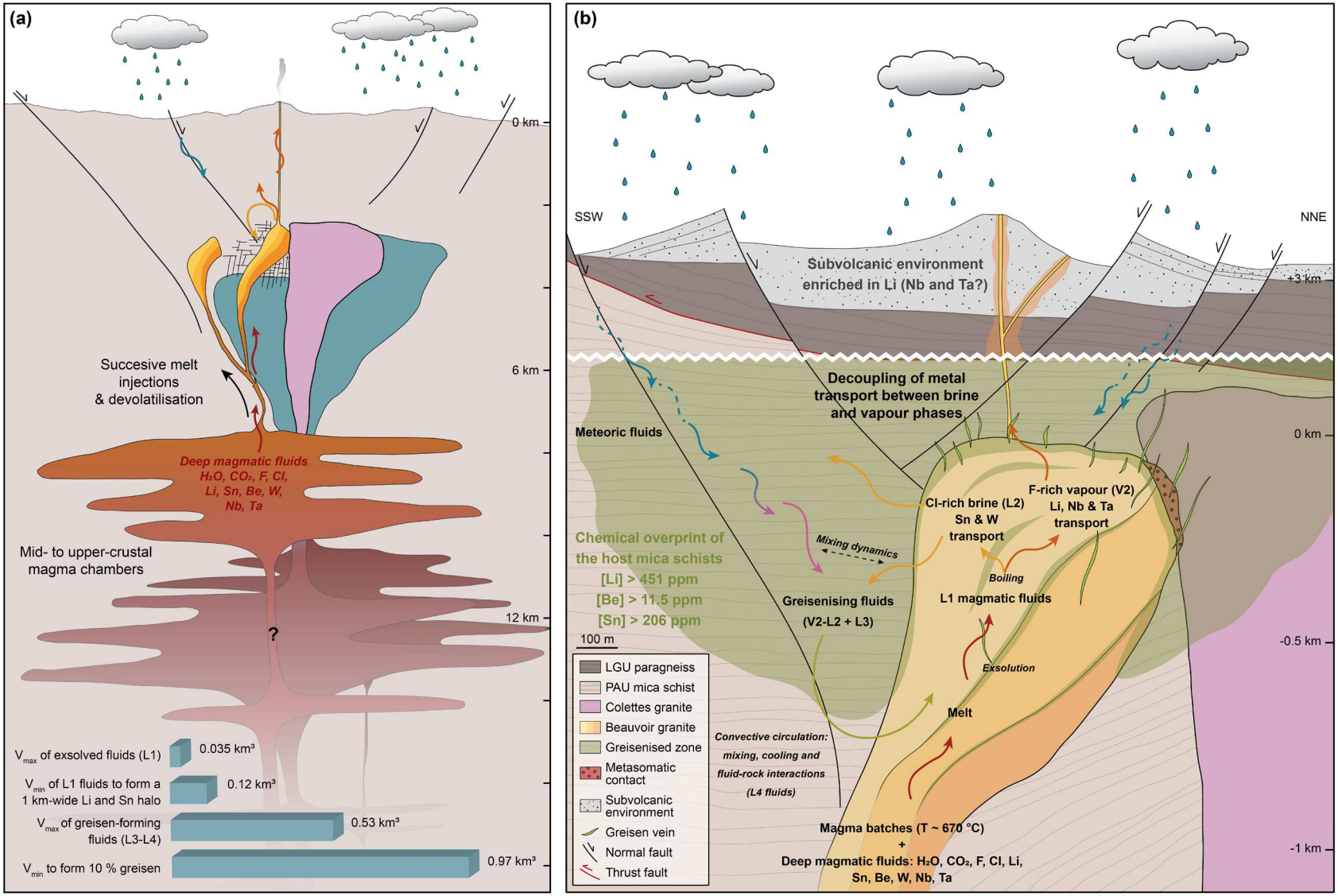
In this equation, $a$ derives from the fluid-to-rock ratio, which is assumed to range between 2:1 and 10:1 (Reed et al., 2013; Launay et al., 2023), meaning that 200–1000 % of the intrusion's mass would need to be supplied as water. As mentioned above, values of 2.3 g/cm$^3$ and 1 g/cm$^3$ are assumed to represent good approximations of magma and fluid densities, respectively. From this equation, the volume of fluid required to metasomatise 10 % of the volume of the Beauvoir intrusion varies between 9.7x10$^8$ and 4.8x10$^9$ m$^3$, significantly higher than the volume of 1.7–3.5 x10$^7$ m$^3$ exsolved from the Beauvoir melts (Fig. IV.4d). Therefore, a magma volume 27 to 278 times greater than that of Beauvoir would be required to generate greisenised zones directly from exsolved fluids. However, greisen-forming fluids (L3-L4) likely represent a mixture of magmatic and meteoric fluids (Cuney et al., 1992; this study), with proportions up to 5:95, as deciphered from the analysis of fluid inclusions (Fig. III.24; section 3 of Part III). As mentioned above, the maximal volume estimated for L3–L4 fluids is of 5.3x10$^8$ m$^3$. The circulation of L3-L4 fluids therefore appears insufficient to account for the observed greisen alteration, supporting that an additional external magmatic fluid source likely contributed to the system (Fig. IV.4d).

The existence of additional fluid contributions to the Beauvoir magmatic-hydrothermal system is consistent with its open nature, highlighted by the detailed petrographic and geochemical study of Esteves et al. (2024b). The Beauvoir PRMG is shown to have formed though the injection of multiple melt batches originating from a deeper reservoir, from which residual liquids (and possibly fluids) were incrementally extracted, ultimately resulting in the stacking of at least eighteen decametre-sized sills (Esteves et al., 2024b) (Fig. IV.5). In the Echassières granitic complex, the extension of elevated anomalies of Li, F and Sn up to 1 km south of the Beauvoir intrusion, as well as gravimetric data, support the possible existence of a second Beauvoir-like intrusion buried at depth, likely derived from the same parental magma chamber (Aubert, 1969; Cuney and Autran, 1987; Harlaux et al., 2025) (Fig. IV.5). A similar genetic model for rare-metal granites, involving the accumulation of fertile magma at different intermediate crustal levels and their transfer through the crust with protracted fractionation to form rare-metal intrusions at shallow levels was proposed by Cuney and Barbey (2014). Here, I

propose an updated model whereby such deep seated magma dynamics below the Beauvoir granite was accompanied by devolatilisation events with resulting fluids channelled toward the upper part of the magmatic column.

Comparatively, the presence of large magma chambers at depth, exsolving low-density bubbly magma and significant volumes fluids that form porphyry ore deposits, is widely acknowledged (e.g., Sillitoe, 2010; Richards, 2022). However, while parallels can be drawn between the development of porphyry-epithermal systems and the Beauvoir magmatic-hydrothermal system, these geological objects differ substantially in scale. The Beauvoir system is significantly smaller, characterised by relatively small volumes of highly evolved magmas, and fluid contributions reaching up to 1 $km^3$. In contrast, porphyry-epithermal systems are much larger, involving the circulation of 1 to 100 $km^3$ of exsolved fluids from deep magma chambers (e.g., Sillitoe, 2010). To fully understand the magmatic-hydrothermal evolution of peraluminous rare-metal granites such as the Beauvoir PRMG, it seems necessary to extend the perspective beyond the scale of the intrusion itself and consider processes operating at the crustal scale. This aligns with models for porphyry-epithermal deposits, where ore formation is driven by the devolatilisation of a large magma reservoir at depth, mineralising relatively small dyke systems at shallower levels. Similarly, in the case of the Beauvoir PRMG, a deep-seated magma chamber likely played a dual role: not only supplying residual melts that formed the stacked sills (Esteves et al., 2024b) but also contributing substantial volumes of metal-rich fluids ($\geq 10^8$–$10^9$ $m^3$), which may have been critical to the magmatic-hydrothermal evolution. The Beauvoir magmatic-hydrothermal system nonetheless stands out as an exceptional case, distinct from porphyry-epithermal systems, as its evolution is profoundly influenced by its extremely high F content, which not only facilitates the increase of the oxidation state during devolatilisation (section 1 of Part IV) but also significantly affects the transport of metals, particularly Nb and Ta (section 3.1 of Part IV).

*Figure IV.5. Proposed open-system model for the genesis and magmatic-hydrothermal evolution of the Beauvoir PRMG: (a) The crustal model illustrates the sequence from magma accumulation at upper- to mid-crustal levels, successive magma injections, and extensive devolatilisation, to final emplacement in the upper crust (modified from Cuney and Autran, 1987). Fluid volumes are proportional to the volume of the Beauvoir PRMG. (b) Fluid and metal dynamics around the Beauvoir intrusion, emphasing the exsolution of magmatic fluids from the Beauvoir melts and their subsequent interaction with meteoric fluids under sub-solidus conditions. A contribution from deep magmatic fluids appears necessary, as the volume of fluids exsolved solely from the Beauvoir melts is insufficient to account for the extent of the alteration halo in the host rocks and the greisen alteration within the intrusion itself.*



# CONCLUSIONS & PERSPECTIVES

Through the case of the Beauvoir PRMG, this study provides new insights into the evolution of rare-metal magmatic-hydrothermal systems. It addresses key unresolved questions regarding the timing of fluid circulation, the origin and evolution of involved fluids, the nature of fluid-melt and fluid-fluid interactions during the magmatic-hydrothermal transition, as well as the dynamics of meltal mobilisation. By integrating U-Pb dating of apatite, geochemical investigations of apatite, quartz and cassiterite, and fluid inclusion analyses, this work refines existing models of rare-metal granite evolution, highlighting the critical – yet often underestimated – role of fluids in controlling crystallisation and mineralisation processes, and the necessity of considering open-system dynamics at both supra- and sub-solidus stages. The key conclusions drawn from this study are summarised below:

- **Apatite as a key geochemical archive:** *In-situ* analyses of apatite – including major and trace elements, O isotopic systematics, and U-Pb geochronology – provided essential constraints on the timing of magmatic and hydrothermal events, as well as on the nature and chemistry of the involved fluids.
- **Prolonged magmatic and hydrothermal evolution:** The Beauvoir PRMG underwent a multi-stage evolution, with four major phases identified through apatite petrography and U-Pb geochronology. These span from magma emplacement at 314.6 ± 4.7 Ma, to the early hydrothermal stage at *ca.* 315 ± 5 Ma, ultimately evolving in two late, non-magmatic hydrothermal stages driven by regional thermal activity, dated at 268.3 ± 20.4 Ma and 148.5 ± 26.6 Ma, respectively.
- **Influence of extensive devolatilisation on melt crystallisation:** Strong evidence of melt devolatilisation is recorded in the REE distribution of magmatic apatite from all three magmatic units, the O isotopic signature of magmatic quartz from the B1 unit, and fluid inclusion petrography. This process was particularly intense in the B1 unit, leading to an increase in oxygen fugacity, promoting the crystallisation of the first cassiterite generation (Cst I), and ultimately evolving toward a volatile-rich residual melt from which snowball quartz crystallised.
- **Exceptional hydrothermal mobility or rare metals:** Magmatic fluids (L1, L2, V2, and L7) are systematically enriched in Be, Cs, Sn, and W compared to average bulk-rock composition of the evolved B1 unit, with notable concentrations of Li, Nb, and Ta, highlighting the exceptional hydrothermal mobility of metals in the system.
- **Role of magmatic vapours in metal transport:** Phase separation of magmatic fluids resulted in metal partitioning between brine (L2) and vapour (V2) phases: Sn and W were predominantly mobilised by the brine phase, whereas Li, Nb, and Ta appear to have been transported by the vapour phase. Although the brine phase undoubtedly remains a key ore-bearing fluid, the significantly larger volume of vapour in such systems suggests a complex metal transport mechanism, with vapour potentially playing a major – yet previously

underappreciated – role in shaping metal distribution. Analogous to porphyry-epithermal deposits, where magmatic brines essentially mineralise the porphyry stock and vapours create Au-As(-Cu) epithermal deposits, a similar subvolcanic environment enriched in Li, Nb, and Ta could be envisioned for the Beauvoir PRMG (Fig. IV.5).

- **Sub-solidus meteoric water infiltration and greisen alteration:** Progressive infiltration of meteoric fluids at sub-solidus conditions played a key role in the widespread greisen alteration and influenced the precipitation of a second, though minor, cassiterite generation.
- **Open nature of the Beauvoir magmatic-hydrothermal system:** Beyond the open-system behaviour emphasised under sub-solidus conditions and marked by meteoric water incursion, mass balance calculations suggest the contribution of deep magmatic fluids during the supra-solidus evolution of the Beauvoir melts. This is consistent with the melt injection dynamics from a deeper magma chamber inferred by Esteves et al. (2024b), likely influencing the metal budget of the Beauvoir intrusion.

While this study has enriched genetic models for magmatic-hydrothermal rare-metals deposits, several key research directions remain open, offering exciting opportunities to further refine our understanding of these complex systems.

- **Quantifying the impact of devolatilisation on mineral crystallisation:** A key future direction is assessing the extent to which devolatilisation has influenced the crystallisation of the B1 unit. While the study has demonstrated its impact on the geochemical signatures of quartz and apatite, it is likely that devolatilisation also played a role in the crystallisation of other magmatic phases, particularly ore-bearing minerals such as lepidolite. Investigating this process could involve *in-situ* O isotopic analyses across a broader range of minerals, as well as the development of physico-chemical models to simulate the effects of devolatilisation on mineral crystallisation. Additionally, a more detailed characterisation of melt inclusions could provide critical insights into the volume of exsolved fluids during late-stage crystallisation and the evolution of metal concentrations in the residual melt, helping to better constrain the mechanisms of rare-metal enrichment and transport.
- **Refining the understanding of fluid evolution through fluid inclusions:** The chemical evolution of hydrothermal fluids remains a fundamental aspect of metal mobilisation and deposition. While this study has provided initial constraints based on LA-ICP-MS analyses of fluid inclusions in magmatic quartz, further investigations are needed to track fluid composition across different hydrothermal minerals. Greisen alteration in the Beauvoir PRMG has been shown to involve multiple boiling events, which likely played a critical role in controlling metal transport and deposition (Monnier et al., 2020). Furthermore, hydrothermal minerals formed during the two late, non-magmatic stages identified through apatite petrography and geochronology may contain fluid inclusions that record key information about the origin and

evolution of these fluids. A systematic analysis of these fluid inclusions could yield valuable insights into the physico-chemical conditions that governed metal redistribution during the later stages of the system's evolution.

- **From micro-scale dynamics to intrusion-scale architecture:** Moving beyond the mineral- and fluid inclusion-scale, an important next step is to investigate the broader architectural controls of the Beauvoir magmatic-hydrothermal system. Hydrothermal fluids extensively interacted with both the intrusion and its host rocks, as evidenced by widespread greisenisation and the formation of late-stage quartz-fluorite, quartz-illite, and quartz-oxide veins (Merceron et al., 1987, 1992; Monnier et al., 2020). At the quarry scale, greisens appear to be organised into large, sub-vertical structures with a predominant NE-SW orientation (Bargain, 2022). If this architecture is confirmed at greater depths, it would contrast sharply with the more typical dome-shaped greisen bodies observed in other rare-metal granites (Launay et al., 2021). A comprehensive structural analysis of hydrothermal features using the extensive borehole imaging dataset from the exploration phases conducted by Imerys could provide critical insights into the system's three-dimensional architecture and its influence on fluid pathways.

# REFERENCES

Aïssa M. (1987) Reconstitution d'un système de paléocirculations hydrothermales et ses conséquences métallogéniques : le district d'Echassières (Massif central français). PhD dissertation, Université de Lorraine.

Aïssa M., Weisbrod A. and Marignac C. (1987) Caractéristiques chimiques et thermodynamiques des circulations hydrothermales du site d'Échassières. *Géologie de la France* **1**, 335–350.

Akinfiev N. N., Korzhinskaya V. S., Kotova N. P., Redkin A. F. and Zotov A. V. (2020) Niobium and tantalum in hydrothermal fluids: Thermodynamic description of hydroxide and hydroxofluoride complexes. *Geochimica et Cosmochimica Acta* **280**, 102–115.

Albrecht M. (2017) The role of the fluid composition in the formation of hydrothermal Sn-W ores: Insights from in situ analyses of fluid inclusions by UV-fs-LA-ICP-MS. Master dissertation, Gottfried Wilhelm Leibniz Universität Hannover.

Allan M. M., Yardley B. W. D., Forbes L. J., Shmulovich K. I., Banks D. A. and Shepherd T. J. (2005) Validation of LA-ICP-MS fluid inclusion analysis with synthetic fluid inclusions. *American Mineralogist* **90**, 1767–1775.

Andersen C. and Weis P. (2020) Heat transfer from convecting magma reservoirs to hydrothermal fluid flow systems constrained by coupled numerical modeling. *Geophysical Research Letters* **47**, e2020GL089463.

Andersson S. S., Wagner T., Jonsson E., Fusswinkel T. and Whitehouse M. J. (2019) Apatite as a tracer of the source, chemistry and evolution of ore-forming fluids: The case of the Olserum-Djupedal REE-phosphate mineralisation, SE Sweden. *Geochimica et Cosmochimica Acta* **255**, 163–187.

Angrand P. and Mouthereau F. (2021) Evolution of the Alpine orogenic belts in the Western Mediterranean region as resolved by the kinematics of the Europe-Africa diffuse plate boundary. *Bulletin de la Société Géologique de France - Earth Sciences Bulletin* **192**, 42.

Araujo F. P., Muchez P. and Hulsbosch N. (2023) The magmatic-hydrothermal transition in P-rich pegmatitic melts: Crystal-melt-fluid interactions recorded by phosphate minerals. *Geochimica et Cosmochimica Acta* **356**, 129–148.

Arribas Jr A., Hedenquist J. W., Itaya T., Okada T., Concepción R. A. and Garcia Jr J. S. (1995) Contemporaneous formation of adjacent porphyry and epithermal Cu-Au deposits over 300 ka in northern Luzon, Philippines. *Geology* **23**, 337–340.

Arthaud F., Mattauer M. and Proust F. (1966) La structure et la microtectonique des nappes Hercyniennes de la Montagne Noire. In *Colloque "Étages Tectoniques"* **4**, 229–241.

Ashworth L., Kinnaird J. A., Nex P. A. M., Erasmus R. M. and Przybyłowicz W. J. (2018) Characterization of fluid inclusions from mineralized pegmatites of the Damara Belt, Namibia: insight into late-stage fluid evolution and implications for mineralization. *Mineralogy and Petrology* **112**, 753–765.

Ashworth L., Kinnaird J. A., Nex P. A. M., Harris C. and Müller A. B. (2020) Origin of rare-element-mineralized Damara Belt pegmatites: A geochemical and light stable isotope study. *Lithos* **372–373**, 105655.

Aubert G. (1969) Les coupoles granitiques de Montebras et d'Echassieres (Massif central francais) et la genese de leurs mineralisations en etain, lithium, tungstene et beryllium. PhD dissertation, BRGM Paris.

Audétat A. (2019) The Metal Content of Magmatic-Hydrothermal Fluids and Its Relationship to Mineralization Potential. *Economic Geology* **114**, 1033–1056.

Audétat A. (2023) A plea for more skepticism toward fluid inclusions: Part II. Homogenization via halite dissolution in brine inclusions from magmatic-hydrothermal systems is commonly the result of postentrapment modifications. *Economic Geology* **118**, 43–55.

Audétat A. and Edmonds M. (2020) Magmatic-Hydrothermal Fluids. *Elements* **16**, 401–406.

Audétat A., Garbe-Schönberg D., Kronz A., Pettke T., Rusk B., Donovan J. J. and Lowers H. A. (2015) Characterisation of a Natural Quartz Crystal as a Reference Material for Microanalytical Determination of Ti, Al, Li, Fe, Mn, Ga and Ge. *Geostandards and Geoanalytical Research* **39**, 171–184.

Audétat A., Günther D. and Heinrich C. A. (2000a) Causes for Large-Scale Metal Zonation around Mineralized Plutons: Fluid Inclusion LA-ICP-MS Evidence from the Mole Granite, Australia. *Economic Geology* **95**, 1563–1581.

Audétat A., Günther D. and Heinrich C. A. (1998) Formation of a magmatic-hydrothermal ore deposit: Insights with LA-ICP-MS analysis of fluid inclusions. *Science* **279**, 2091–2094.

Audétat A., Günther D. and Heinrich C. A. (2000b) Magmatic-hydrothermal evolution in a fractionating granite: a microchemical study of the sn-w-f-mineralized mole granite (Australia). *Geochimica et Cosmochimica Acta* **64**, 3373–3393.

Audétat A. and Pettke T. (2003) The magmatic-hydrothermal evolution of two barren granites: a melt and fluid inclusion study of the Rito del Medio and Cañada Pinabete plutons in northern New Mexico (USA). *Geochimica et Cosmochimica Acta* **67**, 97–121.

Audétat A., Pettke T., Heinrich C. A. and Bodnar R. J. (2008) Special paper: the composition of magmatic-hydrothermal fluids in barren and mineralized intrusions. *Economic Geology* **103**, 877–908.

Audétat A. and Zhang D. (2019) Abundances of S, Ga, Ge, Cd, In, Tl and 32 other major to trace elements in high-temperature (350–700 °C) magmatic-hydrothermal fluids. *Ore Geology Reviews* **109**, 630–642.

Badanina E. V., Sitnikova M. A., Gordienko V. V., Melcher F., Gäbler H.-E., Lodziak J. and Syritso L. F. (2015) Mineral chemistry of columbite–tantalite from spodumene pegmatites of Kolmozero, Kola Peninsula (Russia). *Ore Geology Reviews* **64**, 720–735.

Badanina E. V., Veksler I. V., Thomas R., Syritso L. F. and Trumbull R. B. (2004) Magmatic evolution of Li–F, rare-metal granites: a case study of melt inclusions in the Khangilay complex, Eastern Transbaikalia (Russia). *Chemical geology* **210**, 113–133.

Baertschi P. (1976) Absolute18O content of standard mean ocean water. *Earth and Planetary Science Letters* **31**, 341–344.

Bai T. B. and Van Groos A. K. (1999) The distribution of Na, K, Rb, Sr, Al, Ge, Cu, W, Mo, La, and Ce between granitic melts and coexisting aqueous fluids. *Geochimica et Cosmochimica Acta* **63**, 1117–1131.

Bakker R. J. (2012) Package FLUIDS. Part 4: thermodynamic modelling and purely empirical equations for H2O-NaCl-KCl solutions. *Mineralogy and Petrology* **105**, 1–29.

Ballèvre M., Bosse V., Dabard M.-P., Ducassou C., Fourcade S., Paquette J.-L., Peucat J.-J. and Pitra P. (2013) Histoire Géologique du massif Armoricain : Actualité de la recherche. *Bulletin de la Société Géologique et Minéralogique de Bretagne* **500**, 5–96.

Ballèvre M., Bosse V., Ducassou C. and Pitra P. (2009) Palaeozoic history of the Armorican Massif: models for the tectonic evolution of the suture zones. *Comptes rendus géoscience* **341**, 174–201.

Ballèvre M., Martínez Catalán J. R., López-Carmona A., Pitra P., Abati J., Fernández R. D., Ducassou C., Arenas R., Bosse V., Castiñeiras P., Fernández-Suárez J., Gómez Barreiro J., Paquette J.-L., Peucat J.-J., Poujol M., Ruffet G. and Sánchez Martínez S. (2014) Correlation of the nappe stack in the Ibero-Armorican arc across the Bay of Biscay: a joint French–Spanish project. *Geological Society, London, Special Publications* **405**, 77–113.

Ballouard C., Carr P., Parisot F., Gloaguen É., Melleton J., Cauzid J., Lecomte A., Rouer O., Salsi L. and Mercadier J. (2024) Petrogenesis and tectonic-magmatic context of emplacement of lepidolite and petalite pegmatites from the Fregeneda-Almendra field (Variscan Central Iberian Zone): clues from Nb-Ta-Sn oxide U-Pb geochronology and mineral geochemistry. *Bulletin de la Société Géologique de France - Earth Sciences Bulletin* **195**, 3.

Ballouard C., Couzinié S., Bouilhol P., Harlaux M., Mercadier J. and Montel J.-M. (2023) A felsic meta-igneous source for Li-F-rich peraluminous granites: insights from the Variscan Velay dome (French Massif Central) and implications for rare-metal magmatism. *Contributions to Mineralogy and Petrology* **178**, 75.

Ballouard C., Elburg M. A., Tappe S., Reinke C., Ueckermann H. and Doggart S. (2020a) Magmatic-hydrothermal evolution of rare metal pegmatites from the Mesoproterozoic Orange River pegmatite belt (Namaqualand, South Africa). *Ore Geology Reviews* **116**, 103252.

Ballouard C., Massuyeau M., Elburg M. A., Tappe S., Viljoen F. and Brandenburg J.-T. (2020b) The magmatic and magmatic-hydrothermal evolution of felsic igneous rocks as seen through Nb-Ta geochemical fractionation, with implications for the origins of rare-metal mineralizations. *Earth-Science Reviews* **203**, 103115.

Ballouard C., Poujol M., Boulvais P., Branquet Y., Tartèse R. and Vigneresse J.-L. (2016) Nb-Ta fractionation in peraluminous granites: A marker of the magmatic-hydrothermal transition. *Geology* **44**, 231–234.

Ballouard C., Poujol M., Boulvais P., Mercadier J., Tartèse R., Venneman T., Deloule E., Jolivet M., Kéré I., Cathelineau M. and Cuney M. (2017) Magmatic and hydrothermal behavior of uranium in syntectonic leucogranites: The uranium mineralization associated with the Hercynian Guérande granite (Armorican Massif, France). *Ore Geology Reviews* **80**, 309–331.

Ballouard C., Poujol M., Mercadier J., Deloule E., Boulvais P., Baele J. M., Cuney M. and Cathelineau M. (2018) Uranium metallogenesis of the peraluminous leucogranite from the Pontivy-Rostrenen magmatic complex (French Armorican Variscan belt): the result of long-term oxidized hydrothermal alteration during strike-slip deformation. *Mineralium Deposita* **53**, 601–628.

Barbarin B. (1999) A review of the relationships between granitoid types, their origins and their geodynamic environments. *Lithos* **46**, 605–626.

Barbey P., Marignac C., Montel J. M., Macaudière J., Gasquet D. and Jabbori J. (1999) Cordierite Growth Textures and the Conditions of Genesis and Emplacement of Crustal Granitic Magmas: the Velay Granite Complex (Massif Central, France). *Journal of Petrology* **40**, 1425–1441.

Bargain A. (2022) Exploration lithinifère sur le PER dit "Beauvoir" : caractérisation des faciès géologiques du complexe granitique d'Echassières. Master dissertation, Université de Montpellier.

Barsukov V. L., Sokolova N. T. and Ivanitskii O. M. (2006) Metals, arsenic, and sulfur in the Aue and Eibenstock granites, Erzgebirge. *Geochemistry International* **44**, 896–911.

Bartels A., Behrens H., Holtz F., Schmidt B. C., Fechtelkord M., Knipping J., Crede L., Baasner A. and Pukallus N. (2013) The effect of fluorine, boron and phosphorus on the viscosity of pegmatite forming melts. *Chemical Geology* **346**, 184–198.

Bartels A., Vetere F., Holtz F., Behrens H. and Linnen R. L. (2011) Viscosity of flux-rich pegmatitic melts. *Contributions to Mineralogy and Petrology* **162**, 51–60.

Bau M. (1996) Controls on the fractionation of isovalent trace elements in magmatic and aqueous systems: evidence from Y/Ho, Zr/Hf, and lanthanide tetrad effect. *Contributions to Mineralogy and Petrology* **123**, 323–333.

Baubron J. C., Jébrak M., Joannes C., Lhégu J., JC T. and Ziserman A. (1980) Nouvelles datations K/Ar sur des filons à quartz et fluorine du Massif Central français. *Comptes rendus de l'Académie des Sciences* **290**, 951–953.

Bebout G. E., Cooper D. C., Bradley A. D. and Sadofsky S. J. (1999) Nitrogen-isotope record of fluid-rock interactions in the Skiddaw aureole and granite, English Lake District. *American Mineralogist* **84**, 1495–1505.

Belkasmi M., Cuney M., Pollard P. J. and Bastoul A. (2000) Chemistry of the Ta-Nb-Sn-W oxide minerals from the Yichun rare metal granite (SE China): genetic implications and comparison with Moroccan and French Hercynian examples. *Mineralogical Magazine* **64**, 507–523.

Bellahsen N., Mouthereau F., Boutoux A., Bellanger M., Lacombe O., Jolivet L. and Rolland Y. (2014) Collision kinematics in the western external Alps. *Tectonics* **33**, 1055–1088.

Belousova E. A., Griffin W. L., O'Reilly S. Y. and Fisher N. I. (2002) Apatite as an indicator mineral for mineral exploration: trace-element compositions and their relationship to host rock type. *Journal of Geochemical Exploration* **76**, 45–69.

Berger J., Beau-Hurdebourcq L., Serrano J., Benoit M., Grégoire M., Benmammar A., Duchene S., Bruguier O. and Baele J.-M. (2024) Short-lived active margin magmatism preceding Variscan collision in the Western French Massif Central. *Bulletin de la Société Géologique de France - Earth Sciences Bulletin* **195**, 7.

Bernard-Griffiths J., Peucat J. J., Sheppard S. and Vidal P. (1985) Petrogenesis of Hercynian leucogranites from the southern Armorican Massif: contribution of REE and isotopic (Sr, Nd, Pb and O) geochemical data to the study of source rock characteristics and ages. *Earth and Planetary Science Letters* **74**, 235–250.

Bertrand J.-M., Leterrier J., Cuney M., Brouand M., Stussi J.-M., Delaperriere E. and Virlogeux D. (2001) Géochronologie U-Pb sur zircons de granitoïdes du Confolentais, du massif de Charroux-Civray (seuil du Poitou) et de Vendée. *Géologie de la France* **1–2**, 167–189.

Bettencourt J. S., Leite Jr W. B., Goraieb C. L., Sparrenberger I., Bello R. M. and Payolla B. L. (2005) Sn-polymetallic greisen-type deposits associated with late-stage rapakivi granites, Brazil: fluid inclusion and stable isotope characteristics. *Lithos* **80**, 363–386.

Beus A. A. (1982) Metallogeny of Precambrien rare-metal granitoids. *Revista brasileira de geociências* **12**, 410–413.

Beus A. A., Severov E. A., Sitnin A. A. and Subbotin K. D. (1962) *Albitized and Greisenized Granites (Apogranites)*. Moscow: Academy of Sciences of the USSR (Akademiya Nauk SSSR).

Beus A. A. and Zalashkova N. Y. (1964) Post-magmatic high temperature metasomatic processes in granitic rocks. *International Geology Review* **6**, 668–681.

Bhalla P., Holtz F., Linnen R. L. and Behrens H. (2005) Solubility of cassiterite in evolved granitic melts: effect of T, fO2, and additional volatiles. *Lithos* **80**, 387–400.

Bindeman I. N. and Simakin A. G. (2014) Rhyolites—Hard to produce, but easy to recycle and sequester: Integrating microgeochemical observations and numerical models. *Geosphere* **10**, 930–957.

Bindeman I. N. and Valley J. W. (2002) Oxygen isotope study of the Long Valley magma system, California: isotope thermometry and convection in large silicic magma bodies. *Contributions to Mineralogy and Petrology* **144**, 185–205.

Blès J. L., Bonijoly D., Castaing C. and Gros Y. (1989) Successive post-Variscan stress fields in the French Massif Central and its borders (Western European plate): comparison with geodynamic data. *Tectonophysics* **169**, 79–111.

Bodnar R. J. (1995) Fluid-inclusion evidence for a magmatic source for metals in porphyry copper deposits. *Magma, fluid and ore deposit*, 139–152.

Bodnar R. J. (2003) Introduction to aqueous-electrolyte fluid inclusions. In: I. Samson, A. Anderson, & D. Marshall (Eds.), *Fluid Inclusions: Analysis and Interpretation*, Volume 32. Mineralogical Association of Canada, pp. 81–100.

Bodnar R. J. (1993) Revised equation and table for determining the freezing point depression of H2O-Nacl solutions. *Geochimica et Cosmochimica Acta* **57**, 683–684.

Bodnar R. J., Sterner S. M. and Hall D. L. (1989) SALTY: a FORTRAN program to calculate compositions of fluid inclusions in the system NaCl-KCl-$H_2O$. *Computers and Geosciences* **15**, 19–41.

Boiron M.-C., Cathelineau M. and Richard A. (2010) Fluid flows and metal deposition near basement/cover unconformity: lessons and analogies from Pb–Zn–F–Ba systems for the understanding of Proterozoic U deposits. *Geofluids* **10**, 270–292.

Bongiovanni M., Fusswinkel T. and Marks M. A. W. (2024) Unravelling the effects of magmatic fractionation, fluid phase separation and dilution on the composition of magmatic-hydrothermal fluids of the Cornubian Batholith (SW England). *Chemical Geology* **658**, 122119.

Bottinga Y. and Javoy M. (1973) Comments on oxygen isotope geothermometry. *Earth and Planetary Science Letters* **20**, 250–265.

Bouat L., Strzerzynski P., Mourgues R., Branquet Y., Cogné N., Barré G. and Gardien V. (2023) Early, far-field and diffuse tectonics records in the North Aquitaine Basin (France). *Bulletin de la Société Géologique de France - Earth Sciences Bulletin* **194**, 17.

Bouchez J.-L., Bernier S., Rochette P. and Guineberteau B. (1987) Log des susceptibilités magnétiques et anisotropies de susceptibilité dans le granite de Beauvoir : conséquences pour sa mise en place. *Géologie de la France*, 223–232.

Bouchot V., Ledru P., Lerouge C., Lescuyer J.-L. and Milesi J.-P. (2005) 5: Late Variscan mineralizing systems related to orogenic processes: The French Massif Central. *Ore Geology Reviews* **27**, 169–197.

Bouzari F., Hart C. J. R., Bissig T. and Barker S. (2016) Hydrothermal Alteration Revealed by Apatite Luminescence and Chemistry: A Potential Indicator Mineral for Exploring Covered Porphyry Copper Deposits. *Economic Geology* **111**, 1397–1410.

Boynton W. V. (1984) Cosmochemistry of the Rare Earth Elements: Meteorite Studies. In *Developments in Geochemistry*, Volume 2, Elsevier, 63–114.

Breiter K., Ackerman L., Svojtka M. and Müller A. (2013) Behavior of trace elements in quartz from plutons of different geochemical signature: A case study from the Bohemian Massif, Czech Republic. *Lithos* **175–176**, 54–67.

Breiter K., Ďurišová J., Hrstka T., Korbelová Z., Hložková Vaňková M., Vašinová Galiová M., Kanický V., Rambousek P., Knésl I., Dobeš P. and Dosbaba M. (2017) Assessment of magmatic vs. metasomatic processes in rare-metal granites: A case study of the Cínovec/Zinnwald Sn–W–Li deposit, Central Europe. *Lithos* **292–293**, 198–217.

Breiter K., Ďurišová J., Korbelová Z., Lima A., Vašinová Galiová M., Hložková M. and Dosbaba M. (2022) Rock textures and mineral zoning – A clue to understanding rare-metal granite evolution: Argemela stock, Central-Eastern Portugal. *Lithos* **410–411**, 106562.

Breiter K. and Müller A. (2009) Evolution of rare-metal granitic magmas documented by quartz chemistry. *European Journal of Mineralogy* **21**, 335–346.

Breiter K., Müller A., Leichmann J. and Gabašová A. (2005) Textural and chemical evolution of a fractionated granitic system: the Podlesí stock, Czech Republic. *Lithos* **80**, 323–345.

Breiter K., Svojtka M., Ackerman L. and Švecová K. (2012) Trace element composition of quartz from the Variscan Altenberg–Teplice caldera (Krušné hory/Erzgebirge Mts, Czech Republic/Germany): Insights into the volcano-plutonic complex evolution. *Chemical Geology* **326–327**, 36–50.

Briand B., Piboule M., Santallier D. and Bouchardon J. L. (1991) Geochemistry and tectonic implications of two Ordovician bimodal igneous complexes, southern French Massif Central. *Journal of the Geological Society* **148**, 959–971.

Broska I., Williams C. T., Uher P., Konečný P. and Leichmann J. (2004) The geochemistry of phosphorus in different granite suites of the Western Carpathians, Slovakia: the role of apatite and P-bearing feldspar. *Chemical Geology* **205**, 1–15.

Bruguier O., Becq-Giraudon J. F., Bosch D. and Lancelot J. R. (1998) Late Visean hidden basins in the internal zones of the Variscan belt: U-Pb zircon evidence from the French Massif Central. *Geology* **26**, 627–630.

Bruguier O., Becq-Giraudon J. F., Clauer N. and Maluski H. (2003) From late Visean to Stephanian: pinpointing a two-stage basinal evolution in the Variscan belt. A case study from the Bosmoreau basin (French Massif Central) and its geodynamic implications. *International Journal of Earth Sciences (Geologische Rundschau)* **92**, 338–347.

Bucholz C. E., Jagoutz O., VanTongeren J. A., Setera J. and Wang Z. (2017) Oxygen isotope trajectories of crystallizing melts: Insights from modeling and the plutonic record. *Geochimica et Cosmochimica Acta* **207**, 154–184.

Budd D. A., Troll V. R., Deegan F. M., Jolis E. M., Smith V. C., Whitehouse M. J., Harris C., Freda C., Hilton D. R., Halldórsson S. A. and Bindeman I. N. (2017) Magma reservoir dynamics at Toba caldera, Indonesia, recorded by oxygen isotope zoning in quartz. *Scientific Reports* **7**, 40624.

Budzinski H. and Tischendorf G. (1989) Distribution of REE among minerals in the Hercynian postkinematic granites of Westerzgebirge-Vogtland, GDR. *Zeitschrift fur Geologische Wissenschaften* **17**, 1019–1031.

Burgisser A. and Scaillet B. (2007) Redox evolution of a degassing magma rising to the surface. *Nature* **445**, 194–197.

Burisch M., Markl G. and Gutzmer J. (2022) Breakup with benefits-hydrothermal mineral systems related to the disintegration of a supercontinent. *Earth and Planetary Science Letters* **580**, 117373.

Burnard P. G. and Polya D. A. (2004) Importance of mantle-derived fluids during granite-associated hydrothermal circulation: He and Ar isotopes of ore minerals from Panasqueira. *Geochimica et Cosmochimica Acta* **68**, 1607–1615.

Burnham C. W. (1979a) Magmas and hydrothermal fluids. In: H. L. Barnes (Ed.), *Geochemistry of Hydrothermal Ore Deposits*, 2nd edition. John Wiley & Sons, pp. 71–136.

Burnham C. W. (1979b) The importance of volatile constituents. In: H. S. Yoder Jr. (Ed.), *The Evolution of the Igneous Rocks: Fiftieth Anniversary Perspectives*. Princeton University Press, pp. 439–482.

Burnol L. and Viallefond L. (1984) Géochimie complémentaire en sols à Echassières (Allier): Résultats préliminaires. *Documents BRGM* **81**, 57–85.

Burns M. G. G. (2016) A fluid inclusion study of the Little Nahanni LCT-Type Pegmatite Group, NWT Canada: implications for the nature and origin of fluids in LCT-Type Pegmatites and Pegmatite evolution. Master dissertation, Laurentian University, Sudbury, Ontario, Canada.

Burt D. M. (1981) Acidity-salinity diagrams; application to greisen and porphyry deposits. *Economic Geology* **76**, 832–843.

Candela P. A. (1997) A review of shallow, ore-related granites: textures, volatiles, and ore metals. *Journal of petrology* **38**, 1619–1633.

Candela P. A. (1995) Model ore-metal partitioning from melts into vapor and vapor/brine mistures. *Magmas, Fluids, and ore deposits*.

Cao M., Evans N. J., Hollings P., Cooke D. R., McInnes B. I. A. and Qin K. (2021) Apatite texture, composition, and O-Sr-Nd isotope signatures record magmatic and hydrothermal fluid characteristics at the Black Mountain porphyry deposit, Philippines. *Economic Geology* **116**, 1189–1207.

Carignan J., Hild P., Mevelle G., Morel J. and Yeghicheyan D. (2001) Routine analyses of trace elements in geological samples using flow injection and low pressure on-line liquid chromatography coupled to ICP-MS: A study of geochemical reference materials BR, DR-N, UB-N, AN-G and GH. *Geostandards Newsletter* **25**, 187–198.

Carl C., Dill H. G., Kreuzer H. and Wendt I. (1983) U-Pb dating of ores in NE Bavaria. *Terra cognita* **3**, 195–196.

Carr P. A., Mercadier J., Harlaux M., Romer R. L., Moreira E., Legros H., Cuney M., Marignac C., Cauzid J. and Salsi L. (2021) U/Pb geochronology of wolframite by LA-ICP-MS; mineralogical constraints, analytical procedures, data interpretation, and comparison with ID-TIMS. *Chemical Geology* **584**, 120511.

Carrat G. H. (1956) Uranium deposit of Bauzot (Saone et Loire). CEA Saclay.

Cassidy M., Iveson A. A., Humphreys M. C. S., Mather T. A., Helo C., Castro J. M., Ruprecht P., Pyle D. M. and EIMF (2022) Experimentally derived F, Cl, and Br fluid/melt partitioning of intermediate to silicic melts in shallow magmatic systems. *American Mineralogist* **107**, 1825–1839.

Cathelineau M. (1982) Les gisements d'uranium liés spatialement aux leucogranites sud-armoricains et à leur encaissant métamorphique : relations et interactions entre les minéralisations et divers contextes géologiques et structuraux. Sciences de la Terre : Mémoires, **42**. BRGM.

Cathelineau M., Boiron M. C., Holliger P. and Poty B. (1990) Metallogenesis of the French part of the Variscan orogen. Part II: Time-space relationships between U, Au and Sn□W ore deposition and geodynamic events—mineralogical and U□Pb data. *Tectonophysics* **177**, 59–79.

Cathelineau M., Boiron M.-C., Fourcade S., Ruffet G., Clauer N., Belcourt O., Coulibaly Y., Banks D. A. and Guillocheau F. (2012) A major Late Jurassic fluid event at the basin/basement unconformity in western France: 40Ar/39Ar and K–Ar dating, fluid chemistry, and related geodynamic context. *Chemical Geology* **322**, 99–120.

Cathelineau M., Boiron M.-C., Marignac C., Dour M., Dejean M., Carocci E., Truche L. and Pinto F. (2020) High pressure and temperatures during the early stages of tungsten deposition at Panasqueira revealed by fluid inclusions in topaz. *Ore Geology Reviews* **126**, 103741.

Cathelineau M., Marignac C., Boiron M.-C., Gianelli G. and Puxeddu M. (1994) Evidence for Li-rich brines and early magmatic fluid-rock interactionin the Larderello geothermal system. *Geochimica et Cosmochimica Acta* **58**, 1083–1099.

Caumon M.-C., Dubessy J., Robert P. and Tarantola A. (2013) Fused-silica capillary capsules (FSCCs) as reference synthetic aqueous fluid inclusions to determine chlorinity by Raman spectroscopy. *European Journal of Mineralogy* **25**, 755–763.

Cave B. W., Lilly R., Glorie S. and Gillespie J. (2018) Geology, Apatite Geochronology, and Geochemistry of the Ernest Henry Inter-lens: Implications for a Re-Examined Deposit Model. *Minerals* **8**. 405.

Cernuschi F., Dilles J. H., Grocke S. B., Valley J. W., Kitajima K. and Tepley F. J. (2018) Rapid formation of porphyry copper deposits evidenced by diffusion of oxygen and titanium in quartz. *Geology* **46**, 611–614.

Černý P. (1986) Characteristics of Pegmatite Deposits of Tantalum. In: Möller, P., Černý, P., & Saupé, F. (Eds.), *Lanthanides, Tantalum and Niobium*. Springer Berlin Heidelberg, Berlin, Heidelberg, pp. 195–239.

Černý P. (1989) Contrasting geochemistry of two pegmatite fields in Manitoba: Products of juvenile Aphebian crust and polycyclic Archean evolution. *Precambrian Research* **45**, 215–234.

Černý P. (1991) Rare-element granitic pegmatites. Part I: Anatomy and internal evolution of pegmatite deposits. *Geoscience Canada* **18**, 49–67.

Černý Peter, Blevin P. L., Cuney M. and London D. (2005) Granite-related ore deposits. *Episodes*, **28**, 9–21.

Černý P. and Ercit T. S. (2005) The classification of granitic pegmatites revisited. *The Canadian Mineralogist* **43**, 2005–2026.

Černý P., London D. and Novák M. (2012) Granitic Pegmatites as Reflections of Their Sources. *Elements* **8**, 289–294.

Černý Petr, Masau M., Goad B. E. and Ferreira K. (2005) The Greer Lake leucogranite, Manitoba, and the origin of lepidolite-subtype granitic pegmatites. *Lithos* **80**, 305–321.

Chappell B. W. and White A. J. R. (1992) I-and S-type granites in the Lachlan Fold Belt. *Earth and Environmental Science Transactions of the Royal Society of Edinburgh* **83**, 1–26.

Charoy B., Chaussidon M., Le Carlier De Veslud C. and Duthou J. L. (2003) Evidence of Sr mobility in and around the albite-lepidolite-topaz granite of Beauvoir (France): an in-situ ion and electron probe study of secondary Sr-rich phosphates. *Contributions to Mineralogy and Petrology* **145**, 673–690.

Chauris L. (1988) Les leucogranites à béryl de Bretagne méridionale. In: *113ème Congrès National des Sociétés Savantes, Sciences de la Terre*. Paris, France, pp. 123-130.

Cheilletz A., Archibald D. A., Cuney M. and Charoy B. (1992) Ages $^{40}Ar/^{39}Ar$ du leucogranite à topaze-lépidolite de Beauvoir et des pegmatites sodolithiques de Chédeville (Nord du Massif Central, France). Signification pétrologique et géodynamique. *Comptes rendus de l'Académie des sciences. Série 2, Mécanique, Physique, Chimie, Sciences de l'univers, Sciences de la Terre* **315**, 329–336.

Chelle-Michou C., Rottier B., Caricchi L. and Simpson G. (2017) Tempo of magma degassing and the genesis of porphyry copper deposits. *Scientific reports* **7**, 40566.

Chen Y.-K., Ni P., Pan J.-Y., Cui J.-M., Li W.-S., Fang G.-J., Zhao Z.-H., Xu Y.-M., Ding J.-Y. and Han L. (2023) Fluid evolution and metallogenic mechanism of the Xianghualing skarn-type Sn deposit, South China: Evidence from petrography, fluid inclusions and trace-element composition of cassiterite. *Ore Geology Reviews* **154**, 105351.

Chew D. M. and Spikings R. A. (2015) Geochronology and thermochronology using apatite: time and temperature, lower crust to surface. *Elements* **11**, 189–194.

Chu M.-F., Wang K.-L., Griffin W. L., Chung S.-L., O'Reilly S. Y., Pearson N. J. and Iizuka Y. (2009) Apatite Composition: Tracing Petrogenetic Processes in Transhimalayan Granitoids. *Journal of Petrology* **50**, 1829–1855.

Clayton R. N. (1981) Isotopic Thermometry. In: R. C. Newton, A. Navrotsky, & B. J. Wood (Eds.), *Thermodynamics of Minerals and Melts*. Advances in Physical Geochemistry. Springer New York, pp. 85–109.

Cline J. S. (1995) Genesis of porphyry copper deposits: The behavior of water, chloride, and copper in crystallizing melts. *Arizona Geological Society Digest* **20**, 69–82.

Cline J. S. and Bodnar R. J. (1991) Can economic porphyry copper mineralization be generated by a typical calc-alkaline melt? *Journal of Geophysical Research: Solid Earth* **96**, 8113–8126.

Codeço M. S., Weis P. and Andersen C. (2022) Numerical Modeling of Structurally Controlled Ore Formation in Magmatic-Hydrothermal Systems. *Geochemistry, Geophysics, Geosystems* **23**, e2021GC010302.

Costa S. (1989) Age radiométrique 39Ar-40Ar du métamorphisme des séries du Lot et du charriage du groupe leptyno-amphibolique de Marvejols (M.C.F.). *Comptes rendus de l'Académie des sciences. Série 2, Mécanique, Physique, Chimie, Sciences de l'univers, Sciences de la Terre* **309**, 561–567.

Costa S. (1992) East-west diachronism of the collisional stage In the french Massif Central Implications for the European Variscan Orogen. *Geodinamica Acta* **5**, 51–68.

Coulson I. M., Villeneuve M. E., Dipple G. M., Duncan R. A., Russell J. K. and Mortensen J. K. (2002) Time-scales of assembly and thermal history of a composite felsic pluton: constraints from the Emerald Lake area, northern Canadian Cordillera, Yukon. *Journal of Volcanology and Geothermal Research* **114**, 331–356.

Couzinié S., Bouilhol P., Laurent O., Grocolas T. and Montel J.-M. (2022) Cambro–Ordovician ferrosilicic magmatism along the northern Gondwana margin: constraints from the Cézarenque–Joyeuse gneiss complex (French Massif Central). *Bulletin de la Société Géologique de France* **193**, 15.

Couzinié S., Laurent O., Moyen J.-F., Zeh A., Bouilhol P. and Villaros A. (2016) Post-collisional magmatism: Crustal growth not identified by zircon Hf–O isotopes. *Earth and Planetary Science Letters* **456**, 182–195.

Couzinié S., Moyen J.-F., Villaros A., Paquette J.-L., Scarrow J. H. and Marignac C. (2014) Temporal relationships between Mg-K mafic magmatism and catastrophic melting of the Variscan crust in the southern part of Velay Complex (Massif Central, France). *Journal of Geosciences* **59**, 1.

Cuney M. (2014) Felsic magmatism and uranium deposits. *Bulletin de la Société Géologique de France* **185**, 75–92.

Cuney M., Alexandrov P., Le Carlier de Veslud C., Cheilletz A., Raimbault L., Ruffet G. and Scaillet S. (2002) The timing of W-Sn-rare metals mineral deposit formation in the Western Variscan chain in their orogenic setting: the case of the Limousin area (Massif Central, France). *Geological Society, London, Special Publications* **204**, 213–228.

Cuney M and Autran A. (1987) Géologie profonde de la France. Programme national. Echassières. Le forage scientifique d'Echassières (Allier). Une clé pour la compréhension des mécanismes magmatiques et hydrothermaux associés aux granites à métaux rares (Thème 8: Evolution d'un apex granitique). *BRGM, CNRS*, Orléans.

Cuney M. and Autran A. (1987) Objectifs généraux du projet GPF Echassières n.1 et résultats essentiels acquis par le forage de 900 m sur le granite albitique à topaze-lépidolite de Beauvoir. *Géologie de la France* **2–3**, 7–24.

Cuney M. and Barbey P. (2014) Uranium, rare metals, and granulite-facies metamorphism. *Geoscience Frontiers* **5**, 729–745.

Cuney M., Brouand M. and Stussi J.-M. (2001) Le magmatisme hercynien en Vendée. Corrélations avec le socle du Poitou et l'ouest du Massif central français. *Géologie de la France* **1–2**, 117–142.

Cuney M. and Marignac C. (2015) Rare metal, W and U deposits and related granites from the NE French Massif Central. In *Field Guide for the 13th Biennial SGA Meeting* pp. 155.

Cuney M., Marignac C. and Weisbrod A. (1992) The Beauvoir topaz-lepidolite albite granite (Massif Central, France); the disseminated magmatic Sn-Li-Ta-Nb-Be mineralization. *Economic Geology* **87**, 1766–1794.

Davaine J. J. (1980) Les croûtes silico-fluorées mésozoïques du Bazois, description et modèle d'évolution. Mémoires du BRGM **104**, 211–241.

Decrée S., Cawthorn G., Deloule E., Mercadier J., Frimmel H. and Baele J.-M. (2020) Unravelling the processes controlling apatite formation in the Phalaborwa Complex (South Africa) based on combined cathodoluminescence, LA-ICPMS and in-situ O and Sr isotope analyses. C*ontributions to Mineralogy and Petrology* **175**, 34.

Delfour J. (1989) Données lithostratigraphiques et géochimiques sur le Dévono-Dinantien de la partie sud du faisceau du Morvan (NE Massif central français). *Géologie de la France* **4**, 49–77.

Dennen W. H. (1966) Stoichiometric substitution in natural quartz. *Geochimica et Cosmochimica Acta* **30**, 1235–1241.

Dessemond C., Lajoie-Leroux F., Soucy G., Laroche N. and Magnan J.-F. (2019) Spodumene: The Lithium Market, Resources and Processes. *Minerals* **9**, 334.

Deveaud S., Gumiaux C., Gloaguen E. and Branquet Y. (2013) Spatial statistical analysis applied to rare-element LCT-type pegmatite fields: an original approach to constrain faults-pegmatites-granites relationships. *Journal of Geosciences* **58**, 163–182.

Deveaud S., Millot R. and Villaros A. (2015) The genesis of LCT-type granitic pegmatites, as illustrated by lithium isotopes in micas. *Chemical Geology* **411**, 97–111.

Dilles J. H. (1987) Petrology of the Yerington Batholith, Nevada; evidence for evolution of porphyry copper ore fluids. *Economic Geology* **82**, 1750–1789.

Do Couto D., Faure M., Augier R., Cocherie A., Rossi P., Li X.-H. and Lin W. (2015) Monazite U–Th–Pb EPMA and zircon U–Pb SIMS chronological constraints on the tectonic, metamorphic, and thermal events in the inner part of the Variscan orogen, example from the Sioule series, French Massif Central. *International Journal of Geosciences (Geologische Rundschau)* **105**, 557–579.

Dobeš P. (2005) Fluid inclusion planes and paleofluid records in the Podlesí granite, Krušné hory Mts., Czech Republic. *Bull. of Geosciences* **80**, 149–154.

Dolníček Z., René M., Hermannová S. and Prochaska W. (2014) Origin of the Okrouhlá Radouň episyenite-hosted uranium deposit, Bohemian Massif, Czech Republic: fluid inclusion and stable isotope constraints. *Mineralium deposita* **49**, 409–425.

Dostal J., Kontak D. J., Gerel O., Shellnutt J. G. and Fayek M. (2015) Cretaceous ongonites (topaz-bearing albite-rich microleucogranites) from Ongon Khairkhan, Central Mongolia: products of extreme magmatic fractionation and pervasive metasomatic fluid: rock interaction. *Lithos* **236**, 173–189.

Downes H. and Duthou J.-L. (1988) Isotopic and trace-element arguments for the lower-crustal origin of Hercynian granitoids and pre-Hercynian orthogneisses, Massif Central (France). *Chemical Geology* **68**, 291–308.

Downes H., Shaw A., Williamson B. J. and Thirlwall M. F. (1997) Sr, Nd al36 (1997) 99–122 Hercynian granodiorites and monzogranites, Massif Central, France. *Chemical Geology* **136**, 99–122.

Driesner T. (2007) The system $H_2O$–NaCl. Part II: Correlations for molar volume, enthalpy, and isobaric heat capacity from 0 to 1000 °C, 1 to 5000 bar, and 0 to 1 $X_{NaCl}$. *Geochimica et Cosmochimica Acta* **71**, 4902–4919.

Driesner T. and Geiger S. (2007) Numerical Simulation of Multiphase Fluid Flow in Hydrothermal Systems. *Reviews in Mineralogy and Geochemistry* **65**, 187–212.

Driesner T. and Heinrich C. A. (2007) The system $H_2O$–NaCl. Part I: Correlation formulae for phase relations in temperature–pressure–composition space from 0 to 1000 °C, 0 to 5000 bar, and 0 to 1 $X_{NaCl}$. *Geochimica et Cosmochimica Acta* **71**, 4880–4901.

Dubinina E. O. and Borisov A. A. (2018) Structure and Composition Effects on the Oxygen Isotope Fractionation in Silicate Melts. *Petrology* **26**, 414–427.

Duc-Tin Q. and Keppler H. (2015) Monazite and xenotime solubility in granitic melts and the origin of the lanthanide tetrad effect. *Contributions to Mineralogy and Petrology* **169**, 1–26.

Dusséaux C., Gébelin A., Boulvais P., Ruffet G., Poujol M., Cogné N., Branquet Y., Mottram C., Barou F. and Mulch A. (2022) Timing and duration of meteoric water infiltration in the Quiberon detachment zone (Armorican Massif, Variscan belt, France). *Journal of Structural Geology* **156**, 104546.

Dusséaux C., Gébelin A., Ruffet G. and Mulch A. (2021) Late Carboniferous paleoelevation of the Variscan belt of Western Europe. *Earth and Planetary Science Letters* **569**, 117064.

Duthou J. L. (1978) Les granitoides du Haut Limousin (Massif central francais). Chronologie Rb-Sr de leur mise en place. Le thermométamorphisme carbonifère. *Bulletin de la Société Géologique de France* **7**, 229–235.

Duthou J. L., Cantagrel J. M., Didier J. and Vialette Y. (1984) Palaeozoic granitoids from the French Massif Central: age and origin studied by $^{87}Rb$-$^{87}Sr$ system. *Physics of the Earth and Planetary Interiors* **35**, 131–144.

Duthou J.-L. and Pin C. (1987) Etude isotopique Rb-Sr de l'apex granitique d'Echassières (Granite des Colettes, granite de Beauvoir). *Géologie de la France* **2–3**, 63–67.

Eastoe C. J. (1982) Physics and chemistry of the hydrothermal system at the Panguna porphyry copper deposit, Bougainville, Papua New Guinea. *Economic Geology* **77**, 127–153.

Eikenberg J. H. R. (1988) Vergleichende Datierung von Uranmineralien mit den U-Xe, U-Kr und U-Pb Systemen, sowie Untersuchungen der Produktion von Ne und Ar durch Kernprozesse. PhD dissertation, ETH Zürich.

Eiler J. M. (2001) Oxygen Isotope Variations of Basaltic Lavas and Upper Mantle Rocks. *Reviews in Mineralogy and Geochemistry* **43**, 319–364.

Eldursi K., Branquet Y., Guillou-Frottier L. and Marcoux E. (2009) Numerical investigation of transient hydrothermal processes around intrusions: Heat-transfer and fluid-circulation controlled mineralization patterns. *Earth and Planetary Science Letters* **288**, 70–83.

Elphick S. C., Dennis P. F. and Graham C. M. (1986) An experimental study of the diffusion of oxygen in quartz and albite using an overgrowth technique. *Contributions to Mineralogy and Petrology* **92**, 322–330.

Estéoule-Choux J. (1967) Contribution à l'étude des argiles du Massif armoricain. Argiles des altérations et des bassins sédimentaires tertiaires. *Mémoires de la Société géologique et minéralogique de Bretagne* **14**, 319.

Esteves N., France L., Bouilhol P. and Cuney M. (2024a) Plutonic formation through sills stacking and amalgamation: The case of Beauvoir rare-metal granite. *EGU General Assembly 2024*, Vienna, Austria, 14–19 April 2024.

Esteves N., France L., Cuney M. and Bouilhol P. (2024b) Small pluton construction through sills stacking, amalgamation and differentiation: Insight from the Beauvoir granite (Massif Central, France). [In press]

European Commission (2023) *Study on the Critical Raw Materials for the EU 2023*. European Commission, Brussels, Belgium.

Fabre C., Boiron M. C., Marignac C. and Aïssa M. (2001) Li-F-rich magmatic fluids exsolved from rare metal granites: the example of the Beauvoir granite (French Massif Central); a microthermometric and LIBS study. *XVI European Current Research on Fluid Inclusions (ECROFI) Abstracts*, 145–147.

Faure M. (1995) Late orogenic carboniferous extensions in the Variscan French Massif Central. *Tectonics* **14**, 132–153.

Faure M., Lardeaux J.-M. and Ledru P. (2009) A review of the pre-Permian geology of the Variscan French Massif Central. *Comptes Rendus Geoscience* **341**, 202–213.

Faure M., Leloix C. and Roig J.-Y. (1997) L'Evolution polycyclique de la chaine hercynienne. *Bulletin de la Société Géologique de France* **168**, 695–705.

Fekete S., Weis P., Driesner T., Bouvier A.-S., Baumgartner L. and Heinrich C. A. (2016) Contrasting hydrological processes of meteoric water incursion during magmatic–hydrothermal ore deposition: an oxygen isotope study by ion microprobe. *Earth and Planetary Science Letters* **451**, 263–271.

Feybesse J. L. (1985) Etude structurale du massif d'Echassières et de son encaissant métamorphique. *Documents BRGM* **95–8**, 55–72.

Fiannacca P., Williams I. S. and Cirrincione R. (2017) Timescales and mechanisms of batholith construction: Constraints from zircon oxygen isotopes and geochronology of the late Variscan Serre Batholith (Calabria, southern Italy). *Lithos* **277**, 302–314.

Ford M. and Lickorish W. H. (2004) Foreland basin evolution around the western Alpine Arc. *Geological Society, London, Special Publications* **221**, 39–63.

Fouillac A.-M., Kosakevitch A., Merceron T., Meunier A. and Rossi P. (1987) Comportement des fluides dans l'évolution magmatique puis Hydrothermale du granite à Ta, Nb, Li de Beauvoir d'après la géochimie isotopique de l'oxygène et l'hydrogène. *Géologie de la France* **2–3**, 279–293.

Fouillac A.-M. and Rossi P. (1991) Near-solidus delta $^{18}O$ depletion in a Ta-Nb-bearing albite granite: the Beauvoir Granite, France. *Economic Geology* **86**, 1704–1720.

Fournier R. O. (1999) Hydrothermal processes related to movement of fluid from plastic into brittle rock in the magmatic-epithermal environment. *Economic Geology* **94**, 1193–1211.

Foustoukos D. I. and Seyfried W. E. (2007) Trace element partitioning between vapor, brine and halite under extreme phase separation conditions. *Geochimica et Cosmochimica Acta* **71**, 2056–2071.

Gagny C. (1987) Organisation séquentielle évolutive des intrusions successives du Granite de Beauvoir dans son caisson: Arguments géochimiques. *Géologie de la France* **2–3**, 199–208.

Gagny C., Courrioux G., Cuenin O., Jacquot T. and LEISTEL J.-M. (1984) Contrôle structural de la métallogenèse dans la région d'Echassières par une zone de cisaillement régional orientée à N 60E (Massif Central français). *Comptes-rendus des séances de l'Académie des sciences. Série 2, Mécanique-physique, chimie, sciences de l'univers, sciences de la terre* **298**, 459–462.

Gagny C. and Jacquot T. (1987) Contribution de la pétrologie structurale à la connaissance des conditions de mise en place et de structuration complexe du granite des Colettes (Massif d'Echassières, Massif Central Français). *Géologie de la France* **2–3**, 47–56.

García-Arias M., Morales Cámera M. M., Dahlquist J. A., Gao P., Couzinié S. and Díez-Montes A. (2024) The tectonic significance of peri-Gondwanan Late Neoproterozoic-Early Palaeozoic felsic peraluminous magmatism. *Earth-Science Reviews* **254**, 104803.

Gardien V., Lardeaux J.-M., Ledru P., Allemand P. and Guillot S. (1997) Metamorphism during late orogenic extension; insights from the French Variscan belt. *Bulletin de la Société géologique de France* **168**, 271–286.

Gardien V., Thompson A. B., Grujic D. and Ulmer P. (1995) Experimental melting of biotite + plagioclase + quartz ± muscovite assemblages and implications for crustal melting. *Journal of Geophysical Research: Solid Earth* **100**, 15581–15591.

Gaudin A., Ansan V. and Rigaudier T. (2015) Mineralogical and $\delta^{18}O$–$\delta D$ isotopic study of kaolinized micaschists at Penestin, Armorican Massif, France: New constraint in the kaolinization process. *Catena* **133**, 97–106.

Gébelin A., Brunel M., Monié P., Faure M. and Arnaud N. (2007) Transpressional tectonics and Carboniferous magmatism in the Limousin, Massif Central, France: Structural and $^{40}Ar/^{39}Ar$ investigations. *Tectonics* **26**, TC2008.

Ghiorso M. S. and Gualda G. A. R. (2013) A method for estimating the activity of titania in magmatic liquids from the compositions of coexisting rhombohedral and cubic iron–titanium oxides. *Contributions to Mineralogy and Petrology* **165**, 73–81.

Gigoux M. (2015) Origine des minéralisations stratiformes de fluorine de la bordure sud-est du bassin de Paris. PhD dissertation, Université Paris Sud-Paris XI.

Gigoux M., Delpech G., Guerrot C., Pagel M., Augé T., Négrel P. and Brigaud B. (2015) Evidence for an Early Cretaceous mineralizing event above the basement/sediment unconformity in the intracratonic Paris Basin: paragenetic sequence and Sm-Nd dating of the world-class Pierre-Perthuis stratabound fluorite deposit. *Mineralium Deposita* **50**, 455–463.

Giletti B. J., Semet M. P. and Yund R. A. (1978) Studies in diffusion—III. Oxygen in feldspars: an ion microprobe determination. *Geochimica et Cosmochimica Acta* **42**, 45–57.

Giletti B. J. and Yund R. A. (1984) Oxygen diffusion in quartz. *Journal of Geophysical Research: Solid Earth* **89**, 4039–4046.

Gloaguen E., Melleton J., Lefebvre G., Tourlière B., Yart S. and Gourcerol B. (2018) Ressources métropolitaines en lithium et analyse du potentiel par méthodes de prédictivité. *Rapport final. Rapport BRGM/RP-68321-FR*, BRGM, pp. 126.

Goldoff B., Webster J. D. and Harlov D. E. (2012) Characterization of fluor-chlorapatites by electron probe microanalysis with a focus on time-dependent intensity variation of halogens. *American Mineralogist* **97**, 1103–1115.

Götze J., Pan Y. and Müller A. (2021) Mineralogy and mineral chemistry of quartz: A review. *Mineralogical Magazine* **85**, 639–664.

Götze J., Plötze M., Graupner T., Hallbauer D. K. and Bray C. J. (2004) Trace element incorporation into quartz: A combined study by ICP-MS, electron spin resonance, cathodoluminescence, capillary ion analysis, and gas chromatography. *Geochimica et Cosmochimica Acta* **68**, 3741–3759.

Götze J., Schertl H.-P., Neuser R. D., Kempe U. and Hanchar J. M. (2013) Optical microscope-cathodoluminescence (OM–CL) imaging as a powerful tool to reveal internal textures of minerals. *Mineralogy and Petrology* **107**, 373–392.

Gourcerol B., Gloaguen E., Melleton J., Tuduri J. and Galiegue X. (2019) Re-assessing the European lithium resource potential – A review of *hard-rock* resources and metallogeny. *Ore Geology Reviews* **109**, 494–519.

Graupner T., Brätz H. and Klemd R. (2005) LA-ICP-MS micro-analysis of fluid inclusions in quartz using a commercial Merchantek 266 nm Nd:YAG laser: a pilot study. *European Journal of Mineralogy* **17**, 93–102.

Grolier J. (1971) Contribution à l'étude géologique des séries cristallophylliennes inverses du Massif Central français : la série de la Sioule (Puy-de-Dôme, Allier). PhD dissertation, BRGM, Paris.

Groves D. I. and McCarthy T. S. (1978) Fractional crystallization and the origin of tin deposits in granitoids. *Mineralium Deposita* **13**, 11–26.

Guillocheau F., Robin C., Allemand P., Bourquin S., Brault N., Dromart G., Friedenberg R., Garcia J.-P., Gaulier J.-M. and Gaumet F. (2000) Meso-Cenozoic geodynamic evolution of the Paris Basin: 3D stratigraphic constraints. *Geodinamica Acta* **13**, 189–245.

Guillong M. and Heinrich C. A. (2007) LA-ICP-MS analysis of inclusions: improved ablation and detection. In: L. W. Diamond, T. Pettke, & C. Spandler (Eds.), *European Current Research on Fluid Inclusions-ECROFI-XIX, 17-20 July 2007, University of Berne, Programme and Abstracts Volume*. University of Berne, pp. 82.

Guillong M., Meier D. L., Allan M. M., Heinrich C. A. and Yardley B. W. D. (2008) SILLS: A MATLAB-based program for the reduction of laser ablation ICP-MS data of homogeneous materials and inclusions. In: Peter J. W. S. (Ed.), *Laser Ablation Inductively Coupled Plasma Mass Spectrometry in the Earth Sciences: Current Practices and Outstanding Issues*. Mineralogical Association of Canada, Short Course Series, pp. 328–333.

Günther D., Audétat A., Frischknecht R. and Heinrich C. A. (1998) Quantitative analysis of major, minor and trace elements in fluid inclusions using laser ablation–inductively coupled plasmamass spectrometry. *Journal of Analytical Atomic Spectrometry* **13**, 263–270.

Günther D., Frischknecht R., Heinrich C. A. and Kahlert H.-J. (1997) Capabilities of an Argon Fluoride 193 nm Excimer Laser for Laser Ablation Inductively Coupled Plasma Mass Spectometry Microanalysis of Geological Materials. *Journal of Analytical Atomic Spectrometry* **12**, 939–944.

Haapala I. and Lukkari S. (2005) Petrological and geochemical evolution of the Kymi stock, a topaz granite cupola within the Wiborg rapakivi batholith, Finland. *Lithos* **80**, 347–362.

Halter W. E. and Webster J. D. (2004) The magmatic to hydrothermal transition and its bearing on ore-forming systems. *Chemical Geology* **210**, 1–6.

Halter W. E., Williams-Jones A. E. and Kontak D. J. (1998a) Modeling fluid–rock interaction during greisenization at the East Kemptville tin deposit: implications for mineralization. *Chemical Geology* **150**, 1–17.

Halter W. E., Williams-Jones A. E. and Kontak D. J. (1998b) Origin and evolution of the greisenizing fluid at the East Kemptville tin deposit, Nova Scotia, Canada. *Economic Geology* **93**, 1026–1051.

Handy M. R., Schmid S. M., Bousquet R., Kissling E. and Bernoulli D. (2010) Reconciling plate-tectonic reconstructions of Alpine Tethys with the geological–geophysical record of spreading and subduction in the Alps. *Earth-Science Reviews* **102**, 121–158.

Harlaux M., Blein O., Ballouard C., Kontak D. J., Thiéblemont D., Dabosville A. and Gourcerol B. (2025) Geochemical footprints of peraluminous rare-metal granites and pegmatites in the northern French Massif Central and implications for exploration targeting. *Ore Geology Reviews* **176**, 106409.

Harlaux M., Kouzmanov K., Gialli S., Marger K., Bouvier A.-S., Baumgartner L. P., Rielli A., Dini A., Chauvet A., Kalinaj M. and Fontboté L. (2021) Fluid mixing as primary trigger for cassiterite deposition: Evidence from in situ $\delta^{18}O$-$\delta^{11}B$ analysis of tourmaline from the world-class San Rafael tin (-copper) deposit, Peru. *Earth and Planetary Science Letters* **563**, 116889.

Harlaux M., Mercadier J., Bonzi W. M.-E., Kremer V., Marignac C. and Cuney M. (2017) Geochemical Signature of Magmatic-Hydrothermal Fluids Exsolved from the Beauvoir Rare-Metal Granite (Massif Central, France): Insights from LA-ICPMS Analysis of Primary Fluid Inclusions. *Geofluids* **2017**, 1–25.

Harlaux M., Mercadier J., Marignac C., Peiffert C., Cloquet C. and Cuney M. (2018a) Tracing metal sources in peribatholitic hydrothermal W deposits based on the chemical composition of wolframite: The example of the Variscan French Massif Central. *Chemical Geology* **479**, 58–85.

Harlaux M., Romer R. L., Mercadier J., Morlot C., Marignac C. and Cuney M. (2018b) 40 Ma of hydrothermal W mineralization during the Variscan orogenic evolution of the French Massif Central revealed by U-Pb dating of wolframite. *Mineralium Deposita* **53**, 21–51.

Harlov D. E. (2015) Apatite: A Fingerprint for Metasomatic Processes. *Elements* **11**, 171–176.

Hedenquist J. W., Arribas A. and Reynolds T. J. (1998) Evolution of an intrusion-centered hydrothermal system; Far Southeast-Lepanto porphyry and epithermal Cu-Au deposits, Philippines. *Economic Geology* **93**, 373–404.

Hedenquist J. W. and Lowenstern J. B. (1994) The role of magmas in the formation of hydrothermal ore deposits. *Nature* **370**, 519–527.

Heinrich C. A. (2007) Fluid-Fluid Interactions in Magmatic-Hydrothermal Ore Formation. *Reviews in Mineralogy and Geochemistry* **65**, 363–387.

Heinrich C. A. (1990) The chemistry of hydrothermal tin (-tungsten) ore deposition. *Economic Geology* **85**, 457–481.

Heinrich C. A. and Candela P. A. (2014) Fluids and ore formation in the Earth's crust. In: H. D. Holland & K. K. Turekian (Eds.), *Treatise on Geochemistry*, Second Edition, Elsevier, pp. 1–28.

Heinrich C. A., Günther D., Audétat A., Ulrich T. and Frischknecht R. (1999) Metal fractionation between magmatic brine and vapor, determined by microanalysis of fluid inclusions. *Geology* **27**, 755–758.

Heinrich C. A., Pettke T., Halter W. E., Aigner-Torres M., Audétat A., Günther D., Hattendorf B., Bleiner D., Guillong M. and Horn I. (2003) Quantitative multi-element analysis of minerals, fluid and melt inclusions by laser-ablation inductively-coupled-plasma mass-spectrometry. *Geochimica et Cosmochimica Acta* **67**, 3473–3497.

Heinrich C. A., Ryan C. G., Mernagh T. P. and Eadington P. J. (1992) Segregation of ore metals between magmatic brine and vapor; a fluid inclusion study using PIXE microanalysis. *Economic Geology* **87**, 1566–1583.

Hellstrom J., Paton C., Woodhead J. and Hergt J. (2008) Iolite: software for spatially resolved LA-(quad and MC) ICPMS analysis. *Mineralogical Association of Canada short course series* **40**, 343–348.

Hemley J. J. and Hunt J. P. (1992) Hydrothermal ore-forming processes in the light of studies in rock-buffered systems; II, Some general geologic applications. *Economic Geology* **87**, 23–43.

Henley R. W. and McNabb A. (1978) Magmatic vapor plumes and ground-water interaction in porphyry copper emplacement. *Economic Geology* **73**, 1–20.

Herzberg C. T., Fyfe W. S. and Carr M. J. (1983) Density constraints on the formation of the continental Moho and crust. *Contributions to Mineralogy and Petrology* **84**, 1–5.

Hildreth W. and Moorbath S. (1988) Crustal contributions to arc magmatism in the Andes of Central Chile. *Contributions to Mineralogy and Petrology* **98**, 455–489.

Hofmann B. and Eikenberg J. (1991) The Krunkelbach uranium deposit, Schwarzwald, Germany; correlation of radiometric ages (U-Pb, U-Xe-Kr, K-Ar, $^{230}$Th-$^{234}$U). *Economic Geology* **86**, 1031–1049.

Holtz F., Dingwell D. B. and Behrens H. (1993) Effects of F, $B_2O_3$ and $P_2O_5$ on the solubility of water in haplogranite melts compared to natural silicate melts. *Contributions to Mineralogy and Petrology* **113**, 492–501.

Horstwood M. S., Košler J., Gehrels G., Jackson S. E., McLean N. M., Paton C., Pearson N. J., Sircombe K., Sylvester P. and Vermeesch P. (2016) Community-derived standards for LA-ICP-MS U-(Th-) Pb geochronology–Uncertainty propagation, age interpretation and data reporting. *Geostandards and Geoanalytical Research* **40**, 311–332.

De Hoÿm de Marien L., Pitra P., Poujol M., Cogné N., Cagnard F. and Le Bayon B. (2023) Complex geochronological record of an emblematic Variscan eclogite (Haut-Allier, French Massif Central). *Journal of Metamorphic Geology* **41**, 967–995.

Hsieh P.-S., Chen C.-H., Yang H.-J. and Lee C.-Y. (2008) Petrogenesis of the Nanling Mountains granites from South China: Constraints from systematic apatite geochemistry and whole-rock geochemical and Sr–Nd isotope compositions. *Journal of Asian Earth Sciences* **33**, 428–451.

Hu B., Etschmann B., Testemale D., Liu W., Guan Q., Müller H. and Brugger J. (2024) Tantalum in hydrothermal fluids. *Geochimica et Cosmochimica Acta*. [In press]

Hu G., Clayton R. N., Polyakov V. B. and Mineev S. D. (2005) Oxygen isotope fractionation factors involving cassiterite (SnO2): II. determination by direct isotope exchange between cassiterite and calcite. *Geochimica et Cosmochimica Acta* **69**, 1301–1305.

Hu S. (1984) An important metallogenetic model for W, Sn, and rare granitophile element ore deposits related to metasomatically altered granites. In: K.Q. Xu, G.C. Tu (Eds.), *Geology of Granites and Their Metallogenetic Relations, Science Press, Beijing,* pp. 519–537.

Huang R. and Audétat A. (2012) The titanium-in-quartz (TitaniQ) thermobarometer: A critical examination and re-calibration. *Geochimica et Cosmochimica Acta* **84**, 75–89.

Hulsbosch N., Boiron M.-C., Dewaele S. and Muchez P. (2016) Fluid fractionation of tungsten during granite–pegmatite differentiation and the metal source of peribatholitic W quartz veins: Evidence from the Karagwe-Ankole Belt (Rwanda). *Geochimica et Cosmochimica Acta* **175**, 299–318.

Hulsbosch N., Hertogen J., Dewaele S., André L. and Muchez P. (2014) Alkali metal and rare earth element evolution of rock-forming minerals from the Gatumba area pegmatites (Rwanda): Quantitative assessment of crystal-melt fractionation in the regional zonation of pegmatite groups. *Geochimica et Cosmochimica Acta* **132**, 349–374.

Imerys Ceramics France (2020) *Demande de première Prolongation du Permis Exclusif de Recherche de Mines de "BEAUVOIR."*

Ingebritsen S. E., Geiger S., Hurwitz S. and Driesner T. (2010) Numerical simulation of magmatic hydrothermal systems. *Reviews of Geophysics* **48**, 1–33.

Irber W. (1999) The lanthanide tetrad effect and its correlation with K/Rb, Eu/Eu*, Sr/Eu, Y/Ho, and Zr/Hf of evolving peraluminous granite suites. *Geochimica et Cosmochimica Acta* **63**, 489–508.

Jacques D., Vieira R., Muchez P. and Sintubin M. (2018) Transpressional folding and associated cross-fold jointing controlling the geometry of post-orogenic vein-type W-Sn mineralization: examples from Minas da Panasqueira, Portugal. *Mineralium Deposita* **53**, 171–194.

Jacquot T. (1987) Dynamique de l'organisation séquentielle du magma de Beauvoir. Apport de la pétrologie structurale. *Géologie de la France* **2–3**, 209–222.

Jacquot T. and Gagny C. (1987) Pétrologie structurale du granite de Beauvoir (Massif d'Echassières) : données et interprétation a son niveau apical. *Géologie de la France* **2–3**, 57–62.

Jacquot T. and Gagny C. (1985) Pétrologie structurale du massif d'Echassières (Massif Central français): mise en évidence de l'activité de linéaments lors de sa genèse. *Documents BRGM* **95–8**, 39–53.

Jahn B., Wu F., Capdevila R., Martineau F., Zhao Z. and Wang Y. (2001) Highly evolved juvenile granites with tetrad REE patterns: the Woduhe and Baerzhe granites from the Great Xing'an Mountains in NE China. *Lithos* **59**, 171–198.

Jaranowski M., Budzyń B., Rzepa G., Sláma J. and Sawłowicz Z. (2021) Geochemical constraints on the distribution of trace elements and volatiles in fluorapatite from the Panasqueira tin-tungsten deposit (Portugal). *Geochemistry* **81**, 125765.

Jarchovský T. (1962) Entstehung der Feldspatsaume (Stockscheider) an den Kontakten von Granit-und Greisen-Stocken im Erzgebirge. *Krystalinikum* **1**, 71–80.

Jébrak M. and Marcoux E. (2008) *Géologie des ressources minérales*. Ministère des ressources naturelles et de la faune, Québec.

Jochum K. P., Weis U., Stoll B., Kuzmin D., Yang Q., Raczek I., Jacob D. E., Stracke A., Birbaum K. and Frick D. A. (2011) Determination of reference values for NIST SRM 610–617 glasses following ISO guidelines. *Geostandards and Geoanalytical Research* **35**, 397–429.

Johan V., Monier G. and Rossi P. (1988) Etude pétrographique systématique des granites du sondage GPF1 de Beauvoir. *Documents BRGM* **124**, 11–101.

Johan Z. and Johan V. (2001) Les micas de la coupole granitique de Cínovec (Zinnwald), République tchèque: un nouvel aperçu sur la métallogenèse de l'étain et du tungstène. *Comptes Rendus de l'Académie des Sciences-Series IIA-Earth and Planetary Science* **332**, 307–313.

Joseph D., Bellon H., Derre C. and Touray J. C. (1973) Fluorite veins dated in the 200 million year range at La Petite Verrière and Chavaniac, France. *Economic geology* **68**, 707–708.

Kaeter D., Barros R., Menuge J. F. and Chew D. M. (2018) The magmatic–hydrothermal transition in rare-element pegmatites from southeast Ireland: LA-ICP-MS chemical mapping of muscovite and columbite–tantalite. *Geochimica et Cosmochimica Acta* **240**, 98–130.

Kamenetsky V. S., van Achterbergh E., Ryan C. G., Naumov V. B., Mernagh T. P. and Davidson P. (2002) Extreme chemical heterogeneity of granite-derived hydrothermal fluids: An example from inclusions in a single crystal of miarolitic quartz. *Geology* **30**, 459–462.

Karimzadeh Somarin A. and Ashley P. (2004) Hydrothermal alteration and mineralisation of the Glen Eden Mo-W-Sn deposit: a leucogranite-related hydrothermal system, Southern New England Orogen, NSW, Australia. *Mineralium Deposita* **39**, 282–300.

Kendrick M. A., Phillips D., Wallace M. and Miller J. M. (2011) Halogens and noble gases in sedimentary formation waters and Zn–Pb deposits: A case study from the Lennard Shelf, Australia. *Applied Geochemistry* **26**, 2089–2100.

Kesraoui M. and Nedjari S. (2002) Contrasting evolution of low-P rare metal granites from two different terranes in the Hoggar area, Algeria. *Journal of African Earth Sciences* **34**, 247–257.

Klemm L. M., Pettke T., Heinrich C. A. and Campos E. (2007) Hydrothermal evolution of the El Teniente deposit, Chile: Porphyry Cu-Mo ore deposition from low-salinity magmatic fluids. *Economic Geology* **102**, 1021–1045.

Knoll T., Huet B., Schuster R., Mali H., Ntaflos T. and Hauzenberger C. (2023) Lithium pegmatite of anatectic origin – A case study from the Austroalpine Unit Pegmatite Province (Eastern European Alps): Geological data and geochemical modeling. *Ore Geology Reviews* **154**, 105298.

Knoll T., Schuster R., Huet B., Mali H., Onuk P., Horschinegg M., Ertl A. and Giester G. (2018) Spodumene Pegmatites and Related Leucogranites from the AustroAlpine Unit (Eastern Alps, Central Europe): Field Relations, Petrography, Geochemistry, and Geochronology. *The Canadian Mineralogist* **56**, 489–528.

Kontak D. J., Ansdell K., Dostal J., Halter W., Martin R. and Williams-Jones A. E. (2001) The nature and origin of pegmatites in a fluorine-rich leucogranite, East Kemptville Tin Deposit, Nova Scotia, Canada. *Earth and Environmental Science Transactions of The Royal Society of Edinburgh* **92**, 173–200.

Kontak D. J., Groat L., Burns M. G., Archibald D. A. and Creaser R. (2016) Documenting the complex evolution of a rare-metal pegmatite swarm: The Little Nahanni Pegmatite Group, NWT, Canada. *Geological Association of Canada, Mineralogical Association of Canada, Whitehorse, YK, Canada, Program with Abstracts* **39**.

Kontak D. J. and Kyser T. K. (2009) Nature and origin of an LCT-suite pegmatite with late-stage sodium enrichment, Brazil Lake, Yarmouth County, Nova Scotia. II. Implications of stable isotopes ($\delta^{18}O$, $\delta D$) for magma source, internal crystallization and nature of sodium metasomatism. *The Canadian Mineralogist* **47**, 745–764.

Konzett J., Schneider T., Nedyalkova L., Hauzenberger C., Melcher F., Gerdes A. and Whitehouse M. (2018) Anatectic Granitic Pegmatites from the Eastern Alps: A Case of Variable Rare-Metal Enrichment During High-Grade Regional Metamorphism – I: Mineral Assemblages, Geochemical Characteristics, and Emplacement Ages. *The Canadian Mineralogist* **56**, 555–602.

Korges M., Weis P., Lüders V. and Laurent O. (2018) Depressurization and boiling of a single magmatic fluid as a mechanism for tin-tungsten deposit formation. *Geology* **46**, 75–78.

Kovalenko V. I. (1977) *Petrology and geochemistry of rare-metal granitoids*. Akademiia Nauk SSSR, Siberian Division, Novosibirsk.

Kovalenko V. I. and Kovalenko N. I. (1976) *Ongonites (topaz-bearing quartz keratophyre) - subvolcanic analogues of rare-metal Li-F granites*. Nauka, Moscow.

Kovalenko V. I., Kuz'min M. I. and Letnikov F. A. (1970) Magmatic origin of lithium-and fluorine-bearing rare-metal granite. *Doklady Academy of Sciences USSR, Earth Sciences Seet* **190**, 189–190.

Kovalenko V. I., Tsareva G. M. and Cuney M. (1998) Major-, trace elements and water in the magma of the Beauvoir rare metal granite, France (melt inclusion data). *Doklady Akademii Nauk* **359**, 667–671.

Krauskopf K. B. (1964) The possible role of volatile metal compounds in ore genesis. *Economic Geology* **59**, 22–45.

Kříbek B., Žák K., Dobeš P., Leichmann J., Pudilová M., René M., Scharm B., Scharmová M., Hájek A. and Holeczy D. (2009) The Rožná uranium deposit (Bohemian Massif, Czech Republic): shear zone-hosted, late Variscan and post-Variscan hydrothermal mineralization. *Mineralium deposita* **44**, 99–128.

Krneta S., Ciobanu C. L., Cook N. J., Ehrig K. and Kontonikas-Charos A. (2017) Rare earth element behaviour in apatite from the Olympic Dam Cu–U–Au–Ag deposit, South Australia. *Minerals* **7**, 135.

Kroner U. and Romer R. L. (2013) Two plates – Many subduction zones: The Variscan orogeny reconsidered. *Gondwana Research* **24**, 298–329.

Kunz B. E., Warren C. J., Jenner F. E., Harris N. B. W. and Argles T. W. (2022) Critical metal enrichment in crustal melts: The role of metamorphic mica. *Geology* **50**, 1219–1223.

Kusebauch C., John T., Whitehouse M. J. and Engvik A. K. (2015a) Apatite as probe for the halogen composition of metamorphic fluids (Bamble Sector, SE Norway). *Contributions to Mineralogy and Petrology* **170**, 34.

Kusebauch C., John T., Whitehouse M. J., Klemme S. and Putnis A. (2015b) Distribution of halogens between fluid and apatite during fluid-mediated replacement processes. *Geochimica et Cosmochimica Acta* **170**, 225–246.

Laetsch T. and Downs R. (2006) Software for identification and refinement of cell parameters from powder diffraction data of minerals using the RRUFF Project and American Mineralogist Crystal Structure Databases. In: *19th General Meeting of the International Mineralogical Association,* Kobe, Japan, pp. e28.

Landtwing M. R. and Pettke T. (2005) Relationships between SEM-cathodoluminescence response and trace-element composition of hydrothermal vein quartz. *American Mineralogist* **90**, 122–131.

Lardeaux J. M., Schulmann K., Faure M., Janoušek V., Lexa O., Skrzypek E., Edel J. B. and Štípská P. (2014) The Moldanubian Zone in the French Massif Central, Vosges/Schwarzwald and Bohemian Massif revisited: differences and similarities. *Geological Society, London, Special Publications* **405**, 7–44.

Launay G., Branquet Y., Sizaret S., Guillou-Frottier L. and Gloaguen E. (2023) How greisenization could trigger the formation of large vein-and-greisen Sn-W deposits: A numerical investigation applied to the Panasqueira deposit. *Ore Geology Reviews* **153**, 105299.

Launay G., Sizaret S., Guillou-Frottier L., Fauguerolles C., Champallier R. and Gloaguen E. (2019) Dynamic permeability related to greisenization reactions in Sn-W ore deposits: Quantitative petrophysical and experimental evidence. *Geofluids* **1,** 5976545.

Launay G., Sizaret S., Lach P., Melleton J., Gloaguen É. and Poujol M. (2021) Genetic relationship between greisenization and Sn-W mineralizations in vein and greisen deposits: Insights from the Panasqueira deposit (Portugal). *Bulletin de la Société Géologique de France* **192**, 2.

Laurent O., Couzinié S., Zeh A., Vanderhaeghe O., Moyen J.-F., Villaros A., Gardien V. and Chelle-Michou C. (2017a) Protracted, coeval crust and mantle melting during Variscan late-orogenic evolution: U–Pb dating in the eastern French Massif Central. *International Journal of Earth Sciences (Geologische Rundschau)* **106**, 421–451.

Laurent O., Zeh A., Gerdes A., Villaros A., Gros K. and Słaby E. (2017b) How do granitoid magmas mix with each other? Insights from textures, trace element and Sr–Nd isotopic composition of apatite and titanite from the Matok pluton (South Africa). *Contributions to Mineralogy and Petrology* **172**, 1–22.

Lecumberri-Sanchez P. and Bodnar R. J. (2018) Halogen Geochemistry of Ore Deposits: Contributions Towards Understanding Sources and Processes. In: Harlov, D. E., Aranovich, L. (Eds.), *The Role of Halogens in Terrestrial and Extraterrestrial Geochemical Processes*. Springer Geochemistry. Springer International Publishing, Cham, pp. 261–305.

Lecumberri-Sanchez P., Steele-MacInnis M., Weis P., Driesner T. and Bodnar R. J. (2015) Salt precipitation in magmatic-hydrothermal systems associated with upper crustal plutons. *Geology* **43**, 1063–1066.

Lecumberri-Sanchez P., Vieira R., Heinrich C. A., Pinto F. and Wälle M. (2017) Fluid-rock interaction is decisive for the formation of tungsten deposits. *Geology* **45**, 579–582.

Ledru P., Lardeaux J. M., Santallier D., Autran A., Quenardel J. M., Floc'h J. P., Lerouge G., Maillet N., Marchand J. and Ploquin A. (1989) Où sont les nappes dans le Massif central francais? *Bulletin de la Société Géologique de France* **V**, 605–618.

Legros H., Marignac C., Mercadier J., Cuney M., Richard A., Wang R.-C., Charles N. and Lespinasse M.-Y. (2016) Detailed paragenesis and Li-mica compositions as recorders of the magmatic-hydrothermal evolution of the Maoping W-Sn deposit (Jiangxi, China). *Lithos* **264**, 108–124.

Legros H., Marignac C., Tabary T., Mercadier J., Richard A., Cuney M., Wang R.-C., Charles N. and Lespinasse M.-Y. (2018) The ore-forming magmatic-hydrothermal system of the Piaotang W-Sn deposit (Jiangxi, China) as seen from Li-mica geochemistry. *American Mineralogist* **103**, 39–54.

Legros H., Richard A., Tarantola A., Kouzmanov K., Mercadier J., Vennemann T., Marignac C., Cuney M., Wang R.-C. and Charles N. (2019) Multiple fluids involved in granite-related W-Sn deposits from the world-class Jiangxi province (China). *Chemical Geology* **508**, 92–115.

Lehmann B. (1990) *Metallogeny of Tin*. Lecture Notes in Earth Sciences, Volume 32. Springer-Verlag, Berlin.

Lehmann B. (2006) *Metallogeny of Tin*. Springer-Verlag, Berlin, 211 pp.

Lenoir L., Blaise T., Chourio-Camacho D., Richard A., Tarantola A., Agrinier P., Rigaudier T., Monvoisin G., Bardoux G. and Brigaud B. (2023) The origin of fluorite-barite mineralization at the interface between the Paris Basin and its Variscan basement: insights from fluid inclusion chemistry and isotopic (O, H, Cl) composition. *Mineralium Deposita* **59**, 1–21.

Lerchbaumer L. and Audétat A. (2012) High Cu concentrations in vapor-type fluid inclusions: An artifact? *Geochimica et Cosmochimica Acta* **88**, 255–274.

Lerouge G. and Quenardel J. M. (1988) Les zones de cisaillement carbonifères dans les plutons vendéens et leurs prolongations dans le Nord-ouest du Masif central français. *Bulletin de la Société Géologique de France* **IV**, 831–838.

Li J., Huang X.-L., Fu Q. and Li W.-X. (2021) Tungsten mineralization during the evolution of a magmatic-hydrothermal system: Mineralogical evidence from the Xihuashan rare-metal granite in South China. *American Mineralogist* **106**, 443–460.

Li Y., He S., Zhang R.-Q., Bi X.-W., Feng L.-J., Tang G.-Q., Wang W.-Z., Huang F. and Li X.-H. (2022) Cassiterite oxygen isotopes in magmatic-hydrothermal systems: in situ microanalysis, fractionation factor, and applications. *Mineralium Deposita* **57**, 643–661.

Li Y., Selby D., Condon D. and Tapster S. (2017) Cyclic magmatic-hydrothermal evolution in porphyry systems: High-precision U-Pb and Re-Os geochronology constraints on the Tibetan Qulong porphyry Cu-Mo deposit. *Economic Geology* **112**, 1419–1440.

Liebscher A. (2007) Experimental Studies in Model Fluid Systems. *Reviews in Mineralogy and Geochemistry* **65**, 15–47.

Linnen R. L. (1998) Depth of emplacement, fluid provenance and metallogeny in granitic terranes: a comparison of western Thailand with other tin belts. *Mineralium Deposita* **33**, 461–476.

Linnen Robert L. (1998) The solubility of Nb-Ta-Zr-Hf-W in granitic melts with Li and $Li^+$ F; constraints for mineralization in rare metal granites and pegmatites. *Economic Geology* **93**, 1013–1025.

Linnen R. L. and Cuney M. (2005) Granite-related rare-element deposits and experimental constraints on Ta-Nb-W-Sn-Zr-Hf mineralization. In: Linnen, R. L., Samson, I. M. (Eds.), *Rare-Element Geochemistry and Mineral Deposits*. Geological Association of Canada, Short Course Notes **17**, pp. 45–68.

Linnen R. L., Pichavant M. and Holtz F. (1996) The combined effects of fO2 and melt composition on SnO2 solubility and tin diffusivity in haplogranitic melts. *Geochimica et Cosmochimica Acta* **60**, 4965–4976.

Linnen R., McNeil A. and Flemming R. (2019) Some thoughts on metasomatism in pegmatites. *The Canadian Mineralogist* **57**, 765–766.

Liu H., Ding X., Yan H., Liu K., Liu J. and Huang X. (2024) The solubility and complexation of Niobium in hydrothermal fluids. *Solid Earth Sciences* **9**, 100162.

Liu P., Mao J., Jian W. and Mathur R. (2020) Fluid mixing leads to main-stage cassiterite precipitation at the Xiling Sn polymetallic deposit, SE China: evidence from fluid inclusions and multiple stable isotopes (H–O–S). *Mineralium Deposita* **55**, 1233–1246.

Liu X., Yu P. and Xiao C. (2023) Tin transport and cassiterite precipitation from hydrothermal fluids. *Geoscience Frontiers* **14**, 101624.

London D. (2014) A petrologic assessment of internal zonation in granitic pegmatites. *Lithos* **184–187**, 74–104.

London D. (2005) Granitic pegmatites: an assessment of current concepts and directions for the future. *Lithos* **80**, 281–303.

London D. (2018) Ore-forming processes within granitic pegmatites. *Ore Geology Reviews* **101**, 349–383.

London D. (1992) Phosphorus in S-type magmas: the $P_2O_5$ content of feldspars from peraluminous granites, pegmatites, and rhyolites. *American Mineralogist* **77**, 126–145.

London D., Morgan G. B. and Wolf M. B. (1996) Boron in granitic rocks and their contact aureoles. *Reviews in Mineralogy and Geochemistry* **33**, 299–330.

Longerich H. P., Jackson S. E. and Gunther D. (1997) Laser ablation inductively coupled plasma mass spectrometric transient signal data acquisition and analyte concentration calculation. *Journal of Analytical Atomic Spectrometry* **12**, 391-391.

Lotout C., Pitra P., Poujol M. and Van Den Driessche J. (2017) Ordovician magmatism in the Lévézou massif (French Massif Central): tectonic and geodynamic implications. *International Journal of Earth Sciences (Geologische Rundschau)* **106**, 501–515.

Lotout C., Poujol M., Pitra P., Anczkiewicz R. and Van Den Driessche J. (2020) From Burial to Exhumation: Emplacement and Metamorphism of Mafic Eclogitic Terranes Constrained Through Multimethod Petrochronology, Case Study from the Lévézou Massif (French Massif Central, Variscan Belt). *Journal of Petrology* **61**, egaa046.

Madayipu N., Li H., Elatikpo S. M., Ghaderi M., Heritier R. N., Hu X.-J., Zheng H. and Wu Q.-H. (2024) Tracing fluid exsolution and hydrothermal alteration signature of the Mufushan Nb-Ta-(Li-Be-Cs) deposit, South China: An apatite perspective. *Journal of the Geological Society* **181**, jgs2023-087.

Malavieille J., Guihot P., Costa S., Lardeaux J. M. and Gardien V. (1990) Collapse of the thickened Variscan crust in the French Massif Central: Mont Pilat extensional shear zone and St. Etienne Late Carboniferous basin. *Tectonophysics* **177**, 139–149.

Maluski H. and Monié P. (1988) $^{40}$Ar-$^{39}$Ar laser probe multi-dating inside single biotites of a Variscan orthogeneiss (Pinet, Massif Central, France). *Chemical Geology: Isotope Geoscience section* **73**, 245–263.

Mao M., Rukhlov A. S., Rowins S. M., Spence J. and Coogan L. A. (2016) Apatite Trace Element Compositions: A Robust New Tool for Mineral Exploration. *Economic Geology* **111**, 1187–1222.

Mao W., Rusk B., Yang F. and Zhang M. (2017) Physical and Chemical Evolution of the Dabaoshan Porphyry Mo Deposit, South China: Insights from Fluid Inclusions, Cathodoluminescence, and Trace Elements in Quartz. *Economic Geology* **112**, 889–918.

Marchand L., Joseph D., Touray J. C. and Treuil M. (1976) Critères d'analyse géochimique des gisements de fluorine basés sur l'étude de la distribution des lanthanides – application au gite de Maine (71–Cordesse, France). *Mineralium Deposita* **11**, 357–379.

Marignac C. and Cathelineau M. (2009) The nature of ore-forming fluids in peri-batholitic Sn-W deposits and a classification. In *Proceedings of the Tenth Biennial SGA Meeting* pp. 245–247.

Marignac C., Cuney M., Cathelineau M., Lecomte A., Carocci E. and Pinto F. (2020) The Panasqueira Rare Metal Granite Suites and Their Involvement in the Genesis of the World-Class Panasqueira W–Sn–Cu Vein Deposit: A Petrographic, Mineralogical, and Geochemical Study. *Minerals* **10**, 562.

Marks M. A. W., Wenzel T., Whitehouse M. J., Loose M., Zack T., Barth M., Worgard L., Krasz V., Eby G. N., Stosnach H. and Markl G. (2012) The volatile inventory (F, Cl, Br, S, C) of magmatic apatite: An integrated analytical approach. *Chemical Geology* **291**, 241–255.

Martínez Catalán J. R., Arenas R., Abati J., Martínez S. S., García F. D., Suárez J. F., Cuadra P. G., Castiñeiras P., Barreiro J. G., Montes A. D., Clavijo E. G., Pascual F. J. R., Andonaegui P., Jeffries T. E., Alcock J. E., Fernández R. D. and Carmona A. L. (2009) A rootless suture and the loss of the roots of a mountain chain: The Variscan belt of NW Iberia. *Comptes Rendus. Géoscience, Mécanique de l'orogénie varisque : Une vision moderne de la recherche dans le domaine de l'orogénie* **341**, 114–126.

Masterton W. L., Slowinski E. J. and Stanitski C. L. (1981) *Chemical Principles*, 5th edition, Saunders College Publishing, Philadelphia, 641 pp.

Masuda A., Kawakami O., Dohmoto Y. and Takenaka T. (1987) Lanthanide tetrad effects in nature: two mutually opposite types, W and M. *Geochemical Journal* **21**, 119–124.

Matte P. (1991) Accretionary history and crustal evolution of the Variscan belt in Western Europe. *Tectonophysics* **196**, 309–337.

Matte P. (1986) Tectonics and plate tectonics model for the Variscan belt of Europe. *Tectonophysics* **126**, 329–374.

Matte P. (2001) The Variscan collage and orogeny (480–290 Ma) and the tectonic definition of the Armorica microplate: a review. *Terra Nova* **13**, 122–128.

Matte P. (2007) Variscan thrust nappes, detachments, and strike-slip faults in the French Massif Central: Interpretation of the lineations. In: Hatcher Jr. R. D., Carlson, M. P., McBride, J. H., Martínez Catalán, J. R. (Eds.), *4-D Framework of Continental Crust*. Geological Society of America Memoir **200**, pp. 391–402.

Matzel J. E., Bowring S. A. and Miller R. B. (2006) Time scales of pluton construction at differing crustal levels: Examples from the Mount Stuart and Tenpeak intrusions, North Cascades, Washington. *Geological Society of America Bulletin* **118**, 1412–1430.

McDowell F. W., McIntosh W. C. and Farley K. A. (2005) A precise $^{40}$Ar–$^{39}$Ar reference age for the Durango apatite (U–Th)/He and fission-track dating standard. *Chemical Geology* **214**, 249–263.

McNeil A. G., Linnen R. L., Flemming R. L. and Fayek M. (2020) An experimental approach to examine fluid-melt interaction and mineralization in rare-metal pegmatites. *American Mineralogist* **105**, 1078–1087.

Melfou M., Richard A., Tarantola A., Villeneuve J., Carr P., Peiffert C., Mercadier J., Dean B. and Drejing-Carroll D. (2023) Tracking the origin of metasomatic and ore-forming fluids in IOCG deposits through apatite geochemistry (Nautanen North deposit, Norrbotten, Sweden). *Lithos* **438–439**, 106995.

Melleton J., Cocherie A., Faure M. and Rossi P. (2010) Precambrian protoliths and Early Paleozoic magmatism in the French Massif Central: U–Pb data and the North Gondwana connection in the west European Variscan belt. *Gondwana Research* **17**, 13–25.

Melleton J., Gloaguen E. and Frei D. (2015) Rare-elements (Li–Be–Ta–Sn–Nb) magmatism in the European Variscan belt, a review. In: André-Mayer, A. S., Cathelineau, M., Muchez, P., Pirard, E., Sindern, S. (Eds.), *Proceedings of the 13th Biennial SGA Meeting*, 24–27 August 2015, Nancy, France, Volume 2, pp. 807–810.

Mercer C. N., Reed M. H. and Mercer C. M. (2015) Time scales of porphyry Cu deposit formation: Insights from titanium diffusion in quartz. *Economic Geology* **110**, 587–602.

Merceron T., Bonhomme M. G., Fouillac A. M., Vivier G. and Meunier A. (1987) Pétrologie des altérations hydrothermales du sondage GPF Echassières N. 1. *Géologie de la France* **2–3**, 259–269.

Merceron T., Inoue A., Bouchet A. and Meunier A. (1988) Lithium-Bearing Donbassite and Tosudite from Echassières, Massif Central, France. *Clays and Clay Minerals* **36**, 39–46.

Merceron T., Vieillard P., Fouillac A.-M. and Meunier A. (1992) Hydrothermal alterations in the Echassières granitic cupola (Massif central, france). *Contributions to Mineralogy and Petrology* **112**, 279–292.

Merino Martínez E. (2014) Geochemistry, U–Pb Geochronology and Hf-Isotope Zircon Composition of Variscan Granitoids from the Montes de Toledo Batholith. PhD dissertation, Universidad Complutense Madrid, Spain.

Michaud J. A.-S., Gumiaux C., Pichavant M., Gloaguen E. and Marcoux E. (2020) From magmatic to hydrothermal Sn-Li-(Nb-Ta-W) mineralization: The Argemela area (central Portugal). *Ore Geology Reviews* **116**, 103215.

Michaud J. A.-S. and Pichavant M. (2020) Magmatic fractionation and the magmatic-hydrothermal transition in rare metal granites: Evidence from Argemela (Central Portugal). *Geochimica et Cosmochimica Acta* **289**, 130–157.

Michaud J. A.-S., Pichavant M. and Villaros A. (2021) Rare elements enrichment in crustal peraluminous magmas: insights from partial melting experiments. *Contributions to Mineralogy and Petrology* **176**, 96.

Michon G. (1987) Les vaugnerites de l'Est du Massif central francais; apport de l'analyse statistique multivariee a l'etude geochimique des elements majeurs. *Bulletin de la Société Géologique de France* **III**, 591–600.

Miller J. S., Matzel J. E., Miller C. F., Burgess S. D. and Miller R. B. (2007) Zircon growth and recycling during the assembly of large, composite arc plutons. *Journal of Volcanology and Geothermal Research* **167**, 282–299.

Minghai C., Jingwen M., Ting L., Pirajno F. and Huilan H. (2007) The origin of the Tongkeng-Changpo tin deposit, Dachang metal district, Guangxi, China: clues from fluid inclusions and He isotope systematics. *Mineralium Deposita* **42**, 613–626.

Mlynarczyk M. S., Sherlock R. L. and Williams-Jones A. E. (2003) San Rafael, Peru: geology and structure of the worlds richest tin lode. *Mineralium Deposita* **38**, 555–567.

Monecke T., Dulski P. and Kempe U. (2007) Origin of convex tetrads in rare earth element patterns of hydrothermally altered siliceous igneous rocks from the Zinnwald Sn–W deposit, Germany. *Geochimica et Cosmochimica Acta* **71**, 335–353.

Monier G., Charoy B., Cuney M., Ohnensteter D. and Robert J. L. (1987) Evolution spatiale et temporelle de la composition des micas du granite albitique à topaze-lepidolite de Beauvoir (Massif Central, France). *Géologie de la France* **2–3**, 179–188.

Monnier L., Lach P., Salvi S., Melleton J., Bailly L., Béziat D., Monnier Y. and Gouy S. (2018) Quartz trace-element composition by LA-ICP-MS as proxy for granite differentiation, hydrothermal episodes, and related mineralization: The Beauvoir Granite (Echassières district), France. *Lithos* **320–321**, 355–377.

Monnier L., Melleton J., Vanderhaeghe O., Salvi S., Lach P., Bruguier O., Benmammar A., Bailly L., Béziat D. and Gloaguen E. (2021) Episodic precipitation of Wolframite during an orogen: the Échassières district, Variscan belt of France. *Minerals* **11**, 923.

Monnier L., Salvi S., Jourdan V., Sall S., Bailly L., Melleton J. and Béziat D. (2020) Contrasting fluid behavior during two styles of greisen alteration leading to distinct wolframite mineralizations: The Echassières district (Massif Central, France). *Ore Geology Reviews* **124**, 103648.

Monnier L., Salvi S., Melleton J., Bailly L., Béziat D., De Parseval P., Gouy S. and Lach P. (2019) Multiple Generations of Wolframite Mineralization in the Echassieres District (Massif Central, France). *Minerals* **9**, 637.

Monnier L., Salvi S., Melleton J., Lach P., Pochon A., Bailly L., Béziat D. and De Parseval P. (2022) Mica trace-element signatures: Highlighting superimposed W-Sn mineralizations and fluid sources. *Chemical Geology* **600**, 120866.

Montel J.-M. (1993) A model for monazite/melt equilibrium and application to the generation of granitic magmas. *Chemical geology* **110**, 127–146.

Moyen J.-F., Laurent O., Chelle-Michou C., Couzinié S., Vanderhaeghe O., Zeh A., Villaros A. and Gardien V. (2017) Collision vs. subduction-related magmatism: Two contrasting ways of granite formation and implications for crustal growth. *Lithos* **277**, 154–177.

Müller A., Herklotz G. and Giegling H. (2018a) Chemistry of quartz related to the Zinnwald/Cínovec Sn-W-Li greisen-type deposit, Eastern Erzgebirge, Germany. *Journal of Geochemical Exploration* **190**, 357–373.

Müller A., Kerkhof A. M. van den, Behr H.-J., Kronz A. and Koch-Müller M. (2009) The evolution of late-Hercynian granites and rhyolites documented by quartz – a review. *Earth and Environmental Science Transactions of The Royal Society of Edinburgh* **100**, 185–204.

Müller A., Kronz A. and Breiter K. (2002a) Trace elements and growth patterns in quartz: a fingerprint of the evolution of the subvolcanic Podlesí Granite System (Krušné hory Mts., Czech Republic). *Bulletin of the Czech Geological Survey* **77**, 135–145.

Müller A., Lennox P. and Trzebski R. (2002b) Cathodoluminescence and micro-structural evidence for crystallisation and deformation processes of granites in the Eastern Lachlan Fold Belt (SE Australia). *Contributions to Mineralogy and Petrology* **143**, 510–524.

Müller A., Romer R. L. and Pedersen R.-B. (2017) The Sveconorwegian Pegmatite Province – Thousands of Pegmatites Without Parental Granites. *The Canadian Mineralogist* **55**, 283–315.

Müller A. and Seltmann R. (1999) The genetic significance of snowball quartz in high fractionated tin granites of the Krušne Hory/Erzgebirge. *Mineral deposits: processes to processing* **1**, 409–412.

Müller A., Seltmann R. and Behr H.-J. (2000) Application of cathodoluminescence to magmatic quartz in a tin granite – case study from the Schellerhau Granite Complex, Eastern Erzgebirge, Germany. *Mineralium Deposita* **35**, 169–189.

Müller A., Spratt J., Thomas R., Williamson B. J. and Seltmann R. (2018b) Alkali-F-rich albite zones in evolved NYF pegmatites: the product of melt–melt immiscibility. *The Canadian Mineralogist* **56**, 657–687.

Müller A., Wiedenbeck M., Kerkhof A. M. V. D., Kronz A. and Simon K. (2003) Trace elements in quartz - a combined electron microprobe, secondary ion mass spectrometry, laser-ablation ICP-MS, and cathodoluminescence study. *European Journal of Mineralogy* **15**, 747–763.

Murphy J. B., Gutierrez-Alonso G., Nance R. D., Fernandez-Suarez J., Keppie J. D., Quesada C., Strachan R. A. and Dostal J. (2006) Origin of the Rheic Ocean: Rifting along a Neoproterozoic suture? *Geology* **34**, 325–328.

Nabelek P. I., O'Neil J. R. and Papike J. J. (1983) Vapor phase exsolution as a controlling factor in hydrogen isotope variation in granitic rocks: the Notch Peak granitic stock, Utah. *Earth and Planetary Science Letters* **66**, 137–150.

Nance R. D., Gutiérrez-Alonso G., Keppie J. D., Linnemann U., Murphy J. B., Quesada C., Strachan R. A. and Woodcock N. H. (2009) Evolution of the Rheic Ocean. *Gondwana Research* **17**, 194–222.

Nance R. D. and Linnemann U. (2008) The Rheic Ocean: origin, evolution, and significance. *Geological Society of America Today* **18**, 4.

Naumov V. B. and Kamenetsky V. S. (2006) Silicate and salt melts in the genesis of the industrial'noe tin deposit: Evidence from inclusions in minerals. *Geochemistry International* **44**, 1181–1190.

Ni P., Li W.-S., Pan J.-Y., Cui J.-M., Zhang K.-H. and Gao Y. (2022) Fluid processes of wolframite-quartz vein systems: progresses and challenges. *Minerals* **12**, 237.

Nigon P. (1988) La fluorine stratiforme de la bordure Ouest du Morvan: Géologie, Géochimie et modélisation. Unpublished PhD dissertation, Université d'Orléans.

Ohnenstetter D. and Piantone P. (1987) Caractérisation et étude des substitutions dans les minéraux du groupe des columbo-tantalites et des pyrochlores du granite de Beauvoir. *Géologie de la France* **2–3**, 233–235.

Ohnenstetter D. and Piantone P. (1988) Géochimie et évolution des minéraux du groupe des columbotantalites et des minéraux du groupe du pyrochlore du sondage GPF 1 Echassieres (Allier). *Documents BRGM* **124**, 113.

O'Neil J. R. and Chappell B. W. (1977) Oxygen and hydrogen isotope relations in the Berridale batholith. *Journal of the Geological Society* **133**, 559–571.

O'Neil J. R., Shaw S. E. and Flood R. H. (1977) Oxygen and hydrogen isotope compositions as indicators of granite genesis in the New England Batholith, Australia. *Contributions to Mineralogy and Petrology* **62**, 313–328.

O'Reilly C., Jenkin G. R. T., Feely M., Alderton D. H. M. and Fallick A. E. (1997) A fluid inclusion and stable isotope study of 200 Ma of fluid evolution in the Galway Granite, Connemara, Ireland. *Contributions to Mineralogy and Petrology* **129**, 120–142.

O'Sullivan G., Chew D., Kenny G., Henrichs I. and Mulligan D. (2020) The trace element composition of apatite and its application to detrital provenance studies. *Earth-Science Reviews* **201**, 103044.

Pan Y. and Fleet M. E. (2002) Compositions of the Apatite-Group Minerals: Substitution Mechanisms and Controlling Factors. *Reviews in Mineralogy and Geochemistry* **48**, 13–49.

Paterson S. R., Okaya D., Memeti V., Economos R. and Miller R. B. (2011) Magma addition and flux calculations of incrementally constructed magma chambers in continental margin arcs: Combined field, geochronologic, and thermal modeling studies. *Geosphere* **7**, 1439–1468.

Paton C., Hellstrom J., Paul B., Woodhead J. and Hergt J. (2011) Iolite: Freeware for the visualisation and processing of mass spectrometric data. *Journal of Analytical Atomic Spectrometry* **26**, 2508–2518.

Peng H.-W., Fan H.-R., Lecumberri-Sanchez P., Lai J.-Q., Hu H.-L., Lan T.-G. and Li X.-H. (2023a) Fluid evolution and ore genesis of the Tiantangshan granite-related vein-type Rb-Sn-W deposit, south China: constraints from LA-ICP-MS analyses of fluid inclusions. *Mineralium Deposita* **58**, 751–769.

Peng H.-W., Yang L.-L., Lai J.-Q., Li B., Liu X.-H. and Dai Z.-H. (2023b) Mica geochemistry as an indicator of magmatic-hydrothermal processes in the Ta-Nb-Sn-W mineralization of the Limu deposit, South China. *Ore Geology Reviews* **160**, 105584.

Penniston-Dorland S. C. (2001) Illumination of vein quartz textures in a porphyry copper ore deposit using scanned cathodoluminescence: Grasberg Igneous Complex, Irian Jaya, Indonesia. *American Mineralogist* **86**, 652–666.

Peretyazhko I. S. and Savina E. A. (2010) Tetrad effects in the rare earth element patterns of granitoid rocks as an indicator of fluoride-silicate liquid immiscibility in magmatic systems. *Petrology* **18**, 514–543.

Petrus J. A. and Kamber B. S. (2012) VizualAge: A novel approach to laser ablation ICP-MS U-Pb geochronology data reduction. *Geostandards and Geoanalytical Research* **36**, 247–270.

Pettke T., Oberli F., Audétat A., Guillong M., Simon A. C., Hanley J. J. and Klemm L. M. (2012) Recent developments in element concentration and isotope ratio analysis of individual fluid inclusions by laser ablation single and multiple collector ICP-MS. *Ore Geology Reviews* **44**, 10–38.

Pfister J. D., Kontak D. J. and Groat L. A. (2023) Textural and mineralogical evolution of the Little Nahanni pegmatite group (NWT, Canada) with implications for metasomatism, rare-metal mineralization, and pegmatite-wall rock interaction. *The Canadian Journal of Mineralogy and Petrology* **61**, 467–505.

Pfister J. D., Kontak D. J., Groat L. A. and Fayek M. (2024) Stable isotopes (O, H) and quartz geochemistry provide insight to melt source and subsolidus fluid:rock interaction in the Cretaceous Little Nahanni LCT Pegmatites (NWT, Canada). *Chemical Geology* **664**, 122292.

Piccoli P. M. and Candela P. A. (2002) Apatite in Igneous Systems. *Reviews in Mineralogy and Geochemistry* **48**, 255–292.

Pichavant M. (2022) Experimental Crystallization of the Beauvoir Granite as a Model for the Evolution of Variscan Rare Metal Magmas. *Journal of Petrology* **63**, egac120.

Pichavant M., Valencia Herrera J., Boulmier S., Briqueu L., Joron J.-L., Juteau M., Michard A., Sheppard S. M. F., Treuil M. and Vernet M. (1987b) The Macusani glasses, SE Peru: evidence of chemical fractionation in peraluminous magmas. *Magmatic Process: Physicochemical Principles. Geochemical Society, Special Pulications* **1**, 359–373.

Pichavant M., Boher M., Stenger J.-F., Aïssa M. and Charoy B. (1987a) Relations de phase des granites de Beauvoir à 1 et 3 kbar en conditions de saturation en H2O. *Géologie de la France* **2–3**, 77–86.

Pichavant M., Erdmann S., Kontak D. J., Michaud J. A.-S. and Villaros A. (2024) Trace element partitioning in strongly peraluminous rare-metal silicic magmas – Implications for fractionation processes and for the origin of the Macusani Volcanics (SE Peru). *Geochimica et Cosmochimica Acta* **365**, 229–252.

Pichavant M., Kontak D. J., Briqueu L., Herrera J. V. and Clark A. H. (1988) The Miocene-Pliocene Macusani Volcanics, SE Peru: II. Geochemistry and origin of a felsic peraluminous magma. *Contributions to Mineralogy and Petrology* **100**, 325–338.

Pichavant M., Villaros A., Deveaud S., Scaillet B. and Lahlafi M. (2016) The influence of redox state on mica crystallization in leucogranitic and pegmatitic liquids. *The Canadian Mineralogist* **54**, 559–581.

Pin C. (1991) Sr-Nd isotopic study of igneous and metasedimentary enclaves in some Hercynian granitoids from the Massif Central, France. In: Didier, J., Barbarin, B. (Eds.), *Enclaves and Granite Petrology*. Developments in Petrology, Volume 13. Elsevier, Amsterdam, pp. 333–343.

Pin C., Dupuy C. and Peterlongo J.-M. (1982) Répartition des terres rares dans les roches volcaniques basiques dévono-dinantiennes du Nord-Est du Massif Central. *Bulletin de la Société Géologique de France* **7**, 669–676.

Pin C. and Lancelot J. (1982) U-Pb dating of an early paleozoic bimodal magmatism in the french Massif Central and of its further metamorphic evolution. *Contributions to Mineralogy and Petrology* **79**, 1–12.

Pirajno F. (1992) Greisen systems. In: *Hydrothermal Mineral Deposits: Principles and Fundamental Concepts for the Exploration Geologist*. Springer-Verlag, Berlin, pp. 280–324.

Pirajno F. (2009) Hydrothermal processes and mineral systems, first ed. Springer Science & Business Media.

Pochon A., Gloaguen E., Branquet Y., Poujol M., Ruffet G., Boiron M.-C., Boulvais P., Gumiaux C., Cagnard F., Gouazou F. and Gapais D. (2018) Variscan Sb-Au mineralization in Central Brittany (France): A new metallogenic model derived from the Le Semnon district. *Ore Geology Reviews* **97**, 109–142.

Pokrovski G. S., Borisova A. Y. and Harrichoury J.-C. (2006a) The effect of sulfur on vapor-liquid partitioning of metals in hydrothermal systems: an experimental batch-reactor study. *Geochimica et Cosmochimica Acta* **70**, 498.

Pokrovski G. S., Roux J. and Harrichoury J.-C. (2005) Fluid density control on vapor-liquid partitioning of metals in hydrothermal systems. *Geology* **33**, 657–660.

Pokrovski G. S., Tagirov B. R., Schott J., Hazemann J. L., Harrichoury J. C. and Roux J. (2006b) Speciation of gold and associated metals at hydrothermal conditions: in situ experimental approaches and physical–chemical modeling. In: *Colloquium GDR Transmet – Bilan & Perspectives*. University Henri Poincaré, Nancy, pp. 91–94.

Pollard P. J. (1995) A special issue devoted to the geology of rare metal deposits; geology of rare metal deposits; an introduction and overview. *Economic Geology* **90**, 489–494.

Pollard P. J. (1983) Magmatic and postmagmatic processes in the formation of rocks associated with rare-element deposits. *Transactions of the Institutions of Mining and Metallurgy, Section B: Applied Earth Science* **92**, 1–9.

Pollard P. J., Pichavant M. and Charoy B. (1987) Contrasting evolution of fluorine- and boron-rich tin systems. *Mineralium Deposita* **22**, 315–321.

Pollard P. J., Taylor R. G. and Cuff C. (1988) Genetic modelling of greisen-style tin systems. In: *Geology of Tin Deposits in Asia and the Pacific: Selected Papers from the International Symposium on the Geology of Tin Deposits held in Nanning,* China, October 26–30, 1984*,* Springer, pp. 59–72.

Polya D. A., Foxford K. A., Stuart F., Boyce A. and Fallick A. E. (2000) Evolution and paragenetic context of low δD hydrothermal fluids from the Panasqueira W-Sn deposit, Portugal: new evidence from microthermometric, stable isotope, noble gas and halogen analyses of primary fluid inclusions. *Geochimica et Cosmochimica Acta* **64**, 3357–3371.

Polyakov V. B., Mineev S. D., Clayton R. N., Hu G., Gurevich V. M., Khramov D. A., Gavrichev K. S., Gorbunov V. E. and Golushina L. N. (2005) Oxygen isotope fractionation factors involving cassiterite ($SnO_2$): I. calculation of reduced partition function ratios from heat capacity and X-ray resonant studies. *Geochimica et Cosmochimica Acta* **69**, 1287–1300.

Poutiainen M. and Scherbakova T. F. (1998) Fluid and melt inclusion evidence for the origin of idiomorphic quartz crystals in topaz-bearing granite from the Salmi batholith, Karelia, Russia. *Lithos* **44**, 141–151.

Putzolu F., Seltmann R., Dolgopolova A., Armstrong R. N., Shail R. K., Spratt J., Buret Y., Broderick C. and Brownscombe W. (2024) Influence of magmatic and magmatic-hydrothermal processes on the lithium endowment of micas in the Cornubian Batholith (SW England). *Mineralium Deposita* **59**, 1–22.

Raimbault L. (1998) Composition of complex lepidolite-type granitic pegmatites and of constituent columbite-tantalite, Chedeville, Massif Central, France. *The Canadian Mineralogist* **36**, 563–583.

Raimbault L. (1988) Géochimie des terres rares dans les fluorines fissurales du granite de Beauvoir entre 420 et 625 m (sondage GPF, Echassières, Massif central français). *Géologie Profonde de la France* **8**, 419–426.

Raimbault L. and Azencott C. (1987) Géochimie des éléments majeurs et traces du granite à métaux rares de Beauvoir. *Géologie de la France* **2-3**, *1*89–198.

Raimbault L. and Burnol L. (1998) The Richemont rhyolite dyke, Massif Central, France; a subvolcanic equivalent of rare-metal granites. *The Canadian Mineralogist* **36**, 265–282.

Raimbault L., Cuney M., Azencott C., Duthou J.-L. and Joron J. L. (1995) Geochemical evidence for a multistage magmatic genesis of Ta-Sn-Li mineralization in the granite at Beauvoir, French Massif Central. *Economic Geology* **90**, 548–576.

Rankin A. H., Ramsey M. H., Coles B., Van Langevelde F. and Thomas C. R. (1992) The composition of hypersaline, iron-rich granitic fluids based on laser-ICP and Synchrotron-XRF microprobe analysis of individual fluid inclusions in topaz, Mole granite, eastern Australia. *Geochimica et Cosmochimica Acta* **56**, 67–79.

Rapp R. P., Norman M. D., Laporte D., Yaxley G. M., Martin H. and Foley S. F. (2010) Continent Formation in the Archean and Chemical Evolution of the Cratonic Lithosphere: Melt–Rock Reaction Experiments at 3–4 GPa and Petrogenesis of Archean Mg-Diorites (Sanukitoids). *Journal of Petrology* **51**, 1237–1266.

Reed M., Rusk B. and Palandri J. (2013) The Butte magmatic-hydrothermal system: One fluid yields all alteration and veins. *Economic Geology* **108**, 1379–1396.

Reyf F. G. (1997) Direct evolution of W-rich brines from crystallizing melt within the Mariktikan granite pluton, west Transbaikalia. *Mineralium Deposita* **32**, 475–490.

Ribeiro H. B., Guedes K. J., Pinheiro M. V. B., Greulich-Weber S. and Krambrock K. (2005) About the blue and green colours in natural fluorapatite. *Physica Status Solidi (c)* **2**, 720–723.

Richards J. P. (2018) A shake-up in the porphyry world? *Economic Geology* **113**, 1225–1233.

Richards J. P. (2014) Porphyry and Related Deposits in Subduction and Post-Subduction Settings. *Acta Geologica Sinica (English Edition)* **88**, 1–20.

Richards J. P. (2022) Porphyry copper deposit formation in arcs: What are the odds? *Geosphere* **18**, 130–155.

Richards J. P. (2009) Postsubduction porphyry Cu-Au and epithermal Au deposits: Products of remelting of subduction-modified lithosphere. *Geology* **37**, 247–250.

Richards J. P. (2003) Tectono-magmatic precursors for porphyry Cu-(Mo-Au) deposit formation. *Economic geology* **98**, 1515–1533.

Richards J. P. and Porter T. M. (2005) Cumulative factors in the generation of giant calc-alkaline porphyry Cu deposits. *Super porphyry copper and gold deposits: A global perspective* **1**, 7–25.

Robardet M. (2002) Alternative approach to the Variscan Belt in southwestern Europe: Preorogenic paleobiogeographical constraints. In Martínez Catalán, J. R., Hatcher, R. D., Arenas, R., Díaz García, F. (Eds.), *Variscan-Appalachian Dynamics: The Building of the Late Paleozoic Basement*. Geological Society of America Special Paper **364**, pp. 1–17.

Robb L. (2020) *Introduction to Ore-Forming Processes*. 2nd edition, John Wiley & Sons, Ltd., Chichester, UK.

Rocher O., Ballouard C., Richard A., Monnier L., Carr P., Laurent O., Khebabza Y., Lecomte A., Bouden N., Villeneuve J., Barré B., Fullenwarth P., Leisen M. and Mercadier J. (2024) Unravelling the magmatic and hydrothermal evolution of rare-metal granites through apatite geochemistry and geochronology: The Variscan Beauvoir granite (French Massif Central). *Chemical Geology* **670**, 122400.

Roda-Robles E., Gil-Crespo P. P., Pesquera A., Lima A., Garate-Olave I., Merino-Martínez E., Cardoso-Fernandes J. and Errandonea-Martin J. (2022) Compositional Variations in Apatite and Petrogenetic Significance: Examples from Peraluminous Granites and Related Pegmatites and Hydrothermal Veins from the Central Iberian Zone (Spain and Portugal). *Minerals* **12**, 1401.

Roda-Robles E., Villaseca C., Pesquera A., Gil-Crespo P. P., Vieira R., Lima A. and Garate-Olave I. (2018) Petrogenetic relationships between Variscan granitoids and Li-(F-P)-rich aplite-pegmatites in the Central Iberian Zone: Geological and geochemical constraints and implications for other regions from the European Variscides. *Ore Geology Reviews* **95**, 408–430.

Roedder E. (1984) Volume 12: fluid inclusions. *Reviews in mineralogy* **12**, 644.

Romer R. L. and Kroner U. (2016) Phanerozoic tin and tungsten mineralization – Tectonic controls on the distribution of enriched protoliths and heat sources for crustal melting. *Gondwana Research* **31**, 60–95.

Romer R. L. and Kroner U. (2015) Sediment and weathering control on the distribution of Paleozoic magmatic tin–tungsten mineralization. *Mineralium Deposita* **50**, 327–338.

Romer R. L. and Pichavant M. (2020) Rare metal granites and pegmatites. In: *Encyclopedia of Geology* (Second Edition), Elsevier, Amsterdam, pp. 840–846.

Romer R. L., Thomas R., Stein H. J. and Rhede D. (2007) Dating multiply overprinted Sn-mineralized granites—examples from the Erzgebirge, Germany. *Mineralium Deposita* **42**, 337–359.

Rosenbaum G., Lister G. S. and Duboz C. (2002) Relative motions of Africa, Iberia and Europe during Alpine orogeny. *Tectonophysics* **359**, 117–129.

Rossi P., Autran A., Burnol L., Cuney M., Ohnensteter D. and Monier C. (1987) Logs pétrographiques et géochimiques du granite de Beauvoir dans le sondage Echassières I. Minéralogie et géochimie comparées. *Géologie de la France* **2–3**, 111–135.

Rudnick R. L. and Gao S. (2003) The composition of the continental crust. In: Holland, H. D., Turekian, K. K. (Eds.), *Treatise on Geochemistry*, Volume 3, The Crust. Elsevier-Pergamon, Oxford, pp. 1–64.

Ruhlmann F., Gillet Y. and Lissillour J. (1980) Une occurrence uranifère à sélénium et bismuth dans la ceinture métamorphique du leucogranite de Mortagne-sur-Sèvre (Vendée). *Bulletin de Minéralogie* **103**, 245–249.

Russell J. K., Edwards B. R. and Shyder L. D. (1995) Volatile production possibilities during magmatic assimilation: heat and mass-balance constraints. In: Thompson, J. F. (Ed.), *Magmas, Fluids and Ore Deposits*. Mineralogical Association of Canada Short Course Series **23**, pp. 1–24.

Sabatier H. (1991) Vaugnerites: Special lamprophyre-derived mafic enclaves in some Hercynian granites from Western and Central Europe. In: *Short Course Series* **23**, pp. 63–81.

Sánchez V., Cardellach E., Corbella M., Vindel E., Martín-Crespo T. and Boyce A. J. (2010) Variability in fluid sources in the fluorite deposits from Asturias (N Spain): Further evidences from REE, radiogenic (Sr, Sm, Nd) and stable (S, C, O) isotope data. *Ore Geology Reviews* **37**, 87–100.

Sarcia J. A., Carrat J., Poughon A. and Sanselme H. (1958) Geology of uranium vein-deposits in France; Géologie des gites uranifères et filoniens en France. Rapport CEA 1032, France.

Schaltegger U., Brack P., Ovtcharova M., Peytcheva I., Schoene B., Stracke A., Marocchi M. and Bargossi G. M. (2009) Zircon and titanite recording 1.5 million years of magma accretion, crystallization and initial cooling in a composite pluton (southern Adamello batholith, northern Italy). *Earth and Planetary Science Letters* **286**, 208–218.

Schmitz M. D., Bowring S. A. and Ireland T. R. (2003) Evaluation of Duluth Complex anorthositic series (AS3) zircon as a U-Pb geochronological standard: New high-precision isotope dilution thermal ionization mass spectrometry results. *Geochimica et Cosmochimica Acta* **67**, 3665–3672.

Schoene B. and Bowring S. A. (2006) U–Pb systematics of the McClure Mountain syenite: thermochronological constraints on the age of the $^{40}Ar/^{39}Ar$ standard MMhb. *Contributions to Mineralogy and Petrology* **151**, 615–630.

Schulmann K., Edel J.-B., Catalán J. R. M., Mazur S., Guy A., Lardeaux J.-M., Ayarza P. and Palomeras I. (2022) Tectonic evolution and global crustal architecture of the European Variscan belt constrained by geophysical data. *Earth-Science Reviews* **234**, 104195.

Schulz B. (2009) EMP-monazite age controls on P-T paths of garnet metapelites in the Variscan inverted metamorphic sequence of La Sioule, French Massif Central. *Bulletin de la Société Géologique de France* **180**, 271–282.

Schwartz M. O. (1992) Geochemical criteria for distinguishing magmatic and metasomatic albite-enrichment in granitoids—examples from the Ta-Li granite Yichun (China) and the Sn-W deposit Tikus (Indonesia). *Mineralium deposita* **27**, 101–108.

Schwartz M. O. and Surjono (1990) Greisenization and albitization at the Tikus tin-tungsten deposit, Belitung, Indonesia. *Economic Geology* **85**, 691–713.

Scott S., Driesner T. and Weis P. (2017) Boiling and condensation of saline geothermal fluids above magmatic intrusions. *Geophysical Research Letters* **44**, 1696–1705.

Seo J., Choi S.-G., Kim D. W., Park J. W. and Oh C. W. (2015) A new genetic model for the Triassic Yangyang iron-oxide–apatite deposit, South Korea: Constraints from in situ U–Pb and trace element analyses of accessory minerals. *Ore Geology Reviews* **70**, 110–135.

Seo J. H., Guillong M., Aerts M., Zajacz Z. and Heinrich C. A. (2011) Microanalysis of S, Cl, and Br in fluid inclusions by LA–ICP-MS. *Chemical Geology* **284**, 35–44.

Seo J. H. and Heinrich C. A. (2013) Selective copper diffusion into quartz-hosted vapor inclusions: Evidence from other host minerals, driving forces, and consequences for Cu–Au ore formation. *Geochimica et Cosmochimica Acta* **113**, 60–69.

Sha L.-K. and Chappell B. W. (1999) Apatite chemical composition, determined by electron microprobe and laser-ablation inductively coupled plasma mass spectrometry, as a probe into granite petrogenesis. *Geochimica et Cosmochimica Acta* **63**, 3861–3881.

Sharp Z. D., Gibbons J. A., Maltsev O., Atudorei V., Pack A., Sengupta S., Shock E. L. and Knauth L. P. (2016) A calibration of the triple oxygen isotope fractionation in the SiO2–H2O system and applications to natural samples. *Geochimica et Cosmochimica Acta* **186**, 105–119.

Shaw A., Downes H. and Thirlwall M. F. (1993) The quartz-diorites of Limousin: Elemental and isotopic evidence for Devono-Carboniferous subduction in the Hercynian belt of the French Massif Central. *Chemical Geology* **107**, 1–18.

Shcherba G. N. (1970) Greisens. *International Geology Review* **12**, 114–150.

Shepherd T. J., Miller M. F., Scrivener R. C. and Darbyshire D. F. (1985) Hydrothermal fluid evolution in relation to mineralization in southwest England with special reference to the Dartmoor-Bodmin area. In: *High Heat Production (HHP) Granites, Hydrothermal Circulation and Ore Genesis*. Conference Proceedings, pp. 345–364.

Sheppard S. M. (1986) Characterization and isotopic variations in natural waters. *Reviews in Mineralogy and Geochemistry* **16**, 165–183.

Shinohara H. (1994) Exsolution of immiscible vapor and liquid phases from a crystallizing silicate melt: Implications for chlorine and metal transport. *Geochimica et Cosmochimica Acta* **58**, 5215–5221.

Shinohara H. and Hedenquist J. W. (1997) Constraints on magma degassing beneath the Far Southeast porphyry Cu–Au deposit, Philippines. *Journal of Petrology* **38**, 1741–1752.

Shmulovich K. I., Landwehr D., Simon K. and Heinrich W. (1999) Stable isotope fractionation between liquid and vapour in water–salt systems up to 600 °C. *Chemical Geology* **157**, 343–354.

Shuai X., Li S.-M., Zhu D.-C., Wang Q., Zhang L.-L. and Zhao Z. (2021) Tetrad effect of rare earth elements caused by fractional crystallization in high-silica granites: An example from central Tibet. *Lithos* **384**, 105968.

Sillitoe R. H. (1972) A plate tectonic model for the origin of porphyry copper deposits. *Economic geology* **67**, 184–197.

Sillitoe R. H. (2010) Porphyry copper systems. *Economic geology* **105**, 3–41.

Simon A. C., Frank M. R., Pettke T., Candela P. A., Piccoli P. M. and Heinrich C. A. (2005) Gold partitioning in melt-vapor-brine systems. *Geochimica et Cosmochimica Acta* **69**, 3321–3335.

Simon A. C., Pettke T., Candela P. A., Piccoli P. M. and Heinrich C. A. (2006) Copper partitioning in a melt–vapor–brine–magnetite–pyrrhotite assemblage. *Geochimica et Cosmochimica Acta* **70**, 5583–5600.

Singer D. A., Berger V. I. and Moring B. C. (2008) Porphyry copper deposits of the world: Database and grade and tonnage models. U.S. Geological Survey Open-File Report 2008-1155.

Sizaret S., Marcoux E., Boyce A., Jebrak M., Stevenson R. and Ellam R. (2009) Isotopic (S, Sr, Sm/Nd, D, Pb) evidences for multiple sources in the Early Jurassic Chaillac F-Ba ore deposit (Indre, France). *Bulletin de la Société Géologique de France* **180**, 83–94.

Sizaret S., Marcoux E., Jébrak M. and Touray J. C. (2004) The Rossignol fluorite vein, Chaillac, France: multiphase hydrothermal activity and intravein sedimentation. *Economic Geology* **99**, 1107–1122.

Smedley P. L. and Kinniburgh D. G. (2002) A review of the source, behaviour and distribution of arsenic in natural waters. *Applied geochemistry* **17**, 517–568.

Smith M., Banks D. A., Yardley B. W. D. and Boyce A. J. (1996) Fluid inclusion and stable isotope constraints on the genesis of the Cligga Head Sn-W deposit, SW England. *European Journal of Mineralogy* **8**, 961–974.

Sonyushkin, V. E., Sukhorukov, Y. T., Scherbakova, T. F. (1991) PT environment of crystallization of quartz in granites of the Salmi batholith, Russian Karelia. In: Symposium on Rapakivi Granites and Related Rocks. Abstracts, Geological Survey of Finland Guide, pp. 47.

Soulé de Lafont, D., Lhégu, J. (1980) Les gisements stratiformes de fluorine du Morvan (sud-est du bassin de Paris, France). In: 26$^{e}$ Congrès Géologique International, Paris, 7–17 juillet 1980, Mémoires du BRGM **112**, pp. 1–40.

Stacey J. T. and Kramers J. D. (1975) Approximation of terrestrial lead isotope evolution by a two-stage model. *Earth and planetary science letters* **26**, 207–221.

Stampfli G. M., Borel G. D., Marchant R. and Mosar J. (2002) Western Alps geological constraints on western Tethyan reconstructions. *Journal of the Virtual Explorer* **8**, 77–106.

Štemprok M. (1987) Greisenization (a review). *Geologische Rundschau* **76**, 169–175.

Sterner S. M., Chou I.-M., Downs R. T. and Pitzer K. S. (1992) Phase relations in the system NaCl-KCl-$H_2O$: V. Thermodynamic-*PTX* analysis of solid-liquid equilibria at high temperatures and pressures. *Geochimica et Cosmochimica Acta* **56**, 2295–2309.

Sterner S. M., Hall D. L. and Bodnar R. J. (1988) Synthetic fluid inclusions. V. Solubility relations in the system NaCl-KCl-$H_2O$ under vapor-saturated conditions. *Geochimica et Cosmochimica Acta* **52**, 989–1005.

Stewart D. B. (1978) Petrogenesis of lithium-rich pegmatites. *American Mineralogist* **63**, 970–980.

Stormer J. C., Pierson M. L. and Tacker R. C. (1993) Variation of F and Cl X-ray intensity due to anisotropic diffusion in apatite during electron microprobe analysis. *American Mineralogist* **78**, 641–648.

Stussi J.-M. (1989) Granitoid chemistry and associated mineralization in the French Variscan. *Economic Geology* **84**, 1363–1381.

Sun W., Huang R., Li H., Hu Y., Zhang C., Sun S., Zhang L., Ding X., Li C. and Zartman R. E. (2015) Porphyry deposits and oxidized magmas. *Ore Geology Reviews* **65**, 97–131.

Szuszkiewicz A., Pieczka A., Gołębiowska B., Dumańska-Słowik M., Marszałek M. and Szełęg E. (2018) Chemical composition of Mn-and Cl-rich apatites from the Szklary pegmatite, Central Sudetes, SW Poland: Taxonomic and genetic implications. *Minerals* **8**, 350.

Tait J., Schätz M., Bachtadse V. and Soffel H. (2000) Palaeomagnetism and Palaeozoic palaeogeography of Gondwana and European terranes. *Geological Society, London, Special Publications* **179**, 21–34.

Tartèse R. and Boulvais P. (2010) Differentiation of peraluminous leucogranites "en route" to the surface. *Lithos* **114**, 353–368.

Taylor B. E., Eichelberger J. C. and Westrich H. R. (1983) Hydrogen isotopic evidence of rhyolitic magma degassing during shallow intrusion and eruption. *Nature* **306**, 541–545.

Taylor B. E., Foord E. E. and Friedrichsen H. (1979) Stable isotope and fluid inclusion studies of gem-bearing granitic pegmatite-aplite dikes, San Diego Co., California. *Contributions to Mineralogy and Petrology* **68**, 187–205.

Taylor B. E. and Friedrichsen H. (1983) Light stable isotope systematics of granitic pegmatites from North America and Norway. *Chemical Geology* **41**, 127–167.

Taylor H. P. (1978) Oxygen and hydrogen isotope studies of plutonic granitic rocks. *Earth and Planetary Science Letters* **38**, 177–210.

Taylor H. P. (1968) The oxygen isotope geochemistry of igneous rocks. *Contributions to mineralogy and Petrology* **19**, 1–71.

Taylor H. P. and Epstein S. (1962) Relationship Between $O^{18}/O^{16}$ Ratios in Coexisting Minerals of Igneous and Metamorphic Rocks: Part 1: Principles and Experimental Results. *Geological Society of America Bulletin* **73**, 461–480.

Taylor, H. P., Sheppard, S. M. F. (1986) Chapter 8. Igneous rocks: I. Processes of isotopic fractionation and isotope systematics. In: Valley, J. W., Taylor, H. P., O'Neil, J. R. (Eds.), *Stable Isotopes in High Temperature Geological Processes*. De Gruyter, pp. 227–272.

Taylor J. R. and Wall V. J. (1993) Cassiterite solubility, tin speciation, and transport in a magmatic aqueous phase. *Economic Geology* **88**, 437–460.

Taylor, R. G. (1979) *Geology of Tin Deposits*. Developments in Economic Geology, Volume 11. Elsevier Scientific Publishing Company, Amsterdam, New York.

Taylor, R. G., Pollard, P. J. (1988) Pervasive hydrothermal alteration in tin-bearing granites and implications for the evolution of ore-bearing magmatic fluids. In: Taylor, R. P., Strong, D. F. (Eds.), *Recent Advances in the Geology of Granite-Related Mineral Deposits*, Special Volume 39. Canadian Institute of Mining and Metallurgy, Ottawa, pp. 86–95.

Teuscher E. O. (1936) Primäre Bildungen des granitischen Magmas und seiner Restlösungen im Massif von Eibenstock-Neudeck. *Mineralogische und Petrographische Mitteilungen* **47**, 211–262.

Thomas J. B., Bruce Watson E., Spear F. S., Shemella P. T., Nayak S. K. and Lanzirotti A. (2010) TitaniQ under pressure: the effect of pressure and temperature on the solubility of Ti in quartz. *Contributions to Mineralogy and Petrology* **160**, 743–759.

Thomas R. and Webster J. D. (2000) Strong tin enrichment in a pegmatite-forming melt. *Mineralium Deposita* **35**, 570–582.

Thomas R., Webster J. D. and Davidson P. (2011) Be-daughter minerals in fluid and melt inclusions: implications for the enrichment of Be in granite–pegmatite systems. *Contributions to Mineralogy and Petrology* **161**, 483–495.

Thomson S. N., Gehrels G. E., Ruiz J. and Buchwaldt R. (2012) Routine low-damage apatite U-Pb dating using laser ablation–multicollector–ICPMS. *Geochemistry, Geophysics, Geosystems* **13**.

Timofeev A., Migdisov Art. A. and Williams-Jones A. E. (2015) An experimental study of the solubility and speciation of niobium in fluoride-bearing aqueous solutions at elevated temperature. *Geochimica et Cosmochimica Acta* **158**, 103–111.

Tischendorf G. (1977) Geochemical and petrographic characteristics of silicic magmatic rocks associated with rare-metal mineralization. In: Štemprok, M., Burnol, L., Tischendorf. G. (Eds.), *Metallization Associated with Acid Magmatism*, Volume 2, Geological Survey, Prague, pp. 41–96.

Torsvik T. H. and Rehnström E. F. (2003) The Tornquist Sea and Baltica–Avalonia docking. *Tectonophysics* **362**, 67–82.

Touray J. C., Hubert P. and Bourrat X. (1981) *Etude géochimique du filon de fluorine de Burc (analyse des lanthanides en traces, étude d'inclusions fluides). Comparaison avec les autres filons du district du Tarn*. BRGM, Université d'Orléans.

Troch J., Ellis B. S., Harris C., Ulmer P. and Bachmann O. (2018) The effect of prior hydrothermal alteration on the melting behaviour during rhyolite formation in Yellowstone, and its importance in the generation of low-$\delta$18O magmas. *Earth and Planetary Science Letters* **481**, 338–349.

Trotter J. A., Williams I. S., Barnes C. R., Lécuyer C. and Nicoll R. S. (2008) Did cooling oceans trigger Ordovician biodiversification? Evidence from conodont thermometry. *Science* **321**, 550–554.

Turpin L., Cuney M., Friedrich M., Bouchez J.-L. and Aubertin M. (1990a) Meta-igneous origin of Hercynian peraluminous granites in NW French Massif Central: implications for crustal history reconstructions. *Contributions to Mineralogy and Petrology* **104**, 163–172.

Turpin L., Leroy J. L. and Sheppard S. M. (1990b) Isotopic systematics (O, H, C, Sr, Nd) of superimposed barren and U-bearing hydrothermal systems in a Hercynian granite, Massif Central, France. *Chemical geology* **88**, 85–98.

Ulrich T., Günther D. and Heinrich C. A. (1999) Gold concentrations of magmatic brines and the metal budget of porphyry copper deposits. *Nature* **399**, 676–679.

U.S. Geological Survey (2024) *Mineral Commodity Summaries 2024.*, U.S. Geological Survey.

Valley J. W. and Graham C. M. (1996) Ion microprobe analysis of oxygen isotope ratios in quartz from Skye granite: healed micro-cracks, fluid flow, and hydrothermal exchange. *Contributions to Mineralogy and Petrology* **124**, 225–234.

Van Daele J., Hulsbosch N., Dewaele S., Boiron M.-C., Piessens K., Boyce A. and Muchez P. (2018) Mixing of magmatic-hydrothermal and metamorphic fluids and the origin of peribatholitic Sn vein-type deposits in Rwanda. *Ore Geology Reviews* **101**, 481–501.

Van Hinsbergen D. J., Torsvik T. H., Schmid S. M., Maţenco L. C., Maffione M., Vissers R. L., Gürer D. and Spakman W. (2020) Orogenic architecture of the Mediterranean region and kinematic reconstruction of its tectonic evolution since the Triassic. *Gondwana Research* **81**, 79–229.

Van Staal C. R., Dewey J. F., Niocaill C. M. and McKerrow W. S. (1998) The Cambrian-Silurian tectonic evolution of the northern Appalachians and British Caledonides: history of a complex, west and southwest Pacific-type segment of Iapetus. *Geological Society, London, Special Publications* **143**, 197–242.

Vanderhaeghe O., Laurent O., Gardien V., Moyen J.-F., Gébelin A., Chelle-Michou C., Couzinié S., Villaros A. and Bellanger M. (2020) Flow of partially molten crust controlling construction, growth and collapse of the Variscan orogenic belt: the geologic record of the French Massif Central. *Bulletin de la Société Géologique de France* **191**, 25.

Veksler I. V., Dorfman A. M., Kamenetsky M., Dulski P. and Dingwell D. B. (2005) Partitioning of lanthanides and Y between immiscible silicate and fluoride melts, fluorite and cryolite and the origin of the lanthanide tetrad effect in igneous rocks. *Geochimica et Cosmochimica Acta* **69**, 2847–2860.

Velichkin V. I. and Vlasov B. P. (2011) Domal structures and hydrothermal uranium deposits of the Erzgebirge, Saxony, Germany. *Geology of Ore Deposits* **53**, 74–83.

Vermeesch P. (2018) IsoplotR: A free and open toolbox for geochronology. *Geoscience Frontiers* **9**, 1479–1493.

Vho A., Lanari P. and Rubatto D. (2019) An Internally-Consistent Database for Oxygen Isotope Fractionation Between Minerals. *Journal of Petrology* **60**, 2101–2129.

Vigneresse J.-L. (1987) Organisation tridimensionnelle du Massif d'Echassières et bilan des mesures géophysiques de surface. *Géologie de la France* **2–3**, 27–32.

Villaros A., Laurent O., Couzinié S., Moyen J.-F. and Mintrone M. (2018) Plutons and domes: the consequences of anatectic magma extraction – example from the southeastern French Massif Central. *International Journal of Earth Sciences (Geologische Rundschau)* **107**, 2819–2842.

Virmond A. L., Wotzlaw J.-F., Rojas-Arancibia R., Selby D. and Chelle-Michou C. (2024) Multi-million-year magmatic and hydrothermal activity is key to the formation of supergiant to behemothian porphyry copper deposits. *Contributions to Mineralogy and Petrology* **179**, 88.

Von Quadt A., Erni M., Martinek K., Moll M., Peytcheva I. and Heinrich C. A. (2011) Zircon crystallization and the lifetimes of ore-forming magmatic-hydrothermal systems. *Geology* **39**, 731–734.

Waldron J. W. F., McCausland P. J. A., Barr S. M., Schofield D. I., Reusch D. and Wu L. (2022) Terrane history of the Iapetus Ocean as preserved in the northern Appalachians and western Caledonides. *Earth-Science Reviews* **233**, 104163.

Walker G. P. (1989) Gravitational (density) controls on volcanism, magma chambers and intrusions. *Australian Journal of Earth Sciences* **36**, 149–165.

Wang A., Freeman J. J. and Jolliff B. L. (2015) Understanding the Raman spectral features of phyllosilicates. *Journal of Raman Spectroscopy* **46**, 829–845.

Wang D., Liu J., Carranza E. J. M., Zhai D., Wang Y., Zhen S., Wang Jiang, Wang Jianping, Liu Z. and Zhang F. (2019) Formation and evolution of snowball quartz phenocrysts in the Dongping porphyritic granite, Hebei Province, China: Insights from fluid inclusions, cathodoluminescence, trace elements, and crystal size distribution study. *Lithos* **340–341**, 239–254.

Wang H., Cai K., Sun M., Xia X.-P., Lai C.-K., Li P., Wan B. and Zhang Z. (2022) Apatite as a magma redox indicator and its application in metallogenic research. *Lithos* **422**, 106749.

Wang R. (1988) Etude minéralogique et cristallochimique de cassitérite, niobo-tantalates et minéraux disséminés du granite de Beauvoir (Allier): implications métallogéniques. PhD dissertation, Université de Toulouse 3.

Wang X.-S., Timofeev A., Williams-Jones A. E., Shang L.-B. and Bi X.-W. (2019) An experimental study of the solubility and speciation of tungsten in NaCl-bearing aqueous solutions at 250, 300, and 350°C. *Geochimica et Cosmochimica Acta* **265**, 313–329.

Wark D. A. and Watson E. B. (2006) TitaniQ: a titanium-in-quartz geothermometer. *Contributions to Mineralogy and Petrology* **152**, 743–754.

Warr L. N. (2021) IMA–CNMNC approved mineral symbols. *Mineralogical Magazine* **85**, 291–320.

Watt G. R., Wright P., Galloway S. and McLean C. (1997) Cathodoluminescence and trace element zoning in quartz phenocrysts and xenocrysts. *Geochimica et Cosmochimica Acta* **61**, 4337–4348.

Webster J. D. (1997) Chloride Solubility in Felsic Melts and the Role of Chloride in Magmatic Degassing. *Journal of Petrology* **38**, 1793–1807.

Webster J. D. (1992) Fluid-melt interactions involving Cl-rich granites: experimental study from 2 to 8 kbar. *Geochimica et Cosmochimica Acta* **56**, 659–678.

Webster J. D. (1990) Partitioning of F between $H_2O$ and $CO_2$ fluids and topaz rhyolite melt: Implications for mineralizing magmatic-hydrothermal fluids in F-rich granitic systems. *Contributions to mineralogy and petrology* **104**, 424–438.

Webster J. D., Baker D. R. and Aiuppa A. (2018) Halogens in mafic and intermediate-silica content magmas. *The role of halogens in terrestrial and extraterrestrial geochemical processes: surface, crust, and mantle*, 307–430.

Webster, J. D., Holloway, J. R. (1990) Partitioning of F and Cl between magmatic hydrothermal fluids and highly evolved granitic magmas. In: Stein, H. J., Hannah, J. L. (Eds.), *Ore-bearing Granite Systems: Petrogenesis and Mineralizing Processes*. Geological Society of America Special Paper **246**, pp. 21–34.

Webster J. D. and Piccoli P. M. (2015) Magmatic Apatite: A Powerful, Yet Deceptive, Mineral. *Elements* **11**, 177–182.

Webster J. D., Tappen C. M. and Mandeville C. W. (2009) Partitioning behavior of chlorine and fluorine in the system apatite–melt–fluid. II: Felsic silicate systems at 200 MPa. *Geochimica et Cosmochimica Acta* **73**, 559–581.

Webster J. D., Thomas R., Rhede D., Förster H.-J. and Seltmann R. (1997) Melt inclusions in quartz from an evolved peraluminous pegmatite: Geochemical evidence for strong tin enrichment in fluorine-rich and phosphorus-rich residual liquids. *Geochimica et Cosmochimica Acta* **61**, 2589–2604.

Webster J., Thomas R., Förster H.-J., Seltmann R. and Tappen C. (2004) Geochemical evolution of halogen-enriched granite magmas and mineralizing fluids of the Zinnwald tin-tungsten mining district, Erzgebirge, Germany. *Mineralium Deposita* **39**, 452–472.

Wei C.-S. and Zhao Z.-F. (2022) Paradoxically lowered oxygen isotopes of hydrothermally altered minerals by an evolved magmatic water. *Scientific Reports* **12**, 16213.

Weil J. A. (1984) A review of electron spin spectroscopy and its application to the study of paramagnetic defects in crystalline quartz. *Physics and Chemistry of Minerals* **10**, 149–165.

Weil, J. A. (1993) A review of the EPR spectroscopy of the point defects in α-quartz: the decade 1982–1992. In: Helms, C. R., Deal, B. E. (Eds.), *The Physics and Chemistry of $SiO_2$ and the Si-$SiO_2$ Interface 2*. Springer US, Boston, MA, pp. 131–144.

Weis, P. (2012) The dynamic interplay between saline fluid flow and rock permeability in magmatic–hydrothermal systems. In: Fisher, Q. J., Casey, D., Gerdes, A., John, C. M., Knipe, R. J., Niemeijer, A. R., Tenthorey, E. (Eds.), *Crustal Permeability*. John Wiley & Sons, Ltd., pp. 373–392.

Weis P. (2014) The Physical Hydrology of Ore-Forming Magmatic-Hydrothermal Systems. *Society of Economic Geologists, Inc., Special Publication* **18**, 59–75.

Weis P., Driesner T. and Heinrich C. A. (2012) Porphyry-copper ore shells form at stable pressure-temperature fronts within dynamic fluid plumes. *Science* **338**, 1613–1616.

Wendt I., Lenz H., Höhndorf A., Bültemann H. and Bültemann W.-D. (1979) Das Alter der Pechblende der Lagerstätte Menzenschwand, Schwarzwald. *Zeitschrift der deutschen geologischen Gesellschaft* **130**, 619–626.

White A. J. and Chappell B. W. (1977) Ultrametamorphism and granitoid genesis. *Tectonophysics* **43**, 7–22.

Williams-Jones A. E. and Heinrich C. A. (2005) 100th Anniversary Special Paper: Vapor Transport of Metals and the Formation of Magmatic-Hydrothermal Ore Deposits. *Economic Geology* **100**, 1287–1312.

Williams-Jones A. E., Migdisov A. A., Archibald S. M. and Xiao Z. (2002) Vapor-transport of ore metals. *Water-Rock Interactions, Ore Deposits. and Environmental Geochemistry: A Tribute to David A Crerar. Special Publication* **7**, 279–305.

Williamson B. J., Downes H. and Thirlwall M. F. (1992) The relationship between crustal magmatic underplating and granite genesis: an example from the Velay granite complex, Massif Central, France. *Earth and Environmental Science Transactions of The Royal Society of Edinburgh* **83**, 235–245.

Witt W. K. (1988) Evolution of high-temperature hydrothermal fluids associated with greisenization and feldspathic alteration of a tin-mineralized granite, northeast Queensland. *Economic Geology* **83**, 310–334.

Wood S. A. and Samson I. M. (2000) The hydrothermal geochemistry of tungsten in granitoid environments: I. Relative solubilities of ferberite and scheelite as a function of T, P, pH, and m NaCl. *Economic Geology* **95**, 143–182.

Worden R. H. (1996) Controls on halogen concentrations in sedimentary formation waters. *Mineralogical Magazine* **60**, 259–274.

Worden, R.H. (2018). Halogen Elements in Sedimentary Systems and Their Evolution During Diagenesis. In: Harlov, D., Aranovich, L. (Eds) *The Role of Halogens in Terrestrial and Extraterrestrial Geochemical Processes*. Springer Geochemistry. Springer, Cham, Switzerland, pp. 185–260.

Wu M., Samson I. M. and Zhang D. (2018) Textural features and chemical evolution in Ta-Nb oxides: Implications for deuteric rare-metal mineralization in the Yichun granite-marginal pegmatite, southeastern China. *Economic Geology* **113**, 937–960.

Xi B., Zhang D. and Zhou L. (2007) Magmatic evolutions of several granite plutons related to Sn (W) mineralizations in the Nanling region, China. *Geological Bulletin of China* **26**, 1591–1599.

Xiaolin X., Zhenhua Z., Jinchu Z., Bing R. and Mingyuan L. (1998) Partitioning of F between aqueous fluids and albite granite melt and its petrogenetic and metallogenetic significance. *Chinese Journal of Geochemistry* **17**, 303–310.

Xu J., Xia X.-P., Wang Q., Spencer C. J., Zhang L. and Zhu X. (2024) Apatite textures, elemental and isotopic compositions unmask the homogenizing process in silicic magma chambers. *Geophysical Research Letters* **51**, e2023GL106646.

Yang W.-B., Niu H.-C., Shan Q., Sun W.-D., Zhang H., Li N.-B., Jiang Y.-H. and Yu X.-Y. (2014) Geochemistry of magmatic and hydrothermal zircon from the highly evolved Baerzhe alkaline granite: implications for Zr–REE–Nb mineralization. *Mineralium Deposita* **49**, 451–470.

Yardley B. W. D. (2005) 100th Anniversary Special Paper: Metal Concentrations in Crustal Fluids and Their Relationship to Ore Formation. *Economic Geology* **100**, 613–632.

Yin L., Pollard P. J., Shouxi H. and Taylor R. G. (1995) Geologic and geochemical characteristics of the Yichun Ta-Nb-Li deposit, Jiangxi Province, South China. *Economic Geology* **90**, 577–585.

Yoshie Y. (2012) Hydrothermal evolution of ilmenite-series granite in the inner zone of SW Japan. PhD dissertation, University of Tsukuba, Ibaraki, Japan

Yuguchi T., Ogita Y., Kato T., Yokota R., Sasao E. and Nishiyama T. (2020) Crystallization processes of quartz in a granitic magma: Cathodoluminescence zonation pattern controlled by temperature and titanium diffusivity. *Journal of Asian Earth Sciences* **192**, 104289.

Yund R. A., Thomas Anderson F., Yund R. A. and Thomas Anderson F. (1978) The effect of fluid pressure on oxygen isotope exchange between feldspar and water. *Geochimica et Cosmochimica Acta* **42**, 235–239.

Zajacz Z., Halter W. E., Pettke T. and Guillong M. (2008) Determination of fluid/melt partition coefficients by LA-ICPMS analysis of co-existing fluid and silicate melt inclusions: Controls on element partitioning. *Geochimica et Cosmochimica Acta* **72**, 2169–2197.

Žák K., Pudilová M. and Breiter K. (2005) Oxygen isotope study of the highly fractionated Podlesí granite system, Krušné hory Mts., Czech Republic. *Bulletin of Geosciences* **80**, 139–143.

Zalashkova N. Y. and Sitnin A. A. (1967) Features of distribution of rare elements in tantalum-bearing apogranites and biotite granites. *Geochemistry International* **4**, 1013–1025.

Zaraisky G. P., Korzhinskaya V. and Kotova N. (2010) Experimental studies of $Ta_2O_5$ and columbite–tantalite solubility in fluoride solutions from 300 to 550°C and 50 to 100 MPa. *Mineralogy and Petrology* **99**, 287–300.

Zhang F., Guo F., Zhang X., Zhao L., Hua W., Huang X. and Tian X. (2024) Multiple-pulse magmatic intrusion and fluid metasomatism in Mesozoic Qianlishan rare metal granite, South China: Records from apatite geochemistry. *Lithos* **474**, 107580.

Zhang L.-G., Liu J., Chen Z. and Zhou H. (1994) Experimental investigations of oxygen isotope fractionation in cassiterite and wolframite. *Economic Geology* **89**, 150–157.

Zhang X., Guo F., Zhang B., Zhao L., Wu Y., Wang G. and Alemayehu M. (2020) Magmatic evolution and post-crystallization hydrothermal activity in the early Cretaceous Pingtan intrusive complex, SE China: Records from apatite geochemistry. *Contributions to Mineralogy and Petrology* **175**, 1–18.

Zhao Z.-F. and Zheng Y.-F. (2003) Calculation of oxygen isotope fractionation in magmatic rocks. *Chemical Geology* **193**, 59–80.

Zheng Y.-F. (1993a) Calculation of oxygen isotope fractionation in anhydrous silicate minerals. *Geochimica et Cosmochimica Acta* **57**, 1079–1091.

Zheng Y.-F. (1993b) Calculation of oxygen isotope fractionation in hydroxyl-bearing silicates. *Earth and Planetary Science Letters* **120**, 247–263.

Zheng Y.-F. (1991) Calculation of oxygen isotope fractionation in metal oxides. *Geochimica et Cosmochimica Acta* **55**, 2299–2307.

Zheng Y.-F. (1996) Oxygen isotope fractionations involving apatites: Application to paleotemperature determination. *Chemical Geology* **127**, 177–187.

Zhu J.-C., Li R.-K., Li F.-C., Xiong X.-L., Zhou F.-Y. and Huang X.-L. (2001) Topaz–albite granites and rare-metal mineralization in the Limu District, Guangxi Province, southeast China. *Mineralium Deposita* **36**, 393–405.

Zoheir B., Lehmann B., Emam A., Radwan A., Zhang R., Bain W. M., Steele-MacInnis M. and Nolte N. (2020) Extreme fractionation and magmatic–hydrothermal transition in the formation of the Abu Dabbab rare-metal granite, Eastern Desert, Egypt. *Lithos* **352–353**, 105329.

# APPENDICES

# APPENDICES FOR PART II

## II.A1. Imaging and analytical methods

### II.A1.1. Scanning electron microscope (SEM) and cathodoluminescence (CL) imaging

Petrographic observations were carried out through optical microscopy, scanning electron microscopy (SEM) and cathodoluminescence (CL) at GeoRessources laboratory (Nancy, France). A TESCAN VEGA3 LM conventional SEM with two Bruker XFlash6 30 $mm^2$ EDS detectors and a Gatan ChromaCL2UV cathodoluminescence system was used to investigate the mineralogy, textural relationships and chemical zoning of apatite grains. Backscattered electron (BSE) images were acquired using an accelerating voltage of 15 kV and a beam current of 1 nA. CL study was performed on an OPEA Cathodyne connected to a Nikon Eclipse LV100 microscope in order to reveal the distinct micro-textural domains which were further analysed. The accelerating voltage and gun current were respectively 10-15 kV and 250-400 mA.

### II.A1.2. Micro-XRF chemical mapping

Micro-X-Ray Fluorescence (µ-XRF) analyses of thick sections were carried out with a Bruker M4 Tornado µ-XRF benchtop spectrometer at GeoRessources. The M4 Tornado device is equipped with a 30 W Rh-anode X-ray source operating at 50 kV and 400 µA. Primary X-ray beam was focused with polycapillary optics on a 20 µm spot on the sample surface. Two XFlash silicon drift energy dispersive X-ray detectors (SSD-EDS) with an energy resolution not exceeding 145 eV are located on each side of the primary X-ray source. X-ray maps were acquired with a dwell time of 12 ms per pixel and a spacing of 25 µm between each point. Elemental maps for individual atomic species were generated using a Python routine and mineralogical classification was realised using the software XMapTools.

### II.A1.3. Electron microprobe analysis (EMPA)

Apatite chemistry was determined by Electron probe micro-analysis (EPMA) using a Cameca SX100, equipped with five wavelength dispersive spectrometers (WDS) at GeoRessources. The accelerating voltage and beam current were respectively set at 15 kV and 20 nA, with a focused beam (*ca.* 1 µm). Major and minor elements (Ca, P, F, Cl, Mn, Fe, S, Sr, Na, Si, Al, Mg, As, Ba, Y, Ce, La) were analysed within the different micro-textural domains identified through CL imaging. The detection limit is element-dependant and was ranging from 0.01 wt.% for Si to 0.18 wt.% for Ba, with an average value of approximately 0.07 wt.%. Calibration was carried out using well-established natural (Durango fluorapatite (P), andradite (Ca), topaz (F), vanadinite (Cl), hématite (Fe), albite (Na, Si), olivine (Mg)) and synthetic standards ($MnTiO_3$ (Mn), $SrSO_4$ (Sr), $Al_2O_3$ (Al), GaAs (As), $BaSO_4$ (Ba, S), $YPO_4$ (Y), $CePO_4$ (Ce), $LaPO_4$ (La)). Previous works have highlighted that F and Cl X-ray intensities vary with exposure to the electron beam during EMPA analysis of apatite due to diffusion mechanisms (Stormer et al., 1993). This effect is strongly anisotropic and results in changes up to 100% in F content when the electron beam

is parallel to the *c* axis of apatite, less for Cl, Ca and P, or for grains with oblique orientations (Stormer et al., 1993; Webster and Piccoli, 2015). Furthermore, the comparison of SIMS and EMPA data obtained on fluorapatite from the Olserum-Djupedal REE-phosphate mineralisation (Sweden) suggested the lower precision of F analysis using EMPA (Andersson et al., 2019). As the optimal EMPA operating conditions (Stormer et al., 1993; Goldoff et al., 2012) were not applied in this study, the F and Cl concentrations of apatite determined by EMPA may not be fully reliable. In this study, the composition of major and minor halogens (F, Cl, Br, I) of the Beauvoir apatite generations were analysed by SIMS, allowing for a consistent comparison of halogen concentrations.

The structural formulae of the distinct apatite generations was calculated based on 12.5 oxygen atoms per formula unit (12.5 O apfu), following the appendix 1 of Deer et al. (2003). We assumed the anion site to be full and filled only with F, Cl and OH (Piccoli and Candela, 2002).

Furthermore, Wavelength Dispersive X-ray (WDX) element maps were measured on typical grains selected for each apatite generation. Elements analysed for each grain were those with values above the detection limit in EMPA spot analyses. Analytical conditions were similar to those applied for quantitative analysis (i.e. accelerating voltage of 15 kV and beam current of 20 nA). The step size was ranging from 1 to 7 µm depending on the grain size and the counting time was set at 200 ms per step.

#### II.A1.4. Secondary ion mass spectrometry (SIMS)

Measurements of oxygen isotopic composition and halogen concentrations (F, Cl, Br and I) of apatite were carried out at the CRPG (Nancy, France). Oxygen isotopic ratios were determined using a Cameca IMS 1270-E7 large geometry ion microprobe (SIMS) with analytical conditions similar to those set by Decrée et al. (2020). Each spot analysis was realised in the vicinity of the EMPA spots and consisted in (i) 120 s of background noise measurement of the Faraday collectors for subsequent calculation of the internal error, (ii) 90 s of pre-sputtering the target area in the apatite grain with a 20x20 µm raster beam to remove the gold coating and minimize surface contamination, (iii) sputtering of apatite to create a secondary ion beam, (iv) acceleration at 10 kV of the negative secondary $^{16,18}O$ ions and automatic mass centering in the deflector contrast and field apertures, and (v) collecting of 30 to 40 cycles of $^{16}O$ and $^{18}O$ signals. During step (iii), a primary $Cs^+$ ion beam characterised by an intensity of 2 nA and a bombardment energy of 10 kV was focused on a 15x15 µm raster area to sputter oxygen ions from apatite and create the negative secondary ion beam. Charge build-up generated at the sample surface was compensated by a normal-incident electron gun (NEG) beam. Following the mass centering on $^{16}O$ isotope (step (iv)), measurements were carried out on Faraday collectors in multicollection mode with an integration time ranging from 150 to 200 s (30 to 40 cycles of *ca.* 5 s). The mass resolution was set to 3000 M/ΔM and the energy slit opened at 30 eV.

Correction of instrumental mass fractionation (IMF) was conducted by analysing the Durango fluorapatite reference material ($\delta^{18}O$=9.4 ‰; Trotter et al., 2008), whose composition is overall similar to the analysed samples (Marks et al., 2012). The analytical precision can be estimated through the calculation of the internal error (or internal precision) and external error (reproducibility), both depending on the secondary ion beam intensity and integration time. The internal error on $\delta^{18}O$ was below 0.21 ‰ (2SE), with an average value of about 0.08 ‰. The long-term external reproducibility (2s) varied from 0.08 ‰ to 0.20 ‰ between the two sessions because of changes in the analytical conditions, in particular in the integration time. The reported analytical uncertainty corresponds to the quadratic sum of the internal error and of the reference material external error and ranges from 0.08 ‰ to 0.45 ‰, with a mean value of 0.21 ‰. The $^{18}O/^{16}O$ ratios are expressed as $\delta^{18}O$ values and are normalized to the Vienna Standard Mean Ocean Water (VSMOW) composition ($^{18}O/^{16}O$ = 0.0020052; Baertschi, 1976).

The determination of halogen concentrations (F, Cl, Br and I) was carried out within the same micro-textural domains targeted for O isotopic analysis using a Cameca IMS 1280-HR large geometry ion microprobe, and closely following analytical conditions applied by Marks et al. (2012), Kusebauch et al. (2015a, 2015b), Andersson et al. (2019) and Melfou et al. (2023). The analytical procedure is overall similar to the one described above for O isotopic composition measurement. Apatite grains were sputtered by a primary $Cs^+$ ion beam of *ca.* 1.3 nA, accelerated at 10 kV on a 5x5 µm raster area. Prior to data collection, the selected spot was pre-sputtered for 180 s over a 15 µm square raster area. Secondary ion intensities were measured in peak-switching mode, either on Faraday cups for abundant species (i.e. count rate > $10^6$ cps) or on low-noise ion-counting electron multipliers (count rate < $10^6$ cps). Each analysis consisted in 6 cycles of *ca.* 80 s, leading to a total integration time of approximatively 480 s. A high mass resolving power (MRP) of 16,000 M/ΔM was set in order to resolve the interference of CaCl molecular species with $^{81}Br$ and the energy slit was opened at 30 eV. Measurements were normalised to the $^{40}Ca^{31}P$ matrix signal, with the exception of some cases where the $^{31}P$ value was used due to a molecular interference on the $^{40}Ca^{31}P$ signal (probably with $^{55}Mn^{16}O$). Halogen compositions were determined relatively to the Durango fluorapatite standard using concentrations of 33500 ppm for F (1s = 7 %) (Marks et al., 2012), 4099 ppm for Cl (1s = 5%), 0.84 ppm for Br (1s = 16 %) and 0.73 ppm for I (1s = 4%) (Kusebauch et al., 2015b). Detection limits have been estimated by Kusebauch et al. (2015a, 2015b) based on an average $^{40}Ca^{31}P$ signal of 300,000 cps and three times the typical ion counter background of 0.05 cps, yielding 6.6 x $10^{-5}$ ppm for F, 1.3 x $10^{-4}$ ppm for Cl, 3.8 x $10^{-3}$ ppm for Br, and 7.9 x $10^{-4}$ ppm for I. Repeated analysis (n = 24) of the Durango fluorapatite reveals a relative standard deviation (RSD, 1s) of 2.99% for F, 0.45% for Cl, 6.00% for Br, and 1.19% for I.

### II.A1.5. Laser ablation – inductively coupled plasma – mass spectrometry (LA-ICP-MS)

Trace element concentrations and U–Pb isotope compositions of apatite were determined by LA-ICP-MS at Géosciences Environnement Toulouse (GET, France) and GeoRessources laboratories. At GET, measurements were carried out using a Thermo Element XR Sector-field - inductively coupled plasma - mass spectrometer (SF-ICP-MS) coupled to an ESI 293 nm (New Wave Research) NWR Femto laser ablation system with a dual-volume ablation chamber. At GeoRessources, trace elements were analysed with an Agilent 7900 quadrupole single collector ICP-MS, and U-Pb isotope compositions were obtained using a Nu Instruments AttoM ES SF-ICP-MS. Both instruments are coupled to an ESI 193 nm ArF excimer laser ablation system with a two-volume 'TwoVol2' ablation chamber.

Laser ablations were carried out with constant spot size of 30 µm, repetition rate of 7 Hz, laser energy density of *ca.* 2 J.cm$^{-2}$, and a sampling period varying between 20 and 30 s. For U-Pb isotopic analyses at both GET and GeoRessources, the targeted region was pre-ablated with 4 or 8 spots, respectively (and a spot size of 50 µm and energy density 1 J.cm$^{-2}$ at GeoRessources) to remove any surficial Pb contamination prior to each analysis. More details on acquisition parameters are available in Table S3 (Appendix II.A4).

Trace elements data reduction was completed with the Iolite software (version 2.5 at the GET and version 4 at GeoRessources; Hellstrom et al., 2008; Paton et al., 2011) using the "Trace element" data reduction scheme (Paton et al., 2011). The NIST SRM 610 glass was used as primary reference material for the correction of mass bias and instrumental drift (Jochum et al., 2011). The NIST SRM 612 glass (Jochum et al., 2011) and the Durango apatite were used as secondary control materials. Trace elements concentrations determined for the Durango apatite mostly fall within the range of reported values (note that this apatite is not homogenous in most elements; Table S6 in Appendix II.A4). The signal on $^{43}$Ca within apatite was used as the internal standard, assuming a stoichiometric Ca content of 39.74 wt.%. The average limit of detection (LOD) for each element was estimated from the equation of Pettke et al. (2012).

U-Pb data reduction was performed with Iolite (version 2.5 at the GET and version 4 at GeoRessources; Hellstrom et al., 2008; Paton et al., 2011) and the "UPb Geochronology" data reduction scheme (Petrus and Kamber, 2012). $^{207}$Pb/$^{206}$Pb and $^{238}$U/$^{206}$Pb ratios were first normalised to the NIST SRM 610 glass (Jochum et al., 2011) in Iolite. $^{238}$U/$^{206}$Pb ratios were then corrected for the apatite-glass matrix effect in Excel by applying an average correction factor determined based on the offset between measured and reference lower intercept dates of matrix-matched reference materials: the Madagascar apatite (U-Pb age of 474.25 ± 0.41 and 486.58 ± 0.85 Ma; Thomson et al., 2012), the McClure Mountain apatite (U-Pb age of 523.51 ± 2.09; Schoene and Bowring, 2006), and either the Durango apatite at GET (Ar-Ar age of 31.44 ± 0.18 Ma; McDowell et al., 2005) or the Duluth apatite at GeoRessources (U-Pb age 1099.1 ± 0.5 Ma;

Schmitz et al., 2003). The corrected lower intercept dates of apatite reference materials are available in Table S8 (Appendix II.A4). Apatite $^{207}Pb/^{235}U$ ratios were calculated from $^{238}U/^{206}Pb$ and $^{207}Pb/^{206}Pb$ considering a $^{238}U/^{235}U$ value of 137.818 (Horstwood et al., 2016). In Table S8, U, Pb and Th concentrations from GeoRessources were estimated with Iolite 4 using the trace elements DRS and NIST612 glass as a primary reference material. No internal standard was determined, concentrations should then be regarded as semi-quantitative.

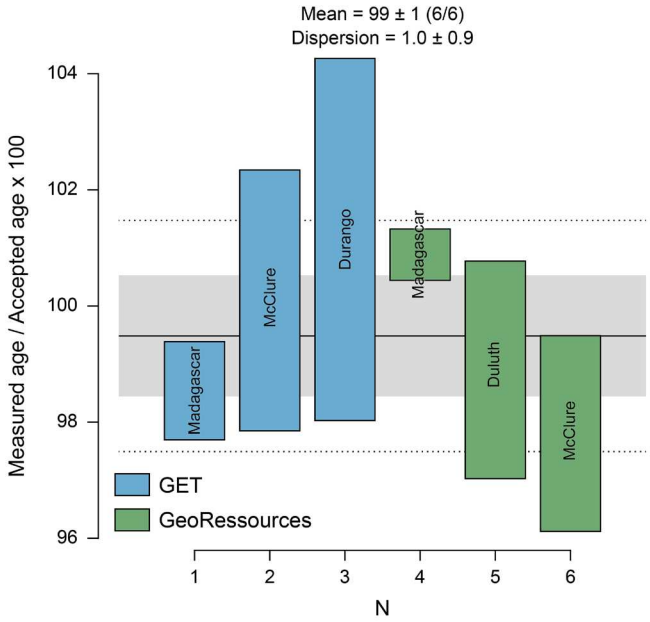



*Figure II.A1. Estimation of the interlaboratory reproducibility from the dispersion of apatite reference material lower intercept ages obtained during this study.*

U-Pb ages presented in this study are lower intercept ages of discordia calculated in $^{238}U/^{206}Pb$ vs. $^{207}Pb/^{206}Pb$ Tera-Wasserburg diagrams with IsoplotR (Vermeesch, 2018) and errors are quoted at the 2-sigma level. Despite similar analytical protocols, systematic bias of U–Pb isotope compositions and ages will exist between both laboratories. We estimate the interlaboratory reproducibility to be ± 1.0 % relative from the dispersion of apatite reference material lower intercept ages obtained during this study (Fig. II.A1). This uncertainty is added in quadrature to any lower intercept date. The resulting total uncertainty is referred to in the following sections and indicated in brackets on Figs. II.11 (Part II) and II.A2 (Appendix II.A2).

### II.A1.6. Whole rock analysis

Samples were crushed to obtain adequate powder fractions using an agate mill. Geochemical analyses were performed by the Service d'Analyses des Roches et Minéraux (SARM, CRPG-CNRS, Nancy, France) using inductively coupled plasma atomic emission spectroscopy (AES) for major elements, inductively coupled plasma mass spectrometry (ICP-MS) for trace elements, absorptiometry for B, flame atomic absorption spectrometry (AAS) for Li and potentiometry for F (Carignan et al., 2001).

## II.A2. Detailed Terra-Wasserburg diagrams for apatite I and IIb from the Beauvoir PRMG

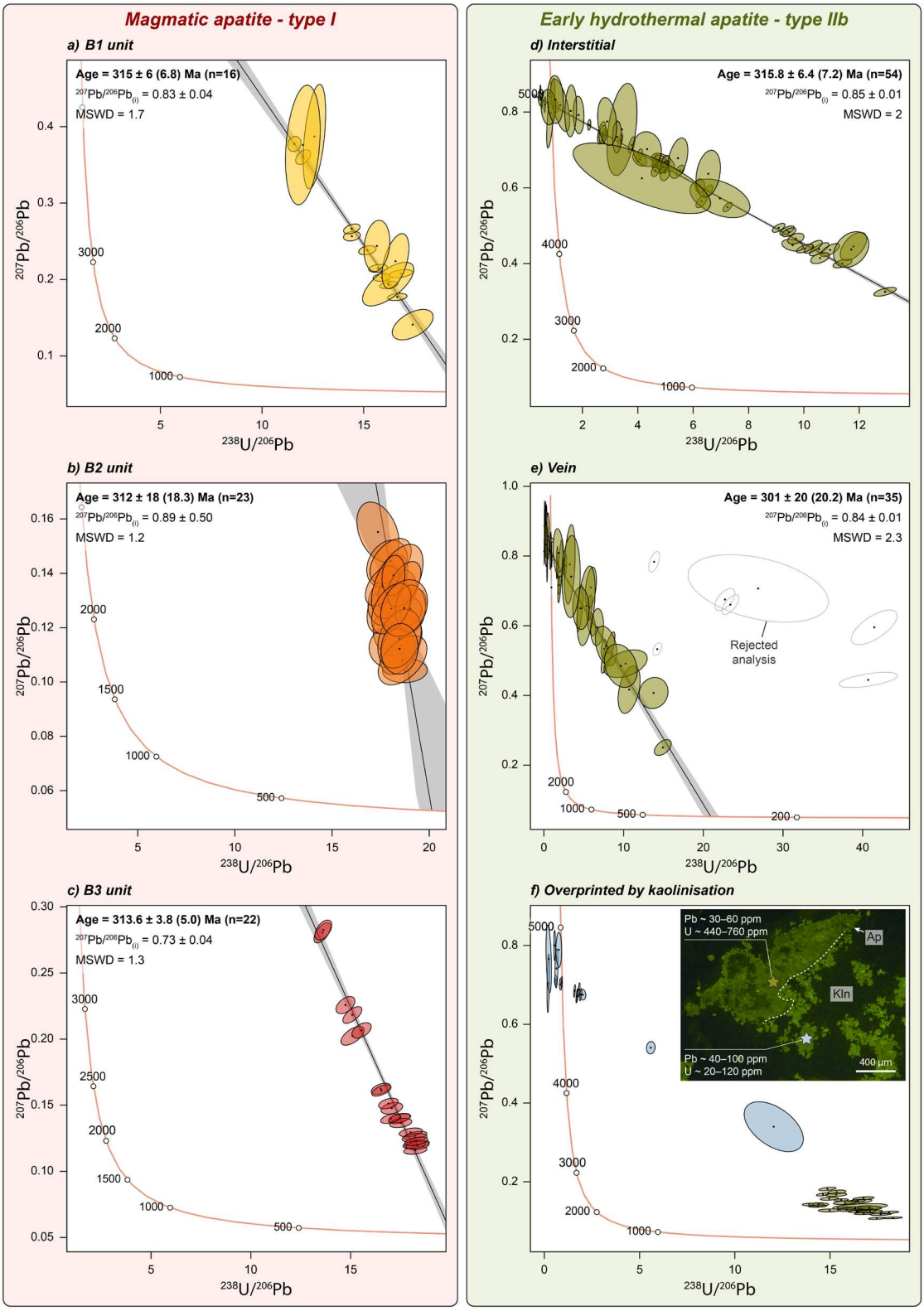



*Figure II.A2. Detailed Tera-Wasserburg diagrams for apatite I and IIb from the Beauvoir PRMG. (a-c) Magmatic apatite (type I) from the B1, B3 and B3 units, respectively; (d-f) Early hydrothermal apatite (type IIb) observed as interstitial apatite replacing magmatic minerals, crystallising within quartz ± muscovite veins and partially overprinted by kaolinisation, respectively. Ellipses and age uncertainties are reported at the 2-sigma level. The first uncertainty indicated corresponds to the analytical uncertainty with overdispersion, while the second one in brackets takes into account interlaboratory reproducibility.*

## II.A3. Trends between Sr and S content and O isotopic composition of apatite

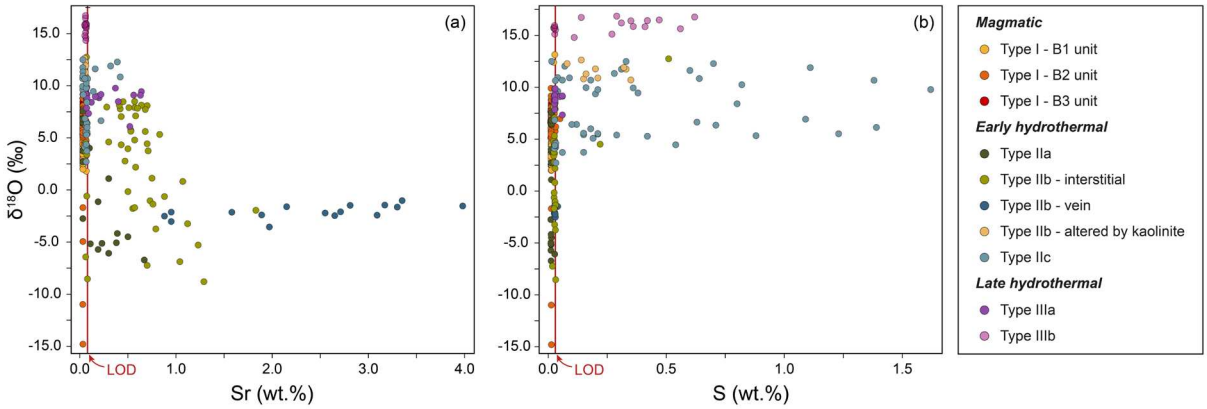



*Figure II.A3. Binary diagrams illustrating trends between Sr and S content and O isotopic composition of apatite. An enrichment in Sr in apatite tends to be associated with low to negative $\delta^{18}O$ values, whereas S-rich apatite exhibits heavier O isotopic signatures. Data are from EPMA. For analysis spots where an element was not detected, half of the detection limit was assigned as the concentration.*

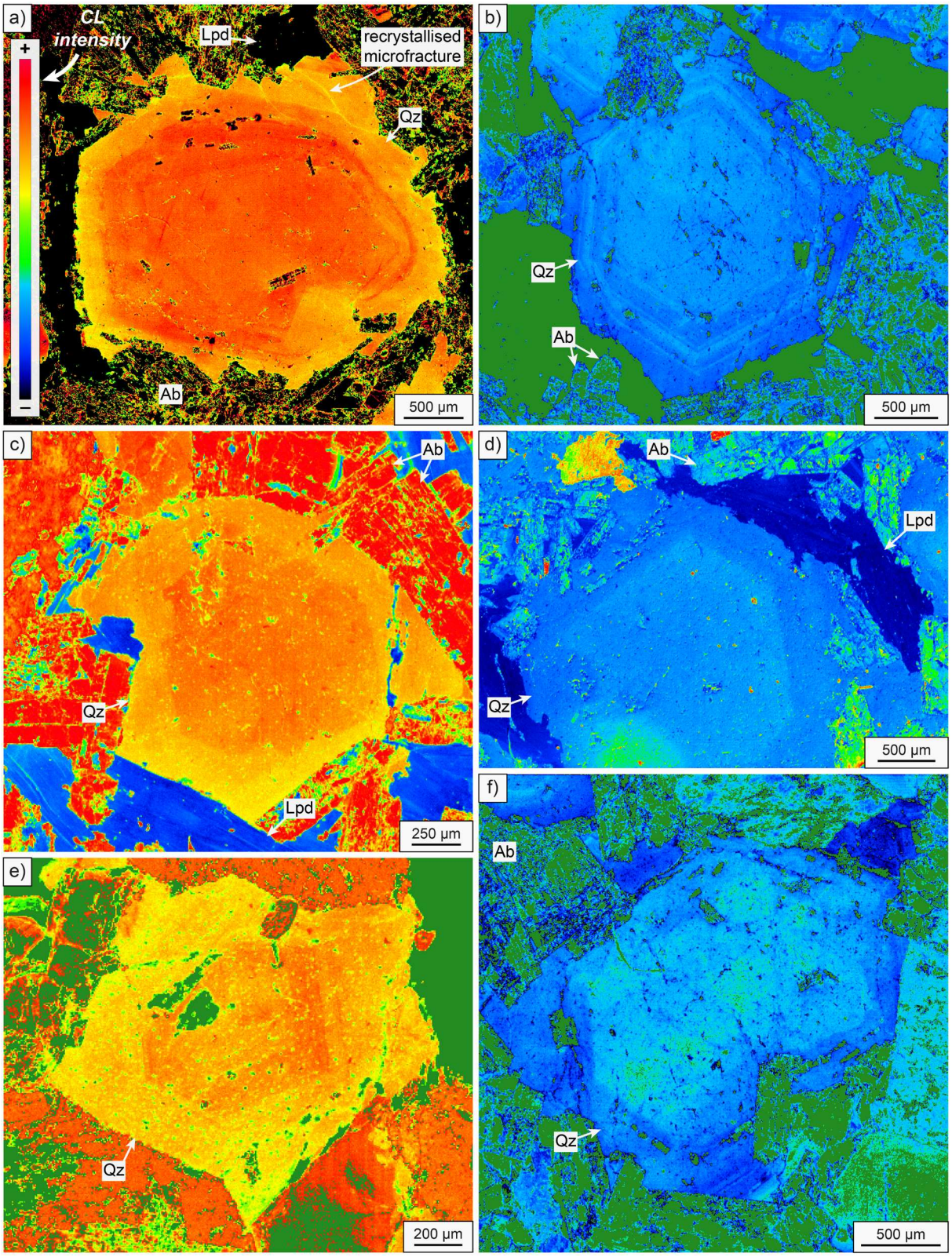
## II.A4. Major and trace elements, halogens, oxygen isotopic compositions, and U-Pb geochronology of apatite generations encountered within the Beauvoir PRMG, with detection limits and analytical parameters

https://drive.google.com/drive/folders/1fg_2RtGm7P91CLvZXN6f5PnbZakrMfTw?usp=sharing

(Appendix II.A4)

# APPENDICES FOR PART III

## III.A1. Supplementary cathodoluminescence images of magmatic quartz from the B1, B2 and B3 units of the Beauvoir PRMG




*(Figure continued on the next page)*

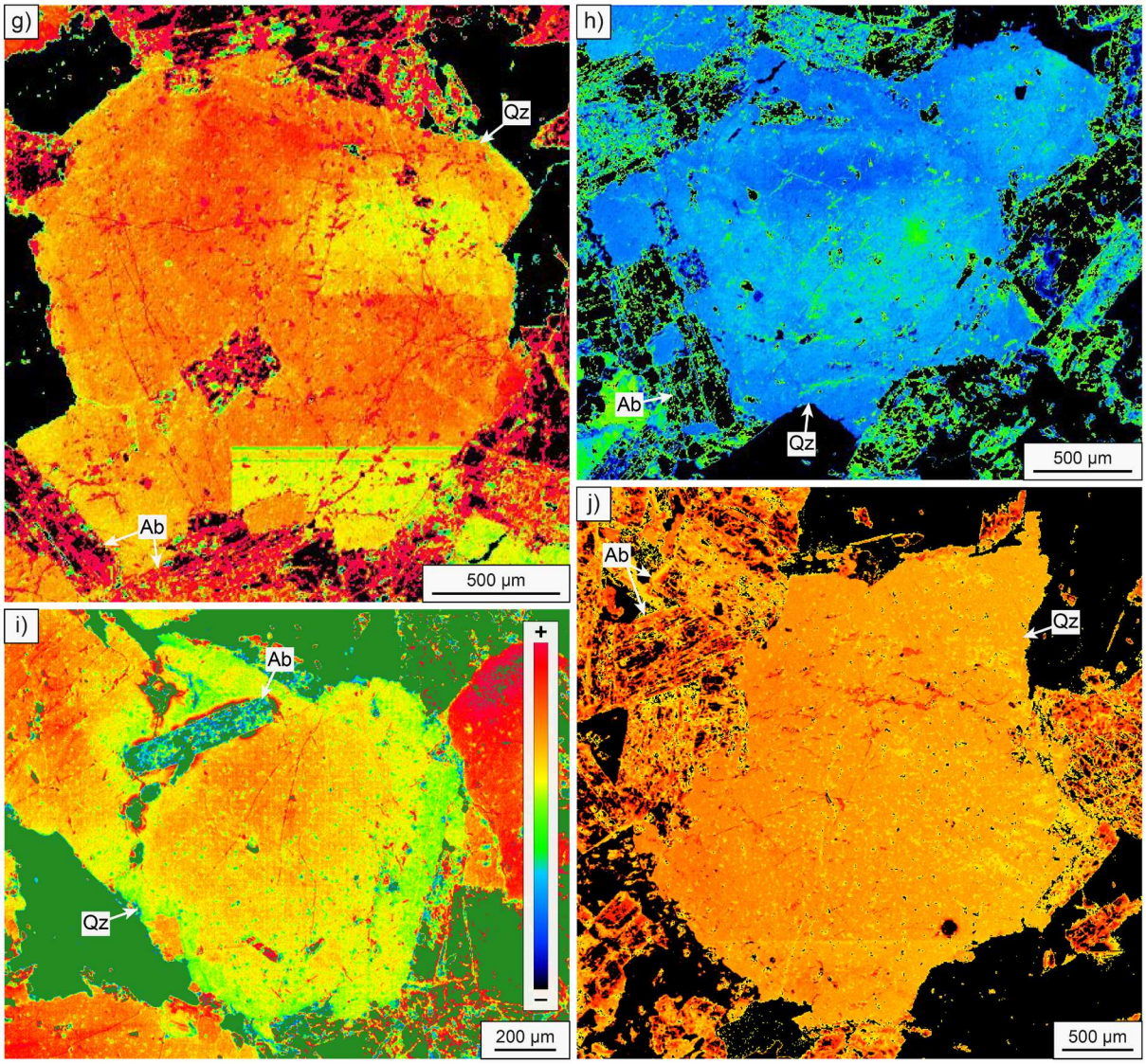



*Figure III.A1. Cathodoluminescence (CL) images revealing zonation in magmatic quartz from the B1 unit of the Beauvoir PRMG. Four main CL textures are identified: (a-b) alternating thin growth bands, several to tens of microns thick, characteristic of oscillatory zoning; (c-f) a sub-euhedral to euhedral core surrounded by a distinct, less-luminescent rim; (g-i) a gradual transition in CL intensity from core to rim; and (j) a homogeneous CL signature. Since the CL detector used was panchromatic, the observed colours do not represent the true luminescence colours of the quartz crystals, although signal intensities can still be qualitatively compared. The colours have been filtered and adjusted to enhance the visibility of quartz zonation. The colour scale representing CL intensity in figures (a) and (i) is consistent across all CL images. Abbreviations follow the IMA conventions compiled by Warr (2021).*

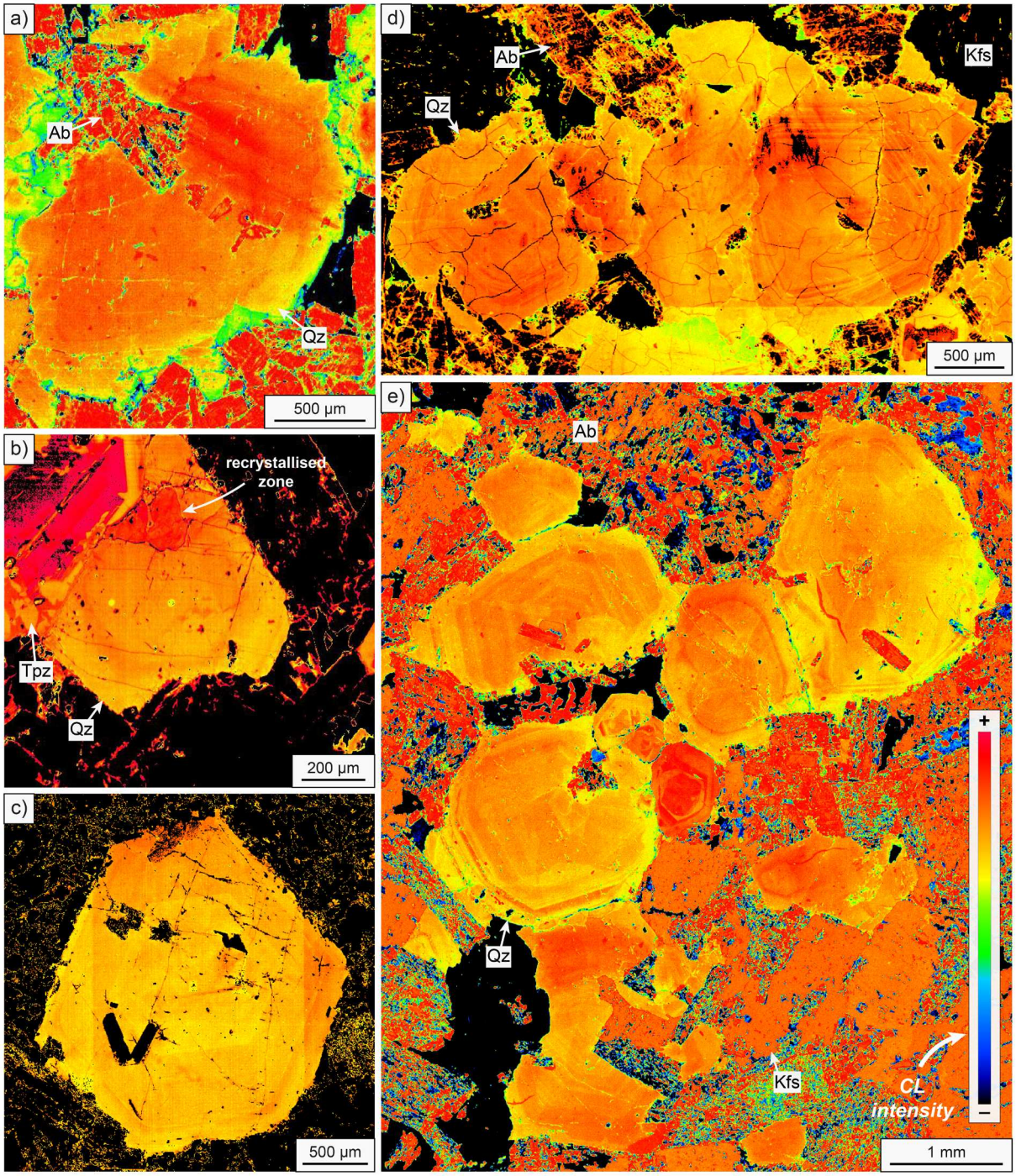



*Figure III.A2. Cathodoluminescence (CL) images showing zonation in magmatic quartz from the B2 unit of the Beauvoir PRMG. Three main CL textures are identified: (a) a gradual transition in CL intensity from the core to a less-luminescent rim; (b-c) a sub-euhedral to euhedral core surrounded by a distinct rim; and (d-e) alternating thin growth bands, several to tens of microns thick, characteristic of oscillatory zoning. Magmatic zonation is occasionally crosscut by dissolution-reprecipitation textures along fractures, particularly in the sample collected at 546.5 m depth in the GPF1 drillhole (d). Since the CL detector used was panchromatic, the observed colours do not represent the true luminescence colours of the quartz crystals, although signal intensities can still be qualitatively compared. The colours have been filtered and adjusted to enhance the visibility of quartz zonation. The colour scale representing CL intensity in (e) is consistent across all CL images. Abbreviations follow the IMA conventions compiled by Warr (2021).*

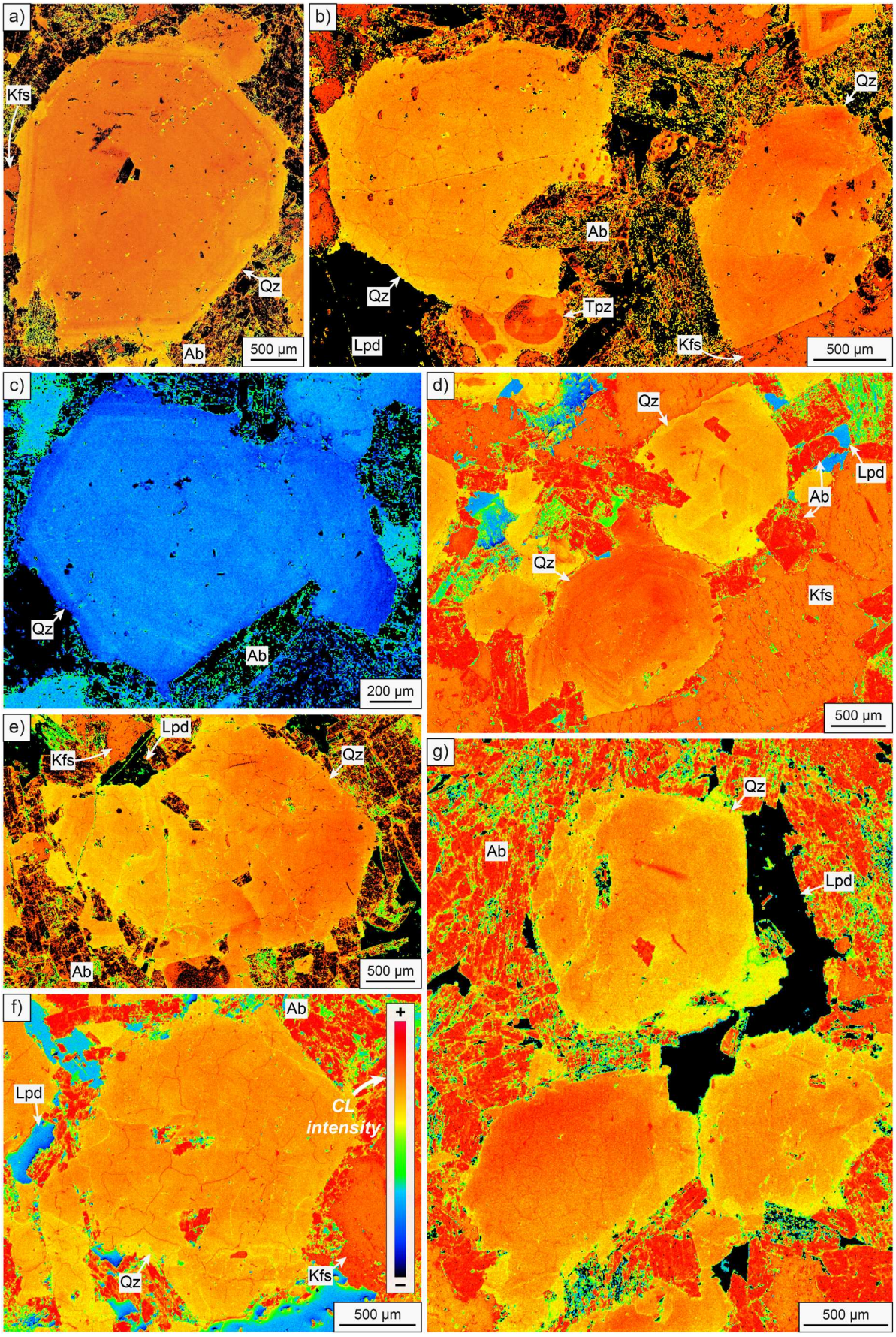



*Figure III.A3. Cathodoluminescence (CL) images showing zonation in magmatic quartz from the B3 unit of the Beauvoir PRMG. (Caption continued on the next page)*

*(Caption continued) Two main CL textures are identified: (a-d) alternating thin growth bands, several to tens of microns thick, characteristic of oscillatory zoning; and (e-g) a more-or-less pronounced gradual transition in CL intensity from the core to a less-luminescent rim. Since the CL detector used was panchromatic, the observed colours do not represent the true luminescence colours of the quartz crystals, although signal intensities can still be qualitatively compared. The colours have been filtered and adjusted to enhance the visibility of quartz zonation. The colour scale representing CL intensity in (f) is consistent across all CL images. Abbreviations follow the IMA conventions compiled by Warr (2021).*

## III.A2. Uncertainty calculations

### III.A2.1. Uncertainty estimation on temperatures of quartz-cassiterite O isotopic equilibrium

The uncertainty associated with the dataset is determined by integrating the individual uncertainties of each temperature estimate with the statistical variability of the population. Individual uncertainties ($\sigma_{ind}$) are consistent across all data points, with an uncertainty of ±0.3 ‰ (2σ) on $\delta^{18}O$ ratios corresponding to an uncertainty of ±10 °C ($2\sigma_{ind}$) on individual temperature estimates (Li et al., 2022). The uncertainty on the mean value of the dataset ($\sigma_{mean}$) is calculated as the quadratic sum of the individual uncertainty ($\sigma_{ind}$) and the standard deviation of the population ($s$):

$$\sigma_{mean} = \sqrt{\sigma_{ind}{}^2 + s^2}$$

This approach ensures that both the intrinsic measurement error and the population variability are accounted for in the final uncertainty. All uncertainties are reported at a 2σ confidence level.

### III.A2.2. Uncertainty propagation methodology for $\delta^{18}O_{fluid}$ calculations

The uncertainty on $\delta^{18}O_{fluid}$ ratios is determined by propagating the uncertainties for mineral (quartz or cassiterite) oxygen isotope measurements and equilibrium temperature estimates. The $\delta^{18}O_{fluid}$ values are calculated using the following equation:

$$\delta^{18}O_{fluid} = \delta^{18}O_{mineral} - 1000 \ln \alpha$$

where 1000 ln α is a function of temperature (T). The total uncertainty ($\sigma_{fluid}$) can be propagated as follows:

$$\sigma_{fluid} = \sqrt{\sigma_{mineral}^2 + \left(\frac{\partial(1000 \ln \alpha)}{\partial T} \times \sigma_T\right)^2}$$

where $\sigma_{mineral}$ is the analytical uncertainty on $\delta^{18}O_{mineral}$, $\sigma_T$ is the uncertainty in the temperature estimate (T), and $\frac{\partial(1000 \ln \alpha)}{\partial T}$ represents the sensitivity of 1000 ln α to temperature. Considering a typical fractionation equation, such as:

$$1000 \ln \alpha = A\frac{1}{T^2} + B\frac{1}{T} + C$$

where A, B, and C are constants specific to the mineral-fluid oxygen isotope fractionation, the sensitivity of 1000 ln α to temperature is:

$$\frac{\partial(1000 \ln \alpha)}{\partial T} = -2A\frac{1}{T^3} - B\frac{1}{T^2}$$

This analytical propagation of uncertainty is a simplified approximation of the Monte Carlo approach used by Li et al. (2022). While this method is widely applied to linear systems or cases where uncertainties are small and symmetric, it might underestimate uncertainties in more complex, nonlinear equations like 1000 ln α. In the context of the quartz-cassiterite greisen from the Beauvoir PRMG, this uncertainty propagation is considered reasonable, as the sensitivity of 1000 ln α to temperature is limited within the temperatures range of *ca.* 460–670 °C for both quartz and cassiterite (Vho et al., 2019; Li et al., 2022).

### III.A3. Petrographic and microthermometric characterisation of fluid inclusions hosted in magmatic quartz from the Beauvoir PRMG, with associated LA-ICP-MS data

https://drive.google.com/drive/folders/1fg_2RtGm7P91CLvZXN6f5PnbZakrMfTw?usp=sharing

(Appendix III.A3)

### III.A4. Trace elements in magmatic quartz from the Beauvoir PRMG and oxygen isotope composition of magmatic quartz, magmatic cassiterite, and greisen-related quartz and cassiterite

https://drive.google.com/drive/folders/1fg_2RtGm7P91CLvZXN6f5PnbZakrMfTw?usp=sharing

(Appendix III.A4)